

MASARYK UNIVERSITY
FACULTY OF SCIENCE
DEPARTMENT OF CHEMISTRY

LASER ABLATION AS A POWERFUL
TOOL FOR THE DETERMINATION OF
ELEMENTAL DISTRIBUTION

HABILITATION THESIS

TOMÁŠ VACULOVÍČ

BRNO 2020

THE BRAIN IS LIKE A MUSCLE. WHEN IT IS IN USE WE FEEL
VERY GOOD. UNDERSTANDING IS JOYOUS.

CARL SAGAN

ABSTRACT

This habilitation thesis is a commented selection of my 16 peer-review papers that are focused on the distribution of elements by laser ablation-based methods. The ability of laser ablation with mass spectrometry of inductively coupled plasma (LA-ICP-MS) for elemental distribution is shown on metallic, geological, and biological materials. In the first part, the development of LA-ICP-MS for identification and description of corrosion processes on Ni-based alloys caused by LiF-NaF mixture is described. For geology, the evolution of the lateral distribution is monitored from the single spot analysis in specific zones in individual grains to the imaging of entire grains. The final part is focused on the distribution in biological tissues. As the distribution of elements by LA-ICP-MS has become a routine analysis, our efforts have forwarded to the imaging of specific biomolecules. For these purposes, we developed two ways for molecular imaging – labelling of antibodies by Au nanoparticles and utilisation of molecularly imprinted polymers (MIPs).

ACKNOWLEDGEMENT

First, I would like to express my gratitude to my wife Markéta for her help and support, without which, none of this would be possible.

During my development from student to scientist, I was lucky enough to have the opportunity to cooperate with many brilliant scientists and co-workers. Above all I else would like to name prof. Viktor Kanický, and prof. Vítězslav Otruba.

Thanks also go to my great colleagues, former and current students. Namely, Markéta Holá, Karel Novotný, Aleš Hrdlička, Miša Tvrdoňová, Lucka Šimoníková and Verča Dillingerová.

Last but not least, my thanks go to my family and friends.

ABBREVIATIONS

| | |
|-----------|--|
| Ab | Antibody |
| CE-LIF | Capillary Electrophoresis Laser-Induced Fluorescence |
| DCC | 2,3-dicarboxycellulose |
| EPMA | Electron Probe Micro Analysis |
| ETV | Electro-Thermal Vaporizer |
| ICP-OES | Inductively Coupled Plasma Optical Emission Spectrometry |
| IR | InfraRed |
| IS | Internal Standard |
| LA-ICP-MS | Laser Ablation with Inductively Coupled Plasma Mass Spectrometry |
| LASER | Light Amplification by Stimulated Emission of Radiation |
| LIP | Laser-Induced Plasma |
| LOD | Limit Of Detection |
| MALDI-MS | Matrix-Assisted Laser Desorption/Ionization Mass Spectrometry |
| MASER | Microwave Amplification by Stimulated Emission of Radiation |
| MeCAT | Metal-Coded Affinity Tagging |
| MeLiM | Melanoma-bearing-Libechev-Minipig |
| MFS | Molten Fluoride Salts |
| MIP | Molecularly Imprinted Polymer |
| MT | Metallothionein |
| Nd:YAG | Neodymium-doped Yttrium-Aluminum-Garnet |
| NIP | Non-Imprinted Polymer |
| NP | NanoParticle |
| PSD | Particle Size Distribution |
| OES | Optical Emission Spectrometry |
| QD | Quantum Dots |
| REE | Rare Earth Elements |
| SSIM | Structural Similarity Index Metric |
| TIMS | Thermal-Ionoization Mass Spectrometry |
| UV | UltraViolet |
| XRF | X-Ray Fluorescence |

CONTENT

| | | |
|----------|--|-----------|
| 1 | Introduction | 7 |
| 1.1 | Structure of the thesis | 7 |
| 1.2 | My contribution to the study of elemental distribution | 8 |
| 2 | Laser ablation | 10 |
| 2.1 | From bulk to the distribution | 10 |
| 2.1.1 | Development of lasers | 11 |
| 2.2 | Suppression of influence of different ablation rate | 14 |
| 2.2.1 | Internal standardisation | 15 |
| 2.2.2 | Normalisation on the total sum of oxides | 16 |
| 2.2.3 | Normalisation on the sum of ion intensities | 17 |
| 2.2.4 | Total mass removal..... | 17 |
| 3 | LA-ICP-MS for lateral distribution | 18 |
| 3.1 | Imaging of corrosion of metallic samples | 20 |
| 3.2 | Elemental imaging in geology | 21 |
| 3.3 | Lateral distribution for bio-applications..... | 23 |
| 3.3.1 | Elemental imaging..... | 23 |
| 3.3.2 | Molecular imaging..... | 27 |
| 4 | Conclusion and Outlook..... | 30 |
| 5 | Literature..... | 32 |
| 6 | Articles..... | 36 |
| 6.1 | Article 1 | 37 |
| 6.2 | Article 2 | 48 |
| 6.3 | Article 3 | 55 |
| 6.4 | Article 4..... | 62 |
| 6.5 | Article 5 | 68 |
| 6.6 | Article 6..... | 81 |
| 6.7 | Article 7..... | 99 |
| 6.8 | Article 8..... | 115 |
| 6.9 | Article 9..... | 124 |
| 6.10 | Article 10..... | 149 |
| 6.11 | Article 11 | 157 |
| 6.12 | Article 12..... | 171 |
| 6.13 | Article 13..... | 178 |
| 6.14 | Article 14..... | 191 |
| 6.15 | Article 15..... | 198 |
| 6.16 | Article 16..... | 208 |

1 INTRODUCTION

The pioneering works devoted to the connection of laser ablation to ICP date back to the 80s of the 20th century. The first connection of laser sampling with ICP published by Thompson et al. in 1981^(*) was carried out with optical detection (ICP-OES). The published results were very promising with both the absolute limit of detection and the precision comparable to solution analysis. When Gray first published the connection of laser sampling with ICP-MS^(†) several problems were found; Gray himself pointed to an inappropriate ICP-MS construction for linking with laser ablation (LA) and the amount of ablated material was so high that it caused its deposition in a sampler cone. On the other hand, the limit of detection lower than 1 mg/kg demonstrated the potential of this technique in the future. At that time, ruby lasers were used for ablation, creating large craters with a diameter of hundreds of μm and producing a huge amount of ablated material (200 $\mu\text{g}/\text{pulse}$). The LA-ICP was introduced as a possible quantitative method for analysis of solid samples without dissolution. As the development of lasers continued, ablation craters became smaller and detection limits at OES became inadequate. Hence, ICPs with mass detection were able to respond to a decreasing amount of ablated material. As the information about total content of elements in the sample may be insufficient for some applications, lateral distribution of elements in the sample is of interest. Therefore, since the beginning of the 21st century, the investigation of the spatial distribution of elements in all possible types of samples has been the focus of LA-ICP-MS.

This work aims to show my contribution to the study of elemental distribution by LA-ICP-MS in various types of materials from metallic samples through geological to biological.

1.1 STRUCTURE OF THE THESIS

This thesis presents collection of 16 peer-reviewed papers published between 2007 and 2020, related to the determination of elemental distribution. As the elemental distribution is analysed in metallic materials¹⁻⁴, geological materials⁵⁻⁹, and bio-applications¹⁰⁻¹⁶ in the form of lateral scans or elemental maps, there are two ways to sort the publications: either by type of distribution – from lateral scans to the elemental mapping, or by type of material. Finally, I decided to sort them by type of analysed material. For better orientation within the cited papers, these works are listed as the first 16 papers and are highlighted bold in the text.

* Thompson, M.; Goulter, J. E.; Sieper, F. *Analyst* **1981**, *106*, 32-39.

† Gray, A. L. *Analyst* **1985**, *110*, 551-556.

1.2 MY CONTRIBUTION TO THE STUDY OF ELEMENTAL DISTRIBUTION

Currently, I have published 74 papers, including 60 journal articles and 14 conference proceedings. I have chosen 16 research articles related to elemental distribution as a part of my thesis. My contribution to these articles is summarised in the following tables with special attention to the experimental work, supervision of students, manuscript preparation and research direction.

1) Novotny, K.; Vaculovic, T.; Galiova, M.; Otruba, V.; Kanicky, V.; Kaiser, J.; Liska, M.; Samek, O.; Malina, R.; Palenikova, K. Applied Surface Science 2007, 253, 3834-3842 (IF=5.155)

| Experimental work (%) | Supervision (%) | Manuscript (%) | Research direction (%) |
|-----------------------|-----------------|----------------|------------------------|
| 20 | 30 | 20 | 10 |

2) Vaculovic, T.; Sulovsky, P.; Machat, J.; Otruba, V.; Matal, O.; Simo, T.; Latkoczy, C.; Gunther, D.; Kanicky, V. Journal of Analytical Atomic Spectrometry 2009, 24, 649-654 (IF=3.646)

| Experimental work (%) | Supervision (%) | Manuscript (%) | Research direction (%) |
|-----------------------|-----------------|----------------|------------------------|
| 20 | - | 80 | - |

3) Vaculovic, T.; Warchilova, T.; Simo, T.; Matal, O.; Otruba, V.; Mikuska, P.; Kanicky, V. Journal of Analytical Atomic Spectrometry 2012, 27, 1321-1326 (IF=3.646)

| Experimental work (%) | Supervision (%) | Manuscript (%) | Research direction (%) |
|-----------------------|-----------------|----------------|------------------------|
| 30 | 50 | 70 | 30 |

4) Warchilova, T.; Dillingerova, V.; Skoda, R.; Simo, T.; Matal, O.; Vaculovic, T.; Kanicky, V. Spectrochimica Acta Part B-Atomic Spectroscopy 2018, 148, 113-117 (IF=3.101)

| Experimental work (%) | Supervision (%) | Manuscript (%) | Research direction (%) |
|-----------------------|-----------------|----------------|------------------------|
| 10 | 100 | 30 | 80 |

5) Novak, M.; Gadas, P.; Filip, J.; Vaculovic, T.; Prikryl, J.; Fojt, B. Mineralogy and Petrology 2011, 102, 3-14 (IF=1.573)

| Experimental work (%) | Supervision (%) | Manuscript (%) | Research direction (%) |
|-----------------------|-----------------|----------------|------------------------|
| 30 | - | 20 | - |

6) Bacik, P.; Uher, P.; Ertl, A.; Jonsson, E.; Nysten, P.; Kanicky, V.; Vaculovic, T. Canadian Mineralogist 2012, 50, 825-841 (IF=1.398)

| Experimental work (%) | Supervision (%) | Manuscript (%) | Research direction (%) |
|-----------------------|-----------------|----------------|------------------------|
| 30 | - | 20 | - |

7) Breiter, K.; Gardenova, N.; Vaculovic, T.; Kanicky, V. Mineralogical Magazine 2013, 77, 403-417 (IF=2.21)

| Experimental work (%) | Supervision (%) | Manuscript (%) | Research direction (%) |
|-----------------------|-----------------|----------------|------------------------|
| 30 | 50 | 20 | 30 |

8) Vaculovic, T.; Breiter, K.; Korbelova, Z.; Venclova, N.; Tomkova, K.; Jonasova, S.; Kanicky, V. *Microchemical Journal* 2017, 133, 200-207 (IF=3.206)

| Experimental work (%) | Supervision (%) | Manuscript (%) | Research direction (%) |
|-----------------------|-----------------|----------------|------------------------|
| 60 | - | 90 | 90 |

9) Petrik, I.; Janák, M.; Klonowska, I.; Majka, J.; Froitzheim, N.; Yoshida, K.; Sasinková, V.; Konečný, P.; Vaculovič, T. *Journal of Petrology* 2020 (IF=3.38)

| Experimental work (%) | Supervision (%) | Manuscript (%) | Research direction (%) |
|-----------------------|-----------------|----------------|------------------------|
| 30 | - | 20 | 10 |

10) Vaculovic, T.; Warchilova, T.; Cadkova, Z.; Szakova, J.; Tlustos, P.; Otruba, V.; Kanicky, V. *Applied Surface Science* 2015, 351, 296-302 (IF=5.155)

| Experimental work (%) | Supervision (%) | Manuscript (%) | Research direction (%) |
|-----------------------|-----------------|----------------|------------------------|
| 20 | 60 | 80 | 40 |

11) Anyz, J.; Vyslouzilova, L.; Vaculovic, T.; Tvrdonova, M.; Kanicky, V.; Haase, H.; Horak, V.; Stepankova, O.; Heger, Z.; Adam, V. *Scientific Reports* 2017, 7 (IF=4.011)

| Experimental work (%) | Supervision (%) | Manuscript (%) | Research direction (%) |
|-----------------------|-----------------|----------------|------------------------|
| 15 | 40 | 30 | 30 |

12) Tvrdonova, M.; Vlcnovska, M.; Vanickova, L. P.; Kanicky, V.; Adam, V.; Ascher, L.; Jakubowski, N.; Vaculovicova, M.; Vaculovic, T. *Analytical and Bioanalytical Chemistry* 2019, 411, 559-564 (IF=3.286)

| Experimental work (%) | Supervision (%) | Manuscript (%) | Research direction (%) |
|-----------------------|-----------------|----------------|------------------------|
| 10 | 30 | 50 | 50 |

13) Munster, L.; Fojtu, M.; Capakova, Z.; Vaculovic, T.; Tvrdonova, M.; Kuritka, I.; Masarik, M.; Vicha, J. *Biomacromolecules* 2019, 20, 1623-1634 (IF=5.667)

| Experimental work (%) | Supervision (%) | Manuscript (%) | Research direction (%) |
|-----------------------|-----------------|----------------|------------------------|
| 20 | 40 | 20 | 15 |

14) Vaneckova, T.; Vanickova, L.; Tvrdonova, M.; Pomorski, A.; Krezel, A.; Vaculovic, T.; Kanicky, V.; Vaculovicova, M.; Adam, V. *Talanta* 2019, 198, 224-229 (IF=4.916)

| Experimental work (%) | Supervision (%) | Manuscript (%) | Research direction (%) |
|-----------------------|-----------------|----------------|------------------------|
| 20 | 40 | 25 | 30 |

15) Vaneckova, T.; Bezdekova, J.; Tvrdonova, M.; Vlcnovska, M.; Novotna, V.; Neuman, J.; Stossova, A.; Kanicky, V.; Adam, V.; Vaculovicova, M.; Vaculovic, T. *Scientific Reports* 2019, 9 (IF=4.011)

| Experimental work (%) | Supervision (%) | Manuscript (%) | Research direction (%) |
|-----------------------|-----------------|----------------|------------------------|
| 15 | 40 | 15 | 30 |

16) Dumkova, J.; Smutna, T.; Vrlikova, L.; Kotasova, H.; Docekal, B.; Capka, L.; Tvrdonova, M.; Jakesova, V.; Pelkova, V.; Krumal, K.; Coufalik, P.; Mikuska, P.; Vecera, Z.; Vaculovic, T.; Husakova, Z.; Kanicky, V.; Hampl, A.; Buchtova, M. *ACS nano* 2020, 14, 3096-3120. (IF=13.903)

| Experimental work (%) | Supervision (%) | Manuscript (%) | Research direction (%) |
|-----------------------|-----------------|----------------|------------------------|
| 10 | 25 | 10 | 25 |

2 LASER ABLATION

The term laser ablation includes a set of events that occur when a laser beam interacts with the surface of a sample. In time sequence, it is the absorption of laser radiation, the transmission of the radiant energy of laser radiation, the removal of atoms, ions and molecular fragments from the surface of the sample and their immediate conversion into a form of dry aerosol. At the same time, the pressure and temperature increases in the surrounding area of the interaction site. This interaction results in a shock wave and a microplasma formation. The carrier of analytical information is thus not only a laser-generated aerosol but also laser-induced plasma (LIP). There are two ways to remove material from the sample surface - thermal (selective evaporation) and non-thermal (ablation). Selective evaporation occurs when the power density is less than 10^6 W.cm^{-2} , or when the laser pulse width is higher than microseconds. Ablation is observed when the power density is larger than 10^9 W.cm^{-2} and the laser pulse width is in the order of ns and less. Selective evaporation is manifested by enrichment of the vapour phase with slightly volatile elements from the surface of the sample. Thus the composition of the aerosol is different from the solid phase composition, causing a systematic error in the result. In the case of ablation, the heating of the solid material is so intense that the evaporation phase is suppressed and the composition of the ablated material is ideally the same as of the solid phase.

Under optimal conditions, laser ablation can be used not only for quantitative analysis but also for the investigation of the lateral distribution of elements - imaging as well as investigation of depth distribution - depth profiling.

2.1 FROM BULK TO THE DISTRIBUTION

The ablated material generated by the explosive interaction of focused laser radiation with the surface of a specimen is carried by the carrier gas (most commonly helium) into the plasma torch of the ICP spectrometer where the atomisation of material occurs. The resulting atoms are excited and ionised. They then enter the evacuated part of the ICP-MS where they are separated in the analyser by their mass/charge ratio (m/z).

LA-ICP-MS is currently a well-established method whose first use dates back to 1985 when Gray¹⁷ introduced a combination of laser ablation with ICP-MS for rock samples that were compressed into tablets. For this purpose, a ruby laser emitting radiation with

a wavelength of 694 nm was used. Since then, the use of LA-ICP has been expanded, and currently, 7107 original works with the topic “LA-ICP” (excluding reviews, conference abstracts, etc.) are available on the Web of Science.

The first publications dealing with the use of laser ablation as a method of sampling for ICP-MS were performed using metallic materials^{18,19} and geological samples that were analysed in the form of compressed tablets^{17,20,21}. The first attempts at semiquantitative analysis were based on the determination of the relative response of the individual isotopes^{19,20}, which were determined experimentally. The relative response depends on the relative representation of the observed isotope in nature, the volatility of the element and its ionisation energy. However, for quantification, this method was insufficient and in 1991 Vanheuzen devised a matrix-matched quantification (matrix-matched standards). This method was based on an approach where the analysed material was mixed with a binder (graphite and cellulose) and pressed into a tablet²² or blended with flux and melted in the form of glass beads²³. Utilisation of both matrix matching methods was affected by considerable problems with memory effects that complicated quantification: even in the case of tablets, quantification was not possible at all. Polyatomic interference was the second major problem complicating the quantification that was revealed in those works^{22,23}. Despite these problems, the use of matrix-matched calibration standards has proved successful and has been used to date with various modifications correcting for systematic errors of determination (e.g. different ablation rates).

2.1.1 DEVELOPMENT OF LASERS

The advances in laser ablation as a sampling technique for ICP-MS are closely connected with the progress of the construction of lasers. The theoretical basis of the laser was laid in 1917 when Einstein postulated the term stimulated emission in his publication "Zur Quantentheorie der Strahlung^(‡)." The first device using stimulated emissions was described in 1952 by Basow and Prokhorov, and built by Townes in the same year. It was a predecessor to the laser - the MASER - Microwave Amplification by Stimulated Emission of Radiation²⁴. The first LASER (Light Amplification by Stimulated Emission of Radiation)²⁵ was constructed in 1960 by T.H. Maiman. It was a ruby laser, whose active environment is corundum with the addition of Cr³⁺. This laser belongs to a group of three-level lasers where the efficiency of radiation generation is low and considerable energy is needed for excitation. For laser ablation,

[‡] Einstein A., Phys.Z., **1917**, 121-128

the ruby laser was used mainly in pioneering work dealing with the combination of laser ablation with ICP spectrometers, both emission²⁶⁻²⁸ and mass^{17,20}. Due to the lower excitation powers for the generation of laser radiation, Nd:YAG (neodymium-doped yttrium-aluminium-garnet) lasers gradually began to emerge. The vast majority of commercial ablation systems are currently working with Nd:YAG lasers, although their development has been delayed by a few years compared to the ruby laser. The first Nd:YAG laser was built in 1964²⁹ and the first use for laser ablation in combination with ICP was published in 1985³⁰. Another reason for replacing ruby lasers was the need for shorter laser radiation wavelengths. Indeed, the effect of fractionation in laser ablation decreases with shorter wavelength (see Fractionation). Consequently, excimer lasers are currently used which, depending on the charge, can emit laser radiation shorter than 200 nm (Table 1). The first excimer laser coupled to the ICP spectrometer was a XeCl laser³¹.

At present, in ablation systems, we can encounter Nd: YAG lasers emitting radiation at the wavelength of 266, 213, and 193 nm with excimer lasers of different fill types; ArF (193 nm), XeCl (308 nm), KrF (248 nm) and F₂ (157 nm). Jeffries et al. observed that by using shorter laser radiation (UV) wavelengths when interacting with glass material (NIST610) fractionation decreases significantly compared to IR laser radiation^{32,33}. This smaller fractionation observed at UV ablation was the reason that excimer lasers (XeCl³³, ArF³⁴, KrF³⁵, and F₂³⁶) became increasingly popular. The indisputable advantage of excimer lasers is the beam profile. In this case, it is "flat-top," which means that the laser radiation energy is the same at every point of the beam profile. The use of a flat-top profile results in the formation of a crater, which has not only a flat bottom but also vertical walls. This shape differs significantly from craters created by solid-state lasers (e.g. Nd:YAG), which have a Gaussian profile - the energy of the laser radiation is highest in the centre of the beam and decreases towards its edges. Thus the obtained crater has oblique walls and the diameter of the crater bottom is smaller than the diameter at the sample surface. Mank et al. described the effect of the aspect ratio - the ratio of crater depth to crater diameter - on the fractionation and found that if this ratio is greater than 6, the signal is reduced by up to 50%³⁷. This implies that if a significant decrease in the signal intensity is observed during a single point ablation, the laser beam diameter has to be reduced.

In addition to adjusting the wavelength of laser radiation, the duration of the laser pulse is also optimised. In the first works on LA-ICP-MS, lasers with pulse lengths in nanoseconds (ns-lasers) were used²⁶. Although the development of lasers moves towards shorter pulse lengths (picosecond-³⁸ and femtosecond lasers³⁹), ns-lasers are still commonly used. If the energy of the laser pulse is emitted within a shorter time (fs), the selective evaporation of the

elements is suppressed. When higher laser pulse energies are used, selective evaporation is suppressed in both ps and ns lasers⁴⁰. Similar conclusions came from Russo et al. even when comparing ns and fs lasers; they found that lasers working in the UV region reduce fractionation in the same way as lasers working in the IR region³⁹. Currently, the development of fs lasers is moving towards the UV region of radiation because this type of laser (fs-UV - 266 nm) provides the lowest fractionation phenomena along with more accurate results compared to fs-IR or ns-UV lasers⁴¹.

Conditions during laser ablation significantly affect the particle size distribution (PSD) generated by ablation. Ideally, particles generated during laser ablation should be as small as possible (in tens of nm). Larger particles entering the ICP source are not entirely vaporised and cannot be completely ionized⁴² which results in a change in the response of the individual analytes being measured⁴³. The changing PSD of the aerosol affects the intensity of the ICP-MS signal, which was demonstrated by inserting an electrothermal vaporiser (ETV) between the ablation system and the ICP source⁴⁴.

The conditions influencing the course of laser ablation include the choice of gas in which the ablation occurs. This effect on the ICP-MS signal was confirmed by Horn et al.⁴⁵, when comparing the effects of noble gases (Ar, He, Ne) used in LA. It was found that ambient gas affects PSD⁴⁵, the amount of material deposited at the edges of the ablation crater^{1,45} and the efficiency of particle transport to ICP. The fact that the choice of ambient gas affects the ablation processes was also determined by the work of Novotny when the influence of air, He and Ar was studied. It was found that there is also a significant influence on the course of emission of microplasma radiation resulting from ablation in dependence on the gas used¹. The crucial problem of LA-ICP-MS, including imaging, is a different ablation rate, but there are some possibilities on how to correct it (see chapter Suppression of influence of different ablation rate).

2.2 SUPPRESSION OF INFLUENCE OF DIFFERENT ABLATION RATE

When laser radiation interacts with different sample matrices, unequal amounts of material are released even with the same laser ablation parameters (radiation wavelength, radiation frequency, beam diameter, radiant energy density, etc.). The different ablation rate is caused mainly due to the different absorption of laser radiation of a given wavelength by a different matrix (see Table 1).

| material | absorption of radiation of various wavelength (%) | | |
|---------------------------------|---|--------|---------|
| | 200 nm | 500 nm | 1000 nm |
| Fused quartz ^a | 8 | 5 | 5 |
| MgF ₂ ^a | 12 | 4 | 4 |
| Sapphire ^a | 35 | 18 | 18 |
| CaF ₂ ^b | 10 | 8 | 8 |
| Si ^c | 15 | 8 | 55 |
| ZnSe ^d | 89 | 95 | 80 |
| Bor-silicate glass ^a | 100 | 8 | 7 |

Table 1: Overview of radiation absorption of different wavelengths by different materials

^a C. Friedrich, Precision Micromanufacturing Processes Applied to Miniaturization Technologies, Michigan Technology University, 1998.

^b http://www.thorlabs.com/NewGroupPage9.cfm?ObjectGroup_ID=3978

^c http://www.thorlabs.com/NewGroupPage9.cfm?ObjectGroup_ID=3979

^d http://www.thorlabs.com/newgroupage9.cfm?objectgroup_id=3981

This effect is the more significant the longer the wavelength of the laser radiation used, and as such, the use of shorter laser radiation wavelengths (213, 193 nm) is more appropriate. Fluctuations in the energy density of the laser radiation contribute to the amount of released material. Both of these phenomena result in a systematic error of the result. Therefore, certain ways are available to suppress it. These corrections may be as follows:

- a) internal standardisation⁴⁶
- b) normalisation on the total sum of oxides^{2,47}
- c) normalisation on the sum of ion intensities⁴⁸
- d) total mass removal¹¹

Each of the listed procedures has its pros and cons, which will be discussed in the following text.

2.2.1 INTERNAL STANDARDISATION

The most common method for compensation of different ablation rates is the utilisation of internal standard (IS) and it is necessary to know the content of the internal standard in the sample to be analysed:

$$w(X)_{corr}^i(\%) = w(X)^i \times \frac{w^{IS}}{w_{EPMA}^{IS}}$$

Where, $w(X)_{corr}^i$ is the content of i -element after compensation of ablation rate, $w(X)^i$ is the content of i -element obtained by LA-ICP-MS, w^{IS} is the content of internal standard obtained by LA-ICP-MS, and w_{EPMA}^{IS} is the content of the internal standard obtained by an independent method.

Most commonly, the content of IS is detected by an independent method (e.g. EPMA - Electron Probe Micro Analysis, XRF - X-Ray Fluorescence, etc.). There are several rules for choosing a suitable IS that should be followed: 1) An element of a high content (one of the matrix elements) should be chosen as the IS to minimise the relative error of determination due to the inaccuracy of the independent method. 2) This element must be detectable by ICP-MS. Therefore, for example, the use of oxygen as an IS element for the analysis of silicates or fluorine in the analysis of fluorites is eliminated, even though its content in the samples is the highest. 3) The distribution of the IS in the sample should be homogeneous to suppress possible errors caused by different contents of the IS at different locations of the sample. When a heterogeneous sample is analysed, it is possible to circumvent this condition by performing the LA-ICP-MS analysis at the same site of the sample as the independent method. This normalisation method was first used in the determination of impurities REE in geological material fused to a glass bead, with the IS being strontium²³. Its use leads to a significant improvement in the precision of the assay. The disadvantage of this method of normalisation is the necessity to use another, very often expensive method, such as EPMA. Nevertheless, this method of normalisation is currently one of the most widely used and has many applications, especially in the analysis of geological samples.

From the view of elemental imaging, this procedure is suitable for imaging of minerals or metallic materials without corrosion.

2.2.2 NORMALISATION ON THE TOTAL SUM OF OXIDES

This normalisation finds application, especially in the analysis of geological samples. The main reasons for applying normalisation to the sum of contents are two: eliminating the need to use a complementary method (EPMA, XRF, etc.) or the inability to use IS. As in the case of internal standardisation, the first step is to use calibration standards, followed by the recalculation of content into the form of oxides. Then the contents are summed and the individual contents are multiplied by factor “100/sum of oxide content”:

$$w(XO)_{corr}^i(\%) = w(XO)^i \times \frac{100}{\sum w(XO)^i}$$

Where $w(XO)_{corr}^i$ is the content of i -element in the form of oxide after compensation of ablation rate, $w(XO)^i$ is the content of i -element in the form of oxide obtained by LA-ICP-MS, 100 means 100 %, and $\sum w(XO)^i$ is the sum of all elements in the form of oxide,

Three requirements should be met for the appropriate application of this method; a) to have information about the matrix composition of the sample, b) ensure the matrix does not contain elements that are not determinable by ICP-MS and can replace each other additionally (typically hydroxy- groups replacing phosphate groups in hydroxyapatites). If these two requirements are met, then the third requirement is the measurement of all matrix and minor elements contained in the sample. Otherwise, there is a systematic error, and the detected contents of the measured elements are higher than the actual. If these requirements are met, then the results obtained by this normalisation are the same as those obtained using the IS⁸.

It should be noted that the requirement regarding non-determinable elements can be circumvented, as in the case of elemental imaging in a mica sample⁸, as follow:

$$w(XO)_{corr} = w(XO) \times \frac{(100 - Y)}{\sum w(XO)}$$

Where Y is the total content of non-determinable elements by LA-ICP-MS (e.g. OH⁻, F⁻) obtained by EPMA.

Both the above-mentioned methods for suppression of different ablation rates are used mainly in combination with external calibration.

2.2.3 NORMALISATION ON THE SUM OF ION INTENSITIES

This approach for the compensation of different ablation rates is suitable for a simple matrix with a well-defined composition as are e.g. alloys⁴⁹, and metallic samples²⁻⁴ (corroded and intact surface). It is based on the measurement of isotopes of all major and minor elements and recalculation of their measured intensities according to their isotope abundance:

$$I_{element1} = \frac{I_{isotope1}}{a_{isotope1}}$$
$$w_{element1}(\%) = \frac{I_{element1}}{\sum I_{element}} \times 100$$

Where $I_{isotope1}$ is the measured intensity of isotope, $a_{isotope1}$ is the abundance of the isotope, $I_{element1}$ is elemental intensity, and $w_{element1}$ is the content of the element.

The advantage is that it is not necessary to use external calibration. On the other hand, this approach works well when the degree of ionisation is close to 100 %. This means that the ionisation energy of the element should be lower than 8 eV – at this ionisation energy, the ionisation efficiency is about 95 %⁵⁰.

2.2.4 TOTAL MASS REMOVAL

The final method for compensating for the different ablation rate is completely different from the previous ones. This way is based on the sample preparation and it is mainly suitable for biosamples^{11,13}. Soft tissue sections are cut with a thickness that allows laser radiation to penetrate the whole thickness of the cut and to reach the substrate (e.g. glass slide). If the substrate is reached in every spot of the tissue section, it means that the sample has been removed completely and the influence of the different ablation rate was suppressed successfully. To verify the total mass removal was reached, it is useful to monitor some isotope released from the substrate (mostly Si from glass substrate¹¹).

3 LA-ICP-MS FOR LATERAL DISTRIBUTION

As mentioned above, the development of lasers was directed towards shorter wavelength (from 1064 to 193 nm for Nd:YAG and ArF laser, respectively) and the related creation of smaller craters. The reduction of the crater size offered the possibility of a new type of laser ablation-based analysis. These can be divided into two groups depending on the amount of ablated material (spot size): a) bulk analysis; and b) spatially resolved analysis. The second one is a very attractive method that allows the gathering of information on the content of the element as well as its distribution within the analysed sample. The distribution information can be beneficial in detecting changes in the development of rocks and crystals, the study of corrosion changes in metallic materials and, last but not least, in studying changes in different biological materials, as shown below. The beginnings of LA-ICP-MS were mainly concerned with geological samples. Therefore, it is not surprising that the first study on the lateral distribution of the elements was carried out on a geological sample. In 1992, Imai showed the possibility of determination of distribution on the sample of stalactite where they reported concentration changes of 25 elements (from Mg to U)⁵¹. Shortly after that, Chenery and Cook performed a lateral scan over the monazite grain and compared the LA-ICP-MS results from the individual zones to the EPMA results⁵². Lateral scanning was performed as a profile of individual points whose distance was significantly larger than their diameter.

However, in the case of really heterogeneous materials, the use of a single profile is insufficient. There is a plenty of missing information about the elemental content in the rest of the sample. The need to know the information about the content of the elements in the whole sample surface increased and thus a study in which the ablation spots covered a larger portion of the sample surface was of interest. Pioneering work devoted to elemental imaging was done on leaves⁵³. The leaf surface was divided into 70 fields. Each of them was analysed by four ablation spots and the signals from these spots were averaged. However, this procedure is not typical for the elemental imaging as we know it now. Today, a line by line or spot by spot approach is used to cover the whole sample surface. From this point of view, the first elemental imaging work was done on sheep liver by Kindness in 2003⁵⁴. Over the next 16 years, LA-ICP-MS imaging has undergone dramatic developments in map quality (resolution improvement and display), acceleration of imaging, 3D mapping and the ability to map not only elements but also molecules (Fig. 1).

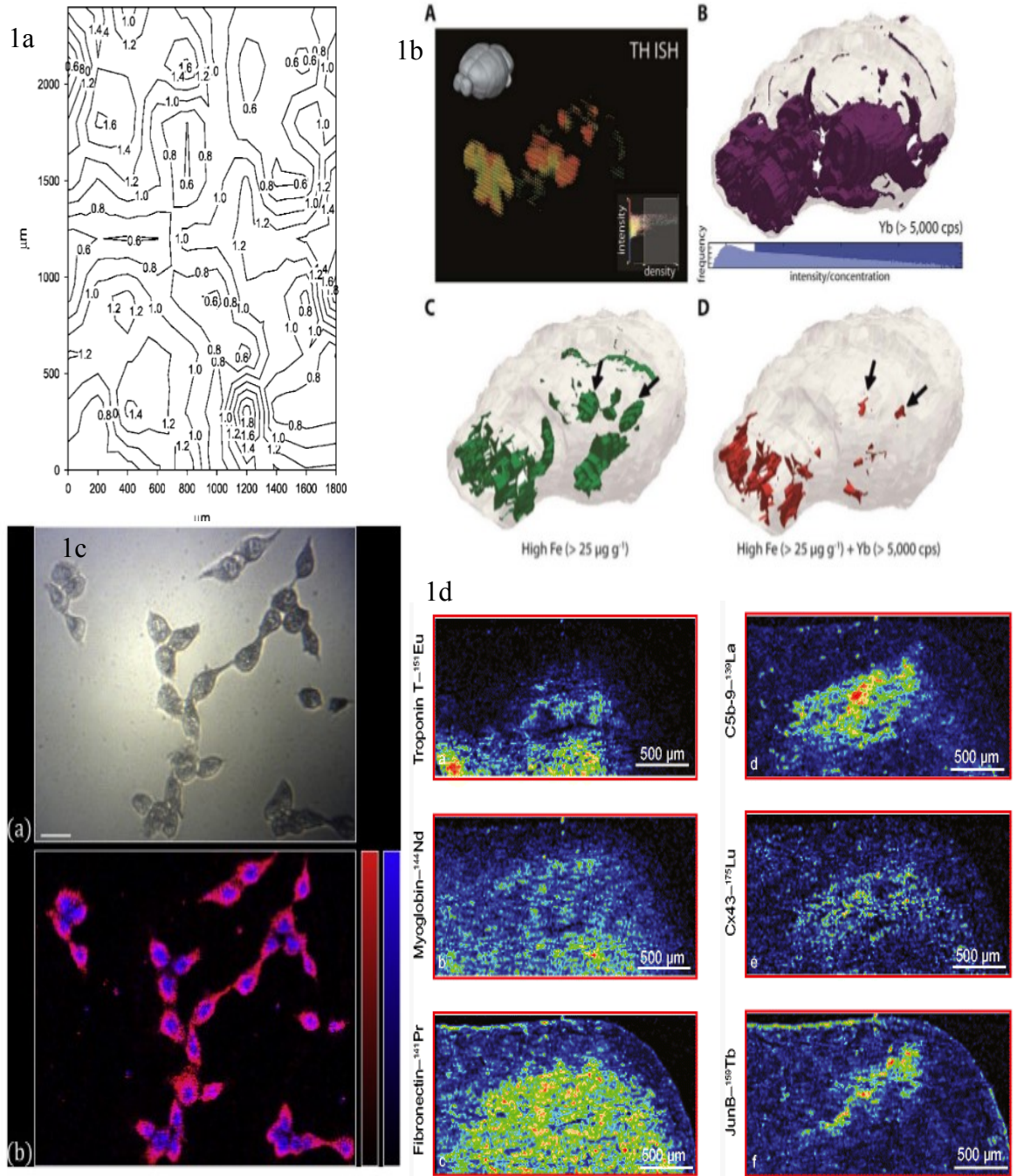


Fig.1: Development of LA-ICP-MS imaging from pioneering work⁵⁴ (a) to 3D model⁵⁵(b), sub-micron resolution⁵⁶ (c) and imaging of proteins⁵⁷ (d).

3.1 IMAGING OF CORROSION OF METALLIC SAMPLES

Determination of lateral distribution in our laboratory started with analysis of metallic samples. This was in relation to the cooperation with the company Energovýzkum Ltd., whose focus was on the development of new materials for a new type of nuclear reactor – Generation IV. As one of them uses molten fluoride salts (MFS) for cooling, the aim of the study was to monitor the progress of corrosion in the presence of MFS.

The MFS represents media of an extremely corrosive and invasive nature, which highly affects the properties of the reactor vessel. The tested candidate materials were treated to 680 °C for up to 1000 h in presence of MFS and the surface was subsequently analysed in order to investigate the corrosion process.

Our first publication was devoted to the corrosion caused by MFS treatment and LA-ICP-MS was used for the determination of the thickness of the corrosion layer². For this purpose, a single line scan across the corrosion layer into the intact material was made and the thickness of the corroded layer was measured according to Na and Li presence in the sample. Inconel A686 and stainless steel 1.4571 were exposed to a LiF-NaF mixture at 680 °C for 380 and 1000 h. In comparison to EPMA, LA-ICP-MS showed a better ability to determine the thickness of the corroded layer, which relates to the inability of EPMA to measure Li and significantly worse LOD for Na. On the other hand, a significantly worse lateral resolution was achieved. Hence, the laser beam diameter was reduced in the following research to improve the lateral resolution.

As the LA-ICP-MS has proved to be suitable for the determination of the thickness of the corroded layer, the method was developed to identify the corrosion damage and elemental changes in structural materials. For this purpose, three candidates of structural materials were tested (nickel, Ni-based alloy, and nickel-coated iron). Both LA-ICP-MS (the thickness of the corroded layer) and ICP-OES (the content of the corrosion products) identified nickel as the most resistant material³. When the more detailed view on the content of the corrosion products was applied, the conspicuous enrichment of Fe was found for nickel-coated iron. This was caused by preferential corrosion of the steel substrate that occurred by MFS penetration through the nickel coating to the iron substrate as seen in Fig. 2.

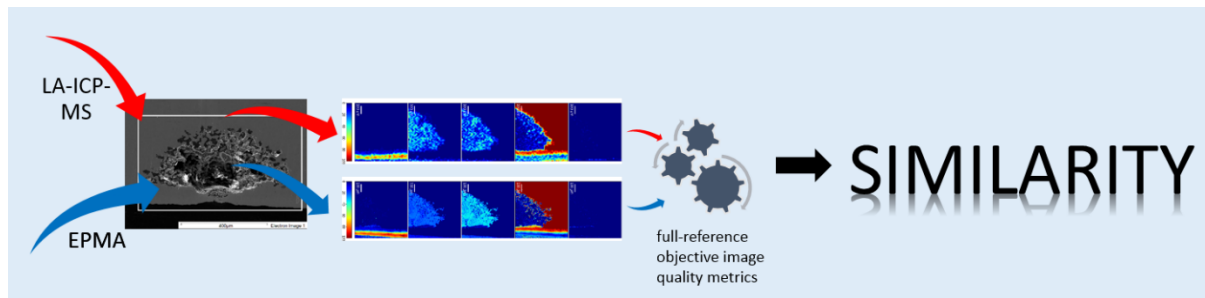


Fig. 2: Similarity of LA-ICP-MS and EPMA elemental maps

Part of the sponge-like corroded area shown in Fig. 2 was subjected to quantitative elemental mapping to demonstrate the penetration of MFS into the exposed specimen and to show relative depletion or enrichment of constituents in the structural material by EPMA and LA-ICP-MS⁴. Full-reference objective image quality metrics were performed for the quantitative comparison of EPMA and LA-ICP-MS elemental maps. These methods compare the original image with distorted images using the structural similarity index metric (SSIM). According to this SSIM, the EPMA and LA-ICP-MS maps are similar (not yet published results).

Our studied system is very specific; however the developed imaging method could be successfully used in other studies, e.g. development of alloys for implants. Most often implants based on Ti-, Ti-Ni- or Zr-alloys and are placed into bones and teeth. Hence, the release of the elements from the developed implants into the tissues could be determined.

3.2 ELEMENTAL IMAGING IN GEOLOGY

The beginning of LA-ICP-MS analysis in geological samples in our laboratory was concerned with single spot analysis without any relation to the distribution. However, since 2011, there have been demands for analysis of specific zones in individual grains (e.g. zoned beryl⁵, or tourmaline crystals⁶) and various minerals (quartz, feldspar, zinnwaldite, topaz)⁷. These requests led to the development of imaging methods for geological samples. As a crucial problem, the quantification of the elemental maps of heterogeneous samples (e.g. zoned muscovite) was identified⁸. When the mineral grain is imaged, the internal standardisation can be successfully used, if the content of the internal standard is uniform. However, our muscovite samples (from Argemela) contained two different zones (Fig. 3a) with non-uniform content of any elements. Hence, the normalisation using IS (chapter 2.2.1) is not applicable in this case. Moreover, the zones differ in the content of species non-determinable by ICP-MS (F, OH, etc.).

For this purpose, the modified normalisation on the total sum of oxides had to be developed. The LA-ICP-MS imaging found the enrichment of Li, Rb, and Mn in the rim, whereas the core is enriched by Fe and Al (Fig. 3). The trueness of LA-ICP-MS results was confirmed by EPMA analysis.

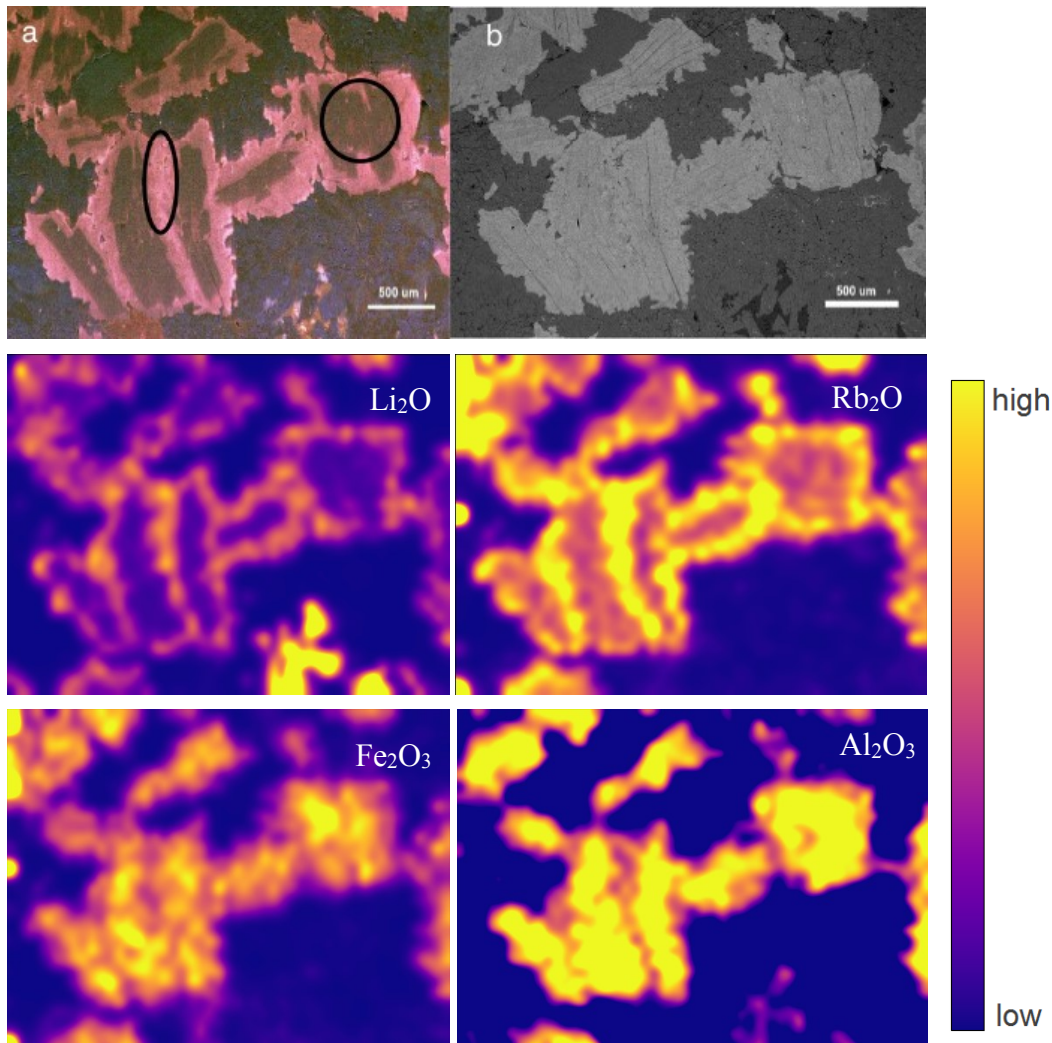


Fig. 3: Cathodo-Luminiscence (CL) (a) and Back Scattered Electron (BSE) (b) images of muscovite grain. The circle and ellipse mark the core and rim, respectively. LA-ICP-MS elemental maps of Li₂O (0-4 %_{m/m}), Rb₂O (0-0.8 %_{m/m}), Fe₂O₃ (0-3 %_{m/m}), and Al₂O₃ (20-50 %_{m/m})

A combination of lateral profiling and imaging was used for the analysis of garnet and monazite grains from Seve Nappe (Sweden)⁹. As the content of SiO₂ is homogeneous across whole grains, the Si could be used as the internal standard. LA-ICP-MS investigation was focused on the REE profile in various parts of the samples. As follows from the obtained results,

the REE profiles vary very strongly depending not only on the minerals (monazite, apatite or garnet) but across the garnet as well.

The advantages of LA-ICP-MS imaging are very similar as at comparison of EPMA and LA-ICP-MS individual spot analysis: speed, very low LODs, and an ability to determine light elements as e.g. Li, and B. This means the determination of the lateral distribution of elements from Li to U in levels of hundreds $\mu\text{g/g}$. As the ICP-MS measures isotopes, the main advantage of LA-ICP-MS imaging lies in the possibility to determine the lateral distribution of isotopic ratios. The most often used isotopic ratios relate to geochronology U-Th-Pb⁵⁸. It is true that Thermal-Ionisation Mass Spectrometry (TIMS) provides much more accurate determination of the age, however there is no possibility of lateral resolution. And this is the gap that can be filled by LA-ICP-MS imaging – dating of highly zoned minerals e.g. zircons.

3.3 LATERAL DISTRIBUTION FOR BIO-APPLICATIONS

In recent years, the interest in the determination of elements in biological samples by LA-ICP-MS has increased significantly. It relates to the fact that many processes in biology are driven by the exchange of elements, which results in a change of their content and lateral distribution. As the content of these elements is, in some cases, very low (at the level of mg/kg) and the changes in distribution are in the level of tens of μm , the LA-ICP-MS is one of the few methods that can be used for this purpose.

3.3.1 ELEMENTAL IMAGING

As the lateral resolution and limit of detection are two crucial parameters in imaging, the influence of the laser ablation parameters such as laser beam diameter, scan speed, and repetition rate were studied¹⁰. Laser repetition rate and laser fluence were investigated in the tapeworm thin-section to attain optimum ablation rate, yielding an appropriately low detection limit which complies with elemental contents in the tissue. The effect of combinations of laser spot size and scan speed on relative broadening (Δw_{rel}) of the image of the ablated pattern (line) was investigated with the aim to quantify the trueness of imaging. The Δw_{rel} is strongly reduced (down to 2%) at low scan speed ($10 \mu\text{m s}^{-1}$) and a laser spot diameter of $10 \mu\text{m}$ but results in an unacceptably long time of mapping (up to 3000 min).

Next, the potential of the LA-ICP-MS imaging was demonstrated in the study that determined Zn and Cu levels in the development of spontaneous regression in melanoma tissue in MeLiM (Melanoma-bearing-Libechev-Minipig) model (Fig. 4A)¹¹. Two cryosections were sliced from tissue (Fig. 4B). A thin slice (8 μm) was used for histological analysis to find uniform spots - red - normally growing melanoma tissue, violet - early spontaneous regression, yellow - late spontaneous regression and green - fibrous tissue. The thicker slice (30 μm) was photographed (Fig. 4C) and analysed by LA-ICP-MS (Fig. 4D). The slices were registered in two steps. Firstly, the elemental maps were registered with slice photography and secondly; the result of the first step was registered with the histological scan. The registration is based on silhouette registration. The output of the process is a layered representation of the tissue consisting of the histological layer with selected spots and metal layers. The layered representation of all tissues was statistically evaluated. Our data confirm the hypothesis that the content of zinc in the zone of growing melanoma tissue is significantly higher than in all remaining zones.

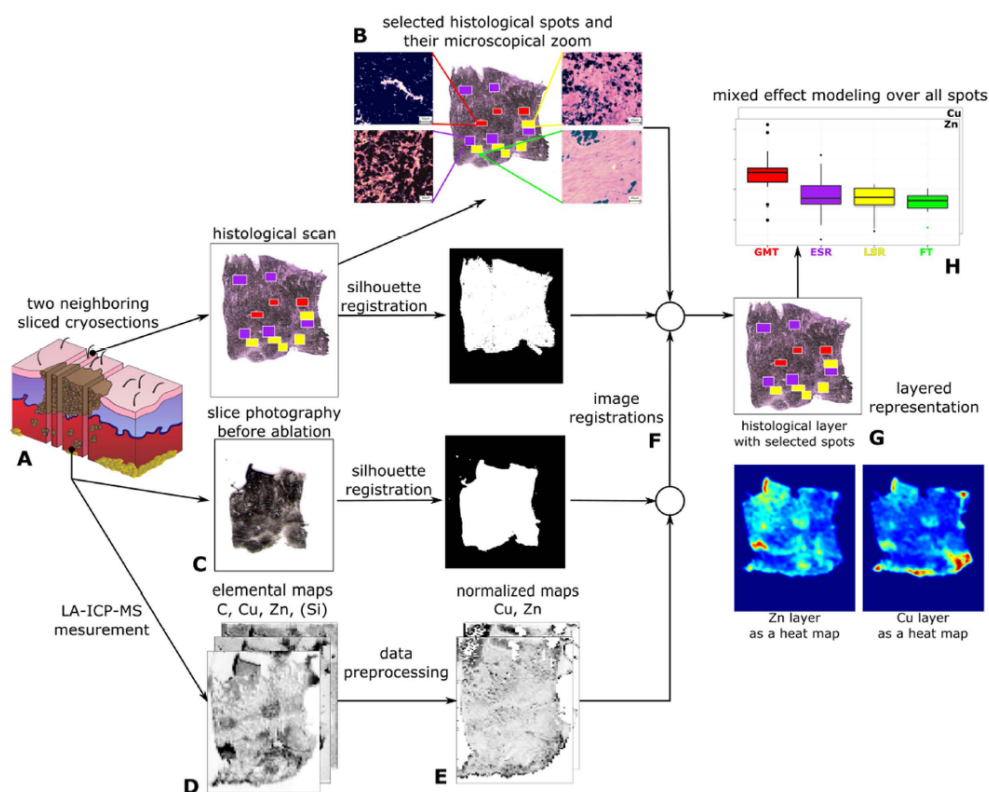


Fig. 4: A schematic description of the transformation process from cryosections to matched layers interpretation¹¹

In addition to the distribution of bio-elements in tissues, we can also determine the distribution of xenobiotics as Pt-based cytostatics¹³ or Pb-based nanoparticles¹⁶. LA-ICP-MS imaging was successfully used in the study where the influence of selectively oxidised cellulose (2,3-dicarboxycellulose – DCC) as a carrier of cisplatin cytostatics (cis-Pt) was compared to bare cis-Pt treatment¹³. It was found that utilisation of DCC- cis-Pt affects the distribution of Pt in tumour tissue. When the mice were treated by cis-Pt, the Pt was localized in the whole tumour (Fig. 5a) and the content of Pt in the majority of the tumour was between 2.5 and 7.5 mg/kg. In contrast, the utilisation of DCC-cis-Pt led to the accumulation of Pt in the centre of the tumour (Fig. 5b) with the content of Pt about 20 mg/kg.

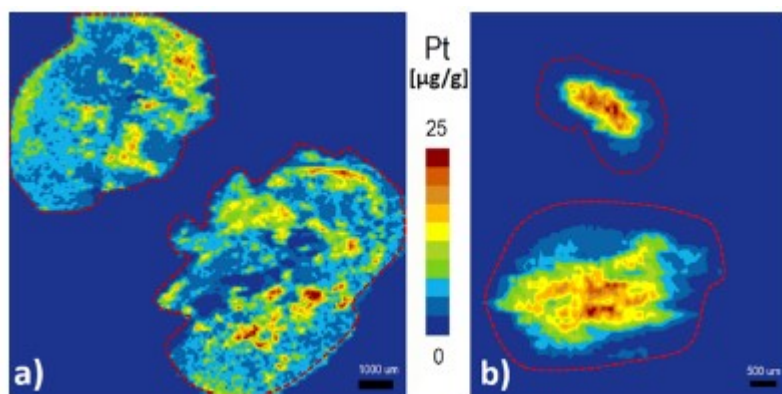


Fig. 5: Distribution of Pt in tumour tissue after treatment by cis-Pt (a) and DCC-cis-Pt (b). The red dashed line represents the boundary of the tumour tissue¹³

In the last research, LA-ICP-MS was used for determination of the distribution of Pb and Pb nanoparticles in mice tissues exposed to treatment by PbO nanoparticles¹⁶. A new method for the imaging of the nanoparticles had to be developed in this study. Moreover, using this method, we were able to distinguish between Pb in ionic or nanoparticle form. The main focus of this study was to identify differences in the ability to clear the inhaled PbO NPs from secondary target organs (clearance). Hence the lateral distribution was determined in lung, liver and kidney tissues after PbO treatment and clearance. The clearance of ionic lead and PbO NPs (Pb/PbO NPs) from the lungs and liver was very effective, with the lead being almost eliminated from the lungs and the physiological state of the lung tissue conspicuously restored. Kidneys exposed to nanoparticles did not exhibit serious signs of damage; however, LA-ICP-MS uncovered a certain amount of lead located preferentially in the kidney cortex even after a clearance period (Fig. 6).

As follows from the above-mentioned results, the information regarding elemental distribution is very useful, especially in the case of monitoring xenobiotics (e.g. Pt and Pb). While the origins and species of these xenobiotics can be well recognisable, in the case of natively present elements, the situation is much more complicated. These elements are present in the organism usually in the form of metalloproteins. For example, there are more than 3000 Zn-binding metalloproteins, each of which is related to a different process in the organism. Furthermore, Zn is often bound to other biomolecules including nucleic acids. Hence, our other work was focused on the development of a bio-recognition tool, allowing the determination of the specific biomolecules by ICP-MS (i.e. molecular imaging).

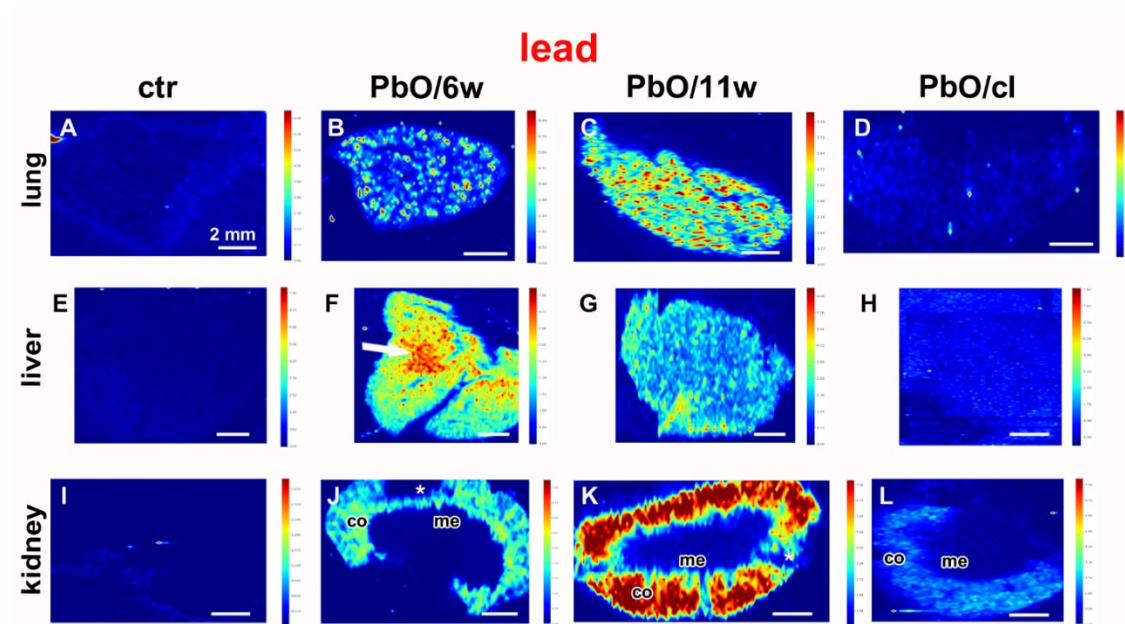


Fig. 6: Lead distribution in lung, liver, and kidney at designated time points after PbONPs inhalation.

3.3.2 MOLECULAR IMAGING

The real breakthrough of LA-ICP-MS in life sciences is the combination of molecularly-specific tools that allow the determination of biomolecules (e. g. proteins, nucleic acids, etc.). Such tools applicable to biomolecular recognition include mainly antibodies (Ab), aptamers, and/or molecularly imprinted polymers (MIPs). Utilisation of metal-containing labels for Ab offered the possibility of the use of ICP-MS detection. The group of metal-containing tags includes mostly metal-containing molecules⁵⁹, chelates^{60,61}, and nanoparticles^{62,63}.

A method for the determination of proteins by labelling the antibody with gold nanoparticles (AuNPs) (10 and 60 nm) with detection by LA-ICP-MS¹² was developed. Additionally, the AuNPs labelling strategy (Fig. 7) was compared with commercially available labelling reagents based on MeCAT (metal coded affinity tagging). Proof of principle experiments based on dot blot experiments were performed using anti-IgG and IgG as the model analyte. The two labelling probes (MeCAT and AuNPs) were compared by sensitivity and limit of detection (LOD). The absolute LODs achieved were in the range of tens of picograms for AuNP labelling compared to a few hundred picograms by the MeCAT labelling¹².

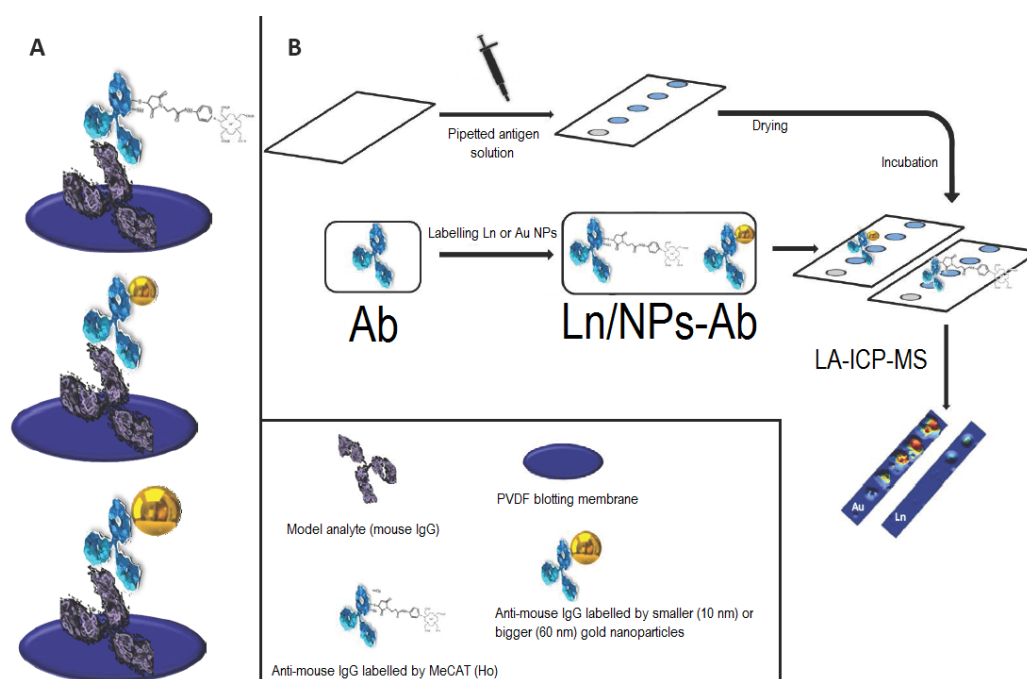


Fig. 7: The workflow of a dot-blot immunoassay with the labelled Ab by Au-NPs and MeCAT.¹⁴

The second approach for the determination of specific biomolecules is the use of MIP as the biorecognition tool. MIP was used as the selector for the determination of metallothionein

(MT) with mass spectrometric detection (matrix-assisted laser desorption/ionization mass spectrometric detection - MALDI-MS and LA-ICP-MS)¹⁴. This method, for the first time, integrated MIPs as a purification/pre-treatment step with MALDI-MS and LA-ICP-MS for analysis of MTs (Fig. 8). The prepared MT-imprinted polydopamine layer showed high binding capacity and specific recognition properties toward the template/analyte. This experimental setup allowed detection μM concentrations of MT. Such concentrations are present in the blood of cancer patients and therefore, this approach can be used for clinical studies recognising MT as a marker of various diseases including tumours. Moreover, two protein isoforms (MT1 and MT3) were successfully separated. The presented approach not only provides fast and selective sample analysis but also avoids the limitations of methods based on antibodies (e.g. high price, cross-reactivity, limited availability in some cases, etc.).

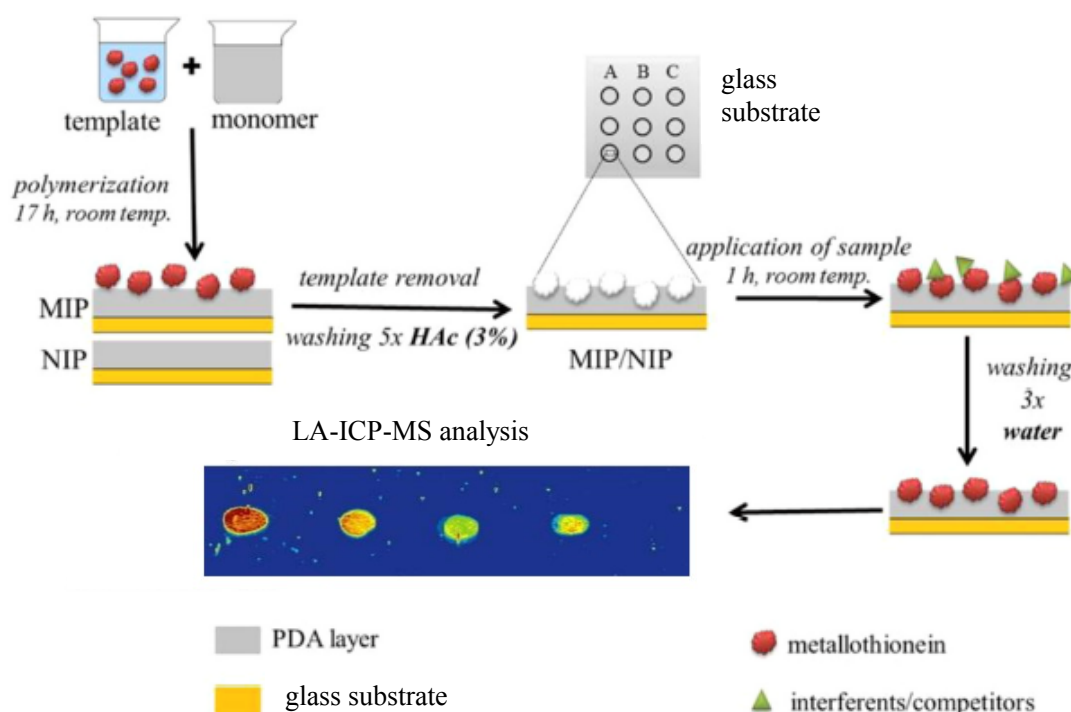


Fig. 8: Workflow of MIP formation, sampling and detection of MT.¹⁵

In this work, a MIP-based pseudo-immunoassay using NP-labelled antibody recognition was introduced and coupled with the sensitive detection technique – LA-ICP-MS¹⁵. Two approaches of specific recognition were tested. The first was based on the immunolabelling of the analyte captured by the MIP layer. The second approach involved immunolabelling of the analyte as a first step and the resulting QD-AB-AG complex was captured by MIP and further analyzed. The double-selective approach comprising of the

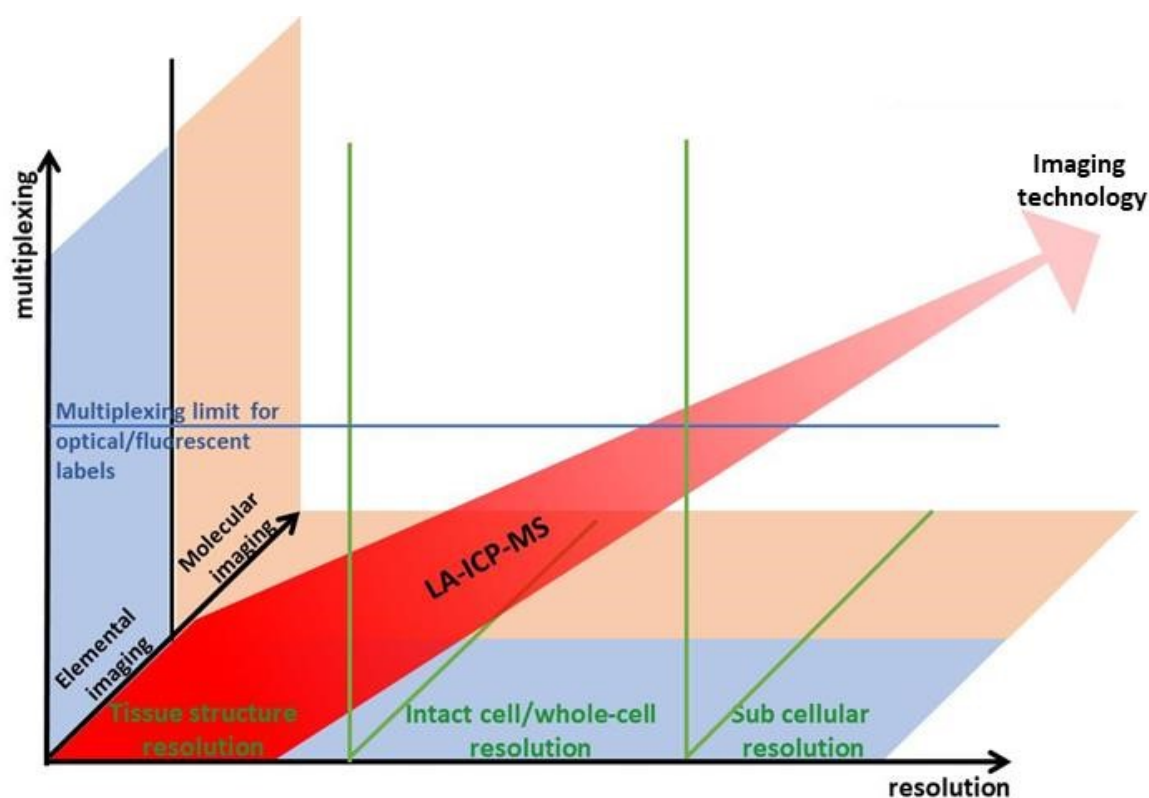
specific immunolabelling reaction combined with isolation by MIP together with the LA-ICP-MS detection represents a viable approach of the IgG detection from a complex sample (LOD 4.2 μg and 1.6 μg , respectively) available for many exciting applications. Considering the overall time of the LA-ICP-MS analysis not exceeding 23 s (scan speed of 2000 $\mu\text{m/s}$), LA-ICP-MS is a promising technology to be used in future in conjunction with MIP technology.

Biorecognition elements (antibodies, aptamers, and MIPs) represent a unique possibility to combine excellent sensitivity and multi-analyte detection of ICP-MS and the ability to determine specific biomolecules. Fluorescence detection, a well-established method for determination of biomolecules based on fluorescence probes offer excellent sensitivity, however, multiplexing capability is limited due to the spectral overlap of the probes. Because of minimal isobaric interference (equivalent to spectral overlap) in ICP-MS the multi-analyte detection is limited only by the number of available labels (REEs, Au, Ag, etc.). Moreover, as follows from our results, utilisation of NPs as the labels improve the sensitivity significantly. As any target (ions, molecules, bacteria, nanoparticles) can be imprinted into an appropriate polymer, the MIP technology can be successfully used for the determination of not only proteins but also others analytes (e.g. metabolites, whole cells, etc.).

4 CONCLUSION AND OUTLOOK

As shown above, LA-ICP-MS offers a great possibility to track elemental changes in any type of material from corroded metals through geological samples to biomaterials. The imaging of each of the studied materials has specific problems that have to be solved. The main problem common to all is the different ablation rate. As we have successfully suppressed this (using different normalisations or total mass removal), LA-ICP-MS elemental imaging is now a routine matter in our laboratory.

In order not to rest on our laurels, our research is focused on the determination of specific biomolecules by LA-ICP-MS. For this purpose, we use antibodies labelled by Au-NPs, which improve the sensitivity significantly and MIPs. Our works with MIPs are the first publications utilising the combination of MIPs with LA-ICP-MS detection.



The future of LA-ICP-MS imaging goes in two directions. The first is to improve the lateral resolution and shorten the analysis time so that we get the multi-element maps of several megapixels in the order of dozens minutes at the most. In this case, the solution is not only the construction of ablation cells with a low dispersion but also the data and image processing. The

second direction is to use biorecognition tools not only for the determination of proteins but of any type of molecule. As many labels (Au, Ag, REE, etc.) can be used for labelling, LA-ICP-MS offers the possibility of multi-molecule imaging. The combination of both directions will lead to multi-target imaging with sub-micron resolution within several minutes, which will be the last step to LA-ICP-MS becoming a molecular microscope. The ability to determine several analytes and their lateral distribution during one analysis opens the door into clinical, diagnostic and medicinal applications.

I believe that our contribution to elemental and molecular imaging will lead to this future.

5 LITERATURE

- (1) Novotny, K.; Vaculovic, T.; Galiova, M.; Otruba, V.; Kanicky, V.; Kaiser, J.; Liska, M.; Samek, O.; Malina, R.; Palenikova, K. *Applied Surface Science* **2007**, *253*, 3834-3842.
- (2) Vaculovic, T.; Sulovsky, P.; Machat, J.; Otruba, V.; Matal, O.; Simo, T.; Latkoczy, C.; Gunther, D.; Kanicky, V. *Journal of Analytical Atomic Spectrometry* **2009**, *24*, 649-654.
- (3) Vaculovic, T.; Warchilova, T.; Simo, T.; Matal, O.; Otruba, V.; Mikuska, P.; Kanicky, V. *Journal of Analytical Atomic Spectrometry* **2012**, *27*, 1321-1326.
- (4) Warchilova, T.; Dillingerova, V.; Skoda, R.; Simo, T.; Matal, O.; Vaculovic, T.; Kanicky, V. *Spectrochimica Acta Part B-Atomic Spectroscopy* **2018**, *148*, 113-117.
- (5) Novak, M.; Gadas, P.; Filip, J.; Vaculovic, T.; Prikryl, J.; Fojt, B. *Mineralogy and Petrology* **2011**, *102*, 3-14.
- (6) Bacik, P.; Uher, P.; Ertl, A.; Jonsson, E.; Nysten, P.; Kanicky, V.; Vaculovic, T. *Canadian Mineralogist* **2012**, *50*, 825-841.
- (7) Breiter, K.; Gardenova, N.; Vaculovic, T.; Kanicky, V. *Mineralogical Magazine* **2013**, *77*, 403-417.
- (8) Vaculovic, T.; Breiter, K.; Korbelova, Z.; Venclova, N.; Tomkova, K.; Jonasova, S.; Kanicky, V. *Microchemical Journal* **2017**, *133*, 200-207.
- (9) Petřík, I.; Janák, M.; Klonowska, I.; Majka, J.; Froitzheim, N.; Yoshida, K.; Sasinková, V.; Konečný, P.; Vaculovič, T. *Journal of Petrology* **2020**.
- (10) Vaculovic, T.; Warchilova, T.; Cadkova, Z.; Szakova, J.; Tlustos, P.; Otruba, V.; Kanicky, V. *Applied Surface Science* **2015**, *351*, 296-302.
- (11) Anyz, J.; Vyslouzilova, L.; Vaculovic, T.; Tvrdonova, M.; Kanicky, V.; Haase, H.; Horak, V.; Stepankova, O.; Heger, Z.; Adam, V. *Scientific Reports* **2017**, *7*.
- (12) Tvrdonova, M.; Vlcnovska, M.; Vanickova, L. P.; Kanicky, V.; Adam, V.; Ascher, L.; Jakubowski, N.; Vaculovicova, M.; Vaculovic, T. *Analytical and Bioanalytical Chemistry* **2019**, *411*, 559-564.
- (13) Muenster, L.; Fojtu, M.; Capakova, Z.; Vaculovic, T.; Tvrdonova, M.; Kuritka, I.; Masarik, M.; Vicha, J. *Biomacromolecules* **2019**, *20*, 1623-1634.
- (14) Vaneckova, T.; Vanickova, L.; Tvrdonova, M.; Pomorski, A.; Krezel, A.; Vaculovic, T.; Kanicky, V.; Vaculovicova, M.; Adam, V. *Talanta* **2019**, *198*, 224-229.
- (15) Vaneckova, T.; Bezdekova, J.; Tvrdonova, M.; Vlcnovska, M.; Novotna, V.; Neuman, J.; Stossova, A.; Kanicky, V.; Adam, V.; Vaculovicova, M.; Vaculovic, T. *Scientific Reports* **2019**, *9*.
- (16) Dumkova, J.; Smutna, T.; Vrlíkova, L.; Kotasova, H.; Docekal, B.; Capka, L.; Tvrdonova, M.; Jakesova, V.; Pelkova, V.; Krumal, K.; Coufalik, P.; Mikuska, P.; Vecera, Z.;

-
- Vaculovic, T.; Husakova, Z.; Kanicky, V.; Hampl, A.; Buchtova, M. *ACS nano* **2020**, *14*, 3096-3120.
- (17) Gray, A. L. *Analyst* **1985**, *110*, 551-556.
- (18) Arrowsmith, P. *Analytical Chemistry* **1987**, *59*, 1437-1444.
- (19) Hager, J. W. *Analytical Chemistry* **1989**, *61*, 1243-1248.
- (20) Mochizuki, T.; Sakashita, A.; Iwata, H.; Kagaya, T.; Shimamura, T.; Blair, P. *Analytical Sciences* **1988**, *4*, 403-409.
- (21) Imai, N. *Analytica Chimica Acta* **1990**, *235*, 381-391.
- (22) Vanheuzen, A. A.; Morsink, J. B. W. *Spectrochimica Acta Part B-Atomic Spectroscopy* **1991**, *46*, 1819-1828.
- (23) Vanheuzen, A. A. *Spectrochimica Acta Part B-Atomic Spectroscopy* **1991**, *46*, 1803-1817.
- (24) Engst, P.; Horák, M. *Aplikace laserů*; SNTL: Praha, 1989.
- (25) Maiman, T. H. *Nature* **1960**, *187*, 493-494.
- (26) Thompson, M.; Goulter, J. E.; Sieper, F. *Analyst* **1981**, *106*, 32-39.
- (27) Hale, M.; Thompson, M. *Transactions of the Institution of Mining and Metallurgy Section B-Applied Earth Science* **1983**, *92*, B23-B27.
- (28) Ishizuka, T.; Uwamino, Y. *Spectrochimica Acta Part B-Atomic Spectroscopy* **1983**, *38*, 519-527.
- (29) Geusic, J. E.; Marcos, H. M.; Vanuitert, L. G. *Applied Physics Letters* **1964**, *4*, 182-&.
- (30) Cremers, D. A.; Archuleta, F. L. *Proceedings of the Society of Photo-Optical Instrumentation Engineers* **1985**, *540*, 542-546.
- (31) Tremblay, M. E.; Smith, B. W.; Leong, M. B.; Winefordner, J. D. *Spectroscopy Letters* **1987**, *20*, 311-318.
- (32) Jeffries, T. E.; Pearce, N. J. G.; Perkins, W. T.; Raith, A. *Analytical Communications* **1996**, *33*, 35-39.
- (33) Bea, F.; Montero, P.; Stroh, A.; Baasner, J. *Chemical Geology* **1996**, *133*, 145-156.
- (34) Gunther, D.; Frischknecht, R.; Heinrich, C. A.; Kahlert, H. J. *Journal of Analytical Atomic Spectrometry* **1997**, *12*, 939-944.
- (35) Borisov, O. V.; Mao, X. L.; Ciocan, A. C.; Russo, R. E. *Applied Surface Science* **1998**, *127*, 315-320.
- (36) Russo, R. E.; Mao, X. L.; Borisov, O. V.; Liu, H. C. *Journal of Analytical Atomic Spectrometry* **2000**, *15*, 1115-1120.

-
- (37) Mank, A. J. G.; Mason, P. R. D. *Journal of Analytical Atomic Spectrometry* **1999**, *14*, 1143-1153.
- (38) Chan, W. T.; Mao, X. L.; Russo, R. E. *Applied Spectroscopy* **1992**, *46*, 1025-1031.
- (39) Russo, R. E.; Mao, X. L.; Gonzalez, J. J.; Mao, S. S. *Journal of Analytical Atomic Spectrometry* **2002**, *17*, 1072-1075.
- (40) Mao, X. L.; Ciocan, A. C.; Russo, R. E. *Applied Spectroscopy* **1998**, *52*, 913-918.
- (41) Koch, J.; Gunther, D. *Applied Spectroscopy* **2011**, *65*, 155A-162A.
- (42) Guillong, M.; Gunther, D. *Journal of Analytical Atomic Spectrometry* **2002**, *17*, 831-837.
- (43) Figg, D. J.; Cross, J. B.; Brink, C. *Applied Surface Science* **1998**, *127*, 287-291.
- (44) Vaculovic, T.; Guillong, M.; Binkert, J.; Kanicky, V.; Gunther, D. *Canadian Journal of Analytical Sciences and Spectroscopy* **2004**, *49*, 353-361.
- (45) Horn, I.; Gunther, D. *Applied Surface Science* **2003**, *207*, 144-157.
- (46) Crain, J. S.; Gallimore, D. L. *Journal of Analytical Atomic Spectrometry* **1992**, *7*, 605-610.
- (47) Halicz, L.; Gunther, D. *Journal of Analytical Atomic Spectrometry* **2004**, *19*, 1539-1545.
- (48) Leach, A. M.; Hieftje, G. M. *Journal of Analytical Atomic Spectrometry* **2000**, *15*, 1121-1124.
- (49) Latkoczy, C.; Muller, Y.; Schmutz, P.; Gunther, D. *Applied Surface Science* **2005**, *252*, 127-132.
- (50) Houk, R. S. *Analytical Chemistry* **1986**, *58*, A97-&.
- (51) Imai, N. *Analytica Chimica Acta* **1992**, *269*, 263-268.
- (52) Chenery, S.; Cook, J. M. *Journal of Analytical Atomic Spectrometry* **1993**, *8*, 299-303.
- (53) Hoffmann, E.; Ludke, C.; Skole, J.; Stephanowitz, H.; Ullrich, E.; Colditz, D. *Fresenius Journal of Analytical Chemistry* **2000**, *367*, 579-585.
- (54) Kindness, A.; Sekaran, C. N.; Feldmann, J. *Clinical Chemistry* **2003**, *49*, 1916-1923.
- (55) Paul, B.; Hare, D. J.; Bishop, D. P.; Paton, C.; Van Tran, N.; Cole, N.; Niedwiecki, M. M.; Andreozzi, E.; Vais, A.; Billings, J. L.; Bray, L.; Bush, A. I.; McColl, G.; Roberts, B. R.; Adlard, P. A.; Finkelstein, D. I.; Hellstrom, J.; Hergt, J. M.; Woodhead, J. D.; Doble, P. A. *Chemical Science* **2015**, *6*, 5383-5393.
- (56) Van Acker, T.; Buckle, T.; Van Malderen, S. J. M.; van Willigen, D. M.; van Unen, V.; van Leeuwen, F. W. B.; Vanhaecke, F. *Analytica Chimica Acta* **2019**, *1074*, 43-53.
- (57) Aljakna, A.; Lauer, E.; Lenglet, S.; Grabherr, S.; Fracasso, T.; Augsburger, M.; Sabatasso, S.; Thomas, A. *International journal of legal medicine* **2018**.

-
- (58) Schaltegger, U.; Schmitt, A. K.; Horstwood, M. S. A. *Chemical Geology* **2015**, *402*, 89-110.
- (59) Hutchinson, R. W.; Cox, A. G.; McLeod, C. W.; Marshall, P. S.; Harper, A.; Dawson, E. L.; Howlett, D. R. *Analytical Biochemistry* **2005**, *346*, 225-233.
- (60) Giesen, C.; Wang, H. A. O.; Schapiro, D.; Zivanovic, N.; Jacobs, A.; Hattendorf, B.; Schuffler, P. J.; Grolimund, D.; Buhmann, J. M.; Brandt, S.; Varga, Z.; Wild, P. J.; Gunther, D.; Bodenmillerthat, B. *Nature Methods* **2014**, *11*, 417-+.
- (61) Giesen, C.; Mairinger, T.; Khoury, L.; Waentig, L.; Jakubowski, N.; Panne, U. *Analytical Chemistry* **2011**, *83*, 8177-8183.
- (62) Seuma, J.; Bunch, J.; Cox, A.; McLeod, C.; Bell, J.; Murray, C. *Proteomics* **2008**, *8*, 3775-3784.
- (63) Baranov, V. I.; Quinn, Z.; Bandura, D. R.; Tanner, S. D. *Analytical Chemistry* **2002**, *74*, 1629-1636.

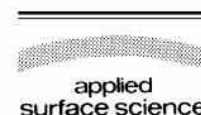
6 ARTICLES

6.1 ARTICLE 1

Novotny, K.; Vaculovic, T.; Galiova, M.; Otruba, V.; Kanicky, V.; Kaiser, J.; Liska, M.; Samek, O.; Malina, R.; Palenikova, K. *Applied Surface Science* 2007, 253, 3834-3842 (IF=5.155)

Available online at www.sciencedirect.com

Applied Surface Science 253 (2007) 3834–3842

www.elsevier.com/locate/apsusc

The use of zinc and iron emission lines in the depth profile analysis of zinc-coated steel

K. Novotný^{a,*}, T. Vaculovič^a, M. Galiová^a, V. Otruba^a, V. Kanický^a,
J. Kaiser^b, M. Liška^b, O. Samek^b, R. Malina^b, K. Páleníková^b

^a Department of Analytical Chemistry, Faculty of Science, Masaryk University in Brno, Kotlářská 2, 611 37 Brno, Czech Republic

^b Institute of Physical Engineering, Faculty of Mechanical Engineering, Brno University of Technology, Technická 2896/2, 616 69 Brno, Czech Republic

Received 17 May 2006; received in revised form 2 August 2006; accepted 4 August 2006

Available online 2 October 2006

Abstract

In this study we report on the results of experiments devoted to the depth profile analysis of zinc-coated steel samples using the laser-induced breakdown spectroscopy (LIBS) technique. The dependence of zinc and iron emissions in three ablation atmospheres (air, argon, helium) was measured using the fundamental wavelength (1064 nm) of the Nd:YAG laser. The highest possible depth resolution was achieved by optimizing the experimental parameters, such as the delay time (which affects the tailing of the zinc emission signal), focusing conditions, energy delivered to the sample, and choice of buffer gases. Current research indicates that there is a constant need to optimize these parameters so that reliable depth-profiling analysis can be performed.

© 2006 Elsevier B.V. All rights reserved.

PACS : 42.62.Fi; 42.62.Cf

Keywords: Laser-induced breakdown spectrometry (LIBS); Laser ablation; Coating; Depth profiling; Depth resolution

1. Introduction

Nowadays several different techniques are employed for depth profiling of multilayered metal materials. Secondary ions mass spectrometry (SIMS) [1], X-ray photoelectron spectroscopy (XPS) [2], Auger electron spectroscopy (AES) [1,2], electron probe microanalysis (EPXMA) and total reflection X-ray fluorescence spectroscopy (TXRF) [3] are widely used (separately or combined with chemical etching or ion sputtering) for depth profiling on a nanometric and sub-micrometric scale. Glow discharge optical emission spectroscopy (GD-OES) [4,5] is very often applied to quantitative depth profiles of coated metal samples in the range from tens of nanometers to tens and hundreds of micrometers.

Pulsed laser ablation (LA) techniques are also powerful tools for depth profiling layered materials. In LA inductively coupled

plasma atomic emission spectrometry (LA-ICP-AES) the ablated material is transported by carrier gas to an ICP and detected through atomic (optical) emission spectrometry. LA-ICP-AES has been used by Kanický et al. [6,7] to perform the depth profiling of a glass coated with a single layer of Sn, steel coated with partially stabilized zirconia, a graded metal-ceramic zone and NiCrAlY alloy layers. In LA inductively coupled plasma mass spectrometry (LA-ICP-MS) the ablated matter is carried in a gas stream to an ICP and detected by mass spectrometry. Coedo et al. [8] used a commercial highly focused (Gaussian) nanosecond UV (266 nm) Nd:YAG laser ablation system coupled to an inductively coupled plasma quadrupole mass spectrometer as a tool for the depth profile analysis of a copper coating on steel. Depth resolution, obtained from normalized in-depth profiles, increased linearly with the coating thickness. For the eight studied samples the ablation rate was approximately 1 $\mu\text{m}/\text{pulse}$. The feasibility of depth profiling of ZrTiN coatings was studied by Kanický et al. [9] using a 193-nm ArF⁺ excimer laser ablation system with a lens array-based beam homogenizer in combination with an

* Corresponding author. Tel.: +420 549 496 231; fax: +420 541 211 214.
E-mail address: codl@sci.muni.cz (K. Novotný).

ICP-MS. The same system using LA-ICP-AES combined with a Nd:YAG laser (1064 nm) has been used to perform the depth profiling of zinc-coated iron sheets in the work of Hrdlička et al. [10]. The comparison of IR-LA and UV-LA profiles indicates that the material-dependent ablation characteristic of the metals is significantly different and the reliable metal ablation for depth profiling needs to change from a nanosecond to a femtosecond laser ablation system.

Laser-induced breakdown spectrometry (LIBS) is based on the detection of photons emitted by the atomized sample constituents in the laser-induced plasma created during laser ablation. In recent years LIBS has been applied successfully to the depth profiling analysis of metal samples with different coatings. Nanometric range depth-resolved analysis of coated steels was reported by Vadillo et al. [11]. The use of a flat energy profile XeCl excimer laser beam in LIBS has been demonstrated as an excellent way to generate craters with an improved depth resolution of up to 8 nm/pulse [12]. The capability of laser-induced breakdown spectrometry to resolve complex depth profiles has also been demonstrated by Vadillo and Laserna [13]. Electrolytically deposited brass samples were analyzed by monitoring the emissions corresponding to Cr, Ni, Cu and Zn emission lines. In the next work [14], a detailed description of the effect of laser irradiance on the averaged ablation rate and depth resolution of Ni-Cu-coated brass samples was presented. Analysis of layered materials using laser-induced plasma spectrometry was also compared with laser-ionization time-of-flight mass spectrometry [15]. St-Onge and Sabsabi [16] used a Nd:YAG laser 1064 nm for quantitative depth profiles of three elements (Al, Fe and Zn) on two galvanized samples. For the calibration of the iron and zinc line intensities, the iron-to-zinc intensity ratio was used and it was assumed that the sum of the iron and zinc concentrations was equal to unity everywhere. The position of the coating substrate interface was estimated by a method based on finding the most negative value of the second derivative on the line intensity profile for the major element in the coating. A steel sample coated with titanium nitride has been depth profiled by laser-induced plasma spectroscopy in an ultraviolet vacuum by Radivojevic et al. [17].

The surrounding atmosphere has a significant influence on the laser-induced plasma characteristic. Time-resolved measurements of temperatures and electron densities of laser-produced plasmas generated in air, argon and helium at atmospheric pressure have been presented by Aguilera and Aragon [18]. The plasmas were obtained by focusing a Nd:YAG laser on a low-alloyed steel sample. Higher temperatures and electron densities were obtained in argon; a faster decrease of measured temperatures and densities takes place in helium. Spatial characterization of laser-induced plasmas obtained in air and argon with different laser focusing distances has also been reported [19].

The delay time, i.e. the time between laser pulse and detection of emission also plays a key role in the evaluation of the signal from the LIBS. The time selection significantly influences the signal/noise ratio. A short time after the laser pulse the signal is dominated by background radiation.

However, the background emission decreases faster than the line emission of the sample constituents. A short delay time also plays a significant role in the self-absorption effect. In principle, the timing parameters (delay and integration times) are highly dependent on the element and the matrix, and must be optimized for each sample [20].

2. Experimental

In order to study the depth profile, zinc-coated iron sheets were ablated using a Nd:YAG laser system (Quantel, Brilliant). The laser operated at the fundamental wavelength (1064 nm) with a pulse width of 4.4 ns, beam diameter 5 mm and repetition rate 10 Hz. The energy of the laser pulse was monitored by an energy meter (Nova-Ophir, Optronics).

The laser-induced sparks were produced by focusing the laser beam with a 170 mm focal-length glass lens. Different power densities on the sample surface were achieved by defocusing the laser light.

Utilizing a gas-filled laboratory-made aluminum ablation chamber with a quartz window, the depth-profiling in different ablation atmospheres (air, argon and helium) was studied (at atmospheric pressure). The 18 cm³ chamber was mounted so that the focused laser beam was inclined at 72° to the sample and the observation angle of the objective was at 90° to the sample surface.

The laser-induced plasma (LIP) radiation was collected with a quartz objective and transported by a 3-m fiber optic system onto the entrance slit of a 0.32 m monochromator (Jobin Yvon TRIAX 320). The monochromator was equipped with three interchangeable holographic gratings of 1200, 2400 and 3600 g/mm. In this study the grating of 2400 g/mm and entrance/exit slits of 50 μm were used. A photomultiplier (Hamamatsu C1392) gated by a laboratory-built control unit was employed as a detector. For the gate-time delay monitoring and time-resolved signal recording, a digital storage oscilloscope Tektronix TDS 1012 was used. The wavelength scale of the spectrometer was calibrated using an ICP source with a nebulizing solution containing 100 mg l⁻¹ zinc or iron. A schematic drawing of the experimental setup is shown in Fig. 1.

The time-resolved emission signal (with a resolution of 10 ns) at the given wavelength was recorded for the each laser shot and the final temporal evolution of the LIP emission was obtained by averaging 16, 64 and 128 laser shots.

The depth profile was evaluated by measuring the intensity of the zinc atomic line at 280.08 nm (background intensity was measured at 279.30 nm) and the iron atomic line at 344.06 nm (background intensity was measured at 343.30 nm). The zinc, iron and background signals were obtained by firing the laser at laterally displaced sites on the sample for consecutive measurements.

For visual inspection and documentation of the created ablation craters a digital camera (Nikon Coolpix 5000) connected to a binocular microscope (PZO Warsaw, Poland) was used. The optical profilometer (Fries Research & Technology GmbH, MicroProf FRT) with a CHR 150 N sensor was utilized for crater depth measurements.

surrounding gases and the delay time between the incident laser pulse and the detected photomultiplier signal. Changing these parameters affected the tailing of the zinc emission signal and the crater shape.

3.1. Influence of laser beam focusing and power density

At a constant laser power (100 mJ/pulse), the power density was varied by moving the focusing lens in relation to the sample surface. The (inner) diameter of the ablation crater was varied in the range 0.8–0.2 mm for different defocusing conditions.

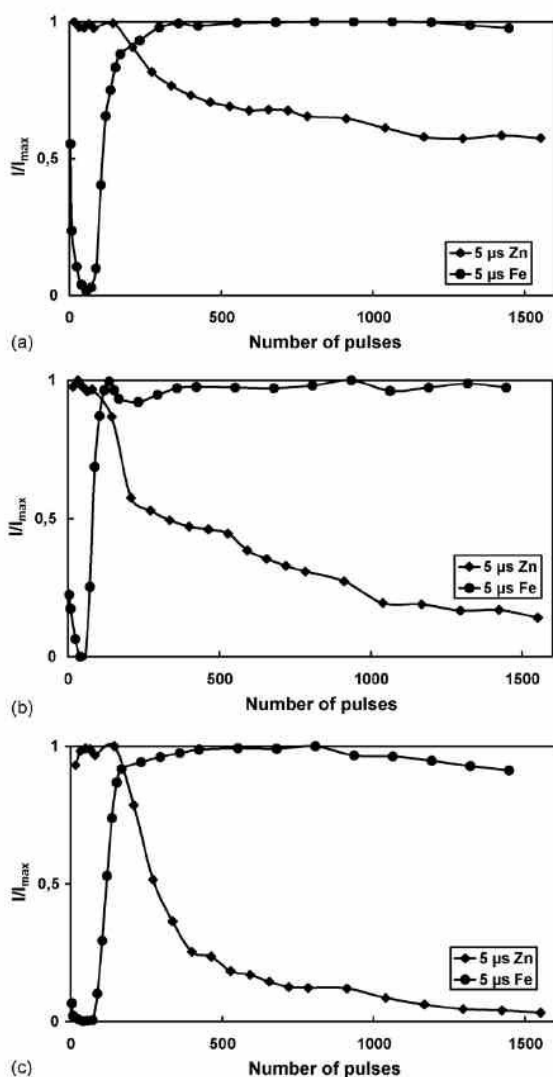


Fig. 5. Influence of the surrounding atmosphere on the depth profile of electroplated Zn coating—Sollac sample. Ablation was performed with an energy of 100 mJ in different atmospheres: (a) in air focusing at -20 mm, (b) in argon focusing at -15 mm, and (c) in helium focusing at -20 mm.

The dependence of the LIP signal on the focusing conditions was studied by measuring the intensity of the Zn(I) atomic line at 280.08 nm. The effect of the laser beam focusing was measured in the range from -40 to $+15$ mm (minus means focusing below sample surface, plus means focusing above sample surface) in each ablation atmosphere (air, argon and helium). The influence of the ablation atmosphere on optimal laser beam focusing is shown in Fig. 2. In the case of air a significant maximum intensity was observed when focusing at -20 mm. In argon the maximal LIP signal was obtained when focusing between -25 and -10 mm. In the helium atmosphere no significant maximum was observed.

At a constant focusing distance the power density was varied by changing the laser energy. As expected, the emission signal increased with the higher laser energy (Fig. 3). This fact can be attributed to the increase in the amount of ablated material. However, for power densities higher than ~ 5 GW cm^{-2} (at ablation crater diameter 750 μm), the Zn(I) emission intensity reached a saturation level. We should note that this value is in the same order of magnitude (1 GW cm^{-2}) as that reported in the work Cabalin and Laserna [23] for similar experimental conditions. The difference between the two results is attributed to the different self-absorption effects of the Zn(I) line at 334.50 nm monitored in the work [23] and the Zn(I) line at 280.08 nm detected in this study.

3.2. Influence of surrounding gasses

The temporal evolution of the zinc signals acquired at optimal focusing distances in each atmosphere is shown in Fig. 4. By comparing these signals it is evident that the microplasma exhibits the shortest lifetime in a helium atmosphere, while in argon the radiation emitted by the microplasma is the longest.

As shown in Fig. 5a–c, the surrounding gases have a critical effect on the temporal behavior of the Zn signal generated during the drilling. At a constant laser pulse energy (100 mJ) and gas pressure (~ 100 kPa), the strongest signal-tailing was observed in an air atmosphere (see Fig. 5a). For argon (Fig. 5b) and helium (Fig. 5c) the signal-tailing was lower. As shown in

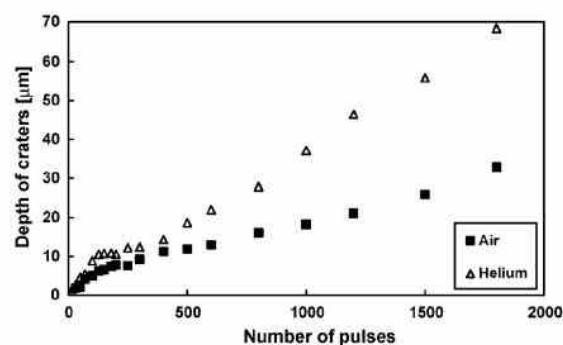


Fig. 6. Dependence of crater depth on the number of laser pulses. Electroplated Zn coating—Sollac sample in air and helium atmospheres. Ablation was performed with an energy of 100 mJ/pulse focusing at -20 mm.

surrounding gases and the delay time between the incident laser pulse and the detected photomultiplier signal. Changing these parameters affected the tailing of the zinc emission signal and the crater shape.

3.1. Influence of laser beam focusing and power density

At a constant laser power (100 mJ/pulse), the power density was varied by moving the focusing lens in relation to the sample surface. The (inner) diameter of the ablation crater was varied in the range 0.8–0.2 mm for different defocusing conditions.

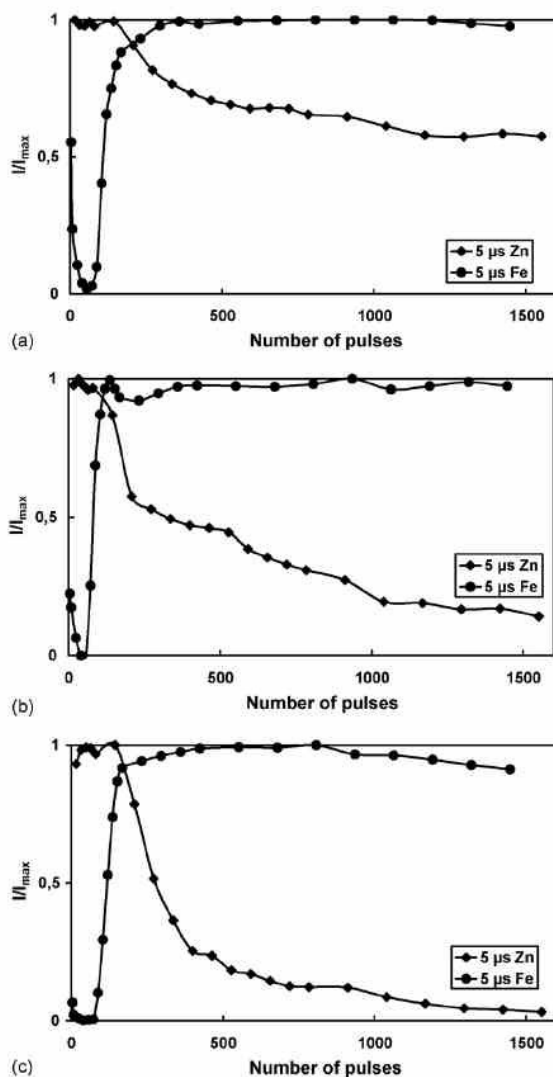


Fig. 5. Influence of the surrounding atmosphere on the depth profile of electroplated Zn coating—Sollac sample. Ablation was performed with an energy of 100 mJ in different atmospheres: (a) in air focusing at -20 mm, (b) in argon focusing at -15 mm, and (c) in helium focusing at -20 mm.

The dependence of the LIP signal on the focusing conditions was studied by measuring the intensity of the Zn(I) atomic line at 280.08 nm. The effect of the laser beam focusing was measured in the range from -40 to $+15$ mm (minus means focusing below sample surface, plus means focusing above sample surface) in each ablation atmosphere (air, argon and helium). The influence of the ablation atmosphere on optimal laser beam focusing is shown in Fig. 2. In the case of air a significant maximum intensity was observed when focusing at -20 mm. In argon the maximal LIP signal was obtained when focusing between -25 and -10 mm. In the helium atmosphere no significant maximum was observed.

At a constant focusing distance the power density was varied by changing the laser energy. As expected, the emission signal increased with the higher laser energy (Fig. 3). This fact can be attributed to the increase in the amount of ablated material. However, for power densities higher than ~ 5 GW cm^{-2} (at ablation crater diameter 750 μm), the Zn(I) emission intensity reached a saturation level. We should note that this value is in the same order of magnitude (1 GW cm^{-2}) as that reported in the work Cabalin and Laserna [23] for similar experimental conditions. The difference between the two results is attributed to the different self-absorption effects of the Zn(I) line at 334.50 nm monitored in the work [23] and the Zn(I) line at 280.08 nm detected in this study.

3.2. Influence of surrounding gases

The temporal evolution of the zinc signals acquired at optimal focusing distances in each atmosphere is shown in Fig. 4. By comparing these signals it is evident that the microplasma exhibits the shortest lifetime in a helium atmosphere, while in argon the radiation emitted by the microplasma is the longest.

As shown in Fig. 5a–c, the surrounding gases have a critical effect on the temporal behavior of the Zn signal generated during the drilling. At a constant laser pulse energy (100 mJ) and gas pressure (~ 100 kPa), the strongest signal-tailing was observed in an air atmosphere (see Fig. 5a). For argon (Fig. 5b) and helium (Fig. 5c) the signal-tailing was lower. As shown in

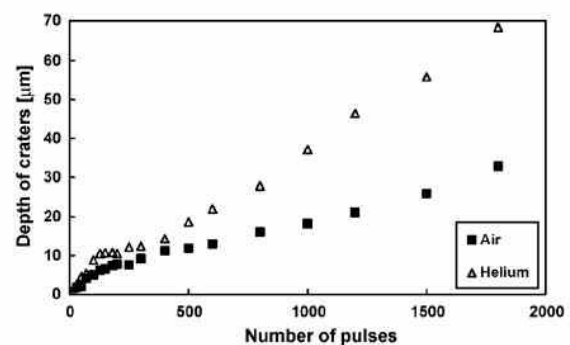


Fig. 6. Dependence of crater depth on the number of laser pulses. Electroplated Zn coating—Sollac sample in air and helium atmospheres. Ablation was performed with an energy of 100 mJ/pulse focusing at -20 mm.

Fig. 5c, only in the helium atmosphere did the intensity of the Zn signal decrease to zero for laser pulses >1500.

The relationship between the crater depth (measured by the optical profilometer) and the laser pulse numbers for air and He is shown in Fig. 6. It is evident that in air a lower ablation rate is

achieved and the ablation rate does not change significantly at the Zn/Fe interface. In contrast, in the case of He a higher ablation rate was observed and the ablation rate changed at the interface. Similar behavior was also observed in Ar. These results correspond to the measurements of the temporal

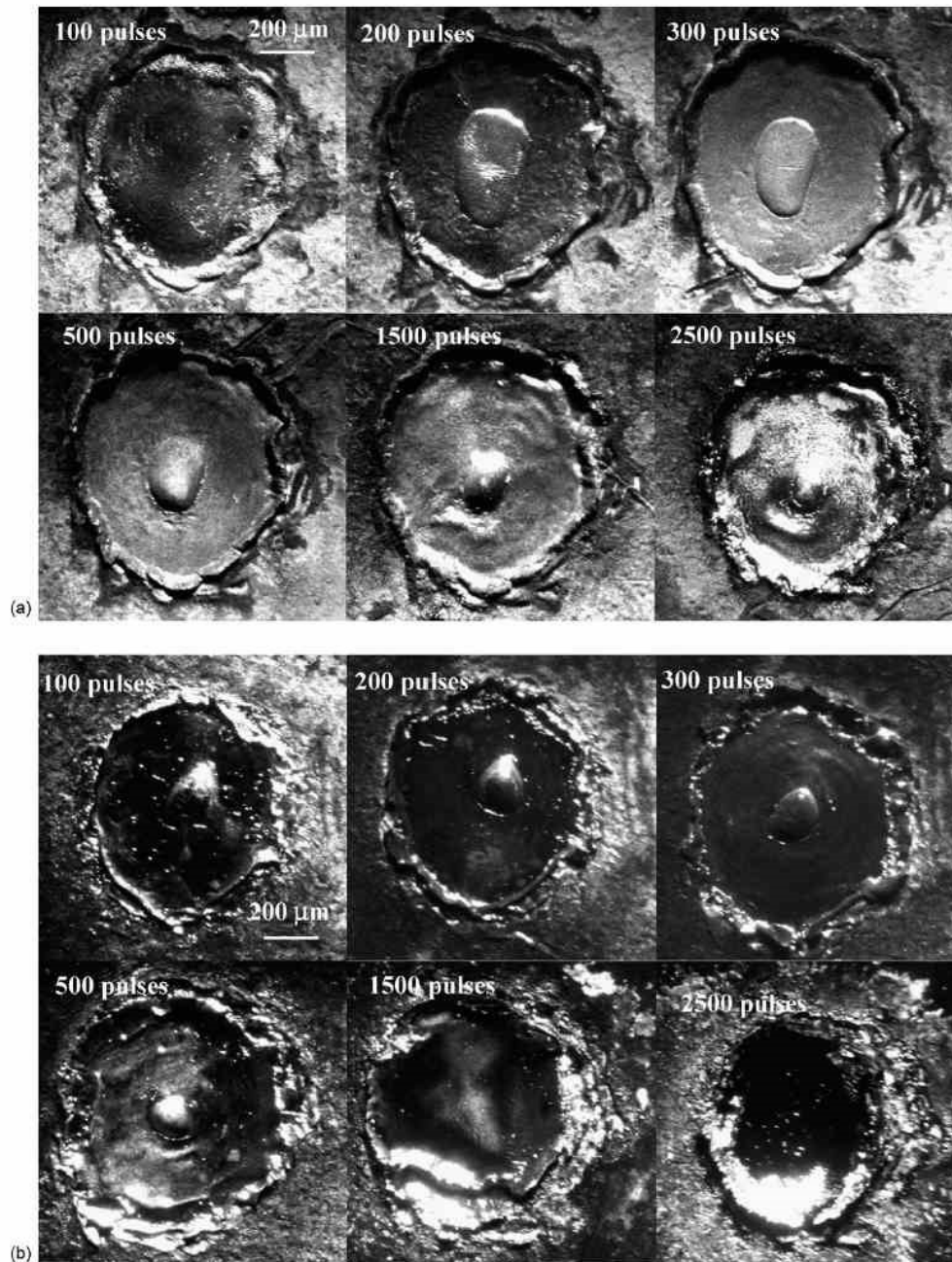


Fig. 7. Photographs of craters on the electroplated Zn coating—Sollac sample surface obtained after 100, 200, 300, 500, 1500 and 2500 pulses with an energy of 100 mJ in different atmospheres: (a) in air focusing at -20 mm, (b) in argon focusing at -15 mm, (c) in helium focusing at -20 mm, and (d) 3D profiles after 200 laser pulses in air, argon and helium atmospheres.

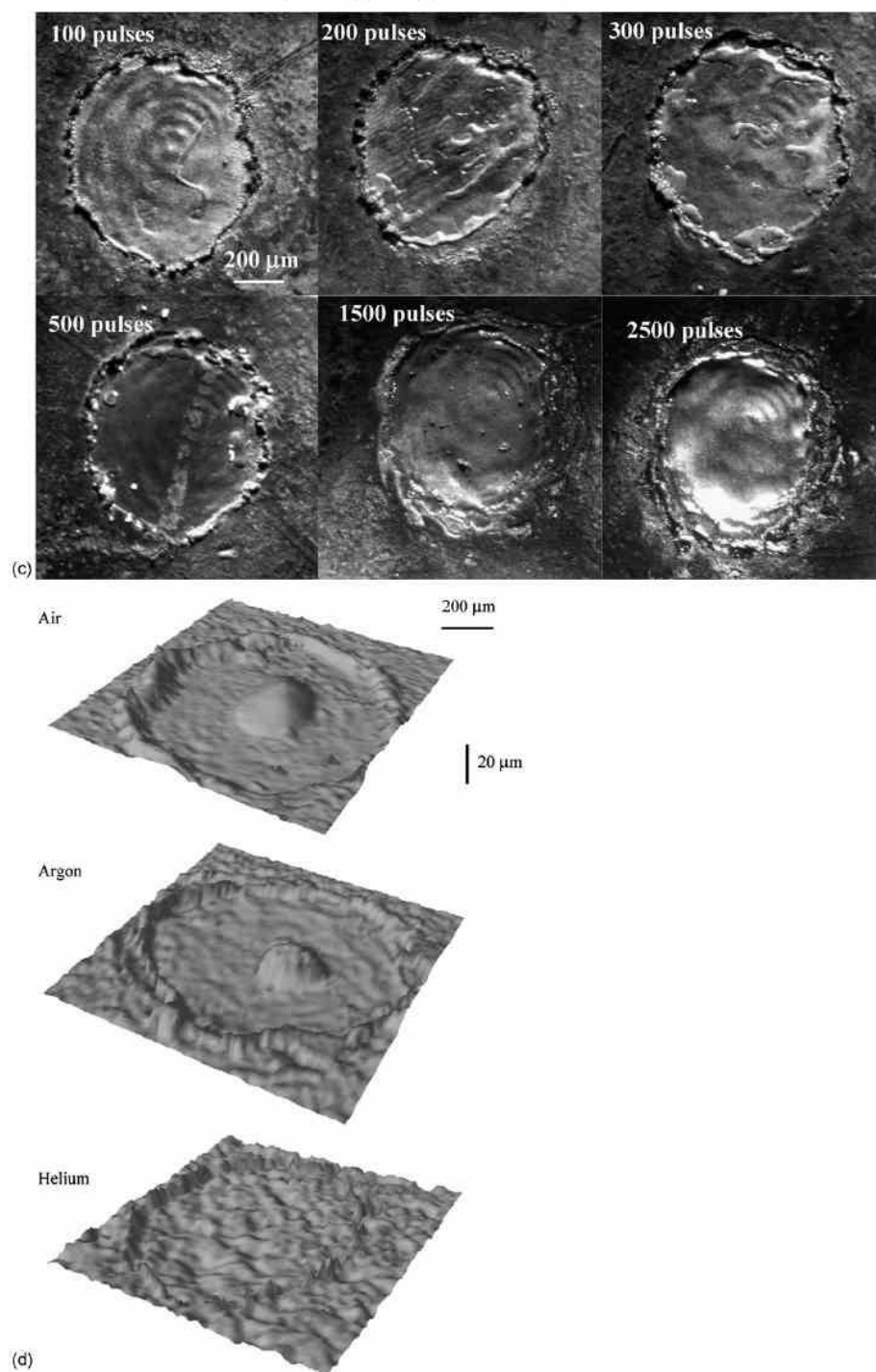


Fig. 7. (Continued).

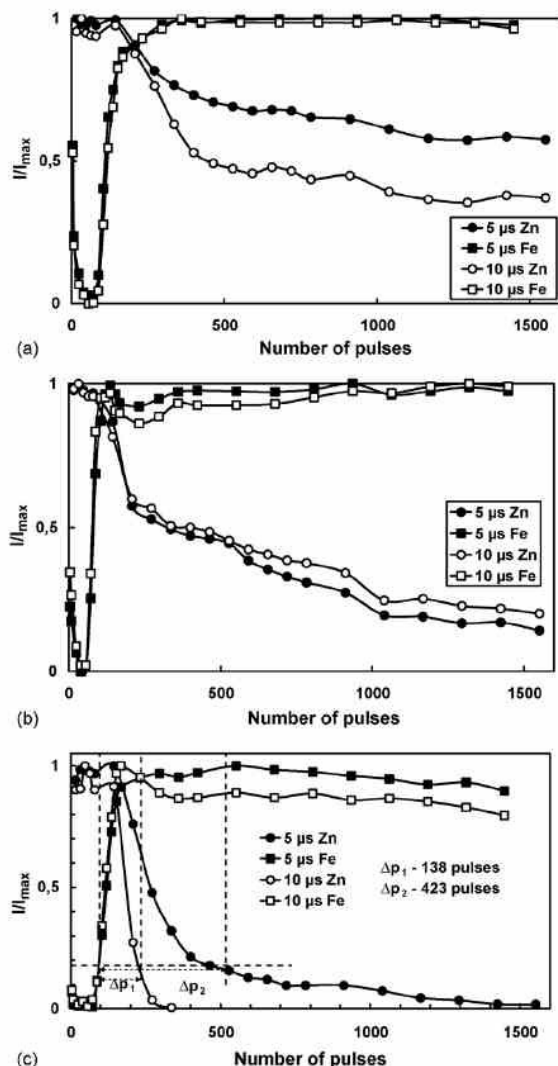


Fig. 8. Influence of the delay time on the depth profile of electroplated Zn coating—Sollac sample in different atmospheres: (a) in air focusing at -20 mm, (b) in argon focusing at -15 mm, and (c) in helium focusing at -20 mm. Comparison of LIB signals of Zn(I) 280.08 nm and Fe(I) 344.06 nm at 5 and 10 μ s delay times. Ablation was performed with an energy of 100 mJ/pulse.

Table 1
Comparison of the ablation rates in air, argon and helium atmospheres determined from LIBS depth profiles and depth measured by optical profilometer

| Atmosphere | Ablation rate (nm/pulse) | |
|------------|--------------------------|-------------------------|
| | From LIBS depth profile | By optical profilometer |
| Air | 49 | 40 |
| Ar | 88 | 73 |
| He | 59 | 53 |

Laser energy 100 mJ/pulse and sample electroplated Sollac.

Table 2
Comparison of the depth resolutions of Zn-coated sheets measured in a helium atmosphere at two different delay times

| Zn-coated sheets | Depth resolution (pulses) | |
|----------------------|---------------------------|------------|
| | 5 μ s | 10 μ s |
| Hot dipped | 493 | 150 |
| Aluzink | 234 | 139 |
| Galfan | 260 | 106 |
| Electroplated Sollac | 423 | 138 |
| Galvanal | 224 | 172 |

Laser beam focusing at -20 mm with laser energy 100 mJ/pulse. Depth resolution of laser ablation depth-profiling technique is evaluated as a depth interval between 16% of the maximum signal of Fe and 16% of the maximum Zn signal.

evolution of the Zn signal (Fig. 5). A helium atmosphere seems to be the most appropriate for depth profiling using 100 mJ laser pulse energy due to the lowest tailing of the zinc emission signal.

Photographs in Fig. 7a–c show craters produced at a laser energy of 100 mJ and an optimized laser beam focusing on the Electroplated Zn coating—Sollac sample in air, Ar and He ambient atmospheres, respectively, for a various number of pulses. In the air (and Ar) during the drilling process melted material accumulates at the bottom of the ablation crater. The composition of this material was analyzed by SEM-EDX and it was shown in [10] that it is Zn. After a higher number of laser pulses the deposition of zinc in these gases is still observable. As an example, the Zn in air is still present after 2500 laser pulses (Fig. 7a) and 500 laser pulses in Ar (Fig. 7b). Craters obtained in a helium atmosphere do not exhibit a strong accumulation of melted zinc on the crater bed (Fig. 7c).

Fig. 7d shows the results of the optical profilometer measurements. The 3D profiles of the ablation craters after 200 shots for the three different gases were measured. The presence of Zn is evident in the ambient gases of Ar and air.

The different Zn signal-tailing in these three gases (Fig. 5) corresponds to the amount of Zn accumulated at the bottom of the ablation crater. Comparing Figs. 5a and 7a for air, it is evident that the longest signal-tailing corresponds to the highest

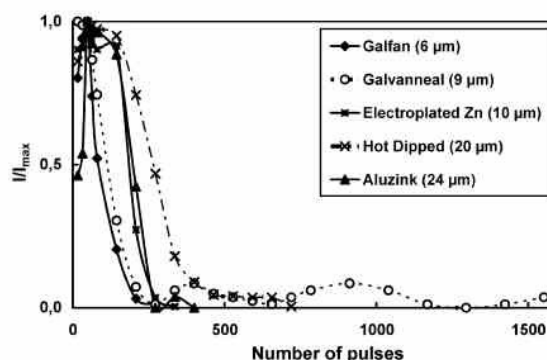


Fig. 9. Depth profiles of five Zn coating samples in helium atmosphere. Comparison of LIB signals of Zn(I) 280.08 nm at 10 μ s delay time. Ablation was performed with an energy of 100 mJ/pulse focusing at -20 mm.

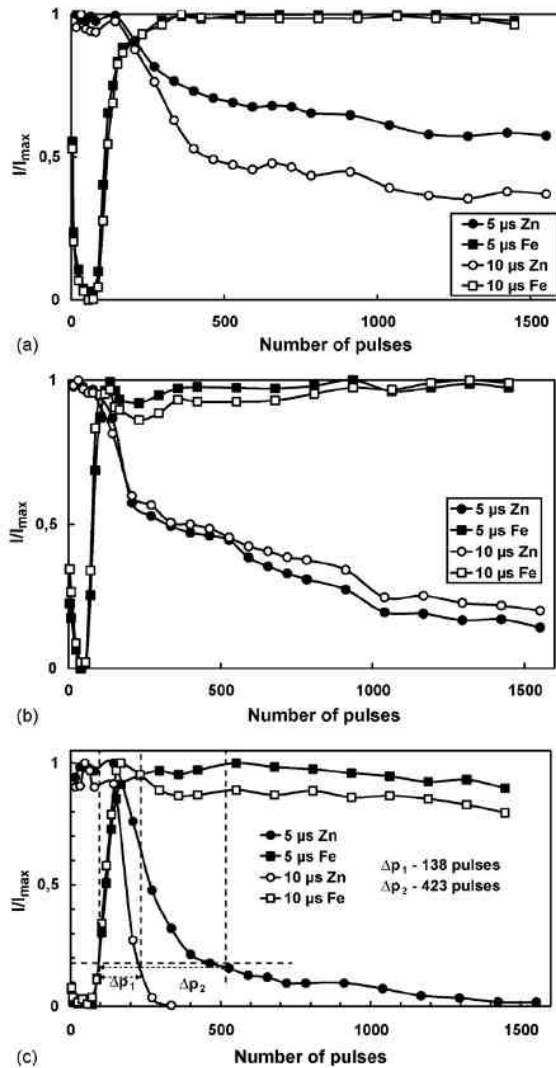


Fig. 8. Influence of the delay time on the depth profile of electroplated Zn coating—Sollac sample in different atmospheres: (a) in air focusing at -20 mm, (b) in argon focusing at -15 mm, and (c) in helium focusing at -20 mm. Comparison of LIB signals of Zn(I) 280.08 nm and Fe(I) 344.06 nm at 5 and 10 μ s delay times. Ablation was performed with an energy of 100 mJ/pulse.

Table 1
Comparison of the ablation rates in air, argon and helium atmospheres determined from LIBS depth profiles and depth measured by optical profilometer

| Atmosphere | Ablation rate (nm/pulse) | |
|------------|--------------------------|-------------------------|
| | From LIBS depth profile | By optical profilometer |
| Air | 49 | 40 |
| Ar | 88 | 73 |
| He | 59 | 53 |

Laser energy 100 mJ/pulse and sample electroplated Sollac.

Table 2

Comparison of the depth resolutions of Zn-coated sheets measured in a helium atmosphere at two different delay times

| Zn-coated sheets | Depth resolution (pulses) | |
|----------------------|---------------------------|------------|
| | 5 μ s | 10 μ s |
| Hot dipped | 493 | 150 |
| Aluzink | 234 | 139 |
| Galfan | 260 | 106 |
| Electroplated Sollac | 423 | 138 |
| Galvaneal | 224 | 172 |

Laser beam focusing at -20 mm with laser energy 100 mJ/pulse. Depth resolution of laser ablation depth-profiling technique is evaluated as a depth interval between 16% of the maximum signal of Fe and 16% of the maximum Zn signal.

evolution of the Zn signal (Fig. 5). A helium atmosphere seems to be the most appropriate for depth profiling using 100 mJ laser pulse energy due to the lowest tailing of the zinc emission signal.

Photographs in Fig. 7a–c show craters produced at a laser energy of 100 mJ and an optimized laser beam focusing on the Electroplated Zn coating—Sollac sample in air, Ar and He ambient atmospheres, respectively, for a various number of pulses. In the air (and Ar) during the drilling process melted material accumulates at the bottom of the ablation crater. The composition of this material was analyzed by SEM-EDX and it was shown in [10] that it is Zn. After a higher number of laser pulses the deposition of zinc in these gases is still observable. As an example, the Zn in air is still present after 2500 laser pulses (Fig. 7a) and 500 laser pulses in Ar (Fig. 7b). Craters obtained in a helium atmosphere do not exhibit a strong accumulation of melted zinc on the crater bed (Fig. 7c).

Fig. 7d shows the results of the optical profilometer measurements. The 3D profiles of the ablation craters after 200 shots for the three different gases were measured. The presence of Zn is evident in the ambient gases of Ar and air.

The different Zn signal-tailing in these three gases (Fig. 5) corresponds to the amount of Zn accumulated at the bottom of the ablation crater. Comparing Figs. 5a and 7a for air, it is evident that the longest signal-tailing corresponds to the highest

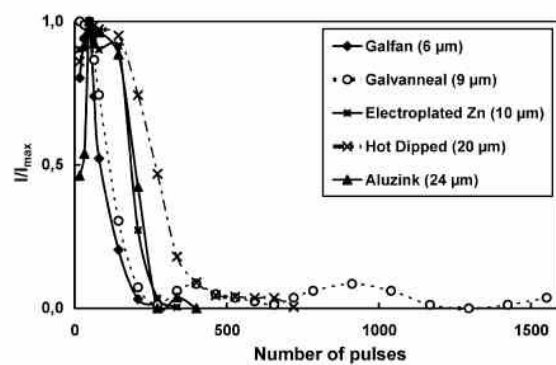


Fig. 9. Depth profiles of five Zn coating samples in helium atmosphere. Comparison of LIB signals of Zn(I) 280.08 nm at 10 μ s delay time. Ablation was performed with an energy of 100 mJ/pulse focusing at -20 mm.

Table 3
Comparison of the depth resolutions and ablation rates of Zn coatings in a He atmosphere

| Sample | Coating thickness (μm) | Ablation rate (nm/pulse) | Depth resolution (μm) |
|----------------------|-------------------------------------|--------------------------|------------------------------------|
| Hot dipped | 20 | 81 | 12 |
| Aluzink | 24 | 152 | 21 |
| Galfan | 6 | 97 | 10 |
| Electroplated Sollac | 10 | 69 | 10 |
| Galvaneal | 9 | 137 | 24 |

Laser ablation energy 100 mJ/pulse, delay time 10 μs , laser beam focusing at -20 mm. Depth resolution of laser ablation depth-profiling technique is evaluated as a depth interval between 16% of the maximum signal of Fe and 16% of the maximum Zn signal.

amount of Zn in the crater. In the case of He the signal-tailing (and the amount of Zn) is smallest (Figs. 5c–7c). We should also note that we did not observe any significant change in the Fe signal for the three different gases.

Comparisons of the ablation rates in Zn coatings estimated from the LIP signal (calculated from intersection of Zn and Fe signals) and from measurements by the optical profilometer are presented in Table 1.

3.3. Influence of the delay time between the incident laser pulse and the detected signal

The delay time appears to be another critical factor in-depth profiling by means of LIBS. Its influence was studied for all three ambient gases. Comparing two different delay times (5 and 10 μs) it was observed that the signal-tailing is lower for a longer delay time (see Fig. 8a–c) for all gases. Choosing the right delay-time was most important for He where the signal-tailing decreased considerably (Fig. 8c). This effect could probably be explained by considerably different microplasma properties at various delay times. The amount of Zn in the microplasma (determined by the ablation) does not change significantly during the LIP lifetime. However, the plasma parameters (electron temperature and density) and so the excitation of the Zn(I) line and also its self-absorption changes considerably. As a result, a roll-off on the signal *versus* content dependence occurs. Consequently, for a given delay time, the Zn(I) emission signal obtained from the pure coating may have the same intensity as the signal generated on the Zn–Fe interface or even at the crater bottom (in Fe substrate splashed with residual Zn). In other words, an incorrectly higher Zn content is attributed to the magnitude of Zn signal-tailing which results in a deformation of the normalized intensity *versus* depth profile. As an example one can refer to the different duration of the signal-tailing in the He atmosphere (Fig. 8c), caused by a stronger self-absorption at the shorter delay time (5 μs).

In order to compare the different zinc-coated steel samples, we expressed the depth resolution as the depth interval corresponding to points at which the Zn signal falls to 16% of its maximum value in the coating and the Fe signal reaches 16% of its maximum value in the substrate (Fig. 8c). The comparison of the depth resolution values for all studied samples measured in the helium atmosphere at the two delay times is presented in Table 2.

Comparison of the LIP signals of Zn(I) line at 280.08 nm at 10 μs delay time in a helium atmosphere for the five different samples is shown in Fig. 9. It was found that the Zn line intensity profile corresponds to the Zn coating thickness for Galfan, electroplated zinc and hot dipped Zn samples. In the case of the Aluzink sample, which contains about 50% aluminum, the presence of Al in the coating significantly influenced the ablation rate. A twice as high ablation rate in Aluzink (in comparison to other coatings) has already been reported by Hrdlička et al. [10]. A similar effect is also observable for Galvaneal which contains aluminium, iron, manganese and phosphorus. The depth resolution values together with ablation rates in He for various Zn coatings are presented in Table 3.

4. Conclusions

The feasibility of depth profiling of zinc-coated iron sheets by LIBS was studied using a 1064 nm Nd:YAG laser system. The LIP plasma emission was measured by applying a monochromator coupled to a “low-cost” detection system consisting of a single photomultiplier detector connected to an oscilloscope. The study of several experimental parameters (energy delivered to the sample, focusing conditions, the delay time and choice of different surrounding gases) influencing zinc and iron emission signals was performed. It follows from the experiments conducted that the choice of surrounding gas affects optimal focusing distance. Microplasma produced in a helium atmosphere exhibits the shortest lifetime while in an argon atmosphere the microplasma emits the longest radiation. The surrounding atmosphere has a critical effect on the temporal behavior of the Zn signal generated in the course of drilling. In the case of an air atmosphere the strongest signal-tailing was observed whereas a helium atmosphere seemed to be most appropriate for depth profiling due to the shortest tailing of the zinc emission signal. It was also found that the surrounding gases crucially influence ablation rates. The lowest ablation rate was observed in an air atmosphere. Ablation rates in Zn coatings estimated from the LIP signal (calculated from the intersection of the Zn and Fe signals) are in agreement with measurements made by means of an optical profilometer.

The delay time appears to be another critical factor in-depth profiling by means of LIBS. Zn signal-tailing is much lower at the delay time of 10 μs than at 5 μs . This could be due to a variation in the degree of self-absorption as the plasma expands and cools. A similar behavior was found for all the samples studied.

Acknowledgements

K. Novotný acknowledges support from Czech Science Foundation GACR 203/02/P097; T. Vaculovič, V. Otruba and V. Kanický acknowledge support from The Ministry of Education, Czech Republic MSM0021622411, J. Kaiser, M. Liška, O. Samek and R. Malina acknowledge support from The Ministry of Education, Czech Republic MSM0021630508. The authors would also like to express their thanks to Zdenek Weiss (LECO Instrumente Plzeň, Czech Republic) for providing the samples and GD-OES depth profile data.

References

- [1] S. Oswald, S. Baunack, *Thin Solid Films* 425 (2003) 9–19.
- [2] R. Balková, J. Zemek, V. Čech, J. Vaněk, R. Příkrýl, *Surf. Coat. Technol.* 174 (2003) 1159–1163.
- [3] R. Klockenkamper, H.W. Becker, H. Bubert, H. Jenett, A. von Bohlen, *Spectrochim. Acta B* 57 (2002) 1593–1599.
- [4] Z. Weiss, *Spectrochim. Acta B* 47 (1992) 859–876.
- [5] R. Payling, M. Aeberhard, D. Delfosse, *J. Anal. At. Spectrom.* 16 (2001) 50–55.
- [6] V. Kanický, V. Otruba, J.M. Mermet, *Fresenius J. Anal. Chem.* 366 (2000) 228–233.
- [7] V. Kanický, I. Novotný, J. Musil, J.M. Mermet, *Appl. Spectrosc.* 51 (1997) 1037–1041.
- [8] A.G. Coedo, T. Dorado, I. Padilla, J.C. Farinas, *J. Anal. At. Spectrom.* 20 (2005) 612–620.
- [9] V. Kanický, H.R. Kuhn, D. Guenther, *Anal. Bioanal. Chem.* 380 (2004) 218–226.
- [10] A. Hrdlička, V. Otruba, K. Novotný, D. Guenther, V. Kanický, *Spectrochim. Acta B* 60 (2005) 307–318.
- [11] J.M. Vadillo, C.C. Garcia, S. Palanco, J.J. Laserna, *J. Anal. At. Spectrom.* 13 (1998) 793–797.
- [12] J.M. Vadillo, J.M.F. Romero, C. Rodriguez, J.J. Laserna, *Surf. Interface Anal.* 26 (1998) 995–1000.
- [13] J.M. Vadillo, J.J. Laserna, *J. Anal. At. Spectrom.* 12 (1997) 859–862.
- [14] M.P. Mateo, J.M. Vadillo, J.J. Laserna, *J. Anal. At. Spectrom.* 16 (2001) 1317–1321.
- [15] C.C. Garcia, J.M. Vadillo, S. Palanco, J. Ruiz, J.J. Laserna, *Spectrochim. Acta B* 56 (2001) 923–931.
- [16] L. St-Onge, M. Sabsabi, *Spectrochim. Acta B* 55 (2000) 299–308.
- [17] I. Radivojevic, C. Haisch, R. Niessner, S. Florek, H. Becker-Ross, U. Panne, *Anal. Chem.* 76 (2004) 1648–1656.
- [18] J.A. Aguilera, C. Aragon, *Appl. Phys. A* 69 (1999) S475–S478.
- [19] J.A. Aguilera, J. Bengoechea, C. Aragon, *Spectrochim. Acta B* 59 (2004) 461–469.
- [20] J.M. Vadillo, J.J. Laserna, *Spectrochim. Acta B* 59 (2004) 147–161.
- [21] Z. Weiss, P.J. Šmíd, *Anal. At. Spectrom.* 15 (2000) 1485–1492.
- [22] Z. Weiss, Application report 98-7P, LECO Pilsen CZ, 1998.
- [23] L.M. Cabalin, J.J. Laserna, *Spectrochim. Acta B* 53 (1998) 723–730.

6.2 **ARTICLE 2**

Vaculovic, T.; Sulovsky, P.; Machat, J.; Otruba, V.; Matal, O.; Simo, T.; Latkoczy, C.; Gunther, D.; Kanicky, V. *Journal of Analytical Atomic Spectrometry* 2009, 24, 649-654 (IF=3.646)

The EPMA, LA-ICP-MS and ICP-OES study of corrosion of structural materials for a nuclear reactor cooling circuit by molten fluoride salt treatment†

T. Vaculovic,^a P. Sulovsky,^b J. Machat,^a V. Otruba,^a O. Matal,^c T. Simo,^c Ch. Latkoczy,^d D. Günther^d and V. Kanicky^{*,a}

Received 24th July 2008, Accepted 9th March 2009

First published as an Advance Article on the web 26th March 2009

DOI: 10.1039/b812766b

Electron probe microanalysis (EPMA), inductively coupled plasma atomic emission spectrometry (ICP-OES), and laser ablation inductively coupled plasma mass spectrometry (LA-ICP-MS) were applied to study the interaction of molten LiF-NaF salt mixtures with candidate structural materials (alloys) for a nuclear reactor-transmutor cooling circuit. The corrosion of test ampoules and inserted test specimens made of structural materials was brought about by the action of molten LiF-NaF coolant at 680 °C and its extent and character were examined in dependence on the time of exposure. The material corrosion changes were studied by mapping the sections of ampoule walls and inserted specimen surfaces with EPMA, whereas LA-ICP-MS was employed for linear scanning the salt/ampoule wall boundary. Corrosion-released structural material, dissolved in solidified molten salt, was analyzed by ICP-OES after the salt dissolution. The melt activity was proved to induce a surficial modification of a structural material up to the depth of 15–50 µm, which was associated with the coolant contamination. The X-ray maps by EPMA with its 1-µm lateral resolution revealed compositional changes in alloys, such as regular depletion of Cr to the depth of 10–25 µm. While the lateral resolution of LA-ICP-MS with the applied laser spot diameter of 25 µm was not exactly adequate to dimensions of the corroded regions and, consequently, yielded less information in comparison with EPMA, this technique was quite sufficient for the monitoring of the presence of alloy constituents in an adhered salt layer. It was concluded that: *i*) the EPMA study, involving semi-quantitative elemental mapping/content profiling and detailed spot quantitative analyses makes it possible to obtain quantitative assessment of the corrosion process; *ii*) LA-ICP-MS profiles can be converted from signal domain to elemental contents on a semi-quantitative level when applying signal normalization to the total sum of signals.

1. Introduction

Nowadays, in some countries the spent nuclear fuel from commercial power reactors is accumulated at first in temporary repositories and later, considered as nuclear waste, deposited in a permanent underground repository. In other countries, reprocessing of the spent fuel is carried out to separate uranium and plutonium and produces mixed oxide fuel for power reactors. In the Generation IV of power reactors, molten salt reactors (MSR) and partitioning and transmutation methods are considered, amongst others, with the aim of utilizing fissile actinides from the nuclear spent fuel and minimizing volume and radiotoxicity of wastes for underground repositories. In the

MSRs, molten fluoride salts (*e.g.* LiF-BeF₂, NaBF₄-NaF)¹ are considered, amongst others, as coolants.

Molten fluoride salts at 500 °C represent a considerably invasive and corrosive media for the material of piping and other circuit parts. It is known that fusion with alkali fluorides is used in chemical analysis for the decomposition of resistant materials, *e.g.* minerals and rocks.² Similarly, fluoride coolant attacks also to some extent corrosion-resistant materials of the heat exchanger circuit.³ Consequently, besides mechanical and thermal influence of molten fluoride salts it is important to investigate their chemical effect on the constructional material.

Corrosion of the piping inner surface and composition of the fluoride in contact with the piping needs to be studied in relation both to the construction material type, and the coolant composition, as well as to the duration of the melt-exchanger contact, melt temperature and some other conditions. For the study of corrosion processes, methods of local surface elemental analysis were employed, involving glow discharge with optical emission detection (GD-OES),⁴ electron probe X-ray microanalysis (EPMA),⁵ atomic force microscopy⁶ and scanning electron microscopy (SEM).^{6,7} Changes in coolant composition, including the main constituents (*e.g.* F⁻, Li⁺, Na⁺, K⁺) as well as elements released from the construction material by corrosion

^aLaboratory of Atomic Spectrochemistry, Faculty of Science, Masaryk University, Kotlarska 2, 611 37 Brno, Czech Republic. E-mail: viktork@chemi.muni.cz

^bLaboratory of Electron Microscopy and Microanalysis, Faculty of Science, Masaryk University, Kotlarska 2, 611 37 Brno, Czech Republic

^cEnergovyzkum, Ltd., Bozotechova 17, 612 00 Brno, Czech Republic

^dLaboratory of Inorganic Chemistry, ETH Zurich, Wolfgang-Pauli Strasse 10, 8093 Zurich, Switzerland

† This article is dedicated to Professor Jean-Michel Mermet, in recognition of his contributions to the field of atomic spectrometry.

(particularly Cr, Mo, Ni and Fe) need to be monitored—at first during optimization of a fluoride mixture composition and selection of a construction material type, and later for the routine operation checking.

For the analysis of fresh and used fluoride salts, atomic spectrometry methods might be appropriate, such as atomic absorption spectrometry (AAS),⁸ optical emission spectrometry with inductively coupled plasma (ICP-OES).⁹ Unlike local surface analysis, which is indispensable for the characterization of material changes at the boundary between the coolant and the piping, determination of contaminants in solidified fluoride coolant requires representative sampling of sufficient amount of salt due to expected inhomogeneous distribution of corrosion products. Such a sample is dissolved in (acidified) aqueous medium and analyzed by using flame AAS or ICP-OES/MS with pneumatic nebulization of the solution.⁹

The aim of this work is to evaluate the applicability and performance of selected analytical techniques for characterization of the corrosive action of fluoride (LiF-NaF) melts at temperatures above 500 °C on candidate structural materials when selecting the most resistant metal or alloy. A coolant based on a binary mixture of fluorides has been selected and included in optimization experiments designed for realization of a secondary circuit that would be used in a future transmutor. This study is applicable generally to heat exchangers that use corrosive media for heat exchange/transfer.

Besides EPMA and SEM, ICP-MS coupled with laser ablation (LA) as a means of local solid sampling was employed for the inspection of boundary alloy–solidified coolant. Unlike EPMA and SEM, which are considered routine techniques for surface elemental analysis, LA-ICP-MS has only been used very rarely so far for acquisition of elemental distribution across the boundary of this kind and therefore, it presents a novelty.¹⁰

The advantage of LA-ICP-MS in comparison with EPMA might consist in faster analysis and in its capability to detect lithium in corroded structural material. As the diameter of the focused laser beam is of the order of tens of micrometers while the electron beam of EPMA has typical diameter of 1 micrometer, a single line scan with LA-ICP-MS would bring information on compositional changes of a sufficiently representative area of the material section within a shorter time in comparison with EPMA, which requires the use of a raster scan for the same area. On the other hand, EPMA has excellent lateral resolution which it uses to possibly detect small material defects. The technique of LA-ICP-MS is operated at atmospheric pressure whereas EPMA operates at vacuum conditions. Degasification of porous material and evacuation of the EPMA working space needs also some time while LA-ICP-MS requires only a few seconds for ablation cell purging with the working gas.

The technique of GD-OES makes it possible to perform depth profiling perpendicularly to the corroded surface. A depth profile with a good depth resolution, which is averaged and smoothed over the sputtered area, can be obtained up to tens or hundreds of micrometers in depth. However, lateral resolution (discharge diameter of the order of mm) is not sufficient in the case of laterally inhomogeneous surfaces. However, the resulting depth profile is averaged from a large sputtered area and small material defects are not detectable. In depth profiling of corrosion layers the technique of GD-OES presents advantage over possible

LA-ICP-MS depth profiling when we are not interested in lateral resolution. In contrast to LA-ICP-MS, GD-OES is capable of detecting and determining oxygen in the corroded layer, which possesses crucial information for nuclear technology development.

Concerning the corroded sample section imaging, the best results are obtained with SEM, which is ideally complementary to GD-OES depth profiling.

Consequently, LA-ICP-MS might be complementary to EPMA and comparable with GD-OES with the above limitations.

As far as the ICP-OES solution analysis of fluoride salts is concerned, the chemical reactivity of fluoride ions complicates the application of the current instrumental equipment due to corrosion of glass and quartz parts of the ICP spectrometer. Usually, a spectrometer with standard sample introduction equipment is not adapted for nebulization of sample solutions with a high content of fluorides and therefore, it was necessary to replace glass parts with components made of resistant materials, such as PFA or Teflon.⁹

2. Experimental

Inconel (A 686) and stainless steel 1.4571 were tested as candidate materials for the construction of a reactor secondary cooling circuit. Nickel and iron are base constituents of Inconel A 686 and stainless steel 1.4571, respectively. The composition of candidate materials is given in Table 1.

Corrosion by the action of the fluoride salt mixture with the molar composition of 60% LiF and 40% NaF was studied in this work. Of the whole fluoride salt family intended for heat exchange and transfer, this candidate cooling medium was chosen for its relatively high melting temperature of 655 °C. The corrosion tests were performed in ampoules^{11,12} (height 185 mm, inner diameter 21.3 mm, wall thickness 2 mm), made of candidate structural materials and filled with a mixture of LiF and NaF. Ampoules were exposed to a constant temperature of 680 °C for 380 and 1000 hours, respectively. After cooling down, the ampoule with solidified melt was cut along its axis. The melt was then ground in a ball mill. Powdered material was further processed for ICP-OES solution analysis and for titrimetric determination of fluorides.⁹ The precipitation titrimetric method based on reaction of fluoride and thorium(IV) nitrate solution was applied for quantification of fluoride content. Glycine–perchloric acid–sodium perchlorate buffer was applied for adjusting the pH value to 3.4 while ascorbic acid served as a masking agent for Fe(III), otherwise interfering with indication of equivalence. Methylthymol blue indicates equivalence and changes from blue [complex indicator–Th(IV)] to yellow (free indicator).¹³

Table 1 Composition of candidate materials for construction of a transmutor secondary cooling circuit obtained by EPMA on the examined samples

| Material | Elemental content (% m/m) | | | | | | | | | | | |
|----------|---------------------------|-------|------|------|------|------|-------|------|------|-------|------|-------|
| | Si | P | Mn | Co | W | Fe | S | Ti | Mo | Cr | Ni | Total |
| 1.4571 | 1.0 | 0.045 | 2.0 | — | — | 64.3 | 0.03 | 0.8 | 2.25 | 17.5 | 12 | 99.93 |
| Inconel | 0.05 | 0.001 | 0.25 | 0.04 | 3.83 | 0.32 | 0.001 | 0.11 | 16 | 20.26 | 59.1 | 99.96 |

Annular pieces of ampoule cut with a diamond saw were further sectioned to obtain cuts perpendicular to the ampoule wall. These were embedded into epoxy resin (Araldite) disks and lapped and polished with diamond pastes for EPMA and LA-ICP-MS measurements.

Electron probe microanalysis was performed with an SX100 microprobe (CAMECA, France). The acceleration voltage was set on 15 kV. The analysis spot size was 1 μm . The standardization was checked for interferences and cross-checked with a stainless steel standard SRM 460b (SPI). The acquired quantitative data were corrected using the modified ZAF method (PhiRoZet, CAMECA).

Instrumentation for LA-ICP-MS consists of a laser ablation system LSX 500 (Cetac, Omaha, USA) and an ICP-MS spectrometer Element2 (Thermo Electron, Bremen, Germany). Optimized parameters of the ICP source and the sector field MS are summarized in Table 2. A commercial Q-switched Nd:YAG laser ablation device is designed for operation at the 4th harmonic frequency which corresponds to the wavelength of 266 nm. The ablation device is equipped with programmable XYZ-stages which makes it possible to set the required XY-position on the target surface and/or to move the sample along a programmed trajectory during ablation. Optimization of the LA-ICP-MS facility (gas flow rates, sampling depth, electrostatic lenses voltages of the MS) was performed with the glass reference material NIST SRM 612 in respect to maximum S/N ratio and minimum oxide formation (ThO⁺/Th⁺ count ratio 0.2%, U⁺/Th⁺ count ratio 1.1%).¹⁴ A single line scan perpendicular to the alloy surface was used for LA-ICP-MS measurements with a 25 μm laser spot diameter.

For quantification purposes a normalization method which uses a total sum of signals of isotopes was employed.¹⁰ The blank-corrected isotope signal was abundance-corrected to obtain the elemental signals. Particular elemental signals were normalized to the sum of all element signals to obtain elemental content. ICP-MS signals were measured for all elements shown in Table 1 and for Li and Na, which are present in molten fluoride salts. The fluorine signal was calculated as the sum of the Li and Na signals.

Analysis of solutions was accomplished by means of a Jobin-Yvon 170 Ultrace ICP spectrometer (JY-Horiba, Longjumeau, France), equipped with a poly- and monochromator. The standard glass sample introduction system (Meinhard concentric nebulizer and cyclonic spray chamber) was replaced with sample introduction system for fluoride solutions, which consisted of the PFA cross-flow nebulizer with solution capillary made of Pt and

Table 2 ICP-MS operating conditions used for laser ablation study of elemental content profiles within the salt layer on the ampoule wall inner surface

| ICP-MS | Element2 (Thermo Electron) |
|--------------------------------|----------------------------|
| rf power | 1350 W |
| sample gas flow | 0.95 l/min Ar |
| auxiliary gas flow | 0.6 l/min Ar |
| cooling gas flow | 15.0 l/min Ar |
| carrier gas flow | 0.86 l/min He |
| m/ Δ m | 300 |
| sampler/skimmer cones material | Pt |

a spray chamber made of PFA. Matrix-matched calibration solutions were used for determination of the content of corrosion products in molten fluoride salts.

3. Results and discussion

3.1. Analysis of corroded surfaces by EPMA

The **Inconel 686** test samples exposed to melt for 1000 hours show significant compositional changes at the boundary. Quantitative results of electron microprobe analyses are presented in Table 3 and corresponding modifications of surface layer are shown in Figs. 1 and 2. In the layer between 0 and 10–20 μm below the surface, nickel is enriched by one third of the original content in the intact material (Fig. 1a). Similarly, molybdenum exhibits increased content in this layer, too. Iron and cobalt are distinctly enriched in the outermost layer between 0 and 5 μm . On the other hand, chromium content drops in the same layer to less than one-fourth of its value found in the intact material and the zone depleted in Cr exhibits quite a sharp boundary with the intact material (Fig. 1b). Besides, a part of chromium released from this surficial layer reacts with oxygen dissolved in the salt melt and forms a thin, more or less continuous chromium trioxide crust. This is evident in Fig. 1b as a thin white zone where chromium content attains double the value for the intact material. Manganese exhibits similar depletion as Cr (Fig. 1c). The crust of Cr₂O₃ is evident from the BSE (back scattered electron) surface image in Fig. 2a as well as from the BSE image of polished sections in Fig. 2b. In areas where this crystalline crust is absent

Table 3 Comparison of composition of Inconel A686 exposed to molten LiF-NaF salt mixture (microgranular phase) and of unaffected zone of Inconel A686 by means of EPMA spot analyses

| Inconel A686 Elements | EPMA, Elemental content (% m/m) | | | | | |
|-----------------------|---------------------------------|----|----|-----|------|------|
| | Cr | Ni | Mo | Mn | Fe | Co |
| Unaffected | 20.7 | 59 | 16 | 0.3 | 0.09 | 0.01 |
| Corroded | 5.1 | 74 | 21 | 0.1 | 1.30 | 0.04 |

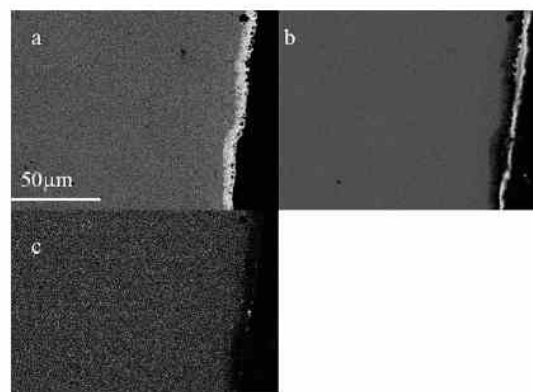


Fig. 1 X-ray elemental mapping of Inconel after 380-hours exposure to LiF-NaF at 680 °C: (a) Ni, (b) Cr, (c) Mn; lighter colour corresponds to higher content.

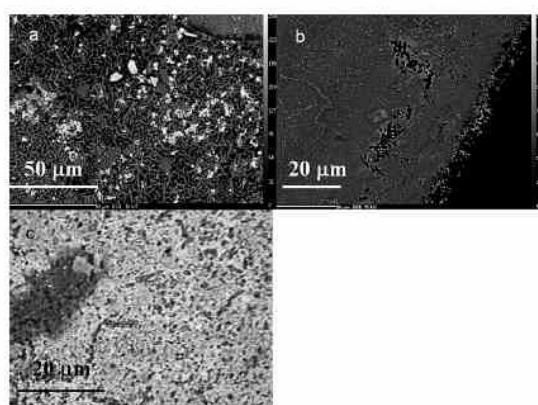


Fig. 2 Inconel after 380-hours exposure to LiF-NaF at 680 °C: (a) BSE image of surface with Cr_2O_3 crystalline salt layer (bright grey platelets) and fragments of Inconel alloy, enriched in Mo (white grains); (b) BSE image of polished section with Cr_2O_3 crust on the wall/melt boundary and voids following grain boundaries, rimmed with W, Ni-enriched material; (c) BSE image of the test body surface, area without Cr_2O_3 crust, showing pitting; in all BSE images lighter colour corresponds to higher content.

or removed the surface appears to be punched by tiny channels or pits formed preferably at grain boundaries (Fig. 2c). These channels, which exhibit a depth less than 20 μm , are always rimmed with a narrow zone of Ni (Mo) enrichment (Fig. 2b). Based on EPMA measurements and observations it can be concluded that the corrosion of Inconel by LiF-NaF melt is characterized by two processes: *i*) diffusion and dissolution of the alloy, and *ii*) oxidation of released chromium by a trace amount of oxygen present in the argon atmosphere in the space above the fluoride melt level. The intergranular corrosion is combined with diffusional substitution of elements leached out by the melt (particularly Cr), leading to enrichment in Ni, W and Mo.

The stainless steel exposed for 1000 hours to the LiF-NaF melt exhibits a granular texture characterized with grains ranging from 7 to 15 μm . Lateral distribution of chromium is not homogeneous, because it contains small (1–4 μm) inclusions of a Cr/Mo-rich phase, which means weak depletion of chromium at the grain boundaries. The stainless steel 1.4571 corrosion proceeds preferentially along grain boundaries, which is evidenced by the formation of narrow etched channels (crevices) or chains of pores. The depth of these channels depends on the duration of contact with the fluoride melt and on the fact whether the static or dynamic regime is considered. The channels are rimmed with narrow Fe/Ni-enriched and Cr/Mn-depleted zones (Figs. 3a–d). The thickness of the contiguous zone of Fe/Ni enrichment is about 7 μm . The degree of enrichment of Fe, Ni, and Co represents about one fourth to one third of their original contents. Of minor and trace elements, Mn, Mo, Si and Ti are depleted in the 50- μm surficial zone. Besides the general decrease (from 2 to 1% m/m) in this zone, Mn shows also local spot enrichment up to the depth of 10 μm . The Mn-rich spots do not match the Fe/Ni enrichment zone and they are localized in some pores or parts of channels depleted in Cr (Fig. 3d). Beneath the

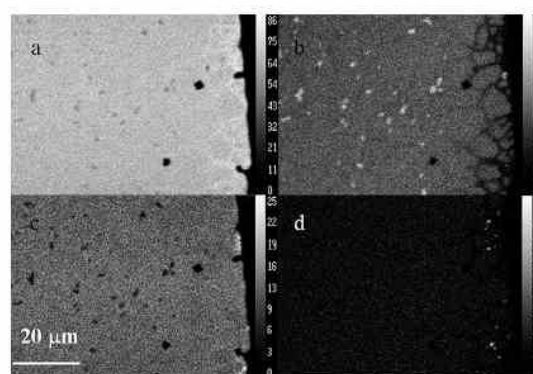


Fig. 3 X-ray elemental mapping of Stainless steel 1.4571 after 1000-hours exposure to LiF-NaF at 680 °C: (a) Fe, (b) Cr, (c) Ni, (d) Mn; lighter colour corresponds to higher content.

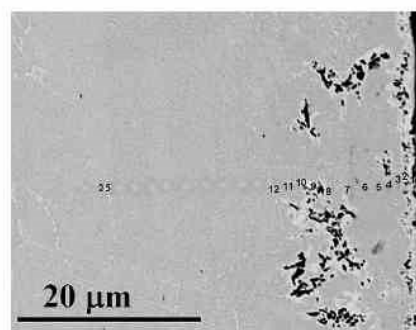


Fig. 4 Stainless steel 1.4571 after 1000-hours exposure to LiF-NaF at 680 °C: BSE image, a close-up view of the near-surface area of polished section; lighter colour corresponds to higher content.

7- μm Fe/Ni enrichment zone the Fe/Ni enrichment continues, but it follows only some grain boundaries or chained pores (Fig. 4).

3.2. Analysis of used fluoride salt coolant

The main cationic constituents of the coolant—sodium and lithium—were determined by ICP-OES, similarly to the products of ampoule wall corrosion. Mutual non-spectral interferences of the main cationic constituents (Li, Na) are observed even when measuring the signal in the normal analytical zone. These multiplicative interferences were eliminated by using matrix-matched calibration solutions containing theoretically the same amount of both elements as analyzed samples. This precaution compensates for the Li and Na signal depression observed with solution containing at the same time both Li and Na in comparison to single-element Li, Na solutions. On the contrary, the matrix effect of fluoride ion on Na/Li signals was not observed despite a relatively high F^- concentration (500 mg/l). This can be explained by the high first ionization energy of fluorine which causes only insignificant fluorine ionization in the plasma. Hence it has only negligible impact on excitation processes in the ICP source.

Contents of corrosion products (major and medium constituents of the particular construction materials, *i.e.* Ni, Cr, Fe and Mo) were determined using matrix-matched calibration solutions. For the quantification of the overall corrosion process, the total content of corrosion products was calculated. It was found that the content of corrosion products increased with the time of exposure for both materials and it was observed that stainless steel exhibited higher corrosion rate in comparison to Inconel (Table 4). The sum of corrosion products of the stainless steel was close to 0.6% m/m after 1000 h of exposure. In the case of Inconel the sum of corrosion products was three times lower in comparison with stainless steel. Detailed information on the presence of individual elements of corroded structural material in exposed salt mixture was published in ref. 9.

3.5. Qualitative profiling of metal/salt boundaries by LA-ICP-MS

Compositional changes along the boundary salt layer/ally were determined for Inconel A686 and stainless steel 1.4571 exposed to LiF-NaF mixture at 680 °C after the 380-hours and 1000-hours exposure. The samples were ablated perpendicularly to the sample surface in several areas of the sample surface. The concentration of all elements was calculated using the total sum of signal normalization method. The thickness of the affected zones is determined based on lithium and sodium contents because these elements are not present in the original candidate material and their presence is caused by molten fluoride salt treatment only. Fig. 5 represents a single line scan over Inconel A686 sample after 380-hours exposure. Compositional changes are observed in the affected zone. Nickel, molybdenum and iron are enriched in this layer in comparison with non-affected material whereas chromium and manganese are depleted in this

Table 4 Total content of corrosion products in the salt mixture after 380-h and 1000-h exposure at 680 °C determined by means of ICP-OES

| Sample | Inconel A686 | | Steel 1.4571 | |
|-----------------------------------|--------------|------|--------------|------|
| Exposure time [h] | 380 | 1000 | 380 | 1000 |
| Sum of corrosion products (% m/m) | 0.12 | 0.19 | 0.23 | 0.63 |

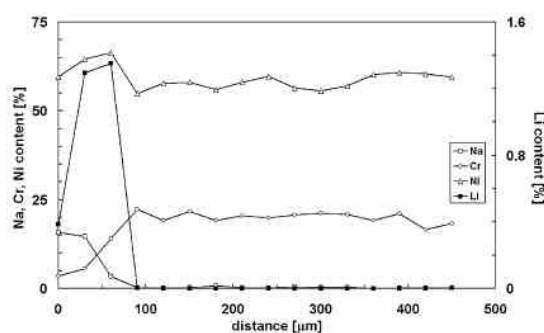


Fig. 5 The LA-ICP-MS single-line scan of Inconel after 380-hours exposure to LiF-NaF at 680 °C.

zone. Elemental contents of corroded and non-affected materials are shown in Table 5. Elemental content is not homogeneous in the corroded layer hence the concentration interval is used in Table 5. Inconel A686 exposed to 1000-hours molten salt treatment shows similar behavior; same elements are enriched and depleted, respectively. The main difference consists in the thickness of the affected zone (Table 6). Longer molten salt treatment causes larger damage of the sample surface; 90 µm for 380 hours and 120 µm for 1000 hours.

Stainless steel exposed to molten fluoride salt treatment during 1000 hours shows great inhomogeneity in lateral elemental distribution, which is evident in Table 7. First the line scan shows a large depletion of Fe, Ni and Mo in the corroded layer in comparison with non-affected material. The content of Cr and

Table 5 Composition changes on Inconel A686 induced by the action of molten LiF-NaF salt mixture at 680 °C for 380 h and 1000 hours, found by means of LA-ICP-MS measurements performed in two affected areas of a sample, and for comparison in adjacent unaffected regions

| Inconel A686 sample | | | | |
|----------------------|------------------|--------------------|------------------|--------------------|
| Time of exposure (h) | | | | |
| Element | 380 | | 1000 | |
| | Corroded (% m/m) | Unaffected (% m/m) | Corroded (% m/m) | Unaffected (% m/m) |
| Li | 0.42–1.40 | — | 0.22–0.96 | — |
| Na | 0.36–15.8 | — | 1.05–9.13 | — |
| Cr | 3.51–14.1 | 20.0 | 1.71–13.3 | 20.5 |
| Mn | 0.04–0.10 | 0.40 | 0.03–0.43 | 0.32 |
| Fe | 0.18–0.70 | 0.05 | 0.11–0.55 | 0.05 |
| Ni | 69.7–76.4 | 60.2 | 68.3–74.6 | 59.9 |
| Mo | 18.3–19.5 | 15.4 | 16.3–18.6 | 15.6 |

Table 6 Thickness of affected zone of the candidate materials after 380 h and 1000 h exposure at 680 °C

| Material | Inconel A686 | | Steel 1.4571 | |
|------------------------------|--------------|------|--------------|------|
| Exposure time [h] | 380 | 1000 | 380 | 1000 |
| Affected zone thickness [µm] | 90 | 120 | 125 | 240 |

Table 7 Composition changes on stainless steel 1.4571 induced by the action of molten LiF-NaF salt mixture at 680 °C for 1000 hours, found by means of LA-ICP-MS measurements performed in two affected areas of a sample, and for comparison in adjacent unaffected regions

| Stainless steel 1.4571 sample | | | | |
|-------------------------------|------------------|--------------------|------------------|--------------------|
| Element | Analyzed area 1 | | Analyzed area 2 | |
| | Corroded (% m/m) | Unaffected (% m/m) | Corroded (% m/m) | Unaffected (% m/m) |
| Li | 0.09–1.94 | — | 0.24–1.57 | — |
| Na | 0.64–19.5 | — | 0.10–9.31 | — |
| Cr | 15.2–18.6 | 17.9 | 2.25–5.70 | 17.8 |
| Mn | 1.85–1.95 | 2.15 | 0.80–1.42 | 2.20 |
| Fe | 30.9–34.5 | 67.5 | 71.9–74.0 | 66.2 |
| Ni | 3.17–4.88 | 11.4 | 6.79–8.16 | 11.6 |
| Mo | 0.60–1.68 | 2.68 | 1.26–2.13 | 2.71 |

Mn in this layer is close to the content in the non-affected layer. A different course is observed for the line scan in the other part of the sample; Fe is enriched in this part of the corroded layer whereas Cr, Mn, Mo and Ni are depleted in this zone. However, differences are not visible in the case of the thickness of the corroded layer, which is 240 μm for both line scans. Similarly to Inconel, the duration of molten salt treatment affects the thickness of the corroded layer; which attains 125 μm for 380 hours and 240 μm for 1000 hours of treatment (Table 6).

The main advantage of LA-ICP-MS in comparison with EPMA is the possibility to detect and determine Li (Na) as constituents of molten fluoride salts, which are present on the surface of the examined material due to corrosion processes during molten fluoride salt treatment. Hence LA-ICP-MS allows more accurate determination of the thickness of the corroded layer than EPMA.

4. Conclusions

Investigation of molten LiF-NaF mixture-induced corrosion of alloys that are designed as candidate structural materials for transmutor cooling circuit construction was performed in laboratory-built test equipment. The corrosion of surfaces of test ampoules and test bodies was evaluated based on results of electron probe X-ray microanalysis. Corrosion products in used fluoride salts were determined by solution analysis with ICP-OES. An elemental content profile of the solidified salt layer/alloy boundary was also obtained by means of EPMA. The results are in accordance in previous observations,³ stating the crucial role of chromium content in the candidate alloy. The laser ablation ICP-MS technique was used for chemical mapping of the solidified salt layer/wall sections. The latter technique offers quantitative profiles with lateral resolution suitable particularly for the salt layer description. The novelty of the results consists in a detailed description of the alloy/molten salt boundary, especially of the chemical composition of the corrosion-influenced surficial zone in the alloy and its microstructure, obtained by EPMA and LA-ICP-MS.

Acknowledgements

V. Kanický, T. Vaculovic, O. Matal, and T. Simo acknowledge the Czech Science Foundation for support of project GA 101/08/1100. V. Kanický acknowledges the Ministry of Education, Youth and Sports, Czech Republic for support in the framework of the project MSM0021622410. V. Otruba and T. Vaculovic acknowledge the Ministry of Education, Youth and Sports, Czech Republic for support in the framework of the project MSM0021622411. J. Machát acknowledges the Ministry of Education, Youth and Sports, Czech Republic for support in the framework of the project MSM0021622412.

References

- 1 H. Moriyama, A. Sagara, S. Tanaka, R. W. Moir and D. K. Sze, *Fusion Eng. Des.*, 1998, **39**, 627.
- 2 M. Q. Li and G. L. Messing, *Thermochim. Acta*, 1984, **78**, 9.
- 3 C. A. C. Sequeira, *High Temperature Corrosion in Molten Salts*, Trans Tech Publications, Erfield, USA, 2003.
- 4 L. Martinelli, F. Balbaud-Celrier, G. Picard and G. Santarini, *Corros. Sci.*, 2008, **50**, 2549.
- 5 M. Suarez, S. Bellayer, M. Traisnel, W. Gonzales, D. Chicot, J. Lesage, E. S. Puchi-Cabrera and M. H. Staia, *Surf. Coat. Technol.*, 2008, **202**, 4566.
- 6 R. M. Pidaparti and R. R. Patel, *Mater. Lett.*, 2008, **62**, 4497.
- 7 A. Pardo, M. C. Merino, A. E. Coy, F. Viejo, R. Arrabal and S. Feliu, *Electrochim. Acta*, 2008, **53**, 7890.
- 8 M. Colognesi, O. Abollino, M. Aceto, C. Sarzanini, E. Mentasi and M. Braglia, *Analyst*, 1996, **24**, 299.
- 9 O. Matal, T. Simo, L. Nesvadba, V. Dvořák, V. Kanický and J. Machát, *Z. Naturforsch. Sect. A*, 2007, **62**, 769.
- 10 C. Latkoczy, Y. Muller, P. Schmutz and D. Günther, *Appl. Surf. Sci.*, 2005, **252**, 127.
- 11 O. Matal, T. Simo, L. Nesvadba, V. Kanický, P. Sulovsky and J. Machat, *Proceedings of the 7th Int. Symp. on Molten Salt Chemistry and Technology*, Toulouse, 2005.
- 12 L. Nesvadba, T. Simo, O. Matal, M. Vávra, J. Machát, P. Sulovsky and V. Kanický, *5th Nicholas Meeting of the Young Generation of the Czech Nuclear Society*, Brno, 2005.
- 13 Anonymous, *Analyst*, 1972, **97**, 734.
- 14 I. Rodushkin, M. D. Axelsson, D. Malinovsky and D. C. Baxter, *J. Anal. At. Spectrom.*, 2002, **17**, 1231.

6.3 **ARTICLE 3**

Vaculovic, T.; Warchilova, T.; Simo, T.; Matal, O.; Otruba, V.; Mikuska, P.; Kanicky, V.
Journal of Analytical Atomic Spectrometry 2012, 27, 1321-1326 (IF=3.646)

Cite this: DOI: 10.1039/c2ja30037k

www.rsc.org/jaas

TECHNICAL NOTE

Elemental mapping of structural materials for a nuclear reactor by means of LA-ICP-MS†

T. Vaculovič,^{ab} T. Warchilová,^{ab} T. Šimo,^c O. Matal,^c V. Otruba,^a P. Mikuška^d and V. Kanický^{e,ab}

Received 6th February 2012, Accepted 23rd April 2012

DOI: 10.1039/c2ja30037k

Laser ablation inductively coupled plasma mass spectrometry (LA-ICP-MS) was applied to the study of the interaction of molten LiF–NaF salts with candidate structural materials for a nuclear reactor-transmutor cooling circuit. At a working temperature of 680 °C structural materials of heat exchangers are attacked and the melt–alloy interaction provokes microstructural and composition changes of the contact surface. The resulting corrosion-influenced zones were studied by LA-ICP-MS and the maps of elemental distribution were created on the semiquantitative level using the procedure based on the normalization of particular isotopic signals to the sum of signals of all isotopes present in the examined zone. Consequently, LA-ICP-MS signals were measured for structural material constituents (Ni, Cr, Fe, W, Mo, Ti, and Mn) and for cationic constituents of the cooling medium (Li and Na). The hypothetical fluorine signal was calculated as a sum of Li and Na signals. Corrosion products in the exposed cooling medium were determined by ICP-OES after dissolution. Of the three examined candidate structural materials (pure nickel, nickel-based alloy A071EV and nickel-coated iron) pure nickel exhibits the best resistance.

Introduction

Spent nuclear fuel (SNF) is deposited in repositories as nuclear waste. However, after reprocessing the SNF can be exploited *e.g.* in the so-called Molten Salt Reactors (MSRs), which utilize fissionable actinides from the SNF and minimize the volume and radiotoxicity of waste for underground repositories.^{1–3}

The MSR systems employ mixtures of molten salts either as solid fuel coolants or as media carrying molten fissile material and accomplishing heat transfer at the same time. The molten fluoride salts (MFS) and their mixtures such as LiF–BeF₂ or NaBF₄–NaF are utilised as high-temperature heat transfer media due to their favourable physical properties.^{4–9}

The MFS circulating in the MSR cooling system at temperatures above 500 °C represent corrosive media that can possibly damage the conduit and other heat exchanger parts.¹⁰ Corrosion needs to be studied in relation to both the structural material type and the coolant composition, as well as the melt temperature and

the duration of the melt–material contact. The rate of even corrosion should be up to 2.5 μm per year.¹¹ At present, pure nickel, nickel-based alloys and Hastelloy are considered as the most resistant structural materials for MSRs.^{12–14}

Corrosion processes are studied by methods of local surface elemental analysis, such as glow discharge with optical emission detection (GD-OES),¹⁵ electron probe X-ray microanalysis (EPMA),¹⁶ atomic force microscopy¹⁷ and scanning electron microscopy (SEM).^{17,18}

The application of laser ablation (LA) inductively coupled plasma (ICP) spectrometry analysis of structural materials tested for their utilisation in the technology of nuclear reactor cooling systems makes it possible to obtain spatially resolved information on elemental distribution changes at the inner surface of the cooling conduit, which may be the result of contact with the corrosive cooling medium. Similarly, a solidified coolant, such as a molten fluoride salt or a salt mixture, adhering to the inner surface of the piping, may be subjected to local or depth profile analysis to find out the thickness of the adjacent salt layer, where a contamination by dissolved conduit material extends, and to determine trace element contents.

Recently, LA-ICP-OES has been used for laboratory tests of the sodium-cooled fast reactor (SFR) cooling system¹⁹ utilizing the supercritical CO₂ for heat transfer. In case of heat exchanger boundary failure the intermixing of high-pressure CO₂ in a sodium circuit causes pressurization which together with chemical reactions may endanger the integrity of the heat exchanger.²⁰ The developed LA-ICP-OES method has been used

^aLaboratory of Atomic Spectrochemistry, Department of Chemistry, Faculty of Science, Masaryk University, 611 37 Brno, Czech Republic. E-mail: viktork@chemi.muni.cz

^bCentral European Institute of Technology, Kamenice 5, Brno, 62500, Czech Republic

^cENERGOVÝZKUM, spol. r. o., 61200 Brno, Czech Republic

^dInstitute of Analytical Chemistry of the Academy of Sciences of the Czech Republic, v.v.i., 602 00 Brno, Czech Republic

† Electronic supplementary information (ESI) available. See DOI: 10.1039/c2ja30037k

for the determination of carbon in sodium after its exposure to CO₂ at high temperatures. The depth-profile analysis of the exposed solidified sodium provided evidence of the penetration of the chemical reaction into the sodium coolant.²¹

The influence of exposition time on corrosion depth for the selected candidate structural materials Inconel A686 and stainless steel 1.4571 in the presence of LiF–NaF molten salt mixture at 680 °C has recently been studied by EPMA and laser ablation inductively coupled plasma mass spectrometry (LA-ICP-MS), while the concentration of corrosion products in the exposed LiF–NaF mixture was determined by ICP-OES. It was concluded that EPMA makes it possible to obtain quantitative assessment of the corrosion process, and LA-ICP-MS single-line raster profiles can be converted from a signal domain to elemental contents on a semi-quantitative level by using signal normalization to the total sum of signals of isotopes. However, the lateral resolution of LA-ICP-MS with a laser spot diameter of 25 μm was not sufficiently adequate in comparison with the depth of the affected zones (100–200 μm).^{22,23}

The aim of this study consists in the development of an LA-ICP-MS quantitative elemental 2D-mapping procedure for the description of composition changes throughout the depth of the corrosion-affected layer formed by the action of the molten mixture of LiF and NaF at 680 °C for 1000 h.

Contrary to our previous work²² we have now focused the study on nickel-based materials which seem to be the most promising for MSR.^{1,12} Nickel is covered with a compact layer of NiF₂ in molten fluoride salts which protects the material against further attack. The corrosion resistance of elements to the action of molten fluoride salts increases with their values of Gibbs free energy of fluoride formation, which are highest for the fluorides of Mo, Co, Ni, and W.¹ Consequently, a smaller depth of the layer affected by corrosion was expected for nickel-based materials in comparison to those studied in ref. 22,23 and thus better resolution of mapping was required. Therefore, instead of the single-line raster of spots with the 25 μm diameter used in ref. 22,23, the grid of spots with the 8 μm diameter was employed. An aerosol density was measured in this study to monitor different ablation rates in the attacked and intact alloys.

It is expected that differences in the corrosion resistance of examined structural materials will be distinct from elemental maps obtained. Accordingly, the most resistant material will be assessed and the selection will be supported by analysis of the dissolved used fluoride salt previously exposed to interaction with the particular examined alloy.

Experimental

Studied structural materials, corrosion tests and sample preparation

The following candidate structural materials were studied: (i) A071EV which is a Ni-based alloy containing (in % m/m) 76.3 Ni, 7.0 Cr, 4.5 W, 9.0 Mo and 1.7 Ti; (ii) pure nickel; and (iii) iron with Ni coating. The test specimen in the form of a tetrahedral prism with a square base was made of each of the tested candidate materials and suspended into an ampoule made of the same material. The ampoule was filled with a mixture of salts with the molar composition of 60% LiF and 40% NaF and maintained at

a constant temperature of 680 °C for 1000 h in a furnace with argon atmosphere which eliminated the undesirable presence of oxygen. The details of the corrosion test procedure have been described in our earlier papers.^{22,23} After cooling, the ampoule containing the solidified fluoride mixture was cut along its axis. The solidified fluoride mixture was ground in a ball mill, dissolved in nitric acid and the corrosion products were determined with ICP-OES.^{22,23} Test specimens were cut with a diamond saw and were further sectioned to obtain cuts perpendicular to the block wall. These were embedded into the epoxy resin disks (Araldite®, Huntsman Advanced Materials), lapped and polished with diamond paste.

LA-ICP-MS instrumentation and conditions

The instrumentation for LA-ICP-MS consists of a laser ablation system UP213 (New Wave Research, Inc., ESI, Fremont, CA, USA) and an ICP-MS apparatus Agilent 7500CE (Agilent, Japan). Optimization of the LA-ICP-MS facility (gas flows, sampling depth, mass spectrometer parameters) was carried out using the glass NIST SRM 612 with the aim of obtaining maximum *S/N* ratio and minimum oxide formation. A collision–reaction cell (octopole reaction system) was switched on for the removal of interfering species. A commercial Q-switched Nd:YAG laser based ablation device is designed for operation at the 5th harmonic frequency which corresponds to a wavelength of 213 nm. The ablation device is equipped with the computer-controlled XYZ-stages which makes it possible to adjust the requested position on the target surface and/or to translate the sample along a programmed path. Single hole drilling was selected as the ablation mode and a grid consisting of lines of isolated spots was used for the mapping. Operating conditions of LA-ICP-MS are listed in Table 1. A ten-second delay between individual hole drilling events was chosen for the ICP-MS signal decreased to background level (Fig. S1†). The thickness of the corrosion-affected zone was evident from the image acquired by the electron microprobe and was consistent with the course of the signals of isotopes of sodium and lithium through the corrosion layer.

Aerosol particle number measurement

The concentration of the particles released during laser ablation was measured with an Aerosol Spectrometer Welas 2000 Series (Palas GmbH, Karlsruhe, Germany). The optical spectrometer Welas operates on the principle of the single particle scattering of

Table 1 Operating conditions of LA-ICP-MS

| | |
|---|--------------------------|
| Generator power input | 1500 W |
| Outer plasma gas flow rate (Ar) | 15.0 l min ⁻¹ |
| Intermediate plasma gas flow rate (Ar) | 1.0 l min ⁻¹ |
| Sample gas flow rate (Ar) | 0.6 l min ⁻¹ |
| Fluence | 25 J cm ⁻² |
| Laser repetition rate | 20 Hz |
| Hole drilling time | 5 s |
| Time delay between hole drilling events | 10 s |
| Laser spot diameter | 8 μm |
| Distance between craters in line | 12 μm |
| Distance between lines | 15 μm |
| Carrier gas flow rate (He) | 1.0 l min ⁻¹ |

white light. The intensity of the scattered light detected at an angle of 90° is a measure of the particle size while the number of scattered-light impulses determines the concentration of particles. The Welas sensor 2200 measures the size distribution of the particles in the size range from 0.25 to 17 μm with a maximum concentration of 10^4 particles cm^{-3} . The Welas Condensation Nucleus Counter (CNC) module combined with the Welas sensor 2100 allows time-resolved particle counting within the nanometer range for particles larger than 8 nm with a maximum concentration of 10^5 particles cm^{-3} . This CNC module operates on the principle of 2-propanol condensation on the particles.

ICP-OES analysis of exposed fluoride salts

Analysis of dissolved samples of corrosion-exposed fluoride salts was performed using ICP-OES JY 170 Ultrace (Jobin Yvon Horiba, Longjumeau, France). Details of the instrumentation have been described in our previous paper.²² For the determination of the contents of corrosion-released metals, the matrix-matched calibration solutions were prepared in the unused fluoride salt mixture. Due to the presence of hydrofluoric acid that results from the dissolution of fluoride salts with acids, the standard glass sample introduction system was replaced with that made of perfluoroalkoxy (PFA) material.

Results and discussion

Influence of the corrosion extent on the ablation rate

The influence of corrosion and its extent on the ablation rate was studied by using the Welas spectrometer with both sensor 2200 and CNC modules. Aerosol particles released as a result of laser ablation of studied materials were observed only when the CNC module was used for the measurement. It implies that the size of ablated particles is smaller than 250 nm. A section of the corroded sample A071EV was ablated in seven positions. Six ablation pits are situated within a distance of less than 100 micrometers from the edge of embedded section, *i.e.* in the corroded surface layer, and one spot is situated at a distance of 550 micrometers from the specimen edge, *i.e.* within the intact area. It is obvious from Fig. S2† that the amount of the released aerosol particles decreases from the edge of the specimen section with increasing distance toward the unaffected area. The number of aerosol particles released from the corroded surface is five times higher compared with the unaffected material as a result of more efficient ablation of material attacked by molten fluoride salts. Consequently, determination of contents of structural material constituents in a corroded area cannot be calibrated based on signals measured in an uncorroded area.

LA-ICP-MS quantification procedure

As it was shown, external calibration based on the known composition of the intact part of a particular test specimen cannot be used for quantification due to different ablation rates in the corroded layer and the unaffected bulk material. Normalization to the internal reference signal fails due to an inhomogeneous distribution of alloy constituents caused by their local depletion or enrichment as a result of corrosion by molten fluoride salts. Hence, the quantification was accomplished with

a normalization method based on a total sum of signals of isotopes.²⁴ This method has already been used in our earlier work.²² The blank-corrected isotope signal was abundance-corrected to obtain the elemental signal. Particular elemental signals were normalized to the sum of signals of all elements to obtain the elemental content. ICP-MS signals were measured for all elements contained in unaffected materials (Ni, Cr, Mo, Ti, W) and Li and Na which are present in molten fluoride salts. The fluorine signal was calculated based on the stoichiometry and composition of the fluoride salt mixture, *i.e.* in this case as the sum of the Li and Na signals.²²

First, applicability of the above described quantification procedure was confirmed by LA-ICP-MS analysis of the *E4* setting up standard (once produced by the now non-existent company Hilger) used for the spark-source optical emission spectrometry. The LA-ICP-MS signals were measured at eight different points on the *E4* standard. The results obtained on the *E4* standard using the quantification procedure based on a total sum of signals of isotopes provide excellent agreement with the reference values (Table 2). Consequently, this analysis can be considered as evidence that the sum of signals can be used to quantify the elemental distribution in the test specimen section where the matrix-induced variation of ablation rate makes it impossible to use external calibration.

Corrosion products in molten salt

Contents of major and minor constituents of candidate materials (Ni, Cr, Fe, W, Mo, Ti, Al, V, Nb and Mn) in the solidified fluoride mixture were determined after dissolution by ICP-OES. For the quantification of the corrosion process the total content of corrosion products is expressed as the sum of contents of all elements contained in candidate materials. It follows from the results summarized in Table 3 that the nickel-based alloy

Table 2 Elemental content obtain on *E4* setting-up standard (once produced by the now non-existent company Hilger) by LA-ICP-MS measurement with total sum of signal normalization (with standard deviation for 8 measurements) and reference values

| Element | Determined value, content (% m/m) | Reference value, content (% m/m) |
|---------|-----------------------------------|----------------------------------|
| Cr | 4.5 ± 0.4 | 4.3 |
| Mn | 0.8 ± 0.1 | 0.7 |
| Ni | 28 ± 2 | 28.5 |
| Fe | 62 ± 2 | 62.7 |
| W | 0.017 ± 0.008 | 0.02 |
| Mo | 1.1 ± 0.2 | 0.97 |

Table 3 The total content of corrosion products in solidified fluoride mixture after the exposure of examined materials to the mixture melt for 1000 h at 680 °C. The salt mixture before exposure is considered as a blank. The standard deviation is calculated from 5 measurements

| Sample | Corrosion products, total content (% m/m) |
|--------------------|---|
| Blank | 0.020 ± 0.002 |
| Pure Ni | 0.055 ± 0.004 |
| A071EV | 0.129 ± 0.009 |
| Nickel-coated iron | 0.061 ± 0.003 |

A071EV exhibits a twice higher total content of corrosion products than pure nickel and nickel-coated iron.

LA-ICP-MS semiquantitative elemental mapping of specimen/salt boundaries

The laser ablation parameters were optimized with respect to the acceptable lateral resolution and sufficient limit of detection (LOD). The lateral resolution which is lower than 10 μm is required in principle, because the thickness of the corroded layer typically reaches tens of micrometers. The laser beam spot diameter of 8 μm was employed as a good compromise between resolution and LOD values, which are presented in Table 4. The LOD values for ICP-OES are better in comparison with LA-ICP-MS which is caused by using very small laser spot (8 μm).

Table 4 Summarization of LODs obtained by means of ICP-OES and LA-ICP-MS (using 8 μm laser ablation spots), respectively

| Element | LOD (% m/m) | |
|---------|-------------|-----------|
| | ICP-OES | LA-ICP-MS |
| Ni | 0.0004 | 0.001 |
| Fe | 0.0002 | 0.02 |
| Mn | 0.0002 | 0.003 |
| Cr | 0.0002 | 0.04 |
| Al | 0.0006 | 0.06 |
| Na | — | 0.1 |
| Li | — | 0.07 |

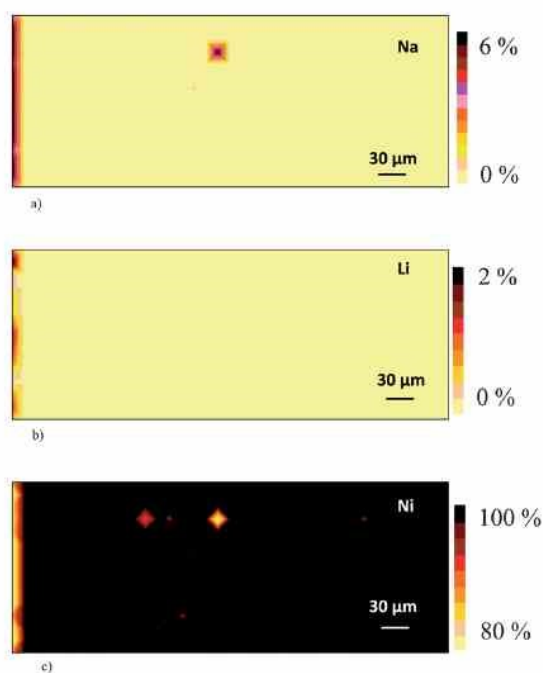


Fig. 1 Elemental distribution of (a) Li, (b) Na, and (c) Ni on the section of the test specimen of pure nickel exposed to the molten fluoride salt mixture for 1000 h at 680 °C.

The elemental mapping of the specimen section embedded in the epoxy resin disk was accomplished using the single hole drilling mode with a distance of 12 μm between the centers of adjacent spots. The analyzed area (approximately 400 \times 200 μm) was defined by a grid consisting of lines of isolated spots. The mapping of the section was initiated in the epoxy resin area close to the edge of the specimen and then continued through the corroded area until the unaffected zone was reached (Fig. S3†).

Compositional changes in pure nickel are distinct to a depth varying between 25 and 36 μm as is visible in the left parts of the elemental maps in Fig. 1. This corrosion-affected zone exhibits enrichment by lithium and sodium up to 2% and 6%, respectively (Fig. 1a and b) and depletion of the nickel content to 82% (Fig. 1c).

The nickel-coated iron specimen is affected, as apparent from Fig. 2a where the sodium distribution indicates the penetration

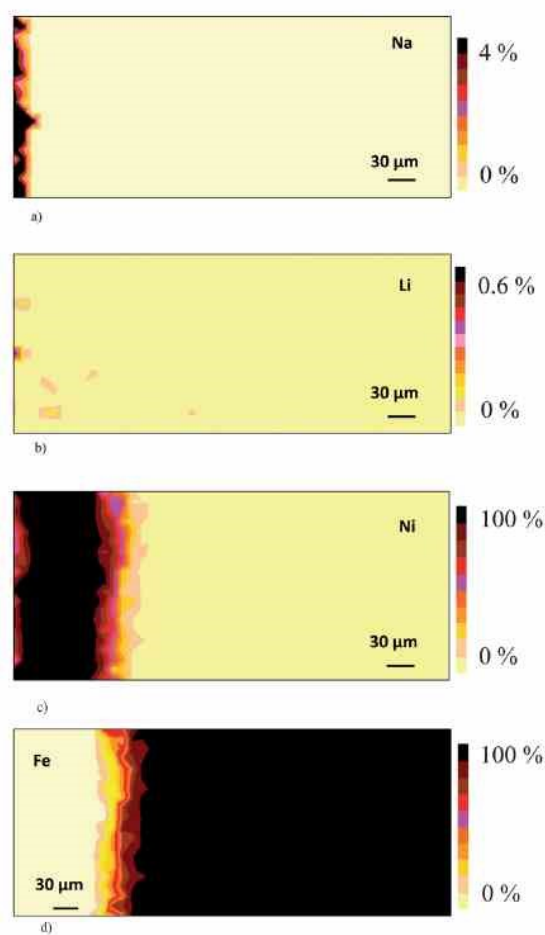


Fig. 2 Elemental distribution of (a) Na, (b) Li, (c) Ni, and (d) Fe on the section of the nickel-coated iron specimen exposed to molten fluoride salt mixture for 1000 h at 680 °C.

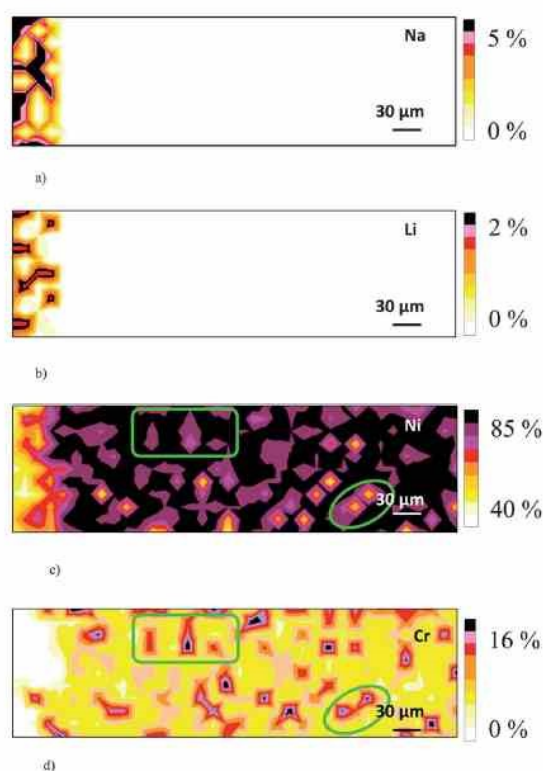


Fig. 3 Elemental distribution of (a) Na, (b) Li, (c) Ni, and (d) Cr on the section of the nickel-based alloy A071EV test specimen exposed to the molten fluoride salt mixture for 1000 h at 680 °C. Areas on the unaffected part of the alloy specimen section showing complementary enrichment/depletion of Ni/Cr and *vice versa* are marked out with a rectangle and an ellipse.

of the LiF–NaF mixture to the depth of 25 μm. This corrosion-affected zone exhibits enrichment by sodium of up to 8%. Contrary to the pure nickel specimen lithium is not distributed homogeneously and its content reaches 0.8% at the maximum (Fig. 2b). The surficial zone is depleted in Ni to a depth from 12 to 25 μm where the Ni content decreases to 80% (Fig. 2c). The Ni/Fe gradient of the coating–substrate interface exhibits a thickness of about 50 μm (Fig. 2c and d).

The nickel-based alloy A071EV specimen shows the highest corrosion damage characterized by the occurrence of Na and Li (Fig. 3a and b) and depletion in Ni and Cr (Fig. 3c and d) up to a depth of 65 μm. The nickel content in the corrosion-affected zone ranges from 41 to 65% whereas its content in the non-affected zone is in the range from 70 to 83% (the average value is 78.5%). In the case of chromium, its content varies in the corroded layer from 0.1 to 1.2%. The average chromium content in the non-affected layer is 6.8%. Besides, inhomogeneity of the unaffected part of the alloy specimen section is obvious on the Ni and Cr maps in Fig. 3c and d where the complementary enrichment/depletion of Ni/Cr and *vice versa* are marked out with a rectangle and an ellipse.

Conclusion

The influence of the extent of corrosion caused by molten fluoride salts on the ablation rate in studied structural materials in the nuclear industry was proved by measuring the amount of aerosol generated by laser ablation. The number of aerosol particles released from the corroded surface is (in the particular presented case) five times higher compared with the unaffected material. As a result, neither the calibration based on signals measured in the uncorroded area, nor the calibration relying on usual metallic reference materials can be applied for the determination of the corrosion-induced changes. Consequently, the normalization of particular isotopic signals to the sum of signals of all isotopes represents an acceptable solution for the semi-quantitative determination. The applicability of this procedure has been confirmed by the LA-ICP-MS analysis of the setting up standard for metallurgical analyses.

The size of aerosol particles was proved to be smaller than 250 nm by the fact that the aerosol was observed only when the CNC module was used for measurement. This applies both for the corroded and non-affected parts of a test specimen.

A procedure has been developed for elemental mapping of corrosion damage of alloys designed for construction of nuclear reactor cooling circuits. Elemental maps characterize the zones where penetration of molten fluoride salts into the structural materials occurs, detect the depletion of affected zones in major alloy constituents, and depict gradients of coating–substrate interfaces and even elemental inhomogeneities in the unaffected parts of a specimen.

Both LA-ICP-MS and ICP-OES analyses have unambiguously identified the material with the lowest and the highest corrosion damage. Of the three examined candidate structural materials (pure nickel, nickel-based alloy A071EV and nickel-coated iron) pure nickel exhibits the best resistance.

Acknowledgements

This work was supported by the European Regional Development Fund project “CEITEC” (CZ.1.05/1.1.00/02.0068), by Czech Science Foundation project 101/08/1100 and by an Institutional research plan no. AV0Z40310501 of Institute of Analytical Chemistry of the Academy of Sciences of the Czech Republic.

References

- 1 L. C. Olson, J. W. Ambrosek, K. Sridharan, M. H. Anderson and T. R. Allen, *J. Fluorine Chem.*, 2009, **130**, 67–73.
- 2 U.S. DOE Nuclear Energy Research Advisory Committee and the Generation IV International Forum, *A Technology Roadmap for Generation IV Nuclear System*, GIF-002–00, December 2002.
- 3 T. Aram and S. Ion, *Energy Policy*, 2008, **36**, 4323–4330.
- 4 D. F. Williams, L. M. Toth and K. T. Claro, *Assessment of Candidate Molten Salt Coolants for the Advanced High-Temperature Reactor (AHTR)*, ORNL/TM-2006/12, March 2006.
- 5 Ch. Le Brun, *J. Nucl. Mater.*, 2007, **360**, 1–5.
- 6 M. Salanne, C. Simon, P. Turk and P. A. Madden, *J. Fluorine Chem.*, 2009, **130**, 38–44.
- 7 O. Beneš and R. J. M. Konings, *J. Fluorine Chem.*, 2009, **130**, 22–29.
- 8 H. Moriyama, A. Sagara, S. Tanaka, R. W. Moir and D. K. Sze, *Fusion Eng. Des.*, 1998, **39**, 627–637.
- 9 R. W. Moir, *Energy Convers. Manage.*, 2008, **49**, 1849–1858.

- 10 A. C. Sequeira, *High Temperature Corrosion in Molten Salts*, Trans Tech Publications, Enfield, USA, 2003.
- 11 W. R. Grimes, *Nucl. Appl. Technol.*, 1970, **8**, 137–155.
- 12 V. V. Ignatév, A. I. Surenkova, I. P. Gnidoi, V. I. Fedulov, V. S. Uglovi, A. V. Panov, V. V. Sagaradze, V. G. Subbotin, A. D. Toropov, V. K. Afonichkin and A. L. Bove, *At. Energy*, 2006, **101**, 730–738.
- 13 M. Samaras, W. Hoffelner and M. Victoria, Modelling of advanced structural materials for GEN IV reactors, *J. Nucl. Mater.*, 2007, **371**, 28–36.
- 14 S. H. Cho, S. S. Hong, D. S. Kang, J. M. Hur and H. S. Lee, *Met. Mater. Int.*, 2009, **15**, 51–55.
- 15 L. Martinelli, F. Balbaud-Celerier, G. Picard and G. Santarini, *Corros. Sci.*, 2008, **50**, 2549–2559.
- 16 M. Suarez, S. Bellayer, M. Traisnel, W. Gonzales, D. Chicot, J. Lesage, E. S. Puchi-Cabrera and M. H. Staia, *Surf. Coat. Technol.*, 2008, **202**, 4566–4571.
- 17 R. M. Pidaparti and R. R. Patel, *Mater. Lett.*, 2008, **62**, 4497–4499.
- 18 A. Pardo, M. C. Merino, A. E. Coy, F. Viejo, R. Arrabal and S. Feliu, *Electrochim. Acta*, 2008, **53**, 7890–7902.
- 19 V. Dostal, P. Hejzlar and M. J. Driscoll, *Nucl. Technol.*, 2006, **154**, 283–301.
- 20 L. Gicquel, N. Latge, C. Simon, P. Hobbes, A. Saboni, J. C. Buvat and J. L. Gustin, *Proceedings of an International Congress on Advances in Nuclear Power Plants (ICAPP 2010)*, San Diego, USA, June 13–17, 2010, paper 10215.
- 21 T. Vaculovic, V. Otruba, O. Matal and V. Kanicky, *Chem. Pap.*, 2011, **65**, 620–626.
- 22 T. Vaculovic, P. Sulovsky, J. Machat, V. Otruba, O. Matal, T. Simo, C. Latkoczy, D. Gunther and V. Kanicky, *J. Anal. At. Spectrom.*, 2009, **24**, 649–654.
- 23 O. Matal, T. Simo, L. Nesvadba, V. Dvorak, V. Kanicky, P. Sulovsky and J. Machat, *Z. Naturforsch., A: Phys. Sci.*, 2007, **62**, 769–774.
- 24 C. Latkoczy, Y. Muller, P. Schmutz and D. Gunther, *Appl. Surf. Sci.*, 2005, **252**, 127–132.

6 . 4 A R T I C L E 4

Warchilova, T.; Dillingerova, V.; Skoda, R.; Simo, T.; Matal, O.; Vaculovic, T.;
Kanicky, V. *Spectrochimica Acta Part B-Atomic Spectroscopy* 2018, 148, 113-117
(IF=3.101)



Contents lists available at ScienceDirect

Spectrochimica Acta Part B

journal homepage: www.elsevier.com/locate/sab

Corrosion of nickel-based structural materials for nuclear reactors by molten fluoride salt: From bulk content of corrosion products to elemental imaging of corrosion changes



T. Warchilová^{a,b}, V. Dillingerová^{a,b}, R. Škoda^c, T. Šimo^d, O. Matal^d, T. Vaculovič^{a,b,*},
V. Kanický^{a,b}

^a Laboratory of Atomic Spectrochemistry, Department of Chemistry, Faculty of Science, Masaryk University, Kotlářská 2, 611 37 Brno, Czech Republic

^b Central European Institute of Technology, Masaryk University, Kamenice 5, 625 00 Brno, Czech Republic

^c Department of Geological Sciences, Faculty of Science, Masaryk University, Kotlářská 2, 611 37 Brno, Czech Republic

^d ENERGOVÝZKUM, s. r. o., Božetěchova 17, 612 00 Brno, Czech Republic

ARTICLE INFO

Keywords:

Molten fluoride salt
LA-ICP-MS
EPMA
Corrosion
Elemental imaging
Ni-based structural material

ABSTRACT

This work is focused on the study of corrosion treatment of molten fluoride salt (MFS) on three candidate structural materials (Ni, ferritic steel with protective Ni coating, and Ni-based alloy). The samples were exposed to an MFS mixture (60 mol% LiF + 40 mol% NaF) at a temperature of 680 °C for 112, 350 and 1000 h. Their corrosion resistance was tested by the determination of the content of corrosion products in MFS by ICP-OES (Inductively Coupled Plasma with Optical Emission Spectrometry) analysis and comparison of elemental ratios. Distinctive differences in the ratios were found for ferritic steel with protective Ni coating. Morphological changes induced by MFS treatment were revealed and studied by EPMA (Electron Probe Micro Analysis) and LA-ICP-MS (Laser Ablation Inductively Coupled Plasma of Mass Spectrometry). Elemental maps of the corroded area were acquired by both methods. The analyses of corrosion products show that the best candidate material is nickel.

1. Introduction

The Molten Salt Reactor (MSR) is a promising nuclear reactor type, which belongs to the group of Generation IV reactor systems [1]. The great benefits of this reactor design are its efficient fuel utilization, minimum radioactive waste and economical use with a safe and environmentally friendly operation [2–4]. Molten salts, exhibit the most appealing properties; they can be used as reactor coolant or a transfer medium in high temperature process heat loops from nuclear reactors to hydrogen production. This explains why they were taken into consideration in the development of nuclear energy technology.

These salts are characterized by a high thermal conductivity, low viscosity, high boiling points, the largest heat capacity per unit volume without any need of pressurization, and insensitivity to radiation [4]. Compared to chloride salts, fluoride salts are more frequently used because fluorine does not require an expensive isotope separation process. Potential coolants for MSR's are BeF₂-salts and alkali fluoride salts. The construction of MSR is a complex process with many difficulties such as finding compatible and resistant structural material for the application and development of the system. The chemical attack of

MFS at working temperature level (570 °C) is highly corrosive. The corrosion in MFS is driven by several factors involving thermodynamic aspects such as Gibbs free energy of fluorides formation, corrosion due to the presence of impurities (moisture, oxygen, metals) and fission products [5]. Alloy dissolved from hotter zones is transported by convection and then plated to colder areas. The major impurities must be removed in order to prevent severe corrosion of the container metal. Typical impurities include moisture and oxide contaminants, which together with a temperature gradient and galvanic corrosion are considered the main driving forces for the corrosion [6, 7]. Additionally, alloying elements dissolved into molten salts accelerate the corrosion due to thermodynamic transportation [8, 9]. Moreover, the production of helium due to neutron irradiation and the formation of helium bubbles can cause extreme swelling, surface roughening and surface blistering [10].

The most promising corrosion-resistant structural materials are Ni-based alloys, e.g. Monels, Inconels, Hastelloys, pure nickel and Ni-plated alloys [11–13]. The tendency for common alloying constituents to corrode in MFS increases in the order of Ni, Co, Fe, Cr and Al, with Al being the most prone to dissolution [14].

* Corresponding author.

E-mail address: vaca@mail.muni.cz (T. Vaculovič).

<https://doi.org/10.1016/j.sab.2018.06.010>

Received 27 November 2017; Received in revised form 12 June 2018; Accepted 13 June 2018

Available online 15 June 2018

0584-8547/ © 2018 Elsevier B.V. All rights reserved.

Electrochemical techniques such as voltammetry are ideal for the study of corrosion thermochemistry and kinetics [15, 16]. For the investigation of the corrosion processes of materials various measurement techniques are typically applied, including e.g. Scanning Electron Microscopy (SEM) [13, 17], EPMA [17], synchrotron radiation techniques [13], laser ablation based methods - LA-ICP-MS [18, 19] and Laser Induced Breakdown Spectroscopy (LIBS) [20, 21].

This work is devoted to the study of the corrosion behavior of three candidate structural materials when exposed to MFS treatment for various time. Resistance to corrosion of ferritic steel with protective Ni coating, Ni, and Ni-based alloy A071EV was expressed and compared in terms of content of steel constituents dissolved in MFS and their elemental ratios. The dissolution of particular steel constituents in MFS was assessed based on the determination of corrosion products in exposed MFS by ICP-OES solution analysis. Elemental maps of corroded area over the Ni-coating/steel substrate interface on a perpendicular section were acquired by EPMA and LA-ICP-MS.

2. Experimental

2.1. Corrosion test

The ferritic steel S355 J0 (> 95%_{w/w} Fe) coated with an 80 μm nickel protective layer, nickel (99.0%_{w/w} Ni, 0.80%_{w/w} Fe, 0.20%_{w/w} Mn), and A071EV alloy (in %_{w/w}: 76.3 Ni, 7.0 Cr, 4.5 W, 9.0 Mo and 1.7 Ti) were tested as candidate structural materials. For this purpose, the specimen (rectangular prism, 2 × 5 × 7 mm) of investigated material was suspended into an ampoule (height 185 mm, inner diameter 21.3 mm, wall thickness 2 mm) made of the same material. The ampoule was filled with the mixture of LiF-NaF (60:40 by mol%) of certified elemental composition 12.9%_{w/w} Li, 28.4%_{w/w} Na, and 58.7%_{w/w} F. The ampoule was evacuated and then heated to 200 °C for 2 h for degassing, after which it was maintained at a constant test temperature of 680 °C in a furnace with an argon atmosphere thus preventing oxygen penetration. After the isothermal exposure (112, 350 and 1000 h) the ampoule and the specimen were allowed to cool to room temperature.

2.2. Determination of corrosion products in MFS and preparation of the test specimen for elemental mapping

The ampoule with the specimen was cut along its axis, the test sample was removed and the solidified fluoride mixture was separated and ground in a ball mill. A 250 mg portion of homogenized fluoride mixture was dissolved in nitric acid, diluted to 250 ml and the resulting

solution was used to determine the corrosion products (Ni, Fe, Mn, Cr, W, Mo, and Ti) by the ICP-OES Jobin-Yvon 170 Ultrace (Jobin-Yvon, France) [22, 23]. The Ni-coated steel specimen was cut with a diamond saw and both resulting parts were embedded into epoxy resin disks (Araldite®, Huntsman Advanced Materials), lapped and polished with diamond paste for EPMA and LA-ICP-MS elemental mapping.

2.3. EPMA/WDS and LA-ICP-MS elemental mapping of corroded Ni-steel interface

The spatial 2D distribution of elements of interest was determined by means of electron probe microanalyser Cameca SX100. The X-Ray maps were collected at an accelerating voltage of 15 kV, beam current of 40 nA, beam diameter < 1 μm. The K α X-rays of F, Na, Cr, Fe, and Ni were simultaneously collected in the wavelength-dispersion mode (WDS) on PCL, TAP, PET, PET and LIF monochromators, respectively. The grid of the map was set at 250 × 188 pixels with a step size of 3 μm to cover an area of 747 × 561 μm². The dwell (counting) times for the peak and the background were 250 ms each. The stage-moving mode at static beam was chosen to keep the detector, monochromator and X-ray source aligned in ideal geometry. The background intensities were subtracted from the peak intensities for further data interpretation. The acquired data were quantified using albite (Na), CaF₂ (F), and pure metals Cr, Fe, Ni as calibrants and X-PHI matrix correction routine [24].

The UP213 laser ablation system with a 213 nm lasing wavelength and a 4.2 ns pulse width (New Wave Research, Inc., ESI, Fremont, CA, USA) coupled with the quadrupole ICP-MS Agilent 7500ce (Agilent Technologies, Japan) was used for elemental mapping. The operating parameters of the LA-ICP-MS experiments were the same as used in previous work [19]. The analyzed area was the same as for EPMA elemental mapping. For the ablation series of individual non-overlapped spots were used. The distance between spots in one line and between lines was 8 μm. Each row of isolated ablation spots originated outside the test specimen in the epoxy resin material, continued through the Ni-coating and coating/substrate interface into the corroded area of steel substrate and ended in the unaffected substrate zone. The quantification was performed using the total sum of signals of isotopes [19, 23].

3. Results and discussion

3.1. Determination of corrosion products in exposed MFS and evaluation of corrosion resistance

The content of corrosion products in MFS is an indicator for the

Table 1

Content of corrosion products in MFS resulting from exposure of nickel-coated steel S355 J0, nickel, and alloy A071EV depending on the time of exposure.

| Exposure time (h) | Corrosion products content in MFS (% _{w/w}) | | | | | | | Total content |
|--------------------------------|---|--------|---------|--------|--------|--------|--------|---------------|
| | Ni | Fe | Mn | Cr | W | Mo | Ti | |
| Ni-coated S355 J0 steel | | | | | | | | |
| 112 | 0.0019 | 0.0198 | 0.0014 | < | < | < | < | 0.0231 |
| 350 | 0.0044 | 0.0215 | 0.0029 | < | < | < | < | 0.0287 |
| 1000 | 0.0067 | 0.0464 | 0.0069 | < | < | < | < | 0.0599 |
| Ni | | | | | | | | |
| 112 | 0.0164 | 0.0039 | 0.0008 | < | < | < | < | 0.0211 |
| 350 | 0.0195 | 0.0055 | 0.0017 | < | < | < | < | 0.0267 |
| 1000 | 0.0320 | 0.0072 | 0.0031 | < | < | < | < | 0.0423 |
| Alloy A071EV | | | | | | | | |
| 112 | 0.0056 | 0.0012 | 0.0008 | 0.0011 | 0.0190 | 0.0270 | 0.0036 | 0.0584 |
| 350 | 0.0083 | 0.0036 | 0.0012 | 0.0012 | 0.0229 | 0.0193 | 0.0047 | 0.0612 |
| 1000 | 0.0150 | 0.0067 | 0.0035 | 0.0010 | 0.0224 | 0.0219 | 0.0054 | 0.0758 |
| LOD (%_{w/w}) | | | | | | | | |
| | 0.0002 | 0.0005 | 0.00005 | 0.0001 | 0.001 | 0.001 | 0.0005 | |

Table 2

Ratio of content of corrosion products to content of Ni in MFS resulting from exposure of nickel-coated steel S355 J0, nickel, and alloy A071EV depending on the time of exposure and their ratio of intact material.

| | Exposure (h) | Fe/Ni | Mn/Ni | Cr/Ni | W/Ni | Mo/Ni | Ti/Ni |
|-------------------|--------------|-------|-------|-------|-------|-------|-------|
| Ni-coated S355 J0 | 112 | 10.7 | 0.76 | – | – | – | – |
| | 350 | 4.9 | 0.65 | – | – | – | – |
| | 1000 | 7.0 | 1.0 | – | – | – | – |
| Ni | Intact | 0.002 | 0.008 | – | – | – | – |
| | 112 | 0.24 | 0.051 | – | – | – | – |
| | 350 | 0.28 | 0.087 | – | – | – | – |
| | 1000 | 0.22 | 0.095 | – | – | – | – |
| Alloy A071EV | Intact | 0.002 | 0.008 | – | – | – | – |
| | 112 | 0.21 | 0.15 | 0.20 | 3.3 | 4.8 | 0.64 |
| | 350 | 0.43 | 0.15 | 0.14 | 2.8 | 2.3 | 0.56 |
| | 1000 | 0.45 | 0.23 | 0.16 | 1.5 | 1.5 | 0.36 |
| | intact | 0.001 | 0.001 | 0.092 | 0.059 | 0.118 | 0.022 |

Table 3

Ratio of content of particular element in MFS after exposure to its content in intact material.

| | Exposure (h) | $W_{\text{LiFNaF}}/W_{\text{material}} \cdot 10^3$ | | | | | | |
|-------------------|--------------|--|-----|-----|------|-----|-----|-----|
| | | Ni | Fe | Mn | Cr | W | Mo | Ti |
| Ni-coated S355 J0 | 112h | 0.019 | 99 | 1.8 | – | – | – | – |
| | 350h | 0.044 | 107 | 3.6 | – | – | – | – |
| | 1000h | 0.067 | 232 | 8.6 | – | – | – | – |
| Ni | 112h | 0.165 | 19 | 1.0 | – | – | – | – |
| | 350h | 0.197 | 27 | 2.1 | – | – | – | – |
| | 1000h | 0.323 | 36 | 3.8 | – | – | – | – |
| Alloy A071EV | 112h | 0.074 | 12 | 12 | 0.16 | 4.2 | 3.0 | 2.1 |
| | 350h | 0.109 | 36 | 17 | 0.17 | 5.1 | 2.1 | 2.8 |
| | 1000h | 0.197 | 67 | 50 | 0.14 | 5.0 | 2.4 | 3.2 |

selection of the most resistant material. The results of ICP-OES solution analysis of MFS are summarized in Table 1. Generally, corrosion rate decreases with exposure time for all constituents, but it differs for particular elements. Due to the substantially lower content of Cr, W, Mo and Ti in nickel coating and in nickel the amount of these elements released by corrosion into MFS is lower than the LOD of the ICP-OES method. The relative standard deviation (RSD) of the analysis ranges from 1 to 7% except for values of content near to the LOD where the RSD increased to 20%.

The comparison of total content values of corrosion products in MFS for each period of exposure indicates that both the coated steel and Ni is more resistant than A071EV alloy. The total content values of corrosion products released from coated steel and Ni into MFS after 112 and

350 h of exposure are very close, whereas 1000 h exposure results in a significantly higher amount of corrosion products coming from coated steel than from Ni. The content of elements in MFS differs distinctly depending on examined candidate material. The ratios of Fe/Ni, Mn/Ni, (and where possible also of Cr/Ni, W/Ni, Mo/Ni and Ti/Ni) were calculated both for original (intact) structural materials and for MFS after exposure in order to compare the individual candidate materials in terms of corrosion rate. The content of corrosion products in MFS is nonlinear increasing with time. The steep increase of corrosion products during the first 112 h is observed for all candidate material, can be caused by the presence of impurities in the system, mainly moisture in the MFS that reacts with fluorides to form highly corrosive HF [5]. This observation is consistent with Koger who found that the amount of Cr in MFS after the first 3 h of exposure was 25 mg/kg and increased to 551 mg/kg after 30,000 h [25]. Moreover, the corrosion rate is driven by diffusion of the metals from the alloy surface into the MFS [26]. The diffusion slows down due to equalization of the concentration on the alloy-MFS interface. They observed that the long-term corrosion attack can be predicted by a logarithmic fitting curve.

It is evident from Table 2 that pronounced enrichment of Fe and Mn (and also of Cr, W, Mo and Ti where determinable) occurred with respect to Ni in exposed salt in comparison to elemental ratios in all three intact materials. The most conspicuous enrichment of Fe and Mn in MFS is observed for Ni-coated steel (10.7 vs. 0.002 in MFS and intact material, respectively). It is remarkable that this enrichment is substantially higher for Ni-coated steel than for Ni, although the coating material and “bulky” Ni have the same composition (99%_{w/w} Ni, 0.8%_{w/w} Fe, 0.2%_{w/w} Mn). Thus, it can be assumed that corrosion occurred mainly on the coating/substrate interface and the increased content of Fe (Mn) might predominantly originate from steel substrate. Corrosion products than probably penetrate into the MFS through the damaged nickel coating. To confirm this assumption, a section of the exposed specimen of Ni-coated steel was subjected to surface imaging by EPMA. It is obvious from the EMPA image of the section (Fig. 2) that porous caverns developed in the steel substrate in positions opposite the areas of distinctly thinned nickel coating. Due to different thermal expansion coefficients of Ni and Fe (13 and 12 μm/K) the micro cracks probably existed at locations of thinned Ni-coating before MFS attack or they formed during the test due to increased temperature, and MFS consequently came into contact with the steel substrate. Thus provoked corrosion has produced an increased content of substrate constituents in MFS. Diffusion and convection during the test transported corrosion products outside the specimen into MFS.

The significant rise of the Fe/Ni ratio in MFS with increasing exposure time is observed for the nickel-based alloy A071EV (Table 2) which indicates that the rate of Fe release from the alloy into MFS was higher than that of Ni. Different corrosion rates for Ni and Fe are also

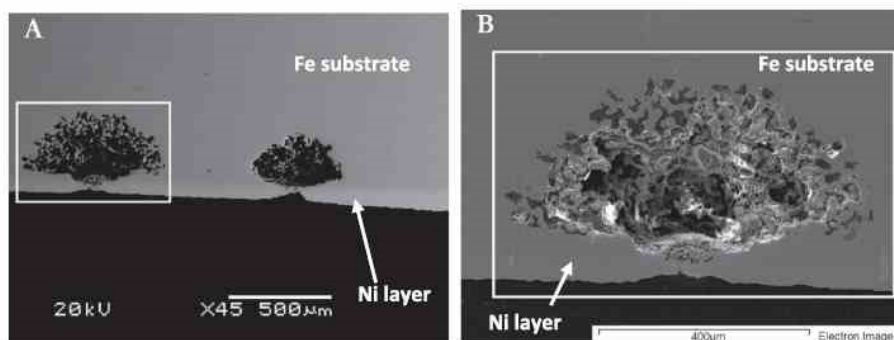


Fig. 1. Nickel-coated steel specimen after 350-hours exposure to LiF-NaF at 680 °C, corroded area EPMA image: the black area corresponds to epoxy resin, the white frames enclose the analyzed area; A) light rim on the edge of specimen – Ni coating; two perforated loci are shown; B) detail of analyzed porous cavern below the corrosion pit.

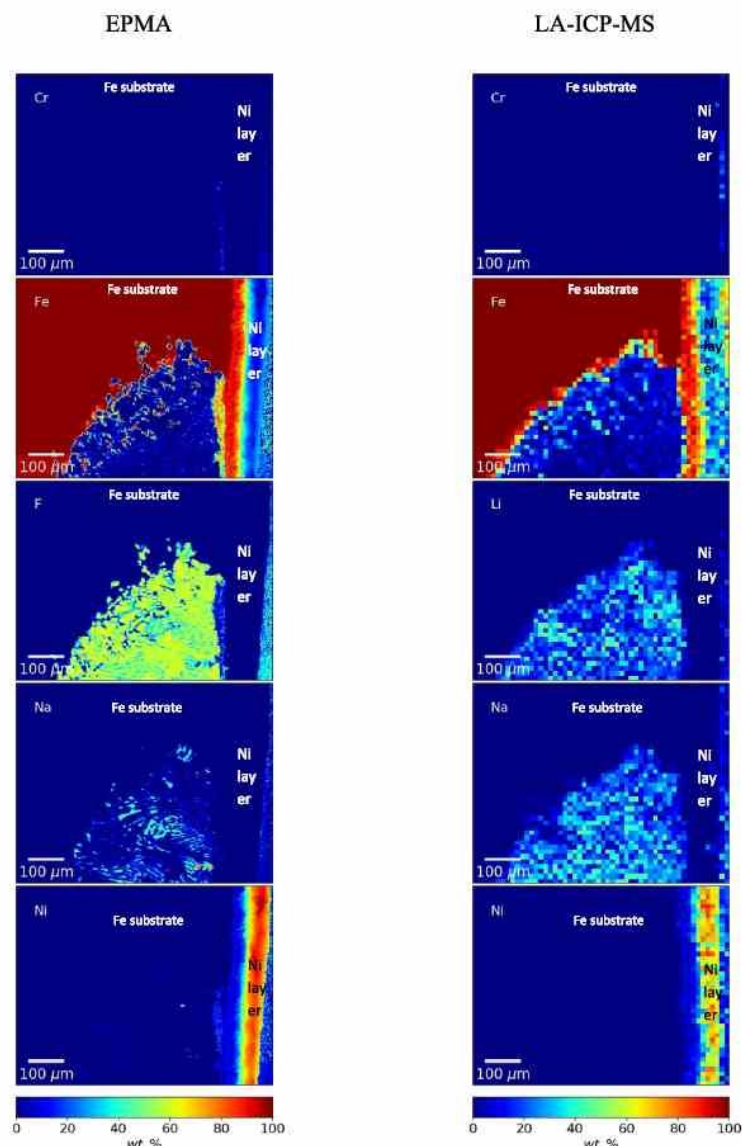


Fig. 2. Elemental maps of Cr, Fe, Li, Na and Ni obtained by LA-ICP-MS and EPM analysis of nickel-coated steel specimen after 350-hours exposure to LiF-NaF at 680 °C.

evident from Table 1. On the other hand, the Mn/Ni and Cr/Ni ratios in MFS remain approximately the same during exposure. Besides, the Mn/Ni ratio is increased in MFS in comparison to the intact specimen by two orders while Cr/Ni ratio no more than twice. Different behavior is visible for W/Ni, Mo/Ni, and Ti/Ni. Important enrichment of W, Mo, and Ti in fluoride salt occurred during 112 h, however, W/Ni, Mo/Ni and Ti/Ni ratios then decrease with increasing MSR exposure. The decrease in these ratios is related to the fact that the amount of Ti, Mo and W increases in the MFS more slowly than the amount of Ni. This may be due to the fact that the amount of Ti, Mo and W in the MFS is close to their amount on the surface of the alloy and their diffusion slows down.

The resistance of the candidate material to the LiF-NaF exposure can be scored as a ratio of the content of given elements in the LiF-NaF mixture after exposure ($w_{\text{LiF-NaF}}$) to the content of particular elements in

the tested material (w_{material}), as well. The most resistant elements exhibit the lowest ratio and *vice versa*. It is evident from Table 3 that nickel is the most resistant element to MFS exposure whereas iron is the most susceptible to corrosion. The noticeable enrichment in the case of Ni-coated steel is caused by preferential corrosion of steel substrate that occurred by penetration of nickel coating by MFS to iron substrate as is clearly seen in Fig. 1. In case of alloy A071EV the most resistant elements are Ni and Cr, Ni, Fe, Mn exhibit similar behavior – a significant enrichment in LiF-NaF mixture with increasing time of exposure (Table 1 and Table 3). On the contrary, in the case of Cr, W, and Mo no significant enrichment is observed. For Ti, slight enrichment occurred. The behavior of Cr, W, Mo and Ti could be caused by their passivation which suppresses the corrosion rate. The results from Tables 2 and 3 show the same conclusion regarding the resistance of candidate

materials and amount of corrosion products.

3.2. Surface analysis

Part of the sponge-like corroded area shown in Fig. 1 was subjected to quantitative elemental mapping to demonstrate penetration of MFS into the exposed specimen and to show relative depletion or enrichment of constituents in the structural material. As EPMA does not allow measuring soft radiation of light elements (in our case of Li) and fluorine ionization in the ICP source is very weak, both EPMA and LA-ICP-MS were used for obtaining 2-D elemental distributions (Fig. 2). All maps are quantified and the scale is from 0 to 100%_{w/w}.

The elemental maps on right hand side of Fig. 2 show the Ni coating on the steel substrate. The corrosion penetrates up to 500 μm under the Ni coating and outstanding depletion of Fe (up to 5%_{w/w}) and enrichment in Li, F and Na content. Moreover, the wide boundaries can be clearly seen between the Ni-coating and the Fe-substrate. In the outermost part of Ni-coating depletion of Ni and enrichment of Li and Na are evident.

4. Conclusion

Three candidate structural materials for the nuclear industry were tested for their corrosion resistance to MFS exposure, with the most appropriate material being selected based on corrosion products content in the solidified exposed melt. The analyses show that the best candidate material is nickel, whereas the nickel alloy A071EV releases the largest amount of metals into the melt and is thus most susceptible to corrosion. A disproportionately higher amount of Fe in MSF after exposure of the Ni-coated steel specimen indicates, together with EPMA and LA-ICP-MS mapping, the coating failure followed by massive corrosion of the steel substrate to a depth of 600 μm.

Acknowledgement

This work was supported by the project CEITEC2020 (LQ1601) made by the Ministry of Education, Youth and Sports of the Czech Republic.

References

- [1] T. Abram, S. Ion, Generation-IV nuclear power: a review of the state of the science, *Energy Policy* 36 (2008) 4323–4330.
- [2] J. Uhlir, Chemistry and technology of Molten Salt Reactors – history and perspectives, *J. Nucl. Mater.* 360 (2007) 6–11.
- [3] R.W. Moir, Recommendations for a restart of molten salt reactor development, *Energy Convers. Manag.* 49 (2008) 1849–1858.
- [4] C. Le Brun, Molten salts and nuclear energy production, *J. Nucl. Mater.* 360 (2007) 1–5.
- [5] G. Zheng, Corrosion Behavior of Alloys in Molten Fluoride Salts, University of Wisconsin, 2015.
- [6] J.H. Shaffer, Preparation and Handling of Salt Mixtures for the Molten Salt Reactor Experiment, Oak Ridge National Laboratory, 1971, pp. 1–45 ORNL-4616.
- [7] J. De Van, Effect of Alloying Additions on Corrosion Behavior of Nickel-molybdenum Alloys in Fused Fluoride Mixtures, Oak Ridge National Laboratory, 1969, pp. 1–51 ORNL-TM-2021.
- [8] L.C. Olson, J.W. Ambrosek, K. Sridharan, M.H. Anderson, T.R. Allen, Materials corrosion in molten LiF-NaF-KF salt, *J. Fluor. Chem.* 130 (2009) 67–73.
- [9] M.W. Rosenthal, P.N. Haubenreich, R.B. Briggs, The Development Status of Molten-salt Breeder Reactors, Oak Ridge National Laboratory, 1972 ORNL-4812.
- [10] H. Trinkaus, Energetics and formation kinetics of helium bubbles in metals, *Radiation Effects and Defects in Solids* 78 (1983) 189–211.
- [11] L. Olson, K. Sridharan, M. Anderson, T. Allen, Nickel-plating for active metal dissolution resistance in molten fluoride salts, *J. Nucl. Mater.* 411 (2011) 51–59.
- [12] V. Ignatiev, A. Surenkov, Alloys compatibility in molten salt fluorides: Kurchatov Institute related experience, *J. Nucl. Mater.* 441 (2013) 592–603.
- [13] M. Liu, J.Y. Zheng, Y.L. Lu, Z.J. Li, Y. Zou, X.H. Yu, X.T. Zhou, Investigation on corrosion behavior of Ni-based alloys in molten fluoride salt using synchrotron radiation techniques, *J. Nucl. Mater.* 440 (2013) 124–128.
- [14] A.K. Misra, Fluoride salts as phase-change materials for thermal-energy storage in the temperature-range 1000–1400-k - thermal-analysis and heat of fusion measurements, *J. Electrochem. Soc.* 135 (1988) 850–854.
- [15] T.K. Abdullaha, C. Petitjean, P.J. Pantreix, S. Mathieu, C. Rapin, M. Vilasi, Z. Hussain, A.A. Rahim, Electrochemical characterization of chromia- and alumina-forming nickel-based superalloys in molten silicates, *Appl. Surf. Sci.* 360 (2016) 510–518.
- [16] S. Fabre, C. Cabet, L. Cassayre, P. Chamelot, S. Delepech, J. Finne, L. Massot, D. Noel, Use of electrochemical techniques to study the corrosion of metals in molten fluoride melts, *J. Nucl. Mater.* 441 (2013) 583–591.
- [17] X.X. Ye, H. Ai, Z. Guo, H.F. Huang, L. Jiang, J.Q. Wang, Z.J. Li, X.T. Zhou, The high-temperature corrosion of Hastelloy N alloy (UNS N10003) in molten fluoride salts analysed by STXM, XAS, XRD, SEM, EPMA, TEM/EDS, *Corros. Sci.* 106 (2016) 249–259.
- [18] D. Walaszek, M. Senn, M. Faller, L. Philippe, B. Wagner, E. Baska, A. Ulrich, Metallurgical and chemical characterization of copper alloy reference materials within laser ablation inductively coupled plasma mass spectrometry: method development for minimally-invasive analysis of ancient bronze objects, *Spectrochimica Acta Part B-Atomic Spectroscopy* 79–80 (2013) 17–30.
- [19] T. Vaculovic, T. Warchilova, T. Simo, O. Matal, V. Otruba, P. Mikuska, V. Kanicky, Elemental mapping of structural materials for a nuclear reactor by means of LA-ICP-MS, *J. Anal. At. Spectrom.* 27 (2012) 1321–1326.
- [20] R. Cerrato, A. Casal, M.P. Mateo, G. Nicolas, Dealloying evidence on corroded brass by laser-induced breakdown spectroscopy mapping and depth profiling measurements, *Spectrochimica Acta Part B-Atomic Spectroscopy* 130 (2017) 1–6.
- [21] M.A. Gomez-Moron, P. Ortiz, R. Ortiz, J.M. Martin, M.P. Mateo, G. Nicolas, Laser-induced breakdown spectroscopy study of silversmith pieces: the case of a Spanish canopy of the nineteenth century, *Appl. Phys. Mater. Sci. Process.* (2016) 122.
- [22] O. Matal, T. Simo, L. Nesvadba, V. Dvorak, V. Kanicky, P. Sulovsky, J. Machat, Interaction of pipeline materials with molten fluoride salts, *Zeitschrift Fur Naturforschung Section A-A Journal of Physical Sciences* 62 (2007) 769–774.
- [23] T. Vaculovic, P. Sulovsky, J. Machat, V. Otruba, O. Matal, T. Simo, C. Latkoczy, D. Gunther, V. Kanicky, The EPMA, LA-ICP-MS and ICP-OES study of corrosion of structural materials for a nuclear reactor cooling circuit by molten fluoride salt treatment, *J. Anal. At. Spectrom.* 24 (2009) 649–654.
- [24] C. Merlet, An accurate computer correction program for quantitative electron-probe microanalysis, *Mikrochim. Acta* 114 (1994) 363–376.
- [25] J.W. Koger, Evaluation of Hastelloy N alloys After Nine Years Exposure to Both a Molten Fluoride Salt and Air at Temperatures From 700 to 560 °C, Oak Ridge National Laboratory, 1972 ORNL-TM-4189.
- [26] G.Q. Zheng, B. Kelleher, G.P. Cao, M. Anderson, T. Allen, K. Sridharan, Corrosion of 316 stainless steel in high temperature molten Li2BeF4 (FLiBe) salt, *J. Nucl. Mater.* 461 (2015) 143–150.

6.5 ARTICLE 5

Novak, M.; Gadas, P.; Filip, J.; Vaculovic, T.; Prikryl, J.; Fojt, B. *Mineralogy and Petrology* 2011, 102, 3-14 (IF=1.573)

Blue, complexly zoned, (Na,Mg,Fe,Li)-rich beryl from quartz-calcite veins in low-grade metamorphosed Fe-deposit Skály near Rýmařov, Czech Republic

Milan Novák · Petr Gadas · Jan Filip ·
Tomáš Vaculovič · Jan Příkryl · Bohuslav Fojt

Received: 2 December 2010 / Accepted: 4 July 2011 / Published online: 30 July 2011
© Springer-Verlag 2011

Abstract Syn-tectonic quartz-calcite veins containing blue beryl are enclosed in hematite > magnetite-rich portions of the low-grade metamorphosed Fe-deposit Skály near Rýmařov, Czech Republic. Aggregates of pale to deep blue beryl, up to 2 cm in diameter, are associated with euclase, clinocllore, hematite, albite and dravite. Complexly zoned beryl crystals consist of skeletal aggregates of beryl I randomly distributed within volumetrically dominant beryl II with narrow rims of beryl III. All types of beryl have similar contents of Na (0.32–0.49 apfu) and Mg (0.31–0.41 apfu) but variable contents of Fe_{tot} (0.05–0.34 apfu) and Al (1.20–1.62 apfu). The LA-ICP-MS study yielded elevated contents of Li, up 1,314 ppm (0.28 wt.% Li₂O) in beryl I. The quartz-calcite veins represent an unusual type of low-T metamorphic-hydrothermal vein related to Fe-ore deposit characterized by single-stage fracturing and mobilization in a

closed system at T~200–300°C and CO₃²⁻ as a major complexing agent for the mobility of Be.

Introduction

The chemical composition of beryl is commonly close to the ideal formula Be₃Al₂Si₆O₁₈; however, more complicated compositions are also quite frequent, leading to the following general formula for beryl-group minerals written as: ${}^{\text{CH}}(\text{Na}, \text{Cs}, \text{Rb}, \text{K}, \text{H}_2\text{O}, \text{He}, \text{Ar}) {}^{\text{T}(2)}(\text{Be}, \text{Li}, \square)_3 {}^{\text{O}}(\text{Al}, \text{Fe}^{3+}, \text{Sc}, \text{Cr}, \text{V}, \text{Fe}^{2+}, \text{Mg}, \text{Mn}^{2+})_2 {}^{\text{T}(1)}[\text{Si}_6\text{O}_{18}]$ (see e.g., Černý 2002). Compositional variations in natural members of the beryl group tend to three general compositions, where R⁺ = Na, Cs, Rb, K; R²⁺ = Mg, Fe²⁺ and R³⁺ = Al, Sc, Fe³⁺: (i) beryl with an idealized formula Be₃R₂³⁺Si₆O₁₈ (beryl—Be₃Al₂³⁺Si₆O₁₈, bazzite—Be₃Sc₂³⁺Si₆O₁₈; stoppaniite—Be₃Fe₂³⁺Si₆O₁₈); (ii) O-beryl with dominant substitutions at the O site and CH site (channel site) leading to the simplified general formula R⁺Be₃R³⁺R²⁺Si₆O₁₈ (Hawthorne and Huminicki 2002; Barton and Young 2002); (iii) T-beryl with a dominant substitution at the T(2) site and CH site leading to the simplified general formula R⁺Be₂LiR₂³⁺Si₆O₁₈ (pezzotaite—CsBe₂LiAl₂Si₆O₁₈). Iron is a typical minor to major element in beryl-group minerals (see Ferraris et al. 1998; Groat et al. 2010 and review therein). Spectroscopic studies suggest that Fe may enter, along with the O site, also the CH site, the T(1) site (Groat et al. 2010) and the 6 g and the 4 d positions in the beryl structure (Platonov et al. 1979; Taran and Rossman 2001); however, the amount of Fe at these positions is typically very low to nil. Lithium enters the T(2) site via the substitution ${}^{\text{CH}}\square {}^{\text{T}(2)}\text{Be}^{2+} = {}^{\text{CH}}\text{R}^{+} {}^{\text{T}(2)}\text{Li}^{+}$, but traces of Li may also be present at the CH site (Sherriff et al. 1991). Small amount of Si is considered to enter T(2) site

Editorial handling: I. Broska and D. Harlov

M. Novák (✉) · P. Gadas · J. Příkryl · B. Fojt
Department of Geological Sciences, Masaryk University,
Kotlářská 2,
611 37 Brno, Czech Republic
e-mail: mnovak@sci.muni.cz

J. Filip
Regional Centre of Advanced Technologies and Materials,
Palacký University,
Šlechtitelů 11,
783 71 Olomouc, Czech Republic

T. Vaculovič
Department of Chemistry, Masaryk University,
Kotlářská 2,
611 37 Brno, Czech Republic

(Beal and Lentz 2010). Also molecular H₂O along with He and Ar frequently enters into the CH site, on two distinct positions - type I H₂O and type II H₂O (e.g., Brown and Mills 1986; Sherriff et al. 1991).

Novák and Jilemnická (1986) first described blue beryl from quartz-calcite veins in a low-grade metamorphosed Lahn-Dill type Fe-deposit at Skály near Rýmařov, Northern Moravia, Czech Republic; the petrography, mineralogy and fluid inclusion characteristics of the Skály Fe-deposit were reported by Fojt et al. (2007). Our study shows that this unusual (Na,Mg,Fe)-enriched beryl is complexly zoned (beryl I, beryl II, beryl III) and contains minor but variable concentrations of Li. Based on EMPA and LA-ICP-MS data, and Mössbauer and FTIR spectroscopy we discuss potential substitution mechanisms, miscibility/immiscibility in this texturally and compositionally unusual beryl as well

as mobility of Be and Li in low-grade metamorphic-hydrothermal conditions and a genetic type of the beryl occurrence Skály near Rýmařov.

Geological setting

The low-grade metamorphosed Lahn-Dill type Fe-deposit Skály near Rýmařov (former name of the locality - Pittenwald), mined intermittently from the 17th to 19th centuries, is located at the easternmost part of the Vrbno Group (Devonian) close to the tectonic border with overlying greywackes and schists of the Andělská Hora Formation (Carboniferous) (Fig. 1) in the eastern termination of the Rhenohercynian Zone of the Variscan chain (Franke and Żelaźniewicz 2000). The Vrbno Group is made

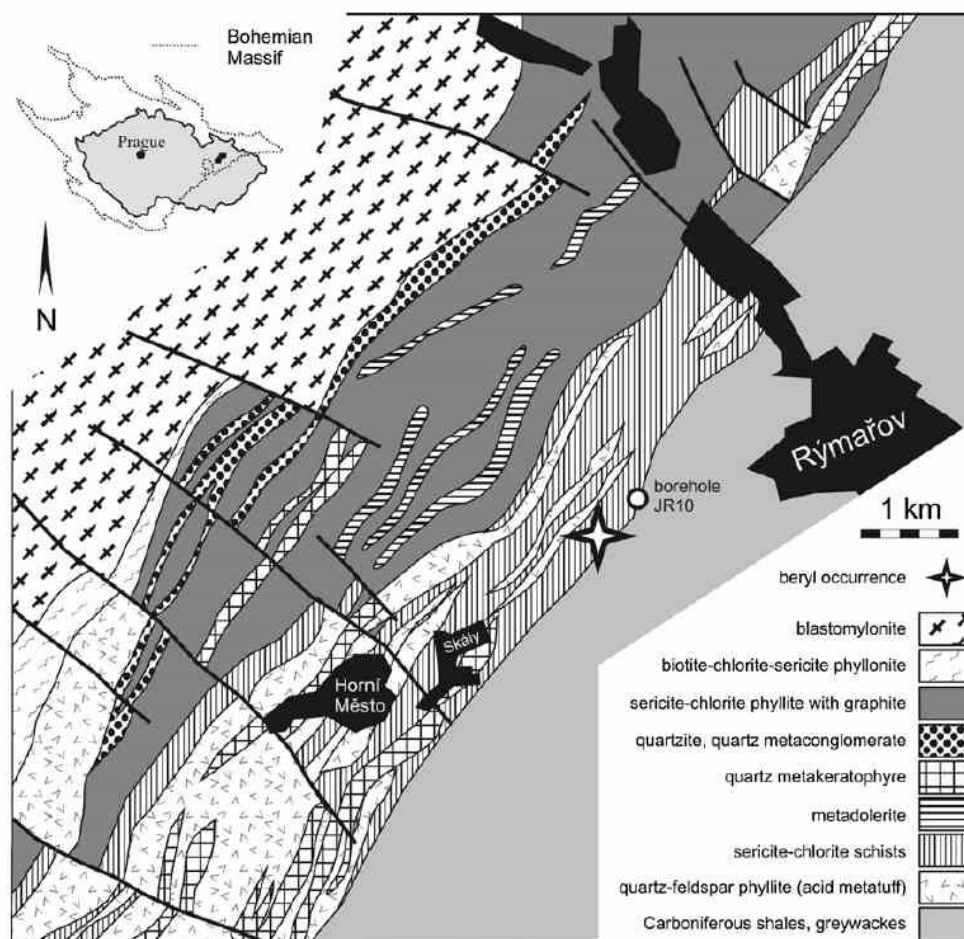


Fig. 1 Schematic geological map of the Vrbno Group and the Andělská Hora Formation; the locality Skály near Rýmařov is marked by a star. Modified from Opletal and Koverdýnský et al. (1998)

up of dominant sericite-chlorite and chlorite schists alternating with less common metarhyolites, graphite schists and Fe-rich ores in the examined area. Metavolcanics of the eastern part of the Vrbno Group are affiliated with a back-arc rift-related alkaline suite (Hanžl et al. 2007) and such a scenario is in line with the current palaeogeographic models for the region (Kalvoda et al. 2008). The rocks underwent complicated tectonic and metamorphic evolution with several stages of deformation and low-grade metamorphism. The peak conditions at $T \sim 350\text{--}400^\circ\text{C}$ and $P \sim 4\text{--}5.5$ GPa (René and Šrein 2001) were attained in chloritoid schists located several km S of the Skály Fe-deposit. The chlorite thermometer (Cathelineau and Nieva 1985) yielded $278\text{--}308^\circ\text{C}$ for chlorite from chlorite schist at Skály (Fojt et al. 2007) and $291\text{--}320^\circ\text{C}$ for chlorite from a hematite + magnetite-rich ore at Horní Město (Fig. 1; Rozmáněk 1981), respectively.

The rock sequence of the Skály Fe-ore deposit is composed of dominant sericite-chlorite schists with minor calcite and accessory titanite, pyrite, chalcopryrite, hematite and stilpnomelane. Coarse-grained portions of sericite-chlorite schists with abundant calcite and minor albite, quartz and accessory tourmaline are rare. Common intercalations of hematite > magnetite-rich layers (Fe-ore mined in the past) reached a thickness of up to several m and a length of up to several hundreds m. Along with abundant hematite and common minor chlorite and magnetite, calcite, quartz, accessory to locally minor pyrite and chalcopryrite also were identified (Fojt et al. 2007). A geochemical study of rocks at the Horní Město locality (Fig. 1) and from the borehole JR-10, situated about 0.5 km N of the Skály deposit (Fig. 1), yielded concentrations of Be of 2–6.3 ppm (Vlčková 1984; Valová-Tomšíková 1987). At the Skály Fe-deposit, 6–10 ppm Be in schist and hematite-calcite rock, and up to 106 ppm Be in magnetite-chlorite rock (Vavrošová 1987), were found.

The syn-tectonic quartz-calcite veins are exclusively enclosed in hematite > magnetite-rich portions of the Skály Fe-deposit (Novák and Jilemnická 1986). They are up to ~10 cm thick and their length of ~1 m was estimated from common fragments in old dumps; no outcrops with quartz-calcite veins have been found at the locality. These veins are typically concordant to a well-developed foliation of the host rock; thin discordant veinlets are very rare. The fluid-inclusion study of quartz and calcite from quartz-calcite veins yielded temperatures of homogenization of aqueous inclusions at $110\text{--}180^\circ\text{C}$, and $124\text{--}156^\circ\text{C}$, respectively, low fluid salinity (2.2–4.3 wt.% of NaCl equivalent) and Na-Mg-Cl salt composition (Fojt et al. 2007). Isotopic composition of calcite ^{13}C (+0.9 to +2.2 PDB) and ^{18}O (–8.1 to 13.5 PDB) indicate a metamorphic origin for H_2O and a marine source for C (Fojt et al. 2007).

Experimental methods

The chemical compositions of beryl and associated minerals were determined with a Cameca SX100 electron microprobe at the Joint Laboratory of Electron Microscopy and Microanalysis, Department of Geological Sciences, Masaryk University, Brno and Czech Geological Survey, Brno, P. Gadas analysts. The analytical conditions were an accelerating voltage of 15 kV, a beam current of 10 nA, and a beam size of 5 μm . The following standards and analytical lines were used: (K_α) lines: sanidine (Si, Al, K), albite (Na), almandine (Fe), pyrope (Mg), titanite (Ca, Ti), rhodonite (Mn), ScVO_4 (Sc,V); (L_α) lines: pollucite (Cs), Rb-leucite (Rb). The analytical data were corrected using the PAP correction procedure (Pouchou and Pichoir 1985). Crystal formulae of beryl were calculated in three different ways: a) normalized on Si=6 apfu, because most studies show that this site is occupied only (or almost exclusively) by Si and the presence of Si at the T(2) site is negligible if any (Černý 2002, Groat et al. 2010); b) calculated on the basis: 18 oxygens, $\text{Fe}_{\text{tot}} = \text{FeO}$ and stoichiometric Be + Li = 3 apfu (beryl I, beryl III); c) calculated on the basis: 18 oxygens, 5–20% Fe^{3+} of total Fe and stoichiometric Be = 3 apfu (beryl II).

Instrumentation for LA-ICP-MS at the Department of Chemistry, Masaryk University, Brno, T. Vaculovič analyst, consists of a laser ablation system UP 213 (New Wave, USA) and an ICP-MS spectrometer Agilent 7500 CE (Agilent, Japan). A commercial Q-switched Nd:YAG laser ablation device works at the 5th harmonic frequency which corresponds to the wavelength of 213 nm. The ablation cell was flushed with helium (carrier gas), which transported the laser-induced aerosol to the inductively coupled plasma mass spectrometer (1 l/min). For LA-ICP-MS measurements we used a hole drilling mode (fixed sample position during laser ablation) with a duration of 75 s for each spot. Laser ablation was performed with laser spot diameter 40 μm , laser fluence 24 Jcm^{-2} and repetition rate 10 Hz.

The amount of Fe^{3+} was estimated by the Mössbauer spectroscopy. The transmission ^{57}Fe Mössbauer spectra of powdered beryl (ground under acetone using an agate mortar and subsequently washed in cold diluted hydrochloric acid) were acquired at constant acceleration mode using a ^{57}Co in Rh source and 1,024 channel detector at a temperature range of 5–300 K. The isomer shift was calibrated against an $\alpha\text{-Fe}$ foil at room temperature. Spectra were fitted by Lorentz functions using the computer program CONFIT2000 (Žák and Jirásková 2006).

Fourier transform infrared (FTIR) spectra were recorded using a Nicolet Nexus 670 spectrometer equipped with DTGS detector and XT-KBr beamsplitter. The sample was prepared by mixing 1 mg of powdered sample with 300 mg of KBr (dried beforehand at 150°C)

with an automated mortar and pressing in an evacuated die at 10 tons. A total of 32 scans in air were done for the sample in the wavenumber range 4,000–400 cm^{-1} at a resolution of 4 cm^{-1} .

The methods used in this study differ significantly in terms of the volume of analyzed material. The electron microprobe has a beam-spot diameter of $\sim 5 \mu\text{m}$, whereas the LA-ICP-MS employs a laser spot diameter of $\sim 40 \mu\text{m}$. Bulk amounts of 0.2 g and 0.1 mg were used in Mössbauer spectroscopy and FTIR-spectroscopy, respectively. Consequently, each method is able to analyze a distinct scale of zoning, and we took this fact into account in the discussion. In all compositional types of beryl, apparent in the BSE images, EMPA and LA-ICP-MS data can be generally correlated; however, Mössbauer spectroscopy, FTIR-spectroscopy and X-ray powder diffraction data were applicable only to volumetrically dominant beryl II.

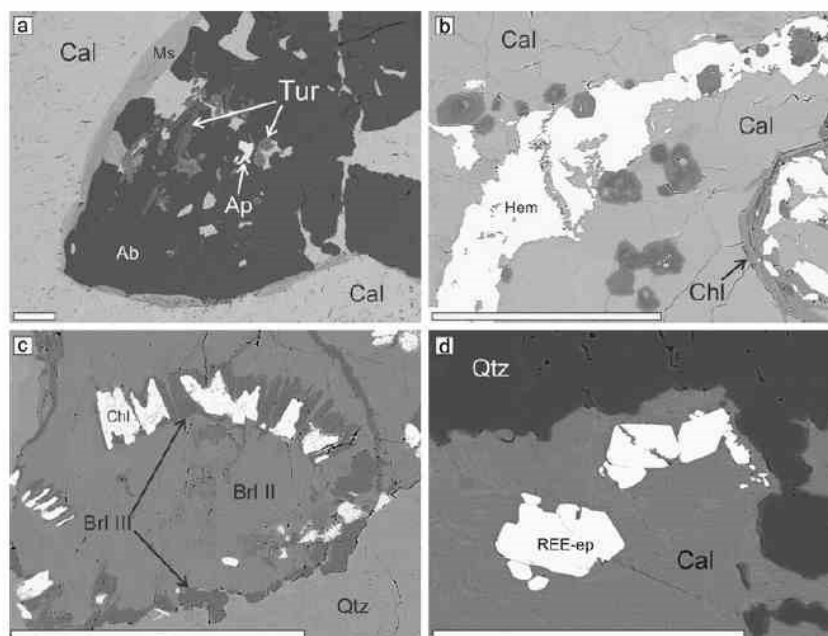
Results

Mineral assemblages of quartz-calcite veins

The syn-tectonic quartz-calcite veins containing blue beryl are typically enclosed in hematite > magnetite-rich portions of the Fe-ore deposit. Dominant white to grayish quartz consists of anhedral grains, up to 5 mm in size, with common undulose extinction in the optical microscope. Moreover, thin quartz veins typically cut beryl. Grayish to

pale brownish calcite only locally predominates over quartz, commonly close to the contact with the host rock; otherwise, its distribution in the veins is rather irregular. In thin sections, two texturally distinct types of calcite were recognized. Calcite I forms medium- to coarse-grained aggregates in the vein matrix (Fig. 2a); calcite II cuts through early minerals, including beryl, in thin veinlets. Large grains of calcite I show locally folded polysynthetic twinning. Small grayish green flakes of chlorite and thin flakes of hematite are typically present close to the generally sharp contact with the host rock. Chlorite also occurs as aggregates in beryl (Fig. 2c). Several common to rare accessory minerals were identified. Common albite (Ab_{100-99}) forms subhedral grains, up to 3 mm in size, irregularly distributed in veins mostly situated close to beryl (Fig. 2a). Oscillatory zoned, dark brown-green to dark green euhedral crystals of tourmaline, up to 200 μm long (Fig. 2b), were found enclosed in calcite, quartz, albite, and only rarely in beryl. They are also associated with hematite and chlorite (Fig. 2b) near the contact or form folded thin veinlets composed of acicular crystals enclosed in quartz or calcite. Small flakes of muscovite are commonly associated with tourmaline and albite (Fig. 2a). Rare bornite, digenite, chalcopyrite, monazite-(Ce), REE-rich epidote and fluorapatite form small euhedral to subhedral grains, commonly from ~ 10 to $\sim 100 \mu\text{m}$ in diameter (Fig. 2a,d). Most minerals are fresh with no evident alterations. Only REE-rich epidote is locally replaced by Ca,REE-fluorocarbonates and rarely by monazite-(Ce).

Fig. 2 BSE images of selected minerals from the quartz-calcite veins. **a** Aggregate of albite grains in calcite. Note small inclusions of tourmaline and fluorapatite in albite and laths of muscovite at the contact between albite and calcite. **b** Calcite with flakes of hematite and chlorite and oscillatory zoned euhedral crystals of tourmaline. **c** Aggregate of subhedral grains of chlorite in beryl II with a narrow rim of beryl III. **d** Euhedral grains of REE-rich epidote in calcite. Scale bar = 200 μm . Abbreviations (according to Kretz 1983): *Cal* calcite; *Qtz* quartz; *Tur* tourmaline; *Ap* apatite; *Eu* euclase; *Ms* muscovite; *Ab* albite; *Hem* hematite; *Chl* chlorite; *Brl* beryl; *REE-ep* REE-rich epidote



Copper sulphides are weathered to malachite and unspecified Fe-oxyhydroxides (Fojt et al. 2007).

Homogenous **calcite** (both aggregates and thin veinlets) with low concentrations of Mg (0.01 apfu), Fe (0.01 apfu) and Mn (0.005 apfu) is very similar to the data of Fojt et al. (2007). The chlorite composition matches Al-rich **clinochlore** with $Fe_{tot}/(Fe_{tot} + Mg)$ varying about 0.35 (wet chemical analyses of chlorite from host rocks yielded 0.36 and 0.44; Fojt et al. 2007), containing slightly increased Ni (up to 0.03 apfu, 0.32 wt.% NiO) and low Li ($Li_2O=0.06$ wt.%; Fojt et al. 2007). The chlorite thermometer (Cathelineau and Nieva 1985) yielded 242–246°C. Cores of the oscillatory zoned tourmaline (Fe-rich **dravite**) usually display a slightly elevated X-site vacancy (~0.1–0.2 pfu), $Fe_{tot}/(Fe_{tot} + Mg)=0.33–0.40$ and contents of Al within the range of 5.73–5.86 apfu compared to the rims which show lower Al (5.34–5.71), higher $Fe_{tot}/(Fe_{tot} + Mg)=0.41–0.47$, low X-site vacancy (0–0.11 pfu) and, in some cases, slightly increased Ca (up to 0.16 apfu). Both cores and rims yielded low contents of F (0.03–0.17 apfu) and, occasionally, slightly elevated contents of Ni (up to 0.08 apfu, 0.62 wt.% NiO). **Hematite** is homogenous with elevated Ti (up to 0.02 apfu, 0.85 wt.% TiO_2) and trace Ca (up to 0.01 apfu, 0.37 wt.% CaO). Crystals of apatite are homogenous and the composition is close to the **fluorapatite** end-member. Patchy zoned **REE-rich epidote** shows variable content of $\sum REE=0.5–0.71$ apfu, Al=1.84–1.95 apfu and $Fe_{tot}^{3+}=1.04–1.02$ apfu. Phengitic **muscovite** has high Si=3.25–3.35 apfu, low contents of Al=2.12–2.20 apfu, high to moderate concentrations of $Fe^{2+}=0.07–0.26$ apfu, Mg=0.25–0.39 apfu, and $Fe_{calc}^{3+}=0.08–0.20$ apfu, but very low contents of Na \leq 0.04, Ca \leq 0.01, Ti \leq 0.01 and F \leq 0.06 (all in apfu).

Beryl description and its mineral assemblage

Subhedral to euhedral, short prismatic crystals of beryl, up to 8 mm long and their aggregates, up to 2 cm in diameter, range in color from pale blue to a sporadic deep blue color. While translucent, no gem-quality beryl has been found. Position and orientation of the crystals and their aggregates within the veins are uneven. They occur close to the contact with host rock or are situated in central parts of the veins. Complexly zoned beryl crystals consist of three individual zones commonly well-defined in BSE images (Fig. 3a) and showing equal optical orientation. Beryl I forms solitary euhedral grains, up to ~200 μm in size, typically with hexagonal shape, frequently arranged in skeletal aggregates, which also show hexagonal symmetry, both randomly distributed within beryl II (Fig. 3b,c). Volumetrically dominant beryl II (Fig. 3d) comprises 90–95 vol. % of the individual beryl crystals. Beryl III forms narrow rims of large beryl II crystals from ~10 to 200 μm thick (Fig. 3c,d).

Commonly, late quartz \pm calcite veins cutting beryl II also are rimmed by thin zone of beryl III (Fig. 3c,d). Beryl II contains rare relics of chlorite, which also show a narrow zone of beryl III (Fig. 2c). Most crystals of beryl contain subhedral inclusions of euclase, up to ~200 μm in size, typically associated with euhedral grains and skeletal aggregates of beryl I (Fig. 3e,f). The textural relations suggest that euclase + beryl I \pm calcite I crystallized simultaneously as the earliest minerals in the complex beryl crystals. Beryl crystals are locally cut by late veinlets of quartz + calcite II. Beryl II occasionally shows corrosive contacts chiefly with calcite II (Fig. 3c,d).

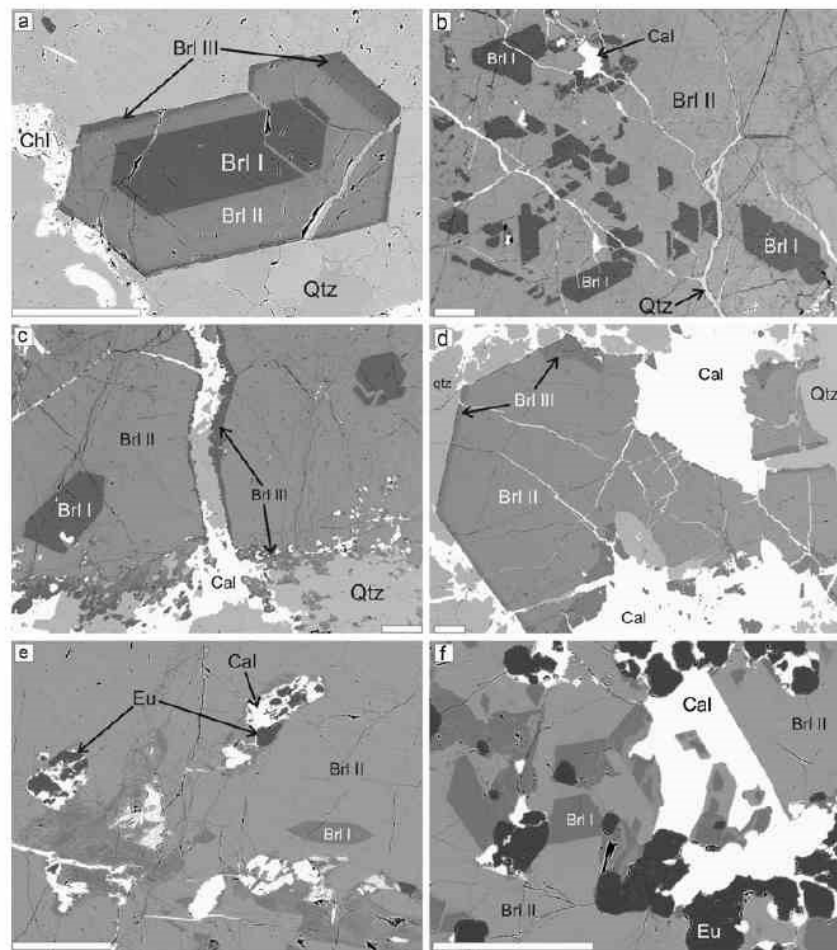
Textural relations suggest that beryl, quartz, calcite and minor to accessory euclase, chlorite, albite, hematite, muscovite I, tourmaline and Cu-sulfides crystallized simultaneously. In the beryl crystals, the detailed succession of crystallization is evident—euclase + beryl I \pm calcite I \rightarrow beryl II \rightarrow beryl III + quartz \pm calcite II. No alterations of beryl except corrosion along contacts with calcite (Fig. 3d) were observed. Beryl I, beryl II, beryl III and calcite in a spatial contact are locally intact (Fig. 3e), whereas euclase is commonly replaced by calcite or muscovite (Fig. 3e,f).

Chemical, spectroscopic and X-ray diffraction study of beryl

Electron microprobe study of about 10 individual crystals revealed three distinct but individually rather homogeneous compositions. All three types of beryl have high but similar contents of Na (0.43–0.49; 0.42–0.48; 0.32–0.45 apfu) and Mg (0.37–0.41; 0.35–0.39; 0.31–0.38 apfu) but variable contents of Fe (0.05–0.08; 0.24–0.34; 0.09–0.15 apfu) and Al (1.49–1.62; 1.20–1.34; 1.43–1.55 apfu) in beryl I, beryl II and beryl III, respectively (Table 1). The only minor cations above the detection limits of EMP are Zn (0.15 wt.% ZnO) and Rb (0.14 wt.% Rb_2O) in beryl I and Ca (0.12 wt.% CaO) in beryl III. The other detected oxides (MnO, K_2O , Cs_2O , TiO_2) were found below or close to the detection limits in all compositional types of beryl.

The LA-ICP-MS study revealed similar concentrations of some trace elements (Sc, V, Mn, Co, Ni, Ga) in beryl I, beryl II and beryl III (Table 2). Other elements (Ti, Zn, Ge, Cs) are more or less partitioned into the individual beryl types (Table 2). The concentrations of Li in beryl I, beryl II and beryl III are lower relative to the preliminary data given by Novák et al. (2010) with the concentrations of Li up to 2,135 ppm obtained using LA-ICP-MS. Recalculation to Li_2O yielded 0.25–0.28 wt.% Li_2O in beryl I and 0.08 wt.% Li_2O in beryl III. Calculation of H_2O using the empirical relationship of Giuliani et al. (1997) for emeralds gave high values up to 3.4 wt.% H_2O .

Fig. 3 BSE images of beryl and euclase from quartz-calcite veins. **a** Simple zoned euhedral crystal of beryl in quartz showing three compositional types of beryl from centre outwards – beryl I, beryl II and beryl III. **b** Skeletal aggregate of euhedral grains of beryl I in beryl II. Note thin late veinlets of quartz and calcite. **c** Two beryl crystals with inclusions of beryl I in beryl II and narrow anhedral rims of beryl III along late quartz \pm calcite veinlets. **d** Large crystal of beryl II with euhedral rims of beryl III. Note absence of beryl I and evident corrosion of beryl II by calcite. **e** Beryl II with inclusions of beryl I associated with subhedral grains of euclase replaced by calcite. **f** Skeletal aggregate of beryl I in beryl II closely associated with subhedral grains of euclase, which is evidently replaced by calcite, whereas beryl is more stable and corrosion is less intensive. Note that quartz is commonly absent in the assemblage euclase + beryl I + beryl II + calcite in Fig. 4e,f. Scale bar=200 μ m. Abbreviations as in Fig. 2



Typical feature of ^{57}Fe Mössbauer spectra of beryl is high asymmetry of dominant Fe^{2+} doublet (da Costa et al. 2006; Groat et al. 2010; Price et al. 1976; Viana et al. 2002) with very broad low-velocity peak and isomer shift $\delta=1.2$ mm/s and quadrupole splitting $\Delta E_Q=2.7$ mm/s (Groat et al. 2010; Novák and Filip 2010). Accordingly, Mössbauer spectra collected from beryl II are highly asymmetric at room temperature and down to 25 K (Fig. 4). With respect to the asymmetry and strong overlap of Fe^{2+} and Fe^{3+} doublets in spectra measured between 300 and 25 K, we fit exclusively the 5 K spectrum where the strong asymmetry of the main paramagnetic Fe^{2+} doublet disappeared. All the spectral components have hyperfine parameters typical for Fe in a high-spin state. The most intense Fe^{2+} doublet with parameters $\delta=1.30$ mm/s and $\Delta E_Q=2.77$ mm/s is assigned to octahedral Fe^{2+} occupying the O site. However, partial substitution of Fe^{2+} into a channel site could not be unambiguously excluded/confirmed on the basis of Mössbauer spectra, where

another Fe^{2+} doublet with parameters comparable to OFe^{2+} , but with very broad spectral lines, could be fitted (see 5 K spectrum in Fig. 4). Ferric iron seems to be solely octahedrally coordinated (O site) with doublet parameters $\delta=0.50$ mm/s and $\Delta E_Q=0.69$ mm/s and resulting relative contribution, calculated from subspectral areas, roughly 5 to 20 at.% Fe^{3+} from total Fe. Such a high uncertainty is given by the fact that the fitting procedure is highly model-dependent. An inner doublet typically ascribed to Fe^{2+} at the T site was not observed in this blue beryl (cf. Novák and Filip 2010).

Unpolarized FTIR spectrum of the blue beryl show characteristic bands at $3,655$, $3,592$ cm^{-1} and the $1,624$ cm^{-1} (Fig. 5). According to literature data we interpret the $3,655$ cm^{-1} band as the ν_3 stretching mode of type II H_2O in the channel site bonded to Na and $1,624$ cm^{-1} band as a corresponding ν_2 bending mode (cf. Della Ventura et al. 2007 and references therein). The $3,592$ cm^{-1} band is, on the other hand, interpreted as either the ν_3 stretching mode of type I

Table 1 Representative EMP analyses of the individual types of beryl and euclase. The detected oxides (MnO, K₂O, Cs₂O, TiO₂) were found below or close to the detection limits (Mn - 620, K - 255, Cs - 333, Ti - 217 all in ppm) in all compositional types of beryl

| Sample | beryl I | | | beryl II | | | beryl III | | | euclase |
|--------------------------------|---------|--------|--------|----------|--------|--------|-----------|--------|--------|---------|
| | 5/1 | 13/1 | 11/1 | 7/1 | 12/1 | 18/1 | 8/1 | 9/1 | 20/1 | 2/1 |
| SiO ₂ wt. % | 66.13 | 65.98 | 65.73 | 64.89 | 65.30 | 65.09 | 65.87 | 66.11 | 65.99 | 42.41 |
| Al ₂ O ₃ | 14.14 | 14.19 | 13.89 | 11.24 | 11.47 | 11.37 | 13.95 | 14.02 | 13.43 | 35.01 |
| FeO | 0.78 | 0.90 | 0.85 | 4.17 | 4.50 | 4.25 | 1.29 | 1.31 | 1.55 | 0.31 |
| MgO | 2.85 | 2.77 | 2.80 | 2.74 | 2.70 | 2.78 | 2.49 | 2.46 | 2.79 | b.d.l. |
| ZnO | b.d.l. | 0.10 | b.d.l. | b.d.l. | b.d.l. | b.d.l. | b.d.l. | b.d.l. | b.d.l. | b.d.l. |
| CaO | 0.04 | b.d.l. | b.d.l. | b.d.l. | b.d.l. | b.d.l. | b.d.l. | 0.04 | b.d.l. | b.d.l. |
| Na ₂ O | 2.58 | 2.71 | 2.48 | 2.46 | 2.43 | 2.50 | 2.13 | 2.30 | 2.21 | b.d.l. |
| Rb ₂ O | b.d.l. | b.d.l. | 0.14 | b.d.l. | b.d.l. | b.d.l. | b.d.l. | b.d.l. | b.d.l. | b.d.l. |
| <i>sum</i> | 86.52 | 86.65 | 85.89 | 85.50 | 86.40 | 85.99 | 85.73 | 86.24 | 85.97 | 77.73 |
| Si ⁴⁺ apfu | 6.000 | 6.000 | 6.000 | 6.000 | 6.000 | 6.000 | 6.000 | 6.000 | 6.000 | 1.010 |
| Al ³⁺ | 1.512 | 1.521 | 1.494 | 1.225 | 1.242 | 1.235 | 1.498 | 1.500 | 1.439 | 0.982 |
| Fe ²⁺ | 0.059 | 0.068 | 0.065 | 0.322 | 0.346 | 0.328 | 0.098 | 0.099 | 0.118 | 0.006 |
| Mg ²⁺ | 0.385 | 0.376 | 0.381 | 0.378 | 0.370 | 0.382 | 0.338 | 0.333 | 0.378 | – |
| Zn ²⁺ | – | 0.007 | – | – | – | – | – | – | – | – |
| Ca ²⁺ | 0.004 | – | – | – | – | – | – | 0.004 | – | – |
| Na ⁺ | 0.454 | 0.478 | 0.439 | 0.441 | 0.433 | 0.447 | 0.376 | 0.405 | 0.390 | – |
| Rb ⁺ | – | – | 0.008 | – | – | – | – | – | – | – |
| <i>sum cat</i> | 8.414 | 8.450 | 8.387 | 8.366 | 8.391 | 8.392 | 8.310 | 8.341 | 8.325 | 1.998 |

b.d.l. - below detection limit

H₂O or the stretching vibration of O-H groups substituted for O(2) according to the (Fe²⁺OH)₁Al₁ vector (as proposed for the 3,595 cm⁻¹ band in stoppaniite; Della Ventura et al. 2007). In the FTIR spectrum are also noticeable CO₂ bands at ~2,350 cm⁻¹ (see also Novák and Jilemnická 1986). With respect to the measurement conditions, however, this CO₂ is most probably of atmospheric origin.

X-ray powder diffraction data of blue beryl (very likely volumetrically dominant beryl II) yielded the unit-cell dimensions: *a*=9.253(4) and 9.285(8), *c*=9.208(5) and 9.195(4) Å and *c/a*=0.995 and 0.990 according to Novák and Jilemnická (1986) and Vavrošová (1987), respectively.

These data are consistent with our new data: *a*=9.292(1) and 9.280(5), *c*=9.199(1) and 9.193(1) Å and *c/a*=0.990 and 0.991, and other Fe-enriched blue beryls (cf., Aurisicchio et al. 1988; Hänni 1980; Groat et al. 2010).

Discussion

Chemical composition, substitutions and zoning in beryl

Chemical analyses (EMPA) of beryl were first normalized to 6 Si apfu (see “Experimental Methods” for details). All

Table 2 LA-ICP-MS data of beryl from Skály (in ppm)

| | d.l. (ppm) | beryl I (n=5) | beryl II (n=16) | beryl III (n=6) |
|----|------------|---------------|-----------------|-----------------|
| Li | 1 | 1,148–1,314 | 48–93 | 183–362 |
| Sc | 1 | 13–18 | 20–34 | 19–33 |
| Ti | 1 | 13–29 | 45–144 | 10–15 |
| V | 0.1 | 21–31 | 40–57 | 35–44 |
| Mn | 0.4 | 7–10 | 12–33 | 7–18 |
| Co | 0.1 | 10–13 | 6–9 | 5–6 |
| Ni | 0.4 | 8–9 | 6–9 | 5–7 |
| Zn | 1 | 467–588 | 87–131 | 53–96 |
| Ga | 0.05 | 5–7 | 12–17 | 7–11 |
| Ge | 0.5 | 4–12 | 17–34 | 6–11 |
| Cs | 0.01 | 40–74 | 185–243 | 46–64 |

d.l. - detection limit

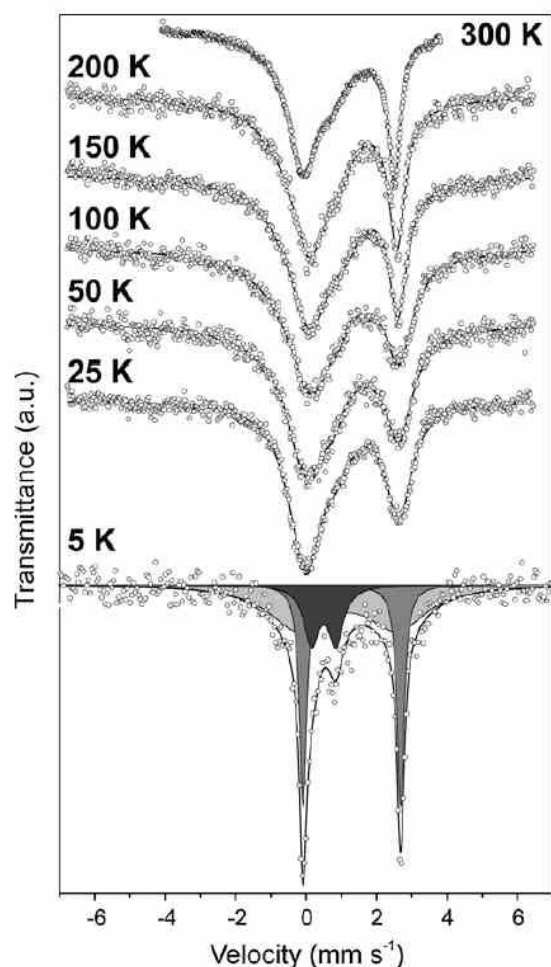


Fig. 4 Room- and low-temperature Mössbauer spectra of beryl II from Skály. Dark gray - $^{\circ}\text{Fe}^{3+}$, medium gray - $^{\circ}\text{Fe}^{2+}$, light gray - $^{\text{CH}}\text{Fe}^{2+}$ (see text for more details)

three compositional types of beryl are characterized by similar and mostly rather constant concentrations of Na and Mg, whereas Fe and Al vary fairly more significantly (Table 1). Poor negative correlation $R^{3+}/\sum R^{2+}$ (Fig. 6a) and poor positive correlation $\text{Na}^+/\sum R^{2+}$ (Fig. 6b) suggest dominant participation of the substitution (1) $^{\text{CH}}\square^{\text{O}}\text{R}^{3+} = ^{\text{CH}}\text{Na}^+ \text{O}^{\text{R}^{2+}}$ for beryl I and beryl III. However, beryl III and particularly Fe-enriched beryl II exhibit the evident excess of R^{2+} cations (Fig. 6b) commonly observed in Fe-rich beryl (Groat et al. 2010). If we plot Na vs. Mg (Fig. 6c), beryl II exhibits a similar pattern to beryl I and beryl III, which may imply that most Fe is present as Fe^{3+} in beryl II. This is supported by the plot Na vs. Fe_{tot} (Fig. 6d), in which no correlation is seen. However, it is in contradiction to the results of the Mössbauer spectroscopy, which yielded only

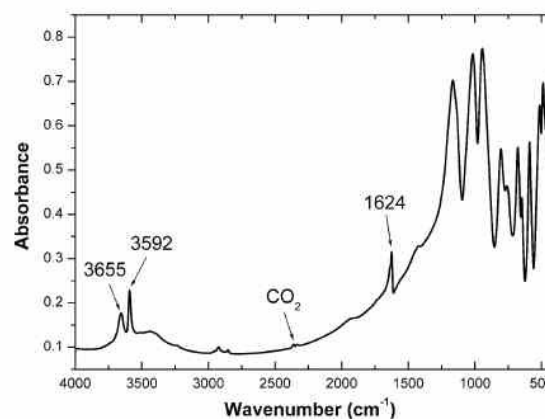


Fig. 5 FTIR spectrum of beryl II from Skály. The ripples at $\sim 2,900 \text{ cm}^{-1}$ are due to impurities of organic matter

5–20% of Fe^{3+} of total Fe (Fig. 4) and also slight excess of Na relative to Mg is evident (Fig. 6c).

Average data for three compositional types of beryl including concentrations of Li in beryl I and beryl III and $\text{Fe}^{2+}/\text{Fe}^{3+}$ in beryl II yielded results very similar to the normalization on 6 apfu Si for beryl I and beryl III with 6.027 and 6.037 apfu Si, respectively (Table 3). Beryl II with a total Fe as FeO has higher Si=6.070 apfu (Table 3). If we consider solely participation of the substitutions (1) and (2) $^{\text{CH}}\square^{\text{T}(2)}\text{Be}^{2+} = ^{\text{CH}}\text{Na}^+ \text{T}(2)\text{Li}^+$ in the beryl, Na^+ should be equal to $\sum R^{2+} + \text{Li}$. In both beryl I and beryl III, there is a deficiency of about 0.05 apfu of $\sum R^+$. These disproportions may be explained by several reasons. A higher amount of Fe^{3+} at the O site is the most probable and most effective, but it is in contradiction with the results of the Mössbauer study. The presence of Fe at the CH site (e.g., Viana et al. 2002; Da Costa et al. 2006), the presence of OH^- at the CH site (Della Ventura et al. 2007) and/or the presence of Si at the T(2) site (see Aurisicchio et al. 1988; Beal and Lentz 2010) may have played a role. Also overestimation of the Li content obtained from LA-ICP-MS may give this difference, although the content of Li is rather low. The current knowledge about the crystal chemistry of beryl and our analytical data do not allow us to distinguish, which of these factors caused the surplus of $\sum R^{2+}$. However, deficiency of R^+ -cations is common in aquamarine and blue beryl (e.g., Beal and Lentz 2010; Groat et al. 2010) but less common in emerald (Groat et al. 2007).

Participation of the substitutions (1) and (2) within a single crystal of beryl is notable because usually substitutions affiliated to the O site or to the T(2) site (plus CH site) are dominant (e.g., Aurisicchio et al. 1988; Franz and Morteani 2002). Aurisicchio et al. (1988) suggested that participation of these substitutions is restricted by crystal-

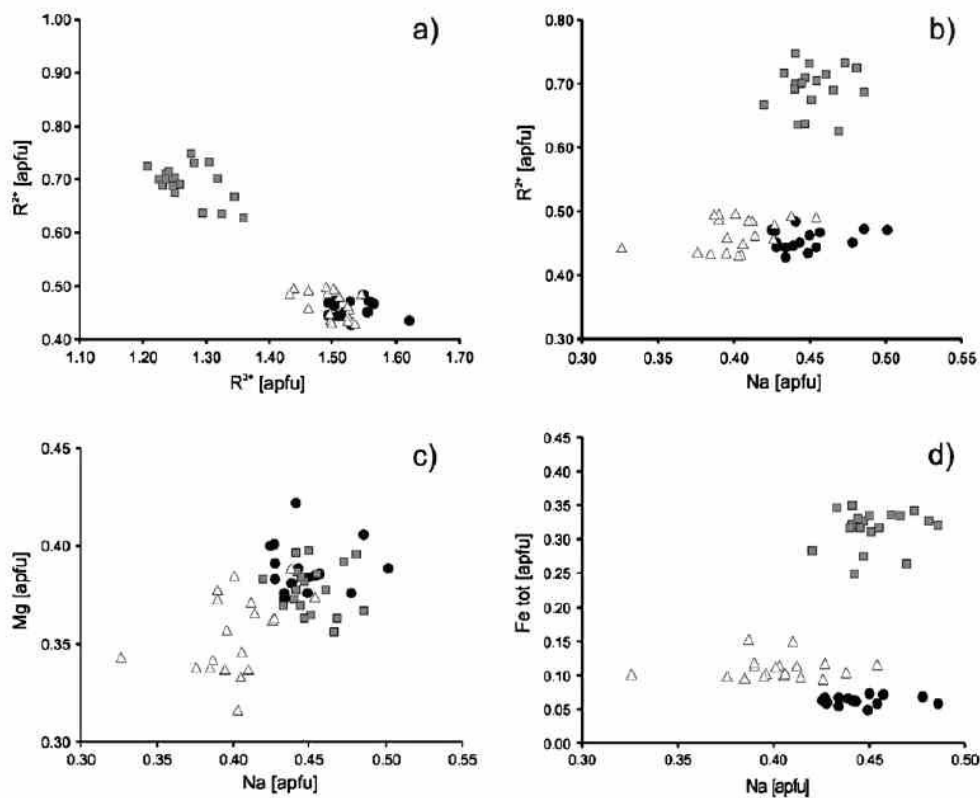


Fig. 6 Plots showing composition of the individual beryl types from Skály. a) R^{3+}/R^{2+} , b) Na/R^{2+} , c) Na/Mg , d) Na/Fe_{tot} , where $R^{2+} = Mg, Fe_{tot}^{2+}$, Zn and $R^{3+} = Al$; beryl I - triangles; beryl II - squares; beryl III - solid circles

structural constraints, whereas Černý (2002) considers concomitant participation of these substitutions simply geologically unlikely. Our results demonstrate that Fe-enriched beryl II contains lower concentrations of Li relative to late beryl III and chiefly to early beryl I. Because there are no discernible indications in the mineral assemblages (with dominant quartz and calcite) or in the change of PTX-conditions (indicated by replacement textures or zoning in minerals) to significantly change chemical activities (Li, Al, Fe) in the system during beryl crystallization, higher contents of Fe and/or higher participation of substitution reaction (1) may constrain lower degrees of substitution reaction (2) in beryl II. A lack of information about the contents of Fe^{3+} in beryl I and beryl III complicates our discussion and this question is still open. Beryl from Skály near Rýmařov is similar to blue beryls—the analyses No. 1, 2, 3 and 4 (see Aurisicchio et al. 1988), but the content of Li is slightly lower for these localities. Because Li has not been routinely determined in beryl from such geological environments (see Turner and Groat 2007; Groat et al. 2007, 2010), a combination of these substitutions in beryl-group minerals is perhaps more

common and routine determination of Li by SIMS or LA-ICP-MS is needed (Groat et al. 2007).

The textural relations of the individual compositional types of beryl are characterized by inclusions and skeletal aggregates of beryl I rather randomly distributed within volumetrically dominant beryl II (Fig. 3b) and exclusive presence of beryl III as the thin outermost rims on beryl II crystals (Fig. 3a,c,d). Distribution and framework of the aggregates of beryl I in beryl II and absence of any compositional changes in the contact of both beryl types (Fig. 3a,b) exclude an exsolution of beryl I from beryl II. Skeletal aggregates rather suggest a rapid crystallization of beryl I. Textural relations of narrow rims of beryl III around beryl II and their shape (Fig. 3a,d) do not indicate any or only insignificant participation of fluid-induced dissolution-precipitation processes (see e.g., Putnis 2002; Harlov et al. 2005) leading to formation of beryl III instead of beryl II. Hence, replacement of the individual beryl types such as described by Novák and Filip (2010) and Novák and Škoda (2010) from granitic pegmatites was not recognized in the Skály occurrence. Sharp contacts of the individual beryl types also point to a lack of post-crystallization diffusion

Table 3 Chemical analyses of beryl, combination of EMPA, LA-ICP-MS and Mössbauer data

| | beryl I | beryl II | | | beryl III |
|--------------------------------|---------|----------|---------|----------|-----------|
| | | 0% Fe3+ | 5% Fe3+ | 20% Fe3+ | |
| SiO ₂ wt.% | 65.55 | 64.67 | 64.67 | 64.67 | 65.61 |
| Al ₂ O ₃ | 14.18 | 11.61 | 11.61 | 11.61 | 13.94 |
| Fe ₂ O ₃ | 0 | 0 | 0.20 | 0.81 | 0 |
| FeO | 0.83 | 4.07 | 3.87 | 3.26 | 1.47 |
| MgO | 2.85 | 2.73 | 2.73 | 2.73 | 2.58 |
| BeO | 13.15 | 13.31 | 13.31 | 13.31 | 13.45 |
| Li ₂ O | 0.26 | 0 | 0 | 0 | 0.07 |
| Na ₂ O | 2.53 | 2.51 | 2.51 | 2.51 | 2.25 |
| <i>sum</i> | 99.35 | 98.90 | 98.90 | 98.90 | 99.37 |
| Si ⁴⁺ <i>apfu</i> | 6.027 | 6.070 | 6.067 | 6.061 | 6.037 |
| Al ³⁺ | 1.537 | 1.284 | 1.284 | 1.282 | 1.512 |
| Fe ³⁺ | – | – | 0.014 | 0.057 | – |
| Fe ²⁺ | 0.064 | 0.319 | 0.304 | 0.255 | 0.113 |
| Mg ²⁺ | 0.391 | 0.382 | 0.382 | 0.381 | 0.354 |
| Be ²⁺ | 2.904 | 3.000 | 3.000 | 3.000 | 2.974 |
| Li ⁺ | 0.096 | – | – | – | 0.026 |
| Na ⁺ | 0.451 | 0.457 | 0.457 | 0.456 | 0.401 |
| <i>sum cat</i> | 11.470 | 11.512 | 11.508 | 11.492 | 11.417 |
| O | 18 | 18 | 18 | 18 | 18 |

within the beryl crystals under low-grade metamorphic-hydrothermal conditions.

Although compositional zoning in beryl crystals is commonly not apparent in macroscopic samples, it has been described from optical microscopy and chiefly in BSE-images by numerous authors. Zoning varies from relatively simple concentric (e.g., Hänni 1980; Turner and Groat 2007; Novák and Filip 2010) through oscillatory (Beal and Lentz 2010), sectorial (Scandale and Lucchesi 2000), complex (Turner et al. 2007; Groat et al. 2010) to late veining (Wang et al. 2009; Novák and Škoda 2010; Uher et al. 2010). Some of these zoned patterns indicate a complex origin for the beryl crystals. The style of zoning in Skály typically has sharp compositional boundaries rather than a homogeneous composition. An absence of replacement textures between the individual beryl types suggest a gradational crystallization. These textures also imply that immiscibility between different individual beryl compositions at low temperature may be the main factor controlling complex zoning in the blue beryl.

Mineral assemblages, PTX conditions, source and mobility of beryllium

Beryl is known from a variety of geological environments (see e.g., Barton and Young 2002; Černý 2002; Franz and

Morteani 2002) including veins in low- to medium-grade metamorphosed Fe(Mn)-deposits (e.g., Hänni 1980; Fontan and Fransolet 1982; Brugger and Gieré 2000) and in altered syenite from the True Blue showing, Yukon Territory (Turner et al. 2007; Groat et al. 2010). Blue beryl mostly occurs in mobilized syn-tectonic to post-tectonic metamorphic-hydrothermal veins at these localities and it is typically associated with quartz, and carbonates (dolomite, ankerite, siderite), and locally also with several accessory to minor minerals such as fluorite, hematite, allanite, phenacite, fluorapatite, pyrophyllite, scheelite-powellite, pyrite, and chalcopyrite. Although the exact PTX conditions of the beryl formation in these localities were not specified in detail, generally low to moderate $T < \sim 300\text{--}400^\circ\text{C}$ are considered (Turner and Groat 2007). The mineral assemblage in the quartz-calcite veins from Skály is similar to these extent occurrence except here calcite is replaced by Fe- and/or Mg-rich carbonates. A temperature of $\sim 200\text{--}300^\circ\text{C}$ is implied for the quartz-calcite veins from Skály. This is based on the low-temperature limit of beryl formation (Barton and Young 2002; Černý 2002), the experimental data in the BASH system for euclase (see e.g., Barton 1986; Barton and Young 2002), chlorite thermometry, and metamorphic conditions of the host rock complex.

Beryllium has been mobilized from host rocks of the low-grade metamorphosed Lahn-Dill type deposit Skály, where one of the rock types (magnetite-chlorite rock) yielded up to 106 ppm of Be (Fojt et al. 2007), whereas the other rock types contain 6–10 ppm of Be. These values are similar to those from low-grade metamorphosed oolitic ironstone and ferruginous sandstone in Sardinia (Franceschelli et al. 2000). For hydrothermal fluids, the dominant complexing agents controlling the solubility of Be are F^- , CO_3^{2-} , OH^- , and $\text{F}^-\text{CO}_3^{2-}$ a pH of 5–7 (Wood 1992). This is consistent with

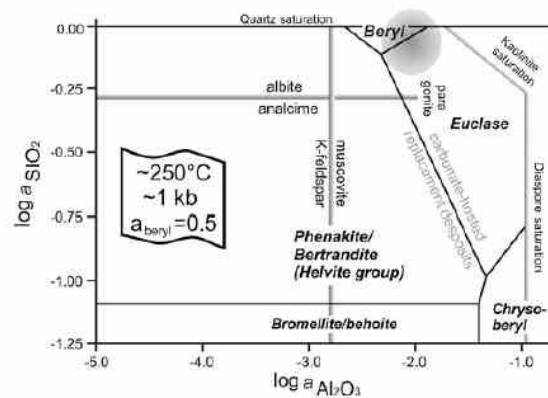


Fig. 7 Stability of Be minerals as a function of silica and alumina activities; slightly modified from Barton and Young (2002). Quartz-calcite veins from Skály are located close to border beryl-euclase (early stage) to beryl + quartz (main stage), see shaded area

the presence of euclase in the mineral assemblage from Skály (Černý 2002). Mineral assemblages from the quartz-calcite veins formed under a high CO_3^{2-} activity, a low S activity, and a very low F activity. This is supported by the absence of fluorite and low contents of F in tourmaline and muscovite. The presence of euclase (+beryl) suggests high activity of Al_2O_3 and slightly acidic to neutral conditions (Barton and Young 2002; Černý 2002). The $f(\text{O}_2)$ is buffered by common hematite in quartz-calcite veins; however, the absence of magnetite may suggest higher $f(\text{O}_2)$ in veins relative to the host hematite-magnetite rock. Because calcite is common in quartz-calcite veins as well as in host schists, the crucial role of CO_3^{2-} as a major complexing agent for the mobility of Be from host rock to syn-tectonic quartz-calcite veins is evident. The influence of CO_3^{2-} complexes on the mobility of Be is also documented by partial corrosion of beryl by calcite (Fig. 3d). The concentrations of Li in beryl (up to 1,314 ppm) manifest elevated contents of Li and its mobility in the host rock sequence of the Skály Fe-deposit. However, bulk rock concentrations of Li in the host rocks were not studied; consequently, further discussion about the origin of Li is not feasible. Nevertheless, concomitant mobility of Be and Li in Skály is apparent.

Conclusions

Zoned blue beryl from quartz-calcite veins in the low-grade metamorphosed Fe-deposit Skály represents O-beryl with the dominant substitution (1) $\text{CH}_\square \text{OR}^{3+} = \text{CHNa}^+ \text{OR}^{2+}$, the minor substitution (2) $\text{CH}_\square \text{T}^{(2)}\text{Be}^{2+} = \text{CHNa}^+ \text{T}^{(2)}\text{Li}^+$ (elevated concentrations of Li up to 1,314 ppm, 0.28 wt.% Li_2O) in beryl I, and the rather negligible substitution (3) $\text{Al} = \text{Fe}^{3+}$ in beryl II. Sharp contacts and absence of any reaction rims in beryl crystals indicate that immiscibility of the individual beryl compositions beryl I, beryl II and beryl III at rather low temperature may be the main factor controlling such a zoned pattern. The mineral assemblages and paragenetic relations of quartz-calcite veins in the Skály Fe-deposit are an example of high mobility of Be (and Li) in the F -poor but CO_2 -rich system at low T -200–300°C. Owing to the absence of a potential magmatic source of Be in the host rocks complex, high concentrations of Be in the host rock, and evident paragenetic and geochemical similarities between the host rock and the quartz-calcite veins classify this metamorphic-hydrothermal occurrence as a closed system (Turner and Groat 2007). The vein mass was sourced via metamorphic-hydrothermal fluids during one-stage fracturing from the host rocks. Because the quartz-calcite veins containing beryl occur exclusively in hematite + magnetite ore and the highest concentrations of Be were detected in magnetite + chlorite schist (Fojt et al. 2007), Fe-

rich portions of the host rock complex seem to be the main source of Be in the veins. Figure 7 illustrates the position of the assemblage beryl + euclase + calcite + quartz + muscovite + albite among other beryl occurrences. It falls within the field of greisens and granitic pegmatites (abundant quartz, minor albite and muscovite, beryl, euclase) tending to carbonate-hosted replacement deposits (common calcite, euclase). Beryl formation is characterized by one-stage fracturing and mobilization in a closed system, CO_3^{2-} as the major complexing agent for the mobility of Be, a high Al_2O_3 activity, and elevated concentrations of Li.

Acknowledgements The authors are very grateful to the reviewers L. Goat and P. Uher, and the Associate Editor I. Broska for constructive criticism that significantly improved the manuscript. The authors thank M. Nepejchal, Šumperk for detailed information about the locality, and J. Sejkora, National Museum, Prague, for technical assistance. This work was supported by the research projects GAČR P210/10/0743 to MN, JF and PG, MSM6198959218 to JF and by the Operational Program Research and Development for Innovations—European Social Fund (CZ.1.05/2.1.00/03.0058).

References

- Aurischio C, Fooravanti G, Grubessi O, Zanazzi P (1988) Reappraisal of the crystal chemistry of beryl. *Amer Mineral* 73:826–837
- Barton M (1986) Phase equilibria and thermodynamic properties of minerals in the $\text{BeO}-\text{Al}_2\text{O}_3-\text{SiO}_2-\text{H}_2\text{O}$ (BASH) system with petrologic applications. *Amer Mineral* 71:277–300
- Barton M, Young S (2002) Non-pegmatitic deposits of Beryllium: Mineralogy, Geology, Phase Equilibria and Origin. In: Grew ES (ed) *Beryllium – Mineralogy, Petrology and Geochemistry*. *Rev Mineral* 50:591–691
- Beal K-L, Lentz DR (2010) Aquamarine beryl from Zealand Station Canada: a mineralogical and stable isotope study. *J Geosci* 55:57–67
- Brown GE Jr, Mills BA (1986) High-temperature structure and crystal chemistry of hydrous alkali-rich beryl from the Harding pegmatite Taos County New Mexico. *Amer Mineral* 71:547–556
- Brugger J, Gieré R (2000) Origin and distribution of some trace elements in metamorphosed Fe–Mn deposits Val Ferrera Eastern Swiss Alps. *Can Mineral* 38:1075–1101
- Cathelineau M, Nieva D (1985) A chlorite solution geothermometer. Los Azures (Mexico) geothermal system. *Contrib Mineral Petrol* 91:235–244
- Černý P (2002) Mineralogy of beryllium in granitic pegmatites. In: Grew ES (ed) *Beryllium – mineralogy, petrology and geochemistry*. *Rev Mineral* 50:405–444
- Da Costa GM, Polli GO, Kahwage MA, de Grave E, Sabioni ACS, Mendes JC (2006) The effect of thermal treatment on the ^{57}Fe Mössbauer spectrum of beryl. *Phys Chem Minerals* 33:161–166
- Della Ventura G, Bellatreccia F, Rossi P (2007) The single-crystal, polarized-light, FTIR spectrum of stoppaniite, the Fe analogue of beryl. *Phys Chem Minerals* 34:727–731
- Ferraris G, Prencipe M, Rossi P (1998) Stoppaniite a new member of the beryl group: crystal structure and crystal-chemical implications. *Eur J Mineral* 10:491–496
- Fojt B, Vavrošová-Konečná J, Dolníček Z (2007) Short characterization of the iron-ore occurrence Skály near Rýmařov Jeseníky

- Mts. Czech Republic. *Čas Slez Muz Opava* 56:1–22 (in Czech with English Summary)
- Fontan F, Fransolet AM (1982) The blue magnesium-iron- and sodium-containing beryl of the Lassur mine Ariège France. *Bul Minéral* 105:615–620
- Franceschelli M, Puxeddu M, Carta M (2000) Mineralogy and geochemistry of Late Ordovician phosphate-bearing oolitic ironstones from NW Sardinia Italy. *Mineral Petrol* 69:267–293
- Franke W, Żelaźniewicz A (2000) The eastern termination of the Variscides: terrane correlation and kinematic evolution. In: Franke W, Haak V, Oncken O, Tanner D (eds) *Orogenic Processes: Quantification and Modelling in the Variscan Belt*. Geological Society London Special Publications 179:63–86
- Franz G, Morteani G (2002) Be-Minerals: Synthesis, Stability and Occurrence in Metamorphic rocks. In: Grew ES (ed) *Beryllium – Mineralogy, Petrology and Geochemistry*. *Rev Mineral* 50:551–589.
- Giuliani G, France-Lanord C, Zimmermann JL, Cheil-Letz A, Arboleda C, Charoy B, Coget P, Fontan F, Gard D (1997) Fluid composition δD of channel H_2O and ^{618}O of lattice oxygen in beryls: genetic implications for Brazilian Colombian and Afghanistanian emerald deposits. *Int Geol Rev* 39:400–424
- Groat LA, Giuliani G, Marshall D, Turner D (2007) Chapter 3. Emerald. In: Groat LA (ed) *Geology of gem deposits*. Mineralogical Association of Canada Short Course 37:79–109
- Groat LA, Rossman GR, Dyar MD, Turner D, Piccoli PMB, Schultz AJ, Ottolini L (2010) Crystal chemistry of dark blue aquamarine from the True Blue Showing Yukon Territory Canada. *Can Mineral* 48:597–613
- Hänni HA (1980) Mineralogische und mineral-chemische Untersuchungen an Beryll aus alpinen Zerklüften. p. 1–107 Ph.D. thesis Universität Basel
- Hanzl P, Janoušek V, Žáček V, Willimský D, Eichler J, Erban V, Pudilová M, Chlupáčová M, Buriánková K, Mixa P, Pecina V (2007) Magmatic history of granite-derived mylonites from the southern Deská Unit (Silesicum Czech Republic). *Mineral Petrol* 89:45–75
- Harlov DE, Wirth R, Förster H-J (2005) An experimental study of dissolution–reprecipitation in fluorapatite: fluid infiltration and the formation of monazite. *Contrib Mineral Petrol* 150:268–286
- Hawthorne FC, Huminicki DMC (2002) The crystal chemistry of beryllium. In: Grew ES (ed) *Beryllium – mineralogy, petrology and geochemistry*. *Rev Mineral* 50:333–404
- Kalvoda J, Bábek O, Fatka O, Leichmann J, Melichar R, Nehyba S, Špaček P (2008) Brunovistulian terrane (Bohemian Massif Central Europe) from late Proterozoic to late Paleozoic: a review. *Int J Earth Sci (Geol Rundsh)* 97:497–518
- Kretz R (1983) Symbols for rock-forming minerals. *Amer Mineral* 68:277–279
- Novák M, Filip J (2010) Unusual (Na, Mg)-enriched beryl and its breakdown products (beryl II, bazzite, bavenite) from euxenite-type NYF pegmatite related to the orogenic ultrapotassic Třebíč Pluton Czech Republic. *Can Mineral* 48:615–628
- Novák M, Jilemnická L (1986) Blue beryl rich in magnesium and iron from Skály near Rýmařov Northern Moravia Czechoslovakia. *Čas Mineral Geol* 31:173–178 (in Czech with English summary)
- Novák M, Škoda R (2010) Field stop 7 Myšelec near Protivín Pisek region—Tourmaline-beryl pegmatite with late Mg-rich alteration. In: Novák M, Cempírek J (eds) *IMA2010 Field trip guide CZ 2 Granitic pegmatites and mineralogical museums in Czech Republic*. *Acta Universitatis Szegediensis Field Trip Guide Series* 6:41–45
- Novák M, Filip J, Gadas P, Příklad J (2010) Alkali-rich beryl from Fe-deposit Skály near Rýmařov, Czech Republic; an example of coupled substitutions in CH-, O- and T2-site. *Acta Universitatis Szegediensis Abstract Series* 6:460
- Opletal M, Koverdinský B et al (1998) Geological map of Czech Republic 1:50000 part 14–42 Rýmařov. *Čes geol úst Praha*
- Platonov AN, Polshin EV, Taran MN (1979) On types of iron in beryls. *Zap Vses Mineral Obshchest* 108:725–730 (in Russian)
- Pouchou JL, Pichoir F (1985) “PAP” procedure for improved quantitative microanalysis. *Microbeam Analysis* 20:104–105
- Price DC, Vance ER, Smith G, Edgar A, Dickson BL (1976) Mössbauer effect studies of beryl. *J Phys* 37(C6):811–817
- Putnis A (2002) Mineral replacement reactions: from macroscopic observations to microscopic mechanisms. *Mineral Mag* 66:689–708
- René M, Šrein V (2001) Chloritoid schists of the Hrubý Jeseník Mts. *Acta Univ Palacký Olomouc Fac. Rer Nat Geol* 37:37–45
- Rozmánek A (1981) Mineralogical characterization of the ore district Horní Město-South. MS thesis JE Purkyně University, Brno. (in Czech)
- Scandale E, Lucchesi S (2000) Growth and sector zoning in a beryl crystal. *Eur J Mineral* 12:357–366
- Sheriff BL, Grundy HD, Hartman JS, Hawthorne FC, Černý P (1991) The incorporation of alkalis in beryl: multi-nuclear MAS NMR and crystal-structure study. *Can Mineral* 29:271–285
- Taran MN, Rossman GR (2001) Optical spectroscopic study of tihualite and a re-examination of the beryl cordierite and osumilite spectra. *Amer Mineral* 86:973–980
- Turner D, Groat LA (2007) Chapter 4. Non-emerald gem beryl. In: Groat LA (ed) *Geology of Gem deposits*. Mineralogical Association of Canada Short Course 37:11–143.
- Turner D, Groat LA, Hart CJR, Mortensen JK, Linnen RL, Giuliani G, Wengzynowski W (2007) Mineralogical and geochemical study of the True Blue aquamarine showing southern Yukon. *Can Mineral* 45:202–227
- Uher P, Chudík P, Bačík P, Vaculovič T, Galiová M (2010) Beryl composition and evolution trends: an example from granitic pegmatites of the beryl-columbite subtype Western Carpathians Slovakia. *J Geosci* 55:69–80
- Valová-Tomšíková R (1987) Litogeochemistry of the bore-hole JR-10 near Rýmařov. MS thesis JE Purkyně University, Brno. (in Czech)
- Vavrošová J (1987) Paragenesis of the iron ore occurrence “Skály” near Rýmařov. MS thesis JE Purkyně University, Brno. (in Czech)
- Viana RR, da Costa GM, de Grave E, Evangelista HJ, Stern WB (2002) Characterization of beryl (aquamarine variety) by Mössbauer spectroscopy. *Phys Chem Minerals* 29:78–86
- Vlčková E (1984) Rock-geochemistry of the Horní Město near Rýmařov ore district. MS thesis JE Purkyně University, Bmo. (in Czech)
- Wang RCh, Che XD, Zhang WL, Zhang ACh, Zhang H (2009) Geochemical evolution and late re-equilibration of Na-Cs-rich beryl from the Koktokay #3 pegmatite (Altai NW China). *Eur J Mineral* 21:795–809
- Wood SA (1992) Theoretical prediction of speciation and solubility of beryllium in hydrothermal solutions in 300°C at saturated vapour pressure. Application to bertrandite/phenakite deposits. *Ore Geol Rev* 7:249–278
- Žák T, Jirásková Y (2006) CONFIT: Mössbauer spectra fitting program. *Surf Interface Anal* 38:710–714

6.6 ARTICLE 6

Bacik, P.; Uher, P.; Ertl, A.; Jonsson, E.; Nysten, P.; Kanicky, V.; Vaculovic, T.
Canadian Mineralogist 2012, 50, 825-841 (IF=1.398)

The Canadian Mineralogist
Vol. 50, pp. 825–841 (2012)
DOI: 10.3749/canmin.50.4.825

ZONED REE-ENRICHED DRAVITE FROM A GRANITIC PEGMATITE IN FORSHAMMAR, BERGSLAGEN PROVINCE, SWEDEN: AN EMPA, XRD AND LA–ICP–MS STUDY

PETER BAČÍK[§] AND PAVEL UHER

Comenius University in Bratislava, Faculty of Natural Sciences, Department of Mineralogy and Petrology, Mlynská dolina, SK–842 15 Bratislava, Slovak Republic

ANDREAS ERTL

Institut für Mineralogie und Kristallographie, Geozentrum, Universität Wien, Althanstraße 14, A–1090 Wien, Austria

ERIK JONSSON

Geological Survey of Sweden, Box 670, SE–751 28 Uppsala, Sweden, and Department of Earth Sciences, Uppsala University, SE–752 36 Uppsala, Sweden

PER NYSTEN

Geological Survey of Sweden, Box 670, SE–751 28 Uppsala, Sweden

VIKTOR KANICKÝ

Department of Chemistry, Faculty of Science, Masaryk University, Kotlářská 2, CZ–611 37 Brno, Czech Republic

TOMÁŠ VACULOVÍČ

Central European Institute of Technology, Masaryk University, Kamenice 5, CZ–625 00 Brno, Czech Republic

ABSTRACT

Green to grayish green tourmaline crystals (up to 10 cm across), with distinct optical zoning, occurs with quartz, blocky albite and muscovite in the Forshammar granitic pegmatite, central Bergslagen province, Sweden. Tourmaline contains inclusions of zircon and xenotime-(Y), and it is cut by veinlets of muscovite and hydroxylbastnäsite-(Ce). Microanalytical and structural data (from the rim) indicate that the tourmaline can be classified as a dravite with moderate Al–Mg disorder at the Y and Z sites. Tourmaline displays chemical zoning that reflects the distribution of Fe, Mg, Al, Ca and Na. The Mg/(Mg+Fe) value is high: it decreases from core (~0.85) to intermediate zone (0.76–0.79), but increases in the rim and vein dravite (0.93). The core has the highest proportion of X-site vacancy and Al content, whereas the intermediate zone is the most enriched in Fe and Na. The rim is slightly depleted in Al and has the highest Na compared to inner zones. Tourmaline veins crosscut the pre-existing tourmaline and are relatively more enriched in Na and Ca. The main compositional variations are driven by $\text{Al}^{\text{IV}}\square\text{Mg}_{-1}\text{Na}_{-1}$ and $\text{AlO}\text{Mg}_{-1}(\text{OH})_{-1}$ substitutions. The Forshammar dravite shows the highest known concentrations of REE from pegmatite tourmaline, ≤ 1200 ppm REE, ≤ 210 ppm La, ≤ 670 ppm Ce; the chondrite-normalized patterns reveal high La_N/Yb_N (32 to 464) values and strongly negative Eu anomalies ($\text{Eu}/\text{Eu}^* = 0.005$ to 0.05). The contents of Ti, Mn, Y and REE generally increase at the boundary of the intermediate zone and rim, whereas the contents of Zn, Ga and Sn decrease from the core to the rim. The core is likely a product of an early magmatic process during the late Svecofennian pegmatite formation (~1.8 Ga) as suggested by oscillatory zoning of trace elements. The intermediate zone, rim and tourmaline veins originated during the late magmatic to hydrothermal stage. Hydroxylbastnäsite-(Ce) and muscovite are apparently the final products of the hydrothermal process.

Keywords: tourmaline, dravite, muscovite, zircon, xenotime-(Y), hydroxylbastnäsite-(Ce), REE, EMPA, XRD, LA–ICP–MS, granitic pegmatite, Forshammar, Bergslagen, Sweden.

[§] E-mail address: bacikp@fns.uniba.sk

INTRODUCTION

Dravite, a magnesium-dominant alkali tourmaline, is a relatively widespread mineral, mainly in metamorphic and metasedimentary rocks, especially in metapelites to metapsammites, amphibole gneisses, marbles, dolomites, and skarns. In contrast, dravite is not typical of common granitic pegmatite environments, where schorl-to-foitite and elbaite members of the tourmaline supergroup are the most widespread (*e.g.*, London 2008). Magnesium-rich members of the schorl–dravite solid-solution series occur only in very primitive barren granitic pegmatites or in relatively unusual Mg-rich environments, such as desilicated pegmatites emplaced in (ultra)basic rocks (*e.g.*, Bernard & Hyršl 2006) or NYF pegmatites derived from Mg-rich parental plutonic rocks, *e.g.*, melasyenites to melagranites of the Třebíč Pluton, Czech Republic (Novák *et al.* 2011).

In this contribution, we document an occurrence of distinctly Mg-rich dravite with unusually high REE contents and associated minerals from a granitic pegmatite at Forshammar, Bergslagen ore province, central Sweden. We carried out a detailed X-ray powder and single-crystal study with a crystal-structure refinement, supplemented by EMPA (electron microprobe) and LA-ICP-MS (laser ablation – inductively coupled plasma – mass spectrometry) spot analyses to establish the internal evolution of the tourmaline from the magmatic to subsolidus stage.

GEOLOGICAL SETTING AND OCCURRENCE

The Forshammar area is situated in the western central part of the Paleoproterozoic, *ca.* 2.0–1.8 Ga Bergslagen ore province (Fig. 1). The main metasupracrustal sequence in Bergslagen consists of Svecofennian volcano-sedimentary units dominated by rhyolitic-to-rhyodacitic, alkali-enriched metavolcanic rocks, clastic metasediments, calcite-rich to dolomite-rich marbles, and minor metabasic dykes and flows. The felsic metavolcanic rock units formed primarily in a volcanic arc environment at *ca.* 1.90–1.87 Ga (*cf.* Lundström *et al.* 1998, and references therein), and the sequence was subjected to intense folding, faulting and regional metamorphism during the Svecokarelian orogeny, as well as to the intrusion of large volumes of mostly granitic magma during several successive stages. The resulting rocks have been historically divided into an older and a younger series; characteristically, the younger series is dominated by mostly undeformed granites of overall S-type affinity, as exemplified by the *ca.* 1.8 Ga Stockholm granite (Ivarsson & Johansson 1995, and references therein). The vast majority of rare-element-type granitic pegmatites in central Sweden formed during *ca.* 1.82–1.79 Ga (*cf.* Römer & Smeds 1997), thus overlapping in time with these granites.

Overall, the region around Forshammar hosts abundant pegmatitic to granitic bodies, occurring on several

scales, from thin dykes to large pods. They are considered to belong to the *ca.* 1.8 Ga generation of granites, and are mostly mineralogically simple and unzoned, and dominated by coarse-grained quartz–feldspar rocks with smaller amounts of micas and locally also magnetite (Sundius 1952, Ambros 1983). At some localities, they form distinct pegmatitic units, with a coarse to very coarse grain-size, typically with very coarse radial aggregates of muscovite, and irregularly distributed small (decimeter- to meter-sized) pods of quartz. A relatively coarse-grained graphic intergrowth between quartz and perthitic microcline is generally dominant. Several of these larger pegmatite bodies have been mined, primarily for feldspar, such as in the Klintjämbo and Limbergsbo quarries (K and L, respectively, in Fig. 1), in the Forshammar area. The Limbergsbo quarry is still in operation.

The granitic pegmatites of the area are, to a large extent, hosted by felsic metavolcanic units, in contrast to a majority of pegmatite fields in central Sweden. Furthermore, pegmatites are characteristically Al-rich, shown by the fairly widespread occurrence of andalusite (Flink 1917, Lundegårdh 1971), and the sporadic appearance of chrysoberyl. Mineralogically unspecified tourmaline-supergroup minerals have been observed in the Forshammar pegmatites, as previously noted by Brotzen (1959) and Lundegårdh (1971). The latter author specifically noted the occurrence of “light gray tourmalines” from the Forshammar quarries. Yet, on the basis of observations during a succession of visits to the area, tourmaline must be considered a rare constituent of these pegmatites. Variably altered andalusite, sparse molybdenite and occasional small amounts of an unspecified, black allanite-like mineral have also been noted (*cf.* Lundegårdh 1971).

We sampled a tourmaline-bearing pegmatite body (GPS geographic coordinates: 59°46'6"N, 15°30'56"E) situated about 1 km northeast of the Klintjämbo quarry in the Forshammar area, exposed in relatively recent times through road construction work. In the remaining exposed portion of the pegmatite, a half-meter-size local quartz core occurs within a muscovite-bearing, coarse-grained graphic intergrowth of K-feldspar and quartz. The euhedral prismatic tourmaline crystals occur at the boundary or immediately inside the quartz at the core margin, in some cases projecting some 10 centimeters into the quartz core. A large part of this particular small core is asymmetrically filled by a single, euhedral and megacrystic internally graphic K-feldspar crystal.

ANALYTICAL METHODS

Electron-microprobe analysis (EMPA)

The composition of tourmaline and associated minerals was established with a CAMECA SX100 electron microprobe in wavelength-dispersion mode at the State Geological Institute of Dionýz Štúr, Bratislava,

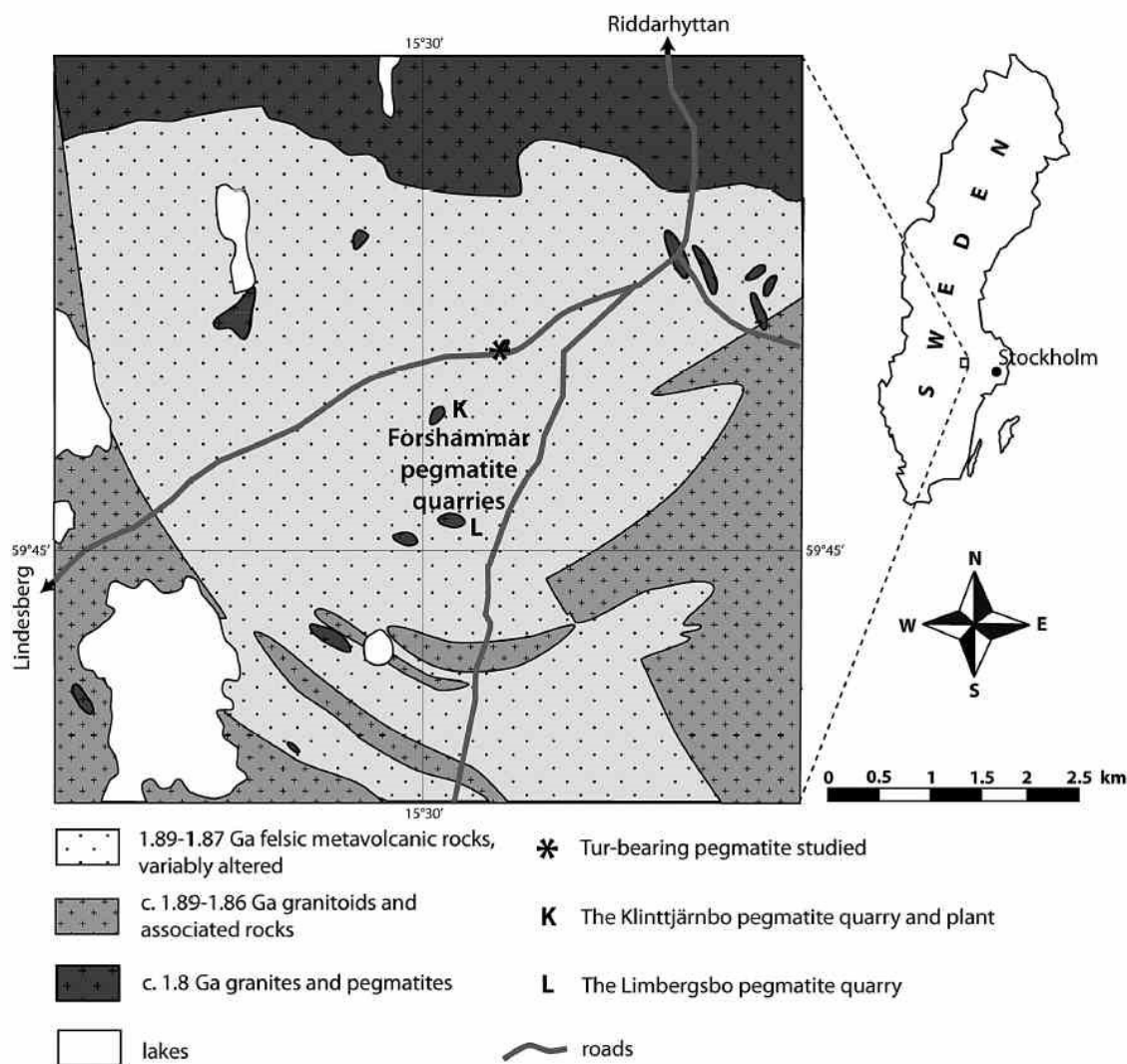


FIG. 1. Simplified geological map of the bedrock in the Forshammar area. The map is based on data from the Geological Survey of Sweden, including the findings of Ambros (1983).

under the following conditions: accelerating voltage 15 keV, beam current 20 nA, and beam diameter 3 to 5 μm . The tourmaline samples were analyzed with the following standards: wollastonite ($\text{SiK}\alpha$, $\text{CaK}\alpha$), TiO_2 ($\text{TiK}\alpha$), Al_2O_3 ($\text{AlK}\alpha$), pure Cr ($\text{CrK}\alpha$), pure V ($\text{VK}\alpha$), fayalite ($\text{FeK}\alpha$), rhodonite ($\text{MnK}\alpha$), forsterite ($\text{MgK}\alpha$), willemite ($\text{ZnK}\alpha$), pure Ni ($\text{NiK}\alpha$), albite ($\text{NaK}\alpha$), orthoclase ($\text{KK}\alpha$), BaF_2 ($\text{FK}\alpha$) and NaCl ($\text{ClK}\alpha$). The lower limits of detection of the measured elements vary between 0.01 and 0.05 wt.%; Zn, Ni and Cl were invariably found to be below their detection limits. The analytical data were normalized according to the PAP procedure. The calculation procedure of tourmaline formula is presented in Table 1. Analytical details

on the electron-microprobe measurements of zircon, xenotime-(Y) and hydroxylbastnäsite-(Ce) are given in Pršek *et al.* (2010).

Powder X-ray diffraction

Powder X-ray-diffraction analyses were made on a BRUKER D8 Advance diffractometer (Laboratory of X-ray diffraction SOLIPHA, Comenius University in Bratislava, Faculty of Natural Sciences) under following conditions: Bragg-Brentano geometry ($\theta-2\theta$), Cu anticathode ($\lambda_{\text{Cu}} = 1.54060 \text{ \AA}$), accelerating voltage 40 kV, beam current 40 mA. We used Ni $K\beta$ filters to strip the $K\beta$ radiation on the primary and diffracted beam,

and data were obtained with the BRUKER LynxEye detector. The step size was $0.01^\circ 2\theta$, the step time was 5 s per step, and the range of measurement was $4 - 65^\circ 2\theta$. The measured data were evaluated with the DIFFRAC^{plus} EVA software package (Bruker 2010a). Analyzed scans were fitted and lattice parameters were refined with the DIFFRAC^{plus} TOPAS software using a pseudo-Voigt function (Bruker 2010b).

Crystal-structure refinement

A fragment of the rim (sample TSW an3) of a tourmaline crystal (originally ~5 cm in length) from

TABLE 1. REPRESENTATIVE COMPOSITIONS OF DRAVITE FROM FORSHAMMAR, BERGSLAGEN PROVINCE, SWEDEN

| | TSW an13 core | TSW an44 core | TSW an10 int. z. | TSW an14 int. z. | TSW an3 rim | TSW an5 rim | TSW an47 vein | TSW an50 vein |
|---------------------------------|---------------------|---------------------|------------------------|------------------------|-------------------|-------------------|---------------------|---------------------|
| SiO ₂ | 37.90 | 38.27 | 37.32 | 37.76 | 37.97 | 38.14 | 38.47 | 38.24 |
| TiO ₂ | 0.08 | 0.09 | 0.16 | 0.14 | 0.18 | 0.14 | 0.01 | 0.01 |
| B ₂ O ₃ * | 11.03 | 11.05 | 10.92 | 10.99 | 11.01 | 11.04 | 11.05 | 11.02 |
| Al ₂ O ₃ | 36.11 | 35.92 | 35.24 | 35.34 | 34.78 | 34.91 | 33.67 | 33.47 |
| FeO | 2.62 | 2.48 | 3.58 | 3.38 | 1.23 | 1.22 | 1.37 | 1.31 |
| MnO | 0.05 | b.d.l. | 0.06 | 0.07 | 0.05 | b.d.l. | b.d.l. | b.d.l. |
| MgO | 7.80 | 7.76 | 7.67 | 7.63 | 9.24 | 9.31 | 10.23 | 10.37 |
| CaO | 0.03 | 0.02 | 0.08 | 0.04 | 0.30 | 0.27 | 0.51 | 0.69 |
| Na ₂ O | 1.81 | 1.91 | 2.23 | 2.35 | 2.32 | 2.26 | 2.32 | 2.35 |
| K ₂ O | 0.04 | 0.03 | 0.03 | 0.04 | 0.05 | 0.04 | b.d.l. | b.d.l. |
| H ₂ O* | 3.42 | 3.31 | 3.32 | 3.26 | 3.25 | 3.29 | 3.33 | 3.28 |
| F | b.d.l. | b.d.l. | 0.13 | 0.07 | 0.08 | 0.08 | 0.23 | 0.27 |
| Total | 100.89 | 100.90 | 100.79 | 101.12 | 100.49 | 100.72 | 101.23 | 101.07 |
| Si <i>apfu</i> | 5.974 | 6.020 | 5.939 | 5.974 | 5.995 | 6.004 | 6.053 | 6.033 |
| Al | 0.026 | 0.000 | 0.061 | 0.026 | 0.005 | 0.000 | 0.000 | 0.000 |
| ΣT | 6.000 | 6.020 | 6.000 | 6.000 | 6.000 | 6.004 | 6.053 | 6.033 |
| B | 3.000 | 3.000 | 3.000 | 3.000 | 3.000 | 3.000 | 3.000 | 3.000 |
| Ti | 0.009 | 0.011 | 0.019 | 0.017 | 0.022 | 0.017 | 0.001 | 0.001 |
| Al | 6.682 | 6.658 | 6.548 | 6.564 | 6.467 | 6.476 | 6.244 | 6.224 |
| Fe | 0.345 | 0.327 | 0.477 | 0.447 | 0.163 | 0.160 | 0.181 | 0.173 |
| Mn | 0.006 | - | 0.008 | 0.009 | 0.006 | 0.002 | - | - |
| Mg | 1.833 | 1.820 | 1.820 | 1.798 | 2.174 | 2.185 | 2.400 | 2.439 |
| ΣY+Z | 8.875 | 8.815 | 8.871 | 8.835 | 8.832 | 8.841 | 8.826 | 8.837 |
| Ca | 0.005 | 0.004 | 0.013 | 0.006 | 0.050 | 0.046 | 0.086 | 0.116 |
| Na | 0.554 | 0.582 | 0.687 | 0.722 | 0.711 | 0.689 | 0.706 | 0.718 |
| K | 0.007 | 0.006 | 0.006 | 0.007 | 0.010 | 0.007 | 0.005 | 0.004 |
| X | 0.434 | 0.408 | 0.294 | 0.265 | 0.228 | 0.258 | 0.203 | 0.161 |
| ΣX | 0.566 | 0.592 | 0.706 | 0.735 | 0.772 | 0.742 | 0.797 | 0.839 |
| F | - | - | 0.067 | 0.036 | 0.038 | 0.041 | 0.114 | 0.134 |
| OH | 3.597 | 3.474 | 3.527 | 3.439 | 3.420 | 3.451 | 3.495 | 3.455 |
| O | 0.403 | 0.526 | 0.406 | 0.523 | 0.542 | 0.507 | 0.390 | 0.411 |
| ΣV+W | 4.000 | 4.000 | 4.000 | 4.000 | 4.000 | 4.000 | 4.000 | 4.000 |
| ΣCat. | 18.444 | 18.433 | 18.583 | 18.577 | 18.608 | 18.588 | 18.679 | 18.714 |
| ΣAl | 6.708 | 6.658 | 6.609 | 6.590 | 6.473 | 6.476 | 6.244 | 6.224 |

The analytical data, acquired with an electron microprobe, is first reported in wt%, and then converted to atoms per formula unit on the basis of 15 cations per formula unit. A component is not considered significant unless its value exceeds the uncertainty (b.d.l.: below detection limit). * B₂O₃ was calculated assuming 3.00 *apfu*; ** OH and Y^{OH} were calculated from the charge-balanced formula, H₂O was calculated for OH + O = 4 *apfu*. Notation: int. z.: intermediate zone.

Forshammar was examined on a Kappa APEX II CCD single-crystal X-ray diffractometer from Bruker AXS equipped with a monochromator, graphite-monochromatized MoK α radiation (Universität Wien). Data were collected at room temperature with six-fold redundancy (up to $80^\circ 2\theta$), integrated and corrected for Lorentz and polarization factors; an absorption correction was applied by evaluation of multiple scans. The structure was refined with SHELXL-97 (Sheldrick 1997) using scattering factors for neutral atoms and a tourmaline starting model from Ertl *et al.* (2010b). The refinement converged at $R1(F)$ value of 1.5%. Table 2 provides crystal data and details of the structure refinement. The H atom bonded to the O3 atom was located from a difference-Fourier map and subsequently refined. Refinement was performed with anisotropic thermal parameters for all non-hydrogen atoms. Site occupancies were refined according to well-known characteristics of the tourmaline structure (Na was refined at the X site, and Mg and Fe were refined at the Y site; for further details see Table 3). In Table 3, we list the atomic parameters, and in Table 4 we present selected interatomic distances. A table of structure factors and a cif file are available from the Depository of Unpublished Data on the Mineralogical Association of Canada website [document Dravite CM50_825].

Laser-ablation ICP-MS spot analysis (LA-ICP-MS)

Instrumentation for LA-ICP-MS analysis consists of a laser-ablation system UP 213 (New Wave, USA) and an Agilent 7500 CE ICP-MS spectrometer (Agilent, Japan). A commercial Q-switched Nd-YAG laser-ablation device works at the fifth harmonic frequency, which corresponds to a wavelength of 213 nm. The ablation device is equipped with programmable XYZ-stage to move the sample along a programmed trajectory during ablation. Visual inspection of the target and photographic documentation are accomplished by

TABLE 2. CRYSTALLOGRAPHICAL DATA AND REFINEMENT DETAILS FOR TOURMALINE FROM FORSHAMMAR

| Sample | TSW an3 (nm) |
|---|------------------------------|
| <i>a</i> , <i>c</i> (Å) | 15.921(1), 7.175(1) |
| <i>V</i> (Å ³) | 1575.1(4) |
| Crystal dimensions (mm) | 0.15 × 0.20 × 0.20 |
| Collection mode, $2\theta_{max}$ (°) | full sphere, 80.24 |
| <i>h</i> , <i>k</i> , <i>l</i> ranges | -28 → 25, -28 → 28, -13 → 12 |
| Total reflections measured | 23334 |
| Unique reflections | 2370 (R_{int} 2.14%) |
| $R_1(F)$, $wR_2(F^2)$ | 1.51%, 3.79% |
| Flack <i>x</i> parameter | 0.060(44) |
| *Observed> reflections [$F_o > 4\sigma_{F_o}$] | 2323 |
| Extinction coefficient | 0.00371(15) |
| Number of refined parameters | 95 |
| Goof | 0.916 |
| $\Delta\sigma_{min}$, $\Delta\sigma_{max}$ (e/Å ²) | -0.27, 0.36 |

TABLE 3. COORDINATES AND DISPLACEMENT PARAMETERS OF ATOMS IN TOURMALINE FROM FORSHAMMAR

| Site | x | y | z | U_{11} | U_{22} | U_{33} | U_{23} | U_{13} | U_{12} | U_{eq} | Occupancy |
|------|--------------------|--------------------|---------------------|--------------------|--------------------|--------------------|---------------------|---------------------|--------------------|--------------------|--|
| X | 0 | 0 | 0.2307 0.0002 | 0.0191 0.0004 | 0.0191 0.0004 | 0.0197 0.0006 | 0 | 0 | 0.0096 0.0002 | 0.0193 0.0003 | Na _{0.86(1)} |
| Y | 0.12439 0.00003 | ½x | 0.63110 0.00005 | 0.00682 0.00015 | 0.00470 0.00011 | 0.01074 0.00016 | -0.00172 0.00005 | -0.00344 0.00010 | 0.00341 0.00007 | 0.0072 0.0001 | Mg _{0.923(1)} Fe _{0.076} |
| Z | 0.29771 0.00002 | 0.26139 0.00002 | 0.61062 0.00003 | 0.00682 0.00015 | 0.00470 0.00011 | 0.01074 0.00016 | -0.00172 0.00005 | -0.00344 0.00010 | 0.00341 0.00007 | 0.00540 0.00004 | Al _{1.00} |
| B | 0.10976 0.00003 | 2x | 0.4540 0.0002 | 0.00528 0.00008 | 0.00555 0.00008 | 0.00533 0.00007 | 0.00038 0.00006 | -0.00007 0.00006 | 0.00267 0.00007 | 0.0060 0.0001 | B _{1.00} |
| T | 0.19176 0.00001 | 0.18981 0.00001 | -0.00040 0.00003 | 0.00462 0.00007 | 0.00423 0.00007 | 0.00521 0.00007 | -0.00060 0.00006 | -0.00044 0.00006 | 0.00220 0.00005 | 0.00469 0.00003 | Si _{1.00} |
| H3 | 0.259 0.002 | ½x | 0.402 0.004 | 0.0052 0.0003 | 0.0057 0.0004 | 0.0071 0.0004 | 0.0007 0.0003 | 0.00034 0.00014 | 0.00286 0.00018 | 0.034 0.007 | H _{1.00} |
| O1 | 0 | 0 | 0.7716 0.0002 | 0.0131 0.0003 | 0.0131 0.0003 | 0.0071 0.0005 | 0 | 0 | 0.00655 0.00017 | 0.0111 0.0002 | O _{1.00} |
| O2 | 0.06098 0.00003 | 2x | 0.4863 0.0001 | 0.0126 0.0003 | 0.0050 0.0003 | 0.0127 0.0003 | 0.0002 0.0002 | 0.00010 0.00011 | 0.00252 0.00013 | 0.0110 0.0001 | O _{1.00} |
| O3 | 0.26378 0.00008 | ½x | 0.5095 0.0001 | 0.0246 0.0004 | 0.0120 0.0002 | 0.0057 0.0003 | 0.00008 0.00014 | 0.0002 0.0003 | 0.0123 0.0002 | 0.0127 0.0001 | O _{1.00} |
| O4 | 0.09353 0.00003 | 2x | 0.0705 0.0001 | 0.00715 0.00019 | 0.0145 0.0003 | 0.0097 0.0003 | -0.0015 0.0003 | -0.00075 0.00013 | 0.00727 0.00017 | 0.0096 0.0001 | O _{1.00} |
| O5 | 0.18512 0.00007 | ½x | 0.0924 0.0001 | 0.0150 0.0003 | 0.00726 0.00019 | 0.0093 0.0003 | 0.00088 0.00012 | 0.0018 0.0002 | 0.00750 0.00017 | 0.0097 0.0001 | O _{1.00} |
| O6 | 0.19549 0.00004 | 0.18515 0.00004 | 0.77620 0.00007 | 0.0093 0.0002 | 0.0098 0.0002 | 0.00527 0.00018 | -0.00128 0.00015 | -0.00083 0.00015 | 0.00521 0.00017 | 0.00792 0.00008 | O _{1.00} |
| O7 | 0.28536 0.00004 | 0.28518 0.00004 | 0.07831 0.00007 | 0.00649 0.00019 | 0.00625 0.00018 | 0.00760 0.00019 | -0.00101 0.00015 | -0.00103 0.00015 | 0.00121 0.00015 | 0.00766 0.00008 | O _{1.00} |
| O8 | 0.20954 0.00004 | 0.27033 0.00004 | 0.43993 0.00008 | 0.00467 0.00018 | 0.0090 0.0002 | 0.0118 0.0002 | 0.00257 0.00016 | 0.00093 0.00016 | 0.00336 0.00016 | 0.00851 0.00008 | O _{1.00} |

Note: For the definition of U_{eq} , see Fischer & Tillmanns (1988).

TABLE 4. SELECTED INTERATOMIC DISTANCES IN TOURMALINE FROM FORSHAMMAR

| | | | | | |
|------|-------|-----------|------|-------|------------|
| X- | O2 ×3 | 2.488(1) | Y- | O1 | 1.9894(8) |
| | O5 ×3 | 2.739(1) | | O2 ×2 | 1.9911(6) |
| | O4 ×3 | 2.824(1) | | O6 ×2 | 1.9953(6) |
| Mean | | 2.684(1) | | O3 | 2.1108(11) |
| | | | Mean | | 2.0122(7) |
| T- | O7 | 1.6070(5) | Z- | O6 | 1.8863(6) |
| | O6 | 1.6071(6) | | O7 | 1.8984(6) |
| | O4 | 1.6242(3) | | O8 | 1.8922(6) |
| | O5 | 1.6394(4) | | O8' | 1.9210(6) |
| Mean | | 1.6194(5) | | O7' | 1.9532(6) |
| B- | O2 | 1.365(1) | | O3 | 1.9889(5) |
| | O8 ×2 | 1.3794(8) | Mean | | 1.9233(6) |
| Mean | | 1.375(1) | | | |

The standard deviation is given in brackets. Distances are quoted in Å.

means of a built-in microscope-CCD camera system. The ablation cell was flushed with helium (carrier gas) that transported the laser-induced aerosol to the inductively coupled plasma. A sample gas flow of argon was admixed to the helium carrier gas flow behind the laser-ablation cell. Optimization of the LA-ICP-MS

conditions (gas flow rates, sampling depth, voltages of electrostatic lenses of the mass spectrometer) was performed with the glass reference material NIST SRM 612 in order to obtain the maximum signal-to-noise ratio and minimum oxide formation (ThO⁺/Th⁺ counts ratio 0.2%, U⁺/Th⁺ counts ratio 1.1%). The hole-drilling mode (fixed position of the sample during laser ablation) was used for a duration of 40 seconds for each spot. Laser ablation was performed with a laser-spot diameter of 65 µm (samples TSW), laser fluence 13 J cm⁻² and repetition rate 10 Hz. All element contents were normalized using Si as an internal standard. Its concentration was obtained by means of EMPA measurements.

RESULTS

Chemical composition, structure and zoning of tourmaline

Tourmaline from the pegmatite studied at Forshammar occurs as distinctly optically zoned crystals up to 10 cm in length and 2 cm in width, scattered in white quartz and white blocky albite. Tourmaline

crystals consist macroscopically of a green core and grayish green rim. Moreover, there is a darker green zone in between the core and rim observable in the

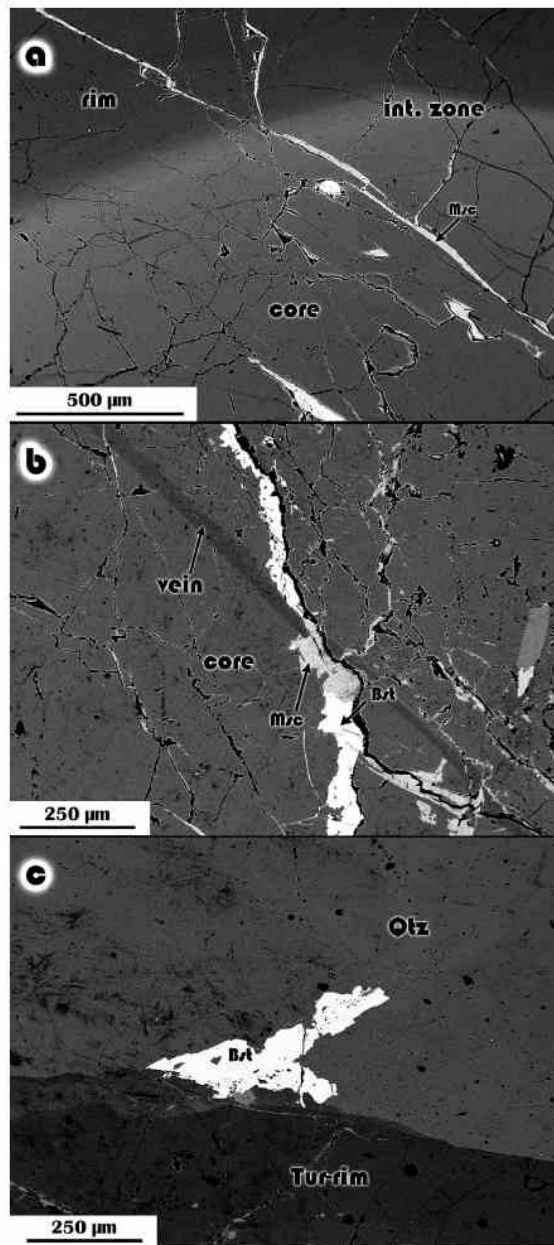


FIG. 2. BSE photomicrographs of dravite and associated minerals from the Forshammar pegmatite. (a) The contacts of the tourmaline core, intermediate zone and rim, cut by veins of muscovite (Ms). (b) Core of tourmaline cut by younger tourmaline vein and even later vein with muscovite and hydroxylbastnäsite-(Ce) (Bst). (c) Aggregate of hydroxylbastnäsite-(Ce) in quartz (Qtz) growing on the rim of tourmaline (Tur-rim).

thin section. Optical zoning is related to chemical zoning, as observed in back-scattered (BSE) images (Fig. 2a). Tourmaline crystals are cut by veins of younger tourmaline and even later veins of muscovite and hydroxylbastnäsite-(Ce) (Figs. 2b, c).

Microchemical data demonstrate that tourmaline from the Forshammar pegmatite belongs to the alkali subgroup (Fig. 3) and has a dravite composition, poor in Fe (Figs. 4b, d); the Mg/(Mg+Fe) value decreases from core (~0.85) to an intermediate zone (0.76–0.79), but increases in rim and vein dravite (0.93) (Table 1). In dravite from the Forshammar pegmatite, chemical zoning is the best displayed in the distribution of Fe, Mg, Al, Ca and Na, as well as in REE and other trace elements (see below). The core has the highest proportion of X-site vacancy (0.34–0.43) and the highest content of Al (6.62–6.71 *apfu*), whereas the intermediate zone is the most enriched in Fe (0.44–0.54 *apfu*) and Na (0.69–0.75 *apfu*), although the Mg content is similar in both zones (1.74–1.89 *apfu*) (Table 1). The rim is slightly depleted in Al (6.46–6.47 *apfu*), and it has the lowest content of Fe (0.16–0.18 *apfu*) and highest content of Mg (2.12–2.18 *apfu*) and Na (0.74–0.77 *apfu*) compared to the inner zones (Table 1). The latest thin vein of tourmaline has a composition similar to the rim, but it is even more enriched in Na (0.79–0.84 *apfu*), Mg (2.40–2.49 *apfu*) and has the lowest content of Al (6.18–6.25 *apfu*). The calcium content is very low in the core and intermediate zone (<0.01 *apfu*), but increases at the rim and in vein dravite (0.05–0.12 *apfu*) (Fig. 3). Moreover, the vein tourmaline is enriched in F (0.11–0.17 *apfu*), whereas other zones except the intermediate zone (0.04–0.07 *apfu*) are generally F-poor, with up to 0.04 *apfu* (Table 1). The chemical zoning of dravite from Forshammar causes only slight changes in the lattice parameters: *a* 15.9252(7), *c* 7.1627(3) Å in the core (powder XRD data); *a* 15.9223(6), *c* 7.1706(5) Å in the rim according to powder XRD data, or *a* 15.921(1), *c* 7.175(1) Å from the crystal-structure refinement.

Variability in the chemical composition is the result of several substitutions, none of which is predominant. An increase of Al compared to an ideal composition of dravite (Fig. 4a) is driven by $\text{Al}^{\text{X}}\square\text{Mg}_{-1}\text{Na}_{-1}$ (Fig. 4c) and $\text{AlOMg}_{-1}(\text{OH})_{-1}$ substitutions. The influence of $\text{AlOMg}_{-1}(\text{OH})_{-1}$ substitution is manifested by a shift in composition from the ideal dravite – magnesiofoitite trend to “oxy-dravite” in the core, intermediate zone and rim; the dravite composition corresponds to the $\text{Al}^{\text{X}}\square\text{Mg}_{-1}\text{Na}_{-1}$ substitution trend only in the vein (Fig. 4b). However, the extent of the $\text{AlOMg}_{-1}(\text{OH})_{-1}$ substitution is not sufficient to attain the composition of “oxy-dravite” (Fig. 4b). The excess of Al at the Y octahedra and also the lower Fe content result in a lower correlation of the FeMg_{-1} substitution (Fig. 4d), which in contrast decrease the impact of the $\text{Al}^{\text{X}}\square\text{Mg}_{-1}\text{Na}_{-1}$ substitution in the intermediate zone (Fig. 4c). Slightly increased Ca contents concomitant with a decrease in

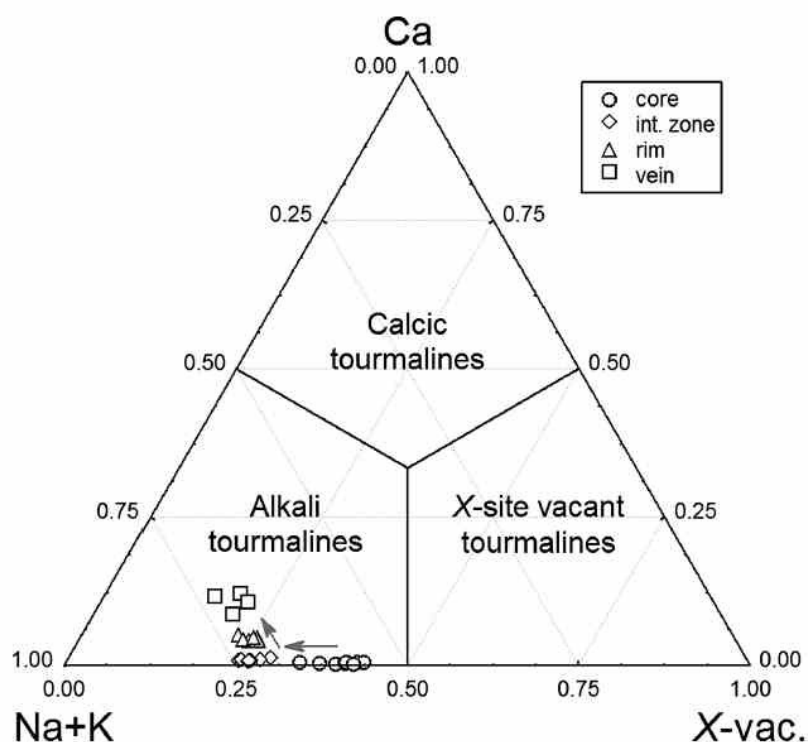


FIG. 3. Classification of dravite from the Forshammar pegmatite based on X-site occupancy (atomic proportions). Arrows indicate evolutionary trend of dravite from core (o), through intermediate zone (\diamond), to rim (Δ) and vein (\square).

^{YZ}Al in the rim and vein dravite (Table 1) indicate also a limited role of the uvite $^{XCa}ZMg^XNa_{-1}ZAL_1$ substitution.

The crystal-structure refinement shows that the average $\langle T-O \rangle$ bond length, 1.6194(5) Å (Table 3), is within one standard deviation equivalent to a T site that is occupied only by Si (1.620 Å; see Ertl *et al.* 2010b). Hence there is no evidence for tetrahedrally coordinated B or Al. By using the correlation between Mg at the Z site and the average $\langle Z-O \rangle$ distance from Ertl *et al.* (2010a), which can be used for Fe-poor tourmalines, where the Z site is only occupied by Al and Mg, we can assign ~ 0.7 apfu Mg to the Z site of our tourmaline by using the $\langle Z-O \rangle$ distance, 1.923 Å (Table 4). By using the data acquired from the crystal-structure refinement and the chemical composition of the tourmaline rim (sample TSW an3; Table 2), we can propose the following formula: $\sim^X(Na_{0.7}Ca_{0.1}\square_{0.2})_{\Sigma 1}Y(Mg_{1.5}Al_{1.2}Fe_{0.2}\square_{0.1})_{\Sigma 3}Z(Al_{5.3}Mg_{0.7})_{\Sigma 6}(BO_3)_3(Si_6O_{18})(OH)_3[(OH),O]$. Hence this tourmaline shows a moderate Al–Mg disorder involving the Y and the Z site.

Most of trace elements were found to be below their detection limits; only Li, Ti, Mn Zn, Ga and the REE are significantly above the detection limits (Table 5). Zoning is also expressed in the distribution

of trace elements. The contents of Ti, Mn, Y and REE are generally higher in the rim, whereas the contents of Zn, Ga and Sn decrease from the core to the rim (Table 5). Moreover, trace elements in the core display an oscillatory zoning that is not apparent in the major-element contents. Titanium, manganese and the REE accumulate on the contact of intermediate zone and rim and decrease toward the outer parts of the rim (Figs. 5a, b). The intermediate zone expresses a similar content of trace elements as the inner part of the rim, but it has the highest contents of Zn and Ga (Table 5).

The LA–ICP–MS data for the REE were normalized to chondritic values. All zones in tourmaline display a distinct enrichment in LREE, with Ce the most abundant in comparison to the HREE; La_N/Yb_N is in the range 32–464 (Fig. 6). The chondrite-normalized REE values regularly decrease with increasing atomic number; Ce_N shows a slight enrichment over La_N (Fig. 6). All zones of tourmaline display very strong negative Eu anomaly ($Eu/Eu^* = 0.005$ to 0.05). The content of ΣREE increases from the core to the intermediate zone and the inner part of the rim, and then decreases to the outer part of the rim (Fig. 6).

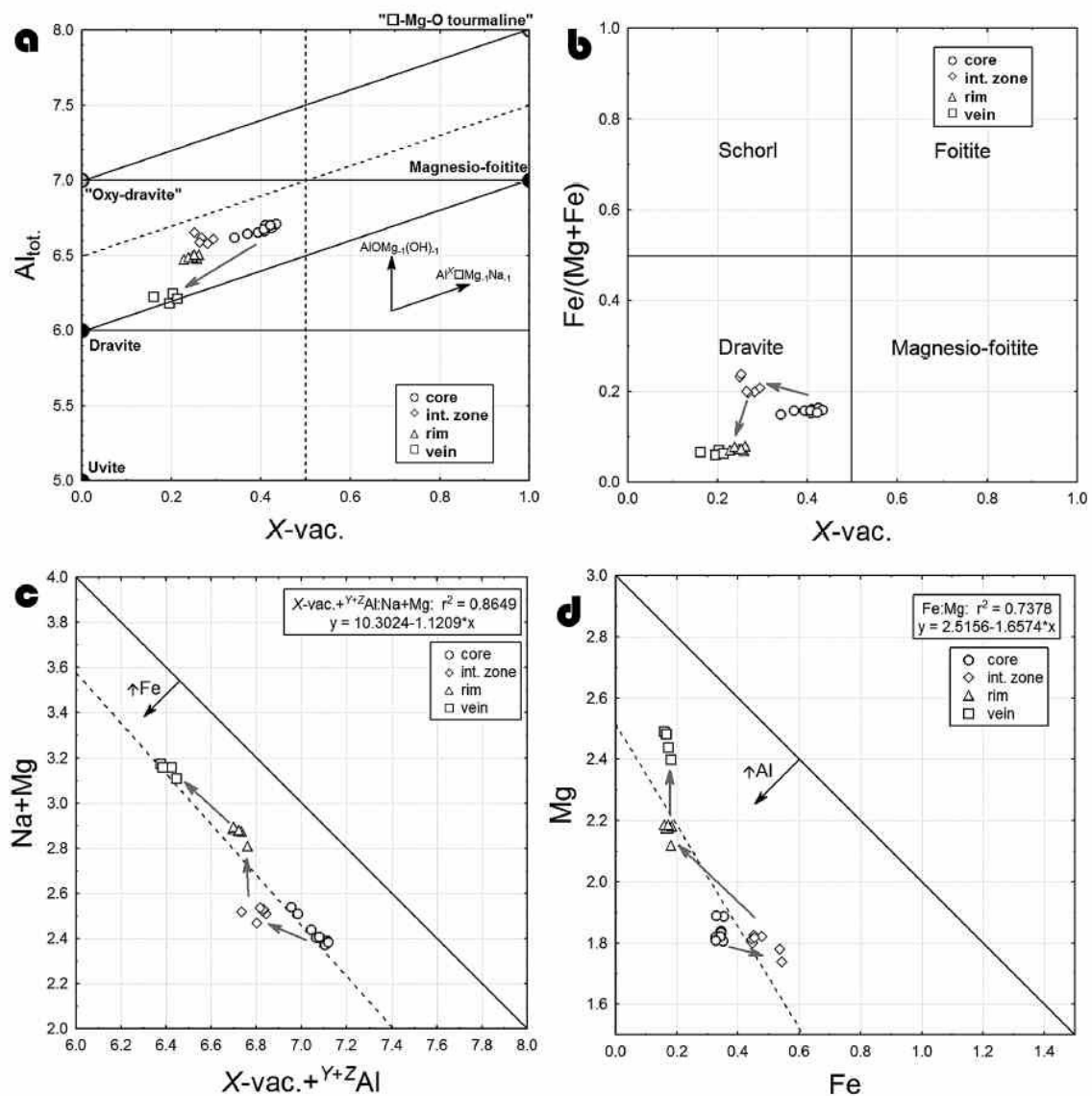


Fig. 4. Diagrams of tourmaline chemical composition (in *apfu*). a. Al_{total} versus X_{vac} diagram. b. $Fe/(Mg + Fe)$ versus X_{vac} diagram. c. $Na + Mg$ versus $X_{vac} + Y + ZAl$ diagram. d. Mg versus Fe diagram. Gray arrows represent change of chemical composition within tourmaline zones. Black arrows represent substitution vectors (a) or trends of cation increase (c, d). Solid lines represent ideal substitution trends (a, c, d) or borders of mineral composition (b). Dashed lines represent borders of mineral composition (a) or correlation trend-line of analyzed samples (c, d).

Associated minerals

Dravite from the Forshammar pegmatite contains thin veinlets and inclusions of other minerals. Muscovite occur in veinlets cutting tourmaline crystals (Figs. 2a, b); it has higher content of Mg than Fe, an atomic $Fe/(Fe+Mg)$ value in the range 0.07–0.10, which is similar to the host tourmaline (Table 6). Zircon and xenotime-

(Y) occur as tiny euhedral inclusions (usually 50 to 150 μm across) in dravite (Fig. 7). The zircon is Hf-rich (3.6 to 6.3 wt.% HfO_2 , 0.03–0.06 *apfu* Hf, $Zr/Hf_{wt.} = 6.9$ to 12.2). The content of Y+REE is relatively low (0.01–0.03 *apfu*); some crystals are slightly enriched in U (up to 1.5 wt.% UO_2 , 0.011 *apfu*; Table 7). Irregular zoning and fractures in zircon could indicate (partial) metamictization. Moreover, zircon contains numerous

tiny inclusions of xenotime-(Y) (Fig. 7). Xenotime-(Y) shows a high atomic $Y/(Y+REE)$ value (0.80), 0.19 *apfu* ΣREE ; Dy (0.043 *apfu*) and Yb (0.048 *apfu*) are the most abundant REE (Table 7). Hydroxylbastnäsite-(Ce) forms tiny veinlets or irregular fillings (up to ~300 μm across) with muscovite in host dravite or at the tourmaline-quartz boundary (Fig. 2). It shows a relatively homogeneous composition, with a distinct dominance of Ce over the other REE, negligible contents of Th, U (both <0.01 *apfu*), and a low F concentration (~0.25 *apfu*) (Table 8).

The chondrite normalization of the REE in accessory minerals was only possible from the electron-microprobe data, as their minute size did not allow for LA-ICP-MS analysis. Hydroxylbastnäsite-(Ce) is distinctly enriched in LREE (Fig. 8a), whereas xenotime-(Y) is enriched in HREE; both of them display a strong negative Eu anomaly (Fig. 8b).

DISCUSSION AND CONCLUSIONS

Crystal chemistry of tourmaline

As suggested by our EMPA and LA-ICP-MS data, the Forshammar tourmaline shows relatively minor chemical variability. It is controlled by substitutions of major cations including Al, Mg and Na; other cations play only negligible roles in the observed crystallochemical variations. Our tourmaline has a poor correlation of $FeMg_{-1}$ substitution; its deviation from the ideal trend is due to a low Fe content.

TABLE 5. CONTENTS OF TRACE ELEMENTS IN TOURMALINE FROM FORSHAMMAR

| | d.l. | core | int. zone | rim |
|----|------|---------------|-----------|---------------|
| Li | 170 | b.d.l. - 220 | 240 | b.d.l. - 369 |
| Ti | 8 | 380 - 814 | 1127 | 933 - 1611 |
| Mn | 1 | 206 - 406 | 635 | 207 - 977 |
| Co | 0.1 | 0.1 - 1.5 | 0.5 | 0.60 - 1.4 |
| Zn | 0.8 | 34 - 84 | 86 | 16 - 37 |
| Ga | 0.4 | 58 - 115 | 105 | 54 - 86 |
| Y | 0.10 | 0.60 - 1.7 | 5.1 | 1.3 - 6.9 |
| Sn | 1.2 | 1.9 - 9.8 | 6.6 | 2.4 - 5.6 |
| La | 0.1 | 15 - 30 | 155 | 44 - 210 |
| Ce | 0.1 | 53 - 108 | 548 | 112 - 670 |
| Pr | 0.06 | 7.4 - 14 | 63 | 14 - 79 |
| Nd | 0.1 | 27 - 58 | 190 | 45 - 251 |
| Sm | 0.2 | 3.5 - 9.0 | 28 | 5.9 - 30 |
| Eu | 0.01 | b.d.l. - 0.07 | b.d.l. | 0.02 - 0.15 |
| Gd | 0.2 | 1.3 - 3.4 | 13 | 2.8 - 11 |
| Tb | 0.01 | 0.09 - 0.32 | 0.77 | 0.16 - 0.81 |
| Dy | 0.01 | 0.19 - 0.72 | 2.2 | 0.43 - 2.5 |
| Ho | 0.01 | b.d.l. - 0.05 | 0.14 | b.d.l. - 0.24 |
| Er | 0.01 | 0.03 - 0.29 | 0.27 | 0.05 - 0.43 |
| Tm | 0.01 | b.d.l. - 0.03 | b.d.l. | b.d.l. - 0.04 |
| Yb | 0.01 | 0.06 - 0.47 | 0.33 | 0.10 - 0.38 |

These data, expressed in ppm, were acquired by laser-ablation inductively coupled plasma - mass spectrometry (LA-ICP-MS). Notations: d.l.: detection limit, b.d.l.: below detection limit.

The occupancy of Y and Z sites is mainly controlled by exchange of Al and Mg. Their distribution over octahedral sites in dravitic to olenitic tourmalines reflects their disorder (Hawthorne *et al.* 1993, Ertl *et al.* 2008, 2010a, Bosi *et al.* 2010). Our tourmaline exhibits Al-Mg disorder involving the Y and the Z sites, but it is not sufficient to change the composition from dravite to olenite. Charge-balance requirements of the substitution of Al^{3+} for Mg^{2+} are partly satisfied by an alkali decrease (mainly in the core, decreasing to the rim), but the excess of Al in comparison to the proportion of X-site vacancy suggests a deprotonation of $V^{+W}OH$. The observed variation in chemical composition in the Y site with increased content of YAl^{3+} , which is observable in dravite from Forshammar (YAl^{3+} in the range 0.18–0.71 *apfu* from the ordered formula; $YAl^{3+} = 1.2$ *apfu* in the structural formula) is typical of the dravite to “oxy-dravite” trend (Bloodaxe *et al.* 1999, Bosi & Lucchesi 2004, Novák *et al.* 2004). The proportion of $V^{+W}O$ calculated from a charge-balanced formula is not sufficiently accurate, and data from the structural

TABLE 6. REPRESENTATIVE COMPOSITIONS OF MUSCOVITE FROM FORSHAMMAR, BERGSLAGEN PROVINCE, SWEDEN

| | TSW an3 | TSW an4 | TSW an5 | TSW an8 | TSW an9 |
|--------------------------------|---------|---------|---------|---------|---------|
| SiO ₂ wt.% | 50.52 | 50.28 | 47.68 | 49.13 | 48.88 |
| TiO ₂ | 0.10 | 0.12 | 0.12 | 0.04 | 0.04 |
| Al ₂ O ₃ | 30.59 | 29.92 | 34.22 | 34.33 | 35.20 |
| FeO | 0.47 | 0.48 | 0.25 | 0.22 | 0.17 |
| MgO | 2.80 | 2.99 | 1.33 | 1.55 | 1.07 |
| CaO | 0.03 | 0.06 | 0.04 | 0.06 | 0.06 |
| Na ₂ O | 0.09 | 0.20 | 0.12 | 0.13 | 0.10 |
| K ₂ O | 10.94 | 10.61 | 10.73 | 10.49 | 9.93 |
| H ₂ O* | 4.55 | 4.49 | 4.50 | 4.59 | 4.59 |
| Cl | 0.02 | 0.07 | 0.01 | 0.01 | b.d.l. |
| sum | 100.10 | 99.25 | 99.05 | 100.58 | 100.08 |
| O=Cl | -0.01 | -0.03 | 0.00 | 0.00 | 0.00 |
| Total | 100.09 | 99.21 | 99.05 | 100.58 | 100.08 |
| Si ⁴⁺ <i>apfu</i> | 3.328 | 3.341 | 3.173 | 3.209 | 3.194 |
| ^{VI} Al ³⁺ | 0.672 | 0.659 | 0.827 | 0.791 | 0.806 |
| ΣT | 4.000 | 4.000 | 4.000 | 4.000 | 4.000 |
| Ti ⁴⁺ | 0.005 | 0.006 | 0.006 | 0.002 | 0.002 |
| ^{VI} Al ³⁺ | 1.703 | 1.684 | 1.857 | 1.852 | 1.906 |
| Fe ²⁺ | 0.026 | 0.027 | 0.014 | 0.012 | 0.009 |
| Mg ²⁺ | 0.275 | 0.296 | 0.132 | 0.151 | 0.104 |
| ΣM | 2.009 | 2.013 | 2.009 | 2.016 | 2.021 |
| Ca ²⁺ | 0.002 | 0.005 | 0.003 | 0.004 | 0.004 |
| Na ⁺ | 0.011 | 0.026 | 0.016 | 0.017 | 0.013 |
| K ⁺ | 0.920 | 0.899 | 0.911 | 0.874 | 0.828 |
| □ | 0.067 | 0.070 | 0.071 | 0.105 | 0.155 |
| ΣI | 0.933 | 0.930 | 0.929 | 0.895 | 0.845 |
| Cl ⁻ | 0.002 | 0.008 | 0.001 | 0.001 | - |
| OH ⁻ | 1.998 | 1.992 | 1.999 | 1.999 | 2.000 |
| Fe/(Fe + Mg) | 0.09 | 0.08 | 0.10 | 0.07 | 0.08 |

The analytical data, acquired with an electron microprobe, are first reported in wt.%, and then converted to atoms per formula unit on the basis of 100 + 2(OH) anions per formula unit. A component is not considered significant unless its value exceeds the uncertainty (b.d.l.: below detection limit). *H₂O was calculated assuming OH + Cl = 2 *apfu*.

formula do not take any local inhomogeneities into account. However, the calculated $V+W$ O along with dravite to “oxy-dravite” trend (Fig. 4a) are good indicators that the $AlOMg_{-1}(OH)_{-1}$ substitution is the most likely mechanism to balance the local excess in charge (Medaris *et al.* 2003). Thus, if O dominates the W site in the ordered formula, some compositions of tourmaline from Forshammar could be classified as “oxy-dravite” according to Henry *et al.* (2011).

The distribution of the REE and other trace elements

Dravite from the Forshammar pegmatite is markedly enriched in the REE in comparison to all known tourmalines from granitic pegmatites (Neiva 1974, Jolliff *et al.* 1987, Hellingwerf *et al.* 1994, Roda *et al.* 1995, Jiang *et al.* 1997, Roda-Robles *et al.* 2004, Ertl *et al.* 2006, Novák *et al.* 2011). In particular, the rim zones attain up to ~1200 ppm Σ REE, \leq 210 ppm La, \leq 670 ppm

Ce, \leq 250 ppm Nd, \leq 30 ppm Sm (Tables 5, 6). A careful inspection of each area of the tourmaline grain before LA-ICP-MS measurement and the general enrichment in REE in all analyzed spots minimize the possible influence of tiny inclusions of hydroxylbastnäsite-(Ce) on the analytical results.

It seems likely that the REE occupy the X site of the tourmaline structure. Tourmaline with dominant Na^+ and Ca^{2+} cations at the X site prefers LREE with larger ionic radii rather than HREE and Y. The ionic radius of 9-coordinated Na^+ cation is 1.24 Å, similar to $^{91}Ca^{2+}$ (1.18 Å) and La^{3+} to Sm^{3+} in the same coordination (1.216 to 1.132 Å), whereas the ionic radius of the following HREE decrease down to 1.032 Å for $^{91}Lu^{3+}$ (Shannon 1976). The relationship of Ca and REE is also pronounced in tourmaline from Forshammar; the highest content of REE is in the rim and veins, which are also the most enriched in Ca.

The REE content of tourmaline in granitic pegmatites is generally low; usually Σ REE is below ~20 ppm (La and Ce <10 ppm), with wide variations of La_N/Yb_N (0.16 to 433) and Eu/Eu^* (0.03 to over 1) (Table 5). Only a few pegmatite populations include tourmaline remarkably enriched in the REE (Table 9), *e.g.*, elbaite from Nuristan, Afghanistan and Anjanabonoina, Madagascar (Ertl *et al.* 2006) or dravite to schorl from the Třebíč pluton, Czech Republic (Novák *et al.* 2011). The Forshammar dravite also show a high La_N/Yb_N value (32 to 464) and a strikingly negative Eu anomaly ($Eu/Eu^* = 0.005$ to 0.05) in comparison to other known tourmalines from granitic pegmatites (Table 6). A strong negative Eu anomaly in tourmaline and also in xenotime-(Y) and hydroxylbastnäsite-(Ce) suggests low oxygen fugacity or some degree of magmatic fractionation of the host rock (*e.g.*, Möller & Muecke 1984), which is a characteristic feature of granitic pegmatites. However, some features of Forshammar tourmaline, including the high X_{Mg} value, suggest a low degree of fractionation of pegmatite.

The REE concentration in tourmalines from granitic rocks also is generally low (usually <20 ppm La and Ce), with LREE > HREE and a negative Eu anomaly (Bea 1996, Jiang *et al.* 1997, Pesquera *et al.* 2005). Yet, it is noteworthy that a tourmaline from an unspecified pegmatite in the Riddarhyttan area, near Forshammar in central Bergslagen, also attains elevated REE contents, as measured by neutron-activation analysis (Hellingwerf *et al.* 1994). Variable but commonly higher REE contents are characteristic of tourmaline in tourmalinites, gneisses, and metasediments, commonly spatially related to metamorphic, magmatic or hydrothermal ore deposits, where dominant La and Ce locally attain up to ~130 and 280 ppm, respectively (Hellingwerf *et al.* 1994, Torres-Ruiz *et al.* 2003, Pesquera *et al.* 2005, Garda *et al.* 2010, Klemme *et al.* 2011). The tourmaline in tourmaline-quartz veins is usually very poor in REE (<20 ppm La, Ce; <50 ppm Σ REE; *e.g.*, King *et al.* 1988, Yavuz *et al.* 1999, Jiang *et al.* 1999,

TABLE 7. REPRESENTATIVE COMPOSITIONS OF ZIRCON AND XENOTIME-(Y) FROM FORSHAMMAR, BERGSLAGEN PROVINCE, SWEDEN

| | Zrn TSW-2 | Zrn TSW-5 | Xnt TSW-1 | | Zrn TSW-2 | Zrn TSW-5 | Xnt TSW-1 |
|----------------|--------------|--------------|--------------|------------------|--------------|--------------|--------------|
| P_2O_5 wt. % | 0.11 | 2.03 | 36.46 | P <i>apfu</i> | 0.003 | 0.056 | 0.996 |
| As_2O_5 | 0.14 | 0.19 | b.d.l. | As | 0.002 | 0.003 | - |
| SiO_2 | 31.67 | 28.76 | 0.12 | Si | 0.992 | 0.939 | 0.004 |
| TiO_2 | 0.04 | 0.05 | b.d.l. | Ti | 0.001 | 0.001 | - |
| ZrO_2 | 61.22 | 49.83 | 0.13 | Al | 0.001 | - | - |
| HfO_2 | 4.61 | 6.32 | 0.10 | ΣB | 0.999 | 0.999 | 1.000 |
| ThO_2 | b.d.l. | b.d.l. | 0.09 | | | | |
| UO_2 | 0.10 | 0.52 | 0.09 | Zr | 0.935 | 0.794 | 0.002 |
| Al_2O_3 | 0.04 | b.d.l. | b.d.l. | Hf | 0.041 | 0.059 | 0.001 |
| Y_2O_3 | 0.11 | 4.47 | 45.19 | Th | - | - | 0.001 |
| La_2O_3 | b.d.l. | b.d.l. | b.d.l. | U | 0.001 | 0.004 | 0.001 |
| Ce_2O_3 | 0.04 | 0.07 | 0.07 | Y | 0.002 | 0.078 | 0.776 |
| Pr_2O_3 | 0.13 | 0.13 | 0.16 | La | - | - | - |
| Nd_2O_3 | b.d.l. | b.d.l. | 0.08 | Ce | 0.001 | 0.001 | 0.001 |
| Sm_2O_3 | b.d.l. | b.d.l. | 0.60 | Pr | 0.001 | 0.002 | 0.002 |
| Eu_2O_3 | 0.12 | 0.16 | b.d.l. | Nd | - | - | 0.001 |
| Gd_2O_3 | 0.12 | 0.15 | 2.43 | Sm | - | - | 0.007 |
| Tb_2O_3 | b.d.l. | b.d.l. | 0.55 | Eu | 0.001 | 0.002 | - |
| Dy_2O_3 | 0.04 | 0.29 | 4.15 | Gd | 0.001 | 0.002 | 0.026 |
| Ho_2O_3 | b.d.l. | b.d.l. | 0.68 | Tb | - | - | 0.006 |
| Er_2O_3 | 0.31 | 0.80 | 3.46 | Dy | 0.001 | 0.003 | 0.043 |
| Tm_2O_3 | 0.10 | 0.22 | 0.67 | Ho | - | - | 0.007 |
| Yb_2O_3 | 0.21 | 1.64 | 4.85 | Er | 0.003 | 0.008 | 0.035 |
| Lu_2O_3 | b.d.l. | 0.36 | 0.76 | Tm | 0.001 | 0.002 | 0.007 |
| FeO | 0.18 | 0.74 | 0.09 | Yb | 0.002 | 0.016 | 0.048 |
| CaO | 0.08 | 1.33 | b.d.l. | Lu | - | 0.004 | 0.007 |
| SrO | 0.08 | 0.09 | b.d.l. | Fe | 0.004 | 0.018 | 0.002 |
| | | | | Ca | 0.003 | 0.047 | - |
| Total | 99.45 | 98.15 | 100.73 | Sr | 0.001 | 0.002 | - |
| | | | | ΣA | 0.996 | 1.042 | 0.973 |
| | | | | Σ cations | 1.995 | 2.041 | 1.973 |
| | | | | Y+REE | 0.011 | 0.118 | 0.966 |
| | | | | Y/(Y+REE) | 0.18 | 0.66 | 0.80 |
| | | | | Zr/Hf wt. | 11.59 | 6.88 | |

The analytical data, acquired with an electron microprobe, are first reported in wt.%, and then converted to atoms per formula unit on the basis of P + As + Si + Ti + Al = 1 *apfu*. A component is not considered significant unless its value exceeds the uncertainty (b.d.l.: below detection limit). Symbols used: Zrn: zircon, Xnt: xenotime-(Y).

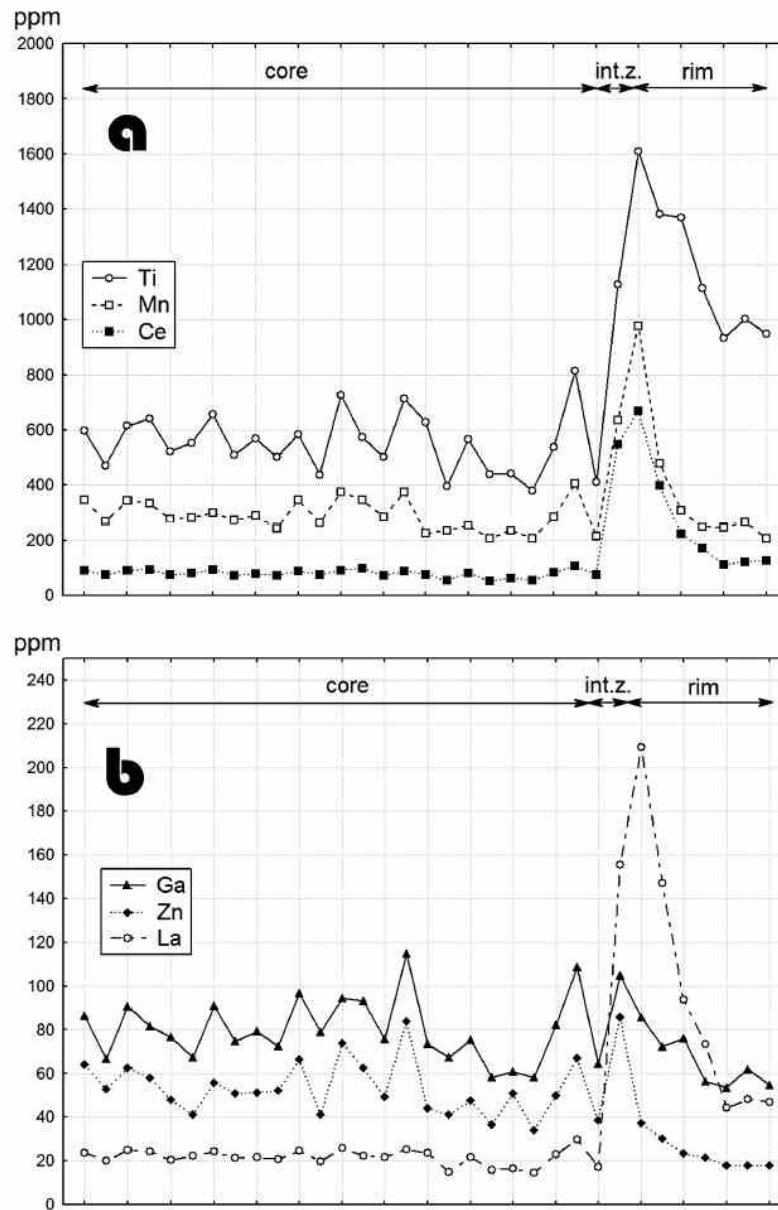


FIG. 5. Cross-section diagrams of trace elements in dravite from the Forshammar pegmatite. The distance between tickmarks on the X axis represents *ca.* 100 μm on the real sample.

2004, Deksissa & Koeberl 2002, Roberts *et al.* 2006). However, the highest REE concentrations observed in tourmaline were reported from veins, also from the Bergslagen ore province in central Sweden (up to 783 ppm La and 1560 ppm Ce; Hellingwerf *et al.* 1994). These highest reported contents of REE in various

genetic types of tourmaline (pegmatites, metamorphic rocks, quartz veins) from same general part of the Bergslagen province indicate an important role of regional lithology on the trace-element (at least REE) concentrations in this mineral group.

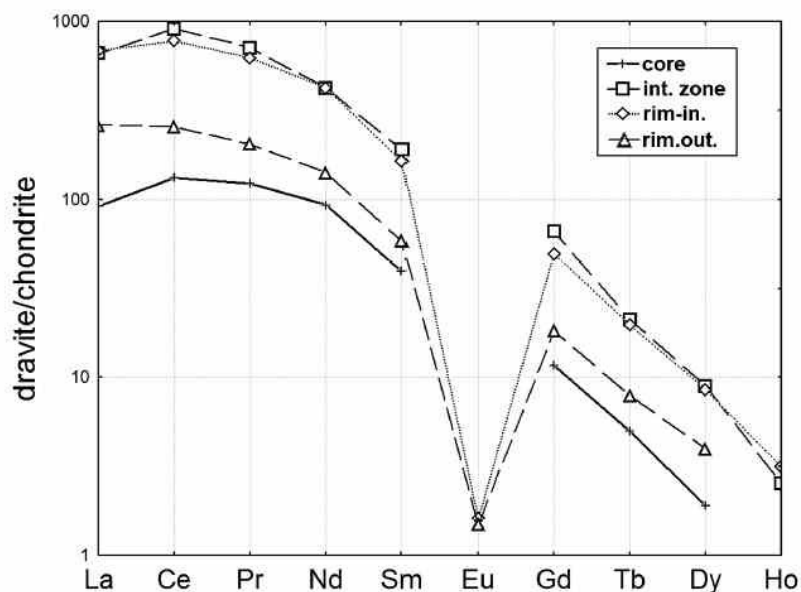
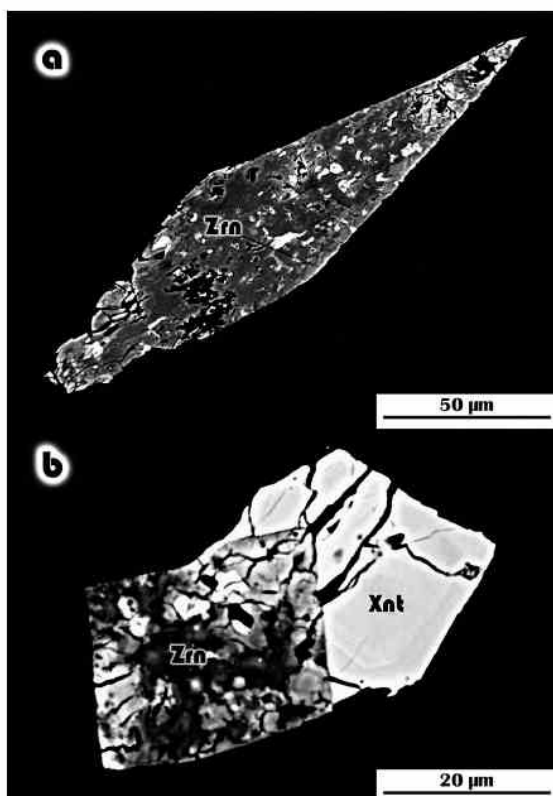


FIG. 6. Average chondrite-normalized REE patterns of several zones in dravite from the Forshammar pegmatite. Chondrite values from Anders & Grevesse (1989).



The tourmaline rim with the highest REE concentrations may also have been influenced or may be the result of a later hydrothermal process that could mobilize the rare earths. The mobilization of the REE is also suggested by formation of hydroxylbastnäsite-(Ce) at a late stage of this hydrothermal process. The behavior of the REE is usually controlled by F (Gramaccioli *et al.* 1999). However, the low content of F in tourmaline and muscovite and the presence of hydroxylbastnäsite-(Ce) in spite of more common bastnäsite-(Ce) suggest only a negligible role of F. Thus, the enrichment in REE in tourmaline from Forshammar could be likely controlled by the activity of CO_2 .

Concentrations of Co and Ga (0.1 to 1.5 and 54 to 115 ppm, respectively; Table 5) are similar, Y (0.6 to 6.9 ppm) reveals higher contents, whereas Zn and Sn (16 to 86 and 1.9 to 9.8 ppm, respectively) show usually lower contents compared to the trace-element concentrations reported from tourmalines in pegmatites (Neiva 1974, Hellingwerf *et al.* 1994, Roda *et al.* 1995, Jiang *et al.*

FIG. 7. BSE photomicrographs of zircon (a) and zircon-xenotime (b) inclusions in dravite from the Forshammar pegmatite. Note the tiny anhedral inclusions of xenotime-(Y) in zircon. Symbols: Zrn: zircon, Xnt: xenotime-(Y).

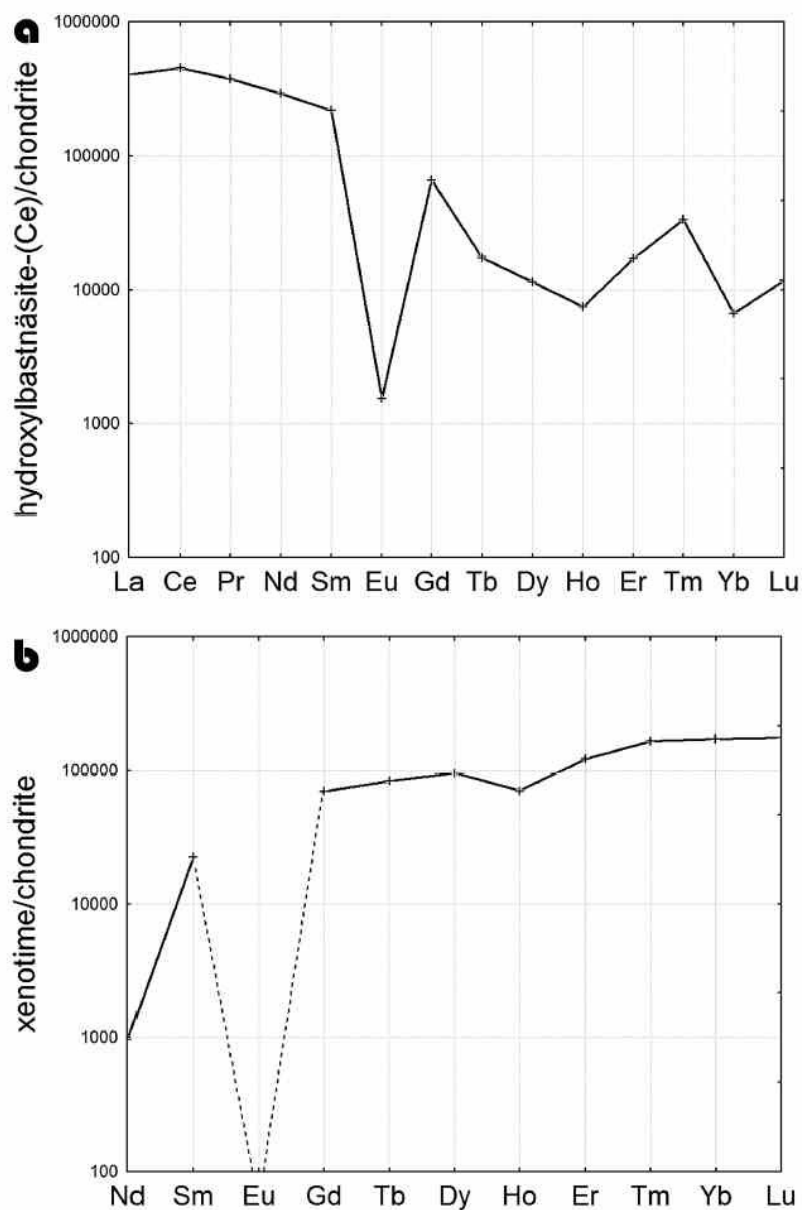


FIG. 8. Average chondrite-normalized REE patterns of a) hydroxylbastnäsite-(Ce) and b) xenotime-(Y) occurring as accessory minerals in tourmaline from Forshammar. Chondrite values from Anders & Grevesse (1989).

1997, Keller *et al.* 1999, Roda-Robles *et al.* 2004, Ertl *et al.* 2006, Novák *et al.* 2011).

The evolution of tourmaline

The observed zoning in the dravite suggests at least two different processes in the growth of tourmaline.

This is suggested by the chemical composition of the core, which differs from other zones in some features. The core has a lower Ca content and distinctly higher X-site vacancy (Table 1) in comparison to other zones. Slight oscillatory zoning apparent in the trace-element distribution suggests that the core is likely the product of a magmatic process. The X_{Mg} value of the rim (0.76)

is similar to that in tourmaline from unusual NYF pegmatites in Třebíč pluton, Czech Republic (up to 0.8; Novák *et al.* 2011). However, dravite from Forshammar has distinctly higher Al content (6.6 – 6.7 *apfu*) and X-site vacancy (0.3 – 0.4) than tourmalines from the Třebíč pluton, with up to 5.7 Al *apfu* and 0.15 of X-site vacancy (Novák *et al.* 2011).

The intermediate zone and rim display increasing Ca and Ti contents and a decreasing proportion of X-site vacancy compared to the core. It could indicate prograde *P–T* conditions during high-grade metamorphism (Henry & Dutrow 1996). However, on the basis of presently available data and observations, the central Swedish pegmatites formed around 1.8 Ga are unlikely to have experienced any significant overprinting geological event other than brittle deformation. The fact that the granitic pegmatites in the Forshammar area are

dominated by a graphic K-feldspar – quartz intergrowth, as well as being unzoned or only marginally so around small, local core pods of quartz, tends to indicate rapid formation from a quickly cooled system. The geochemistry may be an effect of their localized occurrence within a terrane dominated by felsic metavolcanic rock, rather than within metasedimentary units (*e.g.*, Smeds 1990). The lack of tetrahedrally coordinated Al, which usually occurs in significant amounts in tourmaline from higher-grade lithologies (Henry & Dutrow 1996), suggests that the rim of Forshammar tourmaline is not a product of a later metamorphic event. However, it is likely that it grew during a later hydrothermal stage or stages of pegmatite evolution. We can assume that the hydrothermal fluid, which formed intermediate zone, was enriched in Fe, Ca and trace elements including Ti, Mn and REE compared to the rim. The content of Ca and Ti decreases from the contact of the intermediate zone and rim to the outer part of the rim, which could suggest a decrease in the temperature (Henry & Dutrow 1996). A similar trend of enrichment in Ca and Ti was also observed in part of tourmalines in pegmatites from the Třebíč pluton, which suggests an early subsolidus origin (Novák *et al.* 2011). The decrease in Fe, Mn and REE content from core to the rim can be most likely explained by the change of the fluid composition during the formation of the rim. The increased and variable content of REE may indicate a contribution of magmatic–hydrothermal fluids (Garda *et al.* 2010), and it supports the assumption of subsolidus, most likely hydrothermal origin for the intermediate zone and rim of the Forshammar tourmaline. The crystallization of tourmaline ended with the veinlets of tourmaline, which have even lower Al and higher Mg contents than the rim. Even younger hydroxylbastnäsite-(Ce) and muscovite are apparently the products of the final stage or a later hydrothermal process.

ACKNOWLEDGEMENTS

This contribution is dedicated to Professor Petr Černý, University of Manitoba, an eminent mineralogist whose contribution to research on granitic pegmatites, their minerals and genesis is outstanding and influential. We thank Jarek Majka, Jaroslav Pršek and Peter Chudík for their helping hands in the field research and sample collecting. We also thank Daniel Ozdín for assistance with the EMPA analysis. We are indebted to Milan Novák and Robert F. Martin for editorial handling and Darrell J. Henry and Hartmut Beurlen for their detailed reviews and very useful suggestions. This work was supported by the Slovak Research and Development Agency under contracts VVCE–0033–07, APVV–0557–06 (to PB and PU) and by the Austrian Science Fund (FWF) project no. P23012–N19 (to AE).

TABLE 8. REPRESENTATIVE COMPOSITIONS OF HYDROXYLBASTNÄSITE-(Ce) FROM FORSHAMMAR, BERGSLAGEN PROVINCE, SWEDEN

| | TSW51 | TSW52 | | TSW51 | TSW52 |
|--------------------------------|--------|--------|-----------------|-------|-------|
| CO ₂ * wt.% | 18.80 | 18.63 | C <i>apfu</i> | 0.997 | 0.995 |
| SiO ₂ | 0.09 | 0.14 | Si | 0.003 | 0.005 |
| ThO ₂ | b.d.l. | 0.04 | ΣB | 1.000 | 1.000 |
| UO ₂ | 0.06 | 0.05 | | | |
| Y ₂ O ₃ | 0.79 | 1.21 | Th | - | 0.001 |
| La ₂ O ₃ | 11.96 | 10.69 | U | 0.001 | 0.001 |
| Ce ₂ O ₃ | 32.41 | 30.71 | Y | 0.016 | 0.025 |
| Pr ₂ O ₃ | 3.82 | 3.90 | La | 0.171 | 0.154 |
| Nd ₂ O ₃ | 15.19 | 15.85 | Ce | 0.461 | 0.440 |
| Sm ₂ O ₃ | 3.63 | 4.06 | Pr | 0.054 | 0.056 |
| Eu ₂ O ₃ | b.d.l. | 0.04 | Nd | 0.211 | 0.221 |
| Gd ₂ O ₃ | 1.39 | 1.83 | Sm | 0.049 | 0.055 |
| Tb ₂ O ₃ | 0.10 | b.d.l. | Eu | - | 0.001 |
| Dy ₂ O ₃ | 0.28 | 0.43 | Gd | 0.018 | 0.024 |
| Ho ₂ O ₃ | 0.12 | 0.07 | Tb | 0.001 | - |
| Er ₂ O ₃ | 0.26 | 0.34 | Dy | 0.004 | 0.005 |
| Tm ₂ O ₃ | 0.12 | 0.09 | Ho | 0.001 | 0.001 |
| Yb ₂ O ₃ | 0.17 | 0.13 | Er | 0.003 | 0.004 |
| Lu ₂ O ₃ | b.d.l. | b.d.l. | Tm | 0.001 | 0.001 |
| FeO | 0.07 | b.d.l. | Yb | 0.002 | 0.002 |
| MnO | b.d.l. | 0.04 | Lu | - | - |
| CaO | 0.04 | 0.07 | Fe | 0.002 | - |
| SrO | b.d.l. | 0.06 | Mn | - | 0.001 |
| H ₂ O** | 2.90 | 2.82 | Ca | 0.002 | 0.003 |
| F | 2.01 | 2.11 | Sr | - | 0.001 |
| Cl | 0.04 | 0.04 | ΣA | 0.997 | 0.994 |
| O=F | -0.85 | -0.89 | ΣREE+Y | 0.992 | 0.989 |
| O=Cl | -0.01 | -0.01 | Σ cations | 1.997 | 1.994 |
| Total | 93.39 | 92.45 | OH | 0.751 | 0.736 |
| | | | F | 0.247 | 0.261 |
| | | | Cl | 0.003 | 0.003 |
| | | | ΣX | 1.001 | 1.000 |
| | | | O | 3.000 | 3.000 |
| | | | F/(F+OH) | 0.25 | 0.26 |
| | | | 100Ce/(REE+Y) | 46.5 | 44.5 |
| | | | 100LREE/(REE+Y) | 95.4 | 93.7 |

The analytical data, acquired with an electron microprobe, are first reported in wt.%, and then converted to atoms per formula unit on the basis of 4 anions. * C + Si = 1 *apfu*. ** OH + F + Cl = 1 *apfu*. A component is not considered significant unless its value exceeds the uncertainty (b.d.l.: below detection limit).

TABLE 9. COMPARISON OF REE CONTENTS IN TOURMALINES FROM PEGMATITE AT SELECTED LOCALITIES

| Locality | La (ppm) | Ce (ppm) | Yb (ppm) | La _N /Yb _N | Eu/Eu* | Mineral | Reference |
|----------------------------------|------------|------------|--------------|----------------------------------|--------------|-------------------|----------------------------------|
| Alijó-Sanfins area, Portugal | <0.2 – 3.9 | <0.3 – 0.9 | n.d. | n.d. | n.d. | schorl | Neiva (1974) |
| Fregeneda area, Spain | 0.4 – 1.0 | 3.4 | 0.1 – 0.7 | 1.0 – 7.1 | >1 | schorl to dravite | Roda <i>et al.</i> (1995) |
| Bob Ingersoll, U.S.A. | 0.05 – 1.8 | 0.02 – 3.6 | 0.001 – 0.25 | 4.9 – 58 | <0.47 – >1 | schorl to elbaite | Jolliff <i>et al.</i> (1987) |
| Eastern Liaoning, P. R. China | 2.4 | 4.4 | 0.12 | 14 | 5.9 | schorl to dravite | Jiang <i>et al.</i> (1997) |
| Stoffhütte, Austria | 3.5 | 8.3 | 0.24 | 10 | 0.28 | olenite | Ertl <i>et al.</i> (2006) |
| Nuristan, Afghanistan | 13 | 47 | 0.02 | 433 | 0.03 | elbaite | Ertl <i>et al.</i> (2006) |
| Anjanabonoina, Madagascar | 47 | 71 | 0.09 | 359 | 0.46 | elbaite | Ertl <i>et al.</i> (2006) |
| Třebíč pluton, Czech Republic | 6.2 – 51 | 7.6 – 63 | n.d. | n.d. | n.d. | dravite to schorl | Novák <i>et al.</i> (2011) |
| Bergslagen area, Sweden | 0.8–35 | 2.8 – 83 | 0.3 – 5.0 | 0.16 – 14 | <1 | schorl to dravite | Hellingwerf <i>et al.</i> (1994) |
| Forshammar, Sweden | 14.0 – 210 | 55.0 – 670 | 0.06 – 0.38 | 32.0 – 464 | 0.005 – 0.05 | dravite | this study |

n.d.: not determined.

REFERENCES

- AMBRÓS, M. (1983): Beskrivning till berggrundskartan 1:50 000 – VIF Lindesberg NO (description to the map of solid rocks Lindesberg NO). *Sveriges Geologiska Undersökning Af 141*, 75 pp. + map.
- ANDERS, E. & GREVESSE, N. (1989): Abundances of the elements: meteoritic and solar. *Geochim. Cosmochim. Acta* **53**, 197-214.
- BEA, F. (1996): Residence of REE, Y, Th and U in granites and crustal protoliths: implications for the chemistry of crustal melts. *J. Petrol.* **37**, 521-552.
- BERNARD, J.H. & HYRŠL, J. (2006): *Minerals and their Localities* (2nd ed.). Granit, Prague, Czech Republic.
- BLOODAXE, E.S., HUGHES, J.M., DYAR, M.D., GREW, E.S. & GUIDOTTI, C.V. (1999): Linking structure and chemistry in the schorl–dravite series. *Am. Mineral.* **84**, 922-928.
- BOSI, F., BALIĆ-ŽUNIĆ, T. & SUROUR, A.A. (2010): Crystal structure analyses of four tourmaline specimens from the Cleopatra's mines (Egypt) and Jabal Zalm (Saudi Arabia), and the role of Al in the tourmaline group. *Am. Mineral.* **95**, 510-518.
- BOSI, F. & LUCCHESI, S. (2004): Crystal chemistry of the schorl–dravite series. *Eur. J. Mineral.* **16**, 335-344.
- BROTZEN, O. (1959): Mineral-association in granitic pegmatites. A statistical study. *Geol. Fören. Stockholm Förh.* **81**, 231-296.
- BRUKER (2010a): DIFFRACplus EVA. <http://www.brukeraxs.com/eva.html>
- BRUKER (2010b): DIFFRACplus TOPAS. <http://www.bruker-axs.de/topas.html>
- DEKSISSA, D.J. & KOEBERL, C. (2002): Geochemistry and petrography of gold – quartz – tourmaline veins of the Okote area, southern Ethiopia: implications for gold exploration. *Mineral. Petrol.* **75**, 101-122.
- ERTL, A., HUGHES, J.M., PROWATKE, S., LUDWIG, T., PRASAD, P.S.R., BRANDSTÄTTER, F., KÖRNER, W., SCHUSTER, R., PERTLIK, F. & MARSCHALL, H. (2006): Tetrahedrally coordinated boron in tourmalines from the liddicoatite–elbaite series from Madagascar: structure, chemistry, and infrared spectroscopic studies. *Am. Mineral.* **91**, 1847-1856.
- ERTL, A., MALI, H., SCHUSTER, R., KÖRNER, W., HUGHES, J.M., BRANDSTÄTTER, F. & TILLMANN, E. (2010a): Li-bearing, disordered Mg-rich tourmaline from a pegmatite–marble contact in the Austroalpine basement units (Styria, Austria). *Mineral. Petrol.* **99**, 89-104.
- ERTL, A., MARSCHALL, H.R., GIESTER, G., HENRY, D.J., SCHERTL, H.-P., NTAFLAS, T., LUVIZOTTO, G.L., NASDALA, L. & TILLMANN, E. (2010b): Metamorphic ultra high-pressure tourmaline: structure, chemistry, and correlations to P–T conditions. *Am. Mineral.* **95**, 1-10.
- ERTL, A., ROSSMAN, G.R., HUGHES, J.M., MA, CHI & BRANDSTÄTTER, F. (2008) V³⁺-bearing, Mg-rich, strongly disordered olenite from a graphite deposit near Amstall, Lower Austria: a structural, chemical and spectroscopic investigation. *Neues Jahrb. Mineral., Abh.* **184**, 243-253.

- FISCHER, R.X. & TILLMANN, E. (1988): The equivalent isotropic displacement factor. *Acta Crystallogr.* **C44**, 775-776.
- FLINK, G. (1917): Bidrag till Sveriges mineralogi. IV. 112. Andalusit. *Arkiv Kemi, Mineral. Geol.* **6**, 72-74.
- GARDA, G.M., BELJAVSKIS, P., D'AGOSTINO, L.Z. & WIENBECK, M. (2010): Tourmaline and rutile as indicators of a magmatic-hydrothermal origin for tourmalinite layers in the São José do Barreiro area, NE Ribeira Belt, southern Brazil. *Geol. USP Sér. Cient.* **10**(3), 97-117.
- GRAMACCIOLI, C. M., DIELLA, V. & DEMARTIN, F. (1999): The role of fluoride complexes in REE geochemistry and the importance of 4f electrons: some examples in minerals. *Eur. J. Mineral.* **11**, 983-992.
- HAWTHORNE, F.C., MACDONALD, D.J. & BURNS, P.C. (1993): Reassignment of cation site occupancies in tourmaline: Al-Mg disorder in the crystal structure of dravite. *Am. Mineral.* **78**, 265-270.
- HELLINGWERF, R.H., GATEDAL, K., GALLAGHER, V. & BAKER, J.H. (1994): Tourmaline in the central Swedish ore district. *Mineral. Deposita* **29**, 189-205.
- HENRY, D.J. & DUTROW, B.L. (1996): Metamorphic tourmaline and its petrologic applications. In *Boron: Mineralogy, Petrology and Geochemistry* (E.S. Grew & L.M. Anovitz, eds.). *Rev. Mineral.* **33**, 503-557.
- HENRY, D.J., NOVÁK, M., HAWTHORNE, F.C., ERTL, A., DUTROW, B.L., UHER, P. & PEZZOTTA, F. (2011): Nomenclature of the tourmaline supergroup-minerals. *Am. Mineral.* **96**, 895-913.
- IVARSSON, C. & JOHANSSON, Å. (1995): U-Pb zircon dating of Stockholm granite at Frescati. *Geol. Fören. Stockholm Förh.* **117**, 67-68.
- JIANG SHAO-YONG, HAN FA, SHEN JIAN-ZHONG & PALMER M.R. (1999): Chemical and Rb-Sr, Sm-Nd isotopic systematics of tourmaline from the Dachang Sn-polymetallic ore deposit, Guangxi Province, P.R. China. *Chem. Geol.* **157**, 49-67.
- JIANG SHAO-YONG, PALMER, M.R., PENG QI-MING & YANG JING-HONG (1997): Chemical and stable isotopic compositions of Proterozoic metamorphosed evaporites and associated tourmalines from the Houxiyan borate deposit, eastern Liaoning, China. *Chem. Geol.* **135**, 189-211.
- JIANG SHAO-YONG, YU JI-MIN & LU JIAN-JUN (2004): Trace and rare-earth element geochemistry in tourmaline and cassiterite from the Yunlong tin deposit, Yunnan, China: implication for migmatitic-hydrothermal fluid evolution and ore genesis. *Chem. Geol.* **209**, 193-213.
- JOLLIFF, B.L., PAPIKE, J.J. & LAUL, J.C. (1987): Mineral recorders of pegmatite internal evolution: REE contents of tourmaline from the Bob Ingersoll pegmatite, South Dakota. *Geochim. Cosmochim. Acta* **51**, 2225-2232.
- KELLER, P., RODA ROBLES, E., PESQUERA PÉREZ, A. & FONTAN, F. (1999): Chemistry, paragenesis and significance of tourmaline in pegmatites of the Southern Tin Belt, central Namibia. *Chem. Geol.* **158**, 203-225.
- KING, R.W., KERRICH, R.W. & DADDAR, R. (1988): REE distributions in tourmaline: an INAA technique involving pretreatment by B volatilization. *Am. Mineral.* **73**, 424-431.
- KLEMM, S., MARSCHALL, H.R., JACOB, D.E., PROWATKE, S. & LUDWIG, T. (2011): Trace-element partitioning and boron isotope fractionation between white mica and tourmaline. *Can. Mineral.* **49**, 165-176.
- LONDON, D. (2008): *Pegmatites*. The Canadian Mineralogist, Special Publication **10**.
- LUNDEGÅRDH, P.H. (1971): *Nyttosten i Sverige*. Almqvist & Wiksell, Stockholm, Sweden.
- LUNDSTRÖM, I., ALLEN, R.L., PERSSON, P.-O. & RIPA, M. (1998): Stratigraphies and depositional ages of Svecofennian, Palaeoproterozoic metavolcanic rocks in E. Svealand and Bergslagen, south central Sweden. *Geol. Fören. Stockholm Förh.* **120**, 315-320.
- MEDARIS, L.G., JR., FOURNELLE, J.H. & HENRY, D.J. (2003): Tourmaline-bearing quartz veins in the Baraboo Quartzite, Wisconsin: occurrence and significance of foitite and "oxyfoitite". *Can. Mineral.* **41**, 749-758.
- MÖLLER, P. & MUECKE, G.K. (1984): Significance of europium anomalies in silicate melts and crystal-melt equilibria: a re-evaluation. *Contrib. Mineral. Petrol.* **87**, 242-250.
- NEIVA, A.M.R. (1974): Geochemistry of tourmaline (schorl) from granites, aplites and pegmatites from northern Portugal. *Geochim. Cosmochim. Acta* **38**, 1307-1317.
- NOVÁK, M., POVONDRA, P. & SELWAY, J.B. (2004): Schorl-oxy-schorl to dravite-oxy-dravite tourmaline from granitic pegmatites; examples from the Moldanubicum, Czech Republic. *Eur. J. Mineral.* **16**, 323-333.
- NOVÁK, M., ŠKODA, R., FILIP, J., MACEK, I. & VACULOVÍČ, T. (2011): Compositional trends in tourmaline from intragranitic NYF pegmatites of the Třebíč Pluton, Czech Republic: an electron microprobe, Mössbauer and LA-ICP-MS study. *Can. Mineral.* **49**, 359-380.
- PESQUERA, A., TORRES-RUIZ, J., GIL-CRESPO, P.P. & JIANG, S.-Y. (2005): Petrographic, chemical and B-isotopic insights into the origin of tourmaline-rich rocks and boron recycling in the Martínamor Antiform (Central Iberian Zone, Salamanca, Spain). *J. Petrol.* **46**, 1013-1044.
- PRŠEK, J., ONDREJKA, M., BAČÍK, P., BUDZYŃ, B. & UHER, P. (2010): Metamorphic-hydrothermal REE minerals in the Bacúch magnetite deposit, Western Carpathians, Slovakia: (Sr,S)-rich monazite-(Ce) and Nd-dominant hingganite. *Can. Mineral.* **48**, 81-94.
- ROBERTS, S., PALMER, M.R. & WALLER, L. (2006): Sm-Nd and REE characteristics of tourmaline and scheelite from

- the Björkdal gold deposit, northern Sweden: evidence of an intrusion-related gold deposit? *Econ. Geol.* **101**, 1415-1425.
- RODA, E., PESQUERA, A. & VELASCO, F. (1995): Tourmaline in granitic pegmatites and their country rocks, Fregeneda area, Salamanca, Spain. *Can. Mineral.* **33**, 835-848.
- RODA-ROBLES, E., PESQUERA, A., GIL, P.P., TORRES-RUIZ, J. & FONTAN, F. (2004): Tourmaline from the rare-element Pinilla pegmatite, (Central Iberian Zone, Zamora, Spain): chemical variation and implications for pegmatitic evolution. *Mineral. Petrol.* **81**, 249-263.
- ROMER, R.L. & SMEDS, S.-A. (1997): U-Pb columbite chronology of post-kinematic Palaeoproterozoic pegmatites in Sweden. *Precamb. Res.* **82**, 85-99.
- SHANNON, R.D. (1976): Revised effective ionic radii and systematic studies of interatomic distances in halides and chalcogenides. *Acta Crystallogr.* **A32**, 751-767.
- SHELDRIK, G.M. (1997): SHELXL-97, a program for crystal structure refinement. University of Göttingen, Göttingen, Germany.
- SMEDS, S.-A. (1990): Regional trends in mineral assemblages of Swedish Proterozoic granitic pegmatites and their geological significance. *Geol. Fören. Stockholm Förh.* **112**, 227-242.
- SUNDIUS, N. (1952): Kvarter, fältspat och glimmer samt förekomster därav i Sverige. *Sver. Geol. Undersökning C* **520**.
- TORRES-RUIZ, J., PESQUERA, A., GIL-CRESPO, P.P. & VELILLA, N. (2003): Origin and petrogenetic implications of tourmaline-rich rocks in the Sierra Nevada (Betic Cordillera, southeastern Spain). *Chem. Geol.* **197**, 55-86.
- YAVUZ, F., ISKENDERÖĞLU, A. & JIANG SHAO-YONG (1999): Tourmaline compositions from the Salikvan porphyry Cu-Mo deposit and vicinity, northeastern Turkey. *Can. Mineral.* **37**, 1007-1023.

Received July 22, 2011, revised manuscript accepted July 8, 2012.

6.7 ARTICLE 7

Breiter, K.; Gardenova, N.; Vaculovic, T.; Kanicky, V. Mineralogical Magazine 2013, 77, 403-417 (IF=2.21)

Topaz as an important host for Ge in granites and greisens

K. BREITER^{1,*}, N. GARDENOVÁ², T. VACULOVÍČ^{2,3} AND V. KANICKÝ^{2,3}

¹ Institute of Geology, v.v.i., Academy of Sciences of the Czech Republic, Rozvojová 269, CZ-165 00 Prague 6, Czech Republic

² Faculty of Science, Masaryk University, Kotlářská 2, CZ-611 37, Brno, Czech Republic

³ CEITEC, Masaryk University, Kamenice 5, CZ-602 00, Brno, Czech Republic

[Received 21 January 2013; Accepted 18 March 2013; Associate Editor: E. Grew]

ABSTRACT

The composition of topaz from different granites and greisen in the Krušné Hory/Erzgebirge area was investigated using electron microprobe analysis (EMPA) and Laser Ablation Inductively Coupled Plasma Mass Spectrometry (LA-ICP-MS). All topaz grains are rich in F (17.9–19.8 wt.%, 1.73–1.90 a.p.f.u.) and the most important minor/trace elements are P, Ge and Ga. Contents of P up to 1 wt.% P₂O₅ (0.025 a.p.f.u.) were found in topaz from the strongly peraluminous P-rich magmatic systems at Podlesí. Regardless of genetic type, topaz from granites typically contains 50–100 ppm Ge. The greatest amounts (up to 204 ppm Ge) were found in topaz from quartz-topaz-apatite greisen in Krásno. In fractionated granites and greisens, topaz is calculated to contain 23–87% of the bulk Ge content in the rock. In contrast, topaz does not concentrate Ga. The Ga content of topaz (typically 5–35 ppm in S-type granites, <10 ppm Ga in A-type granites) is usually smaller than the bulk Ga content of the rock. In addition, up to 16 ppm Sc, 23 ppm Sn and >400 ppm Fe may be present.

KEYWORDS: topaz, germanium, gallium, LA-ICP-MS, Krušné Hory Mts., Erzgebirge.

Introduction

TOPAZ, Al₂SiO₄(F,OH)₂, is a common component of complex pegmatites (beryl-topaz and lepidolite types of the LCT-family, topaz-beryl type of the NYF-family, according to the classification of Černý and Ercit, 2005), fractionated fluorine-enriched granites and greisens created by their hydrothermal transformation.

Because of its simple composition, topaz is seldom analysed. Only the contents of F (F/OH ratio, Deer *et al.*, 1997 and references therein) have been studied systematically using EMPA. Data for the trace-element contents of topaz are few, but the compilation made by Bernstein (1985) suggests, that topaz could be an important

host for Ge. During a detailed investigation of phosphorus in topaz from different types of granites in the Krušné Hory/Erzgebirge area (Breiter and Kronz, 2004), interesting enrichments in Ge (up to 210 ppm) and Ga (up to 140 ppm) were found. Nevertheless, the contents of both elements were near the detection limits of EMPA. Thus, we decided to study the content of Ge and Ga in topaz from the Krušné Hory/Erzgebirge by a more sensitive method. Moreover, the co-occurrence of fractionated F-enriched granites of S- and A-types (Breiter, 2012) permits comparison of the composition of topaz from these contrasting granite types.

The objectives of our study were as follows: (1) to determine accurately the contents of Ge and Ga in topaz *in situ* using LA-ICP-MS; (2) to evaluate the behaviour of Ge and Ga during the fractionation and subsequent greisenization of F-rich granites.

* E-mail: breiter@gli.cas.cz

DOI: 10.1180/minmag.2013.077.4.01

Previous work

Papish (1928, 1929) examined the emission spectra of 31 topaz samples from 23 localities and found all to contain germanium; although these data could not be quantified. Using chemical extraction, ~0.1 wt.% GeO₂ was found in topaz from the Silver Leaf Mine, Manitoba, (Papish, 1929). Seim and Schweder (1962) found 2–400 ppm Ge in topaz from the Erzgebirge. Oftedal (1963) analysed topaz in 11 Norwegian Precambrian pegmatites and found a surprising enrichment of Ge in the range 100–700 ppm. Shcherba *et al.* (1966) reported 63–320 ppm Ge in topaz from a Sn-W greisen deposit Aktschatau, Kazakhstan. El-Hinnawi and Hofmann (1966) found 95–280 ppm Ge and smaller amounts of Cr, Mn, Co and Ni in 11 topaz samples from the Erzgebirge. Subsequently, Seim and Schweder (1969) conducted a detailed study of the Ge content of topaz. They found 50–86 ppm Ge in topaz from Schneckenstein (37 individual samples), and 11–67 ppm Ge in pycnite (traditional local name for columnar to acicular topaz in some tin deposits in the eastern Erzgebirge) from Zinnwald, Sadisdorf and Altenberg (9 individual samples). Another 25 topaz samples from worldwide occurrences contained 5–440 ppm Ge. The relationship between the genetic type of deposit and Ge content could not be demonstrated. All of the above data were obtained using optical emission spectroscopy. Northrup and Reeder (1994) found 22–24 ppm Ge together with 6–8 ppm Ga, 5–40 ppm As, 153–256 ppm Ti and 172–224 ppm Fe in volcanogenic topaz from San Luis Potosí, Mexico using synchrotron X-ray fluorescence methods. Duck (1986) and Duck and Cohen (1986) analysed Ge and Ga using spectrophotometry in 11 dissolved samples of pegmatitic and hydrothermal topaz and associated quartz. They found 13–238 ppm Ge and 2.5–9.3 ppm Ga in topaz, 0.1–5.6 ppm Ge and 0.01–1.2 ppm Ga in quartz, and concluded that Ge and Ga partitioning into topaz is positively correlated with the fluorine content of topaz and related to induced strain in the crystal structure.

Breiter and Kronz (2004) found 50–100 ppm Ge and ~50 ppm Ga in topaz from peraluminous granites in Erzgebirge using an electron microprobe. Trace-element analyses of three topaz crystals from northern Pakistan using INAA were conducted by Wasim *et al.* (2011), who found 4–10 ppm Ga and 99–138 ppm Ge,

together with 5–977 ppm Ce, which might indicate impurities in the analysed samples. Aigbe *et al.* (2013) recorded 18.7 ppm Sc in topaz from Nigeria using INAA. These two studies examined topaz crystals from the commercial market without any knowledge of their paragenesis.

Although some are only semiquantitative, these published data show that Ge is concentrated in topaz more than Ga. On the basis of ionic size considerations, Ge⁴⁺ is expected to replace Si⁴⁺ in tetrahedral sites whereas Ga³⁺ is expected to replace Al³⁺ in octahedral sites (Goldschmidt, 1954; Northrup and Reeder, 1994), although Ga substitution for tetrahedral Si is also possible (Duck, 1986). Coupled substitution of (GeO)²⁺ for (AlF)²⁺ was proposed by Oftedal (1963). Effective ionic radii for six-fold coordination in topaz are 53.5 pm (Al³⁺) and 62 pm (Ga³⁺), for tetrahedral coordination, 26 pm (Si⁴⁺) and 39 pm (Ge⁴⁺) (Shannon, 1976).

Germanium prefers the least-linked tetrahedral structures (Harris, 1954). Burton *et al.* (1959) and Johan *et al.* (1983) found that the extent of Ge substitution for Si decreases in the order nesosilicates, inosilicates, phyllosilicates and tectosilicates. In contrast, Ga is concentrated in feldspars and micas, and particularly in pegmatites (Bell, 1955). Germanium, but not Ga, tends to be enriched in post-magmatic hydrothermal fluids up to such concentrations that Ge minerals can be formed, e.g. argyrodite [Ag₈GeS₆], in which Winkler (1886) first found the element Ge (Weisbach, 1886; Goldschmidt and Peters, 1933; Schrön, 1969; Bernstein, 1985; Höll *et al.*, 2007).

The crystallochemical similarity between Ge and Si in the structures of topaz-type was confirmed by the discovery of krieselite Al₂GeO₄(F,OH)₂, which is the Ge-analogue of topaz (Schlüter *et al.*, 2010). Krieselite from the Tsumeb copper mine, Namibia, contains up to 0.102 a.p.f.u. Ga substituting for Al. A Ge analogue of hydroxy-topaz Al₂GeO₄(OH)₂ has been synthesized (Wunder and Marler, 1997). This mineral can also be considered the OH analogue of krieselite.

Material investigated

The material investigated (Table 1, Fig. 1) represents the principal types of fractionated tin-bearing granites from the Krušné Hory/Erzgebirge Mountains and the products of their hydrothermal alteration (Breiter *et al.*, 1999; Cháb *et al.*, 2010).

TOPAZ AS A HOST FOR Ge

TABLE 1. Analysed samples.

| Sample | Granite type | Locality and rock description | Topaz description |
|--------|--------------|---|--|
| Po-1 | S | Podlesí, coarse-grained albite-biotite granite of the younger intrusive complex, main facies of the Nejdek pluton, | Euhedral grains 0.1–0.8 mm |
| Po-2 | S | Podlesí stock, medium-grained albite-protolithionite-topaz granite | Euhedral grains 0.1–0.5 mm |
| Po-3 | S | Podlesí stock, medium-grained albite-zinnwaldite-topaz granite | Subhedral grains 0.1–0.5 mm |
| Po-4 | S | Podlesí stock, quartz-topaz-zinnwaldite greisen | Anhedral grains 0.1–0.3 mm |
| Kr | S | Krásno (Schlagenwald in German literature), quartz-topaz-apatite greisen with cassiterite, wolframite and sulphides | Imperfect crystals 2–4 mm |
| Ci | A | Cínovec (Zinnwald in German literature), fine-grained albite-zinnwaldite granite | Subhedral grains 0.1–0.3 mm |
| Alt | A | Altenberg, coarse-grained quartz-topaz-zinnwaldite rock at the upper contact of the granite stock | Aggregates of columnar crystals, individual crystals are ~1 cm long and 1 mm in diameter |
| Sch | A | Schneckenstein, cavities in the explosive breccia | Imperfect wine-yellow crystals up to 1 cm in size |

Strongly peraluminous P-enriched (S-type) granites are represented by samples of typical facies from the Nejdek-Eibenstock (also Eibenstock-Nejdek or Eibenstock-Neudeck according to some German authors) pluton, including the highly fractionated Podlesí stock. The intensity of fractionation and the enrichment of the parent rock in P, F, Li and other lithophile elements increases from the albite-biotite granite with trace amounts of topaz through the albite-protolithionite granite with more abundant topaz to albite-zinnwaldite-topaz granite with up to 3 vol.% of topaz. The associated quartz-topaz greisen originated from the latter type of granite during early post-magmatic rock–fluid interaction (Breiter *et al.*, 2005).

In the Krásno tin deposit, large topaz grains and imperfect crystals (up to 3 mm in diameter) from cm-scale vugs in the greisen cupola of the Hubstock crystallized during the post-magmatic hydrothermal stage of the S-type “Čistá” granite in the Krudum pluton (Jarchovský, 2006).

Sub-aluminous A-type granites from the eastern Erzgebirge are represented by albite-zinnwaldite granite with topaz from the upper part of the Cínovec/Zinnwald granite cupola (Breiter, 2012). Yellow columnar topaz (pycnite) is a typical constituent of the marginal pegmatite (stockscheider) of the granite cupola in Altenberg (Ossenkopf and Helbig, 1975; Seim and Leipe,

1987). Aggregates of pycnite with zinnwaldite, quartz and subordinate wolframite are also common in flat ore veins in the Cínovec/Zinnwald tin-tungsten deposit. The final category of topaz investigated is from Schneckenstein, located at the western edge of the Erzgebirge in Saxony. Here, an explosive phyllite breccia above the stock of A-type granite cemented with a hydrothermal quartz with many cavities, yields extraordinary crystals of gem quality wine-yellow topaz several cm in size (Gottesmann *et al.*, 1994; Förster *et al.*, 2007; Leithner, 2008). In addition, small topaz crystals are quite common.

Analytical methods

Topaz was separated using standard techniques (crushing, sieving, panning, concentration in heavy liquids, hand picking) from eight representative samples (Table 1). Topaz grains (0.2–0.5 mm diameter) were embedded in epoxy resin and polished.

Element abundances of Si, Al, F and P in topaz from Podlesí were determined using a JEOL 8900 RL electron microprobe at the Geowissenschaftliches Zentrum, University of Göttingen (analyst Andreas Kronz; for details, see Breiter and Kronz, 2004). Other samples were analysed using a CAMECA SX100 electron microprobe at the Institute of Geology, Academy of Science of the

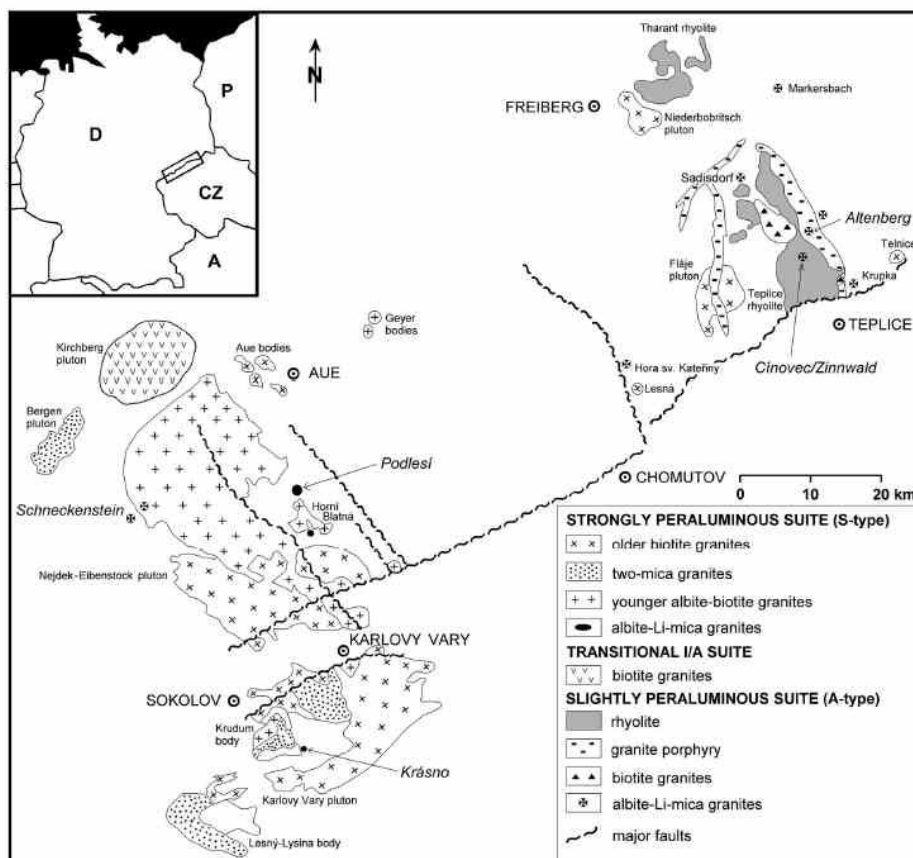
K. BREITER *ET AL.*

Fig. 1. Geological sketch of the Krušné Hory/Erzgebirge area with localities investigated (*in italics*). Modified from Breiter (2012).

Czech Republic, Prague, with an accelerating voltage and beam current of 15 kV and 10 nA, respectively, and a beam diameter 2 μm (analyst Mrs Zuzana Korbelová). The following standards were used: Al, Si, F – topaz, and P – apatite.

The amounts of Ga, Ge, Fe, Sc, In, Tl and Sn in topaz were determined in polished mineral grains using LA-ICP-MS. This instrumentation consists of the laser ablation system UP213 (NewWave Research, USA) and the ICP-MS Agilent 7500CE (Agilent, Japan). The facility is located at the Laboratory of Atomic Spectrochemistry of the Department of Chemistry, Masaryk University, Brno, Czech Republic. Sample aerosols generated by ablation at the laser beam wavelength of 213 nm are transported by He carrier gas (1.0 l min^{-1}) into the ICP source of the quadrupole mass spectrometer, which is equipped with a reaction-collision cell to suppress isobaric inter-

ferences. Ablation was performed at the laser beam flux of 21 J cm^{-2} , a laser spot diameter of 65 μm and a repetition rate of 10 Hz. The following isotopes were measured: ^{27}Al , ^{28}Si , ^{45}Sc , ^{56}Fe , ^{69}Ga , ^{71}Ga , ^{72}Ge , ^{74}Ge , ^{115}In , ^{118}Sn and ^{205}Tl . Two isotopes for both Ga and Ge were measured to detect possible isobaric interferences. Measured isotopic ratios of $^{69}\text{Ga}/^{71}\text{Ga}$ and $^{72}\text{Ge}/^{74}\text{Ge}$ were compared with natural abundance ratios to ensure that neither of the two isotopic pairs exhibited interferences. For quantification ^{71}Ga and ^{74}Ge were employed due to their lower limits of detection (LOD). Calibration with normalization to the ideal formula of topaz with silicon content of 15.41 wt.% was performed using certified reference material NIST612.

The major elements in bulk-rock samples of granites from Podlesí and Cínovec/Zinnwald and fine-grained homogeneous greisen from Podlesí

TOPAZ AS A HOST FOR Ge

were determined using standard wet chemistry methods at the laboratory of the Czech Geological Survey, Prague, Czech Republic. Other samples (breccia, border pegmatite, coarse-grained greisen) were too heterogeneous to be analysed using whole-rock methods. The analyses of the international reference of whole-rock standard (JG-3 granodiorite; Geological Survey of Japan) yielded an average error (1σ) of $\pm 1\%$ with respect to recommended values (Govindaraju, 1994). Rubidium in bulk-rock samples was determined using X-ray fluorescence (LOD 2 ppm) at the laboratory of the Czech Geological Survey, Prague. Gallium and Ge were determined using ICP-MS (Agilent, 7500CE, Japan) after chemical decomposition. Whole-rock samples were decomposed using fusion with LiBO_2 (Spectromelt A20, Merck), (0.2 g of a sample with 1.0 g of LiBO_2). The resulting borosilicate glass bead was dissolved under stirring with 20 ml of 0.7 mol/l HNO_3 , the solution was transferred into a volumetric flask and, after addition of internal reference element (Se), was filled up to 250 ml with deionized water. Blank solutions were prepared in the same way as the samples. The ICP spectrometer is equipped with a collision-reaction cell for suppressing possible isobaric interferences. The generator power input was 1500 W, outer plasma gas flow rate (Ar) 15.0 l min^{-1} , intermediate plasma gas flow rate (Ar) 0.25 l min^{-1} , carrier gas (Ar) flow-rate 0.85 l min^{-1} , sample flow rate $200 \mu\text{l min}^{-1}$, nebulizer temperature 2°C and the He flow-rate in the collision cell was 3 ml min^{-1} . The following isotopes were recorded during analysis: ^{27}Al , ^{28}Si , ^{69}Ga , ^{71}Ga , ^{72}Ge and ^{73}Ge . Due to strong isobaric interferences $^{29}\text{Si}^{40}\text{Ar}$ and $^{16}\text{O}^{56}\text{Fe}$, which were suppressed insufficiently by the collision-reaction cell, the isotopes ^{71}Ga and ^{73}Ge were used for interpretation. For quality control the CRM GBW7406 was analysed in each set of dissolved samples (Table 2).

TABLE 2. Results of analysis of certified reference material GBW7406.

| | Ga | Ge |
|------------------------|------|---------|
| Measured content (ppm) | 32±2 | 3.4±0.3 |
| Certified value (ppm) | 30±3 | 3.2±0.3 |
| LOD (ppm) | 0.02 | 0.08 |

Results

The bulk composition of granites and greisens from Podlesí and Cínovec has been published and discussed previously (Breiter *et al.*, 1999, 2005). Regardless, we decided to perform new bulk-rock analyses from some of the samples investigated (Table 3), to facilitate an accurate correlation between the trace-element contents in topaz and the bulk-rock composition.

Topaz grains were analysed with the electron microprobe and LA-ICP-MS. Si, Al, F and P were determined by EMPA, whereas trace elements (Ga, Ge, Sn, In, Tl, Sc) were determined by means of LA-ICP-MS. Representative EMPA data are summarized in Table 4 and shown in Fig. 2. The Ga, Ge, Fe, Sc and Sn contents, analysed using LA-ICP-MS, are summarized in Table 5 and illustrated in Fig. 3. The In and Tl contents are lower than LOD for these elements (0.1 ppm) in most cases.

The F content is relatively large in all analysed topaz grains, at 17.9–19.8 wt.% (1.73–1.90 a.p.f.u. F). The smallest contents were found in topaz from the Schneckenstein breccia (17.9–18.5 wt.% F, ~1.75 a.p.f.u. F), and in topaz from vugs in the greisen from Krásno (18.6–18.9 wt.% F, ~1.8 a.p.f.u. F). The largest contents were found in late magmatic topaz from the albite-topaz-zinnwaldite granites from Podlesí and Cínovec/Zinnwald (19.5–19.8 wt.% F, ~1.90 a.p.f.u. F). Topaz from other samples ranged between 19.0 and 19.5 wt.% F (1.8–1.9 a.p.f.u. F).

The P contents of topaz correlates well with the P content of the parent rocks. The largest amounts were found in the P-rich (>1 wt.% P_2O_5 in the bulk rock) albite-topaz-zinnwaldite granite and the associated high-temperature greisen in Podlesí (0.1–1.0 wt.% P_2O_5 , 0.003–0.025 a.p.f.u. P). Topaz from other peraluminous rock only rarely exceeds 0.01 wt.% P_2O_5 . Among topaz from A-type environments, pycnite from Altenberg contains 0.1 wt.% P_2O_5 (0.003 a.p.f.u. P), while other samples are generally free of P.

The greatest contents of Ge were found in topaz from greisen in Krásno (62–204 ppm), in topaz from the Cínovec granite (45–132 ppm) and in the topaz from the albite-zinnwaldite granite from Podlesí (47–102 ppm). Topaz from other samples typically contains 40–70 ppm Ge.

The Ga content of topaz is lower than that of Ge. Topaz from the albite-zinnwaldite granite in Podlesí contains the most Ga, typically 9–29 ppm

K. BREITER *ET AL.*

TABLE 3. Bulk-rock composition of selected granites (major elements in wt.%, trace elements in ppm).

| Locality Sample Rock type | Podlesí Po-1 Ab-Bt granite | Podlesí Po-2 Ab-Protol granite | Podlesí Po-3 Ab-Zinw granite | Podlesí Po-4 Qtz-Zinw greisen | Cínovec Ci Ab-Zinw granite |
|---------------------------------|----------------------------------|--------------------------------------|------------------------------------|-------------------------------------|----------------------------------|
| SiO ₂ | 72.52 | 73.17 | 70.10 | 83.52 | 75.85 |
| TiO ₂ | 0.06 | 0.06 | 0.02 | 0.05 | 0.03 |
| Al ₂ O ₃ | 14.95 | 14.67 | 15.77 | 11.63 | 13.04 |
| Fe ₂ O ₃ | 0.24 | 0.28 | 0.11 | 0.26 | 0.44 |
| FeO | 1.05 | 0.69 | 0.67 | 0.26 | 0.39 |
| MgO | 0.08 | 0.03 | 0.04 | 0.01 | 0.04 |
| MnO | 0.03 | 0.04 | 0.02 | 0.02 | 0.05 |
| CaO | 0.39 | 0.45 | 0.43 | 0.28 | 0.38 |
| Li ₂ O | 0.12 | 0.16 | 0.33 | 0.07 | 0.06 |
| Na ₂ O | 3.76 | 3.89 | 4.10 | 0.04 | 3.99 |
| K ₂ O | 4.62 | 4.17 | 4.25 | 0.30 | 4.53 |
| P ₂ O ₅ | 0.44 | 0.47 | 1.03 | 0.33 | 0.01 |
| F | 0.80 | 1.22 | 1.31 | 3.46 | 0.40 |
| H ₂ O ⁺ | 0.85 | 0.87 | 1.34 | 1.11 | 0.48 |
| H ₂ O ⁻ | 0.04 | 0.10 | 0.21 | 0.06 | 0.07 |
| F=O | -0.34 | -0.51 | -0.55 | -1.46 | -0.17 |
| Total | 99.61 | 99.76 | 99.18 | 99.94 | 99.59 |
| ASI | 1.26 | 1.25 | 1.30 | - | 1.07 |
| Rb | 978 | 1257 | 2021 | 87 | 1391 |
| Ga | 35.0 | 34.8 | 67.0 | 7.8 | 31.9 |
| Ge | 2.77 | 3.75 | 4.20 | 7.58 | 4.10 |

ASI: aluminium saturation index is defined as the molecular ratio $[Al/(Ca+Na+K)]$. Calculation of ASI for feldspar-free greisens makes no sense.

Ga, from the greisen from Podlesí 6–22 ppm Ga, from Altenberg 8–10 ppm Ga, from Krásno 2–11 ppm Ga and from Cínovec/Zinnwald and Schneckenstein only 2–4 ppm Ga.

The largest relatively homogeneous Fe contents were found in topaz from Altenberg (155–196 ppm). The Fe content in topaz from the Cínovec, Nejdeč-Eibenstock and Podlesí

TABLE 4. Selected microprobe analyses of topaz (wt.%) and empirical formulae (atoms per formula unit based on Si+Al+P = 3). Data from the Podlesí samples were already published by Breiter and Kronz (2004).

| Locality | Sample | SiO ₂ | Al ₂ O ₃ | P ₂ O ₅ | F | O=F | Total | Si | Al | P | F |
|----------------|--------|------------------|--------------------------------|-------------------------------|-------|-------|--------|-------|-------|-------|-------|
| Cínovec | Cí | 31.75 | 56.86 | 0.00 | 19.59 | -8.25 | 99.95 | 0.964 | 2.036 | 0.000 | 1.882 |
| | | 31.91 | 56.46 | 0.05 | 19.49 | -8.21 | 99.7 | 0.972 | 2.027 | 0.001 | 1.877 |
| | | 32.00 | 56.67 | 0.00 | 19.80 | -8.34 | 100.13 | 0.972 | 2.028 | 0.000 | 1.901 |
| Krásno | Kr | 32.47 | 56.00 | 0.02 | 18.91 | -7.96 | 99.44 | 0.989 | 2.010 | 0.001 | 1.821 |
| | | 31.75 | 56.79 | 0.09 | 18.74 | -7.89 | 99.48 | 0.965 | 2.033 | 0.002 | 1.800 |
| | | 32.27 | 56.34 | 0.00 | 18.65 | -7.85 | 99.41 | 0.981 | 2.019 | 0.000 | 1.793 |
| Altenberg | Alt | 32.20 | 56.50 | 0.13 | 19.37 | -8.16 | 100.04 | 0.977 | 2.020 | 0.003 | 1.858 |
| | | 32.09 | 56.53 | 0.14 | 19.32 | -8.14 | 99.94 | 0.974 | 2.022 | 0.004 | 1.855 |
| | | 32.31 | 56.35 | 0.12 | 19.32 | -8.14 | 99.96 | 0.981 | 2.016 | 0.003 | 1.855 |
| Schneckenstein | Sch | 32.46 | 55.96 | 0.01 | 18.01 | -7.58 | 98.86 | 0.989 | 2.010 | 0.000 | 1.736 |
| | | 32.55 | 55.89 | 0.00 | 17.92 | -7.55 | 98.81 | 0.992 | 2.008 | 0.000 | 1.727 |
| | | 32.85 | 56.40 | 0.00 | 18.54 | -7.81 | 99.98 | 0.992 | 2.008 | 0.000 | 1.771 |

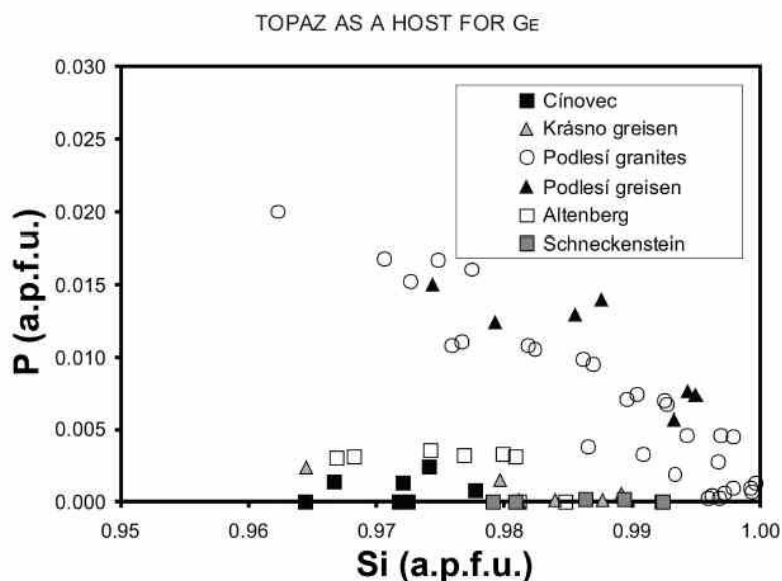


FIG. 2. Phosphorus content of topaz. Phosphorus is incorporated by the berlinite substitution ($\text{Si}+\text{Si} \leftrightarrow \text{P}+\text{Al}$) in topaz from peraluminous granites and greisens in Podlesí. Topaz from greisen in Krásno and from all A-type rocks is free of P.

granites is very variable; usually 40–60 ppm Fe, but unique values up to 1296 ppm Fe were also found. The lowest contents were found in topaz from Schneckenstein (11–55 ppm Fe) and Krásno (<15 ppm Fe). The greatest amounts of Fe (>300 ppm) might result from inadvertent analysis of Fe-bearing mineral inclusions.

The highest Sc concentrations in topaz were encountered in Stockscheider from Altenberg

(‘pyncnite’, 12–16 ppm) and in greisen from Podlesí (2–7 ppm), whereas other samples generally contain <3 ppm Sc. Individual larger Sc contents in topaz from granites from Podlesí coincided with very high Fe and/or high Sn contents, which indicate contamination with an Fe-, Sn-, Sc-bearing phase.

Surprisingly, there was a relatively large Sn content in many topaz grains from several samples.

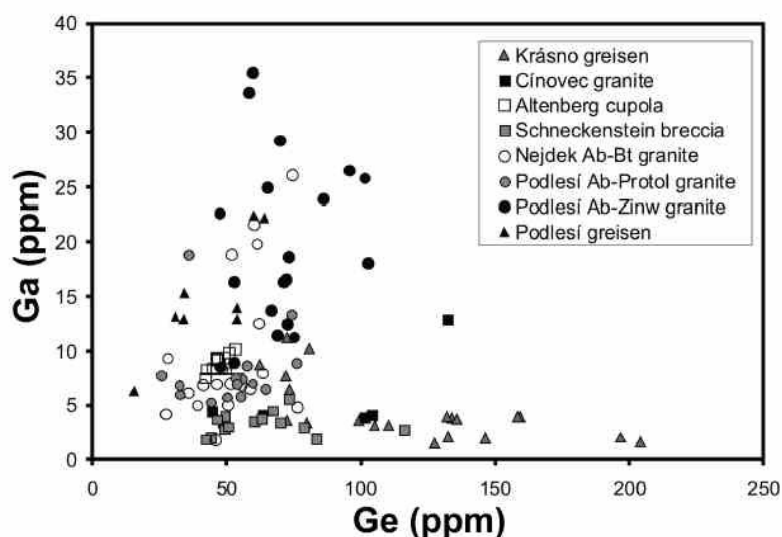


FIG. 3. Topaz Ge and Ga contents (ppm).

K. BREITER *ET AL.*

TABLE 5. Selected LA-ICP-MS analyses of topaz (ppm).

| Locality, sample | Ga | Ge | Sc | Fe | Sn | | Ga | Ge | Sc | Fe | Sn |
|---------------------|------|-------|------|-------|------|---------|------|-------|------|--------|------|
| LOD | 0.1 | 0.4 | 0.4 | 2.0 | 1.0 | Podlesí | 1.8 | 45.8 | 7.9 | 892.4 | 23.2 |
| | | | | | | Po-1 | 6.1 | 35.5 | <LOD | 61.9 | 14.3 |
| Krásno | 4.0 | 159.4 | 2.0 | 9.9 | 8.9 | | 8.4 | 48.2 | <LOD | 516.7 | 7.0 |
| Kr | 7.7 | 71.9 | 1.9 | 11.5 | 4.3 | | 19.9 | 61.2 | 10.6 | 244.2 | 8.6 |
| | 10.2 | 80.9 | 2.0 | 14.6 | 5.3 | | 6.6 | 58.5 | <LOD | 149.7 | 5.4 |
| | 11.2 | 72.5 | 2.0 | 14.0 | 4.0 | | 8.0 | 63.0 | <LOD | 69.1 | 30.8 |
| | 8.7 | 62.4 | 1.7 | 10.7 | 3.1 | | 6.9 | 41.1 | <LOD | 54.2 | 18.8 |
| | 3.4 | 80.0 | 1.8 | 5.1 | 2.7 | | 4.9 | 76.3 | <LOD | 44.2 | 8.7 |
| | 1.6 | 204.2 | 1.6 | 2.8 | <LOD | | 26.1 | 74.4 | 6.3 | 157.9 | 1.5 |
| | 3.9 | 132.1 | 1.7 | 6.0 | <LOD | | 6.9 | 46.0 | <LOD | 41.9 | 3.1 |
| | 2.0 | 196.7 | 1.8 | 3.5 | <LOD | | | | | | |
| | 6.5 | 73.3 | 1.9 | 7.4 | 2.4 | Podlesí | 6.5 | 64.2 | <LOD | 54.1 | 7.1 |
| | | | | | | Po-2 | 5.7 | 50.1 | <LOD | 31.4 | 7.6 |
| Cínovec | 4.4 | 44.6 | 3.5 | 34.3 | <LOD | | 7.4 | 55.7 | <LOD | 67.5 | 3.1 |
| Cí | 3.9 | 101.4 | 2.5 | 46.9 | <LOD | | 5.3 | 44.2 | <LOD | 47.2 | <LOD |
| | 4.1 | 104.1 | 2.3 | 44.3 | <LOD | | 7.7 | 25.6 | <LOD | 56.7 | <LOD |
| | 4.1 | 63.2 | 2.4 | 84.0 | <LOD | | 13.3 | 74.0 | <LOD | 57.0 | 2.1 |
| | | | | | | | 6.0 | 32.7 | <LOD | 42.6 | <LOD |
| Altenberg | 8.4 | 44.8 | 13.2 | 174.7 | 5.9 | | 6.9 | 32.2 | <LOD | 47.5 | <LOD |
| Alt | 8.4 | 45.9 | 13.7 | 167.5 | 5.5 | | 7.5 | 53.4 | <LOD | 63.4 | <LOD |
| | 8.4 | 49.2 | 12.3 | 174.4 | 5.1 | | 8.6 | 57.4 | <LOD | 50.5 | <LOD |
| | 9.4 | 49.2 | 13.5 | 195.7 | 6.6 | | | | | | |
| | 9.2 | 46.6 | 13.4 | 186.0 | 5.2 | Podlesí | 29.2 | 69.8 | 11.8 | 1296.3 | 17.7 |
| | 8.3 | 42.2 | 11.8 | 155.1 | 4.4 | Po-3 | 18.1 | 102.5 | <LOD | 49.0 | 9.3 |
| | 7.5 | 42.0 | 12.1 | 160.0 | 4.0 | | 11.3 | 75.0 | <LOD | 41.1 | 6.0 |
| | 9.4 | 46.1 | 15.2 | 175.6 | 5.0 | | 24.9 | 65.0 | <LOD | 137.2 | 7.0 |
| | 8.9 | 51.2 | 15.1 | 175.0 | 5.5 | | 16.4 | 70.9 | <LOD | 81.4 | 3.9 |
| | 9.9 | 50.8 | 16.3 | 182.4 | 6.1 | | 23.9 | 85.9 | <LOD | 127.2 | 2.4 |
| | | | | | | | 18.6 | 72.9 | <LOD | 99.3 | 5.0 |
| Schneckenstein | 3.5 | 60.2 | 2.3 | 12.0 | <LOD | | 26.5 | 95.5 | <LOD | 40.3 | 3.3 |
| Sch | 3.4 | 48.8 | 2.3 | 18.7 | <LOD | | 22.7 | 47.3 | <LOD | 243.8 | 5.1 |
| | 1.9 | 83.5 | 2.3 | 11.4 | <LOD | | 9.0 | 52.4 | <LOD | 69.6 | 10.5 |
| | 4.0 | 49.4 | 2.6 | 20.8 | 2.5 | | | | | | |
| | 3.7 | 46.2 | 2.7 | 14.9 | <LOD | Podlesí | 13.9 | 53.8 | 6.2 | 107.1 | <LOD |
| | 2.8 | 49.0 | 1.8 | 11.2 | <LOD | Po-4 | 22.2 | 64.0 | 3.0 | 239.4 | <LOD |
| | 2.0 | 44.1 | 2.4 | 13.1 | <LOD | | 12.9 | 53.9 | 2.0 | 67.6 | <LOD |
| | 3.4 | 69.9 | 2.7 | 20.8 | <LOD | | 15.3 | 34.3 | 7.4 | 771.9 | <LOD |
| | 1.9 | 42.3 | 1.7 | 30.8 | <LOD | | 6.2 | 15.6 | 5.0 | 103.8 | <LOD |
| | 2.7 | 116.1 | 2.5 | 55.0 | 2.2 | | 13.1 | 30.9 | 2.6 | 218.0 | <LOD |
| | | | | | | | 12.9 | 34.1 | 2.1 | 119.3 | 10.6 |
| | | | | | | | 22.4 | 60.1 | 2.5 | 176.0 | <LOD |

The largest amounts (2–31 ppm) were found in the biotite and zinnwaldite granite from Podlesí (samples Po-1 and Po-3), whereas topaz from associated protolithionite granite (sample Po-2) contains only 3–8 ppm Sn. Similar amounts of Sn were found also in topaz from Altenberg (4–6 ppm) and Krásno (2–9 ppm). The smallest Sn contents were in topaz from Cínovec/Zinnwald, Schneckenstein and the Podlesí greisen.

Discussion

Comparison between LA-ICP-MS and other methods used for Ge and Ga determination

Most published data for the Ge and Ga contents of topaz were obtained by emission spectroscopy (Papish 1928, 1929; Seim and Schweder, 1962; Oftedal, 1963; etc.) and wet chemistry (Papish, 1929; Duck, 1986). These methods provided reliable results for the bulk composition of topaz

TOPAZ AS A HOST FOR Ge

grains, but were not able to document internal inhomogeneities. Trace element concentrations at the tens of ppm level are at the limits of detection (LOD) for EMPA. Breiter and Kronz (2004) attempted to determine the contents of Ga and Ge in topaz from Podlesí and found 40 to 60 ppm (locally up to 140 ppm) of Ga and 50–100 ppm (locally up to 210 ppm) of Ge with LOD of ~40 and 50 ppm, respectively. The comparison between EMPA and LA-ICP-MS measurements of Ga and Ge show some disagreement. The difference is due to the fact that the Ga and Ge contents in topaz are near the LOD of EMPA whereas the LOD of LA-ICP-MS are significantly lower (0.1 and 0.3 ppm Ga and Ge, respectively). Hence, the ICP data are the more reliable.

Ga and Ge in magmatic and hydrothermal topaz

The Ga vs. Ge plot (Fig. 3) illustrates the different geochemical behaviour of Ge and Ga during evolution of S- and A-type granitic melt and subsequent fluid processes. Topaz from subaluminous A-type granites is poor in Ga (1–10 ppm), but enriched in Ge (mostly 40–100 ppm). Topaz from the peraluminous magmatic environment at Podlesí is relatively rich in Ga (5–35 ppm); Ge contents (mostly 25–100 ppm) are similar to the A-type granites.

Relationships between the Ge and Ga contents and the OH/(OH+F) ratio in topaz are shown in Figs 4 and 5. Our data are compared here with those published by Duck (1986). Topaz crystals from cavities in hydrothermal veins analysed by Duck (1986) are characterized by relatively large contents of (OH)⁻ (OH>0.4 a.p.f.u., F<1.6 a.p.f.u.) and smaller contents of both Ge and Ga (<38.7 ppm and <6.8 ppm, respectively). The only exception is the OH-poor topaz from Adun-Chilon (currently the Sherlovaya Gora tin deposit), E Transbaikalia, Russia (Leithner, 1981; Lyckberg, 2001; Baksheev *et al.*, 2012), although this locality is linked directly to a tin-bearing granite. Topaz from pegmatites (Duck, 1986) is comparable with those from the granites and greisens investigated in this work. It is poor in (OH)⁻ (OH<0.4 a.p.f.u., F>1.6 a.p.f.u.) and can be considerably enriched in Ge: typically 50–100 ppm, and up to 132 ppm in granite, 204 ppm in greisen and 238 ppm in pegmatite. Enrichment in Ga is limited to topaz from peraluminous S-type granites (mostly 5–25 ppm), whereas topaz from A-type granites and pegmatites contains <10 ppm Ga. Duck (1986) concluded that the contents of Ge and Ga are negatively correlated

with the content of (OH)⁻, and that pegmatitic and hydrothermal topaz form two separate lines of correlation. Our results support Duck's conclusions regarding the principal differences between hydrothermal and magmatic (including high-temperature greisen) topaz, although the relation between the (OH) and Ge and Ga contents is more complicated. Relationships between Ge and Ga contents in topaz and in the bulk granites are shown in Figs 6 and 7. There is a poor correlation between the bulk-rock and topaz contents of both elements.

The evolution of the Ge and Ga contents during fractionation of the granitic melt in Podlesí, expressed by the increasing amount of Rb, is shown in Figs 8 and 9. The amounts of both elements increase during the final stage of fractionation, though the range in measured values in a given rock is large. The elevated Ge content in greisen from Podlesí results from the high modal content of topaz in the greisen, although hydrothermal topaz from this greisen contains less Ge than the primary magmatic topaz from the parent granite. In contrast, topaz from the greisen in Krásno is the most Ge-enriched (up to 200 ppm) among all the samples. This demonstrates extensive redistribution of Ge during greisenization.

There is no correlation between the Ga contents of topaz and the whole rock, whereas the major host of Ga, feldspars and mica, usually crystallize before topaz. The large range of Ga contents in topaz from the Ga- and F-enriched albite-zinnwaldite granite from Podlesí is probably related to the order of crystallization of individual grains: early topaz grains crystallized from Ga-rich melt before feldspars, while the later-formed grains crystallized after feldspar from a melt already impoverished in Ga. Similarly, crystallization of dark mica (annite-zinnwaldite group) decreases the Ge content in the melt and late interstitial topaz might be relatively Ge poor.

The inhomogeneity of trace-element distribution within a single grain of topaz has been investigated by Northrup and Reeder (1994). They concluded that no single value of the distribution coefficient of a trace element can be applied for all areas of the crystal surface, and the distribution coefficients depend on the crystal planes.

Estimation of Ge and Ga budget in granites and greisens

Topaz, although quantitatively an unimportant rock-forming mineral, plays an important role in the overall balance of Ge in the rock. To estimate

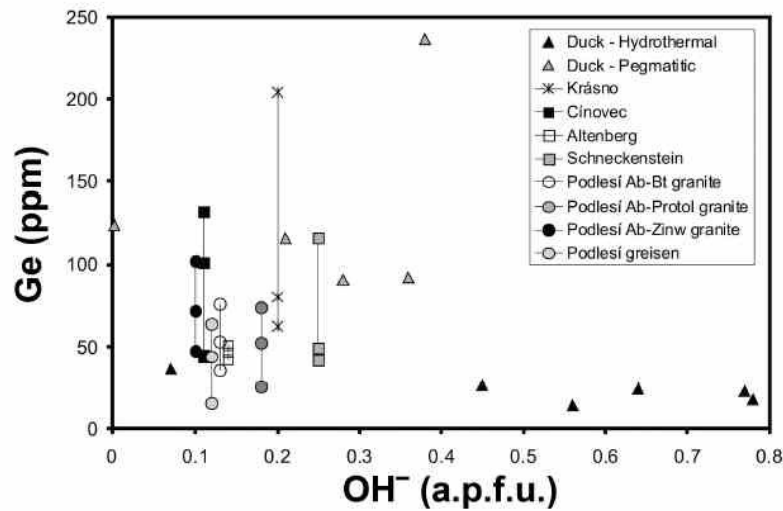
K. BREITER *ET AL.*

FIG. 4. Relations between Ge (ppm) and (OH^-) (a.p.f.u.) contents in topaz. The mean, minimum and maximum Ge contents in each sample are shown. Data from Duck (1986) are shown for comparison.

the contribution of topaz to the Ge and Ga budgets of rock such as granite and greisen, we analysed the Ge and Ga contents in all the associated rock-forming minerals. For these data we used the median of 10–30 analytical points for Ge and Ga in each mineral in selected rocks (Table 6). The quantitative proportions of each mineral in these samples were calculated from bulk-rock analyses and electron microprobe analyses of appropriate minerals. As the analysed minerals and rocks are

not homogeneous, our calculation must be regarded as only semi-quantitative.

The A-type albite-zinnwaldite granite from Cínovec/Zinnwald is composed of ~31 wt.% quartz (0.5 ppm Ge in quartz), 62 wt.% feldspars (3 ppm Ge in feldspar), 5 wt.% zinnwaldite (19 ppm Ge in zinnwaldite), and 1 wt.% topaz (101 ppm Ge in topaz). Thus, topaz is calculated to contain ~23% of the calculated content of 3.9 ppm Ge in this granite (analysed bulk-rock

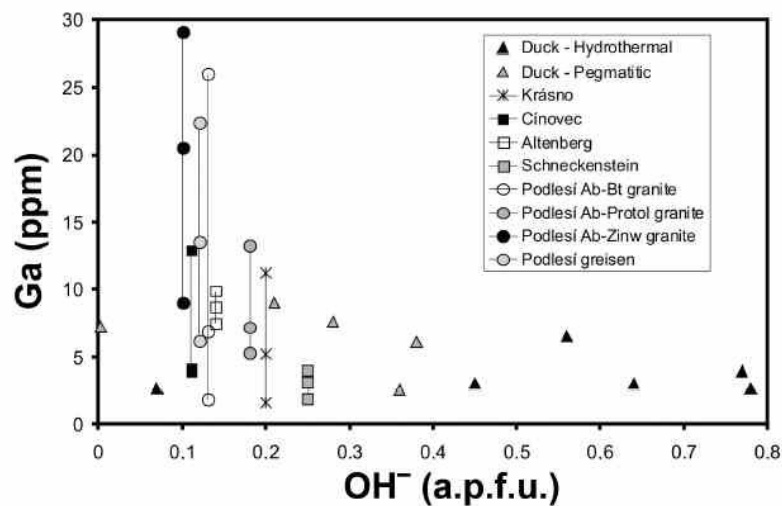


FIG. 5. Relations between Ga (ppm) and (OH^-) (a.p.f.u.) contents in topaz. The mean, minimum and maximum of the Ga contents in each sample are shown. Data from Duck (1986) are shown for comparison.

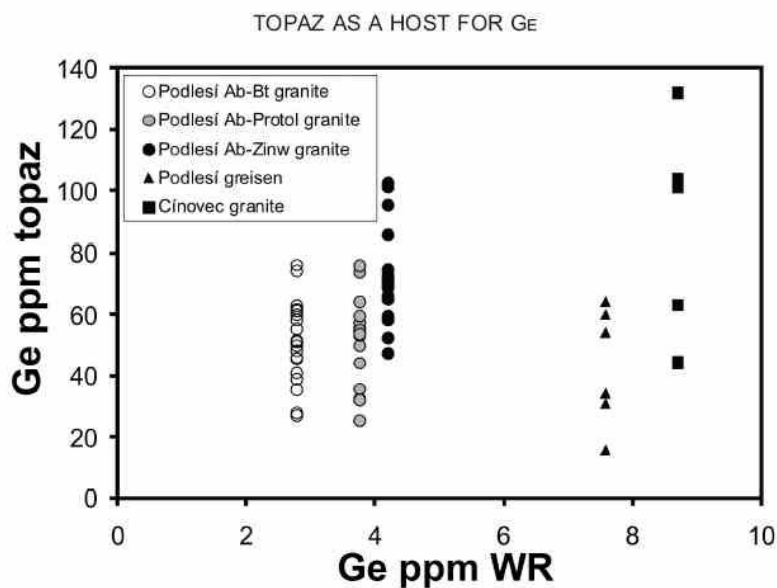


FIG. 6. Relations between Ge contents in topaz and in the bulk rocks (ppm).

content of Ge in this sample was 4.1 ppm, see Table 2).

The S-type albite-zinnwaldite granite from Podlesí is composed of ~30 wt.% quartz (1.3 ppm Ge), 60 wt.% feldspars (2.3 ppm Ge), 7 wt.% zinnwaldite (4.5 ppm Ge) and 3 wt.% topaz (90 ppm Ge). In this case, topaz is calculated to contain ~51% of the calculated content, i.e. 4.8 ppm Ge. The analysed bulk-rock content of this rock was 4.2 ppm Ge.

The quartz-topaz greisen from Podlesí is composed of 79 wt.% quartz (1.0 ppm Ge), 2 wt.% of zinnwaldite (5 ppm Ge) and 19 wt.% topaz (43 ppm Ge). In this example, topaz is calculated to contain ~87% of the calculated content, i.e. 8.9 ppm Ge. The analysed bulk-rock content was 7.6 ppm Ge.

Using Ge data given by Schrön (1969) and mineral proportions calculated by Thomas and Davidson (R. Thomas, pers. comm.) for the topaz-

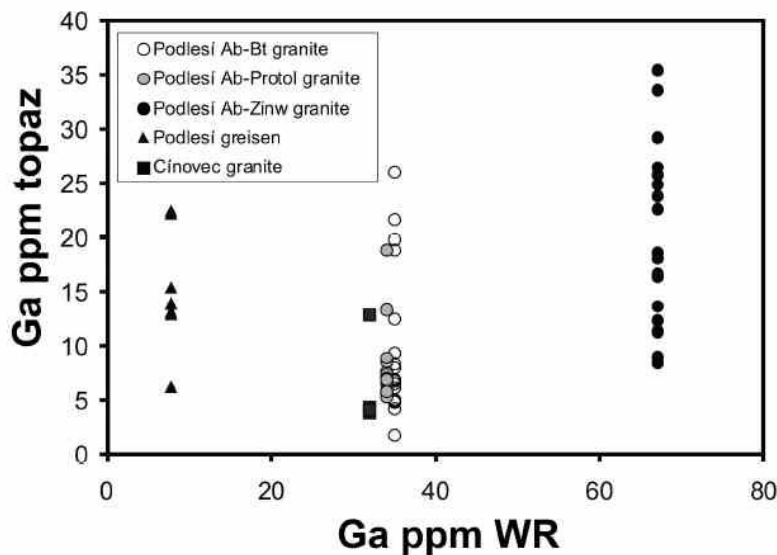


FIG. 7. Relations between Ga contents in topaz and in the bulk rocks (ppm).

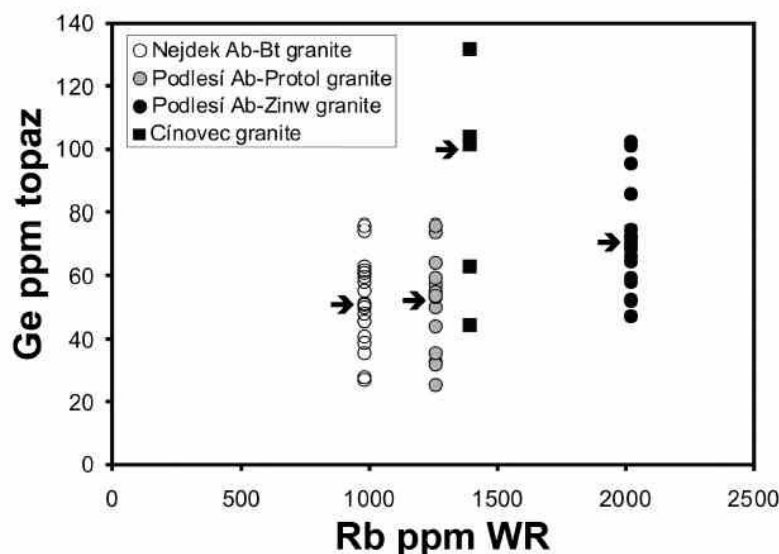
K. BREITER *ET AL.*

FIG. 8. Evolution of the Ge content in topaz during magma fractionation (expressed by the increase in bulk Rb content) in Podlesi S-type granite. Topaz from the A-type granite from Cínovec/Zinnwald is relatively Ge enriched. Small arrows show the medians of the Ge contents in a particular sample.

rich variety of stockscheider ('pyncnite rock') from Altenberg, topaz contains ~84% of the calculated content of 12.5 ppm Ge (compare Table 6). In this case, the bulk rock was not analysed.

In contrast, Ga is hosted mainly by feldspar and mica. Topaz contained generally <1% of the bulk

Ga contents in granites. The only exception is the quartz-topaz (mica poor) greisen from Podlesi. This is composed of 79 wt.% quartz (0.3 ppm Ga), 2 wt.% zinnwaldite (142 ppm Ga) and 19 wt.% topaz (13.5 ppm Ga). Topaz is calculated to contain ~33% of the calculated content of

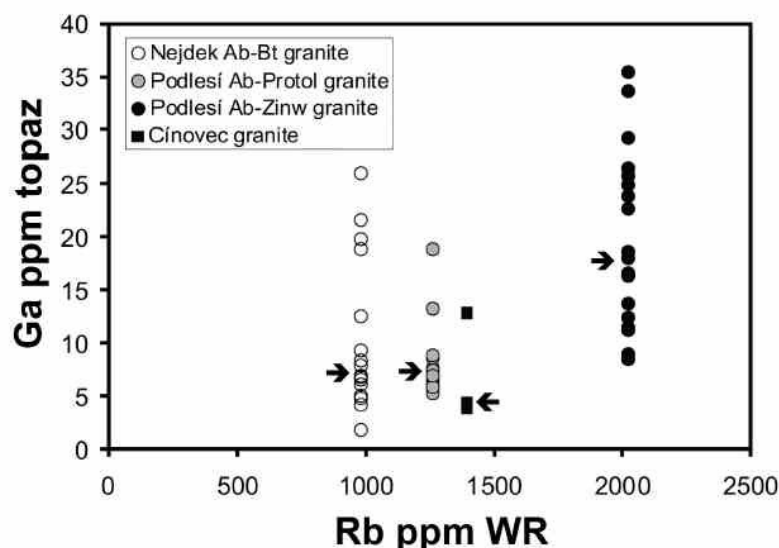


FIG. 9. Evolution of the Ga content in topaz during magma fractionation (expressed by the increase in bulk Rb content) in Podlesi S-type granite. Topaz from the A-type granite from Cínovec/Zinnwald is relatively Ga depleted. Small arrows show the medians of the Ga contents in a particular sample.

TOPAZ AS A HOST FOR GE

TABLE 6. Ge and Ga contents in minerals in granites Ci and Po-3, greisen Po-4 (medians in ppm) and in the pycnite rock from Altenberg (in ppm).

| Locality, sample | Mineral | Content (wt.%) | Ge (ppm) | Ga (ppm) |
|-------------------------|-------------|------------------|-------------------|----------|
| Cinovec, granite Ci | Quartz | 31 | 0.5 | 0.5 |
| | Feldspars | 62 | 3.0 | 37 |
| | Zinnwaldite | 5 | 19 | 62 |
| | Topaz | 1 | 101 | 4.1 |
| | Kaolinite | 1 | – | – |
| Podlesí, granite Po-3 | Quartz | 30 | 1.3 | 0.5 |
| | Feldspars | 60 | 2.3 | 69 |
| | Zinnwaldite | 7 | 4.5 | 142 |
| | Topaz | 3 | 90 | 20 |
| Podlesí, greisen Po-4 | Quartz | 79 | 1.0 | 0.3 |
| | Zinnwaldite | 2 | 5.0 | 142 |
| | Topaz | 19 | 43 | 13.5 |
| | Quartz | 24 ^{*1} | 2.6 ^{*2} | – |
| Altenberg, pycnite rock | Li-Fe mica | 26 ^{*1} | 5.2 ^{*2} | – |
| | Topaz | 50 ^{*1} | 21 ^{*2} | – |

*1 acc. to Thomas, pers. comun., *2 acc. to Schrön (1969)

8.1 ppm Ga. The analysed bulk-rock content was 7.8 ppm Ga.

Differences between analysed and calculated bulk-rock Ge and Ga contents are in the range from –3.8 to + 14.3% of the analysed values, which we consider to be acceptable. The principal source of these discrepancies is related to the relatively large dispersion of the laser-ablation analyses within each mineral sample. The median of these measured data is the best possible, but still not an ideal expression of trace-element content of the mineral.

Phosphorus enrichment in topaz

Enrichment of P up to 1 wt.% P₂O₅ in topaz from peraluminous granites at Podlesí, was reported by Breiter and Kronz (2004) and up to 1.1 wt.% P₂O₅ from the pegmatite in the Ehrenfriedersdorf tin mine (R. Thomas, pers. comm.). Veksler and Thomas (2002) showed experimentally that in topaz the P₂O₅ concentration can increase up to 6.4 wt.% at 600°C and 1 kbar. Our new data confirm that P enrichment in topaz is restricted to magmatic topaz from peraluminous granites and their phosphate-free greisens. Topaz from phosphate (apatite)-bearing greisen in Krásno and from all A-type granite environments is P-poor or P-free.

Conclusions

The most common minor/trace elements in topaz are P, Ge and Ga. The enrichment of P is limited to topaz from strongly peraluminous P-rich magmatic systems such as Podlesí.

Topaz from both A- and S-type granites usually contains 50–100 ppm Ge, locally up to 204 ppm Ge from S-type greisen, which makes topaz the largest concentrator of Ge among all associated silica-bearing minerals. In fractionated granites and greisens, topaz may host 23–87% of the bulk Ge content of the rock. Topaz usually contains less Ga than the host rock: <35 ppm in the S-type granites and <10 ppm in A-type granites. Topaz does not concentrate Ga, except for topaz in the mica-poor/mica-free greisens, in which topaz is the sole Al-bearing mineral.

Acknowledgements

The authors thank Mrs Zuzana Korbelová (Prague) and Mr. Andreas Kronz (Göttingen) for the electron microprobe analyses. Inspiring comments and suggestions made by Peter Bowden, Rainer Thomas, Ed Grew and Roger Mitchell helped to improve the paper substantially. Critical comments by two anonymous reviewers on the previous version of the manuscript are also appreciated. This investigation was

supported by the Czech Science Foundation, project No. P210/10/1309 and by RVO 67985831.

References

- Aigbe, S.O., Ewa, I.O.B., Ogunleye, P.O. and Oladipo, M.O.A. (2013) Elemental characterization of some Nigerian gemstones: tourmaline, fluorite and topaz by instrumental neutron activation analysis. *Journal of Radioanalytical and Nuclear Chemistry*, **295**, 801–805.
- Baksheev, A.I., Prokofev, V.Yu., Zaraisky, G.P., Chitalin, A.F., Yapaskurt, V.O., Nikolaev, Yu.N., Tikhomirov, P.L., Nagornaya, E.V., Rogacheva, L.I., Gorelikova, N.V. and Kononov, O.V. (2012) Tourmaline as a prospecting guide for the porphyry-style deposits. *European Journal of Mineralogy*, **24**, 957–979.
- Bell, C.K. (1955) Some aspects of the geochemistry of gallium. *Bulletin of the Geological Society of America*, **6**, 1529–1530.
- Bernstein, L.R. (1985) Germanium geochemistry and mineralogy. *Geochimica et Cosmochimica Acta*, **49**, 2409–2422.
- Breiter, K. (2012) Nearly contemporaneous evolution of the A- and S-type fractionated granites in the Krušné hory/Erzgebirge Mts., Central Europe. *Lithos*, **151**, 105–121.
- Breiter, K. and Kronz, A. (2004) Phosphorus-rich topaz from fractionated granites (Podlesí, Czech Republic). *Mineralogy and Petrology*, **81**, 235–247.
- Breiter, K., Förster, H. and Seltmann, R. (1999) Variscan silicic magmatism and related tin-tungsten mineralization in the Erzgebirge-Slavkovský les metallogenic province. *Mineralium Deposita*, **34**, 505–521.
- Breiter, K., Müller, A., Leichmann, J. and Gabašová, A. (2005) Textural and chemical evolution of a fractionated granitic system: the Podlesí stock, Czech Republic. *Lithos*, **80**, 323–345.
- Burton, J.D., Culkin, F. and Riley, J.P. (1959) The abundances of gallium and germanium in terrestrial materials. *Geochimica et Cosmochimica Acta*, **16**, 151–180.
- Cháb, J., Breiter, K., Fatka, O., Hladil, J., Kalvoda, J., Šimůnek, Z., Štorch, P., Vašíček, Z., Zajíc, J. and Zapletal, J. (2010) *Outline of the Geology of the Bohemian Massif*. 295 pp., Czech Geological Survey, Prague.
- Černý, P. and Ercit, T.S. (2005) The classification of granitic pegmatites revisited. *The Canadian Mineralogist*, **43**, 2005–2026.
- Deer, W.A., Howie, R.A. and Zussman, J. (1997) *Rock-Forming Minerals*. Second edition, Vol. **1A**, Orthosilicates. The Geological Society, London, pp. 801–815.
- Duck, J.J. (1986) *An investigation of factors controlling the partitioning of trace germanium and gallium between topaz and quartz*. MSc thesis, University of Pittsburgh, Pennsylvania, USA, 76 pp.
- Duck, J.J. and Cohen, A.J. (1986) Partition of trace germanium and gallium between intergrown topaz and quartz. *Abstracts with program 1986; the Fourteenth general meeting of the International Mineralogical Association, Stanford, California, USA* (C.T. Prewitt, chairman), p. 93 (abstract).
- El-Hinnawi, E.E. and Hofmann, R. (1966) Bemerkungen zur Verteilung von Spurenelementen im Topas. *Chemie der Erde*, **25**, 230–236.
- Förster, H.-J., Gottesmann, B., Tischendorf, G., Siebel, W., Rhede, D., Seltmann, R. and Wasternack, J. (2007) Permo-Carboniferous subvolcanic rhyolitic dikes in the western Erzgebirge/Vogtland, Germany: a record of source heterogeneity of post-collisional felsic magmatism. *Neues Jahrbuch für Mineralogie, Abhandlungen*, **183**, 123–147.
- Goldschmidt, V.M. (1954) *Geochemistry*. 730 pp. Oxford University Press, UK.
- Goldschmidt, V.M. and Peters, C. (1933) Zur Geochemie des Germaniums. *Nachrichten von der Gesellschaft der Wissenschaften zu Göttingen. Mathematisch-Physikalische Klasse, Fachgruppe IV*, **33**, 141–166.
- Gottesmann, B., Wasternack, J. and Märtens, S. (1994) The Gottesberg tin deposit (Saxony): Geological and metallogenic characteristic. Pp. 110–115 in: *Metallogeny of Collisional Orogens*, (R. Seltmann, H. Kampf and P. Möller, editors). Czech Geological Survey, Prague.
- Govindaraju, K. (1994) Compilation of working values and sample description for 383 geostandards. *Geostandards Newsletter*, **18**, 1–158.
- Harris, P.G. (1954) The distribution of germanium among coexisting phases of partly glassy rocks. *Geochimica et Cosmochimica Acta*, **5**, 185–195.
- Höll, R., Kling, M. and Schroll, E. (2007) Metallogenesis of germanium – a review. *Ore Geology Reviews*, **30**, 145–180.
- Jarchovský, T. (2006) The nature and genesis of greisen stocks at Krásno, Slavkovský les area – Western Bohemia, Czech Republic. *Journal of the Czech Geological Society*, **51**, 201–216.
- Johan, Z., Oudin, E. and Picot, P. (1983) Analogues germanifères et gallifères des silicates et oxydes dans les gisements de zinc des Pyrénées centrales, France; argutite et carboirite, deux nouvelles espèces minérales. *Tschermaks Mineralogische und Petrographische Mitteilungen*, **31**, 97–119.
- Leithner, H. (1981). Russische Topase und Berylle. *Lapis*, **6**, No. 9, 9–14.
- Leithner, H. (2008) Famous mineral localities: The Königskrone topaz mine, Schneckenstein, Saxony,

TOPAZ AS A HOST FOR GE

- Germany. *Mineralogical Record*, **39**, 355–367.
- Lyckberg, P. (2001) The minerals of Russia – gem beryl and topaz of Sherlovaya Gora, Transbaikal, Russia, a commonly mislabeled locality. *Mineralogical Record*, **32**, 45.
- Northrup, P.A. and Reeder, R.J. (1994) Evidence for the importance of growth-surface structure to trace element incorporation in topaz. *American Mineralogist*, **79**, 1167–1175.
- Ofiedal, I. (1963) The germanium contents in some Norwegian topaz specimens. *Norsk Geologisk Tidsskrift*, **43**, 267–269.
- Ossenkopf, P. and Helbig, C. (1975) Zum geologischen Aufbau der Zinnerzlagstätte Altenberg und speziell zum Pyknitgestein. *Zeitschrift für Angewandte Geologie*, **21**, 57–66.
- Papish, J. (1928) Occurrence of germanium in topaz. *Science*, **68**, 350–351.
- Papish, J. (1929) New occurrences of germanium. II. Occurrence of germanium in silicate minerals. *Economic Geology*, **24**, 470–480.
- Schlüter, J., Geisler, T., Pohl, D. and Stephan, T. (2010) Krieselite, $\text{Al}_2\text{GeO}_4(\text{F},\text{OH})_2$: a new mineral from the Tsumeb mine, Namibia, representing the Ge analogue of topaz. *Neues Jahrbuch für Mineralogie, Abhandlungen*, **187**, 33–40.
- Schrön, W. (1969) Zur Geochemie des Germaniums. II. Lagerstätten-genetische Probleme. *Freiberger Forschungshefte C*, **246**, 5–65.
- Seim, R. and Leipe, T. (1987) Die magmatische Entwicklung einer mehrphasigen Zinngranitintrusion (Altenberg/Erzgebirge). *Chemie der Erde – Geochemistry*, **46**, 247–258.
- Seim, R. and Schweder, P. (1962) Germaniumgehalt im Topas. *Naturwissenschaften*, **49**, 538.
- Seim, R. and Schweder, P. (1969) Untersuchungen zum Germaniumgehalt im Topas. *Chemie der Erde*, **28**, 83–90.
- Shannon, R.D. (1976) Revised effective ionic radii and systematic studies of interatomic distances in halides and chalcogenides. *Acta Crystallographica*, **A32**, 751–767.
- Shcherba, G.N., Zamyatina, G.M., Kalinin, S.K. and Mukhlya, K.A. (1966) Germanium in some greisens in Kazakhstan. *Geokhimiya*, **11**, 1365–1368 (in Russian).
- Veksler, I.V. and Thomas, R. (2002) An experimental study of B-, P- and F-rich synthetic granite pegmatite at 0.1 and 0.2 GPa. *Contributions to Mineralogy and Petrology*, **143**, 673–683.
- Wasim, M., Zafar, W.A., Tufail, M., Arif, M., Daud, M. and Ahmad, A. (2011) Elemental analysis of topaz from northern areas of Pakistan and assessment of induced radioactivity level after neutron irradiation for color induction. *Journal of Radioanalytical and Nuclear Chemistry*, **287**, 821–826.
- Weisbach, A. (1866) Argyrodit, ein neues Silbererz. *Neues Jahrbuch für Mineralogie, Geologie und Paläontologie*, **2**, 67–71.
- Winkler, C. (1886) Germanium, Ge, ein neues nichtmetallisches Element. *Berichte der Deutschen Chemischen Gesellschaft*, **19**, 210–211.
- Wunder, B. and Marler, B. (1997) Ge-analogues of aluminum silicates: high-pressure synthesis and properties of orthorhombic $\text{Al}_2\text{GeO}_4(\text{OH})_2$. *European Journal of Mineralogy*, **9**, 1147–1158.

6.8 ARTICLE 8

Vaculovic, T.; Breiter, K.; Korbelova, Z.; Venclova, N.; Tomkova, K.; Jonasova, S.; Kanicky, V. *Microchemical Journal* 2017, 133, 200-207 (IF=3.206)



Contents lists available at ScienceDirect

Microchemical Journal

journal homepage: www.elsevier.com/locate/microc

Quantification of elemental mapping of heterogeneous geological sample by laser ablation inductively coupled plasma mass spectrometry



T. Vaculovič^{a,b,*}, K. Breiter^c, Z. Korbelová^c, N. Venclová^d, K. Tomková^d, Š. Jonášová^c, V. Kanický^{a,b}

^a Department of Chemistry, Faculty of Science, Masaryk University, Kotlářská 2, Brno 61135, Czech Republic

^b CEITEC, Masaryk University, Kamenice 5, Brno 62500, Czech Republic

^c Institute of Geology, The Czech Academy of Sciences, Kamýcká 6, Praha 16500, Czech Republic

^d Institute of Archaeology, The Czech Academy of Sciences, Letenská 4, Praha 11801, Czech Republic

ARTICLE INFO

Article history:

Received 14 November 2016

Received in revised form 21 March 2017

Accepted 23 March 2017

Available online 24 March 2017

ABSTRACT

Quantification procedures based on the external calibration with total sum content standardization (ECTSCS) and the external calibration with internal standardization (ECIS) were compared in the analysis of glass materials by laser ablation inductively coupled plasma spectrometry (LA-ICP-MS) with a 213 nm Nd:YAG laser ablation device and a quadrupole mass spectrometer. Silicon was used as the internal reference element for ECIS. Applicability of these approaches was statistically tested using both homogeneous and inhomogeneous samples. The former type was represented by the standard reference material NIST 612 and an ancient glass bead (Early Bronze Age), while the latter was a mediaeval glass artefact (8th – 9th century). Homogeneity of samples was examined by EMP analysis. Identical results were obtained by both calibration methods for homogeneous samples, while underestimated contents resulted from quantification with ECIS method in comparison to EMP analyses of the same target area of inhomogeneous glass. Finally, elemental maps of zonal muscovite grain were recorded and quantified using ECTSCS method and verified by EMP analysis.

© 2017 Elsevier B.V. All rights reserved.

1. Introduction

Laser ablation (LA) represents method suitable for sampling of any kind of material (metals [1,2], non-conductive solids [3,4], thin layers [5] liquids and gases [6–8], biological tissues [9,10], archaeological samples [11–13], etc.) and in combination with inductively coupled plasma mass spectrometry (ICP-MS) allows determination of elements in a wide range of contents from major to trace levels. The main difficulties at quantification with LA-based methods follow from both the fluctuations of laser beam energy and dependence of mass of removed target material per laser pulse, the ablation rate, on physical and chemical properties of target matrix. Lack of calibration standards suitable for particular analytical tasks is often the cause of inevitable difference between matrices of available standard and analyzed samples, thus introducing a systematic error into quantification. Summarized, laser energy fluctuations (short-term and drift) and sample vs standard matrix differences result in random and systematic errors due to pulse-to-pulse variability of ablation rate and differences in ablation rate between samples and standards. Therefore in order to ensure conditions for quantification these effects have to be compensated.

Several ways of quantification procedures are used for quantitative LA-ICP-MS analysis. All below mentioned quantifications utilize some normalization procedure which compensates for variations in the ICP-MS signals caused by laser ablation processes [14,15], transport efficiency of ablated material [16,17] and ionization processes in ICP [18,19]. The most widely used method is external calibration with internal standardization (ECIS) first published by Crain and Gallimore [20] in 1992. Since that time this quantification is mainly utilized in analysis of geological samples in spite of a requirement of complementary method for determination of internal standard content, e.g. by electron microprobe (EMP) or X-ray fluorescence (XRF). The EMP represents the most used analytical technique for determination of elemental content in geological samples. It is based on the analysis of the X-ray spectrum emitted after irradiation of the sample by an electron beam [21]. In case of analysis of a sample with a simple matrix and known complete qualitative composition the requirement of the EMP analysis can be avoided by using external calibration with total sum content standardization [22,23] (ECTSCS). This standardization process is based on LA-ICP-MS signal measurement for all elements constituting the sample and yielding measurable signal. In case of oxidic materials (silicate rocks), elemental contents calculated using external calibration are expressed as mass percentages (%_{m/m}) of their oxides. Thus obtained contents of all oxides are normalized to 100%_{m/m}. An important feature of the ECTSC method is the fact that no preliminary analysis by

* Corresponding author at: Department of Chemistry, Faculty of Science, Masaryk University, Kotlářská 2, Brno 61135, Czech Republic.
E-mail address: vaca@mail.muni.cz (T. Vaculovič).

independent method is necessary. The accuracy of this quantification procedure was verified by analysis of homogeneous glass standards, reference materials [22–25] and real relatively homogeneous samples as obsidians as well [26,27]. Liu et al. [28] demonstrated utilization of this procedure by analysis of real anhydrous silicates as are clinopyroxene, orthopyroxene, olivine and garnet. Phase change materials based on AgInSbTe with different stoichiometry were analyzed and quantified by ECTSC approach [29]. In some cases neither of above-mentioned quantification procedures can be used. As an example, analysis of corroded parts of components made of steel or other alloys can be mentioned [30–32]. In this case the laser ablation rate varies depending on whether the corroded or intact part is ablated. For this purpose the total sum of ion intensities normalization [33] (TSHN) was used.

LA-ICP-MS trace analysis capability (mg kg^{-1}) of small spots (from tens to units of μm in diameter) makes this method a powerful tool for elemental mapping. This feature is widely exploited in the study of elemental distribution in biological tissues such as thin sections of tumors [34,35], brain [36,37] or liver [38]. Elemental mapping of tissues relies mostly on internal standardization with carbon, which allows to correct for differences in ablation rate and water content [39] in spite of observation that this matrix element can occur in the form of gaseous species which leads to fractionation [40,41]. However, a necessary prerequisite is a constant content of carbon over examined area, which may not be fulfilled in some cases. Elemental mapping of geological materials is hampered by inhomogeneous distribution of elements which are usually considered as internal standards (Si, Ca). Consequently, acquisition of elemental map is sometimes achieved only on qualitative level [42]. For acquisition of quantitative map of trace elements in iron meteorite authors utilized negative correlation between Ni and Fe content and normalized the results on the sum of Fe and Ni content to 100%_{m/m} [43].

The aim of this study consists in comparison of two quantification procedures based on ECTSCS and ECIS using homogeneous standard reference material and archaeological samples with both homogeneous and heterogeneous distribution of elements. Finally, ECTSCS is proved as suitable quantification procedure for acquisition of quantitative elemental maps of muscovite grain with markedly zonal characterization.

2. Experimental

2.1. Samples

The comparison of ECIS and ECTSCS was performed using 3 different glassy samples. The first one, standard reference material (SRM) NIST 612, represents homogeneous sample with the same matrix as NIST 610, which was used as the calibration standard for analysis of NIST 612. The second one, which is the glass bead originating from the Late Bronze Age burial ground (12th–11th century BC) at Holubice, Bohemia, represents homogeneous real sample. This blue-green translucent specimen belongs to rather exceptional *mixed alkali* glass with CuO as the main colorant. The third one is glass bead from the early mediaeval cemetery (a period of the 8th–9th century) at Iffelsdorf, Bavaria. This specimen represents inhomogeneous material made of soda-lime natron glass with the inclusion of opacifiers.

As an example of mineralogical sample the Li-muscovite grain originating from Argemela Mine in Portugal was subjected to elemental mapping. This grain is composed of two distinctive zones. The core is rich in Al_2O_3 and FeO while the rim is enriched in Li_2O , Rb_2O , and MnO in comparison with the core.

2.2. Instrumentation

LA-ICP-MS experiments were performed using the setup consisting of Nd: YAG laser-based ablation system UP213 (New Wave Research, Inc.) operating at the wavelength of 213 nm with pulse width of 4.2 ns, and quadrupole ICP-MS Agilent 7500ce (Agilent Technologies).

The ablated material was transported from ablation cell (Fig. S1) into the ICP by He (1.0 l min^{-1}) and Ar (0.6 l min^{-1}), which was admixed into He flow prior to entering the torch. The optimization of LA-ICP-MS parameters was performed using NIST610. The sensitivity of the ICP-MS was optimized based on monitoring of ^7Li (low mass), ^{55}Mn (middle mass), ^{89}Y (middle mass), ^{232}Th (high mass) in respect to maximum of S/N ratio, the level of oxide formation was kept below 0.2% (ThO/Th). Laser ablation was performed in two modes: single spot analysis, which was used for comparison of the ECTSCS and ESIC methods, and line scan mode employed for elemental mapping. Single spot analyses were performed with a fluence of 10 J cm^{-2} , spot diameter of 65 μm , repetition rate of 10 Hz, 30 s pre-ablation time for recording of background intensities of measured isotopes, and 60 s ablation time. Each sample was ablated in 10 positions. Isotope ^{28}Si was used as the internal standard. The following isotopes were measured at single spot analyses: ^7Li , ^{11}B , ^{23}Na , ^{24}Mg , ^{27}Al , ^{28}Si , ^{31}P , ^{39}K , ^{43}Ca , ^{45}Sc , ^{47}Ti , ^{51}V , ^{52}Cr , ^{55}Mn , ^{56}Fe , ^{59}Co , ^{60}Ni , ^{63}Cu , ^{66}Zn , ^{69}Ga , ^{72}Ge , ^{85}Rb , ^{88}Sr , ^{89}Y , ^{90}Zr , ^{107}Ag , ^{137}Ba , ^{208}Pb , ^{232}Th , ^{238}U . Prior elemental mapping of the given mica grain we performed bulk analysis of near another mica grain. We analyzed broad range of elements to obtain information about matrix and major elements which have to be imaged. Moreover, where possible we monitored more than one isotope for all imaged elements to reveal possible interferences. Based on these experiments we selected isotopes suitable for imaging to cover all matrix and minor elements whose sum of oxides gives more than 90%_{m/m} (the rest is OH group and fluorine which are non-determinable). Besides laser spot diameter and scan speed the sampling time is critical for lateral resolution of mapping. In order to keep the sampling time of the quadrupole mass spectrometer as short as possible, number of measured isotopes/elements was limited, while all elements contributing substantially to the total content were included.

Elemental mapping was performed with a fluence of 10 J cm^{-2} , spot diameter of 65 μm , repetition rate of 10 Hz, scan speed of $65 \mu\text{m s}^{-1}$ and the spacing between lines of 70 μm . The size of analyzed area was $2400 \times 3132 \mu\text{m}$. Resulting elemental maps consist of 1617 (33×49) pixels.

EMP measurements were performed using CAMECA SX100 electron microprobe (Institute of Geology, The Czech Academy of Sciences). The instrument was operated at an accelerating voltage of 15 kV, a beam current of 10 nA, and with a beam diameter of 2 μm . The following calibration standards were used: apatite (P), diopside (Si, Mg, Ca), rutile (Ti), jadeite (Al, Na), magnetite (Fe), MnCr_2O_4 (Mn), BaSO_4 (Ba), leucite (K), RbCl (Rb), and fluorite (F).

Colour SEM—CL images were obtained using a scanning microscope TESCAN Vega3 (Institute of Geology, The Czech Academy of Sciences). The microscope is equipped with a TESCAN CL detector allowing collection of live colour luminescence in a spectral range of ca. 400–800 nm.

2.3. Testing of normalization methods

Contents obtained by ECTSCS method were plotted against ECIS values and compared using linear regression. The estimated parameters of linear regression a (slope) and b (intercept) were statistically tested against a = 1 and b = 0 using so called single confidence interval: For test of the intercept the expression reads:

$$b_j - t_{1-\alpha}(n-m)\hat{\sigma}\sqrt{c_j} \leq b_j \leq b_j + t_{1-\alpha}(n-m)\hat{\sigma}\sqrt{c_j}$$

where c_{jj} is the j th diagonal element of inverse matrix and $t_{1-\alpha}(n-m)$ is quantile of Student distribution, $\hat{\sigma}$ is the estimate of residual standard deviation [44].

Analogical form is used for slope where b is replaced by a. Confidence intervals were calculated with $\alpha = 0.05$. If confidence interval of slope includes 1 then the slope of regression straight line is considered to be equal 1. If confidence interval of intercept includes 0 then the intercept of regression straight line is considered to be equal to 0.

If both regression parameters are revealed as statistically non-different from

1 and 0, respectively, the systematic constant and proportional errors are not present [44]. Trueness of the ECTSC values was tested in the same manner against reference values for the SRM. Results were also compared with contents obtained by EMP as an independent method. The error bars for LA-ICP-MS data in plots represent twofold standard deviation calculated from 10 replicates while the error bars for EMP data denote twofold standard deviation calculated from 3 replicates. It is to be noted that the ordinate of SiO_2 point (internal standard) in ECIS vs ECTSCS plots is value obtained by EMP analysis (Si as internal standard is not determined by LA-ICP-MS).

3. Results and discussion

We would like to show the applicability of ECTSCS, ECIS and TSIIN quantification methods. We proceeded from the easiest case (homogeneous sample with similar matrix to calibration standard) which is represented by CRM NIST 612 through more complex case (homogeneous real sample with slightly different matrix from calibration standard CRM NIST 610 – high content of K_2O) represented by ancient glass to the most complicated case (heterogeneous mediaeval sample with one part similar to CRM NIST 610 the second one with completely different matrix – lead glass).

As follows from above mentioned description the samples differ in matrix which affects mainly ablation rate. This fact is observable when we monitor the sum of oxide content without previous standardization methods (no matter if ECIS or ECTSCS). If the sum is larger than $100\%_{\text{m/m}}$ it means that the analyzed sample has higher ablation rate in comparison with calibration standard. In case of NIST612 the sum of content was about $98.5\%_{\text{m/m}}$ which means that the ablation rate of both NISTs (610 and 612) is very similar. When the ancient glass was analyzed the sum of content was about $85\%_{\text{m/m}}$ which indicates lower ablation rate in respect to NIST612 (calibration standard). When the heterogeneous mediaeval sample was analyzed, the sum of contents ranges from $80\%_{\text{m/m}}$ to $140\%_{\text{m/m}}$ depending on the location of the analysis.

3.1. Comparison of TSIIN, ECIS, ECTSCS in analysis of glass SRM

The glass SRM NIST 610 and 612 being widely used as calibration standards for LA-ICP-MS analysis of geological and even metallic materials [45] represent homogeneous materials with similar matrices. For comparison of TSIIN, ECTSCS, and ECIS methods the NIST 610 was used as a calibration standard for analysis of NIST 612. The LA-ICP-MS data were collected for 10 spots distributed over the target surface.

First, we have tried to use the total sum of ion intensities normalization (TSIIN) for CRM NIST 612, however we have found out that the obtained results strongly differ from certified values (e.g. SiO_2 : found $36\%_{\text{m/m}}$, certified $72\%_{\text{m/m}}$; Na_2O : found $42\%_{\text{m/m}}$, certified $14\%_{\text{m/m}}$; CaO : found $21\%_{\text{m/m}}$, certified $12\%_{\text{m/m}}$; Al_2O_3 : found $1.2\%_{\text{m/m}}$, certified $2.1\%_{\text{m/m}}$, ...). These extremely large bias follow from combination of several phenomena. First reason consists in differences between ionization energy (E_{ion}) values of particular elements. TSIIN is applicable only when E_{ion} is close for all elements and hence the degree of ionization is virtually the same for all analytes. In our case its value ranges from 5.1 eV for Na to 8.1 eV for Si. Second, the space-charge effect causes the dependence of ion response on the mass of the ions in ion optic. Third, in quadrupole analyzer the lighter ions are transmitted with lower efficiency than heavier. Fourth, the mass discrimination occurs in detection system as well; as the lighter ions produce more secondary electrons when hit the first electrode of the electron multiplier. Combination of all these phenomena causes that the results obtained by TSIIN are not true. When the ECIS or ECTSCS are used these phenomena are suppressed by external calibration. When the TSIIN failed to easiest case (homogenous sample with similar matrix to calibration standard) it was not applied in more complicated cases.

Regression analysis shown in Fig. 1 demonstrates a close match between content values obtained with both quantification methods. The linearity of the dependence was proved by the F-test (lack of fit test). The R^2 says how much of variation in y is described by the linear dependence described by regression equation. It means that if R^2 is equal to 0.999 then 99.9% of variation of y is described by regression straight line and 0.1% is expressed by the residual sum of squares. The test using confidence intervals (confidence intervals of the slope and intercept were 0.976–1.015 and -0.778 – 0.558) proved statistically insignificant difference of the intercept and the slope from “0” and “1”, respectively. It can be concluded that the tests of regression parameters give evidence of the absence of systematic errors. Trueness of the results obtained by the ECTSCS method was tested against reference values of NIST 612 (Fig. 2), which confirmed absence of systematic errors by confidence intervals of slope and intercept which were 0.986–1.056 and -2.578 – 1.412 , respectively. The close match between results obtained with ECIS and ECTSCS methods follows from similarity of matrices of both NIST SRMs, complete information on contents of all constituents (oxygen content is considered based on typical stoichiometry) and homogeneous distribution of internal reference element (Si). Hence, both ECTSCS and ECIS are applicable to analysis of homogeneous glass materials with similar matrix.

3.2. Comparison of ECIS and ECTSCS in analysis of homogeneous ancient glass

Both ECIS and ECTSCS quantification methods were employed for analysis of ancient glass bead from Holubice archaeological site. The ancient glass matrix slightly differs from that of the calibration standard NIST610, while elemental distribution is fairly homogeneous, as follows from RSD of EMP replicates, which does not exceed 3%. The results obtained by both quantification methods are plotted in Fig. 3 and tested as already stated with conclusion that no statistically significant difference exists between the two normalization methods (confidence intervals of slope and intercept were 0.989–1.046 and -0.256 – 0.206 , respectively). Similarly, a close match of contents obtained using ECTSCS with those found with EMP analysis follows from Fig. 4. With absence of systematic (constant and proportional) error (confidence intervals of slope and intercept were 0.931–1.077 and -0.290 – 0.359 , respectively) the EMP analysis confirms reliability of results obtained using ECTSC. For better illustration the content of SiO_2 in Fig. 4 is divided by factor 10. In a detail view the points for Al_2O_3 and K_2O do not lie on the regression line, however, the t -test of difference between EMP and ECTSCS values (for level of significance $\alpha = 0.05$ and degree of freedom $\nu = (n_{\text{LAICPMS}} + n_{\text{EMP}} - 2) = 11$) proved its statistical insignificance. Hence these two values were compared by t -test to find whether EMP and ECTSCS values are same. In case of Al_2O_3 and K_2O the $T = 0.8$ and 2.2, respectively. Both T -values are smaller than $T_{\text{crit}}(11) = 2.343$ which means that the results are not affected by systematic error. It

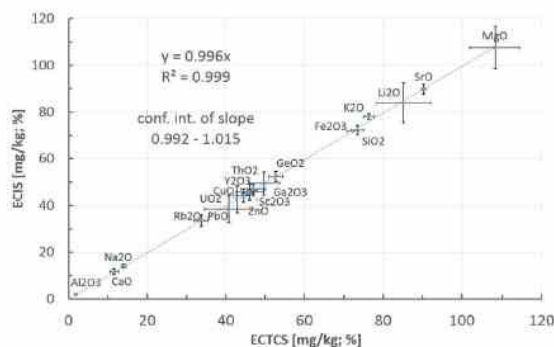


Fig. 1. Comparison of elemental content of SRM NIST 612 obtained by ECTSCS and ECIS.

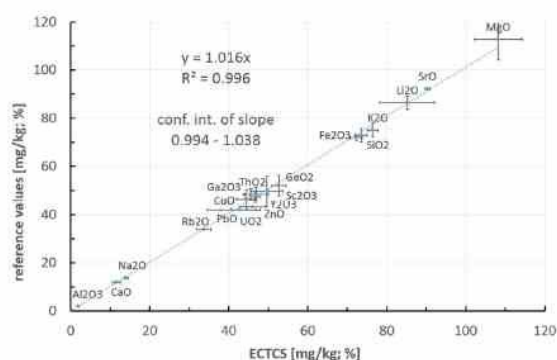


Fig. 2. Elemental contents in SRM NIST 612 obtained by ECTSCS compared to reference values.

follows that both ECTSCS and ECIS yield equal results for homogeneous ancient glass bead. Internal standardization is easily applicable due to homogeneous distribution of silicon, which is characterized by RSD = 0.9% of its content determined by EMP.

3.3. Comparison of ECIS and ECTSCS in analysis of heterogeneous mediaeval glass

As follows from 10 EMP analyses performed at various positions distributed over the whole surface of mediaeval glass bead (Iffeldorf), the SiO_2 content varies ca from 60 to 30%_{m/m}. In such a case, when the average content is calculated based on a limited number of local analyses (sample mean); it may significantly differ from the true mean value. Consequently, a variability of internal standard content over the sample surface together with its biased sample mean are expected to bring about over- and underestimation of analyte content in particular spots when using ECIS.

Nevertheless, ECIS was tested using the "average" (sample mean) content of internal standard, which corresponds to 43.6%_{m/m} SiO_2 , being calculated based on 10 EMP local analyses. Then the artefact was analyzed by LA-ICP-MS at 10 positions, which were intentionally different from those analyzed by EMP but close to each other in order to minimize possible local variability of elemental contents. The absence of constant systematic error between ECTSCS and ECIS results was confirmed by confidence interval of the intercept (−0.301–0.125). In contrast to the variability of EMP analyses of the whole sample surface, this high correlation indicates locally relatively homogeneous area. However, proportional systematic error of ECIS method against ECTSCS occurs, showing underestimation of the results obtained using ECIS

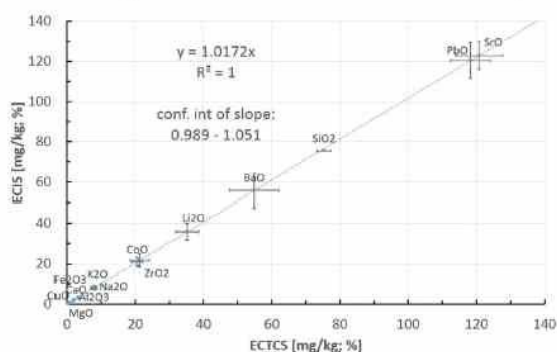


Fig. 3. Comparison of elemental contents in the homogeneous real sample obtained by ECTSCS and ECIS.

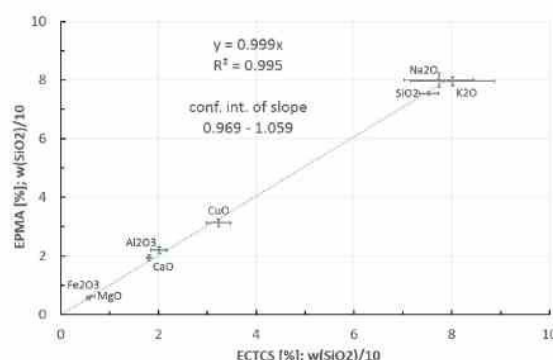


Fig. 4. Elemental contents in the homogeneous real sample obtained by ECTSCS compared to EMP values.

compared with ECTSCS, since the slope (confidence interval 0.720–0.738) is significantly lower than one (Fig.5). This is due to the use of possibly biased sample mean of Si content considered for ECTSCS. This assumption was further confirmed by the EMP analysis of the same area which was subjected to LA-ICP-MS measurement, as substantially higher sample mean of 58.2%_{m/m} SiO_2 was found there.

A close match of contents determined using ECTSCS with those found with EMP analysis in the area characterized with 58.2%_{m/m} SiO_2 follows from Fig. 6. Confidence interval of the slope (0.963–1.102) and intercept (−0.334–0.302) indicate absence of systematic constant and proportional error and confirms reliability of ECTSCS. For better illustration the content of SiO_2 in Fig. 6 was divided by factor 10. It can be concluded that ECTSC yields results which are consistent with those obtained with EMP.

3.4. Elemental mapping of inhomogeneous silicate sample

As an example of inhomogeneous sample mapping, a muscovite grain analysis using ECTSCS method is presented. The studied muscovite sample contains two phases which are clearly distinguished (Fig. 7a) by cathodoluminescence (CL), whereas backscattered electron (BSE) image does not provide differentiation of these areas (Fig. 7b). Grains consist of outer (bright) and inner (dark) zones (Fig. 7a) which differ in composition. According to EMP analysis, the bright zone (the rim of the grain) is enriched with Fe, Mn, Rb and F as compared with the dark core. As follows from the study of inhomogeneous glass, only ECTSCS is applicable for quantification. However, the muscovite sample contains significant amount of fluorine, hydroxy group and hydrogen which cannot be determined by ICP-MS. Knowing their content in the

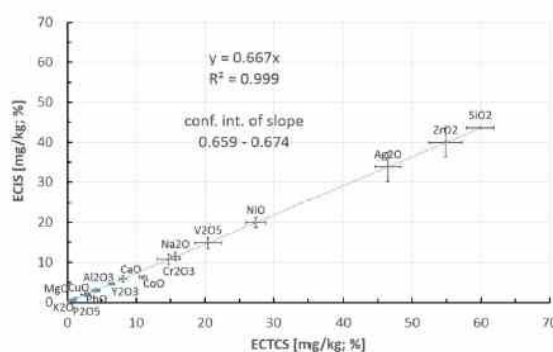


Fig. 5. Comparison of elemental contents in heterogeneous real sample obtained by ECTSCS and ECIS.

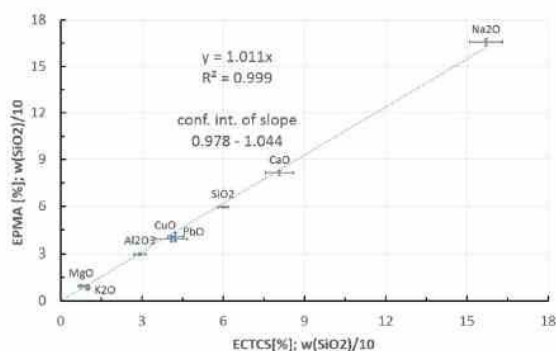


Fig. 6. Elemental contents in the heterogeneous real sample obtained by ECTSCS compared to EMP results.

rim (6.5%_{m/m}) and the core (1.7%_{m/m}) based on EMP analysis, we have to normalize to 93.5%_{m/m} and 98.7%_{m/m}, respectively.

For quantitative elemental mapping of muscovite it is necessary to identify areas where normalization to either 93.5%_{m/m} or 98.7%_{m/m} is to be performed. In the first approximation, the elemental maps were created by ECTSCS considering the sum of 100%_{m/m}. It was found that Li, Mn, Rb are depleted whereas Al and Fe are enriched in core part of the muscovite grain. The most obvious difference between core and rim part was observed in Mn content. Hence Mn was used as a marker of the core part: if the MnO content is lower than 0.2%_{m/m} then the ECTSCS calculates with the sum of 98.7%_{m/m}, if it is higher than 0.2%_{m/m} then the ECTSCS calculation is performed with the sum of 93.5%_{m/m}. Moreover, iron and manganese has two oxidation states (II) and (III) and (II) and (IV), respectively, which can complicate quantification processes. As mica crystallizes from magma it is supposed that Mn is present in the form of Mn (II) due to strongly anaerobic environment. Presence of Mn (IV) is expected at processes occurring in atmosphere which is not the case of our samples. Concerning Fe, the mixture of Fe (II) and Fe (III) is present in micas. Their content in Li-rich micas was determined by wet analysis mentioned in previous work [46]: Five mica samples were analyzed and it was found out that two micas were free of Fe (III), content of Fe (III) in two other mica samples was about 2%_{m/m} of total Fe content and the last sample contained less than 8%_{m/m} of trivalent iron related to the total Fe content. The recalculation considering the higher oxidation states (Fe₂O₃ and MnO₂) yields negligible increase of the content. (Example: when we consider the case with highest portion of trivalent iron (8%_{m/m}) of the total Fe content (3%_{m/m}) in the sample, the calculated content of oxides is 3.55%_{m/m} FeO and 0.34%_{m/m} Fe₂O₃, hence the sum of both oxides is 3.89%_{m/m}.) When we consider that iron is present only in divalent state, we get 3.86%_{m/m} FeO. It is obvious that the difference 0.03%_{m/m}

is insignificant with respect to the sum used for normalization. Hence, calculation of FeO content is sufficient.

We are aware that this approach is possible in the specific case where we know the average content of both iron oxides in the sample determined by bulk analysis after sample decomposition. Quantitative elemental maps shown in Fig. 8 were made with respect to the zones that have been identified and processed according to the above rules.

Elemental mapping confirmed correlation between intensity of red CL (Fig. 7a) and enrichment in Li, Rb, Si, and Mn. Moreover, it sensitively documents evolution of the composition of crystallized silicate melt and enrichment of non-compatible elements in late crystallized mineral grains (zones). Sharp border between cores and rims of muscovite crystals proved crystallization in two independent episodes. Based on LA-ICP-MS images (Fig. 8) we can assume that the crystal nuclei (no CL, low contents of Li, Rb etc.) grown at the initial stage of crystallization of the rock, that is from the primary melt in deep magmatic reservoir. Something later crystallized other minerals, especially quartz and feldspar, and the mixture of crystals with a residual F, Li, Rb-enriched melt was then transported in the vicinity of the ancient surface of the Earth. For a steep temperature gradient and thus a rapid loss of heat, the residual melt crystallized, from geological point of view "very quickly": the old mica grains were embedded with rims with a composition corresponding to the current melt (red CL, high contents of Li, Rb, and Mn).

To verify elemental contents in the maps yielded by LA-ICP-MS method, the EMP analysis by linear scan consisting of 60 individual spots with constant distance of 15 μm was performed through the muscovite grain surface (Fig. 9a,b). The line scan intersects both core and rim part. The distribution of SiO₂ and Al₂O₃ in core part is fairly uniform. Contents determined with EMP are about 47%_{m/m} SiO₂ and 35%_{m/m} Al₂O₃ (Fig. 9a), which matches well with average contents obtained by LA-ICP-MS (47.8%_{m/m} SiO₂ and 35.7%_{m/m} Al₂O₃). More complex situation occurs in the rim part where the distribution of all determined elements is less uniform in comparison with core. The average content of SiO₂ and Al₂O₃ in rim is about 51%_{m/m} and 28%_{m/m}, respectively. This is in good agreement with average content calculated from LA-ICP-MS maps, which is 52.4%_{m/m} and 27.5%_{m/m}, respectively. In case of minor constituents such as FeO and Rb₂O (Fig. 9b), their distribution is not as uniform as that of major constituents. Content of FeO in core and rim varies about 2.7%_{m/m} and 1.9%_{m/m} whereas average content calculated from LA-ICP-MS maps is 2.5%_{m/m} and 1.6%_{m/m}, respectively. Consequently, the EMP line scan analyses confirm quantification of LA-ICP-MS maps.

4. Conclusion

LA-ICP-MS was demonstrated as a powerful tool for quantitative elemental mapping of zonal geological samples in spite of inhomogeneous distribution of all elements and impossibility to use the ECIS

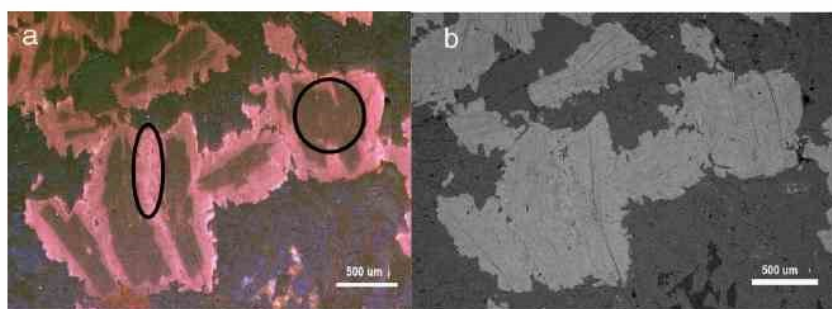


Fig. 7. CL (a) and BSE (b) images of muscovite grain where circle and ellipse mark the core and the rim, respectively.

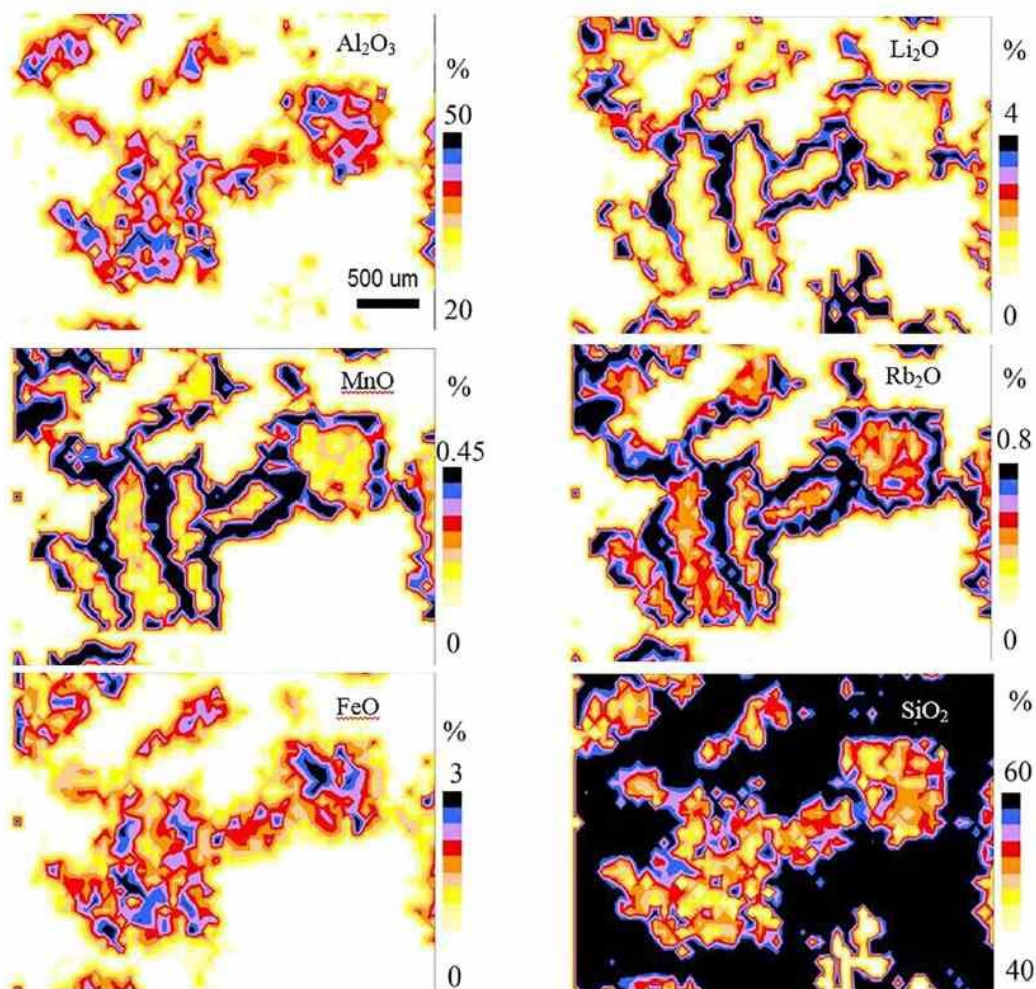


Fig. 8. Elemental maps of muscovite sample created by normalization to the sum of 93.5%_{m/m} and 98.7%_{m/m} for rim and core, respectively.

method. ECIS and ECTSCS provide identical results when homogeneous glassy samples are analyzed, and they give true results if compared to standard reference materials. However, the ECIS yields under- or overestimated results in comparison with true contents when applied

to heterogeneous glassy material analysis. On the other hand, when the ECTSCS is employed the obtained results are in a good agreement with those yielded by some independent method, e.g. EMP analysis. In case of local analysis (not imaging) of zonal sample we can perform

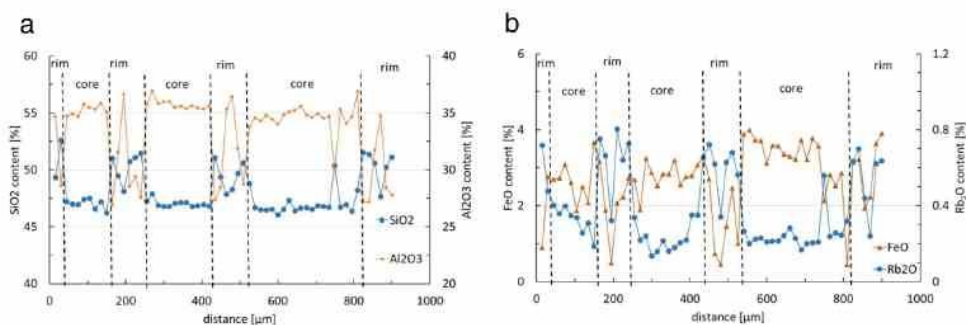


Fig. 9. EMP linear scan across rim and core part of the muscovite grain with spot analyses of (a) SiO₂ and Al₂O₃ and (b) FeO and Rb₂O₃.

LA-ICP-MS analysis in place which is close to the previous EPMA analysis and we know content of IS in this zone. Then we can use ECIS even for zonal samples. However, ECIS is not suitable for quantified imaging of zonal grains due to fact that content of internal standard is in range from 44%*m/m* SiO₂ to 55%*m/m* SiO₂. Its content varies point-by-point hence we do not know the value of IS content which has to be used for normalization. Advantage of the ECTSCS when applied to a sample matrix with known full qualitative composition (e.g. glass) consists in the fact that no additional independent analytical method is required because the content can be normalized to the sum of 100%*m/m*. However, when the sample contains some elements or groups non-determinable by ICP-MS (e.g. fluorine, hydrogen, hydroxy group ...), the normalization has to be performed to the sum obtained by subtracting the content of this element from 100%*m/m* and additional analytical method is required. If these rules are applicable the elemental maps of zonal geological samples can be made and the results are in good agreement with EMP analyses.

Supplementary data to this article can be found online at <http://dx.doi.org/10.1016/j.microc.2017.03.040>.

Acknowledgements

The authors acknowledge the Czech Science Foundation for support of the project GA14-13600S. The results of this research have been acquired within CEITEC 2020 (LQ1601) project with financial contribution made by the Ministry of Education, Youths and Sports of the Czech Republic within special support paid from the National Programme for Sustainability II funds.

References

- [1] S.M. Zaytsev, A.M. Popov, E.V. Chernykh, R.D. Voronina, N.B. Zorov, T.A. Labutin, Comparison of single- and multivariate calibration for determination of Si, Mn, Cr and Ni in high-alloyed stainless steels by laser-induced breakdown spectrometry, *J. Anal. At. Spectrom.* 29 (2014) 1417–1424.
- [2] M.L. Shah, A.K. Pulhani, B.M. Suri, G.P. Gupta, Time-resolved emission spectroscopic study of laser-induced steel plasmas, *plasma, Sci. Technol.* 15 (2013) 546–551.
- [3] K.-y. Chen, C. Fan, H.-l. Yuan, Z.-a. Bao, C.-l. Zong, M.-n. Dai, X. Ling, Y. Yang, High-precision in situ analysis of the lead isotopic composition in copper using femtosecond laser ablation MC-ICP-MS and the application in ancient coins, *Spectrosc. Spectr. Anal.* 33 (2013) 1342–1349.
- [4] M. Singh, V. Karki, R.K. Mishra, A. Kumar, C.P. Kaushik, X.L. Mao, R.E. Russo, A. Sarkar, Analytical spectral dependent partial least squares regression: a study of nuclear waste glass from thorium based fuel using LIBS, *J. Anal. At. Spectrom.* 30 (2015) 2507–2515.
- [5] J.S. Lee, H.B. Lim, Laser ablation of titanium nitride coated on silicon wafer substrate for depth profiling using ICP-MS, *Appl. Surf. Sci.* 327 (2015) 483–489.
- [6] F.-A. Barreda, F. Trichard, S. Barbier, N. Gilon, L. Saint-Jalmes, Fast quantitative determination of platinum in liquid samples by laser-induced breakdown spectroscopy, *Anal. Bioanal. Chem.* 403 (2012) 2601–2610.
- [7] S.H. Lee, H.T. Hahn, J.J. Yoh, Towards a two-dimensional laser induced breakdown spectroscopy mapping of liquefied petroleum gas and electrolytic oxy-hydrogen flames, *Spectrochim. Acta B At. Spectrosc.* 88 (2013) 63–68.
- [8] V. Sturm, R. Noll, Laser-induced breakdown spectroscopy of gas mixtures of air, CO₂, N₂, and C₃H₈ for simultaneous C, H, O, and N measurement, *Appl. Opt.* 42 (2003) 6221–6225.
- [9] M. Bonta, H. Lohninger, V. Laszlo, B. Hegedus, A. Limbeck, Quantitative LA-ICP-MS imaging of platinum in chemotherapy treated human malignant pleural mesothelioma samples using printed patterns as standard, *J. Anal. At. Spectrom.* 29 (2014) 2159–2167.
- [10] D.A. Frick, C. Giesen, T. Hemmerle, B. Bodenmiller, D. Guenther, An internal standardisation strategy for quantitative immunoassay tissue imaging using laser ablation inductively coupled plasma mass spectrometry, *J. Anal. At. Spectrom.* 30 (2015) 254–259.
- [11] S. Conte, T. Chinni, R. Arletti, M. Vandini, Butrint (Albania) between eastern and western Mediterranean glass production: EMPA and LA-ICP-MS of late antique and early medieval finds, *J. Archaeol. Sci.* 49 (2014) 6–20.
- [12] R. Scarpelli, A.M. De Francesco, M. Gaeta, D. Cottica, L. Toniolo, The provenance of the Pompeii cooking wares: insights from LA-ICP-MS trace element analyses, *Microchem. J.* 119 (2015) 93–101.
- [13] J. Farell, D. Amarasiwardena, A.H. Goodman, B. Arriaza, Bioimaging of trace metals in ancient Chilean mummies and contemporary Egyptian teeth by laser ablation-inductively coupled plasma-mass spectrometry (LA-ICP-MS), *Microchem. J.* 106 (2013) 340–346.
- [14] B.K. Kuhn, K. Birbaum, Y. Luo, D. Guenther, Fundamental studies on the ablation behaviour of Pb/U in NIST 610 and zircon 91500 using laser ablation inductively coupled plasma mass spectrometry with respect to geochronology, *J. Anal. At. Spectrom.* 25 (2010) 21–27.
- [15] E. Marillo-Sialer, J. Woodhead, J. Hergt, A. Greig, M. Guillong, A. Gleadow, N. Evans, C. Poin, The zircon 'matrix effect': evidence for an ablation rate control on the accuracy of U-Pb age determinations by LA-ICP-MS, *J. Anal. At. Spectrom.* 29 (2014) 981–989.
- [16] L. Yang, R.E. Sturgeon, Z. Mester, Quantitation of trace metals in liquid samples by dried-droplet laser ablation inductively coupled plasma mass spectrometry, *Anal. Chem.* 77 (2005) 2971–2977.
- [17] C.C. Garcia, M. Waelle, H. Lindner, J. Koch, K. Niemax, D. Guenther, Femtosecond laser ablation inductively coupled plasma mass spectrometry: transport efficiencies of aerosols released under argon atmosphere and the importance of the focus position, *Spectrochim. Acta B At. Spectrosc.* 63 (2008) 271–276.
- [18] M. Iglesias, T. Vaculović, J. Studynkova, E. Poussel, J.M. Memet, Influence of the operating conditions and of the optical transition on non-spectral matrix effects in inductively coupled plasma-atomic emission spectrometry, *Spectrochim. Acta B At. Spectrosc.* 59 (2004) 1841–1850.
- [19] A.C. Lazar, P.B. Farnsworth, Matrix effect studies in the inductively coupled plasma with monodisperse droplets. Part II: the influence of matrix on spatially integrated ion density, *Appl. Spectrosc.* 53 (1999) 465–470.
- [20] J.S. Crain, D.L. Gallimore, Determination of trace impurities in uranium-oxides by laser ablation inductively coupled plasma mass spectrometry, *J. Anal. At. Spectrom.* 7 (1992) 605–610.
- [21] J. Trincavelli, S. Limandri, R. Bonetto, Standardless quantification methods in electron probe microanalysis, *Spectrochim. Acta B At. Spectrosc.* 101 (2014) 76–85.
- [22] L. Halicz, D. Gunther, Quantitative analysis of silicates using LA-ICP-MS with liquid calibration, *J. Anal. At. Spectrom.* 19 (2004) 1539–1545.
- [23] J.T. van Elteren, N.H. Tennent, V.S. Selih, Multi-element quantification of ancient/historic glasses by laser ablation inductively coupled plasma mass spectrometry using sum normalization calibration, *Anal. Chim. Acta* 644 (2009) 1–9.
- [24] J.E. Gagnon, B.J. Fryer, I.M. Samson, A.E. Williams-Jones, Quantitative analysis of silicate certified reference materials by LA-ICPMS with and without an internal standard, *J. Anal. At. Spectrom.* 23 (2008) 1529–1537.
- [25] M. Guillong, K. Hametner, E. Reusser, S.A. Wilson, D. Gunther, Preliminary characterisation of new glass reference materials (GSA-1G, GSC-1G, GSD-1G and GSE-1G) by laser ablation-inductively coupled plasma-mass spectrometry using 193 nm, 213 nm and 266 nm wavelengths, *Geostand. Geoanal. Res.* 29 (2005) 315–331.
- [26] C. Chataigner, B. Gratuze, New data on the exploitation of Obsidian in the southern Caucasus (Armenia, Georgia) and eastern Turkey, part 1: source characterization, *Archaeometry* 56 (2014) 25–47.
- [27] C. Chataigner, B. Gratuze, New data on the exploitation of Obsidian in the southern Caucasus (Armenia, Georgia) and eastern Turkey, part 2: Obsidian procurement from the upper Palaeolithic to the late Bronze age, *Archaeometry* 56 (2014) 48–69.
- [28] Y.S. Liu, Z.C. Hu, S. Gao, D. Gunther, J. Xu, C.G. Gao, H.H. Chen, In situ analysis of major and trace elements of anhydrous minerals by LA-ICP-MS without applying an internal standard, *Chem. Geol.* 257 (2008) 34–43.
- [29] C. Frei, J. Schenzel, F. Waibel, D. Gunther, Stoichiometry of various Ag/In/SbTe phase change materials (PCMs) determined using LA-ICP-MS, *J. Anal. At. Spectrom.* 23 (2008) 217–222.
- [30] T. Vaculović, P. Sulovsky, J. Machat, V. Otruba, O. Matal, T. Simo, C. Latkoczy, D. Gunther, V. Kanicky, The EPMA, LA-ICP-MS and ICP-OES study of corrosion of structural materials for a nuclear reactor cooling circuit by molten fluoride salt treatment, *J. Anal. At. Spectrom.* 24 (2009) 649–654.
- [31] T. Vaculović, T. Warchilova, T. Simo, O. Matal, V. Otruba, P. Mikuska, V. Kanicky, Elemental mapping of structural materials for a nuclear reactor by means of LA-ICP-MS, *J. Anal. At. Spectrom.* 27 (2012) 1321–1326.
- [32] T. Warchilova, T. Vaculović, O. Matal, T. Simo, V. Kanicky, Lateral mapping of metallic materials using laser ablation inductively coupled plasma mass spectrometry, *Chem. List.* 106 (2012) 236–239.
- [33] A.M. Leach, G.M. Hieftje, Methods for shot-to-shot normalization in laser ablation with an inductively coupled plasma time-of-flight mass spectrometer, *J. Anal. At. Spectrom.* 15 (2000) 1121–1124.
- [34] J. Bianga, A. Bouslimani, N. Bec, F. Quenet, S. Mounicou, J. Szpunar, B. Bouysiere, R. Lobinski, C. Larroque, Complementarity of MALDI and LA ICP mass spectrometry for platinum anticancer imaging in human tumor, *Metallomics* 6 (2014) 1382–1386.
- [35] A.E. Egger, S. Theiner, C. Kornauth, P. Heffeter, W. Berger, B.K. Keppler, C.G. Hartinger, Quantitative bioimaging by LA-ICP-MS: a methodological study on the distribution of Pt and Ru in viscera originating from cisplatin- and KP1339-treated mice, *Metallomics* 6 (2014) 1616–1625.
- [36] K. Jurowski, M. Szewczyk, W. Piekoszewski, M. Herman, B. Szewczyk, G. Nowak, S. Walas, N. Miliszewicz, A. Tobiasz, J. Dobrowolska-Iwanek, A standard sample preparation and calibration procedure for imaging zinc and magnesium in rats' brain tissue by laser ablation-inductively coupled plasma-time of flight-mass spectrometry, *J. Anal. At. Spectrom.* 29 (2014) 1425–1431.
- [37] D.J. Hare, J. Lear, D. Bishop, A. Beavis, P.A. Doble, Protocol for production of matrix-matched brain tissue standards for imaging by laser ablation-inductively coupled plasma-mass spectrometry, *Anal. Methods* 5 (2013) 1915–1921.
- [38] M.M. Pornwilard, R. Weiskirchen, N. Gassler, A.K. Bosserhoff, J.S. Becker, Novel Bioimaging Techniques of Metals by Laser Ablation Inductively Coupled Plasma Mass Spectrometry for Diagnosis of Fibrotic and Cirrhotic Liver Disorders, *Plos One*, 8, 2013.
- [39] J.S. Becker, R.C. Dietrich, A. Matusch, D. Pozebon, V.L. Dressier, Quantitative images of metals in plant tissues measured by laser ablation inductively coupled plasma mass spectrometry, *Spectrochim. Acta B At. Spectrosc.* 63 (2008) 1248–1252.

- [40] J.L. Todoli, J.M. Memet, Study of polymer ablation products obtained by ultraviolet laser ablation inductively coupled plasma atomic emission spectrometry, *Spectrochim. Acta B At. Spectrosc.* 53 (1998) 1645–1656.
- [41] D.A. Frick, D. Guenther, Fundamental studies on the ablation behaviour of carbon in LA-ICP-MS with respect to the suitability as internal standard, *J. Anal. At. Spectrom.* 27 (2012) 1294–1303.
- [42] J.R. Chirinos, D.D. Oropeza, J.J. Gonzalez, H. Hou, M. Morey, V. Zorba, R.E. Russo, Simultaneous 3-dimensional elemental imaging with LIBS and LA-ICP-MS, *J. Anal. At. Spectrom.* 29 (2014) 1292–1298.
- [43] S.M. Chernonozhkin, S. Goderis, S. Bauters, B. Vekemans, L. Vincze, P. Claeys, F. Vanhaecke, Evaluation of pneumatic nebulization and ns-laser ablation ICP-MS for bulk elemental analysis and 2-dimensional element mapping of iron meteorites, *J. Anal. At. Spectrom.* 29 (2014) 1001–1016.
- [44] M. Meloun, J. Militký, *Statistical Data Analysis, a Practical Guide*, Woodhead Publishing, India, 2011.
- [45] V. Moza, J. Pisonero, M. Hola, V. Kanický, D. Gunther, Quantitative analysis of Fe-based samples using ultraviolet nanosecond and femtosecond laser ablation-ICP-MS, *J. Anal. At. Spectrom.* 21 (2006) 1194–1201.
- [46] K. Breiter, J. Fryda, R. Seltmann, R. Thomas, Mineralogical evidence for two magmatic stages in the evolution of an extremely fractionated P-rich rare-metal granite: the Podlesi stock, Krušné Hory, Czech Republic, *J. Petrol.* 38 (1997) 1723–1739.

6.9 **ARTICLE 9**

Petrík, I.; Janák, M.; Klonowska, I.; Majka, J.; Froitzheim, N.; Yoshida, K.; Sasinková, V.; Konečný, P.; Vaculovič, T. *Journal of Petrology* 2020 (IF=3.38)

Monazite Behaviour during Metamorphic Evolution of a Diamond-bearing Gneiss: a Case Study from the Seve Nappe Complex, Scandinavian Caledonides

I. Petřík^{1*}, M. Janák¹, I. Klonowska^{2,3}, J. Majka^{2,3}, N. Froitzheim⁴, K. Yoshida⁵, V. Sasinková⁶, P. Konečný⁷ and T. Vaculovic⁸

¹Earth Science Institute, Slovak Academy of Sciences, Dúbravská cesta 9, Bratislava, 840 05, Slovak Republic; ²Department of Earth Sciences, Uppsala University, Villavägen 16, Uppsala, 752 36, Sweden; ³Faculty of Geology, Geophysics and Environmental Protection, AGH University of Science and Technology, Mickiewicza 30, Kraków, 30-059, Poland; ⁴University of Bonn, Institut für Geowissenschaften, Poppelsdorfer Schloss, Bonn, D-53115, Germany; ⁵Research and Development Center for Ocean Drilling Science, Japan Agency for Marine-Earth Science and Technology, 2-15 Natsushima, Yokosuka, 237-0061, Japan; ⁶Institute of Chemistry, Slovak Academy of Sciences, Dúbravská cesta 9, Bratislava, 845 38, Slovak Republic; ⁷Dionýz Štúr State Geological Institute, Mlynská dolina 1, Bratislava, 817 04, Slovak Republic; ⁸Institute of Chemistry, Masaryk University, Kamenice 753/5, Brno, 62500, Czech Republic

*Corresponding author. E-mail: igor.petrik@savba.sk

Received July 25, 2018; Accepted November 2, 2019

ABSTRACT

Monazite is a common mineral in metapelitic rocks including those that underwent ultrahigh-pressure (UHP) metamorphism. During metamorphic evolution monazite adapts its composition to the changing mineral assemblage, especially in its heavy rare earth element contents. We studied this process in diamond-bearing gneiss containing monazite, from Saxnäs in the Seve Nappe Complex of the Scandinavian Caledonides. Although the rock has been re-equilibrated under granulite-facies and partial melting conditions, it still preserves minerals from the UHP stage: garnet, kyanite, rutile, and especially diamond. Microdiamonds occur *in situ* as inclusions in garnet, kyanite and zircon, either as single crystals or as polyphase inclusions with Fe–Mg carbonates, rutile and CO₂. Both monazite and diamond occur in the rims of garnet showing the highest pyrope content and a secondary peak of yttrium. Such a position indicates thermally activated diffusion under high temperature at the end of prograde metamorphism. Monazite compositions show negative Eu anomalies, which we interpret to be inherited from the source rock, not reflecting the coexistence with plagioclase and/or K-feldspar, which are unstable at UHP conditions. Our results suggest that the effect of whole-rock composition may be more important than that of coexisting phases. The UHP monazite was most probably formed from allanite during subduction and prograde metamorphism. The monazites included in garnet and kyanite are mostly unaltered, whereas those in the matrix show breakdown coronas consisting of apatite, REE-epidote/allanite and REE-carbonate, probably formed as a result of pressure decrease and cooling. U–Th–Pb chemical age dating of monazites yields an isochron centroid age of 472 ± 3 Ma. We interpret this age as monazite growth under UHP conditions related to subduction of the Baltica continental margin in Early Ordovician time.

Key words: monazite; diamond; subduction; UHP metamorphism; Scandinavian Caledonides

INTRODUCTION

Monazite is one of the most informative minerals in felsic crustal rocks, providing information not only on the age of metamorphic events but also through its chemistry [light rare earth elements (LREE), Th, U, Y] on equilibria with metamorphic phases such as garnet and feldspars (e.g. Zhu & O'Nions, 1999; Catlos *et al.*, 2002; Spear & Pyle, 2002; Hermann & Rubatto, 2003; Foster *et al.*, 2004; Kohn *et al.*, 2005; Kelsey *et al.*, 2008; Krenn *et al.*, 2009; Gieré *et al.*, 2011; Dumond *et al.*, 2015; Hacker *et al.*, 2019). Only few studies (e.g. Terry *et al.*, 2000; Krenn *et al.*, 2009; Hacker *et al.*, 2015; Holder *et al.*, 2015; Petrik *et al.*, 2016; Klonowska *et al.*, 2017a) have discussed the response of monazite to ultrahigh-pressure (UHP) metamorphism, especially when UHP metamorphism is demonstrated by the presence of diamond, a stable mineral at very high pressure (Dobrzynetska, 2012). Microdiamonds of metamorphic origin can be formed when Earth's crust is subducted beyond the crust–mantle boundary; such diamonds were first identified in crustal rocks from the Kokchetav Massif in northern Kazakhstan (Sobolev & Shatsky, 1990) and subsequently at several localities worldwide (e.g. Gilotti, 2013; Liou *et al.*, 2014).

In UHP gneisses monazite is mostly found as inclusions in garnet (Krenn *et al.*, 2009; Petrik *et al.*, 2016; Klonowska *et al.*, 2017b). The HP–UHP monazites show relatively low Y and Th contents, steep REE patterns with high La/Nd, and relatively weak Eu anomalies, sometimes with elevated Sr (Krenn *et al.*, 2004; Holder *et al.*, 2015). Garnet sequesters Y during prograde metamorphism (e.g. Spear & Pyle, 2002; Hermann & Rubatto, 2003; Foster *et al.*, 2004; Kohn *et al.*, 2005; Kelsey *et al.*, 2008), and a high volume of garnet present in UHP rocks incorporates most of the Y and heavy REE (HREE). If, on decompression from UHP to medium-pressure conditions, the garnet amount decreases, it may liberate Y and REE and cause corresponding changes in the composition of coexisting monazite (Zhu & O'Nions, 1999). It is also known that monazite is strongly soluble in hydrous granitic melts produced during decompression (Rapp & Watson, 1986; Montel, 1993; Skora & Blundy, 2012) and, upon cooling near the solidus, the dissolved monazite can recrystallize. The pre-existing UHP monazite can thus be replaced or overgrown by new monazite.

UHP metamorphism within the Seve Nappe Complex (SNC) of the Scandinavian Caledonides, representing the outermost Baltican margin, has been recognized during recent years in different lithologies, including eclogites, peridotites, pyroxenites and gneisses (e.g. Brueckner *et al.*, 2004; Janák *et al.*, 2013; Majka *et al.*, 2014a; Gilio *et al.*, 2015; Klonowska *et al.*, 2016, 2017a). Microdiamond has been found in gneisses from three localities in the SNC: (1) Mt Tväraklumparna (Majka *et al.*, 2014b) and (2) Mt Åreskutan (Klonowska *et al.*, 2017a), both in west-central Jämtland, and (3) near Saxnäs (Klonowska, 2017;

Klonowska *et al.*, 2017b) in southwestern Västerbotten. Chemical Th–U–Pb dating of monazite in diamond-bearing gneisses from Tväraklumparna and Åreskutan yielded ages between 445 and 435 Ma, which have been interpreted to record post-UHP exhumation of diamond-bearing gneiss with monazite only rarely preserving high-pressure domains, being largely dissolved and re-precipitated from melt at low pressures (Klonowska *et al.*, 2017a). The obtained results corroborated previous Middle to Late Ordovician ages of metamorphism and partial melting known from the SNC in Jämtland (e.g. Williams & Claesson, 1987; Brueckner & van Roermund, 2007; Majka *et al.*, 2012; Root & Corfu, 2012; Ladenberger *et al.*, 2014).

In this study, we have investigated the response of monazite composition to changing mineral assemblage during transition from UHP to granulite-facies metamorphism in the diamond-bearing gneiss from Saxnäs. In addition to previous reports (Klonowska, 2017; Klonowska *et al.*, 2017b) here we provide more details on diamond and other micro-inclusions identified by Raman spectroscopy. Several textural types of monazite have been recognized, including monazite associated with diamond as inclusions in garnet and kyanite, matrix monazite with REE-epidote/allanite + apatite coronas, and former monazite altered to REE-carbonate. The method of electron microprobe U–Th–total Pb dating allowed us to date *in situ* small domains of monazite from the diamond-bearing thin sections. Laser ablation inductively coupled plasma mass spectrometry (LA-ICP-MS) was used to analyse trace elements in garnet and monazite and map the Y distribution in garnet. The results are discussed with respect to the tectono-metamorphic evolution.

GEOLOGICAL BACKGROUND

The Middle Allochthon of the Scandinavian Caledonides (Fig. 1a) comprises lithological units representing the outermost Baltican continental margin. These lithological units currently reside in a structural setting that demonstrates tectonic top-to-the-east emplacement onto Baltica during the final evolutionary stages of the Caledonian orogeny [see, e.g. Gee *et al.* (2013) for comprehensive description]. Recently, a number of papers have provided evidence for Middle and Late Ordovician ultra-deep subduction of some of the uppermost units of the Middle Allochthon, namely the Lower and Middle Seve nappes (e.g. Brueckner *et al.*, 2004; Majka *et al.*, 2012; Klonowska *et al.*, 2016; 2017a, 2017b; Fassmer *et al.*, 2017). These lithological units include sub-UHP and proper UHP eclogites (e.g. Janák *et al.*, 2013; Majka *et al.*, 2014a; Klonowska *et al.*, 2016), garnet-bearing peridotites and pyroxenites (Gilio *et al.*, 2015; Klonowska *et al.*, 2016), and diamond-bearing gneisses (Majka *et al.*, 2014a; Klonowska, 2017; Klonowska *et al.*, 2017a, 2017b). Most of these discoveries have been made in Jämtland, in an area extending

c. 200 km in length from the Tväråklumparna Mts in the SW, where the first metamorphic diamond within the SNC was described by Majka *et al.* (2014b), to the Ertsekey and Tjeliken lenses in the NE, which host numerous eclogites and ultramafic rocks (e.g. Zwart, 1974; van Roermund & Bakker, 1983; van Roermund, 1985, 1989). In Västerbotten (Fig. 1b), the SNC is similarly developed as in the aforementioned UHP areas. Eclogites *sensu stricto* are lacking, but garnet–clinopyroxene–plagioclase gneisses, indicating possible HP metamorphic conditions, are common; for example, in the vicinity of the Kittelfjäll spinel peridotite body occurring at the bottom of the Middle Seve Nappe, which itself records a subduction-related evolutionary path (Clos *et al.*, 2014). Also abundant in the Middle Seve Nappe in this region are metasedimentary kyanite-bearing gneisses, locally referred to as the Marsfjället gneiss (Trouw, 1973), which record at least HP conditions (~14.5–17.5 kbar) but probably experienced higher conditions of metamorphism (Grimmer *et al.*, 2015). In the latter study the researchers investigated several samples of the Marsfjället gneiss collected in the vicinity of Saxnäs and hypothesized that the Marsfjället gneiss may record UHP conditions. Our samples were collected from a thin strip of the Marsfjället gneiss, c. 6 km NW of Saxnäs along Vildmarksvägen (the Wilderness Road).

Only few data exist on the timing of metamorphism in the SNC of the Saxnäs region. Grimmer *et al.* (2015) constrained prograde growth of garnet at 462 ± 3.5 Ma, in schists of the Upper Seve Nappe, based on an Sm–Nd garnet–apatite–feldspar–whole-rock isochron. Subsequent exhumation of both Upper and Middle Seve at c. 438–426 Ma, reaching mid-crustal levels at c. 434 Ma, was dated using a Rb–Sr multi-mineral isochron method on several samples, including mylonites and pegmatites (Grimmer *et al.*, 2015). In contrast, Gademan *et al.* (2011; published in an abstract) dated monazite from the Marsfjället gneiss using an electron microprobe and obtained an age of 507 ± 20 Ma based on a multi-spot ($n = 393$) pseudo-isochron. This age was interpreted to be a record of the controversial ‘Finnmarkian orogeny’ described for regions of the SNC farther north, which resulted from collision of the Baltican outermost margin with an island arc (e.g. Stephens, 1988). In the absence of a detailed documentation of analytical results, this age is difficult to interpret.

SAMPLE PREPARATION AND ANALYTICAL TECHNIQUES

For petrographic observations, electron microprobe analysis, micro-Raman spectroscopy, and LA-ICP-MS analysis, a series of standard thin sections of c. 30–40 μm thickness was prepared from several samples taken from the outcrop. In detail, we studied diamond-bearing thin sections ML-6-12 A, C and LA. The first set of thin sections was polished with a Struers

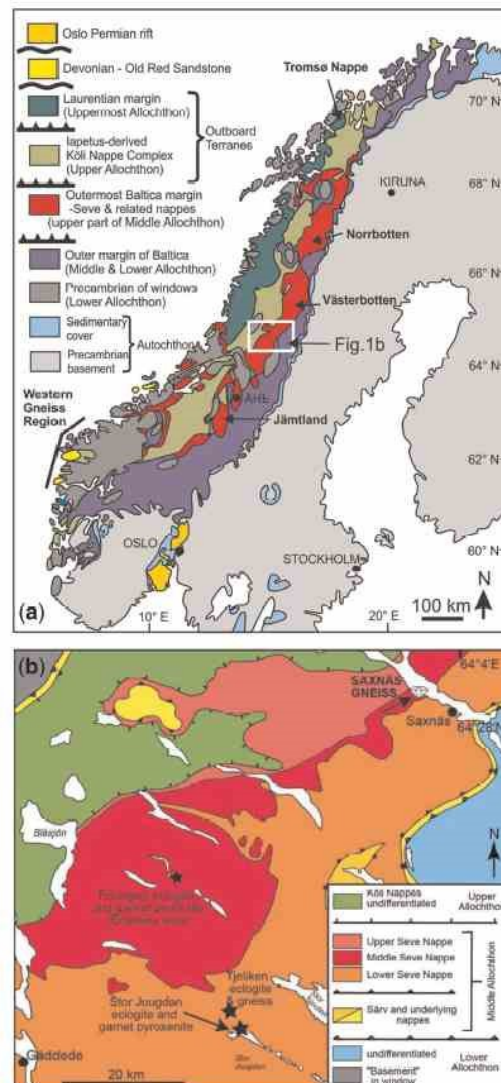


Fig. 1. (a) Simplified tectonic map of the Scandinavian Caledonides. The rectangle indicates the area of the map shown in (b). (b) Simplified tectono-stratigraphic map of northern Jämtland and southern Västerbotten. Sample location of the studied gneiss is marked by a diamond; other HP–UHP rocks in the area are marked by stars. Both maps are modified after Gee *et al.* (2013).

polycrystalline-type diamond spray of 1 μm particle size. To exclude the possibility of diamond being the result of contamination owing to polishing, a second set of duplicate thin sections was polished using Al_2O_3 as a carbon-free medium, and an ultrasonic bath was used to remove any remaining polishing material from the samples. A sample rock was analysed for bulk major and trace elements by inductively coupled plasma

emission spectrometry (ICP-ES) or ICP-MS (Bureau Veritas Minerals).

Electron microprobe WDS analysis of mineral chemistry was performed with a CAMECA SX-100 electron microprobe housed in the Dionýz Štúr State Geological Institute in Bratislava. The analytical conditions were as follows: 15 kV accelerating voltage and 20 nA beam current, peak counting time 20 s, and beam diameter of 2–10 μm . Raw counts were corrected using the on-line PAP routine. Mineral standards (Si, Ca: wollastonite; Na: albite; K: orthoclase; Fe: fayalite; Mn: rhodonite), pure element oxides (TiO_2 , Al_2O_3 , Cr_2O_3 , MgO), and metals (Ni) were used for calibration.

Monazites were dated by the MARC (monazite age reference correction) method developed in the Dionýz Štúr State Geological Institute, Bratislava (Konečný *et al.*, 2018), using microprobe analyses from a CAMECA SX-100. Spot monazite analyses were acquired with conditions of 15 kV accelerating voltage, 180 nA beam current, and 3 μm beam diameter, with the aim of increasing both counting efficiency and spatial resolution. Long counting times were used to increase analytical precision: for Pb, 300 s peak and 2×150 s background; for Th, 35 s peak and 2×17.5 s background; for U, 80 s peak and 80 s background; for Y, 40 s peak and 2×20 s background. Calibration reference materials for REE and Y were phosphates synthesized by Daniel Harlov at the GFZ German Research Centre, Potsdam, Germany; and PbCO_3 for Pb, ThO_2 for Th, UO_2 for U, barite for Sr, wollastonite for Ca and Si, SrTiO_3 for Sr, Al_2O_3 for Al and fayalite for Fe. Irradiation by the electron beam causes gradual degradation of the surface known as beam damage. With increasing analytical time the counting intensity rises non-linearly. Sequential measurement on the spectrometer in the order Pb, Th, U, Y (large PET) was corrected for the acquisition time of these elements. The naturally curved background at Pb-M α was estimated by a novel method (Konečný *et al.*, 2018) based on the positive trend of linear minus exponential background to monazite composition represented by average atomic number. Mutual interferences were resolved by an empirical correction, which included matrix effects on both reference material and on an unknown sample. The Pb-M α line overlaps La-L α , Th-M ζ_1 , Th-M ζ_2 and Y-L γ_2 , 3; weak La-L α overlap was neglected. Weak self-interference Pb-M4-O2 overlapping the background point at relative position $-3255 \sin(\theta) \times 10^5$ was corrected, although its highest values transposed to an error in Pb of only up to 2 ppm. The overlap by tails from more distant U-M ζ_1 and U-M ζ_2 lines at this background point was corrected. 'Background holes' near this background point found by Kato & Suzuki (2014) were not present in our detailed spectrometer scans. The effect of the U-M β overlap by multiple Th-M ζ , Th-M3-N4 and Th-M5-P3 lines was corrected. The U-M β background was measured at the relative position $-1372 \sin(\theta) \times 10^5$. The background slope was estimated by regression through variable Th content down to the zero

concentration. Age estimates were tested on monazites dated by methods involving isotopic ratios of Pb and U, called age reference materials (ARMs). A set of 10 ARMs was utilized for assessment of minor systematic errors that cannot be suppressed in the currently used measuring procedure, but are accumulated regardless of the number of analyses. ARM parameters such as Pb isotopic minus Pb microprobe versus Th and Y improve compositional independence of the age estimation and, thus, the age accuracy and confidence. It is recommended to re-measure ARMs within a dating session of monazites of interest. Principles and details of MARC dating technique have been published by Konečný *et al.* (2018).

Micro-Raman spectroscopy was used to identify diamond and other micro-inclusions with two confocal instruments: (1) the Thermo-Scientific DXR Raman Microscope at the Institute of Chemistry, Slovak Academy of Sciences, Bratislava; (2) the NRS-3100 (JASCO) microspectrometer at the Department of Geology and Mineralogy, Kyoto University, Japan. Raman spectra in Bratislava were excited using the 532 nm line of a Nd:YAG laser, with power emission conditions of 10 mW. An objective lens of 100 \times and a slit or pinhole aperture of 25 μm were used; peak position was calibrated with a polystyrene standard. Each spectrum was collected in two accumulations of 3–30 s to eliminate cosmic ray signals. In Kyoto, Raman analyses were performed with the 532 nm line of a diode-pumped solid-state laser with power emission of 3 mW on the sample surface. An objective lens of 100 \times or 250 \times and a pinhole aperture of 50 μm were used. Peak position was calibrated with 520.7 cm^{-1} of a Si wafer. All measurements were performed at room temperature and Fityk version 0.9.8 (Wojdyr, 2010) was used for spectra analysis and peak fitting.

A field-emission scanning electron microscope (F-SEM), a JEOL JSM 7600F equipped with an EDAX microanalytical system (EDS), was used for observations of microdiamond morphology at the Institute of Materials and Machine Mechanics, Slovak Academy of Sciences, Bratislava. The images were acquired in secondary-electron (SE) mode at 10 kV voltage.

Laser ablation inductively coupled plasma mass spectrometry (LA-ICP-MS) analysis for determination of trace elements and elemental imaging was performed in CEITEC, Masaryk University, Brno, Czech Republic, using instrumentation consisting of a laser ablation system UP213 (NewWaveResearch) and a quadrupole ICP-MS Agilent 7500 ce. The ablated material was transported from the ablation cell into the ICP system by He (1.0 l min $^{-1}$) and Ar (0.6 l min $^{-1}$), which were admixed into a He flow prior to entering the torch. The optimization of LA-ICP-MS parameters was performed using the NIST610 standard with respect to the sensitivity to maximum of S/N ratio of ^7Li , ^{89}Y , ^{232}Th . LA was performed in two modes: (1) single-spot analysis, which was used for analysis of individual points on the sample; (2) line-scan mode employed for elemental mapping. Single-

spot analyses were performed with a fluence of 4 J cm^{-2} , a spot diameter of $40 \mu\text{m}$, a repetition rate of 10 Hz, 30 s pre-ablation time for recording of background intensities of measured isotopes, and 60 s ablation time. The isotope ^{28}Si was used as the internal standard. Elemental mapping was performed with a fluence of 4 J cm^{-2} , a spot diameter of $40 \mu\text{m}$, a repetition rate of 10 Hz, a scan speed of $40 \mu\text{m s}^{-1}$, and a spacing between lines of $40 \mu\text{m}$. The size of the analysed area was $2560 \mu\text{m} \times 2360 \mu\text{m}$. Resulting elemental maps consist of $3900 (65 \times 60)$ pixels. Twenty-five isotopes with total integration time of 1.000 s were determined and ^{28}Si was used as the internal standard.

Zirconium concentrations in rutile obtained by LA-ICP-MS were used for Zr-in-rutile thermometry calibrated by Tomkins *et al.* (2007). To calculate a temperature, equation (9) of Tomkins *et al.* (2007) was used for $P < 39 \text{ kbar}$, and equation (10) for $P > 39 \text{ kbar}$.

RESULTS

Petrography and mineral chemistry

The diamond-bearing gneiss (Fig. 2a) is a medium- to coarse-grained rock showing an inhomogeneous, partly migmatitic texture owing to partial melting, which is strongly deformed and foliated. The deformed matrix consists mostly of dynamically recrystallized quartz, fine-grained biotite, white mica, rutile, and abundant flaky graphite. Porphyroblasts of pink garnet, blue kyanite and dark brown biotite occur within the melanocratic domains, whereas K-feldspar, plagioclase and undulose quartz form leucocratic layers and veins. Representative modal, mineral and whole-rock analyses are shown in Tables 1–4; mineral abbreviations are according to Whitney & Whitney (2010).

Among major rock-forming minerals, garnet forms sub- to euhedral porphyroblasts (Fig. 2b–f) up to 5 mm in diameter (Fig. 2e) with abundant inclusions. These are mostly of quartz, plagioclase, K-feldspar, biotite, white mica, rutile, zircon, apatite, monazite, and microdiamond or graphite. (For the distribution of diamond see Fig. 2c, d and f). Some of the quartz inclusions in garnet are surrounded by radial cracks indicating breakdown of coesite (Fig. 2f inset). Several inclusions in garnet are multiphase, commonly quartz + plagioclase, quartz + white mica + K-feldspar, quartz + plagioclase + biotite, quartz + plagioclase + K-feldspar (Fig. 2e). Kyanite forms prismatic porphyroblasts (Ky I) up to 5 mm in length in the matrix, commonly deformed and fractured (Fig. 2b), with inclusions of zircon, rutile, monazite, quartz and rarely graphitic carbon and diamond. In contrast, a very minor, fine-grained kyanite (Ky II) identified by Raman spectroscopy occurs in the quartz-feldspathic matrix around some garnet grains. Biotite forms red-brownish porphyroblasts growing along the rims and fractures inside garnet and kyanite (Fig. 2b). It has similar Fe and Mg concentrations (Mg#

0.51) and low TiO_2 contents (2.3 wt %). Biotite included in garnet is more Al- and Ti-rich (17.6 wt % Al_2O_3 , 3.9 wt % TiO_2). White mica occurs as inclusions in garnet and in the matrix as medium- to coarse-grained flakes. The white mica composition is muscovite to phengite; Si varies from 3.12 to 3.23 atoms per 11 oxygens regardless of the textural context. Abundant K-feldspar and plagioclase are found in the matrix and as inclusions in garnet, commonly together with quartz. The composition of plagioclase in both the matrix and inclusions in garnet is mostly An_{30-35} , with $\text{CaO} = 6-7 \text{ wt } \%$ and $\text{SrO} = 0.06-0.07 \text{ wt } \%$. Rarely, Ca-rich plagioclase with up to 13 wt % CaO (An_{58-62}) was found within the inclusions in garnet (Fig. 3a–d). Rutile occurs as subhedral, red-brown grains in the matrix and inclusions in garnet; rutile also forms oriented needles in garnet and is further associated with microdiamonds in polyphase inclusions. A large rutile enclosed by garnet (Fig. 2f) was analysed for Zr by LA-ICP-MS. All OH-bearing minerals (micas, allanite) are of chlorine type without detectable fluorine. Further details on monazite, diamond and associated accessory minerals are given below.

Garnet major and trace element chemistry

Compositional maps and profiles of garnet porphyroblasts show the distribution of major and trace elements (Figs 3–6). From core to the rim there is a decrease in Ca and Mn and increase in Mg and Fe expressed by grossular (X_{Grs}), spessartine (X_{Spss}), pyrope (X_{Prp}) and almandine (X_{Alm}) contents; diamond and monazite occur in the rim of garnet (Fig. 3). In contrast, increase in Ca and decrease in Mg is observed at the rims of some garnets penetrated by plagioclase and biotite from the matrix (Fig. 4a–d). Enrichment in Ca within garnet rims has been observed in UHP rocks that underwent partial melting during decompression (e.g. Terry *et al.*, 2000; Stöckhert *et al.*, 2001) and in experiments on dehydration-melting (Auzanneau *et al.*, 2006). Compositional zoning of observed garnets thus suggests occurrence of two generations of garnet, interpreted as a consequence of (1) prograde growth forming UHP garnet (Grt I) with inclusions of diamond and monazite, and (2) partial melting reaction forming a minor, Ca-rich garnet (Grt II) at post-UHP stage.

Trace elements (REE Y, Ti, Cr) were analysed by LA-ICP-MS in garnets of various size (Figs 3f, 4f, 5e and 6). Six garnets of both types were analysed in nine profiles from several thin sections representing two different portions of the rock (see modes in Table 4). Yttrium and REE are significantly higher in garnet I from thin section ML-6-12 LA, with a much lower monazite content: Y in garnet varies from 100 to 1300 ppm, Yb from 50 to 400, and Lu from 5 to 60 ppm. Garnet I in ML-6-12 A, although rich in monazite is poorer in trace elements, Y varying between 50 and 400 ppm, Yb between 5 and 120 ppm, and Lu between 1 and 20 ppm. Garnet II Ca-rich overgrowths (6.5–7 wt % CaO) were analysed in

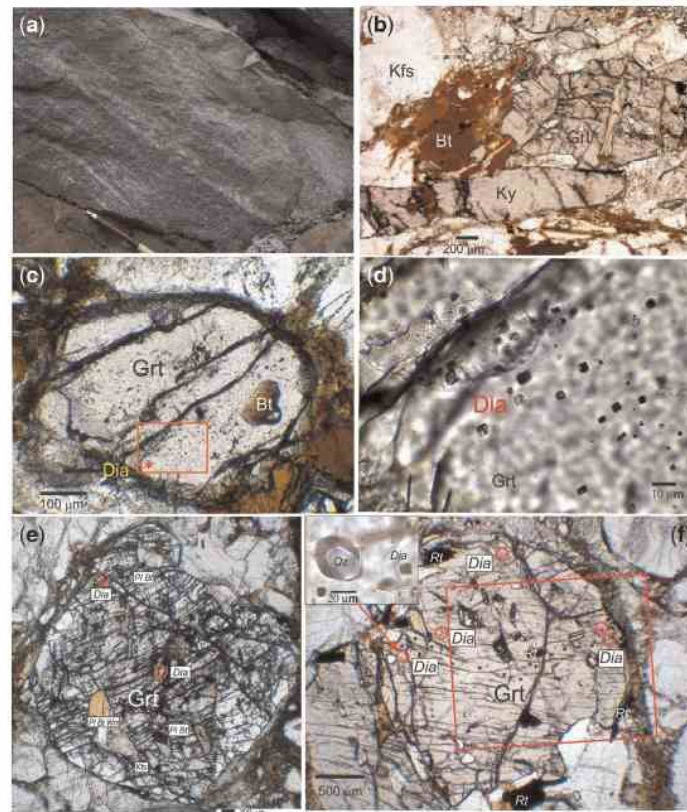


Fig. 2. (a) Photograph of the kyanite–garnet gneiss (sample ML-6-12) with leucocratic, quartzo-feldspathic layers of partial melting. (b) Photomicrograph of the typical texture showing garnet (Grt), kyanite (Ky) and biotite (Bt) porphyroblasts within the quartzo-feldspathic matrix (Kfs). (c) Diamond-bearing inclusions in garnet. (d) Close-up of diamond-bearing inclusions showing the same orientation marked by a rectangle in (c). (e) Diamond inclusions (Dia) in garnet, sample ML-6-12 LA, and (f) sample ML-6-12 A marked by circles. Inset shows the detail of diamond and quartz with radial cracks. Red rectangle marks the area of the X-ray maps shown in Fig. 3. For all microphotographs, (b)–(f), transmitted, plane-polarized light was used.

thin sections ML-6-12 LA and C, typically showing strong depletion in HREE and Y (Fig. 4f), and slight enrichment in LREE, Cr and Ti. Yttrium and HREE profiles in garnet I have generally similar patterns, with a central peak and rim shoulders varying according to the position of the section with respect to the garnet centre. The central peak is usually moderate or weak, except for the large garnet in ML-6-12 LA (Fig. 5e), which shows a prominent central peak. Variable rim enrichment in Y and HREE is observed in all garnets. The same is also shown by the Y distribution (Fig. 6a). The shoulders steeply decrease towards the garnet rims. In some profiles a rimward shift in the position of shoulders is observed from HREE to LREE. The correlation of the normalized HREE patterns with position in the profile shows a moderate decrease from the central peak position to a minimum, then a pronounced increase at rim shoulders, followed by a marked drop of the heaviest REE at very rim (Fig. 6b).

Diamond

Diamond, identified by Raman spectroscopy, occurs as inclusions in garnet, zircon and kyanite I. Diamond-bearing inclusions in host garnet commonly occur as clusters, distributed mostly in the outer part of garnet, except for the outermost, narrow rim (Fig. 2c–f). As shown in Figs 3–5, diamond occurs in garnet I, in some cases together with monazite, whereas diamond and monazite are absent in garnet II.

Diamond-bearing inclusions of cuboid, negative crystal shape in many cases share the same orientation (Figs 2c, d and 7a, b). The size of inclusions is variable from c. 1 to 7 μm in diameter, and the colour is translucent, light brown to yellow or deep brown to opaque in transmitted light (Fig. 7). Diamond itself occurs as a single-crystal inclusion (Fig. 7a) or it is present in poly-phase inclusions (Fig. 7b and d). The Raman peaks of the investigated diamonds are centred between 1333 and 1332 cm^{-1} and their full width at half maximum

Table 1: Garnet major and trace element compositions along the profile (Fig. 5b, black line)

| Point: | an 1 | an 2 | an 3 | an 4 | an 5 | an 6 | an 7 | an 8 | an 9 | an 10 | an 11 | an 12 | an 13 |
|--------------------------------|--------|--------|--------|--------|--------|--------|--------|--------|--------|--------|--------|--------|--------|
| SiO ₂ | 37.90 | 37.98 | 38.19 | 37.68 | 37.70 | 37.63 | 37.61 | 37.60 | 37.52 | 37.83 | 37.58 | 37.43 | 37.70 |
| TiO ₂ | 0.02 | 0.05 | 0.09 | 0.01 | 0.04 | 0.05 | 0.03 | 0.03 | 0.03 | 0.08 | 0.06 | 0.05 | 0.01 |
| Al ₂ O ₃ | 21.32 | 21.57 | 21.54 | 21.29 | 21.27 | 21.04 | 21.10 | 21.08 | 21.21 | 21.16 | 21.40 | 21.30 | 21.32 |
| FeO | 31.62 | 31.45 | 30.87 | 31.18 | 30.73 | 29.26 | 29.39 | 29.80 | 28.98 | 29.90 | 30.08 | 30.05 | 31.67 |
| MnO | 1.22 | 1.15 | 1.19 | 1.33 | 1.59 | 1.71 | 1.77 | 1.77 | 2.28 | 1.44 | 1.05 | 1.10 | 1.09 |
| MgO | 4.98 | 5.13 | 4.90 | 4.87 | 4.41 | 4.03 | 4.11 | 3.77 | 3.19 | 4.15 | 3.79 | 4.30 | 4.70 |
| CaO | 3.28 | 3.61 | 4.05 | 3.46 | 4.51 | 5.59 | 5.23 | 5.73 | 6.80 | 5.38 | 6.17 | 5.15 | 3.43 |
| Total | 100.34 | 100.93 | 100.83 | 99.81 | 100.26 | 99.32 | 99.23 | 99.78 | 100.01 | 99.05 | 100.13 | 99.38 | 99.92 |
| X _{Frp} | 0.24 | 0.25 | 0.23 | 0.23 | 0.21 | 0.20 | 0.19 | 0.17 | 0.18 | 0.14 | 0.17 | 0.20 | 0.23 |
| X _{Grs} | 0.09 | 0.10 | 0.11 | 0.10 | 0.13 | 0.15 | 0.15 | 0.16 | 0.17 | 0.19 | 0.17 | 0.15 | 0.10 |
| X _{Alm} | 0.69 | 0.68 | 0.67 | 0.68 | 0.67 | 0.65 | 0.65 | 0.65 | 0.64 | 0.64 | 0.66 | 0.66 | 0.70 |
| X _{Sps} | 0.03 | 0.03 | 0.03 | 0.03 | 0.04 | 0.04 | 0.04 | 0.04 | 0.04 | 0.05 | 0.02 | 0.02 | 0.02 |
| Sc | 102.0 | 81.9 | 64.3 | 127.8 | 118.3 | 129.6 | 136.1 | 117.5 | 125.7 | 97.6 | 43.9 | 89.8 | 65.7 |
| Ti | 63.9 | 468.6 | 125.1 | 86.6 | 223.1 | 652.9 | 1636.5 | 218.8 | 776.4 | 437.6 | 751.6 | 231.2 | 496.5 |
| Cr | 41.0 | 27.2 | 40.9 | 42.2 | 8.4 | 29.2 | 36.3 | 34.9 | 28.2 | 28.0 | 30.5 | 40.2 | 33.3 |
| Y | 307.3 | 104.4 | 212.0 | 402.6 | 457.3 | 821.7 | 740.6 | 810.8 | 445.2 | 87.9 | 47.0 | 197.5 | 59.9 |
| Zr | 1.21 | 1.46 | 0.93 | 2.63 | 1.95 | 1.10 | 2.14 | 0.58 | 1.36 | 2.73 | 3.07 | 1.41 | 18.92 |
| La | b.d.l. | 0.24 | b.d.l. | b.d.l. | b.d.l. |
| Ce | b.d.l. | b.d.l. | b.d.l. | 0.21 | b.d.l. | b.d.l. | b.d.l. | b.d.l. | 0.49 | 0.43 | b.d.l. | b.d.l. | 0.26 |
| Pr | b.d.l. | b.d.l. | b.d.l. | b.d.l. | b.d.l. | 0.13 | b.d.l. | b.d.l. | b.d.l. | 0.19 | b.d.l. | b.d.l. | b.d.l. |
| Nd | b.d.l. | 0.96 | b.d.l. | 1.46 | b.d.l. | b.d.l. | 0.71 | b.d.l. | 1.19 | 2.06 | 0.73 | 1.07 | 1.27 |
| Sm | 4.0 | 2.9 | 2.2 | 3.6 | 2.1 | 2.0 | 3.0 | 2.4 | 1.2 | 3.1 | 2.6 | 4.2 | 4.4 |
| Eu | 0.29 | 0.44 | 0.37 | 0.16 | 0.32 | 0.33 | 0.36 | 0.32 | 0.60 | 0.40 | 0.93 | 0.38 | 0.76 |
| Gd | 9.5 | 11.8 | 9.8 | 3.9 | 12.5 | 8.9 | 9.4 | 9.1 | 6.3 | 7.1 | 8.9 | 10.0 | 10.9 |
| Tb | 3.5 | 3.9 | 3.6 | 5.2 | 3.8 | 3.3 | 3.4 | 3.4 | 3.4 | 2.2 | 1.6 | 3.6 | 2.6 |
| Dy | 39.6 | 24.7 | 37.9 | 57.9 | 52.3 | 68.0 | 77.4 | 69.2 | 45.0 | 17.0 | 9.5 | 30.2 | 14.7 |
| Ho | 11.7 | 3.6 | 10.1 | 14.8 | 16.6 | 27.3 | 26.3 | 27.4 | 13.2 | 4.0 | 2.5 | 6.4 | 2.2 |
| Er | 42.7 | 7.8 | 32.6 | 47.5 | 77.7 | 104.7 | 97.4 | 108.7 | 55.6 | 13.1 | 6.6 | 15.0 | 6.7 |
| Tm | 7.6 | 1.0 | 5.0 | 6.6 | 13.6 | 17.6 | 17.3 | 16.3 | 8.0 | 1.9 | 1.2 | 1.9 | 1.0 |
| Yb | 62.7 | 5.2 | 37.4 | 49.7 | 98.8 | 108.5 | 117.4 | 117.5 | 61.7 | 13.2 | 8.6 | 10.7 | 10.4 |
| Lu | 8.8 | 1.1 | 5.0 | 6.1 | 13.7 | 11.3 | 11.6 | 12.6 | 8.5 | 2.2 | 1.3 | 1.3 | 1.0 |
| Hf | 0.28 | b.d.l. | 0.20 | 0.13 | 0.22 | 0.13 | b.d.l. | 0.19 | 0.26 | 0.45 | 0.13 | 0.27 | 0.71 |
| Th | b.d.l. | 0.15 | b.d.l. | 0.14 | b.d.l. | b.d.l. | b.d.l. | b.d.l. | b.d.l. | 0.46 | 0.18 | b.d.l. | 0.16 |
| U | b.d.l. | b.d.l. | 0.29 | b.d.l. | 0.21 | 0.16 | 0.28 | 0.12 | 0.25 | b.d.l. | 0.19 | b.d.l. | 0.27 |

b.d.l., below detection limit. Major elements by electron microprobe (wt %); trace elements by LA-ICP-MS (ppm).

(FWHM) varies between 3.6 and 6.9 cm⁻¹ (Fig. 8). Some Raman spectra show bands near 1580 and 1350 cm⁻¹ (Fig. 8) characteristic of the sp²-bonded graphitic carbon (G and D1 bands). Carbonates in the polyphase inclusions with diamond show Raman bands between 1097 and 1087 cm⁻¹ corresponding to Mg-Fe (magnesite, siderite) and Ca-Mg (dolomite, Mg-calcite) carbonates. High-resolution SE images of such polyphase inclusions in garnet (Fig. 7c) show cohesive contacts between host garnet, diamond and carbonate. Raman analysis also revealed the rare presence of CO₂ with diamond and carbonate (Fig. 8c). The Raman band of the diamond associated with CO₂ is shifted to 1329 cm⁻¹ and wider (FWHM = 20.1 cm⁻¹; Fig. 8b) than other diamond peaks. The Raman bands at 1386, 1282 and 1092 cm⁻¹ (Fig. 8b) indicate CO₂ and Mg-Fe carbonate (magnesite-siderite). Diamond and graphitic carbon inclusions in zircon are of 0.5–2 μm size located in the inner parts of the host zircon (Fig. 7e). Microdiamond of 5 μm size (Fig. 7f) and several inclusions of graphitic carbon have been found in kyanite I. Monazite shows only inclusions of graphitic or amorphous carbon (Fig. 7g and h). The Raman peaks of diamond and graphitic carbon inclusions in zircon are shown in Fig. 8e, those of graphitic and amorphous carbon in monazite in Fig. 8f, and those of diamond in kyanite I in Fig. 8g. Carbonate

inclusions in zircon and monazite, identified by Raman analysis, are Ca-Mg carbonates (dolomite, Mg-calcite).

Monazite occurrence and composition

Monazite of 50–200 μm size occurs as inclusions in garnet and kyanite I (Figs 7g, 9a, b and 10a, c) but mostly in the matrix composed of feldspars, biotite, white mica, and quartz (Figs 9e, f and 10e). The sample portion represented by thin section ML-6-12 LA is markedly poorer in monazite (Table 4), which corresponds to higher Y and HREE contents in coexisting garnets. Monazite is found partly or completely enclosed in the outer zones of garnet I close to the diamond and graphitic carbon inclusions (Fig. 7g). Monazite inclusions in kyanite are in many cases associated with zircon (Fig. 10a). The matrix-located monazite is partially broken down to apatite and REE-rich epidote, which form reaction coronas around it (Figs 9e, f and 10e), whereas the monazite crystals enclosed by garnet and kyanite are intact. The extent of this replacement is variable, partly depending on the section position, from thin rims up to major parts of the volume converted to apatite and allanite. The corona is distinctly zoned with apatite forming an inner zone, REE-epidote/allanite an outer zone, and a discontinuous ring of secondary Th-, U- and Y-

Table 2: Representative electron microprobe analyses of biotite, muscovite, plagioclase and K-feldspar

| Mineral: Point: | LA Bt an 21 | A Bt an 14 | A Bt an 7 | A Ms an 16 | A Ms an 10 | LA Pl an 23 | A Pl an 13 | A Pl an 11 | A Kfs an 8 | C Kfs an 12 | |
|--------------------------------|-------------------|------------------|-----------------|------------------|------------------|--------------------------------|------------------|------------------|------------------|-------------------|--------|
| SiO ₂ | 36.45 | 36.39 | 36.87 | 48.57 | 46.32 | SiO ₂ | 59.27 | 51.55 | 59.93 | 64.02 | 64.64 |
| TiO ₂ | 4.00 | 3.92 | 2.31 | 1.35 | 0.24 | Al ₂ O ₃ | 24.98 | 29.26 | 25.24 | 18.92 | 20.05 |
| Al ₂ O ₃ | 17.94 | 17.36 | 18.88 | 33.48 | 35.15 | FeO | 0.14 | 0.16 | 0.01 | 0.19 | 0.06 |
| FeO | 16.30 | 16.59 | 16.48 | 1.38 | 1.45 | CaO | 6.76 | 12.73 | 7.23 | 0.02 | 0.04 |
| MnO | 0.00 | 0.03 | 0.02 | 0.00 | 0.03 | Na ₂ O | 8.02 | 4.29 | 7.24 | 0.85 | 1.12 |
| MgO | 10.06 | 9.91 | 10.80 | 1.49 | 0.56 | K ₂ O | 0.24 | 0.07 | 0.24 | 15.60 | 14.92 |
| CaO | 0.18 | 0.01 | 0.03 | 0.03 | 0.12 | BaO | 0.00 | 0.00 | 0.00 | 0.22 | 0.19 |
| Na ₂ O | 0.10 | 0.05 | 0.07 | 0.20 | 0.34 | SrO | 0.00 | 0.03 | 0.06 | 0.00 | 0.00 |
| K ₂ O | 9.24 | 9.75 | 9.69 | 9.19 | 10.84 | Total | 99.42 | 98.09 | 98.95 | 99.80 | 101.02 |
| Cr ₂ O ₃ | 0.02 | 0.06 | 0.00 | 0.00 | 0.02 | Si | 2.664 | 2.386 | 3.076 | 2.969 | 2.947 |
| Cl | 0.14 | 0.17 | 0.15 | 0.01 | 0.00 | Al | 1.323 | 1.596 | 0.006 | 1.034 | 1.077 |
| H ₂ Oc | 3.99 | 3.97 | 3.99 | 4.56 | 4.50 | Fe ²⁺ | 0.005 | 0.006 | 1.083 | 0.007 | 0.002 |
| Total | 98.43 | 98.20 | 99.30 | 100.24 | 99.58 | X | 3.992 | 3.989 | 4.165 | 4.010 | 4.026 |
| O=Cl | -0.03 | -0.04 | -0.03 | 0.00 | 0.00 | Ba | 0.000 | 0.000 | 0.000 | 0.004 | 0.003 |
| Total | 98.40 | 98.17 | 99.26 | 100.24 | 99.58 | Ca | 0.326 | 0.631 | 0.375 | 0.001 | 0.002 |
| Si | 5.513 | 5.545 | 5.527 | 6.367 | 6.191 | Na | 0.699 | 0.385 | 0.747 | 0.076 | 0.099 |
| Al ^{IV} | 2.487 | 2.455 | 2.473 | 1.633 | 1.809 | K | 0.014 | 0.004 | 0.010 | 0.923 | 0.867 |
| X | 8.000 | 8.000 | 8.000 | 8.000 | 8.000 | Sr | 0.000 | 0.002 | 0.004 | 0.000 | 0.000 |
| Al ^{VI} | 0.711 | 0.663 | 0.862 | 3.540 | 3.728 | Z | 1.039 | 1.022 | 1.137 | 1.004 | 0.972 |
| Ti | 0.455 | 0.449 | 0.260 | 0.133 | 0.024 | Cat. | 5.031 | 5.011 | 5.302 | 5.014 | 4.998 |
| Fe ²⁺ | 2.061 | 2.114 | 2.066 | 0.151 | 0.162 | Cs | 0.000 | 0.000 | 0.000 | 0.004 | 0.004 |
| Mn | 0.000 | 0.003 | 0.003 | 0.000 | 0.003 | Ab | 0.673 | 0.377 | 0.659 | 0.076 | 0.102 |
| Mg | 2.267 | 2.251 | 2.414 | 0.291 | 0.111 | Or | 0.013 | 0.004 | 0.009 | 0.919 | 0.893 |
| Cr | 0.003 | 0.007 | 0.000 | 0.000 | 0.002 | An | 0.314 | 0.619 | 0.331 | 0.001 | 0.002 |
| Y | 5.497 | 5.487 | 5.604 | 4.116 | 4.030 | Total | 1.000 | 1.000 | 1.000 | 1.000 | 1.000 |
| Ca | 0.029 | 0.001 | 0.005 | 0.004 | 0.017 | | | | | | |
| Na | 0.030 | 0.015 | 0.019 | 0.050 | 0.089 | | | | | | |
| K | 1.783 | 1.895 | 1.854 | 1.537 | 1.849 | | | | | | |
| Z | 1.841 | 1.912 | 1.878 | 1.590 | 1.955 | | | | | | |
| Total | 15.338 | 15.399 | 15.482 | 13.706 | 13.985 | | | | | | |
| Cl | 0.037 | 0.043 | 0.039 | 0.002 | 0.001 | | | | | | |
| OH | 3.963 | 3.957 | 3.961 | 3.998 | 3.999 | | | | | | |
| Ani. | 4.000 | 4.000 | 4.000 | 4.000 | 4.000 | | | | | | |
| Cat. | 15.338 | 15.399 | 15.482 | 13.706 | 13.985 | | | | | | |

Formulae based on 22 oxygens (micas) and 8 oxygens (feldspars).

rich phases between them (Fig. 10f). The REE-rich epidote/allanite (compositions lie around the 50% dividing line) crystals are usually cemented by REE-rich carbonate (Fig. 9e).

The monazite composition according to major elements corresponds to 84–86 mol % monazite, 7–11 mol % of cheralite, 1–2 mol % of huttonite, and 1.7–2.5 mol % of xenotime. Thorium content is moderate between 3 and 6 wt % ThO₂, with a maximum of 8 wt %. Uranium varies more, from 0.2 to 1.2 wt % UO₂. Compositional maps of Y, Th and U concentrations in the selected monazite crystals are shown in Fig. 10b, d and f. The monazites enclosed in garnet have slightly lower Y and, owing to similar small ionic radii, show also low UO₂ (0.2–0.6 wt %). All REE were analysed by electron microprobe, but only those from La to Dy were evaluated because the heavier REE have scattered values at or below the microprobe detection limit. Yttrium can be used as a proxy for Ho, which is possible because of the same charge and similar ionic radii (Shannon, 1976). For comparison, three complete monazite analyses obtained by LA-ICP-MS are shown together with average ($n=115$) microprobe analyses indicating twofold underestimation of Ho by microprobe (Fig. 11). The REE

in monazites show typical enrichment in LREE, distinct negative Eu anomalies, and variable Y concentrations (Fig. 10b, d and f). Whereas monazites found in the matrix and enclosed in kyanite form a homogeneous group with increased Y (2500–7500 times chondrite), those found enclosed in garnet have lower Y, typically between 1000 and 2000 times chondrite (Fig. 12). Europium anomalies are similar with Eu/Eu* varying from 0.24 down to 0.07. The monazites only partly enclosed by garnet have the same compositions as those found in the matrix.

The REE-epidote from coronas shows a positive Eu anomaly (Eu/Eu* 1.7–2.8), and low ThO₂ (0.6–1 wt %), HREE, and Y (Fig. 13a and b). By contrast, the REE-carbonates have REE patterns similar to that of monazite, except for the strongly depleted HREE and Y (300–600Y_N), moderate ThO₂ (1.0–3.3 wt %) and detectable F (Fig. 13c).

Th–U–Pb dating of monazite

Th–U–Pb chemical age dating was used to date 31 monazite crystals by 107 point analyses (samples ML-6-12 A, C and LA; see Supplementary Data Electronic Appendix 1) in several domains of monazite crystals

Table 3: Selected electron microprobe analyses of monazite, REE-epidote/allanite and REE-carbonate

| In: | G m1/1 | G m1/2 | G m1/3 | Ky m9/1 | Ky m9/2 | Ky m9/3 | M/C m10/1 | M/C m10/2 | M/C m13/1 | M/C m14/1 | M/C m14/2 | G/m6 REan1 | m10/C RCan3 |
|--------------------------------|-----------|-----------|-----------|------------|------------|------------|--------------|--------------|--------------|--------------|--------------|---------------|----------------|
| Age: | 480 | 454 | 490 | 461 | 475 | 470 | 490 | 476 | 470 | 471 | 467 | n.a. | n.a. |
| 2σ: | 23 | 24 | 26 | 17 | 28 | 25 | 29 | 25 | 21 | 24 | 17 | n.a. | n.a. |
| SiO ₂ | 0.03 | 0.01 | 0.02 | 0.01 | 0.01 | 0.02 | 0.03 | 0.03 | 0.02 | 0.01 | 0.02 | 0.00 | 0.11 |
| P ₂ O ₅ | 29.43 | 28.96 | 28.90 | 29.20 | 28.96 | 30.97 | 29.39 | 29.44 | 28.97 | 28.76 | 28.50 | n.a. | n.a. |
| SiO ₂ | 0.40 | 0.38 | 0.36 | 0.37 | 0.32 | 0.30 | 0.33 | 0.34 | 0.61 | 0.38 | 0.91 | 36.38 | 17.03 |
| TiO ₂ | n.a. | n.a. | n.a. | n.a. | n.a. | n.a. | n.a. | n.a. | n.a. | n.a. | n.a. | 0.16 | 0.87 |
| ThO ₂ | 5.81 | 5.39 | 4.95 | 5.23 | 4.33 | 4.07 | 3.27 | 3.93 | 6.01 | 5.55 | 7.98 | 0.69 | 0.96 |
| UO ₂ | 0.37 | 0.41 | 0.36 | 1.70 | 0.36 | 0.65 | 0.66 | 0.72 | 0.63 | 0.37 | 0.88 | 0.03 | 0.06 |
| Al ₂ O ₃ | n.a. | n.a. | n.a. | n.a. | n.a. | n.a. | n.a. | n.a. | n.a. | n.a. | n.a. | 22.82 | 8.74 |
| Y ₂ O ₃ | 0.25 | 0.44 | 0.48 | 1.36 | 0.73 | 0.65 | 0.88 | 0.76 | 0.56 | 0.25 | 0.69 | 0.15 | 0.15 |
| La ₂ O ₃ | 13.85 | 13.91 | 14.07 | 13.20 | 13.85 | 14.59 | 14.46 | 13.81 | 14.01 | 13.92 | 13.17 | 2.99 | 11.56 |
| Ce ₂ O ₃ | 27.97 | 27.82 | 28.09 | 26.23 | 27.78 | 28.57 | 28.69 | 27.93 | 27.34 | 28.00 | 26.20 | 6.35 | 21.16 |
| Pr ₂ O ₃ | 3.23 | 3.34 | 3.39 | 3.26 | 3.35 | 3.43 | 3.37 | 3.32 | 3.27 | 3.35 | 3.17 | 0.83 | 2.56 |
| Nd ₂ O ₃ | 12.02 | 12.25 | 12.07 | 11.58 | 12.26 | 11.98 | 12.15 | 12.28 | 12.05 | 12.33 | 11.78 | 2.37 | 9.92 |
| Sm ₂ O ₃ | 1.79 | 1.87 | 1.81 | 1.93 | 2.04 | 2.13 | 1.83 | 1.99 | 1.78 | 1.89 | 1.85 | 0.44 | 1.36 |
| Eu ₂ O ₃ | 0.07 | 0.09 | 0.04 | 0.12 | 0.08 | 0.16 | 0.12 | 0.12 | 0.08 | 0.09 | 0.08 | 0.20 | 0.14 |
| Gd ₂ O ₃ | 1.08 | 1.26 | 1.28 | 1.49 | 1.39 | 1.23 | 1.25 | 1.37 | 1.13 | 1.12 | 1.30 | 0.24 | 0.51 |
| Tb ₂ O ₃ | 0.03 | 0.10 | 0.06 | 0.16 | 0.14 | 0.11 | 0.10 | 0.10 | 0.07 | 0.05 | 0.09 | 0.01 | 0.10 |
| Dy ₂ O ₃ | 0.12 | 0.20 | 0.26 | 0.53 | 0.36 | 0.21 | 0.39 | 0.38 | 0.29 | 0.11 | 0.31 | 0.15 | 0.10 |
| Ho ₂ O ₃ | 0.00 | 0.00 | 0.00 | 0.06 | 0.00 | 0.00 | 0.03 | 0.01 | 0.00 | 0.01 | 0.00 | 0.00 | 0.02 |
| Er ₂ O ₃ | 0.28 | 0.28 | 0.28 | 0.39 | 0.30 | 0.34 | 0.26 | 0.32 | 0.33 | 0.32 | 0.27 | 0.24 | 0.31 |
| Tm ₂ O ₃ | 0.11 | 0.09 | 0.08 | 0.10 | 0.07 | 0.08 | 0.12 | 0.11 | 0.10 | 0.11 | 0.04 | 0.02 | 0.01 |
| Yb ₂ O ₃ | 0.09 | 0.09 | 0.07 | 0.16 | 0.11 | 0.17 | 0.13 | 0.15 | 0.08 | 0.07 | 0.11 | 0.04 | 0.09 |
| Lu ₂ O ₃ | 0.09 | 0.10 | 0.06 | 0.08 | 0.09 | 0.19 | 0.08 | 0.11 | 0.08 | 0.08 | 0.06 | 0.14 | 0.13 |
| FeO | 0.26 | 0.17 | 0.42 | 0.00 | 0.00 | 0.00 | 0.04 | 0.08 | 0.00 | 0.00 | 0.01 | 6.42 | 3.09 |
| CaO | 1.14 | 1.06 | 1.01 | 1.35 | 0.86 | 0.93 | 0.76 | 0.97 | 1.01 | 1.08 | 1.26 | 12.96 | 5.51 |
| SrO | 0.02 | 0.01 | 0.00 | 0.01 | 0.02 | 0.02 | 0.03 | 0.02 | 0.03 | 0.02 | 0.00 | 0.37 | 0.14 |
| PbO | 0.14 | 0.13 | 0.12 | 0.21 | 0.11 | 0.12 | 0.11 | 0.12 | 0.16 | 0.13 | 0.21 | | 0.05 |
| MnO | n.a. | n.a. | n.a. | n.a. | n.a. | n.a. | n.a. | n.a. | n.a. | n.a. | n.a. | 0.34 | 0.21 |
| MgO | n.a. | n.a. | n.a. | n.a. | n.a. | n.a. | n.a. | n.a. | n.a. | n.a. | n.a. | 0.31 | 0.36 |
| K ₂ O | n.a. | n.a. | n.a. | n.a. | n.a. | n.a. | n.a. | n.a. | n.a. | n.a. | n.a. | 0.02 | 0.05 |
| F | n.a. | n.a. | n.a. | n.a. | n.a. | n.a. | n.a. | n.a. | n.a. | n.a. | n.a. | 0.00 | 1.07 |
| Cl | n.a. | n.a. | n.a. | n.a. | n.a. | n.a. | n.a. | n.a. | n.a. | n.a. | n.a. | 0.00 | 0.04 |
| Total | 98.57 | 98.38 | 98.19 | 98.73 | 97.50 | 100.90 | 98.46 | 98.42 | 98.61 | 98.00 | 98.92 | 86.54 | |
| O = F | | | | | | | | | | | | 0.00 | 0.45 |
| O = Cl | | | | | | | | | | | | 0.00 | 0.01 |
| Total | | | | | | | | | | | | 96.41 | 86.08 |

m, monazite; G, garnet; Ky, kyanite; C, corona; M/C, matrix monazite with corona; RE, REE-epidote/allanite; RC, REE-carbonate (bastnäsite) in corona. Age and 2σ errors are given in Ma; n.a., not analysed.

(Fig. 10). The weighted average of all single-point dates yields an age of 472.4 ± 2.6 Ma [2σ, mean squared weighted deviation (MSWD) = 0.80]. A relatively wide range in U concentrations (0.2–1.5 wt %) makes the analysed set appropriate for calculation of a U/Pb versus Th/Pb isochron (Cocherie & Albarède, 2001). From the dataset seven points with ages >500 Ma were excluded, either owing to their too low or too high totals (<98, >102 wt %) or because of contamination by surrounding minerals (points close to monazite rim). The resulting isochron constructed from the same set of 107 individual measurements yields the centroid age of 472.4 ± 2.8 Ma, identical to the weighted average, and with a slightly higher MSWD of 1.07 (Fig. 14). The calculated centroid isochron lies just at the border of the tight error envelope close to the regression line, indicating insignificant U/Th mobility. The concordant centroid age is considered the best estimate of the real monazite age. In one case, we found an old age of 519 ± 32 Ma in a Y₂O₃-rich (1.503 wt %) monazite domain (Fig. 10f), which could represent an inherited core.

Table 4: Whole-rock (WR) major and trace elements in sample ML-6-12 by ICP ES/MS, and modal composition of two portions (LA, A) of ML-6-12 sample

| | wt % | | ppm | | ppm | LA (vol. %) | A (vol. %) |
|--------------------------------|-------|----|-------|----|-------|-------------|------------|
| SiO ₂ | 57.1 | Ba | 1058 | Zr | 304.1 | Grt | 19.57 |
| TiO ₂ | 1.03 | Ni | 30 | Y | 68.1 | Kfs | 27.42 |
| Al ₂ O ₃ | 19.48 | Sc | 20 | La | 90.6 | Ky | 1.83 |
| FeO | 7.341 | Ga | 24.5 | Ce | 182.8 | Pl | 10.27 |
| MnO | 0.15 | Hf | 8.4 | Pr | 21.72 | Qz | 17.21 |
| MgO | 2.11 | Nb | 26.3 | Nd | 84.3 | Bt | 17.21 |
| CaO | 2.95 | Rb | 191.8 | Sm | 16.67 | Ms | 4.84 |
| Na ₂ O | 1.81 | Sn | 3 | Eu | 2.2 | Rt | 0.46 |
| K ₂ O | 4.97 | Sr | 328.6 | Gd | 15.87 | Gr | 0.72 |
| P ₂ O ₅ | 0.59 | Ta | 1.7 | Tb | 2.29 | Ap | 0.065 |
| LOI | 1.3 | Th | 25.5 | Dy | 13.29 | Py | 0.33 |
| C | 0.19 | U | 4.9 | Ho | 2.5 | Zrn | 0.065 |
| S | 0.2 | V | 121 | Er | 7.61 | Mnz | 0 |
| Total | 99.22 | W | 6.4 | Tm | 1.21 | Total | 99.99 |
| | | | | Yb | 8.35 | | |
| | | | | Lu | 1.28 | | |

Thermodynamic modelling

Phase diagrams (*P*-*T* pseudo-sections) were calculated using the *Petrelle_X* software, version 6.7.2 (Connolly,

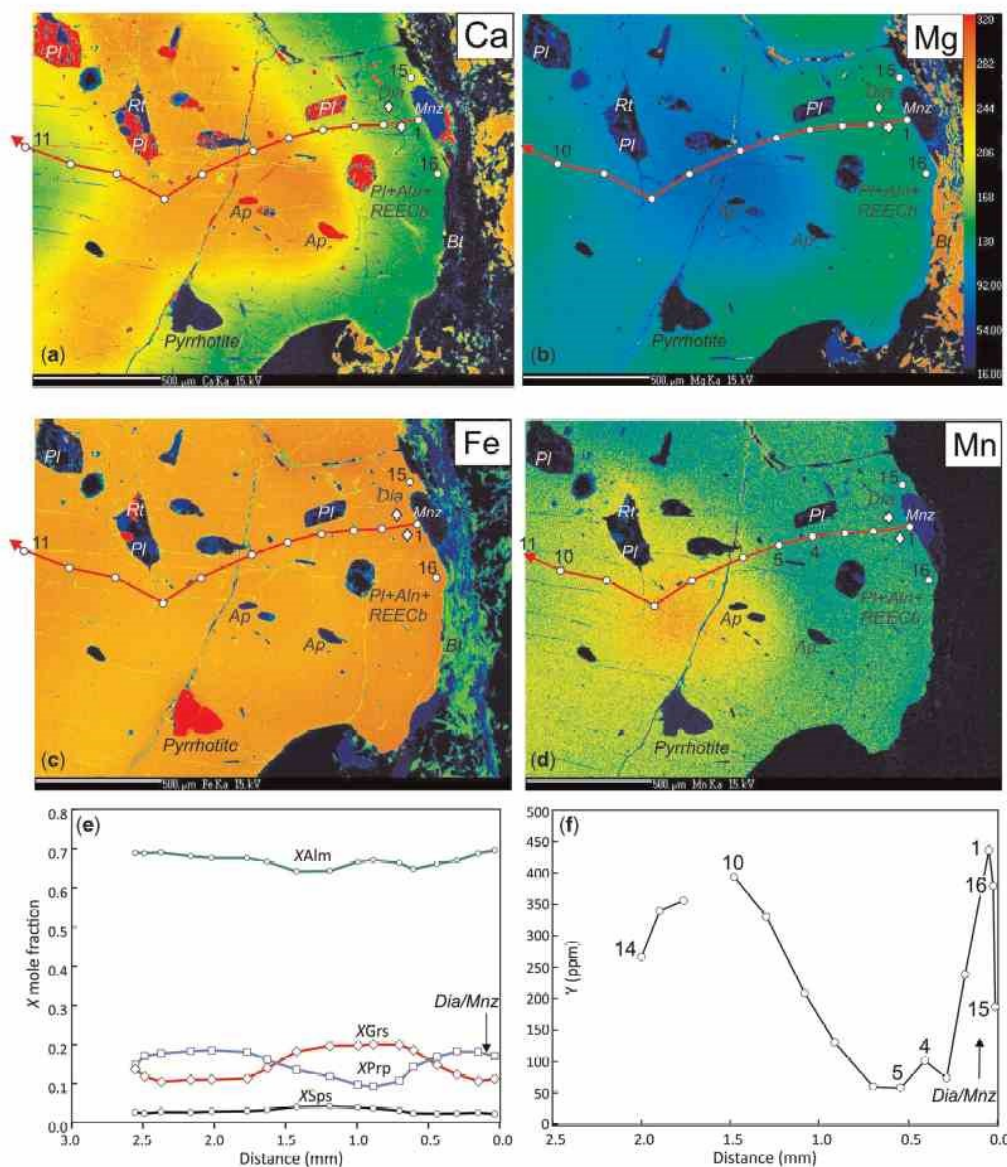


Fig. 3. (a–d) Garnet X-ray maps of Ca, Mg, Fe and Mn; (e) composition profile of X_{Alm} , X_{Prp} , X_{Grs} , X_{SpS} analysed by electron microprobe. (f) Yttrium concentrations analysed by LA-ICP-MS along the profile marked by an arrow. Position of diamond and monazite inclusions is also shown. Sample ML-6-12 A.

1990, 2005) with the internally consistent thermodynamic dataset of Holland & Powell (1998, updated in 2002: hp02ver.dat) to assess mineral assemblages that may have been present during UHP metamorphism. The bulk-rock composition (Table 4) was obtained by ICP-ES analysis and further modified for calculations. Minor elements, $Cr_2O_3 = 0.01$ wt % and $P_2O_5 = 0.59$ wt % have not been taken into account for the modelling.

Cr_2O_3 was neglected because it does not influence the stability of any mineral of the peak-pressure assemblage. The LREE budget shows that more than 95% of the P is bound in apatite and 5% in monazite, and therefore CaO was reduced according to the amount of phosphorus (corrected analysis in wt %: SiO_2 58.58, TiO_2 1.06, Al_2O_3 19.98, FeO 7.53, MnO 0.15, MgO 2.16, CaO 2.23, Na_2O 1.86, K_2O 5.1). P - T phase equilibrium diagrams (Fig. 15)

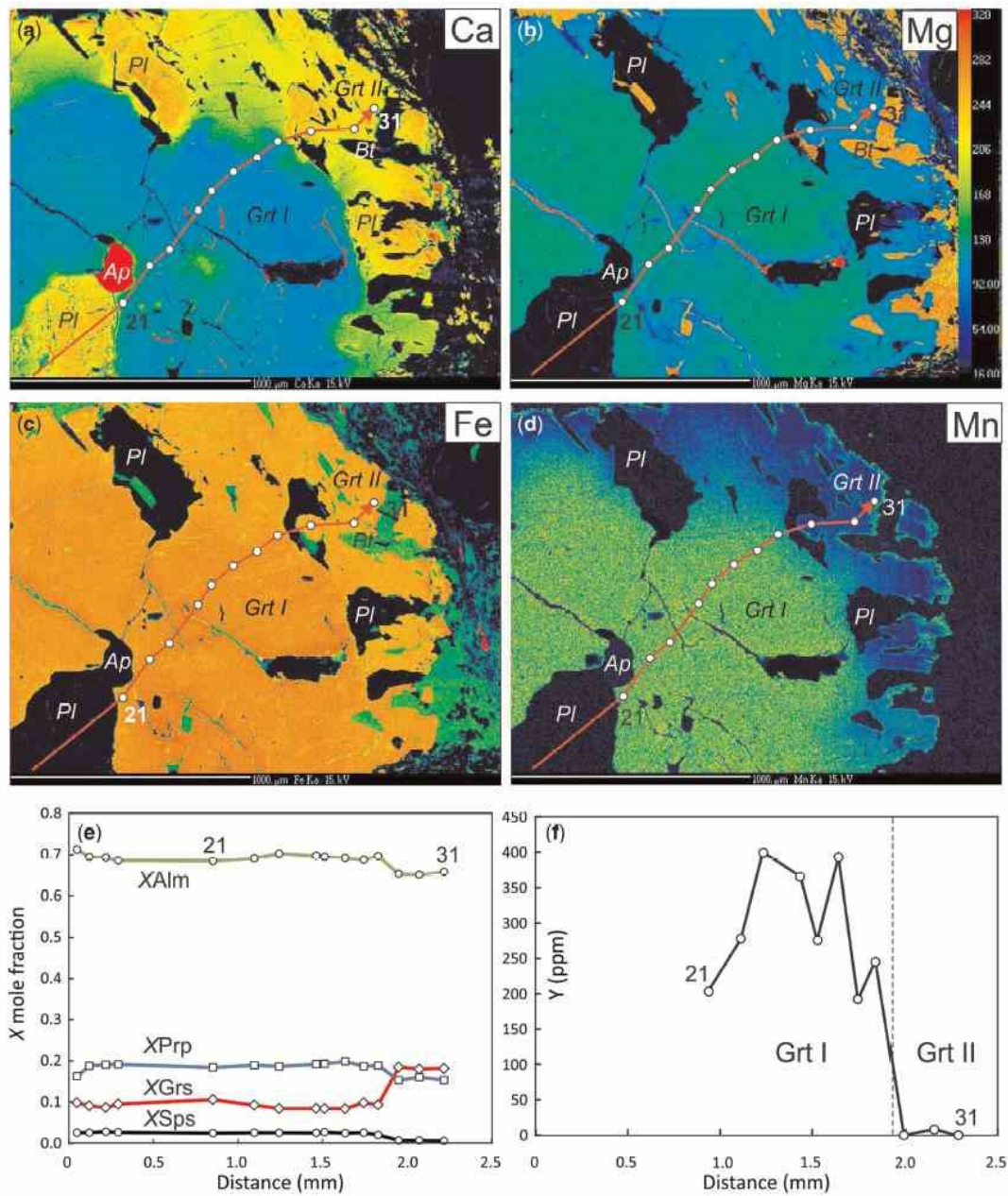


Fig. 4. (a–d) Garnet X-ray maps of Ca, Mg, Fe and Mn; (e, f) composition profile of X_{Alm} , X_{Prp} , X_{Grs} , X_{Sps} and Y. Garnet (Grt I) with Ca-rich (Grt II) rim penetrated by plagioclase and biotite. (e) Mole fractions of Alm, Grs, Prp and Sps. (f) Yttrium concentrations along the profile; Y was analysed by electron microprobe. Sample ML-6-12 C.

were calculated in the $\text{Na}_2\text{O}-\text{CaO}-\text{K}_2\text{O}-\text{FeO}-\text{MgO}-\text{MnO}-\text{Al}_2\text{O}_3-\text{SiO}_2-\text{H}_2\text{O}-\text{TiO}_2$ (NCKFMMnASHT) system with 2.1 wt % of H_2O . This content was chosen to prevent formation of K-feldspar at UHP conditions and to minimize

the amount of melt. This allowed for modelling of partial melting in the investigated rocks, approximating experiments on melting in subducted sedimentary rocks (e.g. Auzanneau *et al.*, 2006; Hermann & Spandler, 2008).

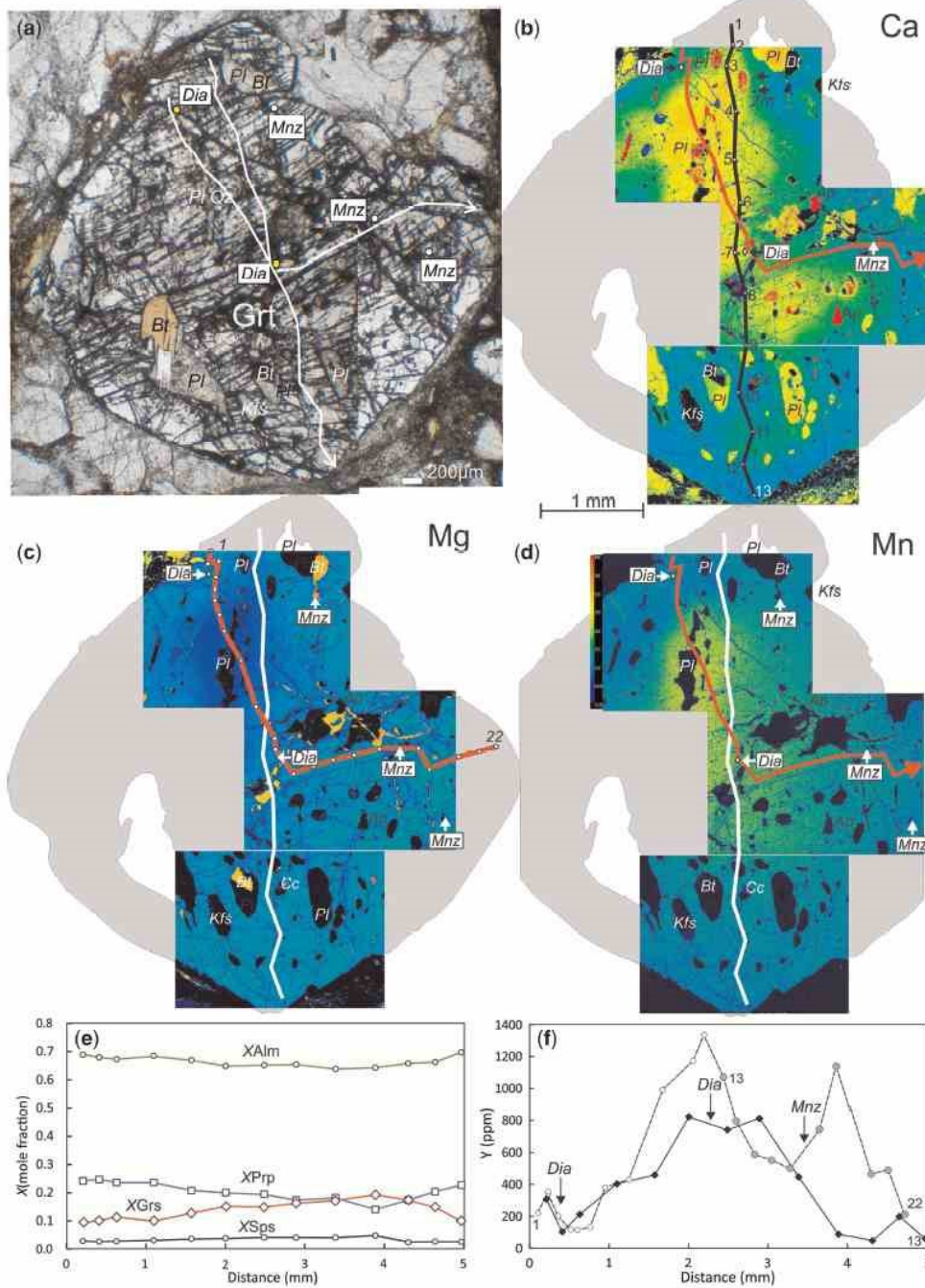


Fig. 5. (a) Garnet I porphyroblast photomicrograph; optical microscope, using transmitted, plane-polarized light. (b–d) X-ray maps of Ca, Mg and Mn analysed by electron microprobe. (e) Mole fractions of Alm, Grs, Prp and Sps. (f) Y concentrations analysed by LA-ICP-MS along two profiles (points 1–13 and 1–22). Position of diamond and monazite inclusions is also shown. Sample ML-6-12 LA.

Downloaded from https://academic.oup.com/ptrology/advance-article-abstract/doi/10.1093/ptrology/egz015/15613903 by Masarykova Univerzita user on 04 February 2020

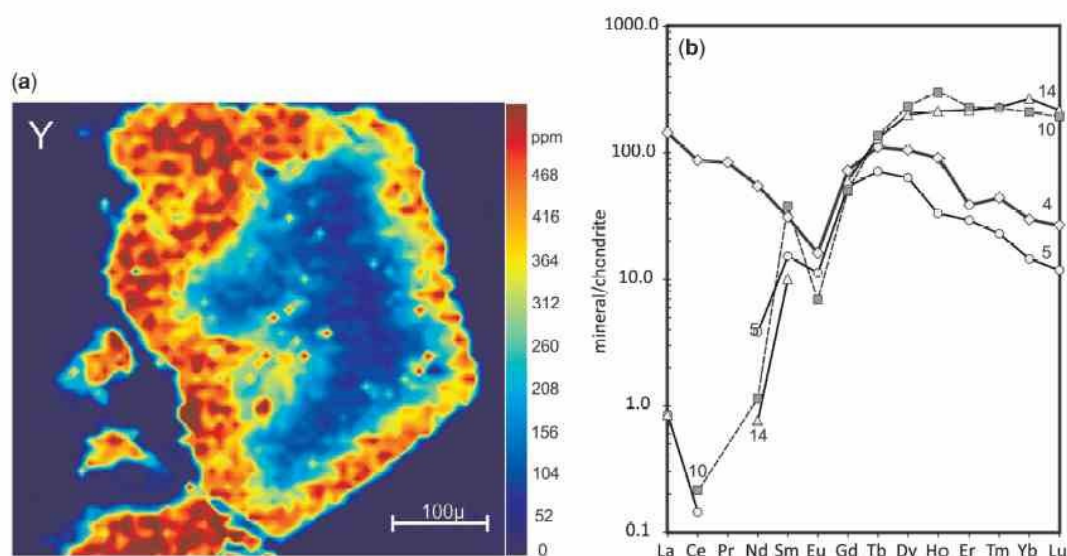


Fig. 6. (a) Yttrium distribution map of garnet (sample ML-6-12 C) analysed by LA-ICP-MS. Enrichment in Y observed in garnet rim corresponds to secondary peaks of Y in the profiles. (b) REE distribution patterns along the profile across the garnet in Fig. 3; numbers refer to the points in Fig. 3f. The elevated LREE values in point 4 are due to contamination by monazite.

Solution models of garnet (Ganguly *et al.*, 1996), phengitic white mica (Holland & Powell, 1998), omphacite (Green *et al.*, 2007), sanidine (Thompson & Hovis, 1979), plagioclase (Newton *et al.*, 1980), biotite (Tajčmanová *et al.*, 2009) and melt (Holland & Powell, 2001) were used as available from the *Perple_X* datafile (*solution_model.dat*). The metamorphic evolution of the diamond-bearing gneiss modelled in pressure–temperature (*P–T*) pseudo-section is shown in Fig. 15.

DISCUSSION

Monazite behaviour during metamorphic evolution

A prograde metamorphic *P–T* path (marked by point 1 in Fig. 15a) is based on a subduction geotherm from Penniston-Dorland *et al.* (2015). Peak metamorphic conditions are inferred in the stability field of kyanite + garnet + omphacite + phengite + coesite + rutile with the presence of diamond as inclusions in kyanite and garnet. The shape-preferred orientation of diamond-bearing inclusions indicates their primary origin (Frezzotti & Ferrando, 2015), and coexistence of diamond with CO₂ indicates crystallization of diamond from a supercritical C–O–H fluid or melt (e.g. Akaishi & Yamaoka, 2000; Stöckhert *et al.*, 2001; Hermann *et al.*, 2006; Frezzotti & Peccerillo, 2007; Janák *et al.*, 2015) trapped by the host mineral (garnet, kyanite, zircon) at UHP conditions. To constrain *T*, we used Zr-in-rutile geothermometry (Tomkins *et al.*, 2007). Zirconium concentrations in rutile obtained by LA-ICP-MS are between

862 and 1102 ppm, with an average 1017 ppm, yielding an average *T* = 851°C at *P* = 29 kbar and 891°C at 45 kbar. The intersection of the Zr-in-rutile univariant line with the diamond–graphite boundary (Day, 2012) (point 2 in Fig. 15a) gives minimal *P–T* constraints for the peak metamorphic stage.

All diamonds were found in garnet I near the rims and close to monazite if both occur together. The only exception is a single diamond found near the centre of a large garnet (Fig. 5). With regard to the HREE and Y profiles, the position of diamond coincides with the secondary Y peak. The mentioned diamond found near the centre of the large garnet is close to the central peak in the Y profile (Fig. 5e). Complex profiles of the HREE and Y are not compatible with single Rayleigh fractionation (e.g. Otamendi *et al.*, 2002), which cannot explain the rise of the concentration in secondary peaks. Moreover, the absence of other Y, REE phases (allanite, xenotime) and the constant garnet volume above 20 kbar (Fig. 15b) do not allow an explanation by interaction with these phases (see Gieré *et al.*, 2011). Skora *et al.* (2006) successfully modelled the behaviour of HREE and Y assuming an increase of diffusion rates owing to the rise of temperature in the prograde stage of garnet growth. The rise is responsible for the formation of secondary peaks and the following steep decrease owing to exhaustion of these elements within a limited diffusion volume. Our profiles (Figs 3f and 5e) appear compatible with this process. The position of most diamonds and monazites, therefore, indicates their incorporation during the final stage of temperature rise when the secondary peak starts to cease.

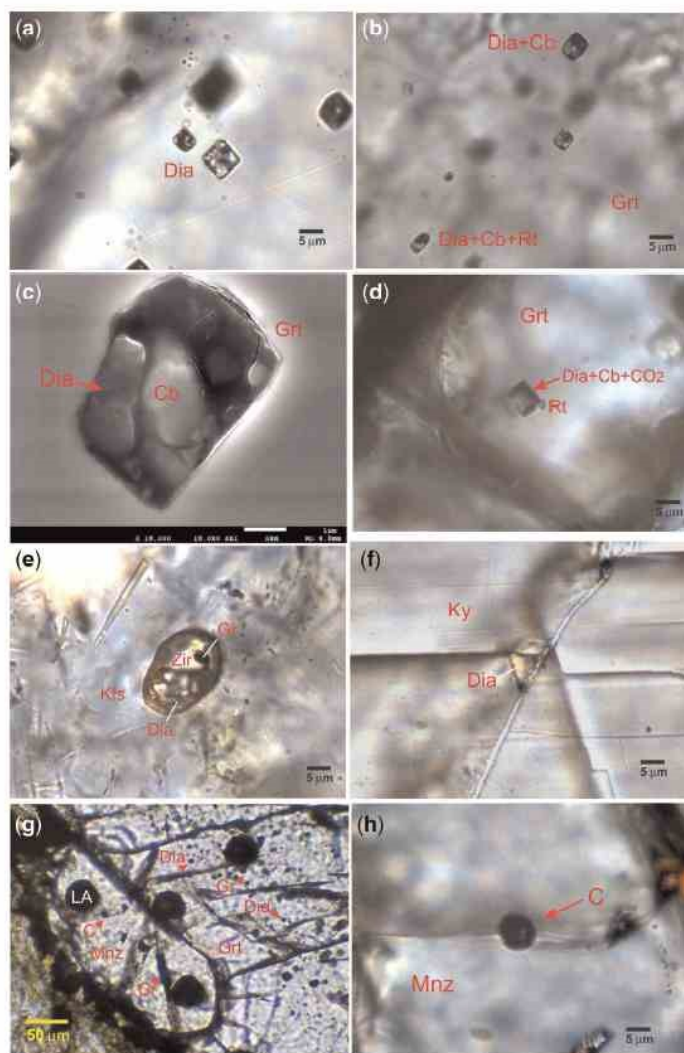


Fig. 7. Photomicrographs of diamond and graphitic carbon inclusions in garnet, zircon, kyanite and monazite using an optical microscope (transmitted, plane-polarized light) and scanning electron microscope. (a) Single crystals of diamond in garnet. (b) Diamond + carbonate + rutile inclusions in garnet. (c) SE image of diamond + carbonate inclusion in garnet. (d) Polyphase diamond + CO₂ + carbonate inclusion in garnet. (e) Diamond and graphitic carbon inclusions in zircon. (f) Diamond inclusion in kyanite. (g) Monazite and garnet with diamond and graphitic carbon inclusions, and laser ablation pits. (h) Detail of graphitic/amorphous inclusion in monazite.

The presence of graphitic carbon with diamond may reflect disordering of the diamond structure from sp³ to sp² bonded (e.g. Smith *et al.*, 2011; Smith & Godard, 2013). Occurrence of diamond and graphitic carbon with CO₂ may indicate transformation of diamond to graphitic carbon in the presence of fluid via a dissolution–precipitation process rather than a solid-state transformation (Korsakov *et al.*, 2015). We argue that the presence of graphitic or amorphous carbon in

monazite, similar to inclusions in associated garnet (Fig. 7g and h), may indicate that former diamond trapped by monazite at UHP conditions was transformed to graphite.

We infer that UHP monazite formed from allanite. Allanite is known to be stable at UHP conditions (Hermann, 2002; Hermann & Spandler, 2008; Engi, 2017). Taking into account the only known UHP allanite–monazite stability boundary of Hermann & Rubatto

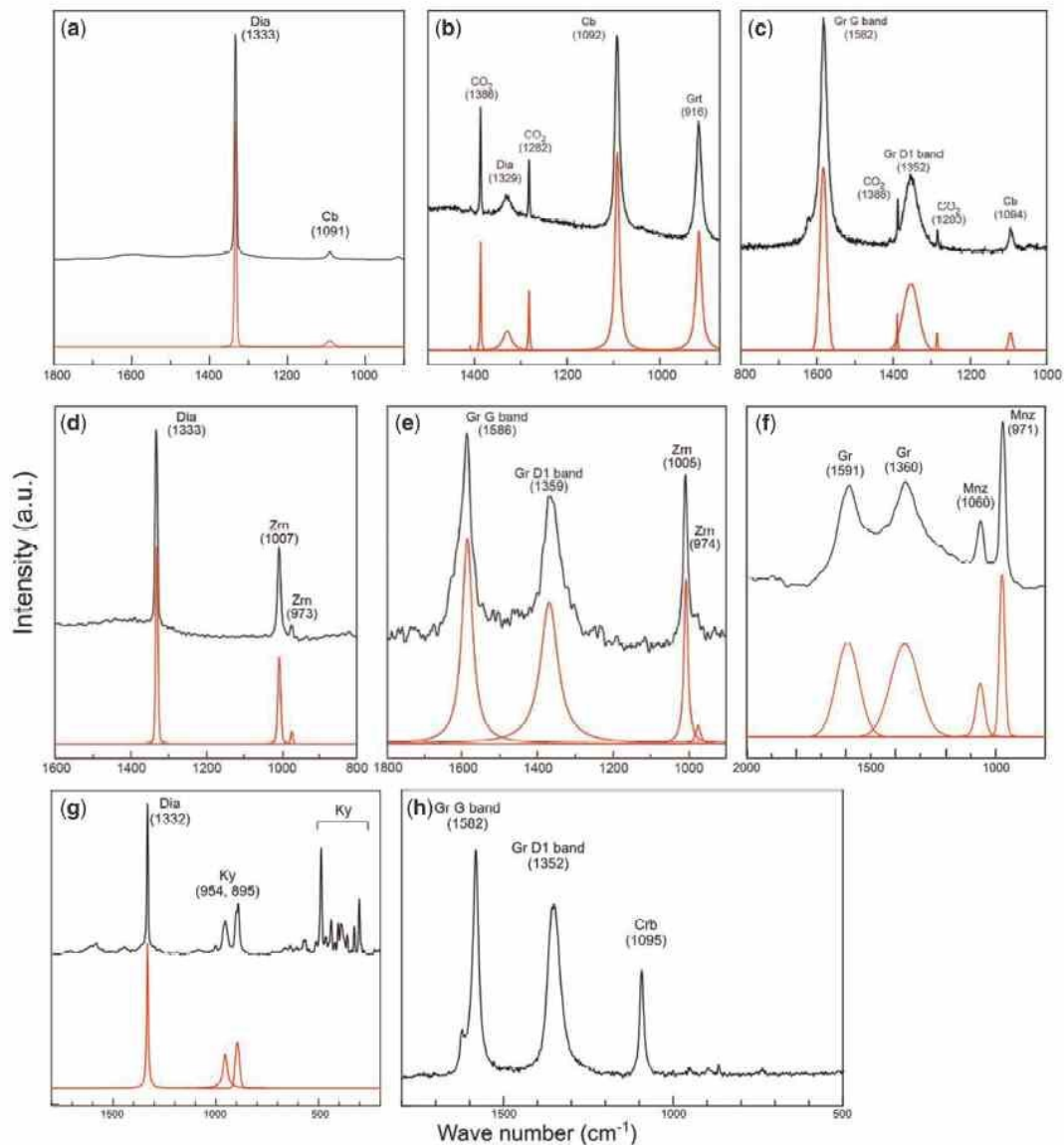


Fig. 8. Representative Raman spectra. (a) Diamond (Dia) together with carbonate (Cb). (b) Polyphase inclusion of diamond, carbonate and CO₂ in garnet (Grt). (c) Graphite G and D1 bands in polyphase inclusion with CO₂ and carbonate in garnet. (d) Diamond in zircon. (e) Graphite carbon in zircon (Zrn). (f) Graphitic/amorphous carbon (Gr) in monazite (Mnz). (g) Diamond in kyanite. (h) Graphitic carbon and carbonate in kyanite. Black curves, raw spectra; red curves, after peak fitting with Fityk software version 0.9.3 (Wojdyr, 2010).

(2009), monazite formed from allanite above 35 kbar and c. 750°C when the rock encountered the monazite stability field.

Yttrium and HREE contents in monazite are commonly used to infer its equilibration with garnet and/or plagioclase (Zhu & O’Nions, 1999; Krenn *et al.*, 2009; Holder *et al.*, 2015; Petrik *et al.*, 2016). Low Y + HREE

and a missing Eu anomaly are related to a high garnet content and absence of plagioclase, which are characteristic of UHP conditions. Vice versa, a distinct negative Eu anomaly and increased Y + HREE should attest to the equilibration with plagioclase and a lower garnet content in granulite-facies metamorphism. As argued above, monazite enclosed in garnet and kyanite is

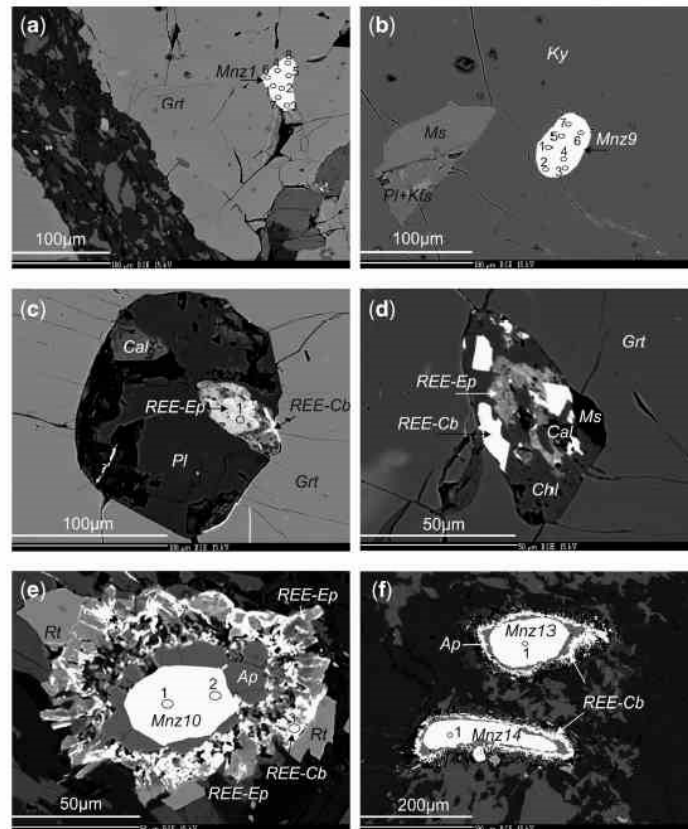


Fig. 9. BSE images of monazite, allanite and associated phases. (a) Mnz1 enclosed in garnet. (b) Mnz9 in kyanite. (c, d) REE-epidote/allanite included in garnet along with REE-carbonate and plagioclase. (e, f) Coronas around matrix monazites (Mnz10, 13, 14) composed of apatite, secondary allanite and late REE-carbonate. Numbers in monazites refer to the analysed points in Table 3 and Supplementary Data Electronic Appendix 1.

considered to be stable at UHP conditions in the absence of plagioclase or K-feldspar. However, monazite chemistry shows a distinct negative Eu anomaly and moderate Y content. Relevant for explaining this discrepancy seems to be the whole-rock REE pattern, which also shows a distinct negative Eu anomaly (Fig. 11). Calculation of the whole-rock budget showed that the whole-rock REE are controlled by three phases: garnet, monazite and apatite. The size of the whole-rock negative Eu anomaly is only slightly moderated by abundant K-feldspar and plagioclase. All three phases (garnet, monazite and apatite; Fig. 11, Supplementary Data Electronic Appendix 2) thus show negative Eu anomalies, which means that this feature was inherited from the source rock. It is concluded that, in the case where the source rock has a negative Eu anomaly, monazite equilibrated at UHP conditions does not necessarily lack a negative Eu anomaly regardless of the presence of feldspars. On the other hand, the uniform garnet content (16 vol. %) predicted by pseudo-section

modeling (Fig. 15b) over a wide P - T window explains well the lack of distinct difference in Y concentrations in monazites (Fig. 12) commonly attributed to the decrease of garnet content with decreasing P .

The lack of difference in chemistry and age of monazite inclusions in garnet and kyanite as well as the matrix monazites suggests that all crystallized simultaneously. We therefore conclude that the bulk of monazite dates the UHP metamorphism at 472 ± 3 Ma (Fig. 14).

The exhumation path crosses the dehydration melting reaction curve of Auzanneau *et al.* (2006) (point 3 in Fig. 15a), approximating the phengite and omphacite breakdown, which produces Ca-rich garnet II, calcic plagioclase and biotite according to reaction $Ph + Omp + Qz = Bt + Pl + Grt + L$. The P - T path becomes isobaric at 10 kbar (point 4 in Fig. 15a) to avoid the sillimanite field as this mineral was not found. At these conditions, the pseudo-section model predicts a maximum of 30 vol. % melt (Fig. 15c). Using the equation of

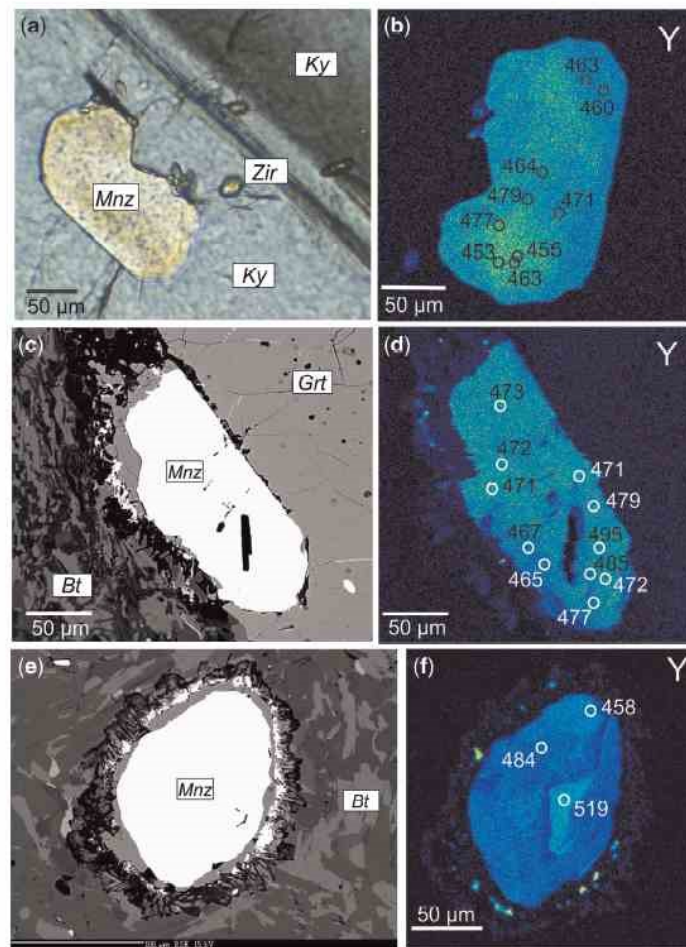


Fig. 10. Monazite photomicrograph, BSE images and X-ray maps of yttrium concentrations with ages of the analysed points. (a, b) Monazite in kyanite; (c, d) in the rim of garnet (sample ML6-12 A); (e, f) matrix monazite with corona.

Stepanov *et al.* (2012) we calculated a maximum 25% dissolution of total monazite (point 4) at pertinent melt H_2O content and melt amount. The model shows that, on cooling to the solidus, the dissolved monazite crystallized again (Fig. 15c) as new overgrowths. However, such rims were not clearly identified in the X-ray maps (Fig. 10d and f). It is possible that the new rims (if they existed) were obliterated by the extensive development of late coronas. If not, it is possible that the complex models overestimate the extent of monazite melting.

The monazite breakdown coronas are a common feature found in several metasedimentary and metaigneous rocks worldwide (Broska & Siman 1998; Finger *et al.*, 1998; Majka & Budzyń, 2006; Gasser *et al.*, 2012; Ondrejka *et al.*, 2012; Lo Pò *et al.*, 2016). These coronas are interpreted as an effect of Ca-rich fluid facilitating monazite breakdown. The Ca activity plays an important role in the stability of monazite, as demonstrated by

thermodynamic modelling for simplified average pelitic compositions with varying Ca content (Janots *et al.*, 2007; Spear, 2010) and experimental results (e.g. Budzyń *et al.*, 2017). The above-cited researchers showed that increased Ca activity generally moves the allanite stability field to higher T (i.e. upper amphibolite- to granulite-facies conditions). In our rocks, we interpret the formation of the apatite–allanite–epidote corona around monazite to be due to exhumation and cooling after the peak-pressure stage rather than a subsequent prograde metamorphic overprint. The boundary between allanite and monazite (red dotted line, Fig. 15a) is for a bulk composition with slightly lower CaO (2.17 wt %) compared with 2.23 wt % used in the model. As the allanite thermal stability is strongly dependent on bulk CaO, the supposed upper boundary is shifted to higher T , following the upper stability limit of zoisite (point 5, red dashed line, Fig. 15a).

When the P - T path crosses the monazite–allanite boundary (point 5 in Fig. 15a) the matrix monazite breaks down to apatite + REE-epidote/allanite + Th, U, Y-rich phases (Fig. 9e and f). An incomplete breakdown assemblage (without monazite and apatite) is also found as inclusions in garnet (Fig. 9c and d), suggesting

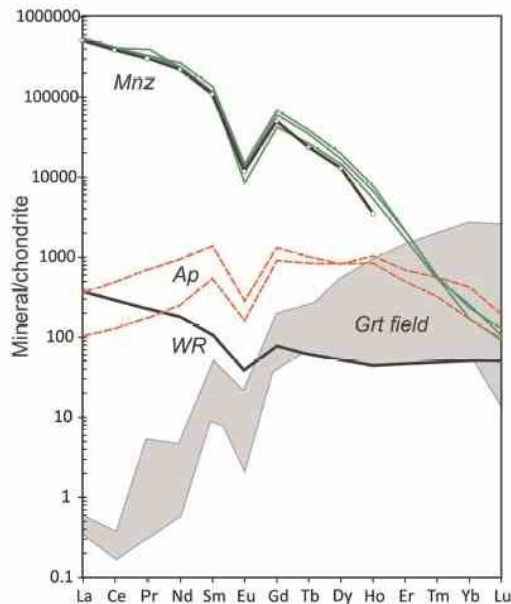


Fig. 11. Comparison of the REE in the minerals analysed by LA-ICP-MS (green lines, Mnz; dashed lines, Ap; field is for all garnets) with whole-rock analysis by ICP-MS (WR). An average of monazite (La–Ho) microprobe analyses is also shown. It should be noted that all analysed phases show negative Eu anomalies.

that not all monazites trapped by garnet have been protected. The REE-epidote/allanite, which partly replaced and partly overgrew monazite crystals, shows REE patterns similar to parental monazite but downshifted to five times lower concentrations. The REE seem to be inherited from monazite with the exception of distinct positive Eu anomalies (Fig. 13a and b). In the reducing regime indicated by abundant hydrothermal graphite in the matrix, Eu occurs as Eu^{2+} , which is mobile. Preference for Eu of allanite was shown in high- P experiments (Hermann, 2002) by allanite/melt partitioning coefficients. At the last cooling stage, low- T , CO_2 -rich fluids altered the corona REE-epidotes to REE-carbonate (bastnäsite-OH). Normalization of the carbonate REE (thick corona around monazites 10, 13, 14 in Fig. 13c) by the monazite composition shows a strong depletion of HREE + Y, and small to moderate positive Eu anomalies (Fig. 13f). The depletion is explained by preferential complexing of HREE with F^- in metamorphic fluids, which (supposing divalent Eu^{2+}) results in a positive slope and negative Eu anomaly of the fluid (Bau, 1991). The only F detected in the analysed gneiss minerals is from the REE-carbonate. Assuming high water/rock ratio at a low temperature, the carbonate crystallizing (in a Ca-rich site among REE-epidote crystals) after the escape of the fluid would have a reciprocal, negative (HREE-depleted) REE pattern and positive (less negative) Eu anomaly, which is observed. The source of this fluid is unknown but the character of REE-carbonate may indicate a late low- T event (see Berger *et al.*, 2008), possibly associated with strong deformation observed in the gneiss.

Tectonic implications

The age of 472 Ma for UHP metamorphism of the diamond-bearing gneiss from Saxnäs in the Middle

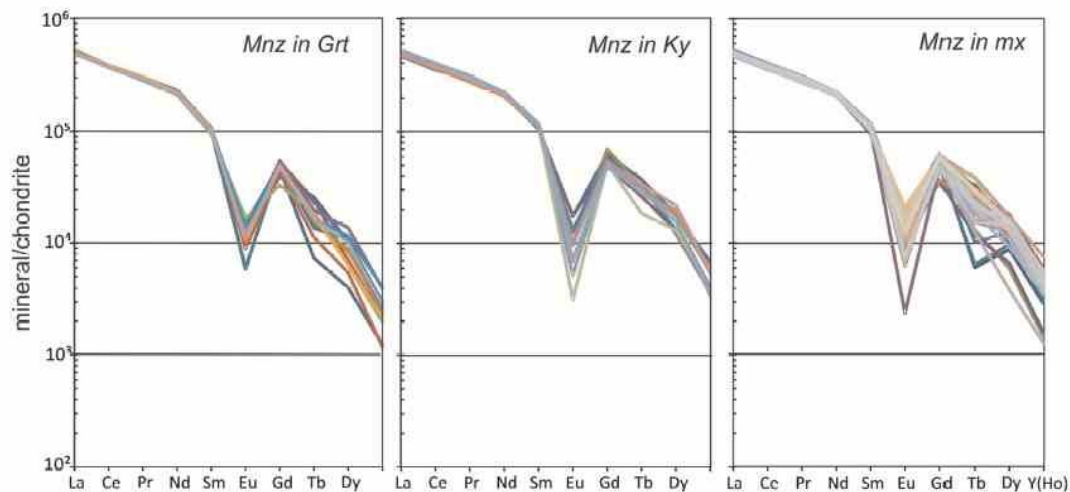


Fig. 12. Comparison of the REE and Y in monazites enclosed in garnet, kyanite and matrix.

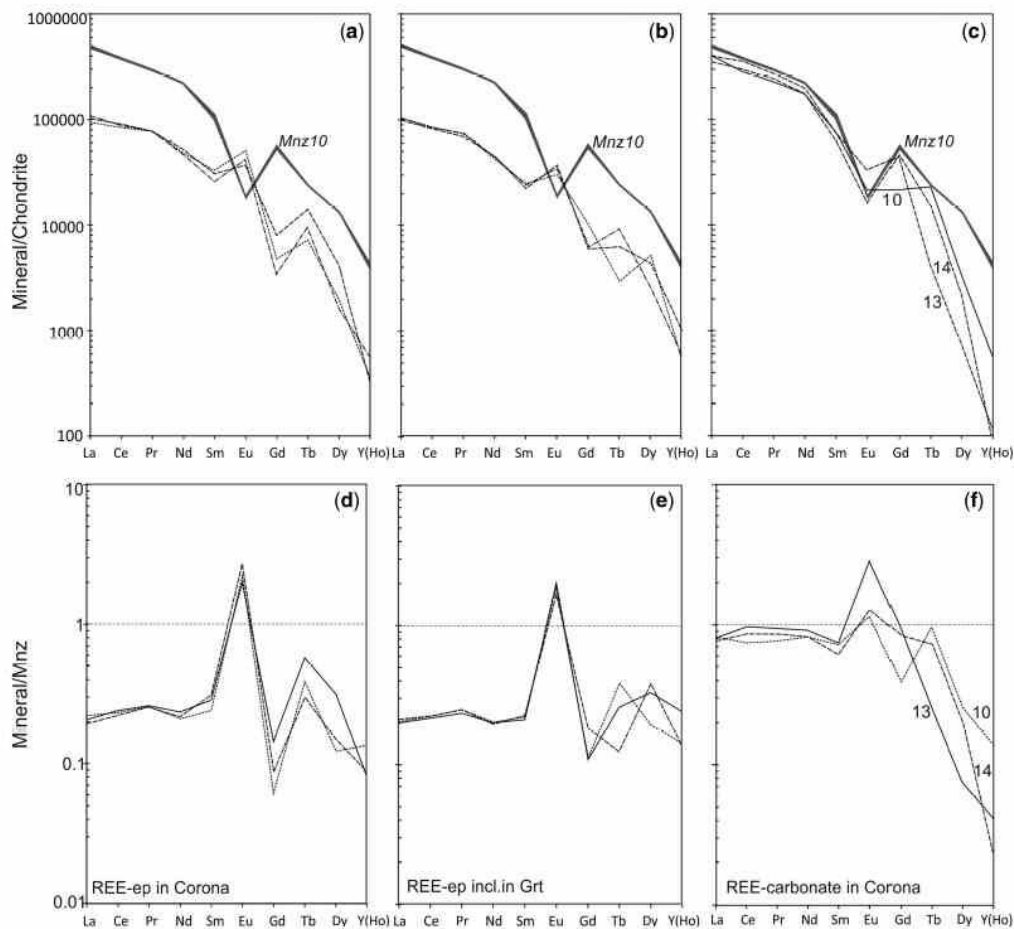


Fig. 13. The REE in allanite/REE epidote (dashed lines) identified as inclusion corona (a, d), garnet, and in REE-carbonate from corona (c, f) normalized by chondrite (a–c) and by parental monazite (d–f).

Seve Nappe is older than the 462 ± 3.5 Ma Sm–Nd garnet–apatite–feldspar–whole-rock isochron age determined by Grimmer *et al.* (2015) from the Upper Seve Nappe in the same area. The sample dated by Grimmer *et al.* (2015) is a mylonitic mica schist consisting of quartz, white mica, garnet, plagioclase, K-feldspar, minor biotite and accessories, recording P – T conditions of ~ 15 kbar and $690 \pm 50^\circ\text{C}$; that is, much lower in pressure than our samples. Grimmer *et al.* (2015) interpreted this age as related to ‘prograde garnet growth and possible incipient subduction’. Assuming that our ~ 473 Ma age is indeed the timing of UHP metamorphism in the Middle Seve Nappe and ~ 462 Ma is the age of incipient eclogite-facies metamorphism in the Upper Seve Nappe, it would follow that the subduction of different parts of the Seve Nappe lying in one profile did not evolve in the usual sequence of thrusting; that is, from more internal and structurally higher units to

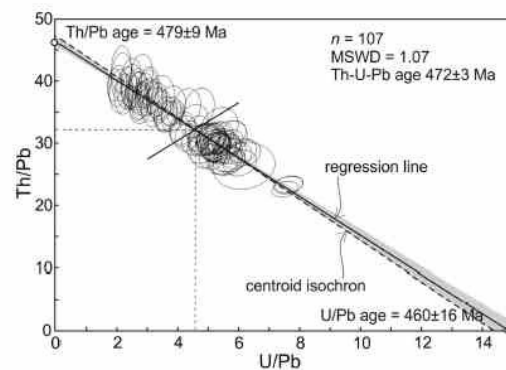


Fig. 14. U/Pb vs Th/Pb isochron (Cocherie & Albarède, 2001) of $n = 107$ dated monazite points showing concordant centroid age of 472 ± 3 Ma. The weighted fit of the data was calculated using Isoplot v. 3.7 (Ludwig, 2001).

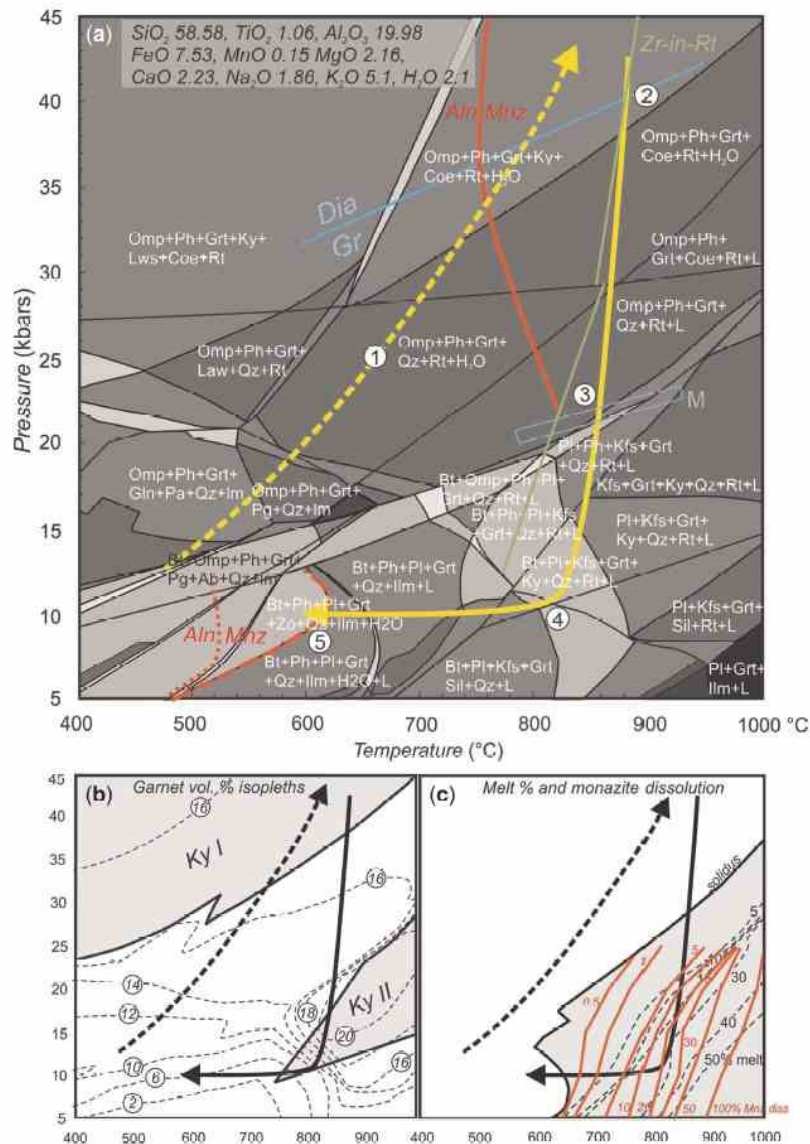


Fig. 15. Phase diagrams (P - T pseudo-sections) showing (a) P - T path of diamond-bearing gneiss in yellow; Aln-Mnz stability boundaries are shown as red dotted line (Spear, 2010, Fig. 7b) and red continuous line (Hermann & Rubatto, 2009). Red dashed line follows the upper stability limit of zoisite. Green lines (Zr-in-Rt) show calculated temperature according to zirconium-in-rutile thermometry (Tomkins *et al.*, 2007). Diamond-graphite (Dia-Gr) transition according to Day (2012) is shown as a blue line and melting reaction (M) according to Auzanneau *et al.* (2006) as a narrow green rectangle. Equilibrium assemblages of major fields are also shown. (b) Garnet modal abundances (vol. % isopleths) with kyanite (Ky I and Ky II) stability fields. (c) Dissolution model of monazite in melt calculated according to Stepanov *et al.* (2012), with amount of monazite in wt % (red isopleths) and modal abundance of melt in vol. % (dashed isopleths). Further details are given in the text.

more external and structurally lower units. It would imply that the kinematic evolution of subduction was more complicated. The 507 ± 20 Ma monazite age of Gademan *et al.* (2011) comes from the same tectonic unit as our sample, the Marsfjället gneiss of the Middle Seve Nappe. The reasons for this age difference remain

unclear, as this age was reported only in an abstract. The ~ 472 Ma age of UHP metamorphism (according to our study) in the Saxnäs area confirms the existence of a north-to-south age gradient for HP-UHP metamorphism in the Seve Nappe Complex. In the Vaimok lens of the Seve Nappe in Norrbotten, ~ 190 km NE of our

sample locality near Saxnäs, UHP metamorphism of eclogites (Bukała *et al.*, 2018) most probably occurred between ~480 and 490 Ma based on recent zircon U/Pb and monazite U–Th–Pb data (Root & Corfu, 2012; Barnes *et al.*, 2019). At Tjeliken in northern Jämtland (Fig. 1b), ~60 km SW of Saxnäs, Lu–Hf garnet dating of a near-UHP eclogite and U–Pb zircon dating of its host rock, garnet–phengite gneiss, yielded identical ages of ~458–459 Ma (Fassmer *et al.*, 2017). Our age results from monazite dating (472 Ma) lie between these, both in terms of locality and time, suggesting that the age difference between Jämtland and Norrbotten reflects southward migration of one tectonic process that caused HP–UHP metamorphism, rather than two independent tectonic processes. If UHP metamorphism of the distal Baltican continental margin represented by the Seve Nappe was caused by the collision of this margin with an intra-oceanic volcanic arc in the Iapetus ocean (e.g. Brueckner & van Roermund, 2004; Brueckner *et al.*, 2004; Majka *et al.*, 2014b), such a high age gradient (>20 Myr over a distance of ~250 km) may have been produced by strong curvature of the arc and/or by irregularities of the continental margin (e.g. promontories and re-entrants). The tectonic map of the Scandinavian Caledonides (Fig. 1) indeed shows changes of the structure along-strike of the orogen, which may reflect such pre-existing irregularities of the continental margin. From Jämtland to Norrbotten, the width of the Lower Allochthon (sedimentary nappes derived from the inner margin of Baltica) decreases significantly so that in Norrbotten, the Middle Allochthon including the Seve Nappe occurs almost at the front of the Caledonide nappe stack. North of Kiruna, the width of the Lower Allochthon increases again northeastward (Fig. 1). This geometry may reflect the existence of a relatively high zone and associated promontory of the continental margin centred in Norrbotten, leading on one hand to a smaller volume of Lower Allochthon sediments and on the other hand to an earlier arc–continent collision. In this case, a northward decrease of HP–UHP ages in the Seve Nappe and related units would be expected from Norrbotten further northward. Determining ages of HP–UHP metamorphism in the Seve Nappe and related units north of Norrbotten would allow for testing of this hypothesis.

CONCLUSIONS

UHP monazite in diamond-bearing gneiss from the SNC shows negative Eu anomalies, in contrast to the general interpretation that the absence of a Eu anomaly is characteristic for UHP monazite reflecting high content of coexisting garnet and the absence of plagioclase. We interpret the negative Eu anomaly to be inherited from the whole-rock chemical composition when the REE source had a negative Eu anomaly. Hence, this feature does not reflect the coexistence with plagioclase and/or K-feldspar, which are unstable at UHP conditions. The UHP stage is evidenced by inclusions of diamond found

together with monazite in the garnet. Both diamond and monazite occur near garnet rims within or close to the secondary peak of Y. Supposing that these Y peaks originated as a result of thermally elevated diffusion rates, such a position indicates a high temperature at the end of the prograde metamorphic stage.

We infer that UHP monazite formed from allanite and the bulk of monazite dates the UHP metamorphism at 472 ± 3 Ma. Monazite inclusions in garnet and kyanite are mostly unaltered, whereas monazite in the matrix shows breakdown coronas of apatite + REE-epidote/allanite + Th, U, Y-rich phases. We interpret this monazite breakdown to be due to cooling after the pressure decrease during exhumation from the UHP stage rather than a subsequent, prograde metamorphic overprint.

ACKNOWLEDGEMENTS

We thank C. Hetherington, F. Finger and E. Catlos for their constructive reviews, and R. Gieré for editorial handling of the paper.

FUNDING

This work was supported by the Slovak Research and Development Agency projects under the contract numbers APVV-14-0278 and APVV-18-0107, the Slovak Scientific Grant Agency VEGA (grant numbers 2/0060/16 and 0008/19), the National Science Center (Poland) 'CALSUB' research project 2014/14/E/ST10/00321, the Swedish Royal Academy of Sciences (KVA) project GS2015-0006, and German Science Foundation (DFG) grant FR700/17-1.

SUPPLEMENTARY DATA

Supplementary data are available at *Journal of Petrology* online.

REFERENCES

- Akaishi, M. & Yamaoka, S. (2000). Crystallization of diamond from C–O–H fluids under high-pressure and high-temperature conditions. *Journal of Crystal Growth* **209**, 999–1003.
- Auzanneau, E., Vielzeuf, D. & Schmidt, M. W. (2006). Experimental evidence of decompression melting during exhumation of subducted continental crust. *Contributions to Mineralogy and Petrology* **152**, 125–148.
- Barnes, C., Majka, J., Schneider, D., Walczak, K., Bukała, M., Kościńska, K., Tokarski, T. & Karlsson, A. (2019). High-spatial resolution dating of monazite and zircon reveals the trimming of subduction–exhumation of the Vaimok Lens in the Seve Nappe Complex (Scandinavian Caledonides). *Contributions to Mineralogy and Petrology* **174**, 5.
- Bau, M. (1991). Rare-earth element mobility during hydrothermal and metamorphic fluid–rock interaction and the significance of the oxidation state of europium. *Chemical Geology* **93**, 219–230.

- Berger, A., Gnos, E., Janots, E., Fernandez, A. & Giese, J. (2008). Formation and composition of rhabdophane, bastnäsite and hydrated thorium minerals during alteration: implications for geochronology and low-temperature processes. *Chemical Geology* **254**, 238–248.
- Broska, I. & Siman, P. (1998). The breakdown of monazite in the West-Carpathian Veporic orthogneiss and Tatric granites. *Geologica Carpathica* **52**, 79–90.
- Brueckner, H. K. & van Roermund, H. L. M. (2004). Dunk tectonics: a multiple subduction/duction model for the evolution of the Scandinavian Caledonides. *Tectonics* **24**, TC2004.
- Brueckner, H. K. & van Roermund, H. L. M. (2007). Current HP metamorphism on both margins of Iapetus: Ordovician ages for eclogites and garnet pyroxenites from the Seve Nappe complex, Swedish Caledonides. *Journal of the Geological Society, London* **164**, 117–128.
- Brueckner, H. K., van Roermund, H. L. M. & Pearsom, N. (2004). An Archean to Paleozoic evolution for a garnet peridotite lens with sub-Baltic Shield affinity within the Seve Nappe Complex of Jämtland, Sweden, Scandinavian Caledonides. *Journal of Petrology* **45**, 415–437.
- Budzyń, B., Harlov, D., Kozub-Budzyń, G. & Majka, J. (2017). Experimental constraints on the relative stabilities of the two systems monazite-(Ce)-allanite-(Ce)-fluorapatite and xenotime-(Y)-(Y, HREE)-rich epidote-(Y, HREE)-rich fluorapatite, in high Ca and Na-Ca environments under *P-T* conditions of 200–1000 MPa and 450–750°C. *Mineralogy and Petrology* **111**, 183–217.
- Bukata, M., Klonowska, I., Barnes, C., Majka, J., Kościńska, K., Janák, M., Fassmer, K., Broman, C. & Luptáková, J. (2018). UHP metamorphism recorded by phengite eclogite from the Caledonides of northern Sweden: *P-T* path and tectonic implications. *Journal of Metamorphic Geology* **36**, 547–566.
- Catlos, E., Gilley, L. D. & Harrison, T. M. (2002). Interpretation of monazite ages obtained via *in situ* analysis. *Chemical Geology* **188**, 193–215.
- Clos, F., Gilio, M. & van Roermund, H. L. M. (2014). Fragments of deeper parts of the hanging wall mantle preserved as orogenic peridotites in the central belt of the Seve Nappe Complex, Sweden. *Lithosphere* **192–195**, 8–20.
- Cocherie, A. & Albarède, F. (2001). An improved U-Th-Pb age calculation for electron microprobe dating of monazite. *Geochimica et Cosmochimica Acta* **65**, 4509–4522.
- Connolly, J. A. D. (1990). Multivariable phase diagrams: an algorithm based on generalized thermodynamics. *American Journal of Science* **290**, 666–718.
- Connolly, J. A. D. (2005). Computation of phase-equilibria by linear programming: a tool for geodynamic modeling and its application to subduction zone decarbonation. *Earth and Planetary Science Letters* **236**, 524–541.
- Day, H. (2012). A revised diamond-graphite transition curve. *American Mineralogist* **97**, 52–62.
- Dobrzhinetskaya, L. F. (2012). Microdiamonds—frontier of ultrahigh-pressure metamorphism: a review. *Gondwana Research* **21**, 207–223.
- Dumond, G., Goncalves, P., Williams, M. L. & Jercinovic, J. (2015). Monazite as monitor of melting, garnet growth and feldspar recrystallization in continental lower crust. *Journal of Metamorphic Geology* **33**, 735–762.
- Engi, M. (2017). Petrochronology based on REE-minerals: Monazite, allanite, xenotime, apatite. In: Kohn, M. J., Engi, M. and Lanari, P. (eds) *Petrochronology: Methods and Applications*. Mineralogical Society of America and Geochemical Society, Reviews in Mineralogy and Geochemistry **83**, 365–418.
- Fassmer, K., Klonowska, I., Walczak, K., Andersson, B., Froitzeim, N., Majka, J., Fonseca, R. O. C., Münker, C., Janák, M. & Whitehouse, M. (2017). Middle Ordovician subduction of continental crust in the Scandinavian Caledonides—an example from Tjeliken, Seve Nappe Complex, Sweden. *Contributions to Mineralogy and Petrology* **172**, 103.
- Finger, F., Broska, I., Roberts, M. P. & Schermaier, A. (1998). Replacement of primary monazite by apatite-allanite-epidote coronas in an amphibolite facies granite gneiss from the eastern Alps. *American Mineralogist* **83**, 248–258.
- Foster, B. R., Parrish, R. R., Horstwood, M. S. A., Chenery, S., Pyle, J. & Gibson, H. D. (2004). The generation of prograde *P-T-t* points and paths; a textural, compositional and chronological study of metamorphic monazite. *Earth and Planetary Science Letters* **228**, 125–142.
- Frezotti, M. L. & Ferrando, S. (2015). The chemical behavior of fluids released during deep subduction based on fluid inclusions. *American Mineralogist* **100**, 352–377.
- Frezotti, M. L. & Peccerillo, A. (2007). Diamond-bearing COHS fluids in the mantle beneath Hawaii. *Earth and Planetary Science Letters* **262**, 273–283.
- Gademan, M., Verbaas, J., van Roermund, H. & Hogerwerf, M. (2011). Evidence for a Finnmarkian (~500 Ma) continental collision/subduction zone in the Central Belt of the Seve Nappe Complex, northern Jämtland-southern Västerbotten, Sweden; Constraints from chemical EMP monazite ages and orogenic mantle wedge garnet peridotite. *Geophysical Research Abstracts* **13**, EGU2011-1340-1.
- Ganguly, J., Cheng, W. & Tirone, M. (1996). Thermodynamics of aluminosilicate garnet solid solution: new experimental data, an optimized model, and thermometric applications. *Contributions to Mineralogy and Petrology* **126**, 137–151.
- Gasser, D., Bruand, E., Rubato, D. & Stüwe, K. (2012). The behaviour of monazite from greenschist facies phyllites to anatectic gneisses; an example from the Chugach metamorphic complex, southern Alaska. *Lithos* **134–135**, 108–122.
- Gee, D. G., Janák, M., Majka, J., Robinson, P. & Van Roermund, H. (2013). Subduction along and within the Baltoscandian margin during closing of the Iapetus Ocean and Baltica-Laurentia collision. *Lithosphere* **5**, 169–178.
- Gieré, R., Rumble, D., Günther, D., Connolly, J. & Caddick, M. J. (2011). Correlation of growth and breakdown of major and accessory minerals in metapelites from Campolungo, Central Alps. *Journal of Petrology* **52**, 2293–2334.
- Gilio, M., Clos, F. & van Roermund, H. L. M. (2015). The Frinningen garnet peridotite (central Swedish Caledonides); a good example of the characteristic *P-T-t* path of a cold mantle wedge garnet peridotite. *Lithos* **230**, 1–16.
- Gilotti, J. A. (2013). The realm of ultrahigh-pressure metamorphism. *Elements* **9**, 255–260.
- Green, E., Holland, T. & Powell, R. (2007). An order-disorder model for omphacitic pyroxenes in the system jadeite-diopside-hedenbergite-acmite, with applications to eclogitic rocks. *American Mineralogist* **92**, 1181–1189.
- Grimmer, J. C., Glodny, J., Drüppel, K., Greiling, R. O. & Kontny, A. (2015). Early- to mid-Silurian extrusion wedge tectonics in the central Scandinavian Caledonides. *Geology* **43**, 347–350.
- Hacker, B., Kylander-Clark, A. & Holder, R. (2019). REE partitioning between monazite and garnet: Implications for petrochronology. *Journal of Metamorphic Geology* **37**, 227–237.
- Hacker, B. R., Kylander-Clark, A. R. C., Holder, R., Andersen, T. B., Peterman, E. M., Walsh, E. O. & Munnikhuis, J. K. (2015). Monazite response to ultrahigh-pressure subduction from U-Pb dating by laser ablation split stream. *Chemical Geology* **409**, 28–41.

- Hermann, J. (2002). Allanite: thorium and light rare earth element carrier in subducted crust. *Chemical Geology* **192**, 289–306.
- Hermann, J. & Rubatto, D. (2003). Relating zircon and monazite domains to garnet growth zones: age and duration of granulite facies metamorphism in the Val Malenco lower crust. *Journal of Metamorphic Geology* **21**, 833–852.
- Hermann, J. & Rubatto, D. (2009). Accessory phase control on the trace element signature of sediment melts in subduction zones. *Chemical Geology* **265**, 512–526.
- Hermann, J. & Spandler, C. J. (2008). Sediment melts at sub-arc depths: an experimental study. *Journal of Petrology* **49**, 717–740.
- Hermann, J., Spandler, C., Hack, A. & Korsakov, A. (2006). Aqueous fluids and hydrous melts in high-pressure and ultra-high pressure rocks: implications for element transfer in subduction zones. *Lithos* **92**, 399–417.
- Holder, R. M., Hacker, B. R., Kylander-Clark, A. R. C. & Cottle, J. M. (2015). Monazite trace-element and isotopic signatures of (ultra)high-pressure metamorphism: Examples from the Western gneiss Region, Norway. *Chemical Geology* **409**, 99–111.
- Holland, T. J. B. & Powell, R. (1998). An internally consistent thermodynamic data set for phases of petrological interest. *Journal of Metamorphic Geology* **16**, 309–343.
- Holland, T. J. B. & Powell, R. (2001). Calculation of phase relations involving haplogranitic melts using an internally consistent thermodynamic dataset. *Journal of Petrology* **42**, 673–683.
- Janák, M., Van Roermund, H., Majka, J. & Gee, D. G. (2013). UHP metamorphism recorded by kyanite-bearing eclogite in the Seve Nappe Complex of northern Jämtland, Swedish Caledonides. *Gondwana Research* **23**, 865–879.
- Janák, M., Froitzheim, N., Yoshida, K., Sasinková, V., Nosko, M., Kobayashi, T., Hirajima, T. & Vrabec, M. (2015). Diamond in metasedimentary crustal rocks from Pohorje, Eastern Alps: a window to deep continental subduction. *Journal of Metamorphic Geology* **33**, 495–512.
- Janots, E., Brunet, F., Goffe, B., Poinssot, C., Burchard, M. & Cemic, L. (2007). Thermochemistry of monazite-(La) and disaksite-(La); implications for monazite and allanite stability in metapelites. *Contributions to Mineralogy and Petrology* **154**, 1–14.
- Kato, T. & Suzuki, K. (2014). 'Background holes' in X-ray spectrometry using a pentaerythritol (PET) analyzing crystal. *Journal of Mineralogical and Petrological Sciences* **109**, 151–155.
- Kelsey, D. E., Clark, C. & Hand, M. (2008). Thermobarometric modelling of zircon and monazite growth in melt-bearing systems: examples using model metapelitic and metapsammitic granulites. *Journal of Metamorphic Geology* **26**, 199–212.
- Klonowska, I. (2017). Deep subduction of the Seve Nappe Complex in the Scandinavian Caledonides. PhD thesis, Acta Universitatis Upsaliensis, Uppsala, 63 pp.
- Klonowska, I., Janák, M., Majka, J., Froitzheim, N. & Košmińska, K. (2016). Eclogite and garnet pyroxenite from Stor Jougdan, Seve Nappe Complex, Sweden: implications for UHP metamorphism of allochthons in the Scandinavian Caledonides. *Journal of Metamorphic Geology* **34**, 103–119.
- Klonowska, I., Janák, M., Majka, J., Petrik, I., Froitzheim, N., Gee, D. G. & Sasinková, V. (2017a). Microdiamond on Åreskutan confirms regional UHP metamorphism in the Seve Nappe Complex of the Scandinavian Caledonides. *Journal of Metamorphic Geology* **35**, 541–565.
- Klonowska, I., Janák, M., Petrik, I., Majka, J., Holmberg, J., Broman, C., Sasinková, V. & Yoshida, K. (2017b). Diamond-bearing UHP Seve Nappe Complex, Scandinavian Caledonides. In: *High- and Ultrahigh-Pressure Rocks—Keys to Lithosphere Dynamics Through Geologic Time. Abstract book and mid-conference excursion field guide, 12th International Eclogite Conference*. Kraków: AGH—University of Science and Technology, p. 66.
- Kohn, M. J., Wieland, M. S., Parkinson, C. D. & Upreti, B. N. (2005). Five generations of monazite in Langtang gneisses: implications for chronology of Himalayan metamorphic core. *Journal of Metamorphic Geology* **23**, 399–406.
- Konečný, P., Kusiak, M. A. & Dunkley, D. J. (2018). Improving U–Th–Pb electron microprobe dating using monazite age references. *Chemical Geology* **484**, 22–35.
- Korsakov, A., Zhimulev, E. I., Mikhailenko, D. S., Demin, S. P. & Kozmenko, O. A. (2015). Graphite pseudomorphs after diamonds: an experimental study of graphite morphology and the role of H₂O in the graphitization process. *Lithos* **236–237**, 16–26.
- Krenn, E., Janák, M., Finger, F., Broska, I. & Konečný, P. (2004). Two types of metamorphic monazite with contrasting La/Nd, Th, and Y signatures in an ultrahigh-pressure metapelite from the Pohorje Mountains, Slovenia: Indications for pressure-dependent REE exchange between apatite and monazite? *American Mineralogist* **89**, 1323–1329.
- Krenn, E., Janák, M., Finger, F., Broska, I. & Konečný, P. (2009). Metamorphic formation of Sr-apatite and Sr-bearing monazite in a high-pressure rock from the Bohemian Massif. *American Mineralogist* **94**, 801–815.
- Ladenberger, A., Be'eri-Shlevin, Y., Claesson, S., Gee, D. G., Majka, J. & Romanova, I. V. (2014). Tectonometamorphic evolution of the Åreskutan Nappe—Caledonian history revealed by SIMS U–Pb zircon geochronology. In: Corfu, F., Gasser, D. and Chew, M. (eds) *New Perspectives on the Caledonides of Scandinavia and Related Areas*. Geological Society, London, Special Publications **390**, 337–368.
- Liou, J. G., Tsujimori, T., Yang, J., Zhang, R. Y. & Ernst, W. G. (2014). Recycling of crustal materials through study of ultrahigh-pressure minerals in collisional orogens, ophiolites, and mantle xenoliths: A review. *Journal of Asian Earth Sciences* **96**, 386–420.
- Lo Pò, D., Braga, R., Massonne, H.-J., Molli, G., Montanini, A. & Theye, T. (2016). Fluid-induced breakdown of monazite in medium-grade metasedimentary rocks of the Pontremoli basement (Northern Apennines, Italy). *Journal of Metamorphic Geology* **34**, 63–84.
- Ludwig, K. R. (2001). *User's manual for Isoplot/Ex ver. 3.7. A geochronological toolkit for Microsoft Excel*. Berkeley Geochronological Centre Special Publication **4**, 65 pp.
- Majka, J. & Budzyń, B. (2006). Monazite breakdown in metapelites from Wedel Jarlsberg Land, Svalbard—preliminary report. *Mineralogia* **37**, 61–69.
- Majka, J., Be'eri-Shlevin, Y., Gee, D. G., Ladenberger, A., Claesson, S., Konečný, P. & Klonowska, I. (2012). Multiple monazite growth in the Åreskutan migmatites: evidence for a polymetamorphic Late Ordovician to Late Silurian evolution in the Seve Nappe Complex of the west-central Jämtland, Sweden. *Journal of Geosciences* **57**, 3–23.
- Majka, J., Janák, M., Andersson, B., Klonowska, I., Gee, D. G., Rosén, Å. & Košmińska, K. (2014a). Pressure-temperature estimates on the Tjeliken eclogite: new insights into the (ultra)-high pressure evolution of the Seve Nappe Complex in the Scandinavian Caledonides. In: Corfu, F., Gasser, D. and Chew, D. M. (eds) *New Perspectives on the Caledonides of Scandinavia and Related Areas*. Geological Society, London, Special Publications **390**, 369–384.
- Majka, J., Rosén, Å., Janák, M., Froitzheim, N., Klonowska, I., Manecki, M., Sasinková, V. & Yoshida, K. (2014b).

- Microdiamond discovered in the Seve Nappe (Scandinavian Caledonides) and its exhumation by the 'vacuum-cleaner' mechanism. *Geology* **42**, 1107–1110.
- Montel, J. (1993). A model for monazite/melt equilibrium and application to the generation of granitic magmas. *Chemical Geology* **110**, 127–146.
- Newton, R. C., Charlu, T. V. & Kleppa, O. J. (1980). Thermochemistry of high structural state plagioclases. *Geochimica et Cosmochimica Acta* **44**, 933–941.
- Ondrejka, M., Uher, P., Putiš, M., Broska, I., Bačík, P., Konečný, P. & Schmiéd, I. (2012). Two-stage breakdown of monazite by post-magmatic and metamorphic fluids: An example from the Veporic orthogneiss, Western Carpathians, Slovakia. *Lithos* **142–143**, 245–255.
- Otamendi, J. E., de la Rosa, J., Patiño-Douce, A. E. & Castro, A. (2002). Rayleigh fractionation of heavy rare earths and yttrium during metamorphic garnet growth. *Geology* **30**, 159–162.
- Penniston-Dorland, S. C., Kohn, M. J. & Manning, C. E. (2015). The global range of subduction zone thermal structures from exhumed blueschists and eclogites: Rocks are hotter than models. *Earth and Planetary Science Letters* **428**, 243–254.
- Petrik, I., Janák, M., Froitzheim, N., Georgiev, N., Yoshida, K., Sasinková, V., Konečný, P. & Milovská, S. (2016). Triassic to Early Jurassic (c. 200 Ma) UHP metamorphism in the Central Rhodopes: evidence from U–Pb–Th dating of monazite in diamond-bearing gneiss from Chepelare (Bulgaria). *Journal of Metamorphic Geology* **34**, 265–291.
- Rapp, R. & Watson, E. (1986). Monazite solubility and dissolution kinetics—implications for the thorium and light rare-earth chemistry of felsic magmas. *Contributions to Mineralogy and Petrology* **94**, 304–316.
- Root, D. B. & Corfu, F. (2012). U–Pb geochronology of two discrete Ordovician high-pressure metamorphic events in the Seve Nappe Complex, Scandinavian Caledonides. *Contributions to Mineralogy and Petrology* **163**, 769–788.
- Shannon, R. D. (1976). Revised effective ionic radii and systematic studies of interatomic distances in halides and chalcogenides. *Acta Crystallographica Section A* **32**, 751–767.
- Skora, S. & Blundy, J. (2012). Monazite solubility in hydrous silicic melts at high pressure conditions relevant to subduction zone metamorphism. *Earth and Planetary Science Letters* **321–322**, 104–114.
- Skora, S., Baumgartner, L. P., Mahlen, N. J., Johnson, C. M., Pilet, S. & Hellebrand, E. (2006). Diffusion-limited REE uptake by eclogite garnets and its consequences for Lu–Hf and Sm–Nd geochronology. *Contributions to Mineralogy and Petrology* **152**, 703–720.
- Smith, D. C. & Godard, G. (2013). A Raman spectroscopic study of diamond and disordered sp³-carbon in the coesite-bearing Straumen Eclogite Pod, Norway. *Journal of Metamorphic Geology* **31**, 19–33.
- Smith, D. C., Dobrzhinetskaya, L. F., Godard, G. & Green, H. (2011). Diamond–lonsdaleite–graphite relations examined by Raman mapping of carbon microinclusions inside zircon at Kumdy Kol, Kokchetav, Kazakhstan: evidence of the metamictisation of diamond. In: Dobrzhinetskaya, L. F., Faryad, S. W., Wallis, S. and Cuthbert, S. (eds) *Ultrahigh Pressure Metamorphism: 25 Years after Discovery of Coesite and Diamond*. Amsterdam: Elsevier, pp. 43–57.
- Sobolev, N. V. & Shatsky, V. S. (1990). Diamond inclusions in garnets from metamorphic rocks. *Nature* **343**, 742–746.
- Spear, F. S. (2010). Monazite–allanite phase relations in metapelites. *Chemical Geology* **279**, 55–62.
- Spear, F. S. & Pyle, J. M. (2002). Apatite, monazite and xenotime in metamorphic rocks. In: Kohn, M. J., Rakovan, J. and Hughes, J. M. (eds) *Phosphates: Geochemical, Geobiological and Materials Importance*. Mineralogical Society of America and Geochemical Society, Reviews in Mineralogy and Geochemistry **48**, 293–335.
- Stepanov, A.S., Hermann, J., Rubatto, D. & Rapp, R. P. (2012). Experimental study of monazite/melt partitioning with implications for the REE, Th and U geochemistry of crustal rocks. *Chemical Geology* **300–301**, 200–220.
- Stephens, M. B. (1988). The Scandinavian Caledonides: a complexity of collisions. *Geology Today* **4**, 20–26.
- Stöckhert, B., Duyster, J., Trepmann, C. & Massonne, H.-J. (2001). Microdiamond daughter crystals precipitated from supercritical CO₂ + silicate fluids included in garnet, Erzgebirge, Germany. *Geology* **29**, 391–394.
- Tajčmanová, L., Connolly, J. A. D. & Cesare, B. (2009). A thermodynamic model for titanium and ferric iron solution in biotite. *Journal of Metamorphic Geology* **27**, 153–165.
- Terry, M. P., Robinson, P., Hamilton, M. A. & Jercinovic, M. J. (2000). Monazite geochronology of UHP and HP metamorphism, deformation, and exhumation, Nordoyane, Western Gneiss Region, Norway. *American Mineralogist* **85**, 1651–1664.
- Thompson, J. B. & Hovis, G. L. (1979). Entropy of mixing in sanidine. *American Mineralogist* **64**, 57–65.
- Tomkins, H. S., Powell, R. & Ellis, D. (2007). The pressure dependence of the zirconium-in-rutile thermometer. *Journal of Metamorphic Geology* **25**, 703–713.
- Trouw, R. A. E. (1973). Structural geology of the Marsfjällen area, Caledonides of Västerbotten, Sweden. *Sveriges Geologiska Undersökning* **689**, 1–155.
- Upadhyay, D. & Pruseth, K. L. (2012). Fluid-induced dissolution breakdown of monazite from Tso Moriri complex, NW Himalayas: evidence for immobility of trace elements. *Contributions to Mineralogy and Petrology* **164**, 303–316.
- Van Roermund, H. L. M. (1985). Eclogites of the Seve Nappe, Central Scandinavian Caledonides. In: Gee, D.G. and Sturt, B.A. (eds) *The Caledonide Orogen—Scandinavia and Related Areas*, 2. Chichester: John Wiley, pp. 873–886.
- Van Roermund, H. L. M. (1989). High-pressure ultramafic rocks from the allochthonous nappes of the Swedish Caledonides. In: Gayer, R.A. (ed.) *The Caledonide Geology of Scandinavia*. London: Graham & Trotman, pp. 205–219.
- Van Roermund, H. L. M. & Bakker, E. (1983). Structure and metamorphism of the Tängene–Inviken area, Seve Nappes, Central Scandinavian Caledonides. *GFF* **105**, 301–319.
- Whitney, D. L. & Whitney, B. W. (2010). Abbreviations for names of rock-forming minerals. *American Mineralogist* **95**, 185–187.
- Williams, I. S. & Claesson, S. (1987). Isotopic evidence for the Precambrian provenance and Caledonian metamorphism of high grade paragneisses from the Seve Nappes, Scandinavian Caledonides. II. Ion microprobe zircon Th–U–Pb. *Contributions to Mineralogy and Petrology* **97**, 205–217.
- Wojdyr, M. (2010). Fityk: a general-purpose peak fitting program. *Journal of Applied Crystallography* **43**, 1126–1128.
- Zhu, X. K. & O'Nions, R. K. (1999). Monazite chemical composition: some implications for monazite geochronology. *Contributions to Mineralogy and Petrology* **137**, 351–363.
- Zwart, H. J. (1974). Structure and metamorphism in the Seve–Köli Nappe Complex (Scandinavian Caledonides) and its implications concerning the formation of metamorphic nappes. In: Bellière, J. and Duchesne, J. C. (eds) *Géologie des Domaines Cristallins. Centenaire de la Société Géologique de Belgique*. Liège: Société Géologique de Belgique, pp. 129–144.

6.10 ARTICLE 10

Vaculovic, T.; Warchilova, T.; Cadkova, Z.; Szakova, J.; Tlustos, P.; Otruba, V.;
Kanicky, V. Applied Surface Science 2015, 351, 296-302 (IF=5.155)



Contents lists available at ScienceDirect

Applied Surface Science

journal homepage: www.elsevier.com/locate/apsusc

Influence of laser ablation parameters on trueness of imaging



T. Vaculovič^{a,b}, T. Warchilová^{a,b}, Z. Čadková^c, J. Száková^c, P. Tlustoš^c, V. Otruba^a, V. Kanický^{a,b,*}

^a Department of Chemistry, Faculty of Science, Masaryk University, Kotlářská 2, Brno 611 37, Czech Republic

^b CEITEC, Masaryk University, Kamenice 5, Brno 625 00, Czech Republic

^c Faculty of Agrobiological, Food and Natural Resources, Czech University of Life Sciences Prague, Kamýčka 129, Praha 165 21, Czech Republic

ARTICLE INFO

Article history:

Received 23 December 2014

Received in revised form 24 April 2015

Accepted 21 May 2015

Available online 29 May 2015

Keywords:

Laser ablation
ICP-MS
Imaging
Tapeworm

ABSTRACT

Influence of laser ablation conditions on limit of detection, spatial resolution and time of analysis was studied for laser ablation inductively coupled plasma mass spectrometry (LA-ICP-MS) applied to elemental mapping. Laser repetition rate and laser fluence were investigated in tapeworm thin section to attain optimum ablation rate, yielding appropriately low detection limit which complies with elemental contents in the tissue. Effect of combinations of laser spot size and scan speed on relative broadening (Δw_{rel}) of image of the ablated pattern (line) was investigated with the aim to quantify the trueness of imaging. Ink lines printed on paper were employed for the study of influence of spot size and scan speed on limit of detection, relative broadening of elemental image and duration of elemental mapping. An uneven distribution of copper in a printed line (coffee stain effect) was observed. The Δw_{rel} is strongly reduced (down to 2%) at low scan speed ($10 \mu\text{m s}^{-1}$) and laser spot diameter of $10 \mu\text{m}$ but resulting in unacceptably long time of mapping (up to 3000 min). Finally, tapeworm thin-section elemental maps ($4 \text{ mm} \times 5 \text{ mm}$) were obtained at the laser spot diameter of $65 \mu\text{m}$ and the scan speed of $65 \mu\text{m s}^{-1}$ within 100 min. A dissimilar lateral distribution of Pb was observed in comparison with that of Cu or Zn due to different pathways of element uptake.

© 2015 Elsevier B.V. All rights reserved.

1. Introduction

In the past few years, there has been a growing interest in spatial distribution imaging of elements in biological materials by physical methods of chemical analysis. The most used techniques are nuclear magnetic resonance imaging (MRI) [1], proton-induced X-ray emission (PIXE) [2], quantitative positron emission tomography (PET) [3], scanning electron microscopy (SEM) [4,5], secondary ion mass spectrometry (SIMS) [6], energy-filtering transmission electron microscopy (EFTEM) [7], and matrix-assisted laser desorption ionization mass spectrometry (MALDI) [8,9]. Unfortunately, some of these techniques do not provide sufficiently low detection limits for trace analysis, although they offer excellent spatial resolution.

Since the inception of laser ablation inductively coupled plasma mass spectrometry (LA-ICP-MS) in 1985 [10], this method has been progressively developed and nowadays ranks among the most widely used mass spectrometry techniques for trace element determination in soft and hard biological tissues [11–13]. LA-ICP-MS

offers in principle satisfactory values of both limits of detection and spatial resolution and therefore can be used as a tool for elemental bio-imaging, e.g. in tree leaves [14], tissues of animals [15,16], and humans [17,18]. Zoriy and Becker [19] studied the feasibility of determination of platinum-based drugs in tissues by LA-ICP-MS as an alternative to autoradiographic imaging, which is more costly and time-consuming. All the above-mentioned techniques require careful optimization of working parameters and properly prepared samples [20].

One of the challenging tasks of LA-ICP-MS imaging is quantification of elemental maps. Three key parameters are of utmost importance for this objective, namely: (i) sensitivity of LA-ICP-MS signal compensated for matrix effects and corrected for spectral interferences; (ii) spatial (lateral) resolution; and (iii) limit of detection. A prerequisite for the implementation of a robust LA-ICP-MS quantification protocol comprises understanding of ablation processes, plasma spectrochemistry and elemental fractionation [21,22].

Signal sensitivity as the first mentioned key parameter of quantitative imaging is matrix-dependent and therefore may differ in calibration and analyzed samples, respectively. Moreover, variability in sensitivity between individual analyzed samples and even between different zones within a sample may occur [23]. Ablation,

* Corresponding author at: Department of Chemistry, Faculty of Science, Masaryk University, Kotlářská 2, Brno 611 37, Czech Republic. Tel.: +420 549494774.
E-mail address: viktork@chemi.muni.cz (V. Kanický).

aerosol transport, and processes influencing ionization efficiency in an ICP source are responsible for variation in sensitivity and for elemental fractionation [24]. Ablation rate, i.e. the amount of target material released per laser shot, represents the onset of these influential processes. In the first approximation, laser ablation rate in calibration and analyzed sample should be ideally the same, but this is not usually fulfilled. What is more, the ablation rate may vary over the mapped surface depending on properties of particular regions.

Variation in aerosol amount, size distribution, and composition of aerosol particles occurs not only during ablation, but also in the course of aerosol transport. Finally, particle size- and composition-dependent vaporization in an ICP source together with water/matrix load of the ICP source determines the sensitivity [25–27]. One must also not forget the spectral interferences. Lack of appropriate calibration materials that at best exactly match the sample composition makes quantitative elemental imaging in biological samples harder. Besides, certified reference materials, which may be used as calibration samples or for a method validation, do not match all sample types. Due to frequent heterogeneity of biological tissue matrices, a section thickness and water content in various tissue regions may affect the analytical signal. The approaches employed for LA-ICP-MS quantification include the following procedures: development of matrix-matched laboratory standards [17,18,28,29], solution-based calibration [30,31], or calibration based on internal standardization with ^{13}C [11,32]. If the elemental composition of sample is known, the normalization method based on the total sum of signals of isotopes can be applied [33,34]. Briefly, sensitivity compensated for matrix effects represents one of the key parameters of LA-ICP-MS imaging.

A particular attention should be paid to another key parameter, namely spatial resolution. The majority of LA-ICP-MS imaging applications usually operate with a resolution of 30–50 μm per pixel and above [11,35]. Thickness of tissue slices varies from 3 to 100 μm , but typically is in the range 10–20 μm [36,37]. Very thin slices allow a clean ablation without tissue cracking and more tissue aerosol may be efficiently transported to the ICP, which results in higher sensitivity. The slight reduction in spot size and scan speed may not lead always to significant improvement in resolution [37].

The limit of detection (LOD) as the third key parameter diminishes with increasing laser spot size, which in turn worsens the spatial resolution. Consequently, compromise operating conditions have to be found.

The goal of the present work consists in the study of influence of scan speed and laser spot diameter on lateral resolution, LOD, and time consumption of analysis. Several works deal with the study of influence of repetition rate, scan speed, and laser spot diameter on ICP-MS signals and particle size distribution using glass reference materials [38–40] even brass sample [41] but not with regard to spatial resolution. It was found that at ns-laser ablation of silicate matrix, the laser-induced fractionation increases with decreasing laser spot size [39,40]. The laser-induced fractionation was confirmed at femtosecond laser ablation by Diwakar et al. [41], who performed fs laser ablation with high repetition rate (up to 1 kHz) in combination with small laser spot size (10 μm) and high scan speed (200 $\mu\text{m s}^{-1}$) which led to successful bulk analysis with very good spatial resolution. The improvement of spatial resolution was achieved by construction of new ablation cells [42,43]. Wang et al. [43] describes improvement of imaging capabilities in new tube cell. Van Malderen et al. [42] use combination of new low-volume ablation cell and deconvolution of overlapping ablation position for better resolution. Optimized operating conditions were employed for acquisition of Cu, Zn, and Pb lateral distributions in tapeworm thin sections. The final step, quantification, will be aim of further study.

2. Experimental

2.1. Instrumentation, operating conditions, and strategy of optimization

Ablation system (model UP 213, New Wave Research, Inc., Fremont, CA, USA) consisting of a Q-switched Nd:YAG laser operating at 213 nm with a pulse width of 4.2 ns, a movable ablation cell (SuperCell™, washout time 1.04 s) and a built-in microscope/CCD camera for inspection of an ablated target was coupled to a quadrupole mass spectrometer with ICP source (ICP-MS model 7500 CE, Agilent Technologies, Inc., Santa Clara, CA, USA). The ICP-MS was operated with a collision cell in He-mode (2.5 ml min⁻¹) for minimization of possible polyatomic interferences. Helium was introduced into the ablation cell as the carrier gas with a flow rate of 1 l min⁻¹ and argon was admixed (0.6 l min⁻¹) prior to entering the ICP torch. Monitored elements were chosen with respect to the analysis of organic matrix (biological tissue, matrix element carbon) deposited on a glass slide (matrix element silicon), and contents of studied trace elements (copper, zinc, and lead) in thin sections. The following isotopes were measured with integration (dwell) times indicated in parentheses: ^{12}C (0.01 s), ^{28}Si (0.1 s), ^{65}Cu (0.1 s), ^{66}Zn (0.1 s), ^{208}Pb (0.3 s). The settling time of the mass spectrometer was 200 μs . The total sampling time (one measuring cycle comprising all isotopes) was 0.384 s.

Operating conditions of the laser ablation system, namely laser beam fluence, laser repetition rate, laser spot diameter, and scan speed were searched for to obtain optimum values of these response functions: (i) minimum limits of detection; (ii) maximum lateral resolution (minimum relative broadening); and (iii) minimum time of analysis for acquisition of elemental maps. Optimization was performed in two steps.

Laser fluence and repetition rate were studied using the tapeworm tissue to obtain maximum amount of ablated material, which is decisive for minimum limit of detection, and at the same time, to penetrate through the thin section just to the surface of the glass slide.

Laser spot diameter and scan speed were searched for obtaining minimum relative broadening of signal corresponding to a structure of defined dimensions, minimum limit of detection (i.e. maximum isotope sensitivity), and minimum time of analysis. This was accomplished by ablation of white bond paper with ink lines printed by an inkjet printer (Color LaserJet Pro M176n, Hewlett Packard). Printed paper was used due to the possibility to design pattern of lines with known dimensions, spacing, and with a sharp interface, which is not fulfilled in case of irregular structure of tapeworm tissue. The approach based on ablation of printed ink was used for calibration purposes [44] even for creation of 2D patterns [45]. Preliminary multielemental analysis of ink led us to conclude that the optimal element is copper for designed experiments. Firstly, its content in ink is the highest of trace elements detected, and, secondly, copper is contained in tapeworm thin slices and its distribution is mapped.

For optimization of laser spot diameter and scan speed, the white bond paper printed with ink lines with the width of 60 μm was employed. Five laser spot diameters were selected (15, 40, 65, 80, and 100 μm) and nine scan speed values were used (10, 30, 50, 65, 80, 100, 200, 300, and 400 $\mu\text{m s}^{-1}$) with each spot diameter. The laser beam fluence and repetition rate were 9 J cm⁻² and 10 Hz, respectively. Prior each ablation scan, a 10 s pre-ablation time was used for recording of background intensities of measured isotopes. Average background intensity was then subtracted from gross intensity recorded during ablation. LOD was calculated as a ratio of triple standard deviation of background signal and sensitivity of ^{65}Cu .

Elemental mapping of tapeworm thin section was performed under the following optimized conditions: laser spot diameter 65 μm , scan speed 65 $\mu\text{m s}^{-1}$, repetition rate 10 Hz, fluence 9 J cm^{-2} .

2.2. Growing and contamination of tapeworm

Two male Wistar rats (Wistar strain; commercial supplier Velaz, s.r.o., Czech Republic) were inoculated at the age of 2 months by *H. diminuta* larvae (cysticercoids). The test animals were placed in individual cages, where they were kept under standardized conditions ($22 \pm 2^\circ\text{C}$, 12/12 h dark/light cycle) and grown for 6 weeks. During this period, host rats were fed at standard pellet diet (ST-1; Velaz, s.r.o., Czech Republic) and were allowed to drink water ad libitum. One rat was given repeated per-oral doses of lead nitrate (p.a. grade; Lach-Ner, s.r.o., Czech Republic). Each individual dose contained 6 mg of Pb (i.e. 36 mg of Pb of the total). The other host rat, which was not subjected to intoxication with lead nitrate, represented comparative sample. After 6 weeks, experimental animals were sedated and euthanized, and individual *H. diminuta* were immediately removed from the intestines using Teflon® dissecting instruments.

2.3. Preparation of tapeworm thin sections

Tapeworm tissues were thoroughly rinsed in double distilled water, fixed in solution of boiling 4% ethyl alcohol (p.a. grade; Lach-Ner, s.r.o., Czech Republic) until subsequent procedures. Segments of the tapeworm strobilae at various stages of maturation were dehydrated in an increasing ethanol series and embedded in paraffin wax (Paraplast Plus®, Sigma-Aldrich). Both the transversal sections and the longitudinal section were prepared using a microtome device (Leica Microsystems GmbH, Germany). The 40 μm thin slices (for LA-ICP-MS analyses) and the 10 μm thin slices (for morphological observation) were alternately sectioned and fixed on Adhesion Microscope Slides HistoBond®+ (Paul Marienfeld GmbH & Co.KG, Laboratory Glassware, Germany). Subsequently, samples for morphological description were stained with Weigert's haematoxylin, counterstained with a 1% eosin B solution, and protected with cover glass, while samples for chemical analyses were left unstained and uncovered for further procedures.

3. Results and discussion

3.1. Optimization of limit of detection, lateral resolution, and time of analysis

First, the effect of laser repetition rate and laser fluence on ablation rate and consequently on limit of detection in tapeworm thin section was investigated with preliminarily selected laser spot size (100 μm) and scan rate (80 $\mu\text{m s}^{-1}$). As a measure of ablation rate, the signal of $^{12}\text{C}^+$ was used. The study of laser repetition rate has shown that the signal of $^{12}\text{C}^+$ increases up to 10 Hz and above this value remains approximately constant, while signal of $^{28}\text{Si}^+$ appears and then rises. This indicates that maximum ablation rate has been achieved and ablation starts to propagate into the glass substrate. The laser beam fluence was varied in the range from 0.5 to 12.0 J cm^{-2} . Maximum fluence is limited again by the requirement that the laser beam just reaches the tissue/glass interface, which is indicated by emerging of $^{28}\text{Si}^+$ signal. Considering this limitation, the optimum fluence value was found to be 9 J cm^{-2} .

Prior to optimization of limit of detection, lateral resolution, and time of analysis as response functions of spot size and scan speed, copper content in printed line was determined because this information is indispensable for calculation of LOD. In order to distinguish between Cu content in unprinted paper and in printed line,

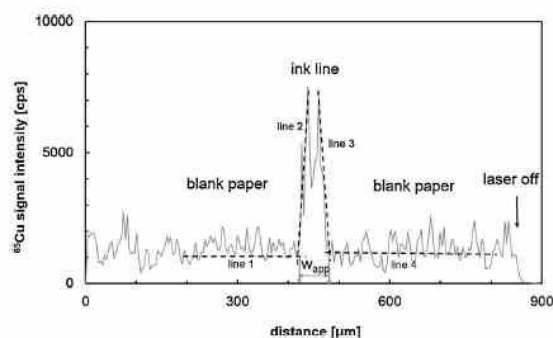


Fig. 1. LA-ICP-MS signal in scan mode recorded for laser beam pass across one printed line at laser spot diameter of 65 μm , scan speed of 10 $\mu\text{m s}^{-1}$, laser beam fluence of 9 J cm^{-2} , and repetition rate of 10 Hz.

analysis by method of standard addition [46] was performed both on printed line ("on line") and on a blank paper ("off line") [46]. Droplets (2 μl) of solutions containing 2, 20, 50, and 250 mg l^{-1} Cu were pipetted on the paper (both "on line" and "off-line"), let dry and then the dried stains and unspiked paper were ablated. Copper content in unprinted/printed area was found to be 30 and 90 mg kg^{-1} , respectively. Besides, statistically insignificant difference between slopes of standard addition regression lines obtained for "on line" and "off line" analyses proved that ablation rate was identical within random errors regardless of color (black/white).

An example of a line scan, an LA-ICP-MS signal record taken with the laser spot diameter of 65 μm and the scan speed of 10 $\mu\text{m s}^{-1}$ is presented in Fig. 1 together with graphical indication of evaluation of apparent width (discussed further in the text). A double-peak was recorded regularly and reproducibly instead of a uniform flat-top/single peak at scan speeds of 10 and 15 $\mu\text{m s}^{-1}$. This can be probably explained by uneven distribution of copper in printed line (coffee stain effect) [47], which was not observed at higher scan speeds when the resolution was getting worse. Nevertheless, this phenomenon does not influence the evaluation of apparent width.

Based on a matrix of LOD values calculated for each combination of laser spot diameter and scan speed, it has been found that the LOD does not depend significantly on scan speed. For example, at the spot diameter of 100 μm , the LOD varies with the scan speed in the range from 1.5 to 1.9 mg kg^{-1} . Such differences are not significant and that is why the LOD values in Table 1 are given for all investigated laser spot diameters but only for a single scan speed (10 $\mu\text{m s}^{-1}$).

On the other hand, significant influence of laser spot size on LOD was observed. Conspicuous decrease in LOD occurs in the range from 15 to 65 μm , whereas no further substantial improvement is attained when increasing the laser spot diameter from 80 to 100 μm . This can be explained as follows. The 3σ -based limit of detection is inversely proportional to the sensitivity supposing that standard deviation of background signal is roughly constant, which has been proved. In the first approximation, sensitivity should be proportional to the amount of ablated material which in turn should

Table 1

Comparison of LOD of copper obtained at various laser beam diameter (15, 40, 65, 80, and 100 μm) and same scan speed (10 $\mu\text{m s}^{-1}$) at laser ablation of paper.

| Laser beam diameter (μm) | LOD (mg kg^{-1}) |
|---------------------------------------|-----------------------------|
| 15 | 40 |
| 40 | 10 |
| 65 | 5 |
| 80 | 3 |
| 100 | 2 |

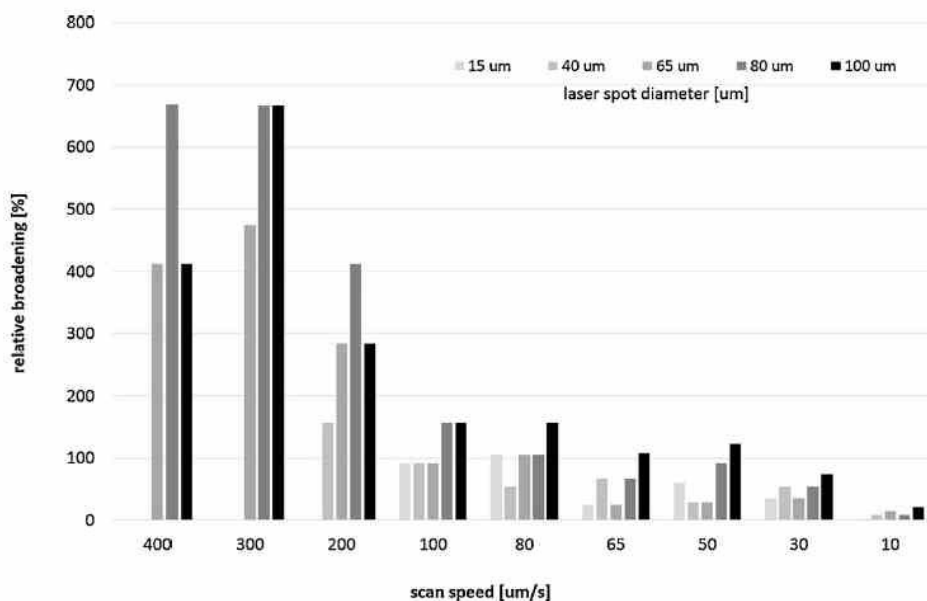


Fig. 2. Relative broadening of a profile of a printed line (expressed in %) with width of 60 μm obtained at various combinations of laser spot diameter (μm) and scan speed ($\mu\text{m s}^{-1}$).

be proportional to the laser spot area (to the second power of the radius) provided that the fluence is constant. Considering random error, the LOD values listed in Table 1 meet this relationship.

For evaluation of distortion of resolution, an apparent width w_{app} of the LA-ICP-MS signal in time/distance scale was introduced, which is a difference between the onset of the signal rise and the end of its drop when the laser spot passes across the testing pattern; in this case, the ink line. Apparent width w_{app} was determined for combinations of laser spot diameter and scan speed values. The onset and end points were obtained as the intersections of trend lines 1 and 2, and trend lines 3 and 4, respectively (Fig. 1). Trend

lines 1 and 4 were obtained from linear regression fitted in domains of signal recorded within the space between printed lines, while trend lines 2 and 3 were obtained by linear regression in domains of signal rise and drop, respectively. The trueness of imaging was expressed as a relative broadening Δw_{rel} of the image w_{app} of the printed line in comparison with its real width w :

$$\Delta w_{\text{rel}}(\%) = \frac{w_{\text{app}} - w}{w} \times 100$$

The values of Δw_{rel} for most of the examined combinations of laser spot diameter and scan speed are displayed in Fig. 2. The

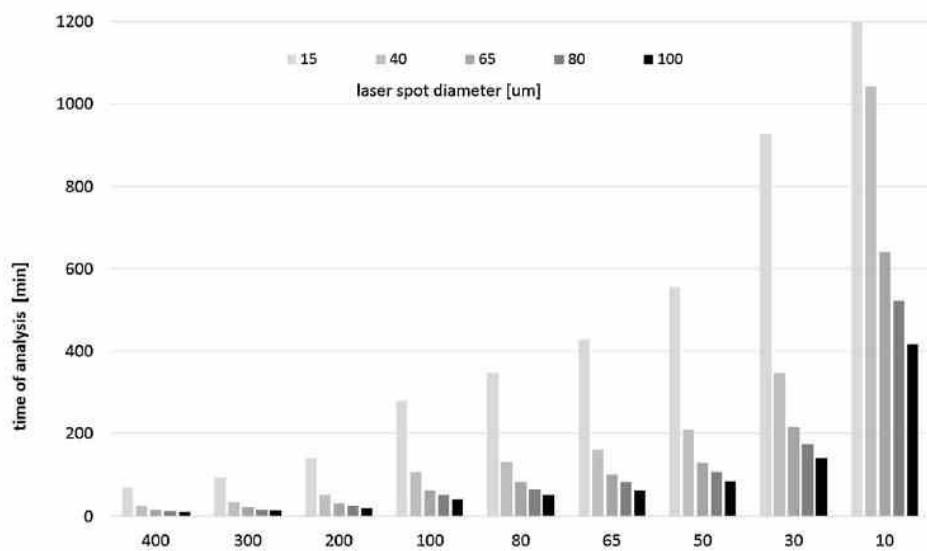


Fig. 3. Duration of scanning of the sample area of 4×5 mm at combinations of laser spot diameter (μm) and scan speed ($\mu\text{m s}^{-1}$).

relative broadening augments with enlarging the laser spot and increasing the scan speed as well, while the scan speed affects the broadening more strongly than the laser spot diameter. This is understandable when one considers that the maximum and minimum spot diameter differ by a factor of 6, while the scan speed by a factor of 40. Above $300 \mu\text{m s}^{-1}$, w_{app} exceeds the real width up to 7 times. For combinations of 300 and $400 \mu\text{m s}^{-1}$ scan speed with laser spot diameters of 15 and $10 \mu\text{m}$, Δw_{rel} could not be determined because only one laser ablation shot occurred onto the printed line. The lowest Δw_{rel} ranging from 2 to 22% is observed at the scan speed of $10 \mu\text{m s}^{-1}$.

The differences in relative broadening relate to a combination of scan speed and a quadrupole mass spectrometer sampling time, which is the time period required for sequential measurement of all isotopes in the measuring method. Besides the sampling time of the used method (0.384 s), a washout time of the ablation cell (1.04 s) contributes to signal broadening.

However, it is not just the limit of detection and lateral resolution that governs the usability of the developed LA-ICP-MS elemental mapping method for a particular task but also duration of analysis is important as it determines the operating cost. Fig. 3 demonstrates the time required for the mapping of a typical thin section area of $4 \text{ mm} \times 5 \text{ mm}$ at several combinations of laser spot diameter and scan speed values. The slowest scan speed of $10 \mu\text{m s}^{-1}$ provides the lowest broadening but is obviously the most time-consuming, as the mapping of this area lasts from 417 to 2778 min depending upon the laser spot diameter. This is obviously unacceptable cost for the best resolution. Therefore, the laser spot diameter of $65 \mu\text{m}$ and the scan speed of $65 \mu\text{m s}^{-1}$ were selected as compromise operating conditions with respect to limits of detection, lateral resolution, and duration of analysis, which is only 100 min. Besides, the time of analysis increases not only because of slower scan speed, but also due to the fact that a longer line scan is necessary to cover the area of interest. The smaller spot diameter

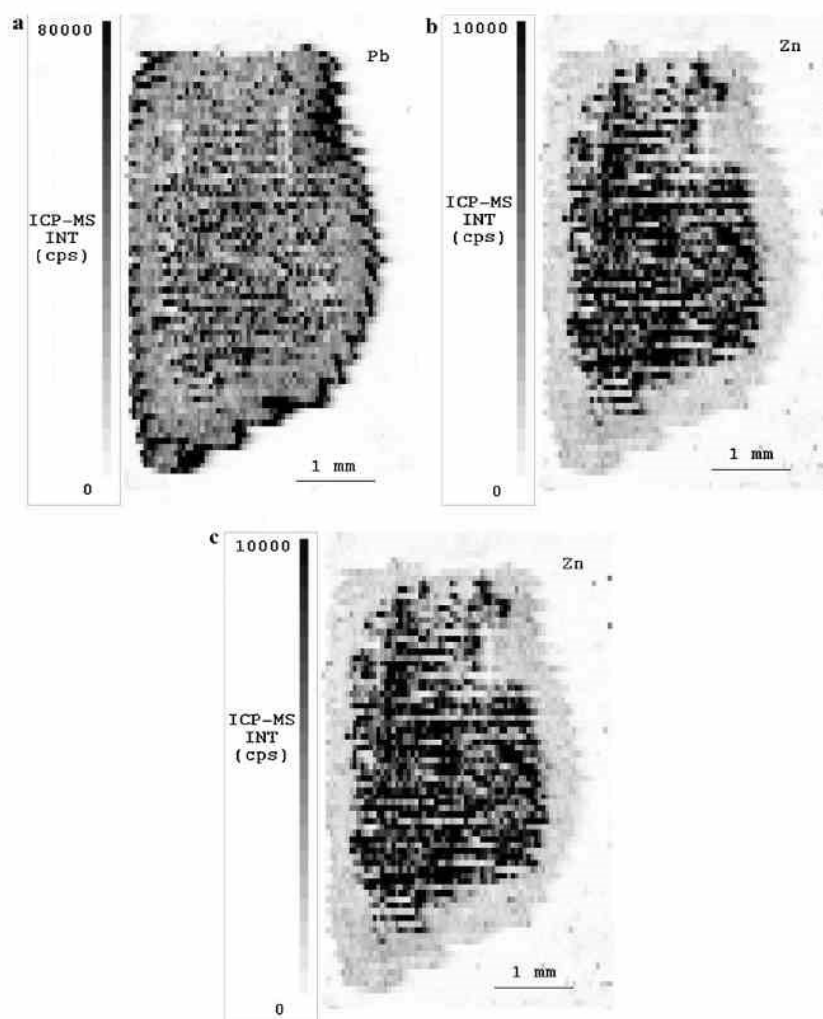


Fig. 4. Distribution of (a) Pb, (b) Zn, and (c) Cu in the tapeworm thin section measured at the laser spot diameter of $65 \mu\text{m}$, the scan speed of $65 \mu\text{m s}^{-1}$, the fluence of 9 J cm^{-2} , and lasing repetition rate of 10 Hz.

is applied, the smaller spacing between scan lines should be used in fact (which was not applied here). However, this would further prolong the analysis because of higher density of ablation raster.

3.2. Elemental mapping of tapeworm thin sections

Mapping of distribution of Pb, Cu, and Zn in 4 mm × 5 mm area (Fig. 4) of a tapeworm thin section took 100 min under compromise operating conditions (laser spot diameter of 65 μm and scan speed of 65 μm s⁻¹). Distribution of lead differs significantly from that of zinc or copper. Circumferential band along the edge of the tapeworm thin section is enriched with lead, and an increased content of Pb is observed also in the central part of the section, being rather randomly distributed (Fig. 4a). In contrast, the map in Fig. 4b, exhibits very low occurrence of Zn in the circumferential band, while the inner part of the section shows almost continuous area of substantially elevated presence of zinc. Copper exhibits the same lateral distribution as zinc (Fig. 4c). A higher lead content in the layer below the surface of the tapeworm body is due to the penetration of lead from surrounding nutrient solution through the body surface. In contrast, copper and zinc are essential elements and therefore are incorporated in keratin tissues and organs. Higher scan speed and larger laser spot diameter (300 μm s⁻¹ and 100 μm) considerably decrease time of analysis (14 min), but the depleted/enriched zones are not identified because of 700% broadening.

4. Conclusion

The influence of operating conditions of a laser ablation system, namely laser repetition rate, laser fluence, laser spot size, and scan speed, on several response functions (limit of detection, lateral resolution, and time of analysis) were studied for LA-ICP-MS elemental mapping of a tapeworm tissue. Ink lines printed on paper were employed for investigation of influence of laser spot size and scan speed on limit of detection, lateral resolution (broadening of pattern), and time of analysis. Uneven (bimodal) distribution of copper across the printed ink line was observed, probably due to the so-called coffee stain effect. Compromise conditions have been found using classical optimization based on varying one parameter at a time. Spatially well-resolved elemental (Cu, Zn, and Pb) maps were obtained for the tapeworm thin section at the laser spot diameter of 65 μm and the scan speed of 65 μm s⁻¹ in 100 min. A dissimilar lateral distribution of Pb was observed in comparison with that of Cu or Zn due to different pathways of element uptake. Thus, the obtained elemental maps can be subjected to quantification with a suitable calibration, which is the aim of further study.

Acknowledgements

The authors acknowledge the Czech Science Foundation (GACR) for a grant to support the project S13-18154. This work was also supported by the European Regional Development Fund project "CEITEC" CZ.1.05/1.1.00/02.0068.

References

- [1] L. Borisjuk, H. Rollitschek, T. Neuberger, Nuclear magnetic resonance imaging of lipid in living plants, *Progr. Lipid Res.* 52 (2013) 465–487.
- [2] D.R. Fernando, E.J. Bakkaus, N. Perrier, A.J.M. Baker, I.E. Woodrow, G.N. Batianoff, R.N. Collins, Manganese accumulation in the leaf mesophyll of four tree species: a PIXE/EDAX localization study, *New Phytol.* 171 (2006) 751–758.
- [3] U. Nestle, W. Weber, M. Hentschel, A.L. Grosu, Biological imaging in radiation therapy: role of positron emission tomography, *Phys. Med. Biol.* 54 (2009) R1–R25.
- [4] H. Kupper, F.J. Zhao, S.P. McGrath, Cellular compartmentation of zinc in leaves of the hyperaccumulator *Thlaspi caerulescens*, *Plant Physiol.* 119 (1999) 305–311.
- [5] A. Goldstein, Y. Soroka, M. Frusic-Zlotkin, I. Popov, R. Kohen, High resolution SEM imaging of gold nanoparticles in cells and tissues, *J. Microsc.* 256 (2014) 237–247.
- [6] J.L. Guerquin-Kern, T.D. Wu, C. Quintana, A. Croisy, Progress in analytical imaging of the cell by dynamic secondary ion mass spectrometry (SIMS microscopy), *Biochim. Biophys. Acta* 1724 (2005) 228–238.
- [7] S. Marco, T. Boudier, C. Messaoudi, J.L. Rigaud, Electron tomography of biological samples, *Biochem. Moscow* 69 (2004) 1219–+.
- [8] B. Balluff, C. Schone, H. Hofer, A. Walch, MALDI imaging mass spectrometry for direct tissue analysis: technological advancements and recent applications, *Histochem. Cell Biol.* 136 (2011) 227–244.
- [9] S.R. Oppenheimer, D.M. Drexler, Tissue analysis by imaging MS, *Bioanalysis* 4 (2012) 95–112.
- [10] A.L. Gray, Solid sample introduction by laser ablation for inductively coupled plasma source-mass spectrometry, *Analyst* 110 (1985) 551–556.
- [11] C. Austin, D. Hare, A.L. Rozelle, W.H. Robinson, R. Grimm, P. Doble, Elemental bio-imaging of calcium phosphate crystal deposits in knee samples from arthritic patients, *Metallomics* 1 (2009) 142–147.
- [12] L. Bartkus, D. Amarasiriwardena, B. Arriaza, D. Bellis, J. Yanez, Exploring lead exposure in ancient Chilean mummies using a single strand of hair by laser ablation-inductively coupled plasma-mass spectrometry (LA-ICP-MS), *Microchem. J.* 98 (2011) 267–274.
- [13] M. Legrand, R. Lam, M. Jensen-Fontaine, E.D. Salin, H.M. Chan, Direct detection of mercury in single human hair strands by laser ablation inductively coupled plasma mass spectrometry (LA-ICP-MS), *J. Anal. At. Spectrom.* 19 (2004) 1287–1288.
- [14] E. Hoffmann, C. Ludke, J. Skole, H. Stephanowitz, E. Ullrich, D. Colditz, Spatial determination of elements in green leaves of oak trees (*Quercus robur*) by laser ablation-ICP-MS, *Fresenius J. Anal. Chem.* 367 (2000) 579–585.
- [15] D. Hare, B. Reedy, R. Grimm, S. Wilkins, I. Volitakis, J.L. George, R.A. Cherny, A.I. Bush, D.I. Finkelstein, P. Doble, Quantitative elemental bio-imaging of Mn, Fe, Cu and Zn in 6-hydroxydopamine induced Parkinsonism mouse models, *Metallomics* 1 (2009) 53–58.
- [16] C. Austin, D. Hare, T. Rawling, A.M. McDonagh, P. Doble, Quantification method for elemental bio-imaging by LA-ICP-MS using metal spiked PMMA films, *J. Anal. At. Spectrom.* 25 (2010) 722–725.
- [17] A. Matusch, A. Bauer, J.S. Becker, Element imaging in formalin fixed slices of human mesencephalon, *Int. J. Mass Spectrom.* 307 (2011) 240–244.
- [18] I. Kozz, B. Fernandez, M.L. Fernandez, R. Pereira, H. Gonzalez-Iglesias, M. Coca-Prados, A. Sanz-Medel, Quantitative elemental bio-imaging of Mn, Fe, Cu and Zn in the human lens by LA-ICP-MS, *Anal. Bioanal. Chem.* 406 (2014) 2343–2348.
- [19] M.V. Zoriv, J.S. Becker, Imaging of elements in thin cross sections of human brain samples by LA-ICP-MS: a study on reproducibility, *Int. J. Mass Spectrom.* 264 (2007) 175–180.
- [20] R.J.A. Goodwin, Sample preparation for mass spectrometry imaging: small mistakes can lead to big consequences, *J. Proteom.* 75 (2012) 4893–4911.
- [21] R.E. Russo, X.L. Mao, H.C. Liu, J. Gonzalez, S.S. Mao, Laser ablation in analytical chemistry—a review, *Talanta* 57 (2002) 425–451.
- [22] R. Hergenroder, Laser-generated aerosols in laser ablation for inductively coupled plasma spectrometry, *Spectrochim. Acta B* 61 (2006) 284–300.
- [23] T. Vaculovic, T. Warchilova, T. Simo, O. Matal, V. Otruba, P. Mikuska, V. Kanicky, Elemental mapping of structural materials for a nuclear reactor by means of LA-ICP-MS, *J. Anal. At. Spectrom.* 27 (2012) 1321–1326.
- [24] D. Gunther, B. Hattendorf, Solid sample analysis using laser ablation inductively coupled plasma mass spectrometry, *Trends Anal. Chem.* 24 (2005) 255–265.
- [25] A. Vogel, V. Venugopalan, Mechanisms of pulsed laser ablation of biological tissues, *Chem. Rev.* 103 (2003) 577–644.
- [26] B. Fernandez, F. Claverie, C. Pecheyran, O.F.X. Donard, Direct analysis of solid samples by fs-LA-ICP-MS, *Trends Anal. Chem.* 26 (2007) 951–966.
- [27] I. Apitz, A. Vogel, Material ejection in nanosecond Er: YAG laser ablation of water, liver, and skin, *Appl. Phys. A* 81 (2005) 329–338.
- [28] M. Tibi, K.G. Heumann, Isotope dilution mass spectrometry as a calibration method for the analysis of trace elements in powder samples by LA-ICP-MS, *J. Anal. At. Spectrom.* 18 (2003) 1076–1081.
- [29] D. Hare, C. Austin, P. Doble, Quantification strategies for elemental imaging of biological samples using laser ablation-inductively coupled plasma-mass spectrometry, *Analyst* 137 (2012) 1527–1537.
- [30] C. Pickhardt, J.S. Becker, H.J. Dietze, A new strategy of solution calibration in laser ablation inductively coupled plasma mass spectrometry for multi-element trace analysis of geological samples, *Fresenius J. Anal. Chem.* 368 (2000) 173–181.
- [31] V.L. Dressler, D. Pozebon, M.F. Mesko, A. Matusch, U. Kumtbatim, B. Wu, J.S. Becker, Biomonitoring of essential and toxic metals in single hair using on-line solution-based calibration in laser ablation inductively coupled plasma mass spectrometry, *Talanta* 82 (2010) 1770–1777.
- [32] D.A. Frick, D. Gunther, Fundamental studies on the ablation behaviour of carbon in LA-ICP-MS with respect to the suitability as internal standard, *J. Anal. At. Spectrom.* 27 (2012) 1294–1303.
- [33] C. Latkoczy, Y. Muller, P. Schmutz, D. Gunther, Quantitative element mapping of Mg alloys by laser ablation ICP-MS and EPMA, *Appl. Surf. Sci.* 252 (2005) 127–132.
- [34] A.M. Leach, G.M. Hieftje, Identification of alloys using single shot laser ablation inductively coupled plasma time-of-flight mass spectrometry, *J. Anal. At. Spectrom.* 17 (2002) 852–857.

- [35] J.S. Becker, A. Matusch, C. Depboylu, J. Dobrowolska, M.V. Zoriv, Quantitative imaging of selenium, copper, and zinc in thin sections of biological tissues (Slugs-Genus arion) measured by laser ablation inductively coupled plasma mass spectrometry, *Anal. Chem.* 79 (2007) 6074–6080.
- [36] D.J. Hare, J.L. George, R. Grimm, S. Wilkins, P.A. Adlard, R.A. Chemy, A.J. Bush, D.I. Finkelstein, P. Doble, Three-dimensional elemental bio-imaging of Fe, Zn, Cu, Mn and P in a 6-hydroxydopamine lesioned mouse brain, *Metallomics* 2 (2010) 745–753.
- [37] E. Moreno-Gordaliza, C. Giesen, A. Lazaro, D. Esteban-Fernandez, B. Humanes, B. Canas, U. Panne, A. Tejedor, N. Jakubowski, M.M. Gomez-Gomez, Elemental bioimaging in kidney by LA-ICP-MS as a tool to study nephrotoxicity and renal protective strategies in cisplatin therapies, *Anal. Chem.* 83 (2011) 7933–7940.
- [38] J.J. Gonzalez, A. Fernandez, D. Oropeza, X. Mao, R.E. Russo, Femtosecond laser ablation: experimental study of the repetition rate influence on inductively coupled plasma mass spectrometry performance, *Spectrochim. Acta B* 63 (2008) 277–286.
- [39] Z. Hu, Y. Liu, L. Chen, L. Zhou, M. Li, K. Zong, L. Zhu, S. Gao, Contrasting matrix induced elemental fractionation in NIST SRM and rock glasses during laser ablation ICP-MS analysis at high spatial resolution, *J. Anal. At. Spectrom.* 26 (2011) 425–430.
- [40] S.M. Eggins, L.P.J. Kinsley, J.M.G. Shelley, Deposition and element fractionation processes during atmospheric pressure laser sampling for analysis by ICP-MS, *Appl. Surf. Sci.* 127 (1998) 278–286.
- [41] P.K. Diwakar, J.J. Gonzalez, S.S. Harilal, R.E. Russo, A. Hassanein, Ultrafast laser ablation ICP-MS: role of spot size, laser fluence, and repetition rate in signal intensity and elemental fractionation, *J. Anal. At. Spectrom.* 29 (2014) 339–346.
- [42] S.J.M. Van Malderen, J.T. van Elteren, F. Vanhaecke, Development of a fast laser ablation-inductively coupled plasma-mass spectrometry cell for sub- μm scanning of layered materials, *J. Anal. At. Spectrom.* 30 (2015) 119–125.
- [43] H.A.O. Wang, D. Grolimund, C. Giesen, C.N. Borca, J.R.H. Shaw-Stewart, B. Bodenmiller, D. Gunther, Fast chemical imaging at high spatial resolution by laser ablation inductively coupled plasma mass spectrometry, *Anal. Chem.* 85 (2013) 10107–10116.
- [44] S. Hoels, B. Neumann, S. Tschrititz, M. Linscheid, F. Theuring, C. Scheler, N. Jakubowski, L. Mueller, Development of a calibration and standardization procedure for LA-ICP-MS using a conventional ink-jet printer for quantification of proteins in electro- and western-blot assays, *J. Anal. At. Spectrom.* 29 (2014) 1282–1291.
- [45] D.J. Bellis, R. Santamaria-Fernandez, Ink jet patterns as model samples for the development of LA-ICP-SPMS methodology for mapping of elemental distribution with reference to biological samples, *J. Anal. At. Spectrom.* 25 (2010) 957–963.
- [46] T. Trejos, A. Flores, J.R. Almirall, Micro-spectrochemical analysis of document paper and gel inks by laser ablation inductively coupled plasma mass spectrometry and laser induced breakdown spectroscopy, *Spectrochim. Acta B* 65 (2010) 884–895.
- [47] W. Nischkauer, F. Vanhaecke, S. Bernacchi, C. Hervvig, A. Limbeck, Radial line-scans as representative sampling strategy in dried-droplet laser ablation of liquid samples deposited on pre-cut filter paper disks, *Spectrochim. Acta B* 101 (2014) 123–129.

6.11 ARTICLE 11

Anyz, J.; Vyslouzilova, L.; Vaculovic, T.; Tvrdonova, M.; Kanicky, V.; Haase, H.; Horak, V.; Stepankova, O.; Heger, Z.; Adam, V. *Scientific Reports* 2017, 7 (IF=4.011)

SCIENTIFIC REPORTS

OPEN

Spatial mapping of metals in tissue-sections using combination of mass-spectrometry and histology through image registration

Received: 26 September 2016

Accepted: 02 December 2016

Published: 10 January 2017

Jiri Anyz¹, Lenka Vyslouzilova², Tomas Vaculovic^{3,4}, Michaela Tvrdonova^{3,4}, Viktor Kanicky^{3,4}, Hajo Haase⁵, Vratislav Horak⁶, Olga Stepankova^{1,2}, Zbynek Heger^{7,8} & Vojtech Adam^{7,8}

We describe a new procedure for the parallel mapping of selected metals in histologically characterized tissue samples. Mapping is achieved via image registration of digital data obtained from two neighbouring cryosections by scanning the first as a histological sample and subjecting the second to laser ablation inductively coupled plasma mass spectrometry. This computer supported procedure enables determination of the distribution and content of metals of interest directly in the chosen histological zones and represents a substantial improvement over the standard approach, which determines these values in tissue homogenates or whole tissue sections. The potential of the described procedure was demonstrated in a pilot study that analysed Zn and Cu levels in successive development stages of pig melanoma tissue using MeLiM (*Melanoma-bearing-Libechov-Minipig*) model. We anticipate that the procedure could be useful for a complex understanding of the role that the spatial distribution of metals plays within tissues affected by pathological states including cancer.

Intensive multidisciplinary cooperation involving the life sciences and technology has produced complete genomic DNA sequences for a number of living organisms, but the differences between normal and pathological cellular functions remain to be fully elucidated. Zn, the most abundant transition metal in most cells, plays a vital role in the functions of more than 300 enzymes, DNA stabilization, and the regulation of gene and protein expression. Zn modulates various biological processes, including apoptosis¹, homeostasis, and oxidative stress², and multiple functions of the immune system³.

Zn is also an important player in various diseases, including cancer and aging-related disorders. One of the largest meta-analyses (22,737 participants) of the role of Zn in cancer yielded somewhat conflicting results: elevated serum Zn levels were not observed in any type of cancer, and decreased serum Zn levels were observed only in lung, head and neck, breast, liver, stomach, and prostate cancers⁴. However, Zn patterns were evident at the tissue level, with increased levels in breast cancer tissue and decreased levels in prostate, liver, lung, and thyroid cancers. Ambiguous results for serum and tissue Zn levels were reported for the other included tumours across the analysed studies. These findings indicate the complex role that Zn plays during the transformation of normal tissue to cancerous one.

The observed range of Zn values suggests that Zn levels are influenced by numerous factors, including the origin of the studied tissue, particularly the structural characteristics of the tissue. Cancerous tissue is histologically

¹Department of Cybernetics, Faculty of Electrical Engineering, Czech Technical University, Technicka 2, CZ-166 27 Prague 6, Czech Republic. ²Czech Institute of Informatics, Robotics, and Cybernetics, CTU in Prague, Jugoslávských partyzánů 1580/3, CZ-160 00 Prague 6, Czech Republic. ³Department of Chemistry, Faculty of Science, Masaryk University, Kotlarska 2, CZ-611 37 Brno, Czech Republic. ⁴Central European Institute of Technology, Masaryk University, Kamenice 5, CZ-625 00 Brno, Czech Republic. ⁵Department of Food Chemistry and Toxicology, Berlin Institute of Technology, Gustav-Meyer-Allee 25, D-133 55 Berlin, Germany. ⁶Laboratory of Tumour Biology, Institute of Animal Physiology and Genetics, Academy of Sciences of the Czech Republic, v.v.i., Rumburska 89, CZ-277 21 Libechov, Czech Republic. ⁷Department of Chemistry and Biochemistry, Mendel University in Brno, Zemedelska 1, CZ-613 00 Brno, Czech Republic. ⁸Central European Institute of Technology, Brno University of Technology, Technicka 3058/10, CZ-616 00 Brno, Czech Republic. Correspondence and requests for materials should be addressed to V.A. (email: vojtech.adam@mendelu.cz)

heterogeneous; cancer cells are unevenly dispersed and form clusters of different sizes that are surrounded by normal stromal cells. To elucidate the underlying processes, data must be obtained from histologically homogeneous parts of the studied cancer sample. New methods that can integrate this additional information are needed. We have therefore designed a method that automates the process of combining and matching spatially resolved results from diverse imaging techniques, namely, histological and spectroscopic descriptions of the studied samples. We validated this new method in a case study whereby the Zn and Cu contents and their distribution in pig melanoma using the MeLiM (*Melanoma-bearing Libechov Minipig*) model were analysed. In cancer-affected MeLiM animals, spontaneous regression of melanoma and rebuilding into fibrous tissue frequently occur during postnatal development⁵. The proposed method was used to detect and quantify both the Zn and Cu biomaterials directly in very small, histologically uniform and mutually distinct zones of melanoma samples, providing an efficient method for monitoring changes in metal levels during the process of spontaneous regression. The same method can be easily modified for applications to other biomaterials and/or tissue samples.

Results

Histological heterogeneity of pig melanoma in the MeLiM model. The MeLiM (*Melanoma-bearing Libechov Minipig*) strain of miniature pigs with heritable cutaneous melanoma is an original animal cancer model with histopathological, biochemical and molecular biological similarities to human melanoma^{6–9}. Multiple skin melanomas appear at birth or shortly thereafter in approximately half of all piglets. More than 2/3 of the affected minipigs display complete spontaneous regression of tumours, which is usually accompanied by skin and bristle depigmentation. After a short postnatal period of tumour growth, the first signs of spontaneous regression, both macroscopic (flattening and grey colour of tumours) and microscopic (gradual destruction of melanoma cells, reduced expression of collagen IV and laminin, and rebuilding of tumour tissue into fibrous tissue), are observed. Ten weeks of age appears to be a turning point in the transition between tumour growth and spontaneous regression in MeLiM melanoma⁵. The incidence of spontaneous regression of melanoma is high in the MeLiM model. Melanoma cells are gradually destroyed after a short postnatal period of tumour growth, and the tumour tissue is rebuilt into fibrous tissue. In connection with this process, four structurally different zones were distinguished in the histological samples and marked with various colours (Fig. 1): GMT (the zone of normally growing melanoma tissue - red rectangles), ESR (the zone of early spontaneous regression - violet rectangles), LSR (the zone of late spontaneous regression - yellow rectangles) and FT (the zone of fibrous tissue - green rectangles). A detailed histological view of the zones and their description are given in Fig. 2A–D. Particularly, using haematoxylin-eosin staining, four histologically different zones were distinguished in the collected melanoma samples (Fig. 2A–D):

- The zone of normally growing melanoma tissue (GMT) was composed of heavily pigmented, intact melanoma cells, which were distributed close together with narrow extracellular spaces (Fig. 2A).
- The zone of early melanoma cell destruction (early spontaneous regression, ESR) included cellular debris from some of the damaged melanoma cells, but a considerable number of melanoma cells were still well preserved (Fig. 2B).
- The zone of late melanoma cell destruction (late spontaneous regression, LSR) was characterized by extensive damage to the melanoma tissue (forming predominantly cellular debris with small groups or individually dispersed melanoma cells) and its incipient rebuilding in the fibrous tissue (Fig. 2C).
- The zone of fibrous tissue (FT) arising by the total rebuilding of tumour tissue. A small number of remaining melanoma cells were occasionally still present (Fig. 2D).

Age-dependent changes in melanoma structure were clearly observed. In the melanoma of the youngest (4-week-old) animals, zones of normally growing melanoma tissue were distinctly prevalent compared with zones of early melanoma cell destruction. The other two zones were entirely missing. The number and size of the GMT zones decreased with age, whereas the opposite tendency was observed in the zones of ESR and late melanoma cell destruction (the latter appeared in 6-week-old animals). The damaged tumour tissue was gradually replaced by fibrous tissue, which was first observed in 15-week-old minipigs. In the melanoma of the oldest animals (22 weeks old), zones of late destruction of melanoma cells were most prevalent, and fibrous tissue occupied the areas between the zones. In these minipigs as well as in the 15-week-old minipigs, zones of GMT were no longer observed. Using the method suggested in the present paper, selected zones were matched with the elemental map (of the neighbouring cryosection) as provided by laser ablation with the aim of comparing Zn and Cu content in melanoma during melanoma growth and successive stages of spontaneous regression.

Elemental imaging. Laser ablation inductively coupled plasma mass spectrometry (LA-ICP-MS) enables the measurement of the metal content in a selected zone ranging from one to several hundred micrometres on the sample surface. LA-ICP-MS provides an ideal, rich source of information because it can match each ablation pixel (the smallest part of the studied sample that can be distinguished using ablation) to the relevant quantified information about the presence of most chemical elements. Laser ablation parameters, such as laser beam fluence, laser spot size, and scan speed rate, determine the time necessary for analysis of any sample as well as the accuracy of the obtained results. These parameters were optimized to ensure the required performance, namely a low limit of detection (LOD) and low broadening of images within a reasonable time period of analysis. This optimization was performed by ablation of white paper with printed ink lines of 800 μm thickness. For this purpose, the ⁶³Cu signal was recorded because this element is present in the used ink¹⁰.

Elemental mapping was performed using line scan mode so that each line started on a glass substrate outside the tumour tissue. The laser beam was moved on the sample surface continuously along a straight line with a constant scan rate of 200 $\mu\text{m}/\text{s}$. The laser beam diameter and the distance between individual straight lines were both 100 μm . The laser beam fluence and the repetition rate were optimized, and respective values of 8 J/cm²

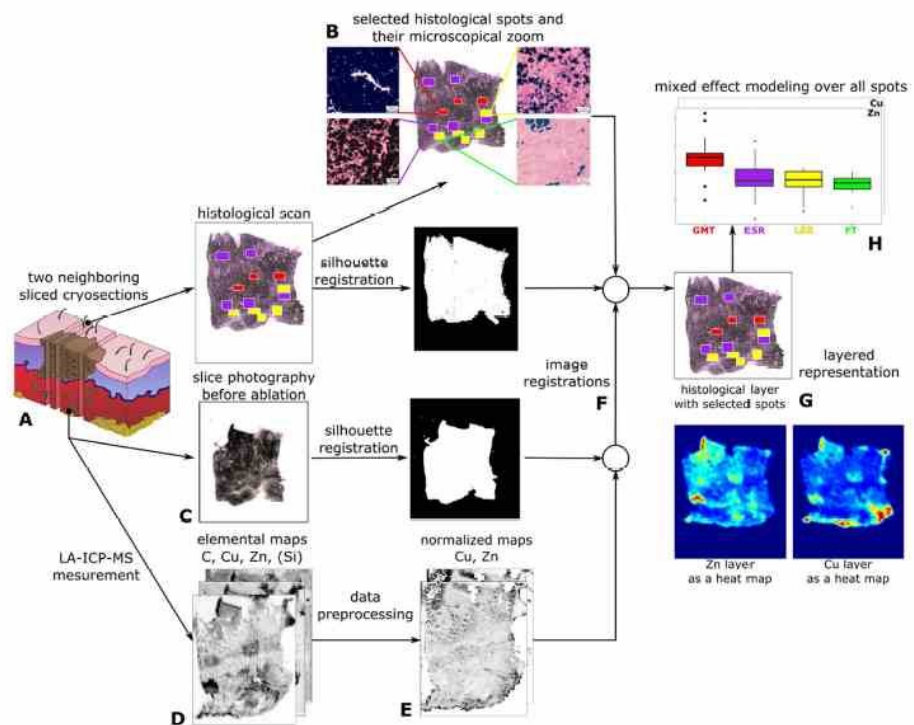


Figure 1. A schematic description of the whole transformation process from cryosections to matched layers representation and statistical evaluation. (A) The two cryosections were sliced from tissue, (B) the narrow slice is used for histological analysis and to find uniform spots - red - GMT (normally growing melanoma tissue), violet - ESR (early spontaneous regression), yellow - LSR (late spontaneous regression) and green - FT (fibrous tissue). (C) The wide slice is photographed and (D) measured by LA-ICP-MS. (E) The measured elemental maps are normalized with respect to dry weight. The slices are registered in two steps. (F) Firstly, the normalized metal maps are registered with the slice photography and secondary, the result of the first step is registered with the histological scan. The registration is based on silhouette registration. (G) The output of the process is a layered representation of tissue consisting of a histological layer with selected spots and metal layers. (H) The layered representation of all tissues is statistically evaluated. Our data confirm the hypothesis that content of zinc in the zone of growing melanoma tissue (GMT) is significantly greater than in all remaining zones.

and 20 Hz were used for all LA-ICP-MS analyses. The high laser beam fluence was used to prevent influence of different ablation rates (see section "2D imaging" for more details) and was optimized to reach the glass substrate during laser ablation.

The quantification was based on calibration performed using agarose gel standards prepared by spiking with known amounts of Cu and Zn, for Cu see in Fig. 3A. The prepared calibration standards contained single metal content of 0, 20, 100, 500 and 2000 mg/kg. Each standard was ablated in triplicate using the same ablation parameters used for imaging. Background correction was performed by subtraction of the average signal obtained using a carrier gas blank (He).

Ablation parameter setting and relative broadening of images. In imaging by means of LA-ICP-MS, a broadening of imaged patterns occurs that can be evaluated as described previously¹⁰⁻¹². The broadening is mainly due to a combination of the laser spot size and scan speed rate. Hence, these parameters must be carefully adjusted with respect to the size of the treated samples (due to time of analysis) and the size of the zones of interest (due to trueness of imaging).

Histologically different zones in minipig tumour tissues were well-defined areas inside the analysed tissue samples with a size of several hundred micrometres in each dimension. Eight scan speed rates were used for the optimization (80, 100, 150, 200, 300, 400, 500 and 1000 $\mu\text{m/s}$). Due to the large dimensions of the imaged tissue samples (approximately 8×5 mm), a laser spot size of 100 μm was selected to reach a minimal LOD. An increase in the laser spot size resulted in a lower LOD^{10,13}. The apparent width w_{app} was calculated to evaluate the broadening caused by the various scan speed rates. w_{app} was obtained as the difference between the onset of the signal increase and the end of its decrease after the laser spot passed across the testing pattern (ink line). The

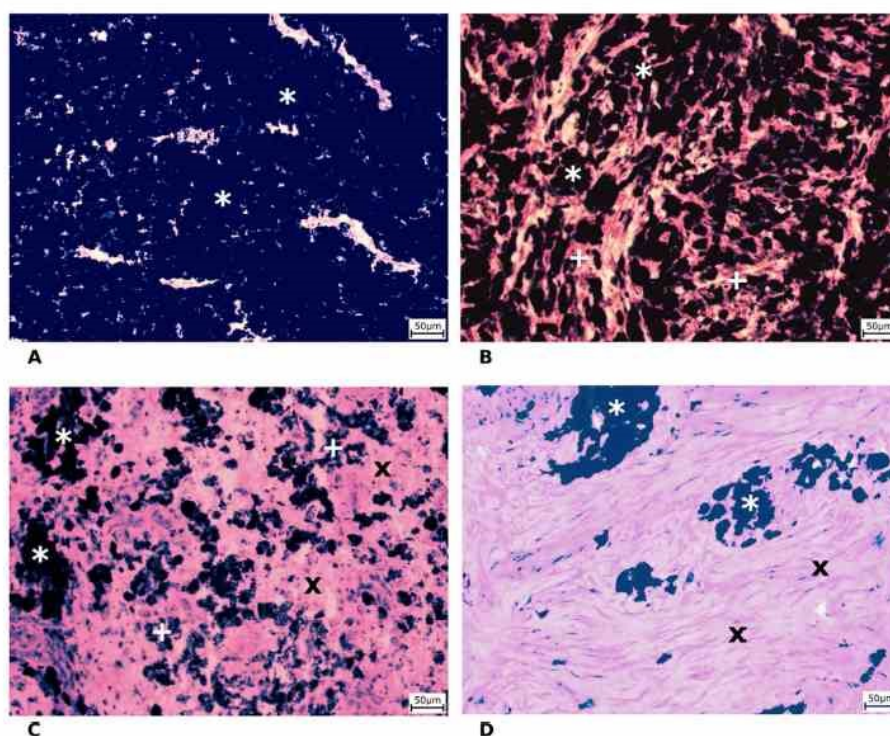


Figure 2. Four histologically differing zones identified in haematoxylin-eosin stained skin porcine melanoma: (A) growing melanoma tissue (GMT), (B) melanoma tissue with early destruction of melanoma cells (early spontaneous regression-ESR), (C) melanoma tissue with late destruction of melanoma cells (late spontaneous regression-LSR), (D) fibrous tissue (FT) with a few remaining melanoma cells. Scale bar = 50 μm (* = melanoma cells; + = cellular debris from damaged melanoma cells; x = fibrous tissue).

onset points were obtained as the intersections of the trend lines **a** and **b**, and the endpoints were obtained as the intersections of the trend lines **c** and **d**. The trend lines **a** and **d** were obtained from linear regression fitted to the domains of the signal between the printed lines, whereas the trend lines **b** and **c** were obtained by linear regression in the domains of signal rise and drop, respectively. The trueness of imaging was expressed as the relative broadening Δw_{rel} of the image w_{app} of the printed line with respect to its real width w .

The dependence of the relative broadening on the scan speed rate is displayed in Fig. 3C. The relative broadening increased from 5% to more than 200% as the scan speed rate increased from 80 to 1000 $\mu\text{m}/\text{s}$.

However, the lateral resolution and LOD were not the only parameters considered in developing the LA-ICP-MS elemental mapping method. The duration of analysis is an important parameter because it affects the operating costs. The times required for mapping are displayed in Fig. 3B and were calculated for typical thin sections of our samples of tumour tissue ($8 \times 5 \text{ mm}$). The time required for analysis decreased with the increasing scan speed rate: whereas approximately 400 minutes was needed for a scan speed rate of 80 $\mu\text{m}/\text{s}$, only 20 minutes was needed for a scan speed rate of 200 $\mu\text{m}/\text{s}$. However, the broadening observed for these parameters was greater than 200%. Hence, a scan speed rate of 200 $\mu\text{m}/\text{s}$ was selected as an optimal compromise because it resulted in a relative broadening of 40% and duration of analysis of 150 min.

2D imaging. Laser beam fluence is one of the most crucial parameters for laser ablation. The laser beam fluence mainly affects the ablation rate, the amount of material released during one laser pulse. Variations of the ablation rate complicate the quantification of LA-ICP-MS experiments because each laser pulse releases different amounts of analysed material in the selected range. There are multiple methods to compensate for this uncertainty. The first approach utilizes normalization to the sum of 100%^{14,15} and can be successfully used for single-spot analysis or imaging of materials with well-known matrix composition to determine the appropriate multiplication coefficient that results in the whole content of 100%. This approach cannot be used for samples with a complex matrix containing large amounts of non-determinable elements or their groups (e.g., fluorapatite, in which OH^- is substituted by F^- , or biological samples containing O, N and H).

In our case, the analysed tumour tissue represents samples containing large amounts of non-determinable elements (O, N, and H). Hence, the normalization approach based on the sum of 100% cannot be used successfully. The second normalization approach is based on utilization of an internal standard¹⁶, i.e., monitoring an isotope

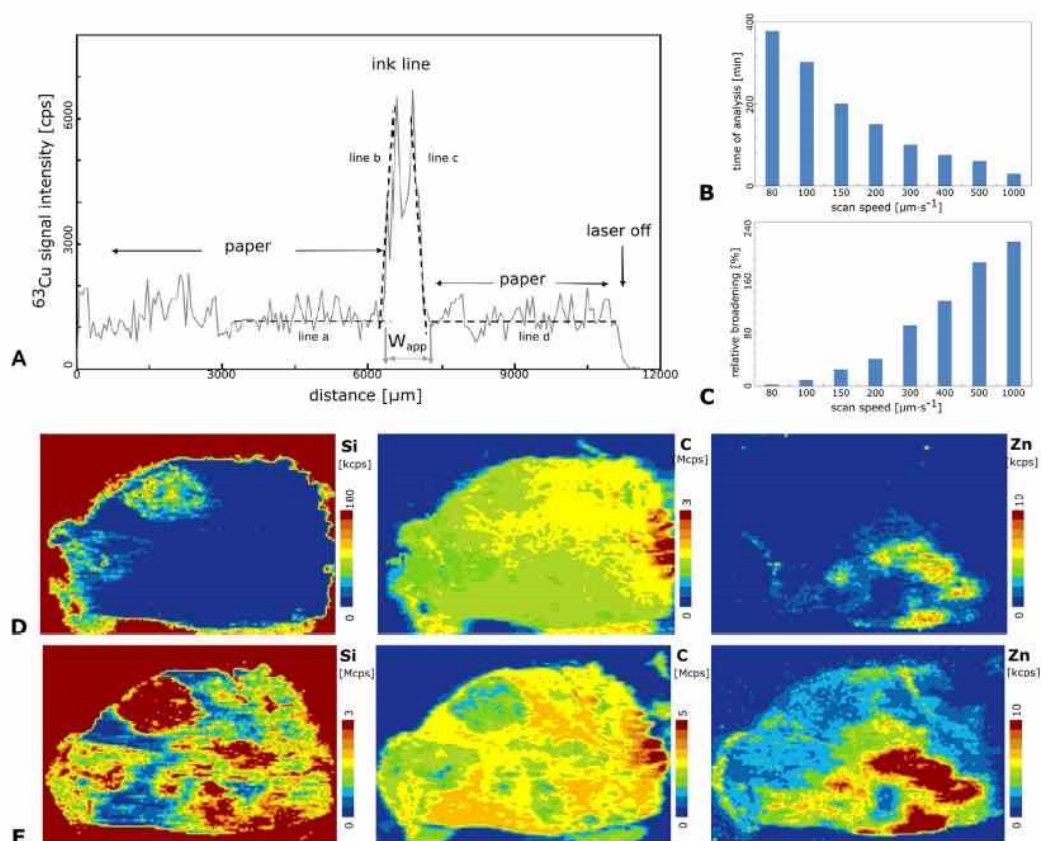


Figure 3. (A) LA-ICP-MS signal in line scan mode recorded for laser beam pass across one printed line at laser spot diameter of $100\mu\text{m}$, scan speed of $20\mu\text{m s}^{-1}$, laser beam fluence of 8 J cm^{-2} and repetition rate of 10 Hz . (B) Duration of scanning of the sample area of $15 \times 15\text{ mm}$ at various scan speeds ($\mu\text{m s}^{-1}$). (C) Relative broadening of a printed line (expressed in %) with width of $800\mu\text{m}$ obtained at various scan speeds ($\mu\text{m s}^{-1}$). (D) Elemental maps of C, Si and Zn obtained at “soft” ablation parameters (2 J cm^{-2}) for tissue K320/1 (12 weeks old). (E) Elemental maps of C, Si and Zn obtained at “hard” ablation parameters (8 J cm^{-2}) for tissue K320/1 (12 weeks old).

with a known amount. It is necessary to rely on internal standards such as C, which is abundant in the sample. However, when carbon is used as an internal standard, marked systematic error arises due to the production of carbon-containing gaseous species, resulting in high losses of the carbon signal during laser ablation¹⁷.

As mentioned above, differences in the ablation rate complicate imaging due to variations in the amount of ablated tissue. This phenomenon could be minimized if controlled amounts of material were released during each laser pulse. Hence, we suggest a total mass removal approach when the whole layer of tissue is completely released. The Si signal indicates when the whole layer of tissue is removed and the glass substrate is ablated as well. Moreover, if the glass substrate does not contain special-interest elements (Zn, Cu and C), there is no danger of contamination from the glass substrate, and the signals of Zn, Cu and C arise from the tissue only.

Elemental images of two nearby thin sections were compared. One section was ablated at high laser beam fluence (8 J cm^{-2} —hard ablation), and the second section was ablated at low laser beam fluence (2 J cm^{-2} —soft ablation), whereas thickness of the given sections were considered to be critical and, thus, were controlled by the slicing machine, where relative standard deviation did not exceed 5% and did not significantly influence further discussed observations. The terms hard and soft ablation are used in this text for explanation only. When soft ablation is applied, the signal of ^{28}Si corresponding to the ablation of the glass substrate under the tissue is not strongly enhanced compared to the gas blank value (Fig. 3D). Thus, the laser beam fluence is not sufficient to ablate the whole layer of the tissue, and the glass substrate is not reached, with the exception of two small regions in the left part of the tissue. When hard ablation is applied, significantly higher intensities of ^{28}Si are observed (Fig. 3E). The range of the ^{28}Si scale is 30 times larger than that of the soft ablation image, indicating that the glass substrate was reached and that the tumour tissue was ablated completely. In the case of the Zn image, we can observe strong enrichment in the lower right corner of tissue. The strongly enhanced Zn signal does not originate from the glass

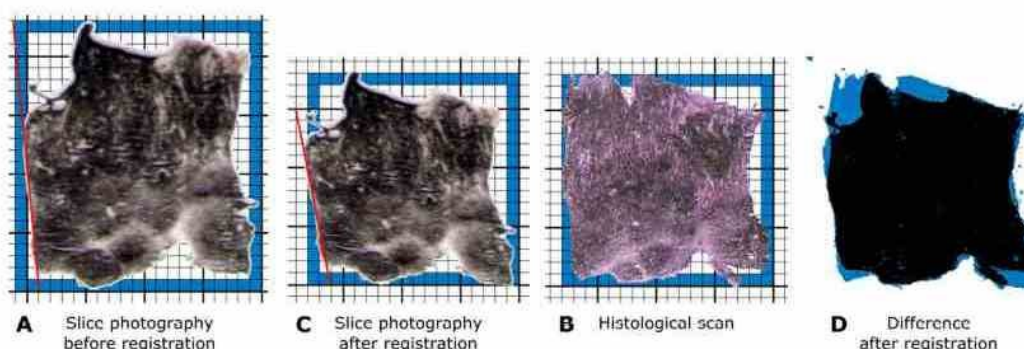


Figure 4. Photographs of two neighboring cryosections prepared to be subjected to laser ablation and to histological analysis (A,B). The image C is the result of registering the images (A,B). The blue rectangle indicates in the images (A–C) the minimal rectangle (with sides parallel to axes) the image fits in. The red line in the image (A,C) accentuates orientation of the corresponding borders on both the images. Images (B,C) are compared in the image (D): while the places appearing in both images have black color, the space in blue corresponds to symmetric difference of both images as explained in Supplementary Note 1.

substrate, as confirmed by comparison with the parts of the image where the glass substrate was analysed only (red part from Si image and blue part of carbon image). The Zn signal is clearly close to zero in all of these regions.

Arguments supporting the need for registration. As it was mentioned above, the data about the spatial distribution of each chemical element can be depicted in the form of an “element heat map” (see Fig. 3D,E). Because the heat maps of all elements can be obtained during one analysis of a single sample, the maps have identical shape, orientation and resolution and are thus ideal for addressing questions such as the relationship between the presence of Zn and Cu in selected ablation pixels of the studied sample. However, the task becomes much more complex when additional information, such as the histological properties of the considered zone, must be incorporated because such information must be determined from another tissue section. Two neighbouring serial cryosections of the original tissue sample must be available, one of which is subjected to ablation, whereas the other is subjected to standard staining for histological analysis. Both treatments produce digital images providing complementary information about the tissue sample. Data corresponding to the selected zone from both treatments must be paired. Fig. 4A and B present photographs of two neighbouring cryosections acquired under the same technical conditions; in an ideal case, the two samples should have identical contours. The two samples are intended for different types of treatment: the sample in Fig. 4A is ready to undergo the ablation procedure, whereas the sample in Fig. 4B will be subjected to a histological analysis. Both samples are so tender that handling them may change both their shape and orientation slightly; the tissue can stretch, or some of its parts may be pinched. Comparison of the two images reveals stretching in both dimensions, with a larger change in the vertical axis: the image in Fig. 4B fits into the blue rectangle with a size of 17.5×18 , whereas an area of 20×23 is necessary for the image in Fig. 4A. Linear transformation of one of the images is suitable to solve this problem. Linear transformation of the image in Fig. 4A is followed by registration to match the histological scan of the sample in Fig. 4B. The resulting image, Fig. 4C (obtained by transformation of Fig. 4A), has a size of 18×18 , which is very close to that of Fig. 4B. The area in which the two images do not match is clearly identified by blue colour in Fig. 4D.

Comparison of the slices before registration of Fig. 4A to B and after this registration (Fig. 4C) indicates that the slices do not have the same orientation. This can be clearly demonstrated through comparison of the angles between the red lines defining one of the borders in both pictures and the horizontal line. Let us estimate the corresponding tangent values using the scale underlying both images: while this value is $23/2 = 11.5$ for the image a, it is $15/3 = 5$ for the image b. The resulting difference in the orientation of both images is approximately 0.055π (or 10°).

Moreover, the size and granularity obtained from the heat map produced from LA-ICP-MS and the histological image can differ by an order of magnitude, depending on the applied magnification. Thus, the absolute size of a pixel in the histological image differs significantly from that of the ablation pixel. To make full use of the information about the spatial distribution of different metals in the sample, a homogeneous cluster of cells must be identified in the histological image, and the corresponding zone must be located in all considered element heat maps. This task can be approximately resolved manually by taking advantage of the human ability to match similar objects, as demonstrated in a breakthrough study of nine samples of invasive breast carcinoma¹⁸. However, manual matching is not a viable solution for frequent analysis of large sample sets. We therefore designed and developed a software method that automates the process of combining and matching spatially resolved results from diverse imaging techniques, namely histological and spectroscopic descriptions. Our method, schematized in Fig. 1, first registers the digital images to project the contours specified in one image to the corresponding pixels of the other images. Consequently, if a zone of interest Z is outlined in one of the images (e.g., histological image), the matching zone Z' is identified automatically in any other image. Thus, it is possible to combine

available complementary data about both matching zones Z and Z' (e.g., histology description of Z and Zn content obtained from Z'), a necessary step towards a modern methodology of analysis, interpretation and integration of biochemical data from diverse sources.

Image registration and creation of layered multidisciplinary description. Each tissue sample was submitted to analysis by two fully independent methods, namely histological scanning and the LA-ICP-MS measurement, and the results for the presence of Zn and Cu in specified histologically uniform locations of the sample were compared. Each of the applied methods processes (and destroys) one of the two bordering serial tissue sections from the same biological sample (Fig. 1A), whereas each delivers its results in the form of a digital image. Morphology of the studied tissue suggests that the corresponding zones in these sections can be assumed to represent identical histological structures provided the selected zones are placed inside of a histologically homogeneous tissue and their diameter is several times bigger than the thickness of the used slices. These conditions were respected during data collection. A standard method for overlaying two different images that has been extensively studied in the context of computer vision and is referred to as image registration was applied¹⁹. Particularly, the methodology of image registration is well developed and offers ample approaches for overlaying two or more images of the same section obtained from different viewpoints or by different sensors¹⁹. The affine transformation²⁰ was chosen for the registration of the studied images after considering other relevant methods. The main benefit of the affine transformation is its simplicity and understandability due to the linear transformation it applies to map the new image on the reference image. Let us assume that an image is a function of two variables $I(x, y)$ that assign an intensity value to the pixel with specific coordinates x and y . The affine transformation of the 2D image is a simple linear mapping in the form of Equation No. 1:

$$\begin{bmatrix} x' \\ y' \\ 1 \end{bmatrix} = \begin{bmatrix} a & b & c \\ d & e & f \\ 0 & 0 & 1 \end{bmatrix} \cdot \begin{bmatrix} x \\ y \\ 1 \end{bmatrix}$$

where x and y are the coordinates of pixels in the original image and x' and y' are the coordinates of the corresponding pixels in the transformed image. The treatment of the image is fully characterized by the constant parameters $a-f$ of the 3×3 transformation matrix T in the middle of the equation. The affine transformation can accomplish translation, rotation, and scaling as well as shear deformation of pixels. The quality of the match between the reference image and the transformed image is characterized by a symmetric difference of both images, as depicted in Fig. 4. This difference should be zero in the ideal case.

Multiresolution image registration²¹ that applies an iterative gradient algorithm is one of the basic procedures for estimation of the parameters $a-f$ of the transformation. It is robust and ensures good results. The registered images were reduced to silhouettes to simplify the parameter estimation and to avoid problems of different modalities of the registered images. The use of silhouettes allows for the definition of the brightness function $I(x, y)$, defined as follows:

$$I(x, y) = 1 \text{ for a pixel belonging to the silhouette} \\ I(x, y) = 0 \text{ elsewhere}$$

First, the registered image must be described in the same coordinate system as the reference image. In the next step, registration can be ensured. The sum of squared differences between the reference image and the registered image (SSD, Fig. 5) was chosen as the criterion to be minimized during the registration procedure. For the silhouettes of the reference image $I_{ref}(x, y)$ and the image to be registered $I_{reg}(x, y)$, the SSD may be defined by Equation No. 2:

$$SSD(I_{ref}, I_{reg}) = \sum_x \sum_y [I_{ref}(x, y) - I_{reg}(x, y)]^2$$

The parameters of the mapping between both images can be determined by minimizing the SSD with the gradient algorithm. To ensure convergence of the gradient algorithm, iterative (gradual) estimation of the parameters on a dyadic decomposition of the images was used [21]. This multiresolution image registration approach decomposes both considered images into a sequence of images with decreasing resolution (the resolution of each successive image is half that of the preceding image). The maximal length I_{max} of the sequence of these decompositions depends on the integer part of the smallest dimension d_{min} (width and/or height "given in pixels of the considered image") of both silhouettes and is given by the following expression as Equation No. 3:

$$I_{max} = \log_2(d_{min}) - 1$$

This upper limit for I_{max} ensures that any of the images in the sequence will have at least 2 pixels in its smallest dimension. The procedure starts with the pair of images (reference and registered) with the lowest level of resolution. The parameters of the transformation are estimated for the given resolution by the gradient algorithm, and their values are used as the initial choice of parameters for the estimation of transformation in the next step, which treats the pair of images with resolution two times higher than the last (the iterative step). These steps are repeated until the original resolution of both images is reached and the final parameter estimates are obtained.

There are even more powerful types of transformations, but affine transformation proved to be sufficient for our purposes. All operations performed by the affine transformation on the image of the tissue sample may be identified with the actual treatment of the sample, such as compressing or stretching of the cryosection during cutting or shifting and rotating during the placement of the cryosection on the slide. The described transformation of coordinates must be followed by the interpolation of the original brightness function to obtain detailed

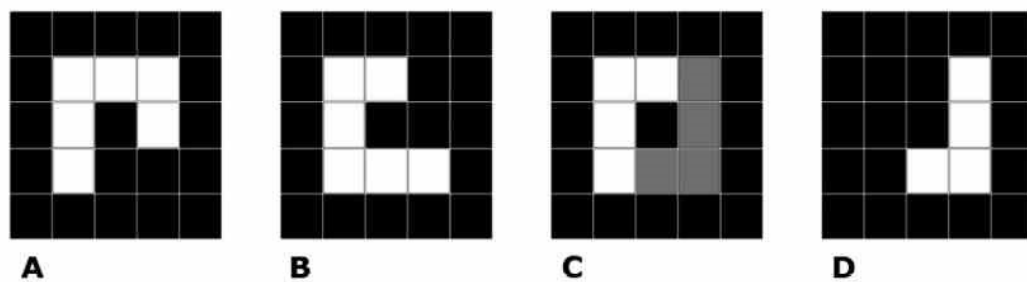


Figure 5. The illustration of the SSD criterion for image registration. The panels (A,B) show the reference image and the image to be registered. The panel (C) shows overlaying of both the images, the gray part corresponds to the difference between the images. The panel (D) shows the difference on itself. As the patterns are 3×3 pixels, the difference part corresponds to SSD of 4.

Information about the transformed image with respect to the new coordinate system. Linear interpolation was used in our case. Our aim is to provide complex information about individual areas of the tissue samples as provided by the considered methods for their analysis. The first step toward this goal is to determine the match between the histological scan and tissue slice photography and also between the tissue slice photography and the laser ablation measurements. The parameters of both transformations were estimated by MATLAB's universal optimizer for unconstrained optimization supplied with the optimization toolbox.

Output of the analysis with biological significance. The preceding procedures provided data for 10 tissue samples each from 10 individual animals of five postnatal ages. Three histologically different zones were observed in each sample obtained from minipigs at 6 weeks of age or older (GMT, ESR and LSR at the age of 6 weeks; ESR, LSR and FT at the age of 15 and 22 weeks), two zones only (GMT and ESR) were detected in the samples from the 4-week-old minipigs. In each individual sample, 10 to 15 spots (3–5 per each zone) were annotated, resulting in 125 annotated spots that were subjected to the statistical analysis described in Supplementary Note 1. The sample means counted from all annotated spots, which were obtained by transforming the histological annotation into content map coordinates, revealed a tendency for decreasing Zn and Cu content during spontaneous disintegration of the melanoma tissue and rebuilding into fibrous tissue (see Fig. 6A–F and Supplementary Table 1). Because the individual animals had different overall metal contents (in the whole tissue sample), a linear mixed effect model^{22,23} was applied to distinguish differences originating from interindividual variation from actual differences among histologically different zones of tissue. Differences among the tissue zones were predicted as fixed effects, and the indicator of an animal was used as a random effect. The resulting *p* values estimated by non-parametric bootstrap test²⁴ were corrected by the Bonferroni correction for multiple comparison²⁵.

The exploration of values depicted in Supplementary Table 1 inspired four hypotheses on the presence of metals in different tissue zones. The testing of these hypotheses is documented in Supplementary Table 2. Table 1 reviews the estimated coefficients of the linear mixed effect model for two hypotheses: “The average Zn (or Cu) content in the GMT zones is lower than that in the remaining zones (ESR, LSR and FT).” To maintain the overall error rate at 0.05, the threshold for *p* values (used in the decision to refute the hypothesis) was 0.0125 according to the Bonferroni correction for multiple comparisons. The presented *p* values indicate that the null hypothesis can be rejected only in case of Zn. Our data confirm that the Zn content in the zone of growing melanoma tissue (GMT) was significantly greater than in all remaining zones, which represent consecutive stages of the tumour tissue that arise as a result of the spontaneous regression of melanoma (ESR, LSR) and its final rebuilding into fibrous tissue.

Discussion

Serum levels of Zn and Cu in melanoma patients have been suggested as valuable diagnostic and prognostic parameters but have yielded conflicting results. The Cu level (but not the Zn level) was generally elevated in melanoma patients, reflecting the degree and extent of tumour activity²⁶. By contrast, serum Cu concentrations were identical in melanoma patients and healthy individuals, whereas the serum Zn concentration was significantly increased in melanoma patients²⁷. In tissue sections, the Zn level was elevated in the majority of melanomas in comparison with the skin of healthy controls. However, the Cu level was increased in some melanoma patients²⁸. The content of melanosomes in skin melanocytes is considerably lower than in melanoma cells, adequately explaining the results of the tissue analysis. Serum concentrations of Zn and Cu are probably greatly influenced by changes in melanosomal membrane permeability due to differences in the cellular milieu, with consequent leakage of reactive melanin precursors (mostly DOPA quinones and semiquinones) whose redox cycling reactions produce H_2O_2 ²⁹. As a type of physiological defence, cells can over-express Zn-containing antioxidant molecules or transport and accumulate them from adjacent tissues. Another pivotal biometal, Cu, acts as a cofactor of tyrosinase, the principal enzyme in the synthesis of melanin pigment from tyrosine³⁰. This process is schematically depicted in Fig. 7.

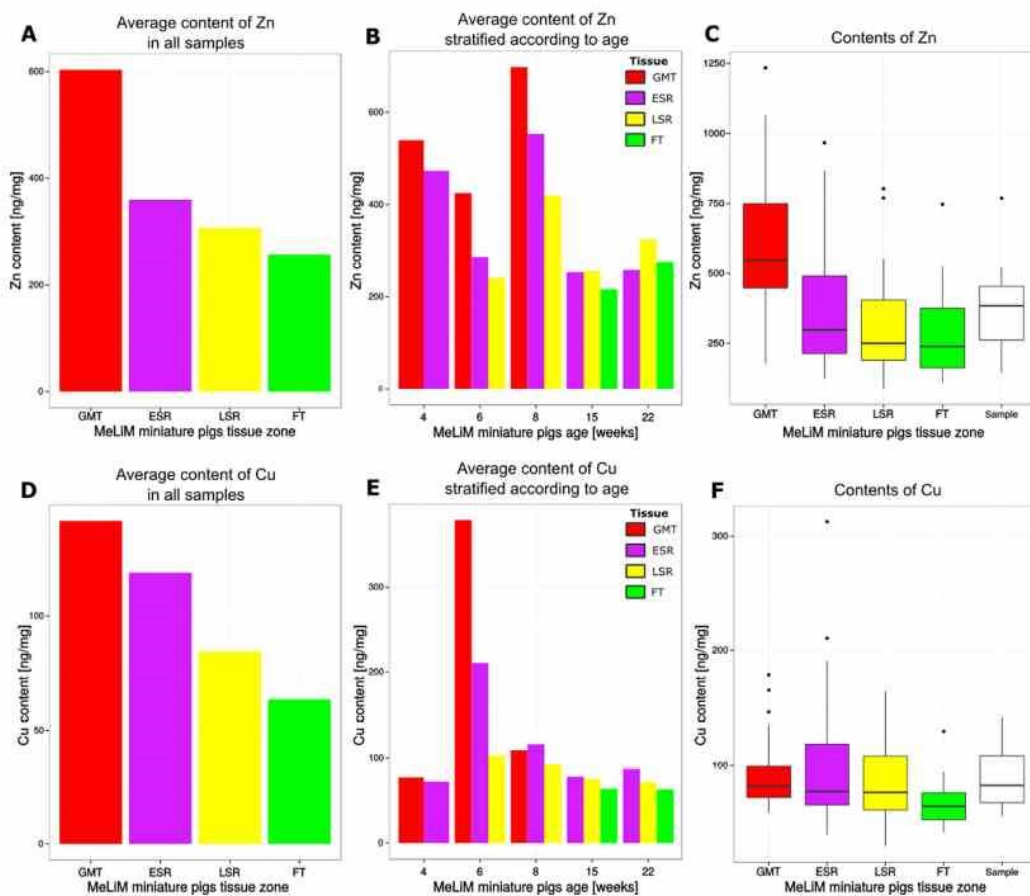


Figure 6. Average content of Zn and Cu in all samples (A,D) and in samples stratified according to age of minipigs (B,E). Box plots (C,F) visualize dispersion of data corresponding to average Zn and Cu content in specified tissue zones by samples as well as by individual samples as a whole for all 10 considered minipigs (the white box plot).

The suggested novel software-supported technique for Zn and Cu mapping permits not only simultaneous quantification in the same tissue cryosection but also detection of both metal ions in very small, histologically characterized zones of tissue, an important advantage compared to their determination in tissue homogenates or in whole tissue sections. We used skin melanoma samples from MeLiM animals of various ages to develop and validate this technique. Our findings (Fig. 6A–C) indicate that the Zn content of a given zone is approximately 3 or 4 times higher than that of Cu (Fig. 6D–F). Moreover, the content of both metals declines as a result of advancing spontaneous regression (due to destruction of melanoma cells by anti-tumour immune reaction). One may suggest that the reason for these changes should be somewhat connected with the expression of proteins, mainly the metal binding ones. From hundreds of the proteins able to bind Cu and Zn, we highlighted tyrosinase and Tyrp 2 (tyrosinase-related protein 2)/Dct (dopachrome tautomerase), two membrane-bound glycoproteins and key enzymes for the synthesis of melanin, where the mentioned metal ions serve as cofactors in the metal-binding sites³¹. Moreover, so called “universal soldiers” metallothioneins (MTs) also have binding capacities for Zn and Cu, whereas these are somewhat related to cancer related processes^{32–34}. On the other hand, imaging metal species in biological tissue presents a complex analytical challenge: a suitable strategy requires a balance of sensitivity, selectivity and spatial resolution³⁵. Hare *et al.* recently showed how they could increase spatial resolution of protein detection using gold-labelled immunohistochemical approach for LA-ICP-MS imaging tyrosine hydroxylase. Their results were associated with iron distribution, whereas findings are critical for further research in the field of neurotransmitters. In addition, our results suggest that the content of Zn and Cu for a given zone fluctuates during the postnatal period, mainly in the earliest ages (4–8 weeks of age). Ten weeks of age appears to be a turning point in the transition between tumour growth and spontaneous regression in MeLiM melanoma⁵. These relations need to be further related to protein spatial distribution, where the above mentioned enzymes and metallothioneins will be further targets.

| | Coefficients | GMT | SR+FT | <i>p</i> values | GMT | SR+FT |
|----|--------------|--------|---------|-----------------|---------|---------|
| Zn | GMT | 495.90 | -146.38 | GMT | 1.00000 | 0.00307 |
| | SR+FT | 146.38 | 349.52 | SR+FT | 0.99693 | 1.00000 |
| Cu | GMT | 126.26 | -44.80 | GMT | 1.00000 | 0.04277 |
| | SR+FT | 44.80 | 81.46 | SR+FT | 0.95723 | 1.00000 |

Table 1. The averages and differences of Zn and Cu contents as estimated by the linear mixed effect model and corrected by random effects are provided in the relevant section of supplementary; the diagonal values are the estimated average contents in the respective zones, and the off-diagonal values indicate their differences.

Material and Methods

Animals and tissue samples. Ten MeLiM animals with multiple skin nodular melanomas (2 pigs each at ages of 4, 6, 8, 15 and 22 weeks) were used in this experiment. One melanoma was excised from each animal under total anaesthesia [premedication with intramuscular (i.m.) atropine 0.5 mg/minipig (Hoechst-Biotika, Slovak Republic), followed by Stresnil 1 mg/kg of body weight (Janssen Pharmaceutica N.V., Belgium) and Narcotan inhalation (Leciva, Czech Republic)]. Vetalgin (0.5 mg/kg of body weight; Intervet International, Germany) was applied i.m. to control pain after tumour excision and wound suturing. This experimental treatment was performed in accordance with the Project of Experiment approved by the Animal Science Committee of the IAPG AS CR, v.v.i. (Libečov, Czech Republic), following the rules of the European Convention for the Care and Use of Laboratory Animals.

Tissue blocks (approximately 8 × 5 mm) of irregular (trapezoidal) shape were obtained from each melanoma. The specific polygonal shape of the cross-section of each block facilitates identical orientation of serial tissue sections used for both histology and LA-ICP-MS. Tissue blocks were placed on a piece of cork, covered with Jung Tissue Freezing Medium (Leica Micro-systems, Germany), and frozen in liquid nitrogen immediately after tumour excision. Serial cryosections (8 μm and 30 μm thick for histology and for LA-ICP-MS, respectively) were prepared by the Leica CM 1850-Cryostat (Leica, Germany), air dried (30 min) and stored at -20 °C until further processing.

Prior to this study, we did a preliminary one, where we tested two issues. The first one was whether we are capable of measuring spatial distribution of metal ions within a tissue section. For this purposes, we prepared sections of various thickness (from 5 to 50 μm) and found 30 μm the best from the point of view of sensitivity and also not influencing variability of a spatial distribution within a tumour.

Histology. Haematoxylin-eosin staining was applied to observe tissue structure. Cryosections (8 μm thickness) were fixed with ethanol (20 min), washed with distilled water (3 times, 5 min each) and treated with Weigert's haematoxylin (20 min) for nuclei staining. Then, the cryosections were washed with running tap water (20 min), followed by distilled water (3 times, 5 min each). The cytoplasm was counterstained with 1% eosin alcoholic solution (1 min). After washing with distilled water (3 times, 5 min each), the stained sections were embedded in glycerine jelly. Whole cryosections were scanned by a VS120 Olympus microscope with OlyVIA software (Olympus, Japan). GIMP software was used to identify four histologically different zones of tissue in the scanned pictures. Three to six rectangular areas of each zone per cryosection were chosen for comparison with Zn and Cu maps to detect their local contents.

Elemental mapping procedure with LA-ICP-MS. Imaging experiments were performed using an LA-ICP-MS setup consisting of the laser ablation system UP213 (Supercell®, NewWave, USA) operated at a wavelength of 213 nm. The system was equipped with a CCD camera for investigation of the sample during laser ablation. The ablated material was washed away using helium (1.0 l/min) from the ablation chamber (Supercell®). Argon flow (0.6 l/min) was admixed into a flow of helium with the sample aerosol behind the ablation cell. Hence, the total gas flow was 1.6 l/min. This mixture was fed into a quadrupole ICP-MS spectrometer Agilent 7500CE (Agilent, Japan) equipped with a collision-reaction cell (CRC) for suppressing possible polyatomic interferences. The CRC was utilized in collision mode with a He (99.999%) flow rate of 2 ml/min. The integration time of monitoring was set to 0.1 s for the isotopes ²⁸Si, ⁶³Cu, ⁶⁶Zn and 0.05 s for ¹²C, yielding a total sampling time of 0.43 s. The measured elements were chosen based on the analysed material (C as a matrix element of biological tissue and Zn as the elements studied in melanoma) and the microscope slide on which the thin section was deposited (silicon as a glass matrix element). The silicon signal emerged immediately once the laser beam reached the tissue/glass interface, thus indicating complete sampling of a tissue layer. The selection of the ablation parameters is explained in Results and Discussion.

Post-processing of collected digital data and statistical analysis. The above-mentioned techniques generated pairs of digital images that were approximately similar but not sufficiently similar for exact indexing among images. These data were submitted to the procedure described by the flow chart in Fig. 1. The registration of the data is described below, and the statistical evaluation based on the mixed effect model is detailed in Supplementary Note 1. To define corresponding zones, the relationship between the registered images was used to map the selected areas identified in the histologically stained cryosections onto the respective maps of Zn, Cu and C (Fig. 3). The distribution of metal contents in the corresponding zones was compared and further explored by means of the mixed effect model described in Supplementary Note 1.

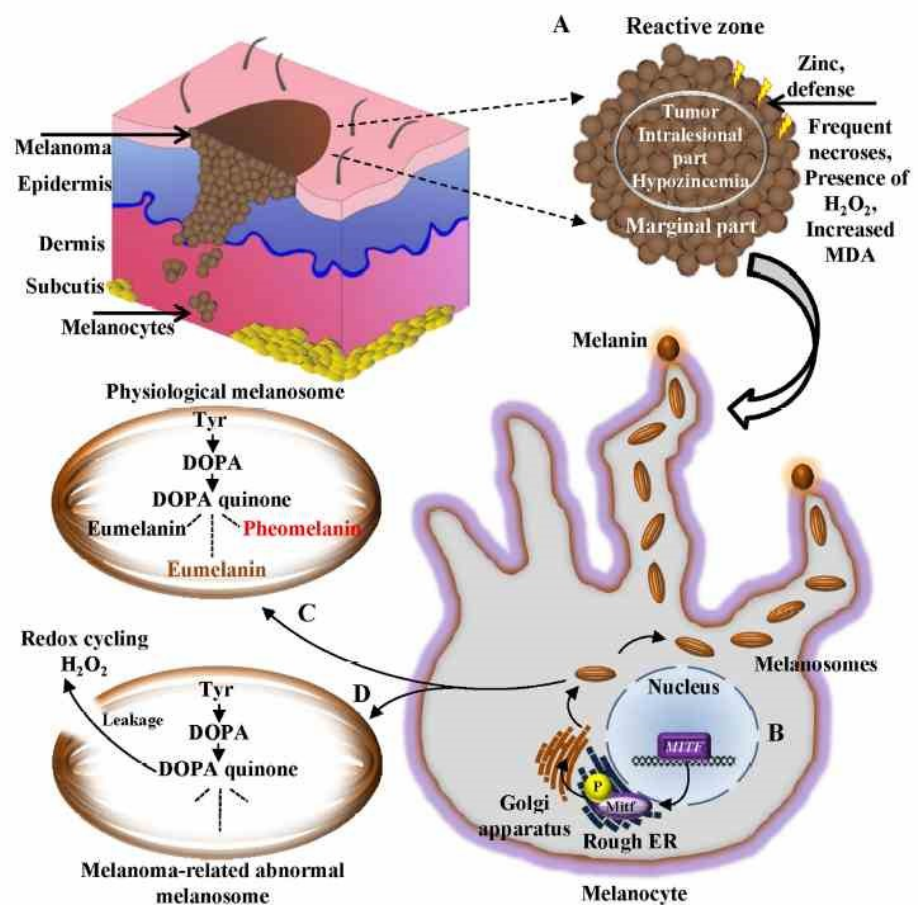


Figure 7. A schematic depiction of a plausible role of zinc in melanoma progression. Marginal parts of tumour border with a reactive zone of an adjacent healthy tissue. In these parts of melanoma, frequent necroses, a presence of H_2O_2 and elevation of malondialdehyde (MDA) can be found. (A) High zinc in marginal sections of melanoma may indicate a physiological defence of zinc-containing antioxidant molecules against the potential danger of ongoing oxidative stress. Although intralesional regions of melanomas generally exhibit hypo-zincemia status, oxidative stress in reactive zones/marginal parts interface can likely result in an oxidative stress-triggered transport of zinc-containing antioxidant molecules from adjacent healthy tissue and temporary accumulation of zinc. (B) Physiologically, an expression of melanosomes is regulated by microphthalmia-associated transcription factor gene (*MITF*) and phosphorylation (P) of the homonymous *MITF*-encoded protein (*Mitf*). (C) Translated melanosomes are the place for entire melanin synthesis, starting by action of tyrosinase, producing L-3,4-dihydroxyphenylalanine (DOPA) from tyrosine (Tyr). Tyrosinase further produces DOPA quinone from DOPA. DOPA quinone can be converted through a sequence of reactions to various types of melanins (black and brown eumelanins or red to yellow pheomelanin). (D) Noteworthy, another plausible reason for the free radicals formation in melanoma is a presence of abnormal and incomplete melanosomes, causing a significant leakage of the reactive melanin precursors, causing oxidative stress in the pigmented tumours through redox cycling and an accumulation of zinc ions originating from antioxidant molecules from adjacent tissues as a kind of physiological protection.

Reproducible analysis of the data. The methods mentioned in the sections on the image registration of the considered images and content maps as well as on the statistical analysis—are provided for the purposes of re-use and reproducible analysis. In the case of image registration, which was performed in the MATLAB programming language, the method is provided in the form of scripts (m-files). The scripts and the necessary data (images and concentration maps) are wrapped in an archive and are designed to simplify the registration process to the execution of only a few scripts. The scripts may be executed by the MATLAB programming language as well as the open source alternative Octave.

The statistical analysis, which was performed using the statistical software R, is provided in a similar form, i.e., as an R script.

Image registration. The archive containing the scripts for the image registration can be downloaded from Dryad. The implementation relies on the Image processing toolbox and the Optimization toolbox in the MATLAB programming language. However, the image registration may be easily performed using the Octave program instead of MATLAB. The image registration is performed by *register_all_at_once.m* script. The script steps through folders containing the images to be registered and performs the registration between the silhouette of the histological scan and the silhouette of the image of the sample to be ablated and measured as well as between the silhouette of the image of the sample to be ablated and measured and the silhouette of the measurements resulting from LA-ICP-MS. The images required for the registration are *hist_si.png*, the silhouette of the histological scan; *abla_si.png*, the silhouette of the image of the sample before ablation; and *matr_si.png*, the silhouette of the concentration map. The results of the script are the transformation matrices stored in the sample folders under the name *trans.mat* and diagnostic images indicating the quality of the registration in the form of differences.

The resulting transformation matrices may be used for direct indexing among images and content maps. For example, the estimation of average metal contents in annotated spots may be performed by the script *means_by_spots.m*. Similar to the *register_all_at_once.m* script, the program steps through the sample folders and estimates average contents in spots annotated in image *anot.png*. The information about the spots is extracted from the image in file *spots.mat*. The result is a csv file. Files for all samples may be combined and used for statistical analysis.

Statistical analysis. Statistical analysis was performed in R statistical software and is presented as a script. The case bootstrap test relies on the output of a random number generator. To ensure the reproducibility of the results, the state of the random number generator is fixed. The analyses in the script *lmer_analyses.R* sequentially tests the two hypotheses on the Zn and Cu meta-concentrations stored in the file *MeLiM_metals_data.csv*, namely “The average Zn (or Cu) content in the GMT zones is lower than that in the remaining zones (ESR, LSR and FT)”. The analysis is very computationally intensive; the execution of the script may last a few hours. The results of the analysis are the fitted linear mixed effect models and the *p* values estimated by the case bootstrap test.

References

- Formigari, A., Gregianin, E. & Irato, P. The effect of zinc and the role of p53 in copper-induced cellular stress responses. *J Appl Toxicol* 33, 527–536 (2013).
- McCord, M. C. & Aizenman, E. The role of intracellular zinc release in aging, oxidative stress, and Alzheimer’s disease. *Front Aging Neurosci* 6, 1–16 (2014).
- Prasad, A. S. Zinc: role in immunity, oxidative stress and chronic inflammation. *Curr Opin Clin Nutr Metab Care* 12, 646–652 (2009).
- Gumulec, J. et al. Serum and Tissue Zinc in Epithelial Malignancies: A Meta-Analysis. *PLoS One* 9, 1–11 (2014).
- Panska, D., Burocziova, M., Strnadel, J. & Horak, V. Immunohistochemical Analysis of Collagen IV and Laminin Expression in Spontaneous Melanoma Regression in the Melanoma-Bearing Libechev Minipig. *Acta Histochem Cytochem* 48, 15–26 (2015).
- Horak, V., Fortyn, K., Hruban, V. & Klauudy, J. Hereditary melanoblastoma in miniature pigs and its successful therapy by devitalization technique. *Cell Mol Biol* 45, 1119–1129 (1999).
- Geffrotin, C. et al. Opposite regulation of tenascin-C and tenascin-X in MeLiM swine heritable cutaneous malignant melanoma. *Biochim Biophys Acta-Gen Subj* 1524, 196–202 (2000).
- Borovansky, J. et al. Biochemical characterization of a new melanoma model the minipig MeLiM strain. *Melanoma Res* 13, 543–548 (2003).
- Vincent-Naulleau, S. et al. Clinical and histopathological characterization of cutaneous melanomas in the melanoblastoma-bearing Libechev minipig model. *Pigm Cell Res* 17, 24–35 (2004).
- Vaculovic, T. et al. Influence of laser ablation parameters on trueness of imaging. *Appl Surf Sci* 351, 296–302 (2015).
- Becker, J. S. et al. Imaging of copper, zinc, and other elements in thin section of human brain samples (Hippocampus) by laser ablation inductively coupled plasma mass spectrometry. *Anal Chem* 77, 3208–3216 (2005).
- Becker, J. S. et al. Bioimaging of metals by laser ablation inductively coupled plasma mass spectrometry (LA-ICP-MS). *Mass Spectrom Rev* 29, 156–175 (2010).
- Latkoczy, C., Muller, Y., Schmutz, P. & Gunther, D. Quantitative element mapping of Mg alloys by laser ablation ICP-MS and EPMA. *Appl Surf Sci* 252, 127–132 (2005).
- Halicz, L. & Gunther, D. Quantitative analysis of silicates using LA-ICP-MS with liquid calibration. *J Anal At Spectrom* 19, 1539–1545 (2004).
- van Elteren, J. T., Tennent, N. H. & Selih, V. S. Multi-element quantification of ancient/historic glasses by laser ablation inductively coupled plasma mass spectrometry using sum normalization calibration. *Anal Chim Acta* 644, 1–9 (2009).
- Crain, J. S. & Gallimore, D. L. Inductively coupled plasma-mass spectrometry of synthetic elements - TC-99. *Appl Spectrosc* 46, 547–549 (1992).
- Frick, D. A. & Gunther, D. Fundamental studies on the ablation behaviour of carbon in LA-ICP-MS with respect to the suitability as internal standard. *J Anal At Spectrom* 27, 1294–1303 (2012).
- Riesop, D., Hirner, A. V., Rusch, P. & Bankfalvi, A. Zinc distribution with in breast cancer tissue: A possible marker for histological grading? *J Cancer Res Clin Oncol* 141, 1321–1331 (2015).
- Zitova, B. & Flusser, J. Image registration methods: a survey. *Image Vis Comput* 21, 977–1000 (2003).
- Preparata, E. P. & Shamos, M. L. *Computational Geometry* Springer-Verlag (2012).
- Corvi, M. & Nicchiotti, G. *Multiresolution image registration* I E E E, Computer Soc Press (1995).
- Pinheiro, J. C. & Bates, M. D. *Mixed-effects models in S and S-PLUS*. Springer (2006).
- Bates, D., Machler, M., Bolker, B. M. & Walker, S. C. Fitting Linear Mixed-Effects Models Using lme4. *J Stat Softw* 67, 1–48 (2015).
- Thai, H. T. et al. A comparison of bootstrap approaches for estimating uncertainty of parameters in linear mixed-effects models. *Pharm Stat* 12, 129–140 (2013).
- Dunn, O. J. Multiple comparisons among means. *J Am Stat Assoc* 56, 52–64 (1961).
- Fisher, G. L., Spitzer, L. E., McNeill, K. L. & Rosenblatt, L. S. Serum copper and zinc levels in melanoma patients. *Cancer* 47, 1838–1844 (1981).

27. Ros-Bullon, M. R., Sanchez-Pedreno, S. & Martinez-Liarte, J. H. Serum zinc levels are increased in melanoma patients. *Melanoma Res* 8, 273–277 (1998).
28. Gorodetsky, R., Sheskin, J. & Weinreb, A. Iron, copper, and zinc concentrations in normal skin and in various nonmalignant and malignant lesions. *Int J Dermatol* 25, 440–445 (1986).
29. Manga, P. *et al.* A role for tyrosinase-related protein 1 in 4-tert-butyl phenol-induced toxicity in melanocytes - Implications for vitiligo. *Am J Pathol* 169, 1652–1662 (2006).
30. Garcia-Borron, J. C. & Sanchez, M. C. O. *Biosynthesis of Melanins* Wiley-VCH Verlag GmbH (2011).
31. Yamaguchi, Y., Brenner, M. & Hearing, V. J. The regulation of skin pigmentation. *J Biol Chem* 282, 27557–27561 (2007).
32. Zalewska, M., Trefon, J. & Milnerowicz, H. The role of metallothionein interactions with other proteins. *Proteomics* 14, 1343–1356 (2014).
33. Weinlich, G. *et al.* Comparison of metallothionein-overexpression with sentinel lymph node biopsy as prognostic factors in melanoma. *J Eur Acad Dermatol Venereol* 21, 669–677 (2007).
34. Weinlich, G. & Zelger, B. Metallothionein overexpression, a highly significant prognostic factor in thin melanoma. *Histopathology* 51, 280–283 (2007).
35. McRae, R., Bagchi, P., Sumalekshmy, S. & Fahrni, C. J. *In Situ* Imaging of Metals in Cells and Tissues. *Chem Rev* 109, 4780–4827 (2009).

Acknowledgements

This research was carried out under the projects CEITEC 2020 (LQ1601) with financial support from the Ministry of Education, Youth and Sports of the Czech Republic under the National Sustainability Programme II, NSP I (project no. LO1609), RVO 67985904, CVUT grant no. SGS16/231/OHK3/3T/13 and AZV CR 15-28334A. This research was also supported by Internal Grant of the Czech Institute of Informatics, Robotics, and Cybernetics, CTU in Prague.

Author Contributions

J.A. was responsible for data registration and statistical analysis. L.V. processed the ablation data and provided visualization of all the results. T.V. and M.T. optimized elemental mapping and analysed samples by LA-ICP-MS. V.K. supervised mass spectrometric analyses. H.H. revised manuscript and contributed to metal metabolism. V.H. performed histology measurements and animal experiments. O.S. and Z.H. contributed to reagents/materials/methods and to revision of manuscript. All members of the team participated in the manuscript writing under coordination of O.S., V.H. and V.A. V.A. contributed to design of a work, revisions and submission of the manuscript.

Additional Information

Supplementary information accompanies this paper at <http://www.nature.com/srep>

Competing financial interest: The authors declare no competing financial interests.

How to cite this article: Anyz, J. *et al.* Spatial mapping of metals in tissue-sections using combination of mass-spectrometry and histology through image registration. *Sci. Rep.* 7, 40169; doi: 10.1038/srep40169 (2017).

Publisher's note: Springer Nature remains neutral with regard to jurisdictional claims in published maps and institutional affiliations.



This work is licensed under a Creative Commons Attribution 4.0 International License. The images or other third party material in this article are included in the article's Creative Commons license, unless indicated otherwise in the credit line; if the material is not included under the Creative Commons license, users will need to obtain permission from the license holder to reproduce the material. To view a copy of this license, visit <http://creativecommons.org/licenses/by/4.0/>

© The Author(s) 2017

6.12 ARTICLE 12

Tvrdonova, M.; Vlcnovska, M.; Vanickova, L. P.; Kanicky, V.; Adam, V.; Ascher, L.; Jakubowski, N.; Vaculovicova, M.; Vaculovic, T. *Analytical and Bioanalytical Chemistry* 2019, 411, 559-564 (IF=3.286)



Gold nanoparticles as labels for immunochemical analysis using laser ablation inductively coupled plasma mass spectrometry

Michaela Tvrdonova^{1,2} · Marcela Vlcnovska³ · Lucie Pompeiano Vanickova^{3,4} · Viktor Kanicky^{1,2} · Vojtech Adam^{3,4} · Lena Ascher⁵ · Norbert Jakubowski⁵ · Marketa Vaculovicova^{3,4} · Tomas Vaculovic^{1,4}

Received: 5 June 2018 / Revised: 20 July 2018 / Accepted: 27 July 2018 / Published online: 14 August 2018
© Springer-Verlag GmbH Germany, part of Springer Nature 2018

Abstract

In this paper, we describe the labelling of antibodies by gold nanoparticles (AuNPs) with diameters of 10 and 60 nm with detection by laser ablation inductively coupled plasma mass spectrometry (LA-ICP-MS). Additionally, the AuNPs labelling strategy is compared with commercially available labelling reagents based on MeCAT (metal coded affinity tagging). Proof of principle experiments based on dot blot experiments were performed. The two labelling methods investigated were compared by sensitivity and limit of detection (LOD). The absolute LODs achieved were in the range of tens of picograms for AuNP labelling compared to a few hundred picograms by the MeCAT labelling.

Keywords Dot blot · Antibody labelling · Gold nanoparticles · LA-ICP-MS · Immunochemistry

Introduction

Since the 1980s, colloidal gold has been used for immuno-histochemical staining of proteins in membrane-based immunoassays [1–3]. The intensive purple color enables a colorimetric detection of the labelled molecules concentrated at the surface of the membrane (after electroblotting) so that limits of detection at the level of attomolar concentrations [4] can be achieved. Sometimes, several labels are used simultaneously (e.g., colloidal gold and peroxidase or alkaline phosphatase) for the detection of multiple antigen spots on a single blot

membrane [4]. Besides this experimentally simple colorimetric detection, other more instrumentally demanding but more sensitive techniques are also discussed, including fluorescent, electrochemical, or calorimetric detection [5].

Metallic nanoparticles had already been applied for detection of biomolecules inside a single cell by use of surface enhanced Raman spectroscopy (SERS). In the case of gold nanoparticles, the local fields generated upon excitation of their localized surface plasmons enable sensitive probing of the molecules interacting with the particle surface on the nanometer scale within living cells by surface-enhanced Raman scattering (SERS) [6–9]. SERS can also be used for sensing of general chemical parameters in the cellular nano-environment. For example, progressing acidification in endosomes [10, 11] using nanoprobe containing a pH-sensitive reporter molecule [12, 13].

Inductively coupled plasma mass spectrometry (ICP-MS) is a well-established method for multi-elemental analysis of elements at trace and ultra-trace levels. It has found acceptance in various application areas over the last decade. ICP-MS is more suitable for detection in the life sciences. For these applications, ICP-MS excels in a high sensitivity which is independent of the molecular structure of the analyte, a wide linear dynamic range and by excellent multi-element capabilities. In combination with laser ablation as a sample introduction system for the analysis of soft materials it has also been used extensively for bioimaging (for more details, see review

Published in the topical collection *Elemental and Molecular Imaging by LA-ICP-MS* with guest editor Beatriz Fernández García.

✉ Tomas Vaculovic
vaca_777@yahoo.com

¹ Department of Chemistry, Faculty of Science, Masaryk University, Kamenice 753/5, 625 00 Brno, Czech Republic

² CEITEC, Masaryk University, Kamenice 753/5, 625 00 Brno, Czech Republic

³ Department of Chemistry and Biochemistry, Mendel University in Brno, Zemedelska 1, 613 00 Brno, Czech Republic

⁴ Central European Institute of Technology, Brno University of Technology, Purkynova 123, 612 00 Brno, Czech Republic

⁵ Bundesanstalt für Materialforschung und -prüfung (BAM), Richard-Willstätter-Straße 11, 12489 Berlin, Germany

[14]). Recently, LA-ICP-MS has also been used to image the distribution of metallic nanoparticles (Au, Ag) in single biological cells [15].

The first immunoassay for detection of thyroxine in solution was described by Zhang et al. [16], and the history of immuno-histochemical approaches developed for ICP-MS applications has already been discussed extensively in review articles [17]. The combination of immunoassays and ICP-MS can be carried out through proper elemental tagging [18]. High multiplexing and signal amplification capabilities are the main advantages of using metal chelates, e.g., 1,4,7,10-tetraazacyclododecane-1,4,7,10-tetraacetic acid (also known as DOTA) coordinated with heteroatoms (typically lanthanide ions) for elemental tagging. Significant signal improvements have been achieved by the use of polymeric tags containing metal ions, such as MAXPAR™ for application in Western blot assays [19]. In the case of polymeric tags, signal amplification has been achieved by the coupling of a single polymer chain carrying more than 100 lanthanide elements per Ab compared to the previously mentioned metal chelates. Waentig et al. found that MAXPAR™ gives better sensitivity than DOTA and MeCAT (metal coded affinity tag), respectively. However, due to a higher background signal, the S/N ratio and finally the limits of detection (LOD: fmol range) are worse than that for MeCAT.

Even higher amplification factors have been achieved in a Western blot approach discussed by Mueller et al. [20]. They followed the concept of Western blotting after separation by gel electrophoresis and used gold cluster-labelled antibodies for detection by laser ablation ICP-MS for the determination of the Mre11 protein in crude lysates of CHO-K1 fibroblasts. This protein is essential for mediating genome stability and DNA repair in mammalian cells. In this approach, high sensitivities have been achieved using an antibody conjugated to gold nanoclusters. More than 50,000 gold atoms can be attached to each antibody at once by this technique, which can help to reach limits of detection below 1 fmol of protein. More recently, Cruz-Alonso et al. used a new immuno-histochemical-based procedure to study the distribution of metallothionein 1/2 (MT 1/2) and metallothionein 3 (MT 3) in human retina tissue. For this purpose, antibodies (Ab) were bio-conjugated by gold nanoclusters (AuNCs) and labelled in combination with laser ablation (LA) coupled to ICP-MS for detection. Each cluster with a diameter of 2.7 nm contained roughly 580 atoms. [21]

Overall, one can summarize that application of Au nanoparticles and clusters look promising for bio-conjugation to improve the signal intensity in LA-ICP-MS; however, as has been mentioned, other factors such as unspecific binding can lead to a reduced S/N ratio or the labelling process can have an impact on the specificity of the antibody. In this work, we have developed a methodology for the tagging of antibodies via gold nanoparticles to enhance the signal intensity in LA-

ICP-MS. Hence, we performed a proof of principle experiment based on dot blot experiments to demonstrate the improvement in sensitivity and specificity of the AuNP conjugation of antibodies in comparison with reagents based on the MeCAT technology as a reference.

Materials and methods

Chemicals

The following chemicals were used: Milli-Q water (purification system, Millipore, Bedford, MA). All solutions were prepared using this ultrapure water. Milk powder, Tris-buffered saline including 0.1% Tween 20, pH 7.3 (TBS-T), Tris buffer (20 mM Tris; 150 mM NaCl; 2.5 mM EDTA (pH 7), metal coded affinity tag MeCAT (Proteome Factory, Berlin, Germany), tris(2-carboxyethyl)phosphine*HCl (TCEP), GOLD Conjugation Kit (60 nm, 20 OD) ab 188,216 and GOLD Conjugation Kit (10 nm, 20 OD) ab201808 Abcam, Goat anti-mouse antibody Abcam (ab6708, Cambridge, UK, 2 mg/ml), Mouse immunoglobulin, Abcam (ab198772, Cambridge, UK).

Nanoparticle-antibody conjugation

Gold nanoparticle (10 and 60 nm) conjugation kits were purchased from Abcam (ab188216, ab201808, Cambridge, UK) and the conjugation was carried out according to the manufacturer's instructions. Briefly, 2 mg/ml of goat anti-mouse antibody was diluted to an appropriate concentration with a buffer provided. This solution was mixed with gold nanoparticles and left to react for 15 min. Finally, a quencher provided in the kit was added and the mixture was left for 5 min to stop the conjugation reaction.

MeCAT antibody labelling

Antibody labelling with metal-coded affinity tag MeCAT (Proteome Factory, Berlin, Germany) containing holmium as the elemental tag was performed in accordance with the publication of Waentig et al. [19]

Dot blot preparation

Mouse immunoglobulin was used as a model antigen and goat anti-mouse antibody was employed as the testing antibody. The dot blot analysis was carried out using a polyvinylidene fluoride (PDVF) membrane (Bio-rad, Prague, Czech Republic). First, the membrane was activated by immersing it in methanol for 30 s and then in blotting buffer containing 50%_(v/v) of buffer (25 mM Trizma base, 150 mM glycine, 10%_(v/v) methanol), and 10%_(v/v) MetOH for 30 s.

0.5 μl of the antigen solution were pipetted onto the membrane which resulted in a dot diameter of approximately 0.8 mm. On each membrane, seven dots with increasing concentration of antigen were applied (0.1, 0.2, 0.5, 1.0, 5.0, and 10 ng/ml). Subsequently, the membrane was blocked for 30 min in blocking buffer (10% milk powder, 90% phosphate buffer saline Sigma Aldrich, USA). The membrane was then incubated in a solution of a marked antibody (6.7 ng/ml) for 1 h at room temperature. Finally, the membrane was washed three times by 0.05% solution of Tween 20 in phosphate buffer saline to remove the non-bound antibodies.

LA-ICP-MS analysis

LA-ICP-MS analysis of the dot blots was undertaken by a laser ablation system UP213 (NewWave, USA) emitting laser radiation of 213 nm with a pulse width of 4.2 ns and a quadrupole ICP-MS spectrometer Agilent 7500ce (Agilent Technologies, Japan). The ICP-MS parameters were optimized with respect to get the best S/N ratio, RSD, and oxide ratio (ThO^+/Th^+) lower than 0.5% using glass reference material NIST610. The imaging of the dot blots was performed using the following ablation parameters: a laser beam diameter of 110 μm , laser beam fluence of 2.5 J/cm², a repetition rate of 10 Hz, a scan speed rate of 150 $\mu\text{m/s}$, and a distance between individual lines of 115 μm .

The whole spot was ablated line by line and the Au signals of monitored isotopes (¹⁹⁷Au, ¹⁶⁵Ho) were measured. The limit of quantification for signal intensity is calculated according to tenfold of standard deviation of the gas level (without ablation). All intensities below the limit of quantification were set to zero. The sum of intensities across the whole spot was then calculated. The images of the dot blots were created using lab-made software Laser Ablation Tool for processing of raw data and Excel for presenting the maps as surface plots with the intensity shown in a color-coded intensity scale.

Results and discussion

In biological workflows proteins are usually detected in a Western blot assay after gel electrophoresis and electroblotting onto membranes. Detection is performed by use of tagged antibodies and signals are measured by colloidal gold, fluorescence signals, or by luminescence in the peroxidase and alkaline phosphatase assay, as discussed previously in the "Introduction" section. The whole procedure is prone to protein losses during the separation and electro-transfer process so all quantitative information can be completely lost. However, one of the authors has recently shown that dot blot experiments can overcome this limitation if the specificity of the antibody is high enough to detect the target protein even in complex protein extracts [22].

The workflow of the dot blot analysis and the type of antibody labelling applied in this study is summarized in Fig. 1. In this study, the sensitivity of antibody labelling by a conventionally used MeCAT method using holmium as a lanthanide element with gold nanoparticle-labelled antibodies will be compared. Moreover, two different sizes of nanoparticles (10 nm and 60 nm) will be investigated (Fig. 1a). The overall workflow of the experiment (antibody labelling, dot blot preparation, and LA-ICP-MS analysis) is shown in Fig. 1b.

The number of Au atoms and thus the signal intensity in LA-ICP-MS of AuNPs bound to antibodies is directly proportional to the volume of the NP with a diameter of 10 or 60 nm, if a single particle binding is assumed. The calculated volume of 60 nm NP is 200 times larger than 10 nm NP. Therefore, the signal ratio should be improved by a factor of approximately 200 for the larger particle.

The AuNP-Ab were pipetted in a dilution series of 1:100; 1:1000 and 1:10,000 onto the surface (without antigen) of preconditioned PVDF membrane to evaluate the signal intensity of Au in relation to the nanoparticle size (Fig. 2a). The Au signal of the 60 nm AuNP-Ab conjugate is approximately five times higher (6.7, 4.9, and 5.9 for 100, 1000, and 10,000 times dilution, respectively) compared to the 10-nm AuNP-Ab conjugate diluted to the same absorbance (Table 1). This means that the amount of 10-nm AuNPs is 50 times higher than 60-nm AuNPs, approximately. This can be caused either by the fact that some nanoparticles are not conjugated to the antibody or that one antibody is labelled by 50 nanoparticles, which is highly improbable. Because the precise mechanism of labelling is not known (commercial conjugation), we believe that a combination of both factors is the most probable (bare nanoparticles as well as multiple labelling of one antibody).

Subsequently, the non-specific adsorption, as well as the washing efficiency of the membrane procedure was verified (Fig. 2b). For this purpose, the experiment described in Fig. 2b was performed a second time, but now, extensive washing was applied. Only a few weak signals were observed which demonstrated that washing is efficient to remove adsorbed antibodies labelled by nanoparticles from the membrane. The Au signal decreased to less than 4% of the original value (without washing shown in Fig. 2a). When the 10,000 times diluted NP-Ab conjugates were spotted and washed, the measured intensities were either not distinguishable or slightly above the blank level. The lowest range of intensities in Fig. 2b is 0–700 cps; hence, no signal of Au is visible for these spots. However, the intensities listed in Table 1 are calculated as a sum across the whole dot, from approximately 1500 points (the dimension of the dot is about 50 \times 30 ablation points). Hence, the sum of integrated intensities for 10,000 times diluted NP-Ab conjugates reaches about 5000 cps.

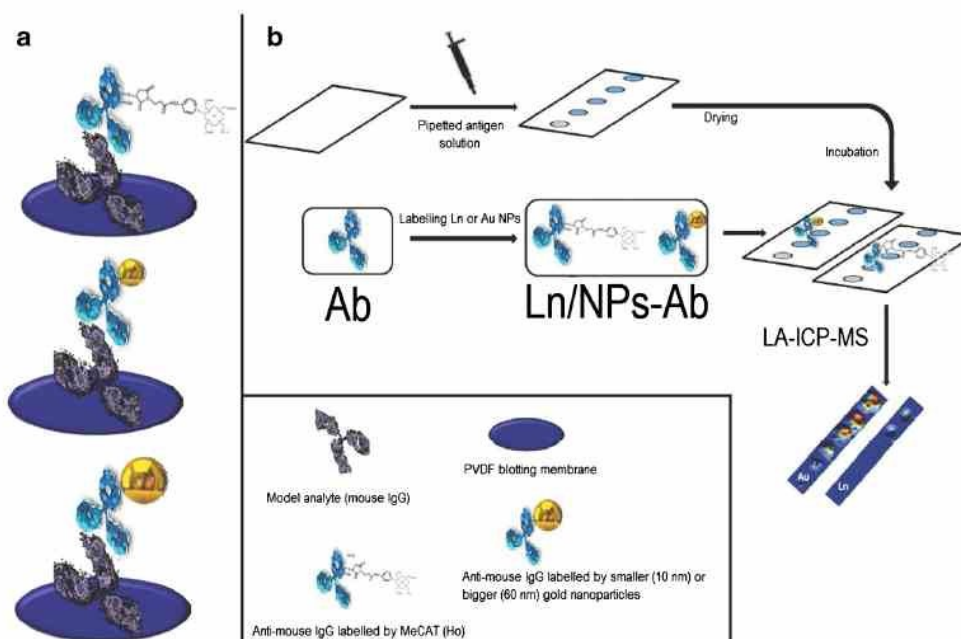


Fig. 1 Workflow of dot blot immunoassay containing the labelled antibodies via non-reduction method (gold nanoparticles) and reduction method MeCAT (Ln). Partially reduced antibodies for MeCAT labelling were obtained by using TCEP solution

Furthermore, the ratio of the Au signal produced by 60 nm NP-Ab and 10 nm NP-Ab conjugates was calculated and its value varied in the range from 4.5 to 8.6 for 100 and 1000 times dilution. These ratios are comparable to the non-washed ratios, which means that the non-specific sorption of the antibody to the PVDF membrane is the same for both types of nanoparticle conjugates and is not dependent on size effects.

Finally, for evaluation of the performance of the labelled antibodies, a titration curve must be measured for a given antigen or AB concentration. For this purpose, we have selected a total antibody amount of 6.66 ng for all antibodies investigated for incubation and changed the total amount of antigen (mouse IgG) in the range from 0.1 to 5 ng. The measured intensities are

shown for 60-nm AuNPs (Fig. 3a), 10-nm AuNPs (Fig. 3b), and Ho-MeCAT labelled (Fig. 3c) anti-mouse IgG. Elemental surface plots of the dot blots measured on the membranes are shown together with the integrated intensity of the whole spot area and the calibration graphs. It is clearly seen that the calibration deviates from a linear function in the whole calibration range, and a saturation curve at a higher amount of mouse IgG is observed. This is not surprising because a full saturation of the antigens is expected already in the upper calibration range where the ratio of AB to antigen reaches a 1:1 ratio (the highest amount of antigen and antibody was 5 ng and 6.66 ng, respectively). On one hand, the curvature of the Ab labelled with 60 nm diameter NP looks more pronounced and hints at a steric obstruction of

Fig. 2 **a** Elemental maps of Au intensities (cps) of 60-nm and 10-nm AuNPs-Ab conjugates at various dilution in unwashed dot blot. **b** Elemental maps of Au intensities (cps) of 60-nm and 10-nm AuNP-Ab conjugates and 60-nm and 10-nm AuNPs at various dilution in washed dot blot

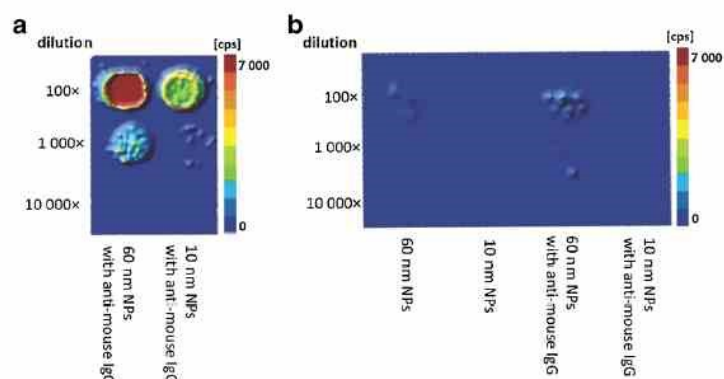


Table 1 Comparison of the sum of Au intensities for AuNP-Ab conjugates and AuNPs measured in washed and unwashed dot blots. The stock solutions were diluted 100, 1000, and 10,000 times before 0.5 μ l was pipetted on the membrane

| Dilution | Sum of Au intensities in unwashed dotblot (kcps) | | Sum of Au intensities in washed dotblot (kcps) | | | |
|----------|--|-----------------------|--|-------------|-----------------------|-----------------------|
| | 60-nm Au-Ab conjugate | 10-nm Au-Ab conjugate | 60-nm AuNPs | 10-nm AuNPs | 60-nm Au-Ab conjugate | 10-nm Au-Ab conjugate |
| 100 | 14,200 | 2400 | 340 | 41 | 370 | 82 |
| 1000 | 1200 | 300 | 13 | 7.4 | 100 | 12 |
| 10,000 | 97 | 16 | 7.4 | 4.3 | 7.8 | 3.3 |

the large NP, which exceeds the size of a typical antibody of about 15 nm. On the other hand, the smaller molecular weight of MeCAT is the reason for a more linear graph.

For a lower total amount of antigens the calibration graph does show a linear behavior, so the measured intensity can be converted directly to a total amount of antigen applied (if an

excess of antibody is used). The slope of the graph can be used for comparison of the three differently labelled antibodies and the following slopes have been calculated: 4.03×10^7 , 6.33×10^5 , and 2.08×10^3 cps kg mg⁻¹ for 60-nm AuNPs, 10-nm AuNPs, and Ho-MeCAT, respectively. It can be concluded from these results that the slopes (sensitivity) of each labelling strategy differs by two orders of magnitude, demonstrating an improvement by four orders of magnitude in the best case. In terms of detection limits (according to 3σ), absolute values at the picogram levels were calculated in particular 11 pg, 51 pg, and 260 pg for 60-nm AuNPs, 10-nm AuNPs, and Ho-MeCAT, respectively, which again demonstrates that the signal to noise ratio and not the improvement in sensitivity plays the important role in an immunoassay. However, in comparison to MeCAT, a significant improvement in the LOD by at least a factor of 5 (20) can be achieved. The last advantage of Ab labelling by NPs compared to MeCAT is the absence of a reduction step. Before MeCAT labelling it is necessary to partially reduce Ab (reduction of disulphide bridges) and thus some Ab could be reduced so much that it can lead to the loss of its biological function. Labelling by nanoparticles does not require this reduction step, and thereby, NP is conjugated to the whole Ab.

Conclusion

The labelling strategy of the antibody by nanoparticles with diameters of 10 and 60 nm, respectively, was developed and compared to widely used labelling via MeCAT. The sensitivity of the 60 nm AuNP labelling was improved by 4 orders of magnitude in comparison to MeCAT strategy whereas the LOD is approximately 20 times better. It shows a higher background level for AuNP labelling caused by their non-specific sorption. The forthcoming work is focused on suppression of the non-specific sorption to minimize signal to noise ratio and improve LOD significantly.

Acknowledgments Financial support was provided by Grant Agency of Czech Republic (GACR 17-12774S) and project CEITEC 2020 (LQ1601) with financial support from the Ministry of Education, Youth and Sports of the Czech Republic under the National Sustainability Program II. LPV was supported by project 6SA17676 that received funding from the European Union's Horizon 2020 research and innovation program under the Marie

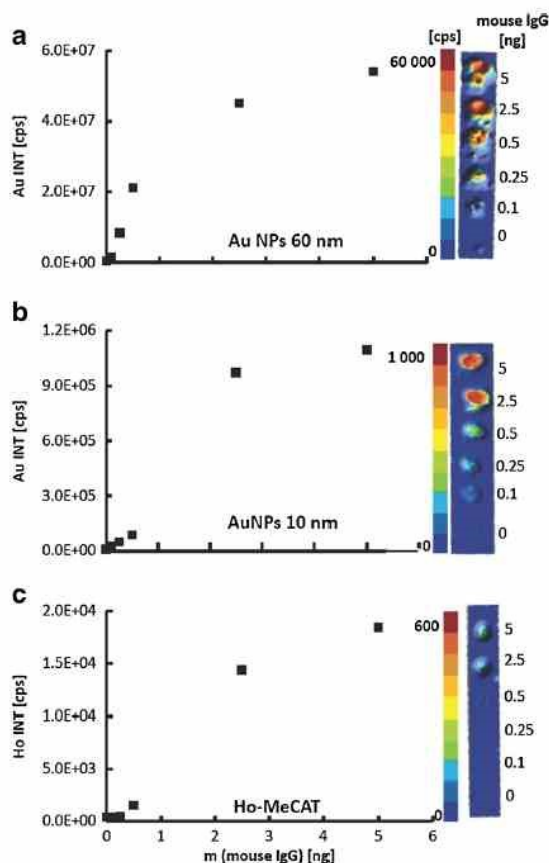


Fig. 3 Au and Ho intensities measured on a PVDF membrane depending on the amount of antigen (mouse IgG). The antibody (anti-mouse IgG) have been labelled by **a** AuNPs—60 nm, **b** AuNPs—10 nm, and **c** Ho-MeCAT; a total amount of 6.66 ng AB has been applied for all three experiments

Skłodowska-Curie and which is co-financed by the South Moravian Region under the grant agreement No. 665860.

Compliance with ethical standards

Conflict of interest The authors declare that they have no conflict of interest.

References

1. Brada D, Roth J. Golden blot - detection of polyclonal and monoclonal-antibodies bound to antigens on nitrocellulose by protein-a gold complexes. *Anal Biochem.* 1984;142:79–83.
2. Surek B, Latzko E. Visualization of antigenic proteins blotted onto nitrocellulose using the immuno-gold-staining (IGS) method. *Biochem Biophys Res Commun.* 1984;121:284–9.
3. Hsu YH. Immunogold for detection of antigen on nitrocellulose paper. *Anal Biochem.* 1984;142:221–5.
4. Dykman L, Khlebtsov N. Gold nanoparticles in biomedical applications: recent advances and perspectives. *Chem Soc Rev.* 2012;41:2256–82.
5. Omidfar K, Khorsand F, Azizi MD. New analytical applications of gold nanoparticles as label in antibody based sensors. *Biosens Bioelectron.* 2013;43:336–47.
6. Kang B, Mackey MA, El-Sayed MA. Nuclear targeting of gold nanoparticles in cancer cells induces dna damage, causing cytokinesis arrest and apoptosis. *J. Am. Chem. Soc.* 2010;132:1517.
7. Kneipp J, Kneipp H, Wittig B, Kneipp K. Following the dynamics of pH in endosomes of live cells with SERS nanosensors. *J Phys Chem C.* 2010;114:7421–6.
8. Kneipp J, Kneipp H, McLaughlin M, Brown D, Kneipp K. In vivo molecular probing of cellular compartments with gold nanoparticles and nanoaggregates. *Nano Lett.* 2006;6:2225–31.
9. Drescher D, Zeise I, Traub H, Guttmann P, Seifert S, Buchner T, et al. In situ characterization of SiO₂ nanoparticle biointeractions using BrightSilica. *Adv Funct Mater.* 2014;24:3765–75.
10. Wilschut J, Hoekstra D. Membrane-fusion - from liposomes to biological-membranes. *Trends BiochemSci.* 1984;9:479–83.
11. Mellman I, Fuchs R, Helenius A. Acidification of the endocytic and exocytic pathways. *Annu Rev Biochem.* 1986;55:663–700.
12. Kneipp J, Kneipp H, Wittig B, Kneipp K. One- and two-photon excited optical pH probing for cells using surface-enhanced Raman and hyper-Raman nanosensors. *Nano Lett.* 2007;7:2819–23.
13. Ochsenkuhn MA, Jess PRT, Stoquert H, Dholakia K, Campbell CJ. Nanoshells for surface-enhanced Raman spectroscopy in eukaryotic cells: cellular response and sensor development. *ACS Nano.* 2009;3:3613–21.
14. Becker JS, Zoriy M, Matusch A, Wu B, Salber D, Palm C. Bioimaging of metals by laser ablation inductively coupled plasma mass spectrometry (LA-ICP-MS). *Mass Spectrom Rev.* 2010;29:156–75.
15. Buchner T, Drescher D, Merk V, Traub H, Guttmann P, Wemer S, et al. Biomolecular environment, quantification, and intracellular interaction of multifunctional magnetic SERS nanoprobe. *Analyst.* 2016;141:5096–106.
16. Zhang C, Wu FB, Zhang XR. ICP-MS-based competitive immunoassay for the determination of total thyroxin in human serum. *J Anal At Spectrom.* 2002;17:1304–7.
17. Giesen C, Waentig L, Panne U, Jakubowski N. History of inductively coupled plasma mass spectrometry-based immunoassays. *Spectrochim Acta B.* 2012;76:27–39.
18. Giesen C, Mairinger T, Khoury L, Waentig L, Jakubowski N, Panne U. Multiplexed immunohistochemical detection of tumor markers in breast Cancer tissue using laser ablation inductively coupled plasma mass spectrometry. *Anal Chem.* 2011;83:8177–83.
19. Waentig L, Jakubowski N, Hardt S, Scheler C, Roos PH, Linscheid MW. Comparison of different chelates for lanthanide labeling of antibodies and application in a Western blot immunoassay combined with detection by laser ablation (LA-)ICP-MS. *J Anal At Spectrom.* 2012;27:1311–20.
20. Muller SD, Diaz-Bobe RA, Felix J, Goedecke W. Detection of specific proteins by laser ablation inductively coupled plasma mass spectrometry (LA-ICP-MS) using gold cluster labelled antibodies. *J Anal At Spectrom.* 2005;20:907–11.
21. M. Cruz-Alonso, B. Fernandez, L. Alvarez, H. Gonzalez-Iglesias, H. Traub, N. Jakubowski, R. Pereiro, Bioimaging of metallothioneins in ocular tissue sections by laser ablation-ICP-MS using bioconjugated gold nanoclusters as specific tags, *Microchim. Acta*, 185 (2018).
22. Waentig L, Techritz S, Jakubowski N, Roos PH. A multi-parametric microarray for protein profiling: simultaneous analysis of 8 different cytochromes via differentially element tagged antibodies and laser ablation ICP-MS. *Analyst.* 2013;138:6309–15.

6.13 ARTICLE 13

Munster, L.; Fojtu, M.; Capakova, Z.; Vaculovic, T.; Tvrdonova, M.; Kuritka, I.; Masarik, M.; Vicha, J. *Biomacromolecules* 2019, 20, 1623-1634 (IF=5.667)

Cite This: *Biomacromolecules* 2019, 20, 1623–1634

pubs.acs.org/Biomac

Article

Selectively Oxidized Cellulose with Adjustable Molecular Weight for Controlled Release of Platinum Anticancer Drugs

Lukáš Münster,[†] Michaela Fojtů,[‡] Zdenka Capáková,[†] Tomáš Vaculovič,[§] Michaela Tvrdoňová,[§] Ivo Kuřitka,[†] Michal Masařík,^{*,†,||,⊥} and Jan Vícha^{*,†,⊥}

[†]Centre of Polymer Systems, Tomas Bata University in Zlín, tř. Tomáše Bati 5678, 760 01 Zlín, Czech Republic

[‡]Department of Physiology, Faculty of Medicine, [§]Department of Chemistry, Faculty of Science, and ^{||}Department of Pathological Physiology, Faculty of Medicine, Masaryk University, Kamenice 5, CZ-625 00 Brno, Czech Republic

[⊥]BIOCEV, First Faculty of Medicine, Charles University, Průmyslová 595, 252 50 Vestec, Czech Republic

Supporting Information

ABSTRACT: The synthesis of selectively oxidized cellulose, 2,3-dicarboxy-cellulose (DCC), is optimized for preparation of highly oxidized material for biological applications, which includes control over the molecular weight of the product during its synthesis. Conjugates of DCC and cisplatin simultaneously offer a very high drug binding efficiency (>90%) and drug loading capacity (up to 50 wt %), while retaining good aqueous solubility. The adjustable molecular weight of the DCC together with variances in drug feeding ratio allows to optimize cisplatin release profiles from delayed (<2% of cisplatin released during 6 h) to classical burst release with more than 60% of cisplatin released after 24 h. The release rates are also pH-dependent (up to 2 times faster release at pH 5.5 than at pH 7.4), which allows to exploit the acidic nature of tumor microenvironment. Extensive *in vitro* studies were performed on eight different cell lines for two cisplatin–DCC conjugates with different release profiles. In comparison with free cisplatin, both cisplatin–DCC conjugates demonstrated considerably lower cytotoxicity toward healthy cells. Conjugates with burst release profiles were found more effective against prostate cell lines, while DCC conjugates with slower release were more cytotoxic against ovarian and lung carcinoma cell lines. *In vivo* studies indicated a significantly longer survival rate, a reduction in tumor volume, and a higher accumulation of platinum in tumors of mice treated with the cisplatin–DCC conjugate in comparison to those treated by free cisplatin.



INTRODUCTION

Despite the number of emerging therapeutic approaches for cancer treatment (monoclonal antibodies and immune checkpoint inhibitors), ~70% of patients diagnosed with lung, ovarian, bladder, or testicular cancer are still treated with the first-generation platinum drug cisplatin, *cis*-[Pt-(NH₃)₂Cl₂].¹ Cisplatin (CP), as well as all other platinum-based chemotherapeutics currently used in clinical praxis, has severe side effects (neurotoxicity, nephrotoxicity, and myelosuppression) originating mostly from its general cumulative toxicity and nonspecific mechanism of action (its inability to selectively target the cancer cells).² This reduces the maximum dosage which can be safely administered to patients and may lead to the development of cancer cells' drug resistance.

Targeted delivery of platinum anticancer therapeutics using macromolecular carriers is thus becoming a key aspect for modern antitumor therapy.³ The conjugation of platinum chemotherapeutics to macromolecular carriers can provide various benefits in comparison to the administration of naked drugs: namely reduced toxicity, increased water solubility, prolonged circulation time in blood (avoiding filtration in kidneys), passive accumulation in tumor tissue due to enhanced permeability and retention (EPR) effect, improved

cellular uptake, easy codelivery of multiple components, and multiple functionalization potential, which allow for a relatively straightforward attachment of targeting vectors without any undesirable modifications to the structure of the carried substance.^{2,3} Active tumor targeting using biological vectors allows the considerable increase of both tumor accumulation and the cellular uptake of carried therapeutics,^{4,5} thus further reducing the side effects associated with the nonspecific mechanism of action.

A number of different approaches for macromolecular drug delivery have been adopted over the years, all having their particular advantages and drawbacks.^{2,3,6,7} Micelles, for instance, offer a high drug-loading capability for lipophilic drugs, but their stability *in vivo* is questionable.⁸ Macromolecular carriers based on synthetic polymers have well-defined structures and properties, but they often suffer from a relatively small drug loading capacity^{5,9} and high complexity.¹⁰ Platinum–dendrimer complexes achieve good platinum loading and show a low toxicity¹¹ but have problematic

Received: December 21, 2018

Revised: February 21, 2019

Published: February 22, 2019



© 2019 American Chemical Society

1623

DOI: 10.1021/acs.biomac.8b01807
Biomacromolecules 2019, 20, 1623–1634

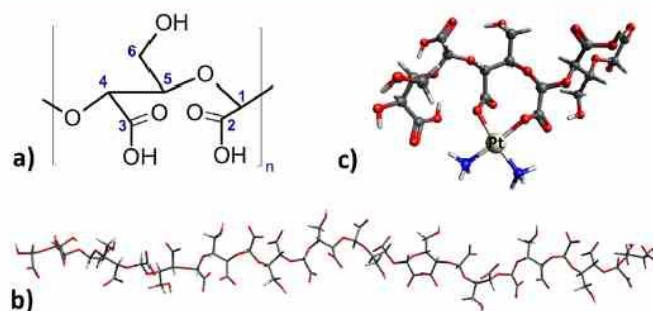


Figure 1. (a) Structural formula of DCC monomeric unit, (b) DFT optimized structure of DCC chain, and (c) DFT optimized structure of CP-DCC conjugate.

water solubility with a tendency to aggregate and very slow platinum release rates due to platinum binding to the secondary and terminal amines in dendrimers structure.^{9,12}

Biopolymers, particularly naturally occurring acidic polysaccharides, are often used as drug delivery vehicles due to their biological origin, biocompatibility, and well-understood chemistry.^{13–15} It is argued that the most studied acidic polysaccharide is hyaluronic acid (HA),^{13,14,16,17} which was used as a platinum anticancer drug carrier on a number of occasions with relatively good results.^{18–20} However, the main drawback of HA as a platinum drug delivery vehicle is the presence of a single carboxylic group per monomeric unit. Because all currently used Pt(II) chemotherapeutics have two binding sites, their monodentate binding leads to undesirable cross-linking reactions, which considerably lowers the aqueous solubility of the drug carrier conjugates and thus also the maximum effective loading of the drug.^{9,21} For instance, the maximum loading capacity of HA for cisplatin does not exceed 25 wt %.^{18,21} Moreover, the reported binding effectiveness of cisplatin to HA is only 50% even at a very low CP:HA reaction ratio of 4:10.¹⁸ Low drug binding effectiveness can easily multiply the cost of a drug delivery system and, in combination with low drug loading capacity, presents one of the key drawbacks for many drug delivery systems (DDS).⁵

Synthetically modified polysaccharides with a high degree of substitution by $-\text{COOH}$ groups (up to 3), such as carboxymethylcellulose or nonspecifically oxidized cellulose, are hypothetically capable of bidentate binding of a large amount of Pt(II) drugs due to a high density of ligating groups. However, synthetically modified polysaccharides were reported to support cell proliferation, which is highly undesirable in cancer treatment.²² Their nonstoichiometric composition and often limited water solubility further reduce their applicability as a DDS.

As we demonstrate in this work, the selectively oxidized cellulose, 2,3-dicarboxycellulose (DCC, Figure 1a,b), does not suffer from such drawbacks. It contains two carboxylic groups per monomeric unit at a distance and orientation suitable for efficient bidentate binding of Pt(II) square-planar complexes, which ensures a high drug binding effectiveness and loading capacity. It is nontoxic and does not support cell proliferation, has a well-defined composition, and allows for good control over its properties.

Although the basic procedure for the selective oxidation of polysaccharide hydroxyl groups at C2 and C3 atoms to the carboxylic groups has been known for a long time,^{23,24} the

applications of DCC were mostly limited to the area of materials and industry. For instance, partially oxidized DCC was proposed as a component of ultrafiltration membranes and chromatography columns,^{25,26} for the preparation of nanopaper,²⁷ water purification,²⁸ and as a material for the preparation of cellulose nanofibrils²⁹ or highly charged cellulose nanocrystals.³⁰

To introduce DCC into the field of drug delivery, it was necessary to optimize its synthesis to obtain a highly oxidized product of sufficient purity and to introduce more direct control over its properties, particularly the molecular weight. The prepared material surpasses current polysaccharide platinum anticancer drug carriers in a number of aspects, particularly in terms of simultaneous drug binding effectiveness, loading capacity, and adjustable drug release profiles. The conjugate of DCC with cisplatin (CP-DCC, Figure 1c) demonstrated a number of advantages in comparison to free cisplatin both *in vitro* and *in vivo*.

METHODS AND MATERIALS

Synthetic Procedures. Preparation of the DCC with Different Molecular Weights. The synthesis of DCC suitable for a DDS application involves the sequential two-step oxidation (primary and secondary) of cellulose. The primary oxidation was performed using 1.2:1 molar ratio of reactants (sodium periodate:cellulose) at 30 °C for 72 h in the absence of light. This allows the preparation of dialdehyde cellulose (DAC) with a degree of oxidation above 95% and with a good reproducibility. The oxidation is terminated by the addition of an excess of ethylene glycol to decompose residual periodate. Subsequently, DAC in a never-dried state is purified by several cycles of centrifugation and mechanical homogenization. The degree of conversion of cellulose is determined by the alkalimetric titration of HCl liberated from the oxime reaction between DAC and hydroxylamine hydrochloride.^{31–33}

The secondary oxidation of the DAC suspension is performed by sodium chlorite in the presence of acetic acid using 1:4:2 molar ratio of reagents ($-\text{CHO}:\text{NaClO}_2:\text{CH}_3\text{COOH}$). The NaClO_2 solution is added dropwise to the reaction mixture to a final concentration of 1.0 ± 0.1 mol/L. To ensure the reproducibility of the results, it is highly recommended to perform the secondary oxidation immediately after the primary one. Otherwise, the DAC may degrade and change its structure during aging, unless it is kept under acidic conditions.^{34,35}

The reaction mixture must be vigorously stirred due to a strong initial increase in viscosity caused by a gradual conversion from DAC to DCC, as DCC oxidized from by less than 70% is unlike fully oxidized DCC, practically insoluble.²⁴ DCC with low degree of oxidation thus can be conveniently separated by filtration or centrifugation. To ensure a quantitative conversion of DAC to DCC, a 7 h secondary oxidation at 30 °C in the absence of light was employed. The reaction

was stopped by the dropwise addition of 10 M NaOH, and the reaction mixture was subsequently dialyzed against distilled water for 48 h. The resulting DCC solution was titrated with 1 M NaOH to pH 7.4, filtered, and lyophilized to obtain a sodium salt of 2,3-dicarboxycellulose (Na-DCC). The obtained Na-DCC has a high purity, a degree of oxidation above 90%, and a mass average molecular weight (M_w) of 82 kDa (estimated by GPC, see Table 1). Its degree

Table 1. Number-Average Molecular Weight (M_n), Weight-Average Molecular Weight (M_w), Peak Molecular Weight (M_p), and Polydispersity Index (PDI) Obtained as M_w/M_n

| | M_n (kDa) | M_w (kDa) | M_p (kDa) | PDI |
|----------|-------------|-------------|-------------|------|
| Na-DCC18 | 12 | 18 | 15 | 1.59 |
| Na-DCC82 | 40 | 82 | 63 | 1.76 |

of polymerization DP = 430 corresponds to that given for the starting material (SigmaCell, M_w = 76100 Da, DP = 460).³⁶ This agrees with earlier observations that both primary and secondary oxidations of cellulose have a minimal impact on the DP of the starting material.³³

Two different approaches were investigated to govern the M_w of DCC. The simplest method of DCC molecular weight reduction is heat degradation. However, this approach leads to very low yields as mostly very low-molecular-weight products are dialyzed away, and its poor selectivity causes a significant increase of polydispersity index (PDI) of the final product. The second approach involves the addition of amidosulfonic acid (H_3NSO_3) to the reaction mixture prior to the secondary oxidation. This has two consequences. First, H_3NSO_3 suppresses the *in situ* formation of the undesirable hypochlorite from $NaClO_2$.³⁴ Second, the M_w of the DCC is indirectly dependent on the molar amount of H_3NSO_3 . The addition of 0.25 mol equiv (relative to the amount of $-CHO$ groups estimated by oxime reaction) of H_3NSO_3 results in a decrease of M_w of the resulting DCC by 30%, i.e., from 82 kDa (Na-DCC from H_3NSO_3 -free synthesis) to 55 kDa. The addition of 0.5 mol equiv of H_3NSO_3 decreases its M_w by nearly 80% relative to Na-DCC prepared without H_3NSO_3 , i.e., down to 18 kDa. The further increase of the H_3NSO_3 amount does not lead to a significant decrease of M_w , as 4 times the molar equivalent of H_3NSO_3 decreases the M_w of Na-DCC only by another 5% to 12 kDa. The careful modification of the H_3NSO_3 : $-CHO$ molar ratio enables the control of the M_w of the final product without negative impacts on its yields or the PDI, as the PDI of Na-DCC prepared with and without amidosulfonic acid are comparable; see Table 1 for the results from GPC analysis.

Preparation of the Cisplatin–DCC Conjugate (CP–DCC). Cisplatin was prepared by using well-established procedures.³⁷ Its aqueous solution (2 mg/mL) was then added dropwise to the DCC dissolved in distilled water (4 mg/mL) at room temperature, and the reaction mixture was gently shaken for 72 h in the absence of light. After this time, the solution was dialyzed against distilled water for 4 h using a membrane of MWCO 3.5 kDa and lyophilized. Reactions were performed using a DCC of M_w of 18 and 82 kDa. The investigated CP:DCC ratio ranged from 4:10 to 12:10 (28 to 55 wt % CP). The formation of CP–DCC was confirmed by infrared spectroscopy (FT-IR) in the far-infrared region as well as 1H , ^{13}C , and ^{195}Pt nuclear magnetic resonance (NMR) spectroscopy and quantified by X-ray fluorescence spectroscopy (XRF).

Drug Release Studies. The drug release rate was investigated using a setup which simulated *in vitro* conditions.²¹ In short, 20 mg of the conjugate was dissolved at 37 °C in 5 mL of PBS and dialyzed against 95 mL of the same medium (MWCO 3.5 kDa) with the pH set to 7.4 and 5.5 by a diluted HCl solution. Aliquots of 5 mL were collected at given times and replaced with 5 mL of fresh PBS of a given pH to conserve the volume. Note that the term cisplatin (CP) is in the text applied also to cisplatin residuum bound to DCC and to the released active form of CP, *cis*-[Pt(NH₃)₂(H₂O)₂]²⁺ complex,³⁸ to simplify the discussion.

Computational Details. The structures of the DCC dodecamer (Figure 1b) and the CP–DCC conjugate (hexamer with bonded CP,

Figure 1c) were optimized using PBE0 functional^{39,40} and a standard def2-SVP basis set⁴¹ for light atoms (DCC chain) and a def2-TZVPP basis set⁴¹ for cisplatin residuum. A relativistic effective core potential (ECP) for Pt, replacing 60 core electrons was used.⁴² The D3 dispersion correction⁴³ and COSMO solvent model⁴⁴ (water) as implemented in Turbomole⁴⁵ were used. This approach is optimized specifically for studies of platinum complexes.^{46–48} The ^{13}C NMR chemical shifts of the DCC were calculated using PBE0 functional with an IGLO-III basis set⁴⁹ and a PCM solvent model⁵⁰ as an average of NMR chemical shifts of ten inner monomeric units of the DCC dodecameric chain. Glycol was used as a secondary reference (63.79 ppm vs TMS).^{46,48}

Because the calculations of ^{195}Pt NMR chemical shifts require rigorous treatment of relativistic effects, a fully relativistic ^{195}Pt NMR chemical shift of cisplatin residuum conjugated to a model of a DCC chain (Figure 1c) was obtained using a four-component relativistic Dirac–Coulomb–Kohn–Sham (DKS) formulation based on the Dirac–Coulomb–Hamiltonian equation and the restricted magnetically balanced basis for the small component,^{51,52} as implemented in the ReSpect 5.1 code.⁵³ The PBE0 functional and an uncontracted Dyall's valence triple- ζ basis set for the Pt and an IGLO-II basis set for light atoms⁵⁷ were used. The use of a smaller model (DCC hexamer) and a locally dense basis set is necessary due to the high computational cost of fully relativistic calculations; the latter was shown to have a minimal impact to the calculated NMR chemical shifts of heavy elements.^{58,59} Solvent effects were simulated by the addition of 12 water molecules in a sphere centered around a platinum atom, which provided the best results in previous work.⁶⁰ The positions of the water molecules and all of the atoms attached to the platinum atom were reoptimized, while the torsion angles of the DCC backbone were fixed to simulate its involvement in the polymeric chain.

Biological Tests. Chemical and Biochemical Reagents. RPMI-1640 medium, Ham's F12 medium, fetal bovine serum (FBS) (mycoplasma-free), penicillin–streptomycin, and trypsin were purchased from PAA Laboratories GmbH (Pasing, Austria). Phosphate buffered saline (PBS) was purchased from Invitrogen Corp. (Carlsbad, CA). Thiazolyl blue tetrazolium bromide (for MTT assay), ethylenediaminetetraacetic acid (EDTA), dimethyl sulfoxide (DMSO), and all other chemicals of ACS purity were purchased from Sigma-Aldrich Co. (St. Louis, MO), unless noted otherwise.

Cell Lines and Cell Culture. Altogether, eight human and mice cell lines were used in this study: The noncancerous cell lines were represented by a normal human epithelial prostate cell line (PNT1A, passage #20) and mice embryonic fibroblasts (NIH/3T3, passage #30). The malignant cell lines were represented by a human ovarian cell line established from a tumor tissue of an untreated patient with ovarian cancer (A2780, passage #10) and its cisplatin-resistant subline (A2780/CP, passage #10), a human cell line derived from pulmonary adenocarcinoma (A549, passage #11), human nonsmall cell lung carcinoma cells derived from the lymph node (H1299, passage #10), a cell line representing human prostate carcinoma (22Rv1, passage #4), and a human prostate cancer cell line established from a bone metastasis (PC-3, passage #25). All of the cell lines except for the NIH/3T3 and PC-3 cell line were cultivated with a RPMI-1640 medium with 10% FBS supplemented with antibiotics (penicillin 100 U/mL and streptomycin 0.1 mg/mL). The cells were grown in an incubator at 37 °C in a humidified 5% CO₂ mixture with ambient air. All of the cell cultures used in this study were purchased from the Health Protection Agency Culture Collections (Salisbury, UK). The PC-3 cell line was cultivated in Ham's medium with 10% FBS supplemented with antibiotics (penicillin 100 U/mL and streptomycin 0.1 mg/mL) and NIH/3T3 in DMEM with 10% calf serum supplemented with antibiotics (penicillin 100 U/mL and streptomycin 0.1 mg/mL).

MTT Cytotoxicity Assessment. The cells were seeded on a 96-well plate at a density of 8×10^4 cells/well (10^4 cells/well in the case of A2780, A2780/CP, A549, and 22Rv1 cell line) in a culture medium containing 10% FBS and 1% penicillin–streptomycin. The cells were then incubated at 37 °C in a humidified 5% CO₂ mixture. After 48 h,

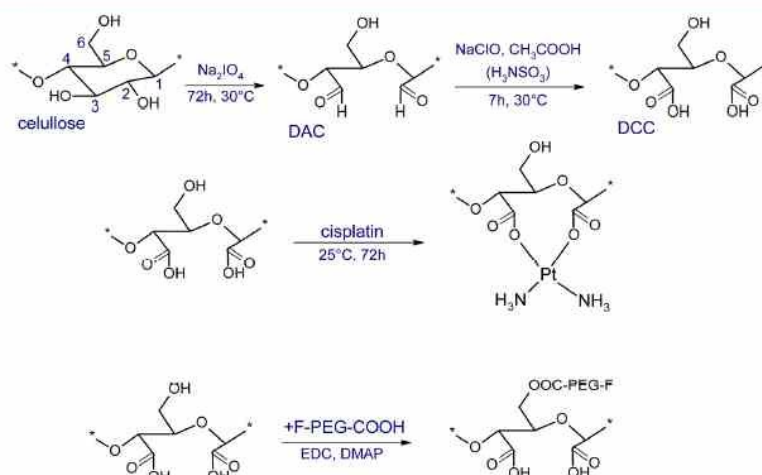


Figure 2. Schematics of CP–DCC preparation. All reactions were performed in the absence of light.

the cell culture medium was removed and replaced with a new medium containing various concentrations of the compounds. The concentrations of conjugates were selected in a way that the concentration of the fully released active compound is equal to that of free CP. After exposure of cells for 24 to 48 h, 200 μL of medium containing 1 mg/mL MTT of reagent per well was added. The plates were kept in the humidified atmosphere at 37 $^{\circ}\text{C}$ for 4 h, wrapped in aluminum foil. After that, the medium containing MTT was exchanged with 200 μL /well of 99.9% DMSO to dissolve the formazan crystals. Then, 25 μL /well of glycine buffer was added to DMSO and gently shaken, and the absorbance was read at a wavelength of 570 nm using a Cytation 3 multimode imaging reader (BioTek Instruments, Winooski, VT). The IC_{50} values are defined as a concentration of compound required to inhibit the cell growth by 50%. All of the measurements were performed in quadruplicates.

Cellular Uptake of Platinum. The A2780 cells were seeded on a cell culture dishes (25 cm^2) in a RPMI-1640 culture medium containing 10% FBS and 1% penicillin–streptomycin and incubated for 48 h. Then, cells were treated with 5 μM CP and CP-DCC18 with a corresponding amount of CP which represents a sub IC_{50} concentration. This concentration was applied to see the platinum accumulation without inducing extensive cell death. After further incubation for 24 or 48 h, the cell culture media above the cells was collected and centrifuged to analyze the concentration of platinum compounds not taken up by cells. The cells itself were harvested by trypsinization. The cell samples were washed three times with PBS followed by centrifugation (4 $^{\circ}\text{C}$, 2700 rpm, 7 min) to remove the surface-bound drugs. Thereafter, cells were mechanically lysed in PBS on ice with a micropestle for 5 min followed by centrifugation (4 $^{\circ}\text{C}$, 2700 rpm, 7 min). Supernatant collected after this centrifugation and the culture media samples collected earlier were analyzed for the platinum concentration by ICP-MS Agilent 7900 (Agilent Technologies, Japan). Prepared lysates were 10 times diluted by deionized water before the analysis and the Pt concentration was measured by isotope ^{195}Pt . The possible matrix effect was suppressed by measuring of Au solution (10 $\mu\text{g}/\text{L}$) as internal standard. The platinum extent was expressed in $\mu\text{g}/\text{l}$ and then converted to nanograms of Pt per 10^6 cells.

In Vivo Cytotoxicity Assessment. The use of the animals followed the European Community Guidelines. The experiments were performed with the approval of the Ethics Commission at the Faculty of Medicine, Masaryk University, Brno, Czech Republic. The tumor distribution of platinum was assessed using 10 eight-week-old untreated Nu-Nu female mice (weight 19.7–25.9 g), which were treated with CP and CP-DCC18. The mice intraperitoneally received

three doses of compounds with an equivalent amount of CP within 2 weeks (200 μL of 1.5 mg/mL solution of CP and 200 μL of 3 mg/mL of CP-DCC18). Each application was followed by a two-day break. The resulting concentration and distribution of platinum in tumors were assessed by LA-ICP-MS.

Tissue Sample Preparation. The surviving animals were terminated two days after the last dose of CP and CP-DCC18. Next, the tumors were extracted and embedded by a CryoGlue embedding medium (Slee Medical, Mainz, Germany) and put inside liquid nitrogen for 10 s. Subsequently, the samples were cut on a cryostat MTC (Slee Medical) with a slice thickness of 25 μm for LA-ICP-MS. The concentration of platinum was proportionate to the weight of the tissue sample.

Instrumentation and Measurement Setup. Infrared Spectroscopy. An FT-IR analysis was performed using a Nicolet 6700 (Thermo Scientific, USA). Spectra were collected in the range of MIR and FIR (4000–400 cm^{-1}) with 64 scans and a resolution of 2 cm^{-1} .

NMR Spectroscopy. ^1H and ^{13}C NMR spectra were recorded at 298 K in D_2O using a Bruker Avance III HD 700 MHz NMR spectrometer equipped with a triple-resonance cryoprobe optimized for ^{13}C detection. Besides the 1D experiments, the ^1H – ^{13}C heteronuclear single quantum correlation (HSQC, $J_{\text{H-C}} = 145 \text{ Hz}$) and ^1H – ^{13}C heteronuclear multiple bond correlation (HMBC, $^2J_{\text{H-C}} = 10 \text{ Hz}$) experiments were performed.³³ The ^{195}Pt NMR chemical shifts were recorded using a Bruker Avance III HD 700 MHz NMR spectrometer equipped with a broad-band probehead at 298 K in a saturated solution of cisplatin in D_2O (2.5 mg/mL) which was necessary to suppress the dynamic processes (CP release from the conjugate) and related NMR signal broadening.

UV-Vis Spectroscopy. The amount of folate bound to the DCC was estimated by a double-beam UV/vis spectrometer Lambda 1050 (PerkinElmer, Inc.) in the span of 250–800 nm using the FA absorption band at 280 nm.

XRF Analysis. The concentration of CP in the prepared sample solutions was determined by an energy-dispersive X-ray fluorescence spectrometer by ARL Quant'X EDXRF Analyzer (Thermo Scientific, Inc.). The calibration standards for determining the platinum amount in the samples were prepared by dissolving a specific amount of CP in distilled water or in a PBS of the required pH.

GPC Analysis. A molecular weight analysis was employed for all of the prepared Na-DCC samples using a Waters HPLC Breeze chromatographic system equipped with a Waters 2414 refractive index detector (drift tube $T = 60 \text{ }^{\circ}\text{C}$), a Tosoh TSKgel GMPW_{XL} column (300 mm \times 7.8 mm \times 13 μm , $T = 30 \text{ }^{\circ}\text{C}$), and a mobile phase composed of 0.1 M of sodium nitrate (NaNO_3) and 0.05 M of

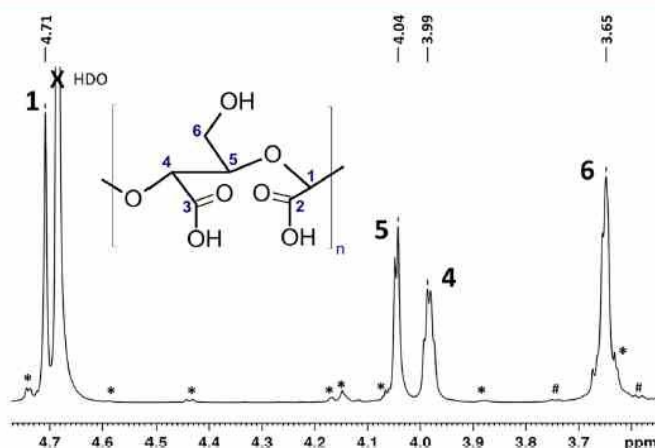


Figure 3. ^1H NMR spectrum of Na-DCC82 in D_2O at 298 K. The signals marked with an asterisk were assigned to the DCC units bonded by 2–6 glycosidic bond; the hashtag marks the signals of unoxidized AGU units.

a disodium phosphate dodecahydrate ($\text{Na}_2\text{HPO}_4 \cdot 12\text{H}_2\text{O}$) aqueous solution. A Pullulan polysaccharide calibration kit SAC-10 (Agilent Technologies, Inc.) in a span of M_w 180–100000 g/mol was used for calibration.

Determination of Platinum Distribution in the Tumor Tissue. Determination of the distribution of platinum in crosscuts of tumors was performed by using LA-ICP-MS. The ablation experiment was undertaken using the commercial laser ablation system UP 213 (New Wave, USA) linked to a quadrupole ICP-MS 7500ce (Agilent Technologies, Japan). The ablated material was performed from the ablation cell by helium (1.0 L/min). Argon was admixed (0.6 L/min) into the flow prior to entering the ICP torch. The ^{195}Pt isotope was measured with an integration time of 0.3 s. The laser ablation parameters influencing the lateral resolution (laser beam diameter and scan speed) were optimized to get a sufficient lateral resolution in a sufficiently short time analysis.⁶¹ The laser spot diameter of 100 μm was adapted with respect to the size of the sample, and the scan speed was 200 $\mu\text{m}/\text{s}$. The laser beam parameters such as fluence and laser repetition rate were 8 J/cm^2 and 10 Hz, respectively. The high laser beam fluence was applied to suppress the influence of a different ablation rate in various zones of the sample.⁶² The possible polyatomic interferences were suppressed by using a collision reaction cell (2.5 mL/min He) that is part of ICP-MS.

Quantification of the Platinum Distribution in the Tumor Tissue. The quantification of the imaged map was done by agarose gels doped with a known amount of platinum to obtain a set of standards with the content of 0–2–5–10 $\mu\text{g}/\text{g}$ of Pt. The calibration standards were ablated under the same laser ablation parameters as the samples.

RESULTS AND DISCUSSION

Preparation and Characterization of DCC for Biomedical Applications. The preparation of highly oxidized DCC and its conjugate with cisplatin is schematically illustrated in Figure 2; see the *Methods and Materials* section for more details.

The synthesis of DCC is based on a two-stage oxidation process,^{23,26,34} which was modified for the preparation of a highly oxidized material with an adjustable M_w . In short, the highly selective periodic oxidation of cellulose hydroxyl groups at C2 and C3 introduces two aldehyde groups per each monomeric unit. The resulting 2,3-dialdehyde cellulose (DAC) is highly reactive^{32,63,64} and decomposes rather fast unless kept under acidic conditions.³³ It is thus not suitable for drug

delivery applications by itself, although DAC-cross-linked hydrogels show certain promise.^{35,65} To avoid the DAC chain scission occurring during the DAC solubilization by hot water,³³ the DAC is oxidized by NaClO_2 directly in a never-dried state in the presence of acetic acid.

The control over the M_w of DCC is achieved by the addition of a given amount of amidosulfonic acid (H_3NSO_3) into the reaction mixture prior to the secondary oxidation because the M_w of Na-DCC is inversely proportional to the molar equivalent of H_3NSO_3 in the reaction mixture (relative to $-\text{CHO}$ groups of DAC). As a result, the M_w of Na-DCC can be tuned in a range between 15 and 100% of that of Na-DCC prepared without H_3NSO_3 (see the *Methods and Materials* section). Notably, unlike heat degradation and solubilization, the H_3NSO_3 -mediated DCC chain scission does not increase the polydispersity index (PDI) of the product (see Table 1).

After the secondary oxidation, the DCC is converted into sodium salt (Na-DCC) and lyophilized. The precipitation of Na-DCC from an aqueous solution by organic solvents such as alcohols, previously employed for the isolation of DCC,²⁴ should be avoided for any material intended for biomedical applications. The product can become contaminated with relatively large quantities of residual solvents, which can persist even after prolonged periods of vacuum drying and are nearly impossible to remove entirely.

In the following, Na-DCC with an M_w of 82 kDa (prepared without H_3NSO_3) is noted as Na-DCC82, while Na-DCC with an M_w of 18 kDa (prepared using 0.5 mol equiv of H_3NSO_3) is termed Na-DCC18.

The FT-IR spectra of all prepared DCC salts revealed strong absorption bands at 1606 and 1294 cm^{-1} , which are consistent with $\text{C}=\text{O}$ and $\text{C}-\text{O}$ stretching vibrations of $-\text{COOH}$ groups (see Figure S3). No evidence of the presence of residual aldehyde groups³³ was found.

The ^1H NMR spectra of Na-DCC82 revealed a 96% conversion of cellulose to DCC. The ^1H NMR spectrum of Na-DCC82 is given in Figure 3. Weak signals in the spectra belong to unoxidized anhydroglucose units (AGU) of the cellulose (<2% of integral intensity relative to DCC, marked with hashtag in Figure 3) and also to the DCC units bonded together by 2–6 glycosidic links (<2% of integral intensity,

Table 2. Experimental (δ) and Calculated (δ_{calc}) ^1H , ^{13}C , and ^{195}Pt NMR Chemical Shifts of Na-DCC82 and CP-DCC82 Conjugate (38% CP, w/w)

| DCC | H1 | H4 | H5 | H6 | C1 | C2 | C3 | C4 | C5 | C6 | MAD |
|------------------------------|------|------|------|------|-------|-------|-------|------|------|------|-------|
| δ (ppm) | 4.71 | 3.99 | 4.04 | 3.65 | 101.0 | 173.7 | 176.1 | 79.9 | 77.7 | 60.8 | |
| δ_{calc} (ppm) | | | | | 100.1 | 174.5 | 175.8 | 81.2 | 80.5 | 61.8 | 0.8 |
| CP-DCC | H1 | H4 | H5 | H6 | C1 | C2 | C3 | C4 | C5 | C6 | Pt |
| δ (ppm) | 4.65 | 4.00 | 4.07 | 3.66 | 101.5 | 175.3 | 175.3 | 80.1 | 78.0 | 61.1 | -1605 |

marked by asterisks in Figure 3), probably the partially oxidized remnants of intermolecular 2–6 hemiacetals formed in large quantities in DAC solutions.³³ These were identified based on distinct correlation signals of H2' and C6 in ^1H – ^{13}C HMBC spectra, which correspond to those previously observed in DAC solutions.³³

The presence of residual unoxidized cellulose units in the DCC structure can be an advantage for a drug carrier as it may provide certain tumor-targeting capabilities because the malignant cells require a large amount of glucose to supply the energy for rapid cell division and tends to have overexpression of glucose membrane transporters and the number of other saccharide and polysaccharide receptors.^{2,66}

The degree of oxidation of Na-DCC18 estimated from ^1H NMR spectra was 82%. The unoxidized part consists from 2% of AGU and from 16% of DCC units bonded together by 2–6 glycosidic links.³³ The ^1H NMR spectrum of Na-DCC18 is given in Figure S1 of the Supporting Information. Instead of an expected increase of effectivity of secondary oxidation,³⁴ the addition of relatively large amounts of amidosulfonic acid seemed to somewhat limit reaction progress in highly oxidized materials. Although no signals of free aldehydes were observed in the spectra, more sterically protected C6–O–C2 links seems to survive the oxidation in the presence of hypochlorite scavenger largely intact. Nevertheless, besides a slightly (5%) decreased CP binding efficiency at CP:DCC reaction ratios 10:10 and higher, the presence of 2–6 linked DCC unit has no negative impact on the biological properties of Na-DCC18 in comparison with Na-DCC82 (see below). The elucidation of the exact reaction mechanism of amidosulfonic acid is currently underway.

The ^{13}C NMR spectra of Na-DCC82 and Na-DCC18 confirmed the presence of COOH groups by signals at 173.7 ppm (C2) and 176.1 ppm (C3) (see Figure S2). Because it was not possible to unambiguously assign C4 and C5 signals directly from the NMR spectra, DFT calculations of ^{13}C NMR chemical shifts were performed on a model structure of a DCC dodecamer (see Figure 1b and Methods and Materials for more details). The calculations reproduced measured ^{13}C NMR chemical shifts with very good accuracy (mean absolute deviation, MAD = 0.8 ppm) (see δ_{calc} in Table 2). On the basis of these results, the C4 resonance was assigned to signal at 79.9 ppm, while C5 was assigned to signal at 77.7 ppm. The corresponding ^1H resonances were identified from the ^1H – ^{13}C HSQC spectra, and the complete ^1H and ^{13}C NMR chemical shift assignments of Na-DCC82 are given in Table 2.

Preparation and Characterization of Cisplatin–DCC Conjugates. The CP–DCC conjugates were prepared by a dropwise addition of an aqueous solution of CP to the solution of Na-DCC18 and Na-DCC82. The CP–DCC conjugates were prepared using the CP:Na-DCC reaction ratio from 4:10 to 12:10, which corresponds to 28 to 55 wt % CP. The reaction was complete after 72 h of gentle shaking in the absence of light. The activation of CP by silver nitride,¹⁸ which

presents a potential source of product contamination, was not necessary. Traces of unreacted CP were removed by dialysis; products were lyophilized and analyzed by FIR, ^1H , ^{13}C , and ^{195}Pt NMR, and XRF spectroscopy.

The FT-IR spectra CP–DCC conjugate measured in the far-infrared region (Figure S3) revealed that the absorption bands corresponding to stretching the Cl–Pt–Cl vibrations of the free CP⁶⁷ at 315 and 323 cm^{-1} were replaced by bands at 338 and 388 cm^{-1} , which were assigned to O–Pt–O vibrations caused by the CP conjugation to the carboxylic groups of DCC.

The NMR spectra of CP–DCC82 prepared using the CP:DCC reaction ratio 6:10 were recorded. The attachment of CP to DCC causes the appearance of a broad signal at 175.3 ppm in the ^{13}C NMR spectra, which was assigned to the C2 and C3 atoms bearing CP moiety (see Figure S4). Notably, the conjugate formation has a minimal effect on the other ^1H and ^{13}C NMR chemical shifts, including signals of unreacted –COOH groups from the CP–DCC82 (see Table 2 and Figure S4). This can be interpreted in a way that the conjugation of CP does not cause any significant distortions to the DCC chain. This is not surprising as the distance of the –COOH groups in DCC (2.65 Å based on DFT-optimized geometry in Figure 1b) is identical to that found in Pt(II) complex oxaliplatin optimized at the same level of theory (2.65 Å, this work). Cisplatin can thus be bound to DCC in a bidentate manner without any energy-extensive deformations to the DCC chain. This agrees with the spontaneous progress of CP conjugation to DCC (see below).

The bidentate binding of CP is evident from the ^{195}Pt NMR spectra, where a very broad signal of the conjugate was observed at –1605 ppm (Figure 4), in a region where the platinum atoms bound by two nitrogen and two oxygen atoms resonate.^{68,69} For instance, the *cis*-[(NH₃)₂PtAc₂] complex, where Ac = –OOCCH₃, essentially a small-molecule analogue of the CP–DCC conjugate, resonates at –1581 ppm,⁷⁰ while the monosubstituted complexes of cisplatin, such as *cis*-[Pt(NH₃)₂(H₂O)Cl]⁺, resonate at a higher field (–1825

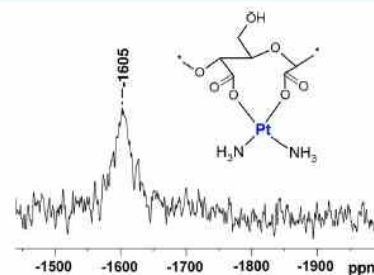


Figure 4. ^{195}Pt NMR spectrum of CP-DCC82 prepared using reaction ratio 6:10 in D_2O at 298 K.

ppm).⁷¹ Signal broadness is probably a result of complex chemical environment related to the attached macromolecular carrier and the presence of dynamic processes in the sample (CP release from the carrier).

The experimental results were further supported by fully relativistic DFT calculations^{48,51,52} of the ¹⁹⁵Pt NMR chemical shifts (see the *Methods and Materials* section) for more details. The calculated ¹⁹⁵Pt NMR chemical shift of a CP moiety conjugated to DCC (Figure 1c) is -1558 ppm, which is consistent with the deshielding of the ¹⁹⁵Pt NMR resonance upon CP–DCC formation.

Cisplatin Binding. The CP binding efficiency toward the DCC was determined by an XRF spectroscopy (see *Methods and Materials*). Nearly quantitative binding with effectivity above 95% was found for both Na-DCC18 and Na-DCC82 using a CP:DCC reaction ratio of up to 8:10 (45 wt % CP) (see Figure 5). Very good binding effectivity, $\geq 90\%$, was observed for Na-DCC18 at up to a 10:10 reaction ratio (50 wt % CP) and for Na-DCC85 even at a 12:10 CP:DCC ratio (55 wt %).

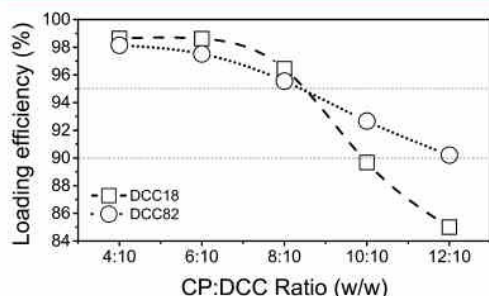


Figure 5. Loading efficiency of CP toward Na-DCC18 and Na-DCC82 as a function of the CP:Na-DCC reaction ratio.

The efficient bidentate binding of CP by Na-DCC results in good solubility of all CP–DCC conjugates (>5 mg/mL) in water and phosphate-buffered saline (PBS). However, while conjugates with <50 wt % CP are dissolved nearly immediately, any conjugates with ≥ 50 wt % CP take ~ 1 h of gentle shaking at 37 °C to fully dissolve. This is not surprising, as the theoretical maximum loading capacity of DCC for cisplatin is 13:10 (assuming 100% oxidation of the cellulose chain and DCC in the form of sodium salt with molar weight of DCC

monomer 236 g/mol). As the DCC chain becomes nearly saturated by CP units, the monodentate binding of an excess of CP molecules is more likely to occur, which leads to undesirable chain cross-linking. Therefore, 50 wt % CP in the CP–DCC conjugate (10:10 ratio) is considered a maximum practical CP loading capacity of the DCC. This is still twice more than loading capacity of HA^{18,21} and is achieved with a much higher CP binding effectivity.

In the following, the CP–DCC conjugates that are prepared using up to 45 wt % CP (8:10) are investigated, as they offer an ideal combination of high drug loading and an excellent binding efficiency ($>95\%$).

Drug Release Studies. The drug release was investigated using a setup mimicking *in vitro* conditions.²¹ The CP–DCC conjugate was dissolved in PBS at 37 °C and dialyzed against neat PBS using a membrane with MWCO 3500 Da. The pH was set to 7.4 and 5.5, respectively. The amount of CP in dialysate was determined by XRF spectroscopy. All of the experiments were performed in triplicate.

Under the experimental conditions, the free CP is quantitatively dialyzed in <2 h, while the CP release from the DCC is considerably slower and depends on the M_w of the carrier and the loading of the drug (see Figure 6a). The conjugate prepared using a “high- M_w ” DCC82 and “low” amount of CP (4:10 or 6:10, 28 or 38 wt %, respectively) leads to a continuous, almost linear drug-release profile, without an initial burst release. The cisplatin release from the conjugate loaded by 28 wt % of the drug is even nearly entirely suspended for the first 6 h (accumulative CP release $<2\%$). This could be exploited for a more targeted drug release, as the active compound is not released prematurely in the bloodstream and the conjugate thus has time to accumulate in the tumor tissue. Another possibility lies in preparation of materials with a continuous drug release, such as DCC-based hydrogels for a sustained and localized drug delivery, e.g., for the suppression of cancer recurrence after resection.⁷²

The influence of the DCC molecular weight to the drug release rate is demonstrated by the comparison of the CP-DCC18 and CP-DCC82 conjugates, which were both prepared using 45 wt % CP (8:10). Although their initial (up to 4 h) release rates are similar, the further release from DCC82 is notably slower. As a result, more than 75% of the CP is released from DCC18 after 3 days, while for DCC82 it is only 58%.

The CP release is also pH dependent, which allows the exploitation of an acidic tumor microenvironment² for a faster

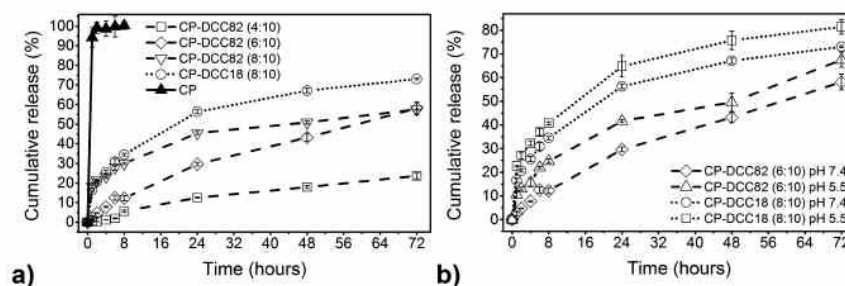


Figure 6. Cisplatin (CP) cumulative release (%) from carriers with a different M_w and drug loading, at 37 °C in PBS at (a) pH 7.4 and (b) pH 5.5. The dashed lines represent conjugates based on Na-DCC82; the dotted lines represent those based on Na-DCC18. The CP:DCC reaction ratio is given in the legend together with different pH values (where applicable).

and more targeted drug release (see Figure 6b). The importance of the pH is best observable at early stages of release from the DCC82 conjugate, where twice the amount (24 vs 12%) of CP is released after 8 h at pH 5.5 than at pH 7.4.

To summarize, the CP–DCC conjugates can offer a broad range of drug release profiles, accessible by a simple optimization of reaction conditions during the preparation of the carrier (changing its M_w) and its conjugates (modification of CP:DCC reaction ratio).

In Vitro Cytotoxicity. The Na-DCC18, Na-DCC82, and CP-DCC18 with 43 wt % of the bound CP (prepared using 45 wt % CP with 96.5% binding efficiency) and the CP-DCC82 with 37 wt % of the bound CP (prepared using 38 wt % CP with 97.5% binding efficiency) were selected for biological testing. In the following, these are referred to only as CP-DCC18 and CP-DCC82. CP-DCC18 is an example of a conjugate with a fast initial platinum release and high CP content, while CP-DCC82 has an approximately linear platinum release profile and moderate CP content.

The cytotoxicity of the free CP, of both the investigated carriers (Na-DCC18, Na-DCC82) and their conjugates (CP-DCC18 and CP-DCC82), was tested by means of MTT using a variety of cell lines, from those representing normal tissue to highly aggressive malignant cancer cells. The noncancerous cell lines were represented by a normal human epithelial prostate cell line (PNT1A) and mice embryonic fibroblasts (NIH/3T3). The malignant primary tumor cell lines were represented by a human ovarian cell line (A2780) and its cisplatin-resistant subline (A2780/CP), a human cell line derived from pulmonary adenocarcinoma (A549) and human prostate carcinoma cell line (22Rv1), while metastatic cell lines were represented by a human prostate cancer cell line established from a bone metastasis (PC-3) and human nonsmall cell lung carcinoma cells derived from the lymph node (H1299). The concentrations of the conjugates were selected in a way that the concentration of the fully released active compound is equal to that of free CP in all cases.

Both Na-DCC18 and Na-DCC82 were found to be nontoxic in the whole span of tested concentrations for all of the tested cell lines (from 0 to 500 μM), disregarding the differences in the M_w and the degree of oxidation (see Table 3). The carriers also do not support the cell proliferation in the given concentration range.

The cytotoxicity of the CP–DCC conjugates toward the cell lines representing normal tissue is 3–9 times lower than for

Table 3. IC_{50} Values for Na-DCC18, Na-DCC82, CP, CP-DCC18, and CP-DCC82 for Noncancerous (NIH/3T3, PNT1A), Primary Tumor (A2780, A2780/CP, A549, 22RV1), and Metastatic (PC-3, H1299) Cell Lines (All Values Are in μM)

| | Na-DCC18 | Na-DCC82 | CP | CP-DCC18 | CP-DCC82 |
|----------|----------|----------|------|----------|----------|
| NIH/3T3 | >500 | >500 | 12.0 | 105.0 | 54.0 |
| PNT1A | >500 | >500 | 5.0 | 14.7 | 16.5 |
| A2780 | >500 | >500 | 6.4 | 9.6 | 5.5 |
| A2780/CP | >500 | >500 | 14.2 | 16.0 | 14.5 |
| A549 | >500 | >500 | 32.1 | 52.4 | 40.4 |
| 22RV1 | >500 | >500 | 8.0 | 11.3 | 14.3 |
| PC-3 | >500 | >500 | 20.5 | 17.5 | 24.6 |
| H1299 | >500 | >500 | 53.4 | 66.9 | 52.4 |

free CP (3–9 times higher IC_{50} values) (see Table 3). On the other hand, the IC_{50} of both conjugates is between 0.8 and 1.6 times of that of free cisplatin. Note that only 65% (CP-DCC18) and 50% (CP-DCC82) of CP are assumed to be released from the conjugates after 48 h under *in vitro* conditions (MTT incubation time). Despite significantly lower overall concentration of released CP, the CP-DCC18 was found to be more effective than free CP against the prostatic PC-3 cell line and only somewhat less effective against the 22RV1 and A2780/CP lines, while the CP-DCC82 conjugate has somewhat better effectivity than free CP against A2780 and is similarly effective against A2780/CP and H1299 cell lines. In absolute values, the conjugates were the most effective against the ovarian A2780 and A2780/CP and prostate PC-3 and 22RV1 cell lines and the least effective against lung cancer cell lines A549 and H1299.

Overall, the physical characteristics of the drug carrier do seem to influence to the certain extent the effectivity of carried CP against individual cell lines. For instance, CP-DCC18 with fast release rates and high platinum content were about 25% more cytotoxic than CP-DCC82 against both tested prostatic cell lines (22RV1, PC-3), while higher molecular weight CP-DCC82 was about 20% more cytotoxic against lung carcinoma cell lines (A549 and H1299) and about 40% more effective against A2780. Additional studies are however required to confirm this interesting observation. The A2780 cell line was selected for further studies as an example of a cell line with one of the best responses based on *in vitro* results.

Cellular Uptake of Platinum. Cisplatin enters the cell via several mechanisms; however, it primarily employs membrane transporters as the copper transporters CTR1 and CTR2 as well as the family of organic cation transporters (OCT).^{73,74} To investigate the influence of cisplatin conjugation to DCC18 on the amount of platinum accumulated inside the cells, cellular uptake studies were performed. A2780 cells were treated with 5 μM concentration of CP and CP-DCC18. This concentration is lower than IC_{50} value of both compounds; therefore, the majority of the cells was viable while accumulating the compounds. Platinum concentration was measured in both lysed cells and culture media treated with CP and CP-DCC18 after 24 and 48 h from the treatment (Table 4). Compared to cisplatin, the resulting data for CP-DCC18 showed slightly reduced platinum uptake after 24 h from treatment. However, the significance of this slight decrease in platinum concentration within cells is debatable considering the high platinum concentration in the surrounding culture media (around 1100 $\mu\text{g/L}$, see Table S1). Observed differences also correlate with measured CP release rates, as

Table 4. Intracellular Concentration of Platinum in A2780 Cells 24 and 48 h after Treatment with CP and CP-DCC18 Determined by ICP-MS^a

| | sample | c ($\mu\text{g/L}$) | c ($\text{ng}/10^6$ cells) |
|------|----------|-------------------------|-------------------------------|
| 24 h | CP | 4.48 \pm 0.12 | 1.41 \pm 0.04 |
| | CP-DCC18 | 3.13 \pm 0.06 | 0.98 \pm 0.02 |
| | control | 0 | 0 |
| 48 h | CP | 7.90 \pm 0.17 | 1.21 \pm 0.03 |
| | CP-DCC18 | 7.73 \pm 0.10 | 1.19 \pm 0.02 |
| | control | 0 | 0 |

^aSee the Methods and Materials section for details. Data are expressed as mean \pm SD.

only about 50% of CP is released from the conjugate after 24 h under *in vitro* conditions (see Figure 6). Besides, platinum content within the cells equalizes 48 h after the treatment with CP and CP-DCC18.

The results imply that cisplatin binding to DCC18 carrier has only minor influence on the amount of platinum accumulated within the cells *in vitro*. In accordance with these findings, no significant difference in platinum concentrations was found within the culture media collected 24 and 48 h after CP and CP-DCC18 treatment (see Table S1).

In Vivo Toxicity Assessment. The pilot *in vivo* toxicity assessment was carried to screen for unexpected side effects of the conjugates in living organism, e.g., high toxicity or irritation. Tests were performed in accordance with the recommendations of the European Community Guide for the Care and Use of Laboratory Animals and in accordance with the experimental protocol approved by the Committee on the Protection of Animals, Faculty of Medicine, Masaryk University. Ten athymic female nude mice (8 weeks old, weight 19.7–25.9 g, five animals in each group), housed under the standard conditions, were inoculated with A2780 ovarian cancer cells. After tumor incubation period (25 days) the mice were injected with three doses of CP and CP-DCC18 (200 μ L of a solution containing 1.5 mg/mL of CP in both cases) within 2 weeks. A statistically significant difference of survival was found between groups treated with free CP and CP-DCC18 ($p = 0.008$) using a log-rank test (see Figure 7).

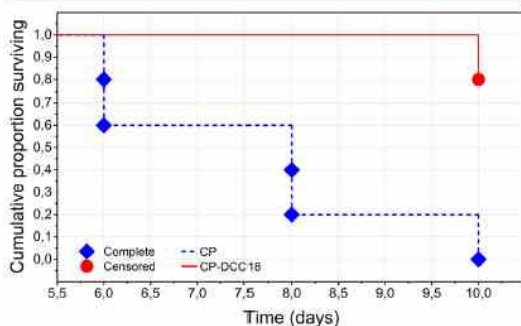


Figure 7. Univariate analysis of overall survival (Kaplan–Meier method). The univariate survival analysis was followed by the log-rank test, and the multivariate analysis was performed using the Cox proportional hazard models.

In general, the mortality of mice receiving free CP was very high already after receiving two doses of the drug (only one mouse out of five survived up to the third injection). On the other hand, the group receiving CP-DCC18 with an equal amount of cisplatin evidenced 80% survival rate (only one mouse out of five did not survive up to the termination of the experiment). Therefore, we conclude the CP-DCC18 conjugate is generally better tolerated in a living organism than free CP.

In general, the tumor volumes in the CP-receiving group were rather enlarging within the duration of experiment. The increase in tumor size was up to 112.5% in comparison with the initial state at the very beginning of the therapy. Contrarily, the tumor sizes of the animals in the CP-DCC18-receiving group were significantly reduced in 75% of cases. The reduction of tumor size ranged between 20 and 66%. Only

in one case was the increase of tumor size (by 67%) observed. The continual tumor growth in the former group was most likely caused by the high toxicity of cisplatin given by bolus injection for the animals, as the effect of drug systemic toxicity was probably acting faster than the tumor-reducing effect. All animals were subsequently terminated, and the tumors extracted and analyzed with respect to the platinum content.

Determination of the Platinum Distribution in the Tumor Tissue. A LA-ICP-MS study was performed to obtain the platinum spatial distribution in tumor tissue. The resulting heat maps illustrate the platinum distribution within the tumor of the mice treated with CP (Figure 8a) and with CP-DCC18

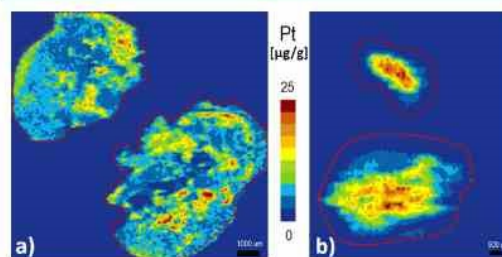


Figure 8. LA-ICP-MS-determined local concentrations of platinum in a tumor tissue of a mouse treated with (a) CP and (b) CP-DCC18. The dashed red lines mark the physical boundary of tumor tissue. The intensity scale indicates platinum concentration (μ g/g).

(Figure 8b). The red dashed line represents the physical boundary of tumor tissue samples. The platinum content in the CP-treated group varied from 0.0 to 18.0 μ g per gram of tumor tissue, while in the CP-DCC18-treated group it varied from 0.0 to 25.0 μ g/g. The dominance of the various shades of blue and light green color in Figure 8a indicates that the platinum concentration in the majority of the tumor tissue is between 2.5 and 7.5 μ g/g, with a randomly distributed maxima up to 18 μ g/g. The prevailing yellow-green and orange-brown in Figure 8b indicate higher platinum concentrations, mostly between 10 and 20 μ g/g, with maxima of up to 25 μ g/g concentrated near the center of the samples (see dashed red line representing boundary of tumor tissue in Figure 8).

The concentrations of platinum per gram of tumor tissue of the CP-DCC18-receiving group was thus higher than in the case of tumors from the CP-receiving group according to ICP-MS analysis. This indicates a better accumulation of active compounds because of the conjugation of CP to the polysaccharide carrier DCC18. Note that the *in vitro* platinum uptake study (see above) did not show any substantial difference in platinum accumulation between A2780 cells treated with CP and CP-DCC18. Therefore, we believe that the higher platinum accumulation within the tumors manifested in mice treated with CP-DCC18 is a result of its improved systemic properties within the organism provided by macromolecular carrier.^{2,3}

Altogether, our results indicate a higher survival rate of animals, a better toleration of the drug, reduced systemic toxicity, and higher tumor accumulation of cisplatin after its complexation with a DCC18 carrier.

CONCLUSION

Highly oxidized 2,3-dicarboxycellulose (DCC) was optimized for the use in biological applications. The control over the

molecular weight of the product during the synthesis was introduced by the addition of the given amounts of amidosulfonic acid into the reaction mixture. The prepared DCC is a nontoxic and well-soluble material with a well-defined composition and a high degree of oxidation, up to 96%. It features two $-\text{COOH}$ groups per each oxidized monomeric unit and is capable of a highly effective bidentate chelation of platinum(II) chemotherapeutics, as demonstrated by its conjugates with cisplatin. The cisplatin–DCC conjugates simultaneously offer a very high binding efficiency (90–98%) and a loading capacity of the drug (up to 50 wt %). The conjugates remain well soluble in an aqueous medium even with maximum drug loading.

The variable drug-release profiles are accessible by simple modifications of the carrier molecular weight (M_w) during the synthesis and conjugate preparation (drug feeding ratio). As a result, the cisplatin release rates can be modified to include a delayed release as well as an initial burst release, e.g., from <10% to >60% after 24 h. The release rates are also pH-dependent (up to 2 times faster release at pH 5.5 than at pH 7.4), which allows to exploit the acidic nature of tumor microenvironment.

The DCC itself was found nontoxic in the whole set of tested concentrations during *in vitro* studies. The CP–DCC conjugates were found considerably less toxic *in vitro* than free CP toward cells representing normal tissues, while having a comparable or better cytotoxicity than CP against the prostatic (PC-3 and 22RV1), human ovarian cell lines (A2780 and A2780/CP), and lung metastatic (H1299) cancer cell lines. This was achieved despite only partial release of CP during the MTT incubation period. Besides, conjugates with burst release profiles were found more effective against tested prostate cell lines, while conjugates with slower release were in general more cytotoxic against lung carcinoma cell lines and human ovarian cell lines. Additional studies are however required to confirm this observation. Conjugation of CP to DCC has only minor influence on the amount of platinum accumulated within the cells *in vitro*.

The pilot *in vivo* tests indicated a significantly higher mice survival rate, a higher accumulation of platinum in tumors, and lower systemic toxicity of mice treated by cisplatin conjugated to the DCC in comparison with those treated by free cisplatin. Reduction of the tumor size was observed for the animals treated with CP–DCC conjugates.

In this study, the 2,3-dicarboxycellulose and its conjugates with cisplatin demonstrated a number of characteristics implying considerable potential in the area of drug delivery. High drug loading efficiency and capacity, broad spectrum of accessible drug release profiles together with no observable toxicity makes DCC a promising candidate for drug delivery systems of the future. The described method for cost-effective modulation of molecular weight of the oxidized cellulose may be exploited not only for preparation of cellulose-based drug delivery systems but is also applicable to other oxidized polysaccharides with number of potential applications outside the area of drug delivery.

■ ASSOCIATED CONTENT

📄 Supporting Information

The Supporting Information is available free of charge on the ACS Publications website at DOI: 10.1021/acs.biomac.8b01807.

^1H NMR spectrum of DCC18, ^{13}C NMR spectra of Na-DCC82 and CP-DCC82, FT-IR spectrum of DCC82 and CP-DCC82, table with platinum concentrations in culture media obtained by ICP-MS (PDF)

■ AUTHOR INFORMATION

Corresponding Authors

*E-mail jvicha@utb.cz.

*E-mail masarik@med.muni.cz.

ORCID

Jan Vicha: 0000-0003-3698-8236

Author Contributions

L.M., I.K., and J.V.: synthesis and characterization of DCC and its conjugates; Z.C.: *in vitro* studies; M.F. and M.M.: *in vitro* and *in vivo* experiments; T.V. and M.T.: ICP-MS studies of platinum content. All authors contributed to manuscript preparation.

Notes

The authors declare no competing financial interest.

■ ACKNOWLEDGMENTS

This work was supported by the Czech Science Foundation grant 16-05961S and Ministry of Education, Youth and Sports of the Czech Republic Program NPU I (LO1504) and by funds from Specific University Research Grant, as provided by the Ministry of Education, Youth and Sports of the Czech Republic in the year 2019 (2018 MUNI/A/1255/2018 and MUNI/A/1553/2018). Computational resources were provided by CESNET (LM2015042), the CERIT Scientific Clouds (LM2015085), and "IT4Innovations National Supercomputing Center – LM2015070". CIISB research infrastructure project LM2015043 funded by MEYS CR is gratefully acknowledged for the financial support of the NMR measurements at the NMR CF at CEITEC MU.

■ REFERENCES

- (1) Dorcier, A.; Ang, W. H.; Bolaño, S.; Gonsalvi, L.; Juillerat-Jeannerat, L.; Laurenczy, G.; Peruzzini, M.; Phillips, A. D.; Zanobini, F.; Dyson, P. J. In Vitro Evaluation of Rhodium and Osmium RAPTA Analogues: The Case for Organometallic Anticancer Drugs Not Based on Ruthenium. *Organometallics* 2006, 25 (17), 4090–4096.
- (2) Johnstone, T. C.; Suntharalingam, K.; Lippard, S. J. The Next Generation of Platinum Drugs: Targeted Pt(II) Agents, Nanoparticle Delivery, and Pt(IV) Prodrugs. *Chem. Rev.* 2016, 116 (5), 3436–3486.
- (3) Tibbitt, M. W.; Dahlman, J. E.; Langer, R. Emerging Frontiers in Drug Delivery. *J. Am. Chem. Soc.* 2016, 138 (3), 704–717.
- (4) Dong, S.; Cho, H. J.; Lee, Y. W.; Roman, M. Synthesis and Cellular Uptake of Folic Acid-Conjugated Cellulose Nanocrystals for Cancer Targeting. *Biomacromolecules* 2014, 15 (5), 1560–1567.
- (5) Dai, L.; Cao, X.; Liu, K.-F.; Li, C.-X.; Zhang, G.-F.; Deng, L.-H.; Si, C.-L.; He, J.; Lei, J.-D. Self-Assembled Targeted Folate-Conjugated Eight-Arm-Polyethylene Glycol-Betulinic Acid Nanoparticles for Co-Delivery of Anticancer Drugs. *J. Mater. Chem. B* 2015, 3 (18), 3754–3766.
- (6) Senapati, S.; Mahanta, A. K.; Kumar, S.; Maiti, P. Controlled Drug Delivery Vehicles for Cancer Treatment and Their Performance. *Signal Transduct. Target. Ther.* 2018, 3 (1), 7.
- (7) Wang, X.; Guo, Z. Targeting and Delivery of Platinum-Based Anticancer Drugs. *Chem. Soc. Rev.* 2013, 42 (1), 202–224.
- (8) Yokoyama, M. Polymeric Micelles as Drug Carriers: Their Lights and Shadows. *J. Drug Target.* 2014, 22 (7), 576–583.
- (9) Haxton, K. J.; Burt, H. M. Polymeric Drug Delivery of Platinum-Based Anticancer Agents. *J. Pharm. Sci.* 2009, 98 (7), 2299–2316.

- (10) Nowotnik, D. P.; Cvitkovic, E. ProLindac™ (AP5346): A Review of the Development of an HPMA DACH Platinum Polymer Therapeutic. *Adv. Drug Delivery Rev.* 2009, 61 (13), 1214–1219.
- (11) Malik, N.; Evagorou, E. G.; Duncan, R. Dendrimer-Platinate: A Novel Approach to Cancer Chemotherapy. *Anti-Cancer Drugs* 1999, 10 (8), 767–776.
- (12) Pellechia, P. J.; Gao, J.; Gu, Y.; Ploehn, H. J.; Murphy, C. J. Platinum Ion Uptake by Dendrimers: An NMR and AFM Study. *Inorg. Chem.* 2004, 43 (4), 1421–1428.
- (13) Huang, G.; Mei, X.; Xiao, F.; Chen, X.; Tang, Q.; Peng, D. Applications of Important Polysaccharides in Drug Delivery. *Curr. Pharm. Des.* 2015, 21 (25), 3692–3696.
- (14) Schanté, C. E.; Zuber, G.; Herlin, C.; Vandamme, T. F. Chemical Modifications of Hyaluronic Acid for the Synthesis of Derivatives for a Broad Range of Biomedical Applications. *Carbohydr. Polym.* 2011, 85 (3), 469–489.
- (15) Maeda, M.; Takasuka, N.; Suga, T.; Uehara, N.; Hoshi, A. Antitumor Activity of a New Series of Platinum Complexes: Trans(±)-1,2-Cyclohexanediammineplatinum(II) Conjugated to Acid Polysaccharides. *Anti-Cancer Drugs* 1993, 4 (2), 167–171.
- (16) Dosio, F.; Arpicco, S.; Stella, B.; Fattal, E. Hyaluronic Acid for Anticancer Drug and Nucleic Acid Delivery. *Adv. Drug Delivery Rev.* 2016, 97, 204–236.
- (17) Zhang, H.; Huang, S.; Yang, X.; Zhai, G. Current Research on Hyaluronic Acid-Drug Bioconjugates. *Eur. J. Med. Chem.* 2014, 86, 310–317.
- (18) Cai, S.; Xie, Y.; Bagby, T. R.; Cohen, M. S.; Forrest, M. L. Intralymphatic Chemotherapy Using a Hyaluronan–Cisplatin Conjugate. *J. Surg. Res.* 2008, 147 (2), 247–252.
- (19) Quan, Y. H.; Kim, B.; Park, J.-H.; Choi, Y.; Choi, Y. H.; Kim, H. K. Highly Sensitive and Selective Anticancer Effect by Conjugated HA-Cisplatin in Non-Small Cell Lung Cancer Overexpressed with CD44. *Exp. Lung Res.* 2014, 40 (10), 475–484.
- (20) Jain, A.; Jain, S. K.; Ganesh, N.; Barve, J.; Beg, A. M. Design and Development of Ligand-Appended Polysaccharidic Nanoparticles for the Delivery of Oxaliplatin in Colorectal Cancer. *Nanomedicine* 2010, 6 (1), 179–190.
- (21) Fan, X.; Zhao, X.; Qu, X.; Fang, J. PH Sensitive Polymeric Complex of Cisplatin with Hyaluronic Acid Exhibits Tumor-Targeted Delivery and Improved in Vivo Antitumor Effect. *Int. J. Pharm.* 2015, 496 (2), 644–653.
- (22) Heinze, T.; Trier, K.; Wollina, U. Use of Carboxy-Substituted Polysaccharides, Such as Carboxy Cellulose or Carboxymethyl Cellulose, for Stimulating Cell Proliferation e.g. to Treat Wounds. DE10319808 A1, November 18, 2004.
- (23) Hofreiter, B. T.; Wolff, I. A.; Mehlretter, C. L. Chlorous Acid Oxidation of Periodate Oxidized Cornstarch2. *J. Am. Chem. Soc.* 1957, 79 (24), 6457–6460.
- (24) Maekawa, E.; Koshijima, T. Properties of 2,3-Dicarboxy Cellulose Combined with Various Metallic Ions. *J. Appl. Polym. Sci.* 1984, 29 (7), 2289–2297.
- (25) Visanko, M.; Liimatainen, H.; Sirviö, J. A.; Haapala, A.; Sliz, R.; Niinimäki, J.; Hormi, O. Porous Thin Film Barrier Layers from 2,3-Dicarboxylic Acid Cellulose Nanofibrils for Membrane Structures. *Carbohydr. Polym.* 2014, 102, 584–589.
- (26) Kim, U.-J.; Kuga, S. Ion-Exchange Chromatography by Dicarboxyl Cellulose Gel. *J. Chromatogr. A* 2001, 919 (1), 29–37.
- (27) Liimatainen, H.; Visanko, M.; Sirviö, J. A.; Hormi, O. E. O.; Niinimäki, J. Enhancement of the Nanofibrillation of Wood Cellulose through Sequential Periodate–Chlorite Oxidation. *Biomacromolecules* 2012, 13 (5), 1592–1597.
- (28) Suopajarvi, T.; Liimatainen, H.; Hormi, O.; Niinimäki, J. Coagulation–Flocculation Treatment of Municipal Wastewater Based on Anionized Nanocelluloses. *Chem. Eng. J.* 2013, 231, 59–67.
- (29) Tejado, A.; Alam, M. N.; Antal, M.; Yang, H.; van de Ven, T. G. M. Energy Requirements for the Disintegration of Cellulose Fibers into Cellulose Nanofibers. *Cellulose* 2012, 19 (3), 831–842.
- (30) Yang, H.; Alam, M. N.; van de Ven, T. G. M. Highly Charged Nanocrystalline Cellulose and Dicarboxylated Cellulose from Periodate and Chlorite Oxidized Cellulose Fibers. *Cellulose* 2013, 20 (4), 1865–1875.
- (31) Veelaert, S.; de Wit, D.; Gotlieb, K. F.; Verhé, R. Chemical and Physical Transitions of Periodate Oxidized Potato Starch in Water. *Carbohydr. Polym.* 1997, 33 (2–3), 153–162.
- (32) Kim, U.-J.; Wada, M.; Kuga, S. Solubilization of Dialdehyde Cellulose by Hot Water. *Carbohydr. Polym.* 2004, 56 (1), 7–10.
- (33) Münster, L.; Vicha, J.; Klofáč, J.; Masař, M.; Kucharczyk, P.; Kuřitka, I. Stability and Aging of Solubilized Dialdehyde Cellulose. *Cellulose* 2017, 24 (7), 2753–2766.
- (34) Sirviö, J. A.; Liimatainen, H.; Visanko, M.; Niinimäki, J. Optimization of Dicarboxylic Acid Cellulose Synthesis: Reaction Stoichiometry and Role of Hypochlorite Scavengers. *Carbohydr. Polym.* 2014, 114, 73–77.
- (35) Münster, L.; Vicha, J.; Klofáč, J.; Masař, M.; Hurajová, A.; Kuřitka, I. Dialdehyde Cellulose Crosslinked Poly(Vinyl Alcohol) Hydrogels: Influence of Catalyst and Crosslinker Shelf Life. *Carbohydr. Polym.* 2018, 198, 181–190.
- (36) Engel, P.; Hein, L.; Spiess, A. C. Derivatization-Free Gel Permeation Chromatography Elucidates Enzymatic Cellulose Hydrolysis. *Biotechnol. Biofuels* 2012, 5 (1), 77.
- (37) Wilson, J. J.; Lippard, S. J. Synthetic Methods for the Preparation of Platinum Anticancer Complexes. *Chem. Rev.* 2014, 114 (8), 4470–4495.
- (38) Chen, Y.; Guo, Z.; Sadler, P. J. 195Pt- and 15N-NMR Spectroscopic Studies of Cisplatin Reactions with Biomolecules. In *Cisplatin*; Lippert, B., Ed.; Verlag Helvetica Chimica Acta: 1999; pp 293–318.
- (39) Adamo, C.; Barone, V. Toward Reliable Density Functional Methods without Adjustable Parameters: The PBE0Model. *J. Chem. Phys.* 1999, 110 (13), 6158–6170.
- (40) Adamo, C.; Scuseria, G. E.; Barone, V. Accurate Excitation Energies from Time-Dependent Density Functional Theory: Assessing the PBE0Model. *J. Chem. Phys.* 1999, 111 (7), 2889–2899.
- (41) Weigend, F.; Ahlrichs, R. Balanced Basis Sets of Split Valence, Triple Zeta Valence and Quadruple Zeta Valence Quality for H to Rn: Design and Assessment of Accuracy. *Phys. Chem. Chem. Phys.* 2005, 7 (18), 3297–3305.
- (42) Andrae, D.; Häußermann, U.; Dolg, M.; Stoll, H.; Preuß, H. Energy-Adjusted Basis Set Pseudopotentials for the Second and Third Row Transition Elements. *Theor. Chim. Acta* 1990, 77 (2), 123–141.
- (43) Grimme, S. A General Quantum Mechanically Derived Force Field (QMDF) for Molecules and Condensed Phase Simulations. *J. Chem. Theory Comput.* 2014, 10 (10), 4497–4514.
- (44) Klant, A.; Schüürmann, G. COSMO: A New Approach to Dielectric Screening in Solvents with Explicit Expressions for the Screening Energy and Its Gradient. *J. Chem. Soc., Perkin Trans. 2* 1993, No. 5, 799–805.
- (45) Furche, F.; Ahlrichs, R.; Hättig, C.; Klopper, W.; Sierka, M.; Weigend, F. Turbomole. *Wiley Interdiscip. Rev. Comput. Mol. Sci.* 2014, 4 (2), 91–100.
- (46) Vicha, J.; Patzschke, M.; Marek, R. A Relativistic DFT Methodology for Calculating the Structures and NMR Chemical Shifts of Octahedral Platinum and Iridium Complexes. *Phys. Chem. Chem. Phys.* 2013, 15 (20), 7740–7754.
- (47) Pawlak, T.; Niedzielska, D.; Vicha, J.; Marek, R.; Pazderski, L. Dimeric Pd(II) and Pt(II) Chloride Organometallics with 2-Phenylpyridine and Their Solvolysis in Dimethylsulfoxide. *J. Organomet. Chem.* 2014, 759, 58–66.
- (48) Vicha, J.; Novotný, J.; Straka, M.; Repisky, M.; Ruud, K.; Komorovsky, S.; Marek, R. Structure, Solvent, and Relativistic Effects on the NMR Chemical Shifts in Square-Planar Transition-Metal Complexes: Assessment of DFT Approaches. *Phys. Chem. Chem. Phys.* 2015, 17 (38), 24944–24955.
- (49) Pawlak, T.; Munzarova, M. L.; Pazderski, L.; Marek, R. Validation of Relativistic DFT Approaches to the Calculation of NMR Chemical Shifts in Square-Planar Pt2+ and Au3+ Complexes. *J. Chem. Theory Comput.* 2011, 7 (12), 3909–3923.

- (50) Tomasi, J.; Mennucci, B.; Cammi, R. Quantum Mechanical Continuum Solvation Models. *Chem. Rev.* **2005**, *105* (8), 2999–3094.
- (51) Komorovsky, S.; Repisky, M.; Malkina, O. L.; Malkin, V. G.; Malkin Ondik, I.; Kaupp, M. A Fully Relativistic Method for Calculation of Nuclear Magnetic Shielding Tensors with a Restricted Magnetically Balanced Basis in the Framework of the Matrix Dirac-Kohn-Sham Equation. *J. Chem. Phys.* **2008**, *128* (10), 104101–104115.
- (52) Komorovsky, S.; Repisky, M.; Malkina, O. L.; Malkin, V. G. Fully Relativistic Calculations of NMR Shielding Tensors Using Restricted Magnetically Balanced Basis and Gauge Including Atomic Orbitals. *J. Chem. Phys.* **2010**, *132* (15), 154101–154108.
- (53) Repisky, M.; Komorovsky, S.; Malkin, V. G.; Malkina, O. L.; Kaupp, M.; Ruud, K.; Bast, R.; Ekstrom, U.; Kadek, M.; Knecht, S.; et al. *Relativistic Spectroscopy DFT Program ReSpect, Developer Version 5.1* (www.Respectprogram.org), 2018.
- (54) Dylla, K. G. Relativistic Double-Zeta, Triple-Zeta, and Quadruple-Zeta Basis Sets for the 5d Elements Hf–Hg. *Theor. Chem. Acc.* **2004**, *112* (5–6), 403–409.
- (55) Dylla, K. G. Relativistic Double-Zeta, Triple-Zeta, and Quadruple-Zeta Basis Sets for the 4d Elements Y–Cd. *Theor. Chem. Acc.* **2007**, *117* (4), 483–489.
- (56) Dylla, K. G.; Gomes, A. S. P. Revised Relativistic Basis Sets for the 5d Elements Hf–Hg. *Theor. Chem. Acc.* **2010**, *125* (1–2), 97–100.
- (57) Jensen, F. Basis Set Convergence of Nuclear Magnetic Shielding Constants Calculated by Density Functional Methods. *J. Chem. Theory Comput.* **2008**, *4* (5), 719–727.
- (58) Vicha, J.; Marek, R.; Straka, M. High-Frequency ¹³C and ²⁹Si NMR Chemical Shifts in Diamagnetic Low-Valence Compounds of TlI and PbII: Decisive Role of Relativistic Effects. *Inorg. Chem.* **2016**, *55* (4), 1770–1781.
- (59) Vicha, J.; Marek, R.; Straka, M. High-Frequency ¹H NMR Chemical Shifts of SnII and PbII Hydrides Induced by Relativistic Effects: Quest for PbII Hydrides. *Inorg. Chem.* **2016**, *55* (20), 10302–10309.
- (60) Truflandier, L. A.; Autschbach, J. Probing the Solvent Shell with ¹⁹⁵Pt Chemical Shifts: Density Functional Theory Molecular Dynamics Study of PtII and PtIV Anionic Complexes in Aqueous Solution. *J. Am. Chem. Soc.* **2010**, *132* (10), 3472–3483.
- (61) Vaculovič, T.; Warchilová, T.; Čadková, Z.; Száková, J.; Tlustoš, P.; Otruba, V.; Kanický, V. Influence of Laser Ablation Parameters on Trueness of Imaging. *Appl. Surf. Sci.* **2015**, *351*, 296–302.
- (62) Anyz, J.; Vyslouzilova, L.; Vaculovic, T.; Tvrdonova, M.; Kanicky, V.; Haase, H.; Horak, V.; Stepankova, O.; Heger, Z.; Adam, V. Spatial Mapping of Metals in Tissue-Sections Using Combination of Mass-Spectrometry and Histology through Image Registration. *Sci. Rep.* **2017**, *7*, 40169.
- (63) Kim, U.-J.; Kuga, S.; Wada, M.; Okano, T.; Kondo, T. Periodate Oxidation of Crystalline Cellulose. *Biomacromolecules* **2000**, *1* (3), 488–492.
- (64) Sulaeva, L.; Klinger, K. M.; Amer, H.; Henniges, U.; Rosenau, T.; Potthast, A. Determination of Molar Mass Distributions of Highly Oxidized Dialdehyde Cellulose by Size Exclusion Chromatography and Asymmetric Flow Field-Flow Fractionation. *Cellulose* **2015**, *22* (6), 3569–3581.
- (65) Kim, U.-J.; Lee, Y. R.; Kang, T. H.; Choi, J. W.; Kimura, S.; Wada, M. Protein Adsorption of Dialdehyde Cellulose-Crosslinked Chitosan with High Amino Group Contents. *Carbohydr. Polym.* **2017**, *163*, 34–42.
- (66) Shaw, R. J. Glucose Metabolism and Cancer. *Curr. Opin. Cell Biol.* **2006**, *18* (6), 598–608.
- (67) Wang, Y.; Liu, Q.; Qiu, L.; Wang, T.; Yuan, H.; Lin, J.; Luo, S. Molecular Structure, IR Spectra, and Chemical Reactivity of Cisplatin and Transplatin: DFT Studies, Basis Set Effect and Solvent Effect. *Spectrochim. Acta, Part A* **2015**, *150*, 902–908.
- (68) Still, B. M.; Kumar, P. G. A.; Aldrich-Wright, J. R.; Price, W. S. ¹⁹⁵Pt NMR—Theory and Application. *Chem. Soc. Rev.* **2007**, *36* (4), 665–686.
- (69) Gabano, E.; Marengo, E.; Bobba, M.; Robotti, E.; Cassino, C.; Botta, M.; Osella, D. ¹⁹⁵Pt NMR Spectroscopy: A Chemometric Approach. *Coord. Chem. Rev.* **2006**, *250* (15–16), 2158–2174.
- (70) Appleton, T. G.; Berry, R. D.; Davis, C. A.; Hall, J. R.; Kimlin, H. A. Reactions of Platinum(II) Aqua Complexes. 1. Multinuclear (Platinum-195, Nitrogen-15, and Phosphorus-31) NMR Study of Reactions between the Cis-Diamminediaqua-platinum(II) Cation and the Oxygen-Donor Ligands Hydroxide, Perchlorate, Nitrate, Sulfate, Phosphate, and Acetate. *Inorg. Chem.* **1984**, *23* (22), 3514–3521.
- (71) Brière, K. M.; Goel, R.; Shirazi, F. H.; Stewart, D. J.; Smith, I. C. P. The Integrity of Cisplatin in Aqueous and Plasma Ultrafiltrate Media Studied by ¹⁹⁵Pt and ¹⁵N Nuclear Magnetic Resonance. *Cancer Chemother. Pharmacol.* **1996**, *37* (6), 518–524.
- (72) Emoto, S.; Yamaguchi, H.; Kamei, T.; Ishigami, H.; Suhara, T.; Suzuki, Y.; Ito, T.; Kitayama, J.; Watanabe, T. Intraperitoneal Administration of Cisplatin via an in Situ Cross-Linkable Hyaluronic Acid-Based Hydrogel for Peritoneal Dissemination of Gastric Cancer. *Surg. Today* **2014**, *44* (5), 919–926.
- (73) Hall, M. D.; Okabe, M.; Shen, D.-W.; Liang, X.-J.; Gottesman, M. M. The Role of Cellular Accumulation in Determining Sensitivity to Platinum-Based Chemotherapy. *Annu. Rev. Pharmacol. Toxicol.* **2008**, *48* (1), 495–535.
- (74) Amable, L. Cisplatin Resistance and Opportunities for Precision Medicine. *Pharmacol. Res.* **2016**, *106*, 27–36.

6.14 ARTICLE 14

Vaneckova, T.; Vanickova, L.; Tvrdonova, M.; Pomorski, A.; Krezel, A.; Vaculovic, T.; Kanicky, V.; Vaculovicova, M.; Adam, V. *Talanta* 2019, 198, 224-229 (IF=4.916)



Contents lists available at ScienceDirect

Talanta

journal homepage: www.elsevier.com/locate/talanta

Molecularly imprinted polymers coupled to mass spectrometric detection for metallothionein sensing

Tereza Vaneckova^{a,b}, Lucie Vanickova^{a,b}, Michaela Tvrdonova^c, Adam Pomorski^d, Artur Krężel^d, Tomas Vaculovic^{c,e}, Viktor Kanicky^{c,e}, Marketa Vaculovicova^{a,b}, Vojtech Adam^{a,b,*}

^a Department of Chemistry and Biochemistry, Mendel University in Brno, Zemedelska 1, CZ-613 00 Brno, Czech Republic

^b Central European Institute of Technology, Brno University of Technology, Parkynova 123, CZ-612 00 Brno, Czech Republic

^c Department of Chemistry, Faculty of Science, Masaryk University, Kamenice 753/5, CZ-625 00 Brno, Czech Republic

^d Department of Chemical Biology, Faculty of Biotechnology, University of Wrocław, Joliot-Curie 14a, 50-383 Wrocław, Poland

^e Central European Institute of Technology, Masaryk University, Kamenice 753/5, CZ-625 00 Brno, Czech Republic



ARTICLE INFO

Keywords:

Metallothionein
Molecularly imprinted polymers
Polydopamine
MALDI-TOF-MS
LA-ICP-MS

ABSTRACT

We report a facile method for detection of metallothionein (MT), a promising clinically relevant biomarker, in spiked plasma samples. This method, for the first time, integrates molecularly imprinted polymers as purification/pre-treatment step with matrix assisted laser desorption/ionization time-of-flight mass spectrometric detection and with laser ablation inductively coupled plasma mass spectrometry for analysis of MTs. The prepared MT-imprinted polydopamine layer showed high binding capacity and specific recognition properties toward the template. Optimal monomer (dopamine) concentration was found to be 16 mM of dopamine. This experimental setup allows to measure μM concentrations of MT that are present in blood as this can be used for clinical studies recognizing MT as marker of various diseases including tumour one. Presented approach not only provides fast sample throughput but also avoids the limitations of methods based on use of antibodies (e.g. high price, cross-reactivity, limited availability in some cases, etc.).

1. Introduction

Metallothioneins (MTs) are low molecular mass (< 7 kDa), cysteine-rich proteins, ubiquitously present in practically all eukaryotes [1–3]. MTs perform a wide range of functions in an organism including essential metal homeostasis, i.e. Zn^{2+} and Cu^+ , heavy metal detoxification, i.e. Cd^{2+} , scavenging of reactive oxygen species and regulation of transcription [4–8]. The elevated concentration of MTs has been observed in blood and/or tissues coming from patients with various tumour diseases (e.g., colon, breast, liver, kidney, lung, nasopharynx, ovary, salivary gland, prostate, thyroid, and urinary bladder cancer) as it was reviewed [9,10], demonstrating that MTs are promising onco-suppressors [11–13].

Numerous analytical approaches have been suggested for detection and determination of MTs as reviewed elsewhere [14,15]. More recently, a method based on the enzyme-linked immunosorbent assay and the real time polymerase chain reaction was used [16]. Another study reported a microfluidic MT electrochemical immunosensor utilizing superparamagnetic agarose beads [17], where a curve fitting approach was used for voltammograms of various isoforms of MTs [18]. Mass

spectrometry coupled with matrix assisted laser desorption/ionization (MALDI) or laser ablation inductively coupled plasma (LA-ICP) ionization was also used for determination of MTs [19]. Recently, bottom-up mass spectrometry-based approach for human MT isoforms quantification has been developed [20], nevertheless combinations of these types of detection with biological molecule recognition elements are needed.

Molecularly imprinted polymers (MIPs) are biorecognition surfaces with high affinity towards desired template. Named as natural receptor mimics, MIPs are being considered as an alternative to biological receptors, such as enzymes, antibodies or aptamers [21,22]. Their major advantages cover predictable specific recognition, low cost, ease of preparation, good mechanical/chemical stability, and reusability [23]. Although MIPs have been successfully applied using wide range of small molecules [24], imprinting of biomacromolecules, such as proteins, faces challenges. Macromolecular templates have a tendency to adsorb to polymers, where it is not trivial to remove them from the polymer matrix, as they produce heterogeneous sites, and may be sensitive to denaturation or presence of organic solvents, which are usually essential for formation of polymers [22,25]. To date, only few

* Corresponding author at Department of Chemistry and Biochemistry, Mendel University in Brno, Zemedelska 1, CZ-613 00 Brno, Czech Republic.

E-mail address: vojtech.adam@mendelu.cz (V. Adam).

<https://doi.org/10.1016/j.talanta.2019.01.089>

Received 5 September 2018; Received in revised form 22 January 2019; Accepted 24 January 2019

Available online 25 January 2019

0039-9140/© 2019 Elsevier B.V. All rights reserved.

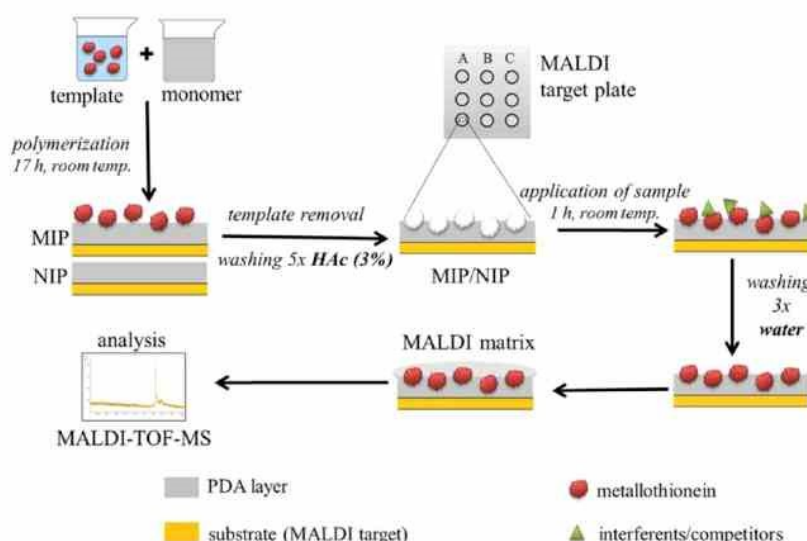


Fig. 1. Overall workflow of molecularly imprinted polymer (MIP) formation, sampling and MALDI-MS detection of MT-1.

studies reported combination of molecular imprinting technology together with MALDI time-of-flight mass spectrometry (MALDI-TOF-MS) [26–33]. However, determination of MT using molecular imprinting technology combined with mass spectrometric detection (neither MALDI-TOF-MS nor LA-ICP-MS) has not been reported yet.

In the present study, we developed an easy method for MT purification from a complex matrix using MT-selective polydopamine layer combined with MALDI-TOF-MS and LA-ICP-MS detection techniques (Fig. 1). The analytical performance of the sensor was evaluated. The obtained results reveal a new perspective in recognition and separation of this template, which is a potential marker of diseases.

2. Material and methods

2.1. Materials

Dopamine hydrochloride, albumin from human serum ($\geq 97\%$), Trizma® (TRIS base), and lysozyme from chicken egg white were purchased from Sigma-Aldrich company (St. Louis, MO, USA). Acetic acid (99.8%) and hydrochloric acid (reagent grade, 35%) was obtained from PENTA (Chrudim, Czech Republic). Amicon® Ultra 0.5 mL 50 K Centrifugal Filters were purchased from Merck Millipore (Billerica, MA, USA). Tris-HCl buffer (20 mM, pH 8.5) was prepared from Trizma® and hydrochloric acid was used for pH adjustment. Aqueous solution of acetic acid (3%, v/v) was used as a washing buffer. Deionized water used during the experiments was prepared with a Milli-Q water purification system (Millipore, Milford, MA, USA).

2.2. Preparation of MT-imprinted polydopamine layer

Polydopamine (PDA) MIP was prepared by self-polymerization inspired by works of [34,35]. In brief, dopamine was dissolved in 1 mL Tris-HCl buffer (20 mM, pH 8.5). Template molecules of MT-1, MT-3 or lysozyme, for initial optimization, were then mixed with the stock solution of dopamine at 1:1 (v/v) ratio. The target concentration was varied depending on the experiment. Next, 1 μ L of the polymerization mixture was applied on the MALDI target plate (Bruker MTP AnchorChip 384 BCE™) or, in case of initial experiments, bottom of the 96 well-plate and let to polymerize and dry at the room temperature for 24 h. Subsequently, the prepared polymeric layer was overlaid with a

sample solution and the incubation was carried for 1 h at room temperature. The resulting self-assembled polymer was then washed with 3% acetic acid to remove the bound MT or lysozyme. Final wash was performed with Milli-Q water. Control, non-imprinted polymer (NIP), was prepared under the same conditions without adding the template (MT/lysozyme). Each of the analysed polymers was prepared in triplicate.

2.3. Sample preparation

2.3.1. Standard solutions

The coding sequences of human metallothionein-1 (MT-1) (UniProt:P13640-2) and metallothionein-3 (MT-3) (UniProt:P25713-1) were purchased from Genscript (Piscataway, NJ, USA) and inserted into the pTYB21 vector (New England Biolabs, UK). Prepared plasmid were transformed into BL21 (DE3)pLysS *E. coli* cells. Protein production and purification was conducted as previously stated [36]. The obtained recombinant protein MT-1 used in the MALDI-TOF-MS experiments had seven bound Zn(II) ions. For LA-ICP-MS experiments were prepared MT-1 with seven bound Cd(II) ions and MT-3 with seven bound Zn(II) ions.

2.3.2. Plasma sample preparation

Whole blood was collected from a healthy volunteer and then centrifuged for 10 min at 2000 rcf and the plasma was further centrifuged for 30 min at 22000 rcf. The plasma was diluted 50 \times with Tris-HCl buffer (20 mM, pH 8.5) and spiked with MT-1 to its final concentration of 5 μ M. All subjects gave their informed consent for inclusion, before participating in the study. The study was conducted in accordance with the Declaration of Helsinki and the protocol was approved by the Ethics Committee of Masaryk University.

2.4. MALDI-TOF-MS

MIP/NIP were analysed using MALDI-TOF-MS (ultrafleXtreme instrument, Bruker Daltonik GmbH, Bremen Germany) equipped with a laser (operating at wavelength of 355 nm with an accelerating voltage of 25 kV, a maximum energy of 43.2 μ J, and a repetition rate of 2000 Hz) in linear positive ion mode for data acquisition. Three different organic matrix solutions were tested, namely α -cyano-4-

hydroxycinnamic acid, sinapinic acid and 2,5-dihydroxybenzoic acid (DHB) (Bruker Daltonik, Bremen, Germany), with DHB diluted in 0.1% trifluoroacetic acid (Sigma-Aldrich) being considered the optimal solution, since less background was produced in the final spectrum [18]. Matrix (0.5 μ L) was applied on the prepared MIP and/or NIP polymerized layer (as previously described in Section 2.2) and dried under atmospheric pressure and ambient temperature (25 $^{\circ}$ C). The laser frequency was set to 1000 Hz and laser energy was optimized prior to each measurement. Calibration was done externally using a protein standard mixture I and II (Bruker Daltonics, Bremen, Germany) in the range of m/z 1–90 kDa. A total of 500 spectra were summed for each spot using the Random Walk raster pattern, with no evaluation criteria and were analysed with the Flex Analysis software (Version 3.4).

2.5. Fluorescence spectrometry

Fluorescence spectrometric measurements were performed using Infinite M200 fluorescence microplate reader (Tecan, Männedorf, CH). Polymerization mixture (50 μ L) was deposited on the bottom of the well of Corning[®] 96 Well Clear Flat Bottom UV-Transparent Microplate (Corning, NY, USA). Fluorescence emission of lysozyme was recorded at λ_{ex} = 280 nm and λ_{em} = 330 nm with gain of the detector set to 100.

2.6. LA-ICP-MS

The analysis of MIP was performed by LA-ICP-MS setup that consists of LA system UP213 (NewWave Research, USA) emitting laser radiation with a wavelength of 213 nm with a pulse width of 4.2 ns. The ablated material was carried out from an ablation cell by a flow of a He (1.0 L/min) into ICP-MS Agilent 7500CE (Agilent Technologies, Japan) with quadrupole analyzer.

The MIP and NIP were ablated with following ablation parameters: laser beam diameter of 110 μ m, the repetition rate of 10 Hz; laser beam fluence of 6 J/cm², the scan speed of 400 μ m/s and distance between individual lines of 100 μ m. The analytes MT-1 and MT-3 were monitored by measuring of isotope ¹¹¹Cd and ⁶⁶Zn, respectively.

3. Results and discussion

3.1. Optimization of MIPs preparation

To address limitations of protein imprinting, several strategies have been investigated including metal ion-coordination polymerization, protein epitope approach, and surface imprinting [22,25,37]. The last approach utilizes polydopamine (PDA), one of the most favourable polymers considering its green chemistry status and facile preparation. Dopamine (DA), a functional monomer, can form a thin, self-polymerizing film on a wide variety of materials in a weak alkaline environment (pH > 8) [38]. It has been shown that PDA forms thin films by the spontaneous polymerization in the presence of oxygen; however some other polymerization methods involving radicals formation have been developed [39]. DA, commonly involved in human body as a neurotransmitter, is also a small-molecule mimicking the adhesive proteins. Its multifunctional groups and properties of hydrophilicity and biocompatibility make it suitable for imprinting of proteins. It can be self-polymerized under mild conditions (room temperature, pH 8.0) resulting in formation of an adherent polydopamine film. For example, approach for imprinting proteins using PDA coating of Fe₃O₄ nanoparticles has been reported [40]. Xia et al. suggested an approach for protein recognition and separation using PDA-coated molecularly imprinted silica nanoparticles [41]. Therefore, it is believed that polydopamine MIPs are expedient and appropriate materials applicable in the identification of proteins.

The simple oxidative polymerization was employed in this study. For non-covalent imprinting, the optimal ratio of template to functional monomer (T/M) has to be achieved empirically [42]. Therefore, the

concentration of monomer (dopamine) was tested in concentrations of 16, 32, 65, and 130 mM (data not shown). The functionality of the imprinted polymer was initially tested utilizing lysozyme as a template. The globular glycoprotein lysozyme (Lys) plays an important role in living organisms. Considering its excellent antibacterial property, Lys is widely used in medical and food industry. Thus, the development of an effective purification method for Lys is broadly valuable [43]. Based on the intrinsic fluorescence of Lys, the efficiency of the polymeric layer preparation was evaluated. According to the fluorescence spectrometry measurements, the dopamine concentration of 16 mM was chosen as the most appropriate due to the highest binding yield.

Subsequently, the effect of template concentration was investigated also by use of Lys in the same manner as optimal dopamine concentration determination. The dopamine concentration of 16 mM was used for polymerization. Concentrations of the template molecules of 9, 17, 35, and 70 μ M were tested (Fig. S1). In our experiment, the evaluation was performed considering the size of the molecule used as a template and was also aimed at use as low amount of protein as possible. The T/M ratio was 0.0005, 0.001, 0.002, and 0.004, even though the T/M ratio is suggested to be 0.5–0.25, however, this depends on the type of the template [42]. As expected, the higher the template concentration, the better signal was obtained due to the fact that more analyte-responsive cavities were formed. Therefore, we selected 70 μ M as the optimum in further experiments.

3.2. MALDI-TOF-MS analysis

DHB was determined as optimal MALDI matrix for MT analysis and therefore it was used in all following MALDI-MS experiments. Consequently, two concentrations of MT-1 (6071.5 [M+H]⁺) as a template in the DA were tested (0.2 mM and 0.02 mM, T/M = 0.013 and 0.0013). The data shown in Fig. 2SA confirm the fact that higher concentration of template increases the signal, as expected.

3.3. Template removal

Numerous approaches to template removal are presented in the literature [44,45]. Based on these works, 3% acetic acid (v/v) was chosen for washing. When the PDA imprinted layer (1 μ L of polymerization mixture) was washed once with 2 μ L of 3% acetic acid (v/v), the vast majority of the template still remained in the PDA layer. Performed experiments revealed that repeated washing (5-times with 2 μ L of 3% acetic acid) was required for the sufficient template removal. As shown in Fig. 2SB, the amount of template molecules remaining on the MIP surface after template removal procedure (background signal) was significantly lower compared to the signal obtained after application of the sample (analyte) solution onto the PDA layer. NIP (PDA polymerized in absence of template) was treated exactly the same way as MIP.

Based on this, the final signal results as a comparison between 1) the signals obtained from MIP with applied sample solution (washed with water) with subtracted signal of MIP after template removal (washed with 3% acetic acid) and 2) the NIP after application of the sample solution (washed with water).

3.4. MIP selectivity

To evaluate the selectivity of prepared MIP, the most abundant protein occurring in blood, albumin, was employed as an interference present in the model sample mixture (c_{MT-1} = 3 μ M, $c_{albumin}$ = 3 μ M). This protein represents a suitable model of interference not only because of its intrinsic presence in blood but also due to its tendency to adsorb on various surfaces that is commonly employed as a blocking agent in immunoassays [46]. As shown in the Fig. S3, metallothionein MIP analysed after application of the model sample solution exhibited only a minor signal of albumin (69368.5 [M+H]⁺), which is shown in

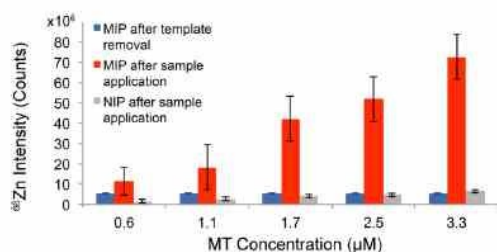


Fig. 2. LA-ICP-MS quantification of ^{66}Zn of different MT-1 concentrations in the sample extracted by MIP (red) and NIP (grey). ^{66}Zn quantification in MIP after template removal is shown in blue. (For interpretation of the references to color in this figure legend, the reader is referred to the web version of this article).

the inset in Fig. S3, whereas MT ($6071.5 [\text{M}+\text{H}]^+$) could be easily identified. PDA exhibits multiple interactions with proteins and weak hydrophilic interactions with salts. Thus the signals of proteins can be improved in spite of contamination by salts [47]. In addition, the MIPs have low nonspecific absorption capacity to non-templates [33]. The above mentioned results validated that the MIPs have specificity toward MT and resulted in a significantly selective enhancement in MS signals of MT.

3.5. Evaluation of different MT concentrations by MALDI-TOF-MS

Based on the literature information, the MT level in blood of healthy persons occurs at the value of $0.5 \mu\text{M}$, however the level in cancer patients ranges from 1.59 to $2.70 \mu\text{M}$ with average and median of 2.12 and $2.07 \mu\text{M}$, respectively [48]. It has to be noticed here that the precise quantification by MALDI-TOF-MS is not trivial and may be problematic even though numerous approaches may be taken to address this issue [49]. Therefore, this work does not aim at exact determination of the MT concentration, but rather targets at development of rapid method to identify the suspicious samples with potentially elevated MT level. Therefore, the $0.6 \mu\text{M}$ concentration of MT occurring in the diseased patients was taken as a threshold value. It should be noted that the samples with elevated MT level provides very high S/N ratio and signal is dependent although in a non-linear fashion on the concentration of the target. Three MT concentrations (0.6 , 1.7 and $3.3 \mu\text{M}$) were, thus, tested in order to investigate the possibility of detection of the MT signal. As shown in Fig. S4, all of these concentrations were well detected after undergoing the MIP extraction procedure (Fig. 4SA) and NIPs were simultaneously performed as a control (Fig. 4SB). Therefore, it can be concluded that the method is sensitive and selective enough to indicate the increased level of MT, leading to further quantitative investigation.

3.6. Zinc and cadmium detection in MT by LA-ICP-MS

As mentioned previously, MALDI-TOF-MS is not a method of choice if precise quantification is needed. Therefore, a quantitative mass spectrometric analysis (LA-ICP-MS) was employed for quantitation of levels of metal ions present in MT. To our best knowledge, this is the first use of LA-ICP-MS in combination with MIP technique. Under physiological conditions metallothioneins bind Zn^{2+} and Cu^+ , participating in metabolism of those metal ions [50]. Furthermore, cadmium (Cd^{2+}) accumulates in MT with exposure and age. For simplification, MT completely saturated with Zn^{2+} ions or with Cd^{2+} ions was used in this study.

First, the efficiency of the template removal from MIP by washing with acetic acid was tested. It was found out that the ^{66}Zn remaining on the MIP surface (and within the PDA layer) after template removal procedure was approximately 1.3% of the original amount. The nonspecific adsorption of analyte on NIP was observed, as well. Similarly to MALDI-TOF-MS experiments, the signal was significantly lower in comparison to MIP, which is extremely beneficial for usage of this protocol as quantification step. To summarize data obtained by LA-ICP-MS we used Fig. 2, where is clearly shown that MIP-MT signal significantly differed from others. LA-ICP-MS technique was further applied for distinction of MT-1 (Cd) from MT-3 (Zn) MIP and NIP as demonstrated in Fig. 3.

3.7. MT analysis in plasma

Our MT-MIP MALDI-TOF-MS approach has been verified using a real biological sample of human plasma. As illustrated in Fig. 4, no peak of MT-1 was revealed when using NIP. However, after enrichment from diluted human plasma, only a sharp peak of MT-1 ($6071.5 [\text{M}+\text{H}]^+$) could be identified on the MT-MIP. Here we have shown that MT-MIPs can capture MT-1 specifically and effectively from complex biosamples. Furthermore, spectrum in the Fig. 4 shows interfering substances (m/z 5539.4) demonstrating the ability of MS detection to identify the interferents and providing additional information level compared to nonspecific detections commonly used with MIP, such as quartz crystal microbalance. Besides precise identification, we further used above mentioned protocol based on LA-ICP-MS and found the level of MT-1 to be $0.05 \mu\text{M}$.

In conclusion, we demonstrated for the first time that MIP may be used as a selective purification step for metalloproteins for MALDI-TOF-MS analyses. Metallothionein-molecularly imprinted polymers were successfully prepared by immobilization of the template and self-polymerization of dopamine directly on the MALDI plate and showed good selectivity toward the template protein. Convenient enhancement in MALDI-TOF-MS signals was achieved for MT from the spiked protein

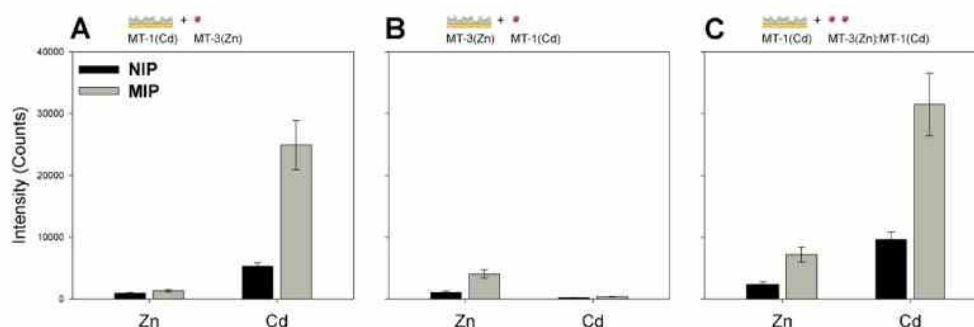


Fig. 3. LA-ICP-MS analyses of MIP and NIP using the MT-1 (Cd) and MT-3 (Zn) templates. (A) Sample containing MT-3(Zn) was applied to MIP/NIP created with template MT-1(Cd). (B) Sample containing MT-1 (Cd) was applied to MIP/NIP created with template MT-3(Zn), (C) Sample containing MT-3(Zn) and MT-1(Cd) was applied to MIP/NIP created with template MT-1(Cd).

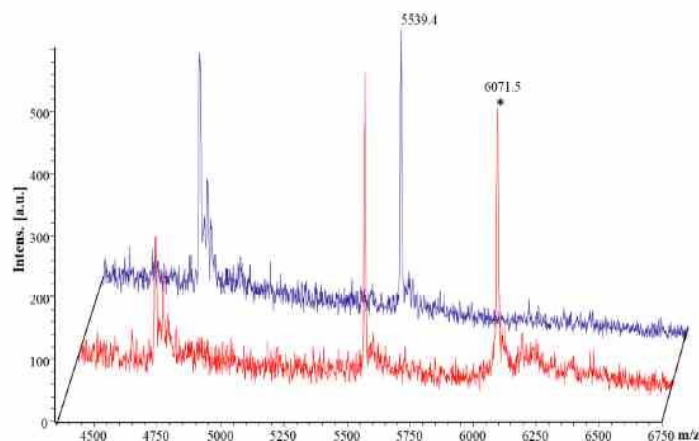


Fig. 4. Stacked overlay of MALDI-TOF-MS data using MT-MIP purification of the plasma spiked with 5 μM MT-1 (red), in comparison with NIP purification (blue), MT-1 peak (m/z 6071.5) is marked with (*). (For interpretation of the references to color in this figure legend, the reader is referred to the web version of this article).

mixture and plasma sample. Furthermore, LA-ICP-MS analyses served for MT quantification and for evaluation of the MIP/NIP isoform selectivity. MIPs combined with MALDI-TOF-MS and LA-ICP-MS techniques enable precise identification and quantification with high mass accuracy, outstanding sensitivity, and relatively fast analysis; showing further prospects in high-throughput testing. For the separation of particular MT isoforms further investigation and optimization of the two mass spectroscopic techniques will be performed together with application of diverse polymers for MIP formation.

Acknowledgments

This research has been financially supported by the Czech Science Foundation (project No. 17-12774S), Ministry of Education, Youth and Sports of the Czech Republic under the project GEITEC 2020 (LQ1601) and National Science Centre Poland (NCN) under Sonata Opus grant no. 2014/13/B/NZ1/00935 (to A.K.). Tereza Vaneckova is a Brno Ph.D. Talent Scholarship Holder – funded by the Brno City Municipality. VA wishes to express his thanks to the European Research Council (ERC) under the European Union's Horizon 2020 research and innovation programme (grant agreement No 759585). LV was supported by project 6SA17676 which received funding from the European Union's Horizon 2020 research and innovation programme under the Marie Skłodowska-Curie and which is co-financed by the South Moravian Region under grant agreement No. 665860.

Conflicts of interest

There are no conflicts to declare.

Appendix A. Supporting information

Supplementary data associated with this article can be found in the online version at doi:10.1016/j.talanta.2019.01.089.

References

- [1] E. Coyle, J.C. Philcox, L.C. Carey, A.M. Rofe, Metallothionein: the multipurpose protein, *Cell. Mol. Life Sci.* 59 (4) (2002) 627–647.
- [2] M.A. Dunn, T.L. Blalock, R.J. Cousins, Metallothionein, *Proc. Soc. Exp. Biol. Med.* 185 (2) (1987) 107–119.
- [3] D.H. Hamer, Metallothionein, *Annu. Rev. Biochem.* 55 (1986) 913–951.
- [4] A.T. Miles, G.M. Hawksworth, J.H. Beattie, V. Rodilla, Induction, regulation, degradation, and biological significance of mammalian metallothioneins, *Crit. Rev. Biochem. Mol. Biol.* 35 (1) (2000) 35–70.
- [5] J.H. Beattie, A.M. Wood, P. Tnyhurn, B. Jasani, A. Vincent, G. McCormack, A.K. West, Metallothionein is expressed in adipocytes of brown fat and is induced by catecholamines and zinc, *Am. J. Physiol. -Regul. Integr. Comp. Physiol.* 278 (4) (2000) R1082–R1089.
- [6] W. Maret, The function of zinc metallothionein: a link between cellular zinc and redox state, *J. Nutr.* 130 (5) (2000) 1455S–1458S.
- [7] B. Ruttkay-Nedecky, L. Nejdil, J. Gumulec, O. Zitka, M. Masarik, T. Eckschlager, M. Stiborova, V. Adam, R. Kizek, The role of metallothionein in oxidative stress, *Int. J. Mol. Sci.* 14 (3) (2013) 6044–6066.
- [8] M. Capdevila, R. Bofill, O. Palacios, S. Airian, State-of-the-art of metallothioneins at the beginning of the 21st century, *Coord. Chem. Rev.* 256 (1–2) (2012) 46–62.
- [9] T. Eckschlager, V. Adam, J. Hrabeta, K. Pigova, R. Kizek, Metallothioneins and cancer, *Curr. Protein Pept. Sci.* 10 (4) (2009) 360–375.
- [10] J. Gumulec, M. Raudenska, V. Adam, R. Kizek, M. Masarik, Metallothionein - immunohistochemical cancer biomarker: a meta-analysis, *PLoS One* 9 (1) (2014) 1–14.
- [11] C. Ferrario, P. Lavagnoli, M. Gariboldi, C. Mimada, M. Losa, L. Cleris, F. Formelli, S. Pilotti, M.A. Pierotti, A. Greco, Metallothionein 1G acts as an oncosuppressor in papillary thyroid carcinoma, *Lab. Invest.* 88 (5) (2008) 474–481.
- [12] J. Fu, H.J. Lv, H.X. Guan, X.Y. Ma, M.J. Ji, N.Y. He, B.Y. Shi, P. Hou, Metallothionein 1G functions as a tumor suppressor in thyroid cancer through modulating the PI3K/Akt signaling pathway, *BMC Cancer* 13 (2013) 1–13.
- [13] M. Kanda, S. Nomoto, Y. Okamura, Y. Nishikawa, H. Sugimoto, N. Kanazumi, S. Takeda, A. Nakao, Detection of metallothionein 1G as a methylated tumor suppressor gene in human hepatocellular carcinoma using a novel method of double combination array analysis, *Int. J. Oncol.* 35 (3) (2009) 477–483.
- [14] M. Ryvolova, S. Krizkova, V. Adam, M. Beklova, L. Trnkova, J. Hubalek, R. Kizek, Analytical methods for metallothionein detection, *Curr. Anal. Chem.* 7 (3) (2011) 243–261.
- [15] V. Adam, I. Fabrik, T. Eckschlager, M. Stiborova, L. Trnkova, R. Kizek, Vertebrate metallothioneins as target molecules for analytical techniques, *Trac-Trends Anal. Chem.* 29 (5) (2010) 409–418.
- [16] A. Houessinon, C. Francois, C. Sauzy, C. Louandre, G. Mongelard, C. Godin, S. Bodeau, S. Takahashi, Z. Saidak, L. Gutierrez, J.M. Regimbeau, N. Barget, J.C. Barbare, N. Ganne, B. Chauffert, R. Cortat, A. Galmiche, Metallothionein-1 as a biomarker of altered redox metabolism in hepatocellular carcinoma cells exposed to sorafenib, *Mol. Cancer* 15 (2016) 1–10.
- [17] L. Nejdil, H.V. Nguyen, L. Richtera, S. Krizkova, R. Guran, M. Masarik, D. Hynek, Z. Heger, K. Lundberg, K. Erikson, V. Adam, R. Kizek, Label-free bead-based metallothionein electrochemical immunosensor, *Electrophoresis* 36 (16) (2015) 1894–1904.
- [18] M.A.M. Rodrigo, J. Molina-Lopez, A.M.J. Jimenez, E.P. Del Pozo, P. Adam, T. Eckschlager, O. Zitka, L. Richtera, V. Adam, The application of curve fitting on the voltammograms of various isoforms of metallothioneins-metal complexes, *Int. J. Mol. Sci.* 18 (3) (2017) 1–11.
- [19] K. Coufalikova, I. Benesova, T. Vaculovic, V. Kanicky, J. Preisler, LC coupled to ESI, MALDI and ICP MS – a multiple hyphenation for metalloproteomic studies, *Anal. Chim. Acta* 968 (2017) 58–65.
- [20] J.B. Shabb, W.W. Muhonen, A.A. Mehus, Quantitation of human metallothionein isoforms in cells, tissues, and cerebrospinal fluid by mass spectrometry, in: A.K. Shukla (Ed.), *Proteomics in Biology*, Pt B, 2017, pp. 413–431.
- [21] G. Wulff, Molecular imprinting in cross-linked materials with the aid of molecular templates - a way towards artificial antibodies, *Angew. Chem. -Int. Ed. Engl.* 34 (17) (1995) 1812–1832.
- [22] L.X. Chen, S.F. Xu, J.H. Li, Recent advances in molecular imprinting technology: current status, challenges and highlighted applications, *Chem. Soc. Rev.* 40 (5) (2011) 2922–2942.
- [23] G. Vaspallo, R. Del Sole, L. Mergola, M.R. Lazzoli, A. Scardino, S. Scorrano,

- G. Mele, Molecularly imprinted polymers: present and future prospective, *Int. J. Mol. Sci.* 12 (9) (2011) 5908–5945.
- [24] K. Smolínska-Kempisty, A. Guerreiro, F. Canfarotta, C. Caceres, M.J. Whitcombe, S. Piletsky, A comparison of the performance of molecularly imprinted polymer nanoparticles for small molecule targets and antibodies in the ELISA format, *Sci. Rep.* 6 (2016) 1–7.
- [25] A. Bossi, F. Bonini, A.P.F. Turner, S.A. Piletsky, Molecularly imprinted polymers for the recognition of proteins: the state of the art, *Biosens. Bioelectron.* 22 (6) (2007) 1131–1137.
- [26] M. Bertolla, L. Cenci, A. Anesi, E. Ambrosi, F. Tagliaro, L. Vanzetti, G. Gueifa, A.M. Bossi, Solvent-responsive molecularly imprinted nanogels for targeted protein analysis in MALDI-TOF mass spectrometry, *ACS Appl. Mater. Interfaces* 9 (8) (2017) 6908–6915.
- [27] Y. Chen, D.J. Li, Z.J. Bie, X.P. He, Z. Liu, Coupling of phosphate-imprinted mesoporous silica nanoparticles-based selective enrichment with matrix-assisted laser desorption/ionization-time-of-flight mass spectrometry for highly efficient analysis of protein phosphorylation, *Anal. Chem.* 88 (2) (2016) 1447–1454.
- [28] A.N. Tang, L.P. Duan, M.J. Liu, X.C. Dong, An epitope imprinted polymer with affinity for kininogen fragments prepared by metal coordination interaction for cancer biomarker analysis, *J. Mater. Chem. B* 4 (46) (2016) 7464–7471.
- [29] R.M. Caprioli, T.B. Farmer, J. Gile, Molecular imaging of biological samples: localization of peptides and proteins using MALDI-TOF MS, *Anal. Chem.* 69 (23) (1997) 4751–4760.
- [30] W.T. Jia, H.X. Wu, H.J. Liu, N. Li, Y. Zhang, R.F. Cai, P.Y. Yang, Rapid and automatic on-plate desalting protocol for MALDI-MS: using imprinted hydrophobic polymer template, *Proteomics* 7 (15) (2007) 2497–2506.
- [31] A. Mathur, S. Blais, C.M.V. Goparaju, T. Neubert, H. Pass, K. Levon, Development of a Biosensor for Detection of Pleural Mesothelioma Cancer Biomarker Using Surface Imprinting, *PLoS One* 8 (3) (2013) 1–8.
- [32] F. Sineriz, Y. Ikeda, E. Petit, L. Bultel, K. Haupt, J. Kovensky, D. Papy-Garcia, Toward an alternative for specific recognition of sulfated sugars: Preparation of highly specific molecular imprinted polymers, *Tetrahedron* 63 (8) (2007) 1857–1862.
- [33] W. Wan, Q. Han, X.Q. Zhang, Y.M. Xie, J.P. Sun, M.Y. Ding, Selective enrichment of proteins for MALDI-TOF MS analysis based on molecular imprinting, *Chem. Commun.* 51 (17) (2015) 3541–3544.
- [34] M. Zhang, X.H. Zhang, X.W. He, L.X. Chen, Y.K. Zhang, A self-assembled polydopamine film on the surface of magnetic nanoparticles for specific capture of protein, *Nanoscale* 4 (10) (2012) 3141–3147.
- [35] R.X. Gao, L.L. Zhang, Y. Hao, X.H. Cui, Y.H. Tang, Specific removal of protein using protein imprinted polydopamine shells on modified amino-functionalized magnetic nanoparticles, *RSC Adv.* 4 (110) (2014) 64514–64524.
- [36] N.E. Wezyńfeld, E. Stefanlak, K. Stachucy, A. Drozd, D. Plonka, S.C. Drew, A. Krezel, W. Bal, Resistance of Cu(A beta 4-16) to copper capture by metallothionein-3 supports a function for the a beta 4-42 peptide as a synaptic Cu-II scavenger, *Angew. Chem. -Int. Ed.* 55 (29) (2016) 8235–8238.
- [37] K. Eersels, P. Lieberzeit, P. Wagner, A review on synthetic receptors for bioparticle detection created by surface-imprinting techniques from principles to applications, *ACS Sens.* 1 (10) (2016) 1171–1187.
- [38] Y.L. Liu, K.L. Ai, L.H. Lu, Polydopamine and its derivative materials: synthesis and promising applications in energy, environmental, and biomedical fields, *Chem. Rev.* 114 (9) (2014) 5057–5115.
- [39] T.P. Chen, T.C. Liu, T.L. Su, J.F. Liang, Self-polymerization of dopamine in acidic environments without oxygen, *Langmuir* 33 (23) (2017) 5863–5871.
- [40] W.H. Zhou, C.H. Lu, X.C. Guo, F.R. Chen, H.H. Yang, X.R. Wang, Mussel-inspired molecularly imprinted polymer coating superparamagnetic nanoparticles for protein recognition, *J. Mater. Chem.* 20 (5) (2010) 880–883.
- [41] Z.W. Xia, Z.A. Lin, Y. Xiao, L. Wang, J.N. Zheng, H.H. Yang, G.N. Chen, Facile synthesis of polydopamine-coated molecularly imprinted silica nanoparticles for protein recognition and separation, *Biosens. Bioelectron.* 47 (2013) 120–126.
- [42] D.A. Spivak, Optimization, evaluation, and characterization of molecularly imprinted polymers, *Adv. Drug Deliv. Rev.* 57 (12) (2005) 1779–1794.
- [43] K.J. Xu, Y.Z. Wang, X.X. Wei, J. Chen, P.L. Xu, Y.G. Zhou, Preparation of magnetic molecularly imprinted polymers based on a deep eutectic solvent as the functional monomer for specific recognition of lysozyme, *Microchim. Acta* 185 (2) (2018) 146–154.
- [44] G.H. Yao, R.P. Liang, C.F. Huang, Y. Wang, J.D. Qiu, Surface plasmon resonance sensor based on magnetic molecularly imprinted polymers amplification for pesticide recognition, *Anal. Chem.* 85 (24) (2013) 11944–11951.
- [45] F. Lan, S.H. Ma, Q. Yang, L.Q. Xie, Y. Wu, Z.W. Gu, Polydopamine-based superparamagnetic molecularly imprinted polymer nanospheres for efficient protein recognition, *Colloid Surf. B-Biointerfaces* 123 (2014) 213–218.
- [46] Y.L. Jeyachandran, E. Mielezarski, B. Raj, J.A. Mielczarski, Quantitative and qualitative evaluation of adsorption/desorption of bovine serum albumin on hydrophilic and hydrophobic surfaces, *Langmuir* 25 (19) (2009) 11614–11620.
- [47] H.M. Chen, C.H. Deng, X.M. Zhang, Synthesis of Fe₃O₄@SiO₂@PMMA core-shell-shell magnetic microspheres for highly efficient enrichment of peptides and proteins for MALDI-TOF MS analysis, *Angew. Chem. -Int. Ed.* 49 (3) (2010) 607–611.
- [48] S. Krizkova, M. Ryzvolova, J. Gumulec, M. Masarik, V. Adam, P. Majzlík, J. Hubalek, I. Provazník, R. Klzék, Electrophoretic fingerprint metallothionein analysis as a potential prostate cancer biomarker, *Electrophoresis* 32 (15) (2011) 1952–1961.
- [49] A.S. Benk, C. Roesli, Label-free quantification using MALDI mass spectrometry: considerations and perspectives, *Anal. Bioanal. Chem.* 404 (4) (2012) 1039–1056.
- [50] A. Krezel, W. Maret, The functions of metamorphic metallothioneins in zinc and copper metabolism, *Int. J. Mol. Sci.* 18 (6) (2017).

6.15 ARTICLE 15

Vaneckova, T.; Bezdekova, J.; Tvrdonova, M.; Vlcnovska, M.; Novotna, V.; Neuman, J.; Stossova, A.; Kanicky, V.; Adam, V.; Vaculovicova, M.; Vaculovic, T. *Scientific Reports* 2019, 9 (IF=4.011)

OPEN

CdS quantum dots-based immunoassay combined with particle imprinted polymer technology and laser ablation ICP-MS as a versatile tool for protein detection

Received: 7 January 2019
Accepted: 1 August 2019
Published online: 14 August 2019

Tereza Vaneckova^{1,2}, Jaroslava Bezdekova^{1,2}, Michaela Tvrdonova⁴, Marcela Vlcnovska^{1,2}, Veronika Novotna³, Jan Neuman³, Aneta Stossova⁴, Viktor Kanicky⁴, Vojtech Adam^{1,2}, Marketa Vaculovicova^{1,2} & Tomas Vaculovic⁴

For the first time, the combination of molecularly imprinted polymer (MIP) technology with laser ablation inductively coupled plasma mass spectrometry (LA-ICP-MS) is presented with focus on an optimization of the LA-ICP-MS parameters such as laser beam diameter, laser beam fluence, and scan speed using CdS quantum dots (QDs) as a template and dopamine as a functional monomer. A non-covalent imprinting approach was employed in this study due to the simplicity of preparation. Simple oxidative polymerization of the dopamine that creates the self-assembly monolayer seems to be an ideal choice. The QDs prepared by UV light irradiation synthesis were stabilized by using mercaptosuccinic acid. Formation of a complex of QD-antibody and QD-antibody-antigen was verified by using capillary electrophoresis with laser-induced fluorescence detection. QDs and antibody were connected together via an affinity peptide linker. LA-ICP-MS was employed as a proof-of-concept for detection method of two types of immunoassay: 1) antigen extracted from the sample by MIP and subsequently overlaid/immunoreacted by QD-labelled antibodies, 2) complex of antigen, antibody, and QD formed in the sample and subsequently extracted by MIP. The first approach provided higher sensitivity (MIP/NIP), however, the second demonstrated higher selectivity. A mixture of proteins with size in range 10–250 kDa was used as a model sample to demonstrate the capability of both approaches for detection of IgG in a complex sample.

The technology of imprinted polymers allows for a selective recognition of targeted analyte. It is based on a formation of an analyte recognition surface that is created after polymerization of a mixture of analyte and suitable monomer^{1,2}. Molecules or ions can be imprinted into polymers then molecularly or ion imprinted polymers (MIP or IIP, respectively) are formed. Nowadays, MIPs are used as specific selectors for pre-concentration of broad groups of analytes in food^{3,4}, beverages^{5,6}, water⁷, soil⁸, and biological samples (e.g. blood plasma⁹). The main benefit of this technology is in its variability. Compared to conventional immunoassay, the use of MIP technology is applicable for analytes for which the antibodies are unavailable. Moreover, MIPs can be employed for a broad range of analytes (from ions to microorganisms) and take advantage of various surface arrangements (well-plates, microscopic slides, mass spectrometric targets, electrode and/or even nanoparticle surfaces). The monomer/polymer system can be also varied to provide not only suitable functional groups increasing the specificity of the interaction with the target analyte, but also suitable polymerization conditions¹⁰. Moreover, a number of detection techniques (e.g. fluorescence spectrometry or microscopy, mass spectrometry, and/or quartz crystal

¹Department of Chemistry and Biochemistry, Mendel University in Brno, Zemedelska 1, CZ-613 00, Brno, Czech Republic. ²Central European Institute of Technology, Brno University of Technology, Purkynova 123, CZ-612 00, Brno, Czech Republic. ³NenoVision s.r.o., Purkynova 649/127, CZ-612 00, Brno, Czech Republic. ⁴Department of Chemistry, Masaryk University, Kamenice 753/5, CZ-625 00, Brno, Czech Republic. Correspondence and requests for materials should be addressed to M.V. (email: marketa.ryvolova@seznam.cz)

microbalance) can be selected. The most commonly employed type of detection method is probably the quartz crystal microbalance¹¹, however extremely sensitive techniques such as inductively coupled plasma mass spectrometry (ICP-MS) may provide benefits for certain applications¹².

One of the polymers used for MIPs is polydopamine offering numerous benefits compared methacrylate and its derivatives¹³. Polydopamine was used for the first time as a surface coating in 2007 by Lee *et al.*¹⁴ and since then, the benefits of this material have been exploited in various fields including molecular imprinting¹⁵. Simple oxidative polymerization of dopamine is involved during the formation of the self-assembly layer¹⁶. Even though the detail mechanism of the polymerization is still not completely clear, it has been widely to create MIP on surfaces such as particles^{17–19}, monolithic columns²⁰ and/or carbon nanomaterials^{15,21}.

MIPs have found its application in biochemistry and bioanalysis providing an alternative to antibodies used in immunoassays. Standard immunoassays are commonly visualized by optical techniques, such as fluorescence^{22,23}, chemi(bio)luminescence²⁴, colorimetric detection^{25–28} or more recently introduced photothermal method²⁹, however in some cases, a more sensitive detection is required. For such applications, metal-labelled antibodies in combination with laser ablation inductively coupled plasma mass spectrometry (LA-ICP-MS) is the method of choice.

Inductively coupled plasma mass spectrometry (ICP-MS) is a well-established analytical method for multi-elemental analysis for elements at trace- and ultra-trace levels. It is outstanding mainly due to the high sensitivity independent of the molecular structure of the analyte, wide linear dynamic range and due to excellent multi-element capabilities. In combination with laser ablation sample introduction, ICP-MS has also been used to image the distribution of metallic nanoparticles (Au, Ag) in single biological cells³⁰.

As it was shown, NP-labelled antibodies in combination with ICP-MS used in dot-blot analysis are providing 4 orders of magnitude improved detection limits compared to standard metal-based labelling approach³¹. The idea of MIP-based technology has been employed in combination with nanoparticles (NPs) made of Fe₃O₄^{32,33}, gold NPs³⁴, CuO NPs³⁵, EuS NPs³⁶, quantum dots^{37–44} and upconversion NPs^{45,46}.

For the first time, the combination of LA-ICP-MS with the technology of imprinted polymers is presented by application on the immunoassay using CdS quantum dots-labelled antibodies. By the technology of imprinted polymers (polydopamine), the analyte is selectively captured, and antibodies tagged by semiconductor NPs provided a high sensitivity signal. This proof-of-concept study combining for the first time the advantages of MIP and LA-ICP-MS is presented with special attention paid to optimization of the LA-ICP-MS method in terms of laser ablation parameters.

Experimental

Materials. Natural Mouse IgG protein (ab198772) and Goat Anti-Mouse IgG H&L (ab6708) were purchased from AbCam (Cambridge, UK). HWRGWVC peptide was obtained from Clonestar Peptide Services, s.r.o., (Brno, Czech Republic). Dopamine hydrochloride, Mercaptosuccinic acid (MSA), Cadmium (Cd), Trizma base, Na₂HPO₄ and NaH₂PO₄ were purchased from Sigma-Aldrich (St. Louis, MO, USA) in ACS purity. 2-propanol and sodium tetraborate decahydrate were obtained from Thermo Fisher Scientific (Waltham, MA, USA).

Preparation of quantum dots. CdS QDs were prepared by mixing 50 μ l Cd solution (3 mM) with 25 μ l 0.1 M sodium phosphate buffer (Na₂HPO₄/NaH₂PO₄) pH 7 and 25 μ l MSA (2.4 mg·ml⁻¹) all 96 wells of UV-transparent well-plate. Then the plate was placed in UV trans-illuminator and was irradiated ($\lambda = 254$ nm) for 10 minutes. Resulted QDs were precipitated by 2-propanol (mixed 1:2 QDs:2-propanol, shaking for 10 minutes, and centrifugation for 10 min at 9000 rpm). Supernatant was removed and pellet was dried by solvent evaporation at 50 °C⁴⁷.

Characterization of prepared QDs. The prepared QDs were characterized by dynamic light scattering measuring the size, polydispersity, and zeta-potential using Zetasizer Nano ZS (Malvern, UK) according to the manufacturer's instruction. Moreover, fluorescence and absorbance spectroscopic characterization was performed using Plate reader Infinite 200 PRO (Tecan, Switzerland). Wavelength 350 nm was used as an excitation radiation and the fluorescence scan was measured within the range from 400 to 700 nm per 2-nm steps. The detector gain was set to 100. The samples were placed in UV-transparent 96 well microplate with flat bottom by CoStar (Corning, USA). To each well 50 μ l of the sample was placed. All measurements were performed at 25 °C.

Preparation of QD-antibody conjugates. 1.7 μ l of solution of conjugation peptide (HWRGWVC) abbreviated as HWR peptide (1.25 mg·ml⁻¹) was added to 25 μ l of CdS QDs (0.125 mg·ml⁻¹) capped with MSA and the mixture was incubated using Thermomixer 5355 (Eppendorf, Germany) at 45 °C, 600 rpm for 1 hour. Subsequently, 1.6 μ l of antibody (AB, 1 mg·ml⁻¹) was added to the QDs-HWR peptide conjugate. The mixture was again reacted using the Thermomixer at 21 °C, 600 rpm for 1 hour. Then the conjugate QD-AB linked *via* HWR peptide was ready to use³¹.

Characterization of QD-AB conjugates by capillary electrophoresis with laser-induced fluorescence detection (CE-LIF). Prepared conjugates were characterized by CE-LIF using Beckman PACE/MDQ with excitation using light emitting diode with emission wavelength of 395 nm. An uncoated fused silica capillary with total length of 47 cm and effective length of 40 cm was used. The internal diameter of the capillary was 75 μ m. 20 mM sodium borate buffer (pH = 9) was used as a background electrolyte and the separation was carried out using 20 kV with hydrodynamic injection by 5 psi for 5 s³¹.

Preparation of imprinted surface. The mixture (1 μ l) of dopamine (5 mg·ml⁻¹ in tris buffer pH 8.5) and the template (quantum dot-antibody = QD-AB, or quantum dot-antibody-antigen = QD-AB-AG complex) in

a ratio of 1:1 was polymerized (overnight at room temperature) on the surface of the glass microscopic slide to form a thin film of polydopamine with specific cavities selective to analyte (QD-AB or QD-AB-AG complex). Non-imprinted layer (NIP) was used as a control. The MIP/NIP spot was in average 2 mm in diameter and all experiments (MIP as well as NIP) were performed in triplicates. The final concentration of the QD and AB in the template was therefore 0.055 mg ml^{-1} and 0.028 mg ml^{-1} , respectively. Then the template was removed by washing for five-times with $10 \mu\text{l}$ of acetic acid (10%) and twice with $10 \mu\text{l}$ of MilliQ water. The surface of polymer was blocked by using $5 \mu\text{l}$ mixture of milk (10%) and 0.1M phosphate buffer, pH 7 (90%) for 10 minutes. Subsequently, the surface was washed three-times with $10 \mu\text{l}$ of MilliQ water. Next, the sample ($1 \mu\text{l}$) containing the analyte was dosed on the imprinted surface and after 1 hour of interaction, the surface was rinsed three-times by MilliQ water ($10 \mu\text{l}$). It was necessary to prepare NIP, formed from polydopamine without the presence of the template. It served as a blank.

Imprinted surface characterization. The sample surface was analyzed using SEM LYRA3 (TESCAN, Czech Republic) with integrated AFM LiteScope (NenoVision, Czech Republic). Correlative Probe and Electron Microscopy (CPEM)⁴⁸ was used for the surface analysis allowing simultaneous acquisition of SEM and AFM images at the same place in the same coordinate system. The SEM contrast is sensitive to the sample composition, while the AFM provides real surface topography. The accelerating voltage of 5 kV, beam current of 13 pA and SE detector was used for SEM imaging. The self-sensing Akiyama probe in tapping mode was used for the AFM measurement.

LA-ICP-MS. The analysis of MIP was performed by LA-ICP-MS setup that consists of LA system UP213 (NewWave Research, USA) emitting laser radiation with a wavelength of 213 nm with a pulse width of 4.2 ns. The ablated material was carried out from an ablation cell by a flow of a He (1.0 l/min) into ICP-MS Agilent 7500CE (Agilent Technologies, Japan) with quadrupole analyzer. The optimized laser ablation parameters used for MIP and NIP analysis were following: laser beam diameter of $250 \mu\text{m}$, the repetition rate of 10 Hz, laser beam fluence of 2 J/cm^2 , the scan speed of $2000 \mu\text{m/s}$ and distance between individual lines of $210 \mu\text{m}$. The signal arising from CdS QD was monitored via isotope ^{111}Cd . The whole spot of the sample was ablated by line patterns and signals of monitored isotopes were observed. The limit of quantification for signal intensity is calculated according to 10-fold of standard deviation of the gas level (without ablation). All intensities below LOQ were replaced by zero. Then sum intensity across the whole spot was calculated.

Limits of detection was calculated according to 3σ : $\text{LOD} = (3 \times \text{Standard deviation of blank})/\text{slope}$.

As a blank value, three spots of NIPs were measured and the standard deviation was then calculated from the sum of intensities of each one. The slope value was obtained from the sum of intensities of MIP ($2.5 \mu\text{g}$ of IgG).

Data processing. First, the threshold value for ^{111}Cd signal was calculated. It was the lowest measured intensity taken into count for data evaluation. It was calculated as a sum of the average blank level of ^{111}Cd signal and 10 fold standard deviation of a blank level. Blank level corresponding to intensities measured in carrier gas before ablation start. Time resolved signal of ^{111}Cd was obtained for each spot and intensities, lower than the threshold value, were removed. Then total sum of intensities of ^{111}Cd was calculated for each spot. The threshold value caused that the sum of intensities did not grow due to background level intensities.

Results

Characterization of prepared QDs. For the characterization of CdS QDs their size, polydispersity, ζ -potential, and absorption and emission spectra were measured. From the DLS analysis follows that the average particle size is 18 nm and the negative value of ζ -potential (-41 mV) indicated that the prepared QDs were stable and did not aggregate. This measurement is supported by their emission spectrum showing the emission maximum to be 548 nm. Size distribution, DLS data as well as TEM micrographs are shown in S1–S3.

CE-LIF of QD-conjugates. To verify the formation of the conjugates, CE-LIF was used. QDs, QDs-HWR, QDs-HWR-AB, and QDs-HWR-AB-AG were measured to confirm that each step of conjugation was successful. As can be seen from the Fig. 1, formation of various species was confirmed. The CdS QDs have negative charge as found by measurement of ζ -potential. Hence they have the highest migration time (5.38 minutes). HWR peptide sequence contains several positively charged amino acids and therefore, the conjugate of QD with HWR exhibited positive charge and its migration time decreased (3.26 minutes). The migration time of QD-HWR-AB complex was 3.78 minutes due to the increase in the size as well as increase of the negative charge. Similarly, when the complex QD-HWR-AB-AG was created (after addition of AG in total concentration 0.026 mg ml^{-1}), further increase in migration time was observed (4.32 minutes). Moreover, significant increase in the fluorescence intensity is observed when the HWR peptide is connected to CdS QDs. It is supposed that the increase relates to the fluorescence resonance energy transfer occurring within the formed complex. HWR peptide contains 1 molecule of histidine with an aromatic ring responsible for absorption maximum at 390 nm ⁴⁹. Hence the light supplied by the excitation LED was absorbed by the histidine and transferred to the connected QD. This is believed to lead to the fluorescence signal enhancement. However this was not the aim of this study and therefore, it was not further investigated in detail.

Optimization of MIP. A non-covalent imprinting approach was employed in this study due to the simplicity of preparation. The polymeric layer was created on the surface of a glass slide according to the method published previously by our group⁹. The concentration of 16 mM (2.5 mg ml^{-1}) dopamine hydrochloride was determined as the most effective considering the imprinting ratio (data not shown).

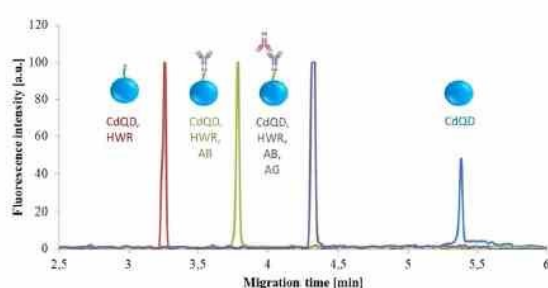


Figure 1. Electropherogram recording consequent complex formation by CE-LIF Fluorescence excitation at 395 nm, total length 47 cm, effective length 40 cm, internal diameter 75 μm , electrolyte - 20 mM sodium borate buffer (pH=9), separation voltage - 20 kV, injection - 5 psi for 5 s.

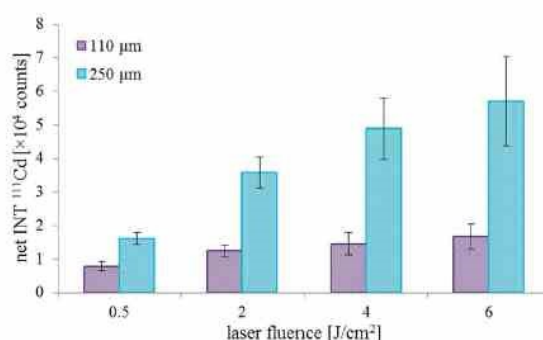


Figure 2. Influence of laser beam diameters (110 and 250 μm) and fluence (0.5, 2, 4, and 6 J/cm^2) on intensity of ^{111}Cd signal.

Optimization of ablation parameters. Laser ablation parameters as the laser beam fluence, laser spot size and scan speed were optimized to get a combination of both parameters with high sensitivity and high stability (low relative standard deviation - RSD) of the measured signal of ^{111}Cd . For all optimization, the slide was covered by a layer of polydopamine surface imprinted with CdS QDs with a diameter of 18 nm. First, optimization of laser beam fluence and laser spot size was carried out. Laser ablation system operates in 2 modes of laser beam focusing: I) Imaging mode – the laser spot size selected by using suitable aperture and II) Focused mode – the laser spot size selected by moving the lens. In the case of the imaging mode, the laser beam energy was more homogeneous across the laser beam cross section than in case of the Focused mode. To get the highest amount of the ablated material the largest available laser beam diameters for each focusing mode were tested – 110 (imaging) and 250 μm (focused). The laser beam fluence was changed in a range from 0.5 to 6.0 J/cm^2 . Under optimal laser beam fluence and laser spot size, the optimization of scan speed was done. Each combination of laser spot size and laser beam fluence was done as a line scan in triplicates on different places on the slide. The arithmetic average and relative standard deviations were calculated. The results of the optimization of laser beam spot size and fluence are summarized in Fig. 2 The pink and blue columns represent the laser beam diameters of 110 and 250 μm , respectively. As expected, the 250 μm laser beam spot provided significantly higher intensities compared to the 110 μm laser beam. In the case of the signal stability, the results obtained by 250 μm laser beam spot exhibited lower RSD compared to 110 μm laser beam spot. Hence, the laser beam spot of 250 μm was selected as optimal. Once the laser beam fluence was optimized, the largest intensities were achieved for 4 and 6 J/cm^2 . However, the lower stability of the signal was obtained. Therefore, the laser beam fluence of 2 J/cm^2 was used as a compromise between the signal sensitivity and stability.

Subsequently, the optimal scan speed was searched. It was found that scan speed affected neither the sensitivity nor the stability of the ^{111}Cd signal. The RSD of the signal intensity varied from 10 to 15% for all 4 tested scan speeds (300, 800, 1200 and 2000 $\mu\text{m}/\text{s}$). Hence, the criterion for selection of scan speed was the duration of the analysis. When the scan speed of 2000 $\mu\text{m}/\text{s}$ was applied, the overall duration of the analysis was about 23 s.

MIP-immunoassay design. Two approaches towards the MIP-immunoassay design (schematically shown in Fig. 3A,B) were tested. In the first concept (concept labelled A), only the AG was used as a template and therefore, the MIP selective only for AG was prepared. After that, AG was selectively isolated from the sample and subsequently, the MIP surface (with AG extracted from the sample) was overlaid by the QD-AB conjugate.

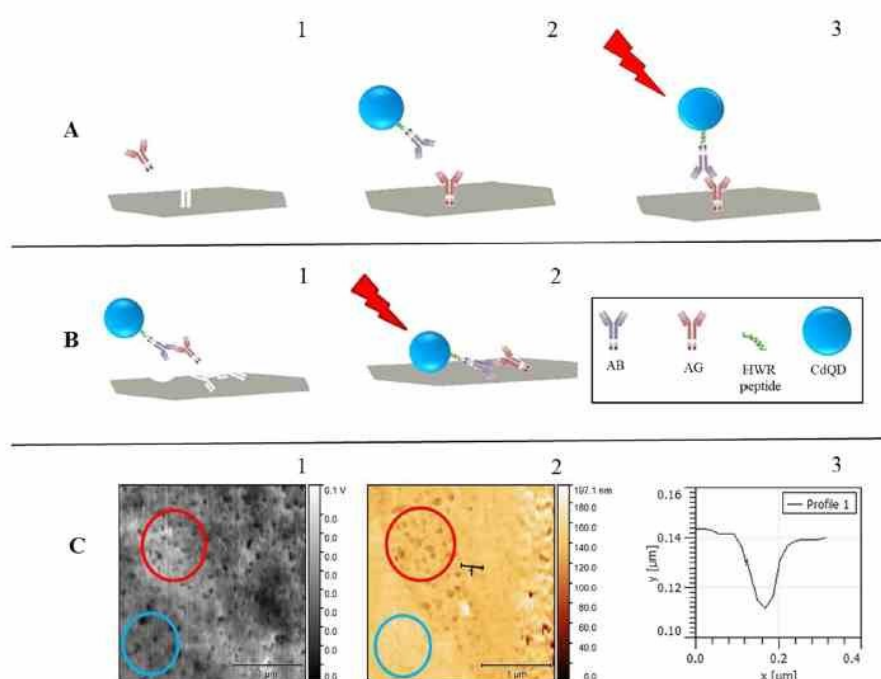


Figure 3. Schematic representation of two concepts of immunoassay combining QD-labelled antibodies and MIP technology. (A) 1-imprinting of the AG, 2-extraction of the AG from the sample by MIP; overlay with QD-AB conjugate, 3-interaction of the conjugate with the extracted AG from the sample, removal of the unreacted conjugate. (B) 1 - imprinting of the complex QD-AB-AG, 2 - QD-AB-AG formed in the sample after addition of QD-AB conjugate into the sample solution and extraction of QD-AB-AG complex from the sample by MIP for removal of interferences from the sample. (C) Correlative Probe and Electron Microscopy (CPEM) imaging of MIP layer with imprinted QD-AB conjugate. 1 - SEM image, 2 - AFM image of the same area and sample in the same coordinate system. 3 - profile of a well formed due to the imprinting process.

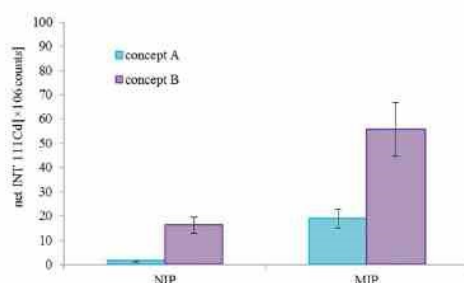


Figure 4. ICP-MS signal intensities (MIPs and NIPs) obtained by analysis of IgG standard sample by assay concepts A and B described in Fig. 3.

In the second approach (concept labelled B), the whole complex QD-AB-AG was imprinted (used as template) and during the analysis, this complex was formed directly within the sample and subsequently extracted by MIP.

In Fig. 3C, the surface visualization obtained by Correlative Probe and Electron Microscopy (CPEM) is shown. SEM image (1) and AFM image (2) were obtained simultaneously from the same region of the sample. Mainly two regions of the surface are of our interest (red and blue circle). Even though SEM image shows similar contrast of both regions, AFM imaging clearly confirms differences between the flat surface (blue circle) and wells formed due to the imprinting process (red circle). Profile of one of the wells is shown in (3).

As shown in Fig. 4, significant differences between MIP and NIP were detected in both concepts. The MIP/NIP signal ratio was 13.5 and 3.4 for concept A and concept B, respectively. This result, however demonstrates

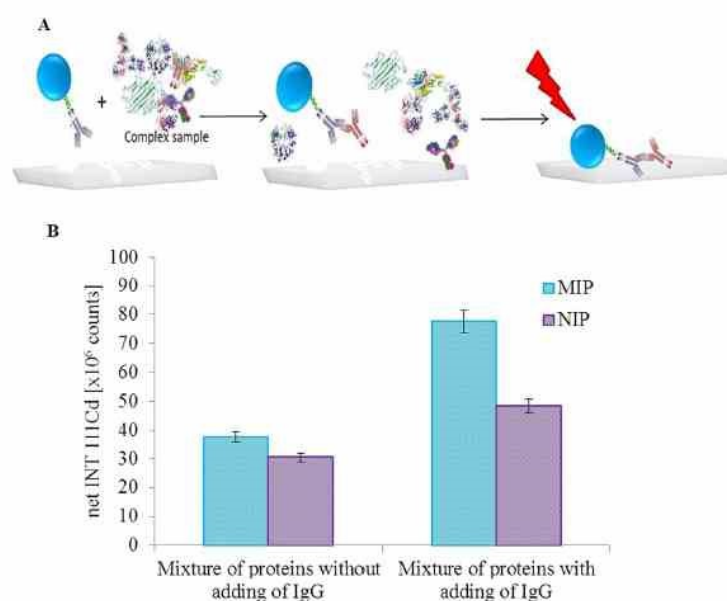


Figure 5. (A) Schematic representation of isolation and detection IgG from the same complex sample. At first the conjugate (QD-Ab) is added to the complex sample. The conjugate reacts with IgG contained in sample and creates the complex (QD-AB-AG) with them. The complex is bound to the cavity in MIP that is specific for this. The bound complex is subsequently detected by LA-ICP-MS. (B) ICP-MS signal intensities obtained by analysis of model protein mixture either with or without added IgG extracted by the assay schematically shown in (A).

the concept A to be less influenced by the non-specific adsorption of the sample components on the polymeric layer (NIP signal).

Lower intensities (both MIP and NIP) are observed in concept A compared to concept B. This is probably due to the fact that when the concept A is applied, the antigen only is imprinted, but its orientation in the polydopamine layer may not always be correct; that means, when the antigen is oriented so that the interaction site is not accessible for the QD-labelled antibody, the antigen-antibody interaction is prevented.

On the other hand, the concept B is providing 2.9-fold higher MIP signal compared to concept A suggesting better sensitivity of this approach. The significantly higher NIP signal (11.6-fold) of B concept compared to approach A is probably given by the fact that some molecules of AA-QD complex are more prone to non-specific adsorption.

The LODs of both concepts were calculated according to 3σ : concept A – 4.2 μg , concept B – 1.6 μg .

NIP is prepared under identical conditions and also with identical construction as MIP. The difference is that NIP is prepared without the presence of the template. It is taken as an indicator of non-specific binding. The NIP has functional groups randomly arranged on its surface that interact with analyte and cause to some extent bindings. These non-specific bindings are weaker than those of the MIP. The difference in binding to the MIP and the NIP are caused by selective binding sites in MIP created by imprinting of template molecule⁵⁰. On the surface of NIP, monomer self-association occurs and reduces the number of free functional groups where the analyte can be bound. Therefore NIP is able to bound less amount of analyte.

Based on the above mentioned facts, concept B was evaluated as more sensitive as it yields in lower LOD and therefore, was used for isolation and detection of IgG from complex model sample. For this purpose, the protein ladder was used. It consists of mixture of proteins in range from 10–180 kDa (lysozyme, α -lactalbumin, trypsin inhibitor, carbonic anhydrase, ovalbumin, bovine serum albumin, phosphorylase B, β -galactosidase; 0.1–0.3 mg/ml each). Scheme of experiment is illustrated in the Fig. 5A. The idea of this experiment is that the conjugate QD-AB-AG (QD-antiIgG-IgG) is imprinted. Then the QD-AB (QD-antiIgG) conjugate is added into the solution of protein ladder and the AG (IgG) from the sample is captured forming QD-AB-AG (QD-antiIgG-IgG) conjugate. After the overlay of the MIP by this solution, QD-antiIgG-IgG conjugate is captured in the cavities and interfering proteins are washed.

Mixture of proteins with and without addition of IgG was measured. The addition of IgG was 2.5 μg . The mixture of proteins and the QD-AB conjugate was mixed in ratio 1:1. The results are shown in Fig. 5B. It is clearly seen that mixture without IgG addition produces the signal intensity indistinguishable from the NIP, which is due to the nonspecific adsorption. However, it is impossible to distinguish whether the sample components are or the QD-AB conjugate are nonspecifically adsorbed on MIP surface. While after the addition of IgG a significant increase of Cd intensity relating to presence of QD-antiIgG-IgG conjugate is observed. It means that the Concept B is able to isolate IgG from the complex sample containing a mixture of proteins. In comparison results for

concept B from Fig. 5 significantly lower sensitivity and higher LOD was found. This deterioration of the parameters is caused probably due to the matrix effect of the proteins present in the sample.

Conclusions

The MIP technology is currently experiencing a rapid development due to the limitations of natural recognition elements such as antibodies or aptamers. However, neither MIP strategies are limitless. Therefore, the combination of these powerful tools in a specific immunoassay may bring highly selective approach. In this work, a MIP-based pseudo-immunoassay using NP-labelled antibody recognition was introduced and coupled with the sensitive detection technique – LA-ICP-MS. Two approaches of specific recognition were tested. The first one was based on the immunolabelling of the analyte captured by the MIP layer. The second approach involved immunolabelling of the analyte as a first step and the resulting QD-AB-AG complex was captured by MIP and further analyzed.

The double-selective approach comprising of the specific immunolabelling reaction combined with isolation by MIP together with the LA-ICP-MS detection represents a viable approach of the IgG detection from a complex sample (LOD 4.2 µg and 1.6 µg, respectively) available for many exciting applications. Considering the overall time of the LA-ICP-MS analysis not exceeding 23 s (scan speed of 2000 µm/s), LA-ICP-MS is a promising technology to be used in future in conjunction with MIP technology.

References

- Vlatakis, G., Andersson, L. I., Muller, R. & Mosbach, K. Drug assay using antibody mimics made by molecular imprinting. *Nature* 361, 645–647, <https://doi.org/10.1038/361645a0> (1993).
- Wulff, G. Molecular imprinting in cross-linked materials with the aid of molecular templates - a way towards artificial antibodies. *Angew. Chem.-Int. Ed. Engl.* 34, 1812–1832, <https://doi.org/10.1002/anie.199518121> (1995).
- Baggiani, C., Anfossi, L. & Giovannoli, C. Solid phase extraction of food contaminants using molecular imprinted polymers. *Anal. Chim. Acta* 591, 29–39, <https://doi.org/10.1016/j.aca.2007.01.056> (2007).
- Ramstrom, O., Skudar, K., Haines, J., Patel, P. & Bruggemann, O. Food analyses using molecularly imprinted polymers. *J. Agric. Food Chem.* 49, 2105–2114, <https://doi.org/10.1021/jf001444h> (2001).
- Manesiotes, P., Borrelli, C., Aureliano, C. S. A., Svensson, C. & Sellergren, B. Water-compatible imprinted polymers for selective depletion of riboflavin from beverages. *J. Mater. Chem.* 19, 6185–6193, <https://doi.org/10.1039/b906117g> (2009).
- Zhu, Q. F., Ma, C., Chen, H. X., Wu, Y. Q. & Huang, J. L. A molecular imprint-coated stirrer bar for selective extraction of caffeine, theobromine and theophylline. *Microchim. Acta* 181, 303–311, <https://doi.org/10.1007/s00604-013-1117-1> (2014).
- Watabe, Y. et al. LC/MS determination of bisphenol A in river water using a surface-modified molecularly-imprinted polymer as an on-line pretreatment device. *Analytical and Bioanalytical Chemistry* 381, 1193–1198, <https://doi.org/10.1007/s00216-004-3031-1> (2005).
- Peng, Y. et al. Molecularly imprinted polymer layer-coated silica nanoparticles toward dispersive solid-phase extraction of trace sulfonurea herbicides from soil and crop samples. *Anal. Chim. Acta* 674, 190–200, <https://doi.org/10.1016/j.aca.2010.06.022> (2010).
- Vaneckova, T. et al. Molecularly imprinted polymers coupled to mass spectrometric detection for metallothionein sensing. *Talanta* 198, 224–229, <https://doi.org/10.1016/j.talanta.2019.01.089> (2019).
- Haupt, K. & Mosbach, K. Molecularly imprinted polymers and their use in biomimetic sensors. *Chem. Rev.* 100, 2495–2504, <https://doi.org/10.1021/cr990099w> (2000).
- Diltemiz, S. E., Kecili, R., Ersoz, A. & Say, R. Molecular Imprinting Technology in Quartz Crystal Microbalance (QCM) Sensors. *Sensors* 17, 454 <https://doi.org/10.3390/s17030454> (2017).
- Shepherd, R. E. Chromatographic and related electrophoretic methods in the separation of transition metal complexes or their ligands. *Coord. Chem. Rev.* 247, 147–184, [https://doi.org/10.1016/s0010-8545\(03\)00125-5](https://doi.org/10.1016/s0010-8545(03)00125-5) (2003).
- Lymge, M. E., van der Westen, R., Postma, A. & Stadler, B. Polydopamine—a nature-inspired polymer coating for biomedical science. *Nanoscale* 3, 4916–4928, <https://doi.org/10.1039/c1nr10969c> (2011).
- Lee, H., Dellatore, S. M., Miller, W. M. & Messersmith, P. B. Mussel-inspired surface chemistry for multifunctional coatings. *Science* 318, 426–430, <https://doi.org/10.1126/science.1147241> (2007).
- Liu, R., Sha, M., Jiang, S. S., Luo, J. & Liu, X. Y. A facile approach for imprinting protein on the surface of multi-walled carbon nanotubes. *Talanta* 120, 76–83, <https://doi.org/10.1016/j.talanta.2013.12.002> (2014).
- Ryu, J. H., Messersmith, P. B. & Lee, H. Polydopamine Surface Chemistry: A Decade of Discovery. *ACS Appl. Mater. Interfaces* 10, 7523–7540, <https://doi.org/10.1021/acsami.7b19865> (2018).
- Jia, X. P. et al. Polydopamine-based molecular imprinting on silica-modified magnetic nanoparticles for recognition and separation of bovine hemoglobin. *Analyst* 138, 651–658, <https://doi.org/10.1039/c2an36313e> (2013).
- Xia, Z. W. et al. Facile synthesis of polydopamine-coated molecularly imprinted silica nanoparticles for protein recognition and separation. *Biosens. Bioelectron.* 47, 120–126, <https://doi.org/10.1016/j.bios.2013.03.024> (2013).
- Zhang, M., Zhang, X. H., He, X. W., Chen, L. X. & Zhang, Y. K. A self-assembled polydopamine film on the surface of magnetic nanoparticles for specific capture of protein. *Nanoscale* 4, 3141–3147, <https://doi.org/10.1039/c2nr30316g> (2012).
- Lin, Z. A. et al. Preparation of boronate-functionalized molecularly imprinted monolithic column with polydopamine coating for glycoprotein recognition and enrichment. *J. Chromatogr. A* 1319, 141–147, <https://doi.org/10.1016/j.chroma.2013.10.059> (2013).
- Yin, Y. L., Yan, L., Zhang, Z. H. & Wang, J. Magnetic molecularly imprinted polydopamine nanolayer on multiwalled carbon nanotubes surface for protein capture. *Talanta* 144, 671–679, <https://doi.org/10.1016/j.talanta.2015.06.067> (2015).
- Klos-Witkowska, A. The phenomenon of fluorescence in immunosensors. *Acta Biochim. Pol.* 63, 215–221, https://doi.org/10.18388/abp.2015_1231 (2016).
- Fu, X. L., Chen, L. X. & Choo, J. Optical Nanoprobes for Ultrasensitive Immunoassay. *Analytical Chemistry* 89, 124–137, <https://doi.org/10.1021/acs.analchem.6b02251> (2017).
- Fan, A. P., Cao, Z. J., Li, H. A., Kai, M. & Lu, J. Z. Chemiluminescence Platforms in Immunoassay and DNA Analyses. *Anal. Sci.* 25, 587–597 (2009).
- Hasanzadeh, M., Shadjou, N., Soleymani, J., Omidinia, E. & de la Guardia, M. Optical immunosensing of effective cardiac biomarkers on acute myocardial infarction. *Trac-Trends Anal. Chem.* 51, 158–168, <https://doi.org/10.1016/j.trac.2013.06.010> (2013).
- Wei, X. F. et al. Multiplexed Instrument-Free Bar-Chart Spin Chip Integrated with Nanoparticle-Mediated Magnetic Aptasensors for Visual Quantitative Detection of Multiple Pathogens. *Analytical Chemistry* 90, 9888–9896, <https://doi.org/10.1021/acs.analchem.8b02055> (2018).
- Sanjay, S. T., Dou, M. W., Sun, J. J. & Li, X. J. A paper/polymer hybrid microfluidic microplate for rapid quantitative detection of multiple disease biomarkers. *Scientific Reports* 6, 30474 <https://doi.org/10.1038/srep30474> (2016).
- Fu, G. L., Sanjay, S. T. & Li, X. J. Cost-effective and sensitive colorimetric immunosensing using an iron oxide-to-Prussian blue nanoparticle conversion strategy. *Analyst* 141, 3883–3889, <https://doi.org/10.1039/c6an00254d> (2016).

29. Fu, G. L., Sanjay, S. T., Dou, M. W. & Li, X. J. Nanoparticle-mediated photothermal effect enables a new method for quantitative biochemical analysis using a thermometer. *Nanoscale* 8, 5422–5427, <https://doi.org/10.1039/c5nr09051b> (2016).
30. Buchner, T. *et al.* Biomolecular environment, quantification, and intracellular interaction of multifunctional magnetic SERS nanopores. *Analyst* 141, 5096–5106, <https://doi.org/10.1039/c6an00890a> (2016).
31. Janu, L. *et al.* Electrophoretic study of peptide-mediated quantum dot-human immunoglobulin bioconjugation. *Electrophoresis* 34, 2725–2732, <https://doi.org/10.1002/elps.201300088> (2013).
32. Bilici, M., Zengin, A., Ekmen, E., Cetin, D. & Aktas, N. Efficient and selective separation of metronidazole from human serum by using molecularly imprinted magnetic nanoparticles. *J. Sep. Sci.* 41, <https://doi.org/10.1002/jssc.201800428> (2018).
33. Chen, G. N. *et al.* Preparation of molecularly imprinted polymers and application in a biomimetic biotin-avidin-ELISA for the detection of bovine serum albumin. *Talanta* 198, 55–62, <https://doi.org/10.1016/j.talanta.2019.01.088> (2019).
34. Lai, Y. X. *et al.* Molecular Imprinting Polymers Electrochemical Sensor Based on AuNPs/PTH Modified GCE for Highly Sensitive Detection of Carcinoembryonic Antigen. *J. Biomed. Nanotechnol.* 14, 1688–1694, <https://doi.org/10.1166/jbn.2018.2617> (2018).
35. Li, Y. X. & Jiang, C. Y. Trypsin electrochemical sensing using two-dimensional molecularly imprinted polymers on 96-well microplates. *Biosens. Bioelectron.* 119, 18–24, <https://doi.org/10.1016/j.bios.2018.07.067> (2018).
36. Babamiri, B., Salimi, A. & Hallaj, R. A molecularly imprinted electrochemiluminescence sensor for ultrasensitive HIV-1 gene detection using EuS nanocrystals as luminophore. *Biosens. Bioelectron.* 117, 332–339, <https://doi.org/10.1016/j.bios.2018.06.003> (2018).
37. Ge, S. G., Lu, J. J., Ge, L., Yan, M. & Yu, J. H. Development of a novel deltamethrin sensor based on molecularly imprinted silica nanospheres embedded CdTe quantum dots. *Spectrochimica Acta Part A-Molecular and Biomolecular Spectroscopy* 79, 1704–1709, <https://doi.org/10.1016/j.saa.2011.05.040> (2011).
38. Jia, M. F. *et al.* A molecular imprinting fluorescence sensor based on quantum dots and a mesoporous structure for selective and sensitive detection of 2,4-dichlorophenoxyacetic acid. *Sensors and Actuators B-Chemical* 252, 934–943, <https://doi.org/10.1016/j.snb.2017.06.090> (2017).
39. Li, J. H. *et al.* Thermosensitive molecularly imprinted core-shell CdTe quantum dots as a ratiometric fluorescence nanosensor for phycocyanin recognition and detection in seawater. *Analyst* 143, 3570–3578, <https://doi.org/10.1039/c8an00811f> (2018).
40. Liu, Y. X., Liu, L., He, Y. H., He, Q. H. & Ma, H. Quantum-dots-encoded-microbeads based molecularly imprinted polymer. *Biosens. Bioelectron.* 77, 886–893, <https://doi.org/10.1016/j.bios.2015.10.024> (2016).
41. Wang, X. Y. *et al.* Quantum dots based imprinting fluorescent nanosensor for the selective and sensitive detection of phycocyanin: A general imprinting strategy toward proteins. *Sensors and Actuators B-Chemical* 255, 268–274, <https://doi.org/10.1016/j.snb.2017.08.068> (2018).
42. Xu, S. F. *et al.* Dummy Molecularly Imprinted Polymers-Capped CdTe Quantum Dots for the Fluorescent Sensing of 2,4,6-Trinitrotoluene. *ACS Appl. Mater. Interfaces* 5, 8146–8154, <https://doi.org/10.1021/am4022076> (2013).
43. Yu, J. L. *et al.* One-pot synthesis of a quantum dot-based molecular imprinting nanosensor for highly selective and sensitive fluorescence detection of 4-nitrophenol in environmental waters. *Environmental Science-Nano* 4, 493–502, <https://doi.org/10.1039/c6en00395h> (2017).
44. Zhang, Z., Li, J. H., Wang, X. Y., Shen, D. Z. & Chen, L. X. Quantum Dots Based Mesoporous Structured Imprinting Microspheres for the Sensitive Fluorescent Detection of Phycocyanin. *ACS Appl. Mater. Interfaces* 7, 9118–9127, <https://doi.org/10.1021/acsami.5b00908> (2015).
45. Tang, Y. W. *et al.* A NIR-responsive up-conversion nanoparticle probe of the NaYF₄: Er,Yb type and coated with a molecularly imprinted polymer for fluorometric determination of enrofloxacin. *Microchim. Acta* 184, 3469–3475, <https://doi.org/10.1007/s00604-017-2387-9> (2017).
46. Wang, Y. *et al.* A label-free detection of diethylstilbestrol based on molecularly imprinted polymer-coated up conversion nanoparticles obtained by surface grafting. *RSC Adv.* 7, 22215–22221, <https://doi.org/10.1039/c6ra26999k> (2017).
47. Nejdli, L. *et al.* Rapid preparation of self-assembled CdTe quantum dots used for sensing of DNA in urine. *New J. Chem.* 42, 6005–6012, <https://doi.org/10.1039/c7nj05167k> (2018).
48. <http://www.nenovision.com/>.
49. Zhang, J., Men, Y. W., Lv, S. S., Yi, L. & Chen, J. F. Protein tetrazinylation via diazonium coupling for covalent and catalyst-free bioconjugation. *Org. Biomol. Chem.* 13, 11422–11425, <https://doi.org/10.1039/c5ob02053k> (2015).
50. Zhou, W. H. *et al.* Mussel-inspired molecularly imprinted polymer coating superparamagnetic nanoparticles for protein recognition. *J. Mater. Chem.* 20, 880–883, <https://doi.org/10.1039/b916619j> (2010).

Acknowledgements

This work has been supported by the Czech Science Foundation (project No. 16-23647Y) and internal grant agency MENDEL IGA grant No. TP_1/2017 This research was carried out under the project CEITEC 2020 (LQ1601) with financial support from the Ministry of Education, Youth and Sports of the Czech Republic under the National Sustainability Programme II. TerVan is Brno Ph.D. Talent holder – funded by the Brno City Municipality.

Author Contributions

TerVan performed the preparation of molecularly imprinted layer, J.B. carried out the electrophoretic characterization of conjugates, M.T. performed the laser ablation data processing and evaluation, MarVc carried out the conjugate preparation, V.N. and J.N. were responsible for microscopic conjugate characterization, A.S. carried out the laser ablation optimization, V.K. performed the data analysis, V.A. was responsible for supervision and experimental design, MarVac and TomVac carried out the manuscript preparation.

Additional Information

Supplementary information accompanies this paper at <https://doi.org/10.1038/s41598-019-48290-2>.

Competing Interests: The authors declare no competing interests.

Publisher's note: Springer Nature remains neutral with regard to jurisdictional claims in published maps and institutional affiliations.



Open Access This article is licensed under a Creative Commons Attribution 4.0 International License, which permits use, sharing, adaptation, distribution and reproduction in any medium or format, as long as you give appropriate credit to the original author(s) and the source, provide a link to the Creative Commons license, and indicate if changes were made. The images or other third party material in this article are included in the article's Creative Commons license, unless indicated otherwise in a credit line to the material. If material is not included in the article's Creative Commons license and your intended use is not permitted by statutory regulation or exceeds the permitted use, you will need to obtain permission directly from the copyright holder. To view a copy of this license, visit <http://creativecommons.org/licenses/by/4.0/>.

© The Author(s) 2019

6.16 ARTICLE 16

Dumkova, J.; Smutna, T.; Vrlikova, L.; Kotasova, H.; Docekal, B.; Capka, L.;
Tvrdonova, M.; Jakesova, V.; Pelkova, V.; Krumal, K.; Coufalik, P.; Mikuska, P.;
Vecera, Z.; Vaculovic, T.; Husakova, Z.; Kanicky, V.; Hampl, A.; Buchtova, M. ACS
nano 2020, 14, 3096-3120. (IF=13.903)

Variability in the Clearance of Lead Oxide Nanoparticles Is Associated with Alteration of Specific Membrane Transporters

Jana Dumková,[#] Tereza Smutná,[#] Lucie Vrlíková,[#] Hana Kotasová, Bohumil Dočekal, Lukáš Čapka, Michaela Tvrdoňová, Veronika Jakešová, Vendula Pelková, Kamil Krůmal, Pavel Coufalík, Pavel Mikuška, Zbyněk Večeřa, Tomáš Vaculovič, Zuzana Husáková, Viktor Kanický, Aleš Hampl, and Marcela Buchtová*



Cite This: *ACS Nano* 2020, 14, 3096–3120



Read Online

ACCESS |

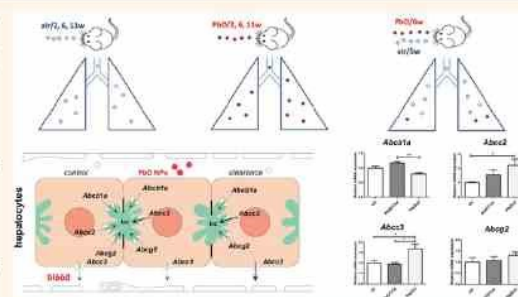
Metrics & More

Article Recommendations

Supporting Information

ABSTRACT: Lead oxide nanoparticles (PbONPs), upon their entry into the lungs *via* inhalation, induce structural changes in primary and secondary target organs. The fate and ultrastructural localization of PbONPs in organs is known to be dependent on the specific organ. Here, we focused on the differences in the ability to clear the inhaled PbONPs from secondary target organs and on molecular and cellular mechanisms contributing to nanoparticle removal. Mice were exposed to PbONPs in whole-body inhalation chambers. Clearance of ionic lead and PbONPs (Pb/PbONPs) from the lungs and liver was very effective, with the lead being almost completely eliminated from the lungs and the physiological state of the lung tissue conspicuously restored. Kidneys exposed to nanoparticles did not exhibit serious signs of damage; however, LA-ICP-MS uncovered a certain amount of lead located preferentially in the kidney cortex even after a clearance period. The concentration of lead in femurs, as representatives of the axial skeleton, was the highest among studied organs at all designated time points after PbONP exposure, and the clearance ability of lead from the femurs was very low in contrast to other organs. The organ-specific increase of ABC transporters expression (ABCG2 in lungs and ABCC3 in the liver) was observed in exposed animals, suggesting their involvement in removing Pb/PbONPs from tissues. Moreover, the expression of *caveolins* and *clathrin* displayed a tissue-specific response to lead exposure. Our results uncovered high variability among the organs in their ability to clear Pb/PbONPs and in the transporters involved in this process.

KEYWORDS: clearance, nanoparticles, lead oxide, inhalation, ABC transporters, caveolins, LA-ICP-MS imaging



Lead is a heavy metal found in various forms in the environment (elemental, inorganic, and organic). Inorganic and organic lead compounds are the most common forms, with many industrial uses. This utilization includes the production of additives in engine oils, car batteries (lead acid batteries), ceramic glazes, paints, plumbing, gas solders (tin–lead solder), ammunition (bullets contain lead stypnate or lead dioxide), crystal glassware (added PbO increases the refractive index of glass), protective aids against X-rays used in medicine (*e.g.*, lead aprons, lead shields), or components of fertilizers and pesticides.¹ Although the effects of lead toxicity on many organs are well-known (lead neurotoxicity, hematotoxicity, cardiotoxicity, nephrotoxicity, and others) and some of its uses (*e.g.*, house paint, ceramic

glaze, leaded gasoline in recent history) are in the process of being phased out due to advances in technology or regulatory control, lead is still widely used not only in developing countries but all over the world.² Metal nanoparticles and especially of their oxides are still broadly used in industry, metallurgy, agronomy, or science,^{3–6} and lead oxide nano-

Received: October 15, 2019

Accepted: February 27, 2020

Published: February 27, 2020

particles (PbONPs) are one of the most industrially used metal nanoparticles.⁷ Traditional or modern technologies of steel production, electric arc welding, and pyrometallurgy of heavy metals or combustion processes including automobile emissions pollute the air with aerosol particles (particulate matter, PM) smaller than one micrometer containing the same metal oxide.^{8,9}

Inhalation (or breathing in) is a vital physiological process necessary for all living organisms. Parts of inhaled air are not only main crustal elements such as Ca, Fe, Al, Mg, and K but also toxic elements such as Zn, Cu, Pb, Cr, Ni, As, Cd, and Sb.¹⁰

Occupational Safety and Health Administration (OSHA) has set a permissible exposure limit for lead in the workplace air of $50 \mu\text{g}/\text{m}^3$ (8 h time-weighted average); however, in some megacities and urban areas in Asia, concentrations of particles in the PM10 fraction (PM smaller than $10 \mu\text{m}$), containing also metals from anthropogenic sources as Zn, Pb, Cd, Cu, Bi, and Sb, can reach pollution peaks at $>250 \mu\text{g}/\text{m}^3$.^{11–14} Risk assessment of air contaminants has received more attention in recent years, and lead was identified as the second most common toxic metal in inhaled air not only in megacities of Asia but also in cities of Europe.^{10,15–17} The World Health Organization determined a limit for airborne lead of $0.5 \mu\text{g}/\text{m}^3$. This limit was exceeded in several cities around the world. In large cities such as Tehran, Athens, or Lahore the concentration of air lead reached $20 \mu\text{g}/\text{m}^3$, and in cities in Spain with petrochemical manufacturers, copper metallurgy, or steel industry concentrations of airborne Pb were measured to be between 10 and $77 \mu\text{g}/\text{m}^3$.^{18,19}

Thus, the human population continues to be exposed to lead. As acute lead toxicity is related rather to occupational exposure (smelters or workers in battery recycling plants), chronic lead exposure linked with adverse health effects is much more common. A number of different nanomaterials including metal nanoparticles is growing worldwide, and the impact on human health will further rise.

The effects of bulk lead are well known, but only some studies have evaluated the potential toxicity of its nanoforms.^{8,20,21} Lead nanoparticles, due to their size, can invade the lower respiratory tract more easily than corresponding larger forms. They can also enter through the alveoli into the blood circulation and consequently induce damage in other organs.²² Here, we have exposed experimental animals to PbONPs at a mass concentration of $78 \mu\text{g}/\text{m}^3$, corresponding to the exposure of inhabitants in cities during pollution peaks, and exposure to metal nanoparticles *via* whole-body inhalation reflects the real conditions in the environment.

To our knowledge, only a few studies have assessed the ability of organs to clear the lead load after long-term exposure to lead particles *via* the respiratory route.^{2,3,24} Despite the serious toxicity caused by lead exposure, the transport mechanisms of lead to organs or from them are not well understood yet.²⁵

Here, we examine the clearing ability of target organs (lung, liver, kidney, spleen, bone, and blood) following subchronic inhalation of PbONPs, using the mouse as a model organism. Next, we evaluate the mechanisms contributing to lead and lead nanoparticles' entrance or withdrawal from cells to reveal possible organ-specific processes contributing to lead removal from exposed organs.

RESULTS AND DISCUSSION

Exposure of Mice to Lead Oxide Nanoparticles in Whole-Body Inhalation Chambers. Lungs are the primary organ for NPs' entrance into an organism during inhalation. Inhaled nanoparticles can easily infiltrate deep parts of the lungs because of their small size. The ability of lung alveolar macrophages to remove nanosized particles is known to be low, so that nanoparticles can directly get into contact with the alveolar epithelium during nanoparticle penetration and pass to secondary organs.²⁶ Therefore, we designed the experiment simulating the real conditions with low concentrations of PbONPs in the air (Table 1) corresponding to the environ-

Table 1. Characterization of Generated PbONPs

| characterization of PbONPs | PbO |
|---|--|
| number concentration | 2.23×10^6 NPs/ cm^3 |
| surface area | 4.96×10^3 $\mu\text{m}^2/\text{cm}^3$ |
| mode | 15.5 nm |
| geometric mean diameter | 19.5 nm |
| geometric standard deviation | 1.74 nm |
| mass concentration | $78.0 \mu\text{g PbO}/\text{m}^3$ |
| estimated deposited dose (after 11 weeks) | $0.88 \mu\text{g PbO}/\text{g}$ |

ment in industrial areas, and mice were exposed to lead oxide particles in whole-body inhalation chambers to simulate physiological conditions.²⁷ We followed our previous findings from subchronic inhalation of nanoparticles, and we focus on the ability of organs to clear the lead burden, to repair the injury, and to induce a physiological response before their exposure.²⁸ Toward this aim, female mice were divided into three groups: a group exposed to PbONPs (PbO), a clearance group of animals who, after 6 weeks of inhalation of PbONPs, inhaled clean air for 5 weeks (PbO/d), and a control group (ctr) (Figure 1A,B,C). At designated time points (2, 6, and 11 weeks) mice were sacrificed and their organs collected for further analyses.

It is necessary to mention that during the whole-body inhalation, the PbO nanoparticles can come into contact with various parts of the mouse body such as the respiratory pathways, the olfactory region, the skin and hair of the animals, and the conjunctiva of the eyes. We constructed a special feeding device to eliminate oral intake of PbO nanoparticles; however, the reciprocal animal licking of hair is not possible to eradicate. Moreover, all inhaled nanoparticles have extrapulmonary effects as nanoparticles are cleared from the lung through the mucociliary transport or are directly ingested while breathing air by mouth.²⁹ Therefore, almost all organs of the body can be exposed to nanoparticles *via* the systemic circulation after translocation of nanoparticles through the alveolo-capillary barrier in the lungs. In summary, our experimental design and exposure in the whole-body inhalation chamber should reflect the complex conditions of how humans are exposed to metal nanoparticles in the environment.

PbONPs were generated continuously *in situ* in a hot-wall tube flow reactor using an evaporation–oxidation–condensation technique.²⁸ The mass concentration of PbO NPs was $78.0 \mu\text{g PbO}/\text{m}^3$ during the inhalation experiment, and the surface area $4.96 \times 10^3 \mu\text{m}^2/\text{cm}^3$ (Table 1). Even this low-concentration exposure caused serious histopathological changes in several target organs in mice after subchronic lead oxide inhalation, similar to that described previously for shorter time inhalations.^{2,2,28}

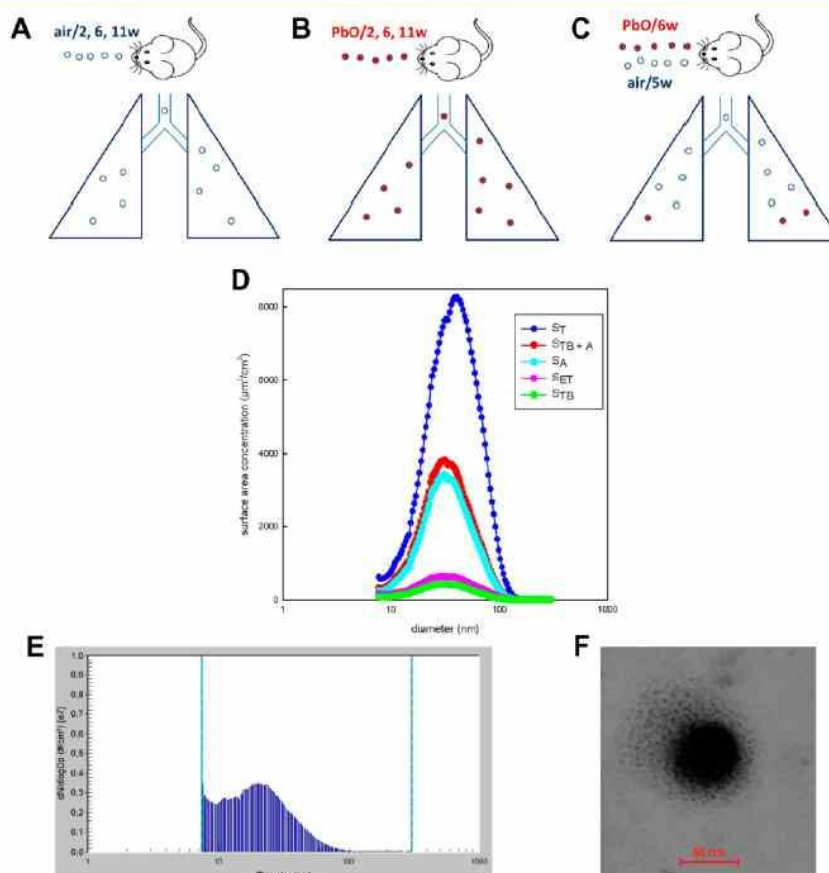


Figure 1. Design of the inhalation experiment. The size distribution with respect to the number of particles per unit volume and characterization of PbONPs in the inhalation chambers. The groups of animals (A) inhaled clean air for a period of up to 11 weeks (ctr), the other groups (B) inhaled air with PbONPs for the same period (PbO), and one group (C) inhaled air with PbONPs for 6 weeks and thereafter clean air for 5 weeks. This group is annotated as clearance group (PbO/d). (D) Surface area PbONP size distribution ($dS/d\log D_p$). S_T is the total surface area of generated PbO NPs, S_{TB+A} is the lung-deposited surface area, S_{ET} is the surface area of fractions deposited in the extrathoracic region, S_{TB} the tracheobronchiolar, and S_A the alveolar region of the lungs. The size distribution of nanoparticles (E) with respect to the number of particles measured by a scanning mobility particle sizer (SMPS) in the inhalation chambers and STEM image of PbONPs (F).

Various studies indicated surface area as an important parameter in assessing the toxicity of nanoparticles.^{30–33} Moreover, recently, the surface area has been shown as the biologically most relevant dose metric for NP (*i.e.*, non- or low-solubility NPs of spherical shape) toxicity in the lung.³⁴ To assess toxicological impacts of NPs as well as their possible risks to human health, information about NP deposition in different human lung regions is needed. Therefore, to further characterize our nanoparticles' effect on organism, we simulated the deposition of inhaled PbONPs in different parts of the human respiratory tract using the deposition fractions calculated by the ICRP deposition model for the extrathoracic, tracheobronchiolar, and alveolar regions.³⁵ The total surface area of generated PbONPs (*i.e.*, $4.96 \times 10^3 \mu\text{m}^2/\text{cm}^3$; S_T) was calculated by a scanning mobility particle sizer (SMPS) spectrometer software from measured particle size distribution.³⁶ Calculations of surface area of the NPs

deposited in the extrathoracic region (S_{ET} ; includes anterior and posterior nasal passage, larynx, pharynx, and mouth), tracheobronchiolar region (S_{TB} ; trachea, bronchi, and bronchioles), and alveolar region (S_A ; respiratory bronchioles and alveolar ducts) indicate the highest surface area of PbONPs deposited in the alveolar region of the lungs (*i.e.*, 38.4% of the total surface area of PbONPs), while the surface area of NPs deposited in the extrathoracic (8.5%) and tracheobronchiolar (5.3%) regions was predicted to be much smaller (Figure 1D).

Lung-deposited surface area (LDSA) concentration is another relevant metric for health effects of aerosol particles.³⁷ The LDSA combines the surface area of the NPs deposited in the alveolar and tracheobronchiolar regions of the lungs. The particle size distributions of the total surface area of PbONPs (S_T) and the surface area fractions deposited in the extrathoracic (S_{ET}), tracheobronchiolar (S_{TB}), and alveolar

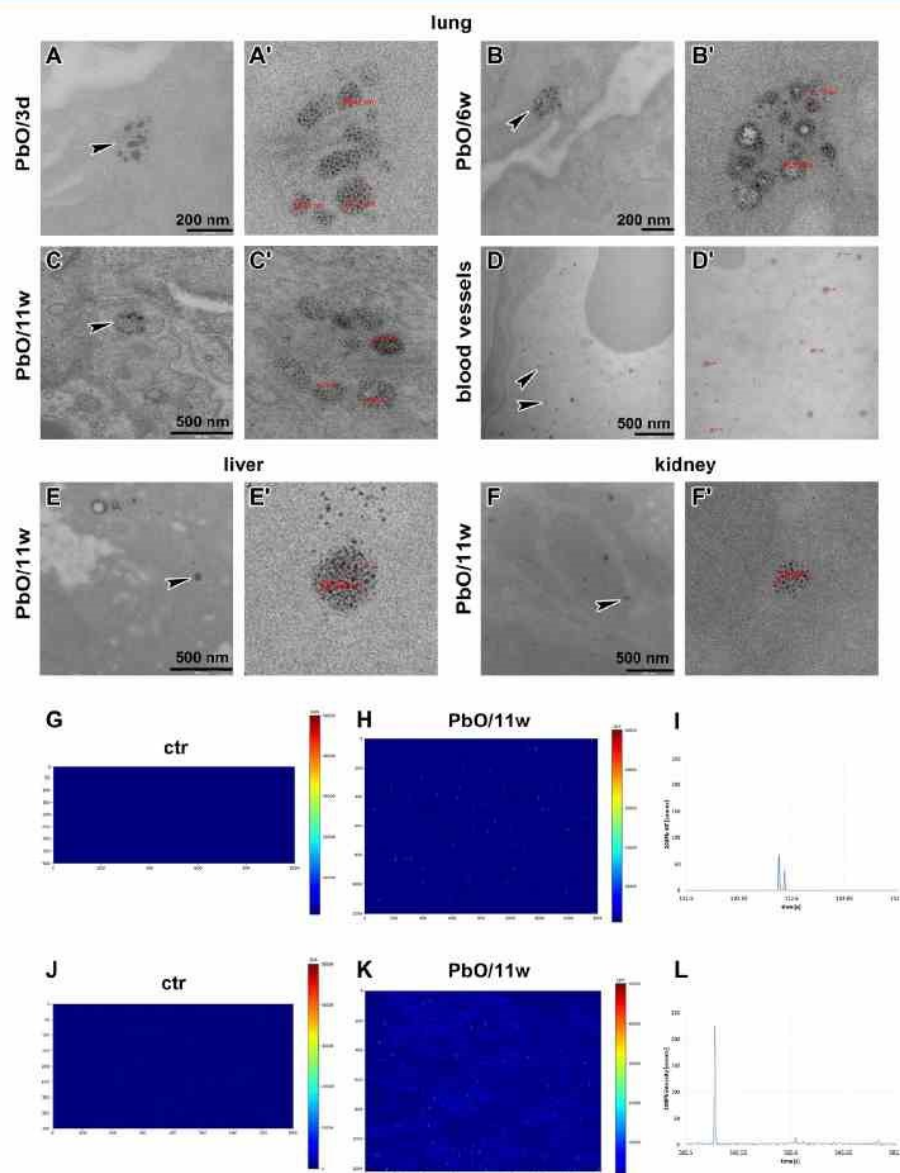


Figure 2. Presence of PbO nanoparticles in the lungs after 3 days (A, A'), 6 weeks (B, B'), and 11 weeks of PbO exposure (C, C'). Arrowheads display clusters of nanoparticles inside endocytic vesicles in pneumocytes I. Nanoparticles inside lung blood vessels (D, D', arrowheads), in hepatocytes in the liver (E, E', arrowhead), and in renal tubular epithelial cells (F, F', arrowhead). (G–I) Detection of Pb in part of the control liver sample (G) and liver after PbONP exposure (H) at week 11 by the LA-ICP-MS method. The different shades of light blue represent Pb in ionic form. Pb-based NPs are imaged as thin bright lines on the map. (I) Time-resolved signal of ^{208}Pb in liver tissue. The highly intensive peak corresponds to PbONPs. The baseline of the signal corresponds to Pb in ionic form. (J–L) Detection of Pb in part of the control kidney cortex (J) and kidney after PbONP exposure (K) at week 11 by the LA-ICP-MS method. The different shades of light blue represent Pb in ionic form. Pb-based NPs are imaged as thin bright lines on the map. (L) Time-resolved signal of ^{208}Pb in kidney tissue. The highly intensive peak corresponds to PbONPs. The baseline of the signal corresponds to Pb in ionic form.

regions (S_A) as well as the LDSA ($S_{\text{TB+A}}$) were evaluated (Figure 1D). The LDSA corresponds to 43.8% of the total surface area of prospectively inhaled PbONPs, while the sum of the surface area of the NPs deposited in the extrathoracic,

tracheobronchiolar, and alveolar regions makes up 52.3% of the total surface area of inhaled PbONPs (Figure 1D).

Moreover, it is well known that the character of nanoparticles can be modified during passage through the

Table 2. Concentration of Lead (ng/g) in Organs Following PbONP Inhalation Determined by AAS^a

| | | ctr/2,6,11w | PbO/2w | PbO/6w | PbO/11w | PbO/cl |
|--------|-------|-------------------|-----------|--------------|--------------|-------------------|
| lung | range | <LOD ^b | 617–1156 | 896–1406 | 903–1695 | ~LOD ^b |
| | mean | | 792 | 1212 | 1419 | |
| | SD | | 245 | 191 | 369 | |
| liver | range | <LOD ^b | 174–283 | 311–475 | 714–1328 | 24–100 |
| | mean | | 229 | 374 | 1018 | 45 |
| | SD | | 46 | 78 | 224 | 31 |
| kidney | range | <LOD ^b | 1329–1728 | 1621–2168 | 2203–2838 | 229–366 |
| | mean | | 1488 | 1981 | 2512 | 282 |
| | SD | | 148 | 213 | 227 | 54 |
| spleen | range | <LOD ^b | 93–171 | 249–354 | 403–711 | 94–155 |
| | mean | | 128 | 288 | 542 | 114 |
| | SD | | 30 | 43 | 148 | 29 |
| femur | range | <LOD ^b | 5001–5864 | 12 429–15879 | 13 835–28946 | 11 474–15 328 |
| | mean | | 5245 | 13 562 | 20 468 | 13 957 |
| | SD | | 352 | 1349 | 7674 | 1737 |

^aComparison of lead concentration in the lung, liver, kidney, spleen, and femur at different time points. ^bLimit of detection in the lung, liver, kidney, spleen, and femur was 26, 3, 9, 29, and 21 ng/g Pb, respectively.

respiratory tract, and metal nanoparticles can dissolve into corresponding ions.³⁸ Previous studies indicated variability in dissolution of metals in different solutions including simulated lung fluids (SLF).^{16,39} Lead was determined to exhibit a relatively high extraction efficiency for saline, deionized water, or artificial lysosomal fluid; however, lead displayed minimal bioaccessible proportions in SLF as Gamble's solution or simulated alveoli fluid.¹⁶ Thus, these results indicate large differences in dissolution of lead according to the chemical composition of used fluids and simulating extraction efficiency in the lungs can be very difficult.

Therefore, also in our experimental conditions, generated PbONPs can be dissolved after *in vivo* deposition in the lungs, leading to ion formation. These ions together with nanoparticles can be released and transported from the site of their deposition in the lungs to other target organs, resulting in continual dissolution of the nanoparticles, as demonstrated in the studies with other metal nanoparticles.^{40,41} On the other hand, a certain fraction of the inhaled nanoparticles was proven to translocate from the lungs to other internal organs.⁴² In agreement with these findings, our ultrastructural analyses of organs also confirmed the presence of nanosized PbO in the lungs, liver, and kidney (Figure 2), and our data confirm that the translocation of lead nanoparticles through the circulation into secondary organs is possible, similar to other metals.²⁹ The majority of PbO nanoparticles were observed in the pulmonary tissue (Figure 2A–D'), which corresponded with the other analyses determining the translocation of nanoparticles through the blood circulation into secondary organs.^{29,43,44} This is also in agreement with our previous studies, where we confirmed the presence of individual PbONPs after acute and subchronic inhalation not only in the lungs but also in all analyzed secondary target organs.^{22,28}

One of the possibilities of how to distinguish between particulate and nonparticulate lead in organs is laser ablation inductively coupled plasma mass spectrometry (LA-ICP-MS).^{40,45} The detection is based on the fact that the intensity of Pb (in counts) in ionic form decreases with decreasing integration time (1 ms), whereas the Pb signal from nanoparticles is the same. Therefore, to distinguish between the ionic and NP form of Pb, we shortened the integration time to 1 ms, measured only one isotope, and diminished the

laser beam spot. The presence of lead in ionic form was manifested by a low signal throughout the measured area, while the nanoparticle form was manifested by a high signal, which was specifically localized (Figure 2). Analysis was performed of kidney and liver samples from mice exposed to PbONPs as well as control mice at the 11 weeks time point. In both tissues, we were able to distinguish the ionic form of lead and the nanoparticle form of lead (Figure 2G–L). In the liver tissue, only a small number of nanoparticles was observed, while lead in the kidney cortex was present in a high amount both in nanoparticle and ionic form (Figure 2K,L).

Enhanced Clearance of Lead Occurred in the Lungs in Contrast to the Failure of Clearance from Bone. First, the final amount of lead was analyzed in all collected tissues (lung, liver, kidney, spleen, blood, femur) at all time points. The highest concentration of lead after 2 weeks of exposure was observed in bone (examined in mice femurs), followed by the kidney (3.5 times lower compared to bone), lungs (seven times lower compared to bone), liver (23 times lower compared to bone), and spleen (Table 2).

After 6 weeks of exposure, the concentration of lead in bone was the highest, being seven times higher in bone compared to kidney or 11 times higher compared to the lungs. After 11 weeks of exposure, the concentration of lead in bone reached 20 $\mu\text{g/g}$, while in kidneys it was 2.5 $\mu\text{g/g}$, in the lungs and liver it was similarly about 1 $\mu\text{g/g}$, and in the spleen it was 0.5 $\mu\text{g/g}$ (Table 2).

Following the clearing period, the concentration of lead in the lungs decreased practically to the limit of detection (26 ng/g). The ability of the liver to eliminate lead was also efficient; the concentration of lead in the liver was eight times lower than its concentration after 6 weeks of PbONP exposure (Table 2). In the kidneys, a significant decrease of lead level after clearance was also observed. The concentration of lead after 5 weeks of clearing was seven times lower than the concentration after PbONP exposure. However, it was still enhanced in comparison to the unexposed controls (Table 2). A similar trend was observed in the spleen. In the femur, the state was quite different, with a very high concentration of lead detected following 2 weeks of PbONP inhalation, which even increased with a prolonged time of exposure. In contrast, no significant clearing effect was observed regarding the level of

Table 3. Lead in the Blood Determined by AAS^{a†}

| | | ctr/2,6,11w | PbO/2w | PbO/6w | PbO/11w | PbO/d |
|---------------------|-----------------------------------|-------------------|-------------------|-------------------|-------------------|-------------------|
| erythrocytes (ng/g) | range | <LOD ^b | 161–232 | 215–323 | 242–488 | 37–64 |
| | mean | | 204 | 277 | 342 | 50 |
| | SD | | 27 | 42 | 91 | 11 |
| proteins (ng/g) | range | <LOD ^b |
| | mean | | | | | |
| | SD | | | | | |
| serum (ng/g) | range | <LOD ^b |
| | mean | | | | | |
| | SD | | | | | |
| blood (ng/g) | | <LOD ^b | 104 | 148 | 174 | 27 |
| | blood ($\mu\text{g}/\text{dL}$) | | 10.4 | 14.8 | 17.4 | 2.7 |

^{a†}The concentration of lead in blood at different time points. ^bLimit of detection in erythrocytes in control animals, in proteins at all data points, in serum at all data points, and in whole blood in control animals was 6, 11, 4, and 3 ng/g Pb, respectively.

lead in bones (femurs) following the clearance period, and the lead concentration was still at a high level similar to that immediately after 6 weeks of exposure.

In summary, lungs are cleared highly effectively so that the 5-week clearing period allowed the lungs to become completely void of detectable PbO particles. The secondary organs, instead, exhibited much less clearing activity, with long bones showing no clearing of PbO particles at all.

Lead in Blood Was Decreased to Normal Values after Clearance. The inhaled lead is transported from the lungs to the secondary organs by the blood. The level of lead in the blood reflects individuals' current exposure, and unfortunately, today, humans working or living in some developing and industrial countries where toxic metals such as lead are present in the environment can have concentrations of lead in the blood that are much higher than the level established as safe by the World Health Organization (WHO). The whole blood lead levels in adults and children residing in some locations in Africa can reach 150 $\mu\text{g}/\text{dL}$, while the recommended WHO value is 5 $\mu\text{g}/\text{dL}$.^{46,47}

In our experimental animals, the concentration of lead in the blood continuously increased with the length of PbONP inhalation. The lead concentration then increased only slightly from 15 $\mu\text{g}/\text{dL}$ to 17 $\mu\text{g}/\text{dL}$ between the sixth and 11th week of exposure (Table 3).

A similar pattern of concentration changes in lead level during exposure progress was described after instillation of PbS NPs in rats following four exposures.⁴⁸

After 5 weeks of clearance, the lead concentration in the blood decreased approximately five times in comparison to 6 weeks of exposure (Table 3) and reached values within physiological limits of lead in the blood recommended by the WHO (<5 $\mu\text{g}/\text{dL}$). This finding is in accordance with the residence time of lead in blood, which was found to be around 4–6 weeks.⁴⁹

Lead Oxide Nanoparticle Inhalation Did Not Cause Extensive Changes in Biochemical Parameters in Experimental Animals' Blood. The blood concentration of total protein and albumin is usually used as a biochemical marker, mainly to test hepatic function (albumin level also reflects kidney function). The blood level of albumin was significantly decreased after 2 and 6 weeks of inhalation, and the level of total protein was significantly decreased after 2 weeks of inhalation. However, all these values were still in the reference range for adult female mice (Table 4).

The level of total bilirubin was significantly decreased after 6 weeks of exposure. Blood levels of triglycerides and cholesterol were in the physiological reference range; however, the clearance visibly decreased their concentrations. The values of specific hepatic enzymes, alanine aminotransferase (ALT), aspartate aminotransferase (AST), and gamma-glutamyl transferase (GGT), were within physiological range. Thus, analysis of biochemical parameters in blood revealed slightly impaired hepatic function after subchronic PbONP inhalation, especially after 2 and 6 weeks of PbONP exposure. Our results are in contrast to a previously observed high elevation of liver enzymes and low-density lipoproteins, which were found in some affected individuals after lead exposure.²⁰ One possible explanation could be the use of relatively lower levels of lead in our experiment, which may not significantly alter liver function. Moreover, the nanoparticle form of lead seems to be less toxic to the liver than its soluble form. In agreement with our findings, another *in vivo* study with PbO nanoparticles revealed that almost all biochemical parameters after 6 weeks of metal nanoparticle exposure were in physiological values for rats, although the lead content in the blood reached 38.7 $\mu\text{g}/\text{dL}$ (0.387 $\mu\text{g}/\text{mL}$).⁵ Interestingly, the same mass dose of CuO and ZnO nanoparticles used in this study exhibited more distinctive, and negative effect on the biochemical parameters in the blood than PbO nanoparticles.

Similar biochemical results to ours were reported also in an *in vivo* study with Ag NPs and Au NPs in mice, where most of the standard biochemical parameters (ALT, AST, albumin, total bilirubin) between control and treated groups were not significantly changed, and the level of alkaline phosphatase (ALP) was significantly reduced only in the Au NPs-treated group.⁵⁰

Biochemical markers of kidney function (predominantly urea and creatinine) were found to be within the standard range in all animals. Also, glycemia was within physiological limits in all groups. The levels of chloride also remained unchanged in all animals.

Exposure to inhaled PbONPs did not influence the calcium level in blood in any time point. Still, calcium levels were altered with the length of the experiment (Table 4). At the end of the experiment, calcium was at its highest level, which corresponds to completion of bone growth at this animal age.⁵¹

Interestingly, blood levels of sodium and potassium in all groups of animals in our experiment were lower than reference values for female mice.⁵² While values for sodium level in all observed groups were similar, the mean concentration of

Table 4. Blood Biochemical Analysis Following PbONP Inhalation

| | | ctr/6w | PbO/6w | ctr/11w | PbO/11w | PbO/d | ref values CD-1 (ICR) | ref values female mice |
|---------------------|-------|-----------|------------------|-----------|-------------------|-----------------|-----------------------|------------------------|
| TP (g/L) | range | 58–67 | 59–69 | 57–62 | 56–63 | 55–60 | 53–60 | 45–62 |
| | mean | 63 | 63 | 60 | 58 | 57 | | |
| | SD | 4 | 4 | 3 | 3 | 2 | | |
| Alb (g/L) | range | 32–34 | 31–33 | 31–35 | 30–34 | 30–33 | 36–43 | 29–43 |
| | mean | 33 | 32 ^b | 33 | 32 | 31 ^b | | |
| | SD | 1 | 1 | 2 | 1 | 1 | | |
| Tbil (μ mol/L) | range | 2.6–3.7 | 1.8–2.2 | 3.3–4.3 | 3.3–4.1 | 3.4–3.8 | 2.7–4.6 | 1.7–15.4 |
| | mean | 3.3 | 2.1 ^c | 3.8 | 3.7 | 3.6 | | |
| | SD | 0.5 | 0.2 | 0.4 | 0.3 | 0.2 | | |
| Ca (mmol/L) | range | 2.30–2.47 | 2.25–2.47 | 2.50–2.80 | 2.38–2.76 | 2.52–2.71 | 2.48–2.88 | 2.28–2.88 |
| | mean | 2.39 | 2.34 | 2.68 | 2.59 | 2.59 | | |
| | SD | 0.06 | 0.10 | 0.13 | 0.16 | 0.07 | | |
| P (mmol/L) | range | 1.64–2.66 | 2.96–3.49 | 1.82–2.95 | 1.24–2.25 | 1.14–2.56 | 2.30–4.52 | 2.06–4.52 |
| | mean | 2.06 | 3.19 | 2.40 | 1.61 ^c | 2.01 | | |
| | SD | 0.42 | 0.24 | 0.62 | 0.39 | 0.68 | | |
| ALP (μ kat/L) | range | 0.6–2.7 | 1.1–1.9 | 1.2–2.3 | 1.1–2.1 | 0.7–1.4 | 0.8–2.2 | 0.7–4.1 |
| | mean | 1.6 | 1.5 | 1.5 | 1.6 | 1.0 | | |
| | SD | 0.8 | 0.5 | 0.5 | 0.5 | 0.3 | | |
| ALT (μ kat/L) | range | 0.3–1.4 | 0.3–3.1 | 0.3–0.4 | 0.3–0.6 | 0.3–0.6 | 0.3–0.7 | 0.2–4.5 |
| | mean | 0.6 | 1.2 | 0.3 | 0.5 | 0.4 | | |
| | SD | 0.4 | 1.3 | 0.2 | 0.2 | 0.1 | | |
| AST (μ kat/L) | range | 2.5–9.4 | 4.6–9.7 | 1.8–3.1 | 1.3–5.5 | 1.6–5.1 | 0.8–1.3 | 0.6–8.4 |
| | mean | 4.9 | 7.2 | 2.3 | 3.1 | 2.5 | | |
| | SD | 3.1 | 2.8 | 0.6 | 1.6 | 1.5 | | |
| urea (mmol/L) | range | 6.2–7.7 | 10.5–14.3 | 7.6–10.0 | 5.6–8.7 | 5.2–6.7 | 4.6–7.5 | 3.9–10.0 |
| | mean | 7.2 | 11.9 | 8.6 | 7.5 | 6.2 | | |
| | SD | 0.6 | 1.7 | 1.0 | 1.2 | 0.6 | | |
| crea (mmol/L) | range | 29.5–36.5 | 29.2–38.8 | 33.5–39.5 | 30.4–33.2 | 33.6–36.3 | 26.5–35.4 | 17.7–35.4 |
| | mean | 32.2 | 33.7 | 37.0 | 32.3 | 35.0 | | |
| | SD | 2.8 | 4.3 | 2.5 | 1.1 | 1.3 | | |
| chol (mmol/L) | range | 1.83–2.54 | 1.52–2.32 | 1.88–3.39 | 1.46–2.68 | 1.19–2.90 | 1.84–3.81 | 1.45–3.86 |
| | mean | 2.23 | 1.80 | 2.66 | 2.19 | 1.89 | | |
| | SD | 0.27 | 0.35 | 0.62 | 0.49 | 0.68 | | |
| TAG (mmol/L) | range | 1.41–1.99 | 1.57–2.32 | 1.05–2.38 | 1.03–3.52 | 0.68–1.42 | 0.27–2.44 | 0.27–3.30 |
| | mean | 1.72 | 1.80 | 1.67 | 1.86 | 1.12 | | |
| | SD | 0.21 | 0.35 | 0.64 | 0.99 | 0.30 | | |
| Na (mmol/L) | range | 141–149 | 141–145 | 146–148 | 144–147 | 142–148 | 151–161 | 149–161 |
| | mean | 144 | 143 | 147 | 146 | 146 | | |
| | SD | 3 | 2 | 1 | 1 | 2 | | |
| K (mmol/L) | range | 5.8–8.9 | 7.5–9.6 | 5.2–6.9 | 4.4–7.0 | 5.0–9.0 | 8.1–12.2 | 7.2–12.2 |
| | mean | 7.2 | 8.3 | 6.2 | 5.7 | 6.6 | | |
| | SD | 1.6 | 0.3 | 0.9 | 1.2 | 1.5 | | |
| Cl (mmol/L) | range | 115–121 | 114–119 | 112–120 | 117–122 | 116–119 | 112–124 | 102–120 |
| | mean | 118 | 117 | 116 | 118 | 118 | | |
| | SD | 2 | 2 | 3 | 2 | 1 | | |
| Glu (mmol/L) | range | 8.4–13.8 | 7.8–10.1 | 8.0–12.0 | 9.6–11.4 | 8.3–11.6 | 8.0–17.8 | 4.57–17.8 |
| | mean | 11.0 | 9.2 | 9.7 | 10.6 | 9.7 | | |
| | SD | 2.1 | 1.1 | 1.7 | 0.7 | 1.6 | | |
| GGT (μ kat/L) | range | <0.07 | <0.07 | <0.07 | <0.07 | <0.07 | | |

^aData were obtained from five animals per group; the values denote average \pm SD. ^b $p < 0.05$, ^c $p < 0.01$ compared with the corresponding control group by unpaired t test. The values of female mice crl:CD-1 (ICR) BR were used as reference standards, and another reference values mentioned in the table are the smallest and the highest values previously published for different strains of female mice.⁵² Reference biochemical values were recounted to our used units.

potassium after 11 weeks of PbONP exposure was the lowest in all studied groups of animals.

Exposure to inhaled PbONPs also affected the phosphorus level in blood. After 2 and 11 weeks of exposure, phosphorus concentration in the blood decreased; after 6 weeks of exposure, in contrast, it was significantly increased. The value

for blood phosphorus following clearance returned to the values of the respective controls. Moreover, ALP, regulating the blood phosphorus level, was decreased in the clearance group. A previously published study also detected significantly decreased levels of ALP in the blood after 6 weeks of exposure to PbO, ZnO, and CuO and after their combinations.⁵

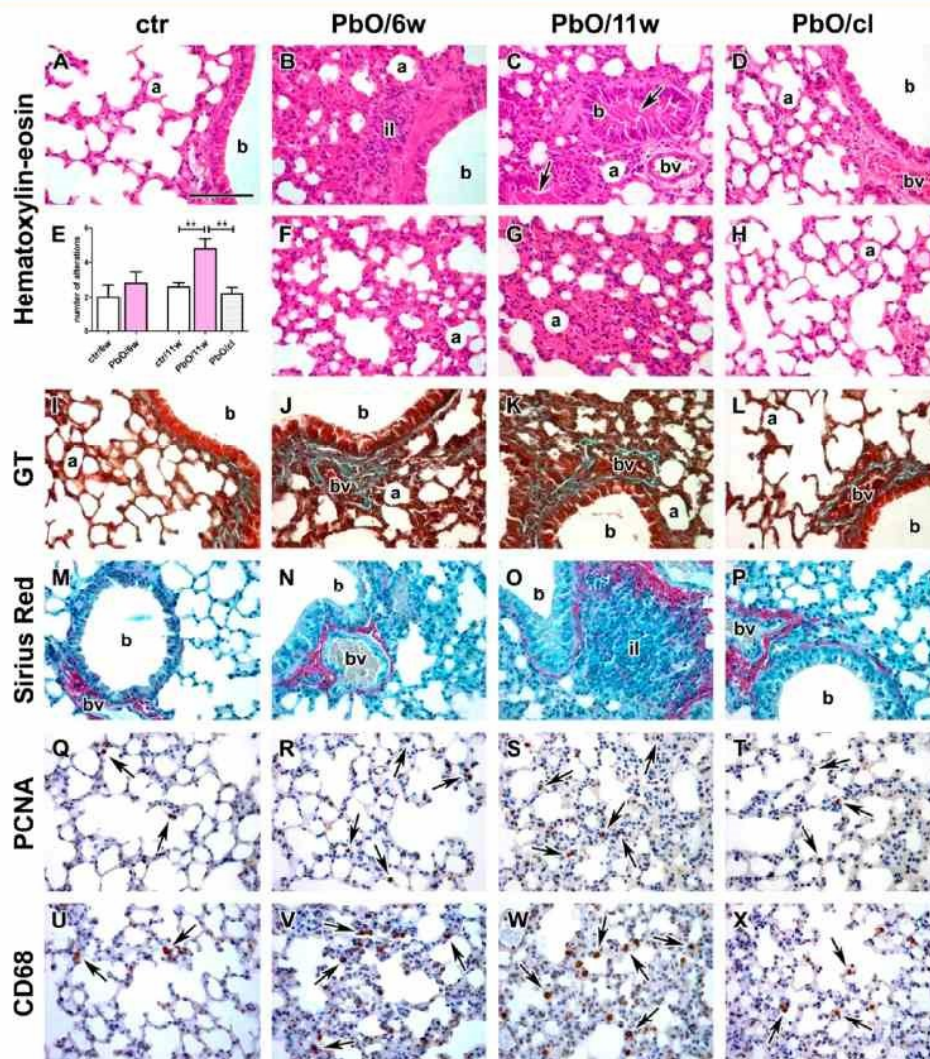


Figure 3. Effect of PbONP inhalation and its clearance on the lung. (A) Lungs in control animals. (B, F) Lungs after 6 weeks of PbONP inhalation exhibited peribronchiolar inflammatory infiltrates of leukocytes (il) and remodeling in alveolar areas (a). Alveolar septa were thickened. (C, G) Remodeling of lung tissue was detected after 11 weeks of PbONP inhalation. Arrows show bronchioles (b) filled with mucous secretion. (D, H) Lung after 5 weeks of clearance without significant pathological changes. (E) Statistical evaluation of the histopathological changes after 6 and 11 weeks of PbONP inhalation in the experiments according to Table S1. The graph values denote average \pm SD; $***p < 0.01$ compared with the corresponding group. (I–P) Collagen fibers (I–L, green; M–P, red) are detected only around blood vessels and bronchioles in all groups. (Q–T) PCNA in lung tissue. Arrows show PCNA-positive cells. There is a higher number of proliferating cells after PbONP exposure in alveolar areas. (U–X) Detection of CD68-positive cells (marker of macrophages) in the lungs. The number of macrophages was increased in the PbONP groups (arrows). Scale bar in all panels = 100 μ m.

However, the relationship of ALP to P and changes of phosphorus level in blood during nanoparticle exposure have not been carefully analyzed and explained yet.

We observed the decrease of ALP at the end of the experiment in the clearance group, and the levels of phosphorus were changed in PbONP-exposed groups during the whole experiment, which can be associated with the alteration in kidney function. During metal exposure, the

kidney can display disruption of phosphate reabsorption in the proximal renal tubules. The kidney damage inflicted by lead poisoning has been previously described, and it is well known.²¹ The proximal renal tubular dysfunctions decrease phosphate levels in the blood, even reaching hypophosphatemia levels.^{53,54} As we observed changes of Na–K-ATPase expression in these proximal canals, fluctuations in blood phosphate level indicate functional alteration of proximal canal

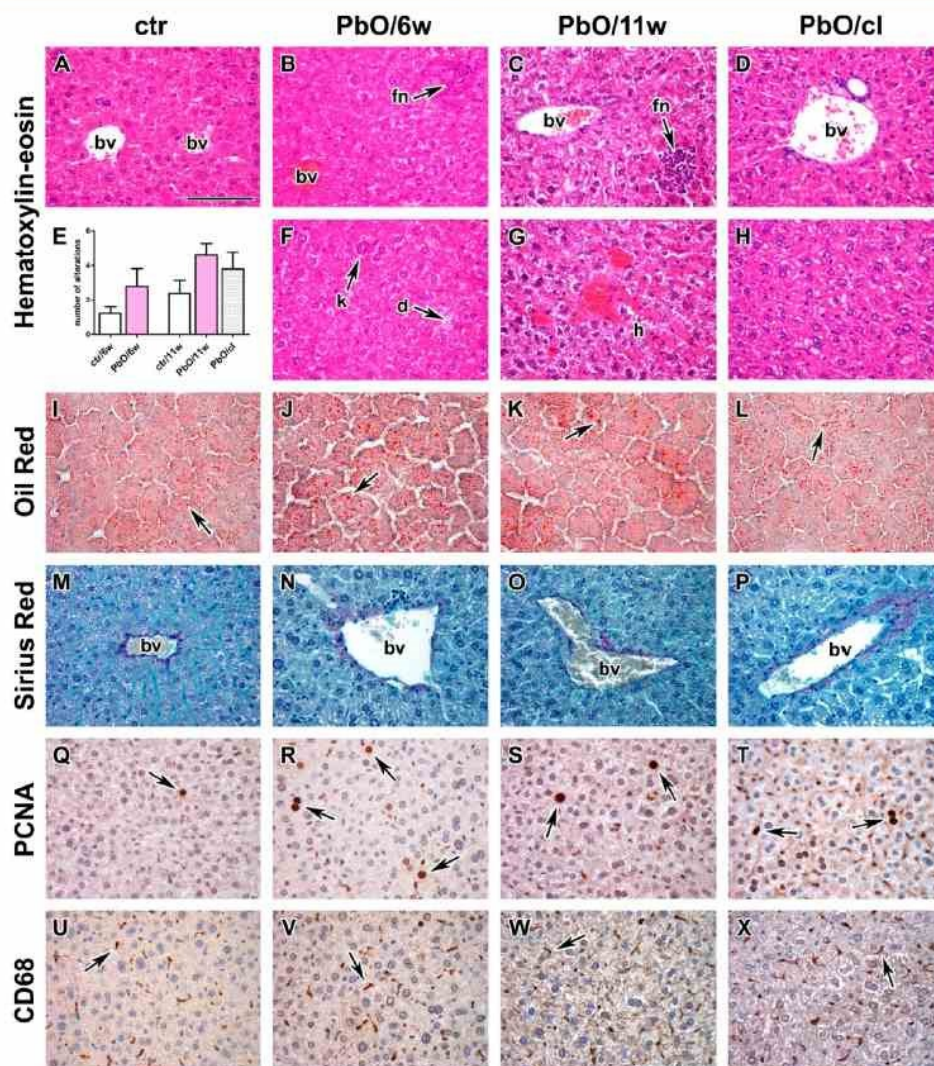


Figure 4. Effect of PbONP inhalation and its clearance on the liver. (A) Liver in control animals. (B, F) Presence of focal necrosis (fc), karyomegaly (k), and dystrophy (d) of hepatocytes after 6 weeks of PbONP inhalation. (C, G) Focal necrosis (fc) and hemostasis (h) in small veins and sinusoids after 11 weeks of exposure to PbONPs. (D, H) Liver without remodeling of parenchyma after 5 weeks of clearance. (E) Statistical evaluation of the histopathological changes after 6 and 11 weeks of PbONP inhalation in the experiments delineated in Table S2. The graphs values denote average \pm SD. (I–L) Oil Red staining of lipid droplets (arrows). Only a small amount of lipid droplets was detected in control samples. Microvesicular steatosis was present after PbONP exposure. Liver after clearance exhibited a decreased level of microvesicular steatosis. (M, P) Sirius Red staining. Collagen fibers (red) were presented only around blood vessels (bv). There was no change in location or amount of collagen in all groups. (Q–T) PCNA in the liver. Arrows show PCNA-positive hepatocytes and macrophages (T). There was no significant change in proliferation. (U–X) Detection of CD68-positive cells (arrows) in the liver (marker of macrophages). The number of macrophages was similar in all groups. Scale bar in all panels = 100 μ m.

membranes and failure of phosphate reabsorption, although significant morphological changes have not been observed following PbONP inhalation at this low concentration.²⁸ One possible significance of low phosphorus level in blood can be related to the instability of cell membranes due to low ATP levels and/or the alteration of cell signaling through different

phosphorylation status of key signaling proteins in affected cells.

However, the elevated phosphate level observed at 6 weeks of exposure could be caused by increased compensatory mechanisms of kidney function after subchronic exposure to metal nanoparticles. To follow these effects and significance of

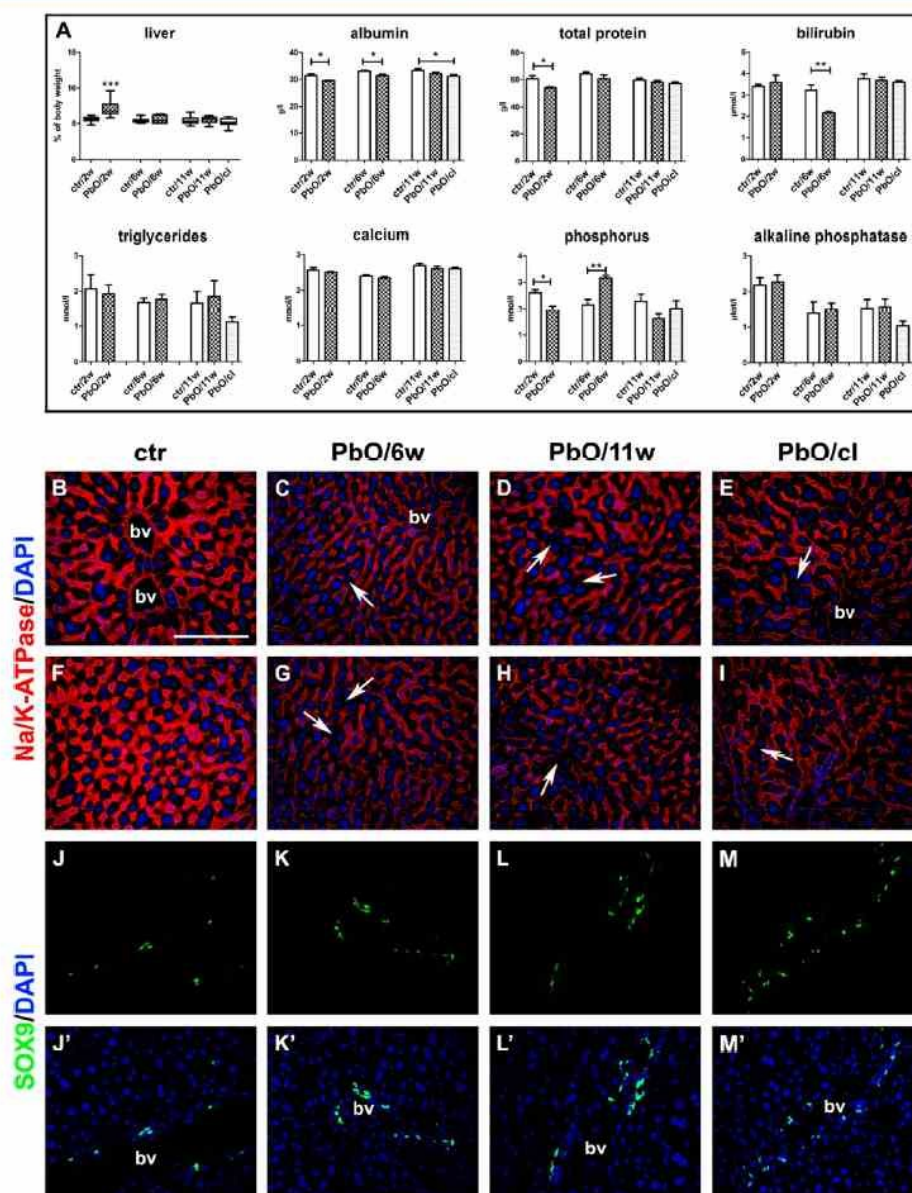


Figure 5. Effect of PbONP inhalation on selected biochemical parameters in the blood. The effect of PbONP inhalation and its clearance on the liver. (A) Graph of liver weight coefficient at designated time points. Graphs of blood level of albumin, total protein, bilirubin, triglycerides, calcium, phosphorus, and alkaline phosphatase at designated time points. Graph values denote average \pm SD for 5 mice/group, $*p < 0.05$, $**p < 0.01$, and $***p < 0.001$ by unpaired *t* test. (B–I) Immunostaining of Na/K-ATPase. Arrows indicate areas without positivity on membranes of hepatocytes in PbONP groups. Hepatocytes exhibited variability in size and irregular organization. (J–M') Immunostaining of protein SOX9 (J–M: SOX9; J'–M': SOX9/DAPI). SOX9-expressing cells were in portal areas and in bile ducts. A higher number of SOX9-positive cells was detected after PbONP inhalation. bv: blood vessel. Scale bar = 100 μ m.

metal nanoparticle exposure on blood, P and ALP levels will probably be a very attractive topic for further research.

Lung Tissue Exhibited Sufficient Ability to Repair the Injury Caused by PbONP Inhalation. The histopathological analysis of the lung after 3 days of PbONP exposure (acute)

revealed no sign of inflammatory infiltration or increased expression of any other analyzed markers of inflammation (Figure S1). Our analysis was focused on the determination of the increased presence of mastocytes (detected by toluidine blue labeling), immunohistochemical labeling of neutrophils

(detection of myeloperoxidase; MPO), and macrophages (CD68 detection). The number of mastocytes, neutrophils, or macrophages was not changed after 3 days of exposure to PbO nanoparticles.

After subchronic PbONP inhalation, morphological alterations and tissue damage were observed mainly in the lungs as a primary target. The level of pathological alteration increased with the duration of inhalation and the amount of inhaled PbONPs. The lungs of exposed animals exhibited several signs of inflammation such as hyperemia, thickened alveolar septa with increased cellularity, a higher number of macrophages (often foamy macrophages were present), regions with peribronchial and perivascular lymphocyte infiltrates, and areas of atelectasis and focal bronchiolitis or alveolitis (Figure 3, Table S1). In some areas, serious damage of the lung parenchyma with destroyed septa and initiated alveolar emphysema were detected.

Despite severe alteration of lung tissue, fibrosis was not detected by Sirius Red staining (Figure 3). The number of TUNEL-positive cells (apoptotic cells) in the lungs of control animals, animals undergoing 11 weeks of PbONP exposure, and animals after clearance was not altered (data not shown). The numbers of proliferating cells (PCNA-positive cells) and CD68-positive cells (macrophages) were significantly increased, predominantly in the alveolar septa, after 11 weeks of inhalation (Figure 3).

The decreased level of pathological changes in the lungs after clearance was observed in all analyzed animals (Figure 3, Table S1). The severity of bronchiolitis and peribronchial infiltrates decreased. Alveolar emphysema destroying the alveolar septa was not observed. The lungs of animals after clearance exhibited mostly hyperemia in the alveolar septa and the presence of perivascular infiltrates. The lungs were evenly ventilated in all parts. All these characteristics observed after clearance were consonant with the sufficient ability of the lungs to repair the injury caused by PbONP inhalation.

Our recent and previously published results indicate that the lungs, after PbONP exposure, exhibit various signs of inflammation and focal destruction of the lung parenchyma depending on the nanoparticle concentration and exposure time, similar to what has been found upon inhalation of TiO₂ NPs or Co NPs.^{28,55,56} Nevertheless, focal microscopic changes in the lungs are often observed after exposure to different types of inhaled pollutants of nonliving etiology, such as metal nanoparticles TiO₂ NPs and NiO NPs as well as living etiology, such as bacteria or viruses.^{55,57–60}

Taken together, after clearance, all analyzed features corresponded with sufficient ability of the lungs to repair the injury caused by PbONP inhalation.

Clearance Period Increased the Amount of Progenitor Cells in the Liver. In our previous study, the liver was identified as the secondary target organ with the most significant changes after subchronic inhalation of PbONPs (6 weeks) in comparison to only a mild effect on the kidney, spleen, or brain.²⁸ After 11 weeks of inhalation, the most significant alterations in the liver were remodeling of the hepatic parenchyma and severe hemostasis (Figure 4).

Further, we observed hypertrophy affecting centrilobular hepatocytes, an increased amount of binucleated and multinucleated hepatocytes, and/or karyomegaly of hepatocytes. Hematopoietic islands were present in a higher amount compared to controls. Hemostasis was seen in small veins and liver sinusoids, while hemorrhages surrounded with necrotic

cells developed in some areas. An increased number of mononuclear cells was observed in portal areas. Microvesicular steatosis was confirmed by the electron microscopy and Sudan staining. Focal necrosis and dystrophy of hepatocytes were also apparent. Despite severe alteration of liver tissues, liver fibrosis was not detected (Figure 4M–P). Liver, after PbONP exposure, exhibited various signs of tissue and cell nuclear remodeling in relation to the duration of the experiment (Table S2), similar to a study with CdO NPs.⁶¹ After 5 weeks of clearance, hemostasis returned to a physiological level and normal liver architecture was restored. Still, some hypertrophic hepatocytes and small infiltrates in the portal area or liver parenchyma remained present.

The number of proliferating (PCNA-positive cells) cells was only slightly increased after 11 weeks of PbONP inhalation. PCNA-positive cells were mainly Kupffer cells, myofibroblasts in the portal area, cells in hematopoietic islands, or some mononucleated or binucleated hepatocytes (Figure 4Q–T). A similar number of PCNA-positive cells was detected in clearance samples. The number of apoptotic cells (TUNEL-positive cells) was found to be the same in controls and PbONP-exposed animals (data not shown). Similarly, clearance did not affect the number of TUNEL-positive cells in the liver (data not shown). The number of Kupffer cells detected by CD68 antigen (Figure 4U–X) was similar in all analyzed groups, indicating only a mild burn in the liver caused by lead exposure.

Na/K-ATPase is the enzyme in the plasmatic membrane of animal cells that is responsible for ion transport and cell size regulation.⁶² The expression of Na/K-ATPase was down-regulated in PbO-treated animals, and the clearance did not rescue the loss of its expression (Figure 5B–I). This result indicates functional changes in hepatocyte membranes following lead exposure, which display no full repair of liver tissue function even after 5 weeks of clearance.

The extent of progenitor cells in adult organs correlates with an organ's ability to replace damaged cells and thus repair an injury. As markers of progenitor cells, we used SOX proteins, which are transcription factors exhibiting tissue specificity in their expression.^{63,64} In the liver, SOX9-positive progenitor cells were found in the epithelial lining of the bile ducts, as was previously described.⁶⁵ SOX9-positive cells were also some hepatocytes in the periportal area, also called hybrid hepatocytes or activated stellate cells.^{66,67} Here, we observed a higher number of SOX9-expressing cells after PbONP exposure at all time points in periportal areas and bile duct epithelial cells (Figure 5J–M), which corresponds to higher regeneration of liver tissue during the entire experimental period. An increased number of SOX9-positive progenitor cells was also documented in other studies after various liver injuries.^{65,68}

Moreover, we noticed a significantly elevated weight of the liver after 2 weeks of PbONP inhalation (Figure 5A). Increased liver weight correlated with a lower blood level of total protein and protein albumin and indicated a higher burden on the liver (Figure 5A). Later (after 11 weeks exposure), levels of albumin and total protein increased, and the values returned to their physiological levels. However, it is necessary to note that all values of total protein and albumin occurred in the reference range for female mice at the analyzed time points. Taken together, these observed liver features illustrate the ability of this organ to effectively react to an increased lead load during the time of the experiment. However, 5 weeks' clearance did

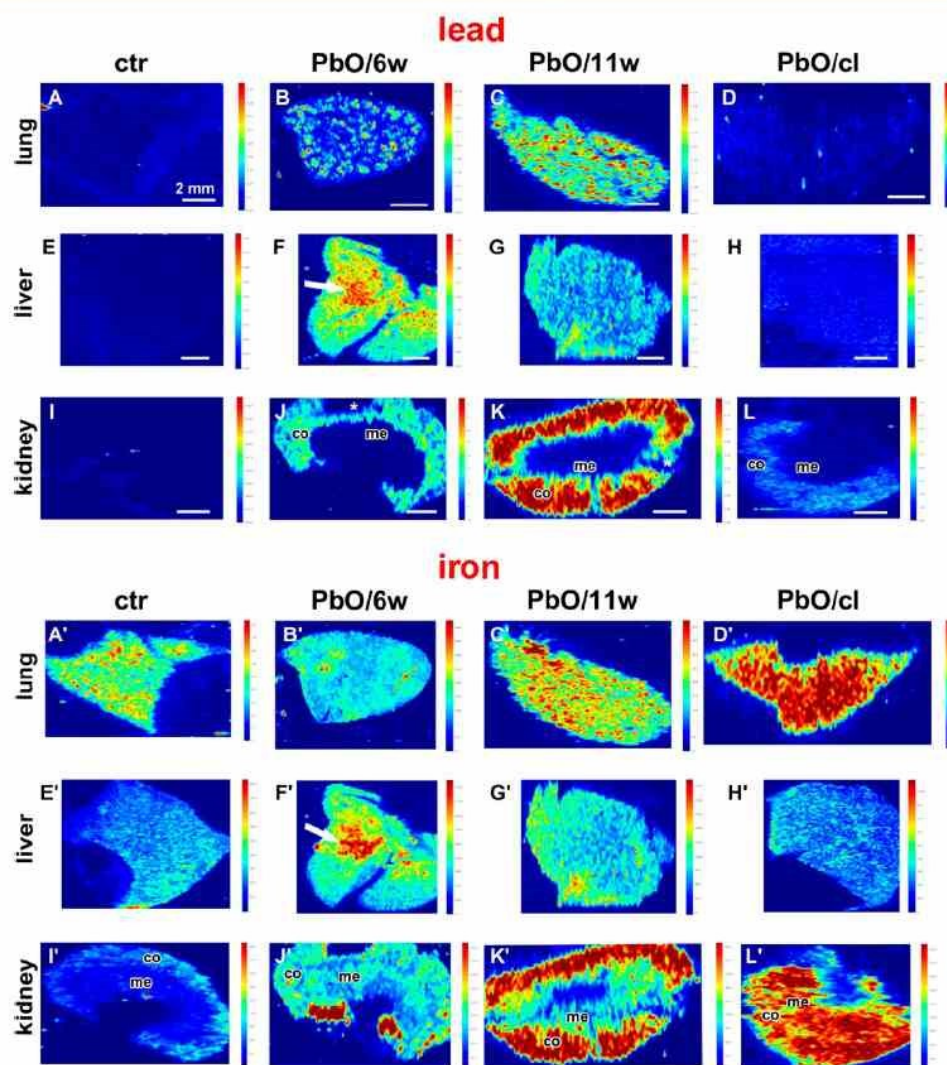


Figure 6. Lead and iron distribution in the lung, liver, and kidney at designated time points after PbONP inhalation. (A–D) Lead distribution in controls, PbO groups, and clearance group of animals analyzed in lung samples using laser ablation inductively coupled plasma mass spectrometry (LA-ICP-MS). Control lungs (A) were without lead positivity. Distribution of lead was regular in all parts of the lung after treatment (6 and 11 weeks (B, C)). Clearance lungs (D) were without lead positivity. (E–H) Lead distribution in controls, PbO groups, and clearance group of animals analyzed in liver samples. Control liver (E) was without lead positivity. Distribution of lead was irregular, with the highest content of lead in central areas of the liver lobule (white arrow) after 6 weeks of PbONP exposure (F), while after 11 weeks, the lead was distributed rather in a symmetric manner in the liver lobule (G). In the clearance group (H), we observed a decreased level of lead in the liver lobule. (I–L) Lead distribution in controls, PbO groups, and clearance group of animals analyzed in kidney samples. Control kidney was without lead positivity (I). After PbONP inhalation, lead was detected only in the kidney cortex (co), not in the medulla (me). The highest positivity for lead was detected after 11 weeks of PbONP inhalation in the kidney cortex (K). Lead was still present in the kidney cortex after 5 weeks of clearance (L). (A'–D') Iron distribution in controls, PbO groups, and clearance group of animals analyzed in lung samples. Distribution of iron depends predominantly on the vascularization in a given organ. The highest level of iron was in the clearance group (D'); the distribution of iron was regular in all parts of the lung at all designated time points. (E'–H') Iron distribution in controls, PbO group, and clearance group of animals analyzed in liver samples. The distribution of iron in controls and clearance group was regular in all parts of the liver parenchyma, contrary to an uneven and high allocation predominantly after 6 weeks of PbONP inhalation. Interestingly, the highest positivity for iron was observed in the same area as for lead (F', G'). (I'–L') Iron distribution in controls, PbO groups, and clearance group of animals analyzed in kidney samples. The highest positivity for iron was observed in large branches of renal vessels adjacent to the renal hilus (J'), followed by the kidney cortex at all designated time points. The higher content of iron was present in the kidney cortex after 11 weeks of PbONP exposure (K') and after the clearance period (L'). *Missing tissue. Scale bar: 2 mm.

3107

<https://dx.doi.org/10.1021/acsnano.9b08143>
ACS Nano 2020, 14, 3096–3120

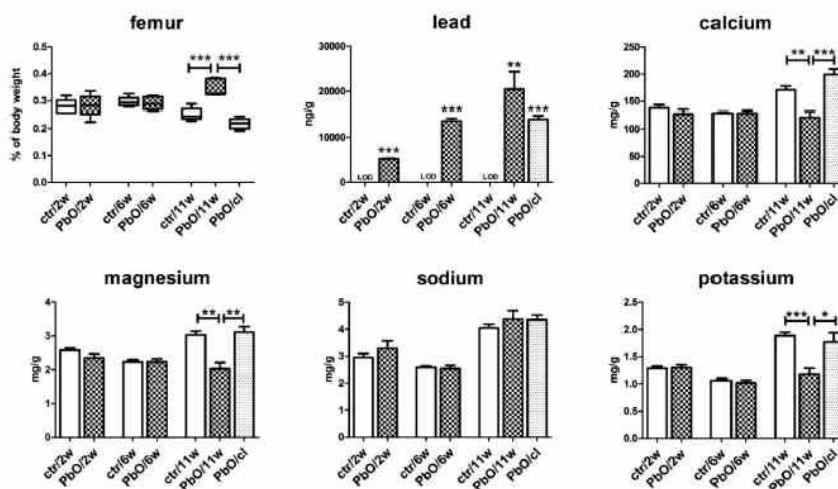


Figure 7. Femur weight coefficient and the concentrations of selected elements in bone after PbONP inhalation at designated time points. The graph values denote average \pm SD, * $p < 0.05$, ** $p < 0.01$, *** $p < 0.001$ by unpaired t test.

not have an outstanding positive effect on hepatocyte function, as shown by disrupted membrane function.

No Significant Changes in Kidney Morphology Were Observed. The kidney was evaluated microscopically, as lead is primarily excreted by this organ. We did not see damage in either the glomerular or tubular parts of the kidney (Figure S2). In humans, there is well-known nephrotoxic effects of lead at blood concentrations higher than 50 $\mu\text{g}/\text{dL}$ in children or 40 $\mu\text{g}/\text{dL}$ in adults.²¹ However, in our study, the lead in the blood reached a maximum of 17 $\mu\text{g}/\text{dL}$, which corresponds to the absence of significant morphological damage of kidney tissues under our experimental conditions.

Lead Was Uniformly Distributed throughout Lung Tissue. Further, we wanted to analyze the distribution of lead throughout the exposed tissues and the possible differences in lead accumulation in certain structures. Different analytical methods such as atomic absorption spectrometry (AAS) or inductively coupled plasma mass spectrometry (ICP-MS) were previously recommended for lead analysis in tissue samples.²¹ Elemental imaging (LA-ICP-MS) is a modern technique of elemental analysis, ideal for bioimaging of metals in tissues; however, quantification of metal levels is sometimes difficult due to a lack of standard reference materials.⁶⁹

The elemental imaging of mouse lungs after inhalation of PbONPs (6 and 11 weeks) uncovered the presence of lead evenly distributed throughout lung tissue (Figure 6B,C). The regions with large branches of bronchi and vessels exhibited the smallest lead content. The main destination areas, with the highest concentration of lead, were small respiratory units such as the alveolar ducts and alveoli. After the clearance period, a reduced level of lead in the lungs was clearly observed, nearly reaching the LOD (limit of detection) (Figure 6D). The concentration of lead in the lungs after 5 weeks of clearance measured by AAS was also below the LOD (26 ng/g), which corresponded with the absence of lead detected by LA-ICP-MS. Thus, this elemental analysis confirmed the efficient clearing of PbONPs from the lungs, leading to a restoration of normal state.

LA-ICP-MS Analysis Revealed Uneven Distribution of Lead in the Liver. In the liver, the analysis of elements demonstrated a specific pattern of lead distribution at all analyzed time points (Figure 6E–H). After 6 weeks of exposure, the main amount of lead was located centrally in the liver tissue with a decreasing level of lead concentration toward the periphery. On the other hand, a more homogeneous distribution of lead in the liver tissue was observed after 11 weeks of exposure. After the clearance period, a reduced level of lead in the liver was distinctly detected, reaching almost the LOD level (Figure 6H). The distribution of iron (Figure 6E'–H') was similar to lead after PbONP inhalation. The highest positivity of tissues for iron was observed in the same area as for lead (compare Figure 6F,G and F',G').

Analysis of Lead Distribution Revealed Its Accumulation in the Kidney Cortex. Elemental imaging revealed the massive amounts of lead unevenly distributed in the kidney. A high concentration of lead was found only in the kidney cortex at all analyzed time points (Figure 6J–L). The kidney medulla did not exhibit a detectable amount of lead. Five weeks of clearance led to a reduction of lead amount in the kidney (Figure 6L); however, the cortex remained positive for lead. This finding is interesting in the context of the unchanged morphology observed in the kidney cortex or extensive ultrastructural alteration in the cortex tubules and/or glomeruli. These are, however, in agreement with our previous findings on kidney morphology upon 6 weeks of high concentration of PbONP inhalation.²⁸

Lead Oxide Nanoparticle Inhalation Significantly Altered the Concentration of Calcium in the Liver and Kidney. Previous studies documented that lead interferes with calcium in various cells and tissues because of similarities in ionic radii.^{20,70} The presence of lead can affect the levels of essential metals in organs, including calcium, which also depends on the route of lead administration. Intraperitoneal application of lead was shown to cause an altered level of calcium in secondary target organs (liver, kidney).⁷¹ However, changes in the metabolism of calcium after lead inhalation have not been extensively studied until now.

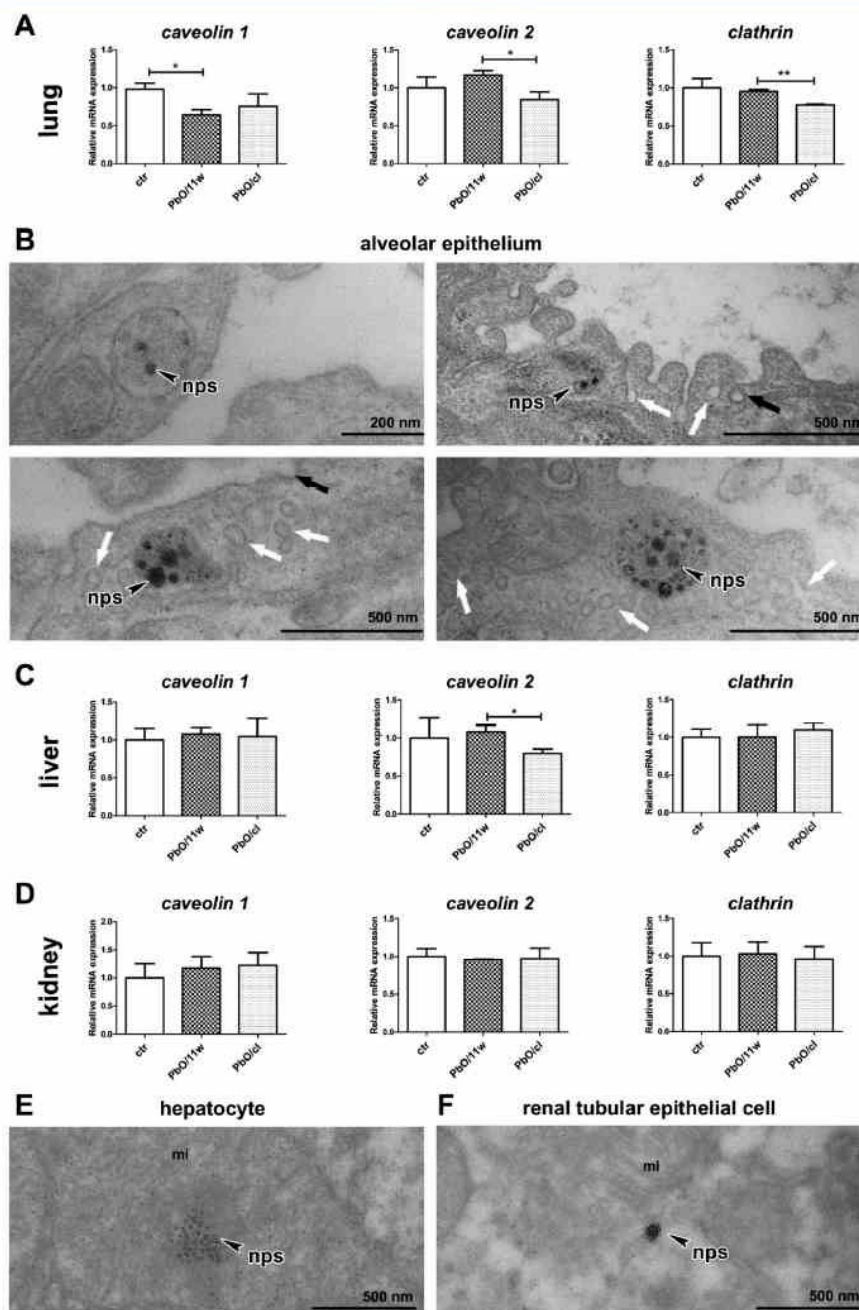


Figure 8. Entry of nanoparticles into cells of lung, liver, and kidney. (A) Effects of PbONP inhalation on relative expressions of genes involved in endocytic pathways (*caveolin 1*, *caveolin 2*, and *clathrin*) in the lung. The graph values denote average \pm SD for 3–5 mice/group, $*p < 0.05$, $**p < 0.01$ by unpaired *t* test. (B) TEM images of alveolar epithelial cells type 1 (PbONPs group) with caveolae (white arrows), clathrin-coated vesicles (black arrows), and clusters of nanoparticles (nps, arrowheads) inside cytoplasmic vesicles. (C, D) Effects of PbONP inhalation on relative expressions of genes involved in endocytic pathways (*caveolin 1*, *caveolin 2*, and *clathrin*) in the liver (C) and kidney (D). The graph values denote average \pm SD for 3–5 mice/group, $*p < 0.05$ by unpaired *t* test. (E) TEM image of hepatocyte mitochondrion (mi, PbONPs group) with agglomeration of nanoparticles inside (nps, arrowhead). (F) TEM image of renal tubular epithelial cell (PbONPs group) with isolated nanoparticle inside the cell cytoplasm (nps, arrowhead) adjacent to a mitochondrion (mi).

Here, we found that PbONP inhalation significantly altered the concentration of calcium in the liver. After 2 weeks of lead inhalation, the calcium concentration in the liver decreased significantly. A similar calcium decrease was previously observed following 3 weeks of intraperitoneal application of cadmium, where the authors expected similarities between cadmium and calcium.⁷² On the other hand, after 11 weeks of PbONP inhalation, we observed significantly increased levels of calcium in the liver in comparison to corresponding controls. The indisputable reason for calcium increase, however, remains unclear.

Similar to the liver, a statistically significant decrease ($p < 0.01$) in calcium concentration was observed in the kidneys after 2 and 6 weeks of exposure. On the other hand, no significant changes in calcium concentration were observed after 11 weeks of exposure and in the clearance group (Figure S3). As calcium and lead are reabsorbed in the same tubule segments, and lead may compete with calcium for reabsorption, impaired calcium reabsorption can cause a reduced level of calcium in the kidney after lead inhalation. However, the opposite behavior was observed in another study, where renal calcium levels increased after lead exposure and were accompanied by higher calciuria.⁷³ Taken together, due to diverse factors (route of application, the length of exposure, used dose) influencing calcium concentration in a given organ during lead inhalation, it is not possible to easily explain the final effect of lead on metabolism of such essential metals such as calcium in internal organs, and further analysis will be necessary.

On the other hand, the levels of other analyzed elements such as sodium and potassium in the liver and kidneys were not affected by PbONPs inhalation (Figure S3).

Clearance Restored the Levels of Calcium and Magnesium in Bones to Their Physiological Values. The main target for lead deposition is the bone matrix, due to its ability to substitute other bivalent cations in the body, such as Ca^{2+} or Mg^{2+} .⁷⁴ The accumulation of lead by replacing calcium in bones was previously described upon exposure to lead salts.^{75–77} However, to our knowledge, only a few studies have analyzed the effect of inhaled lead in the form of submicrometer-sized particles on bone.^{23,78}

Here, the content of lead in bones was the highest among the studied organs (lung, liver, kidney, and spleen) at all time points after PbONP exposure. These results document the ability of PbONPs to incorporate lead into the bone matrix (Figure 7).

After 2 and 6 weeks of PbONP exposure, we did not observe any variations in the content of elements such as calcium, magnesium, sodium, or potassium in bones compared to the respective controls. However, after 11 weeks of PbONP inhalation, the concentrations of calcium ($p < 0.01$), potassium ($p < 0.001$), and magnesium ($p < 0.01$) in bones were significantly reduced in comparison to controls (Figure 7). The level of sodium in bone was not affected by exposure to PbONPs.

After 11 weeks of PbONP exposure, there were also statistically significant differences in the weight of femurs among the exposed, control, and clearance groups, and we observed an unexpectedly higher weight of femurs in exposed animals. In the interpretation of these results, it is necessary to take into account that bone growth continues much longer after sexual maturity in mice and rats than in other animals (e.g., cats, dogs, rabbits).⁷⁹ Female mice achieve sexual

maturity at about one month of age; however, growth plate closure occurs much later, at about the age of five months. There is no synchrony between the onset of puberty and growth plate closure in female mice. At the end of our inhalation experiment (after 11 weeks' exposure), experimental animals reached four months; thus, this time still falls into the period of intensive growth (including the bones) (Figure S4). This is physiologically accompanied by the increased storage of elements (calcium, magnesium, potassium, sodium) into bone tissue, as was also observed in our control animals and clearance group. On the basis of our results, we assume the association of higher deposition of elements into growing bones, which is usual for this specific age, and an increased level of calcium in the blood, which we observed.⁵¹ In our study, the concentrations of analyzed elements (Ca, K, and Mg) were restored to levels corresponding to the controls in bones after 5 weeks of clearance, although the level of lead remained the same.

Interestingly, several other studies with long lead exposure did not find changes in element deposition in the femurs. Following lead exposure of rats, calcium was only slightly decreased after exposure and magnesium was unchanged, even after 90 days.⁸⁰ Additionally, four months of lead exposure in adult mice did not alter calcium levels in bones of controls and lead-treated bones.⁸¹

Together, these data indicate that the effect of lead on bone tissue depends on many factors and that not only the type of lead exposure but also the characteristics of the exposed population have to be considered.

Expression of Genes Controlling the Endocytic Pathway Was Altered in the Lungs and Liver. The type of NPs that enter into cells can influence their final effects on cellular function.⁸² The major process of endocytosis is phagocytosis (occurring in specific immune cells), nonspecific pinocytosis, caveolae endocytosis, and clathrin-mediated endocytosis. Here, we decided to evaluate the cellular mechanisms involved in PbONP entry into cells and analyzed the role of clathrin-mediated and caveolae-mediated endocytosis in mice after 11 weeks of inhalation in primary (lung) and secondary (kidney, liver) target organs.

Alveolar epithelium, especially pneumocytes type I, displayed abundant simple membrane-bounded vesicles and scattered fuzzy clathrin-coated vesicles (CCV) (Figure 8B). The majority of the vesicles present in pneumocytes I are considered as caveolae.⁸³ We observed nanoparticles mainly in membrane-bounded vesicles–caveolae (any case in CCV), so we expected the upregulation of *caveolin 1* or *2* after PbO inhalation, similar to that described in other studies.^{82,84} Moreover, a high level of *caveolin 1* is typical for differentiated epithelial cells such as pneumocytes, endothelial cells, smooth muscle cells, or bronchial epithelial cells in the lungs. On the other hand, low levels of *caveolin 1* can be observed in cancer cell lines originating from lung or breast tumors.^{85,86} Surprisingly, the relative expression of *caveolin 1* in the lungs was statistically significantly reduced after 11 weeks of PbONP inhalation compared to the corresponding control ($p < 0.05$). After clearance, the level of *caveolin 1* increased to the level of the control group of animals. We propose that the observed low expression of *caveolin 1* in exposed animals can be related to the dedifferentiated state of lung epithelial cells after long-term PbONP exposure and an increased number of progenitor cells.

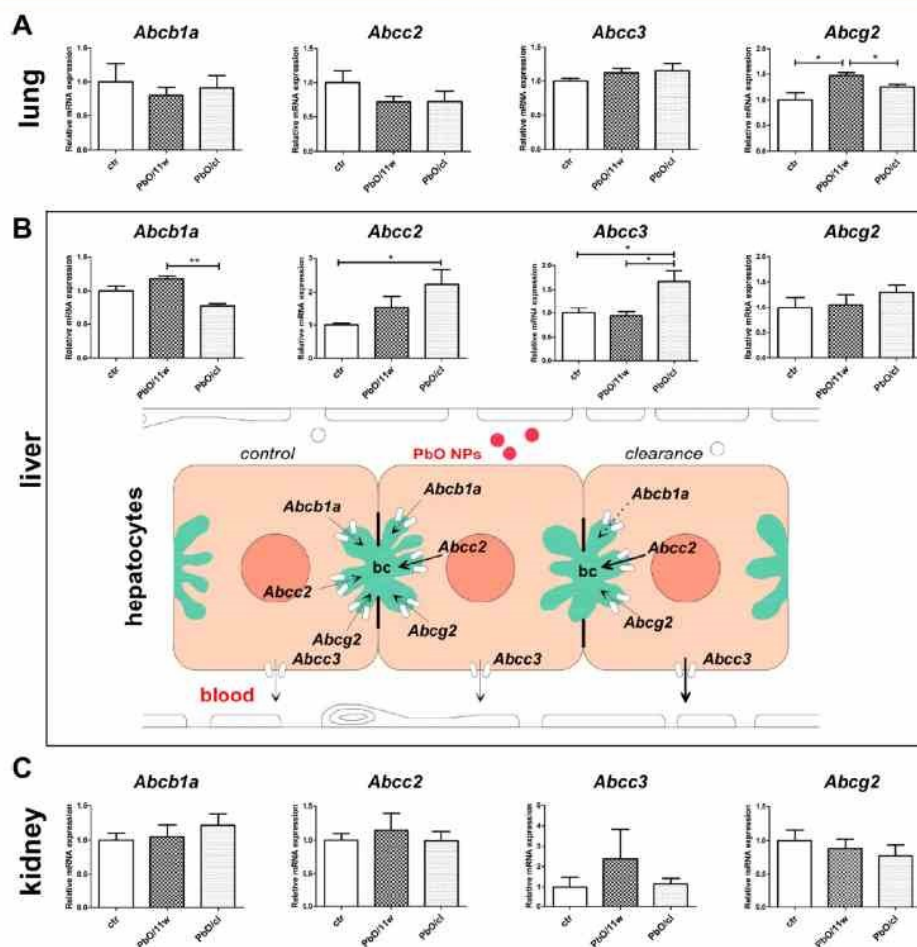


Figure 9. RNA expression levels of ABC transporters in the lung, liver, and kidney after 11 weeks of PbONP inhalation. (A) Effects of PbONP inhalation on relative expressions of transporters *Abcb1a*, *Abcc2*, *Abcc3*, and *Abcg2* in the lung. (B) Effects of PbONP inhalation on relative expressions of transporters *Abcb1a*, *Abcc2*, *Abcc3*, and *Abcg2* in the liver in the graphs and in the scheme of liver parenchyma. *Abcc3* protein is localized in the sinusoidal (basolateral) membrane of hepatocytes, and transporters *Abcb1a*, *Abcc2*, and *Abcg2* are proteins in the canalicular membranes of bile canaliculus (bc). (C) Effects of PbONP inhalation on relative expressions of transporters *Abcb1a*, *Abcc2*, *Abcc3*, and *Abcg2* in the kidney. The graph values denote average \pm SD for 3–5 mice/group, * $p < 0.05$, ** $p < 0.01$ by unpaired *t* test.

On the other hand, the relative expression of *caveolin 2* in lungs was increased after 11 weeks of exposure to PbONPs (Figure 8A). The level of *caveolin 2* after clearance was restored to the level typical for corresponding controls (*caveolin 2* was suppressed significantly ($p < 0.05$)). This means that while PbO exposure caused upregulation of *caveolin 2*, the clearance significantly decreased its expression level. Moreover, the expression of *caveolin 2* in lungs did not correspond to the level of *caveolin 1* previously described in cancer cell lines.⁸⁶ The exact relationships between *caveolin 1* and *2* are still not completely understood. Today, some authors even denote *caveolin 1* and *2* as antagonistic partners in various processes including endocytosis or the inflammatory response.⁸⁷ Our findings support this antagonistic relationship; however, the exact molecular mechanism of their functions and response to lead exposure needs to be further investigated.

Clathrin-coated vesicles were present in alveolar macrophages in higher quantities than in pneumocytes in our exposed animals. This finding corresponds to other previously published studies.^{86,88} In our animals, the relative expression of *clathrin* was not changed after PbO inhalation; however, clearance significantly downregulated *clathrin* expression. These data demonstrate the possible role of lung macrophages, which contain abundant CCV, during lung clearance.

In the liver, PbONP exposure caused upregulation of *caveolin 2*, and clearance statistically significantly decreased its expression. The levels of *caveolin 1* and *clathrin* were not significantly altered, similar to changes observed in lungs after lead inhalation (Figure 8C). The effect of lead inhalation on the level of *caveolins* in the liver does not offer a simple explanation since *caveolins* modulate a wide range of cellular events. *Caveolins* can be found not only in superficial caveolae

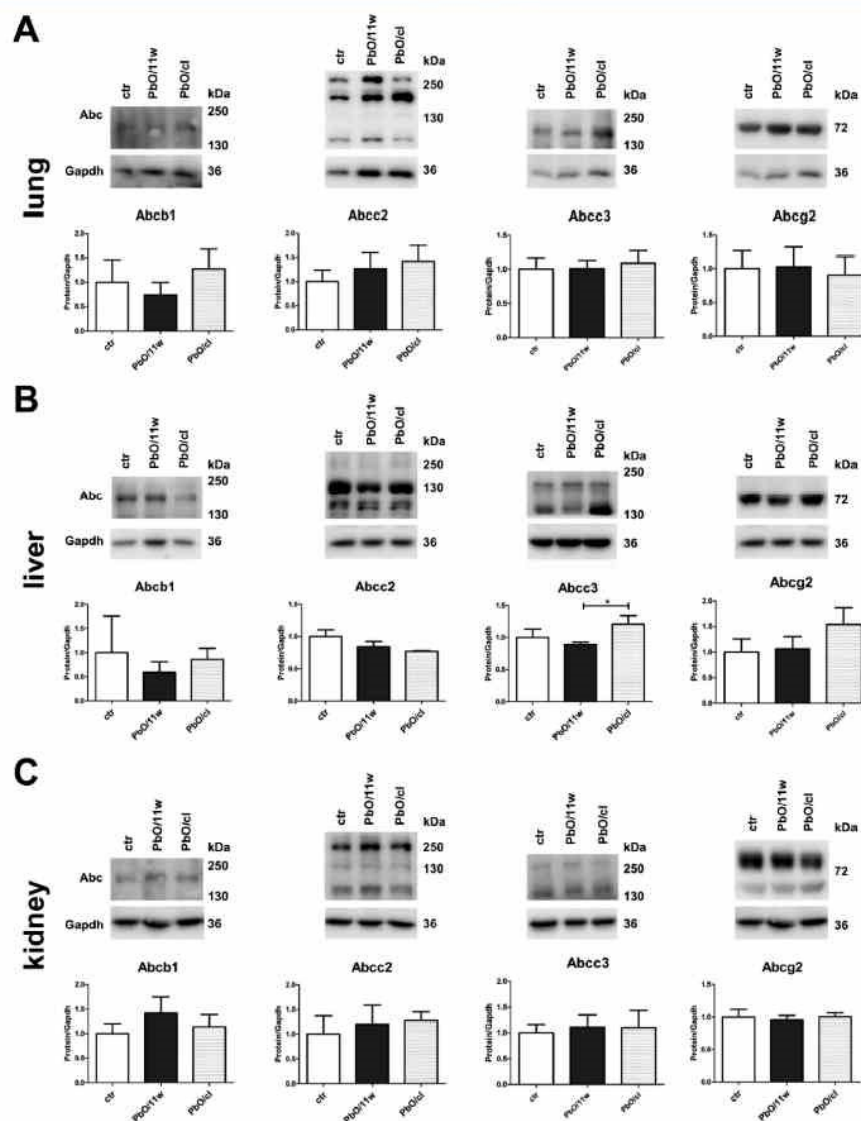


Figure 10. Protein expression levels of ABC transporters in the lung (A), liver (B), and kidney (C) after 11 weeks of PbONP inhalation. The quantitative comparison of ABC transporter levels was normalized to GAPDH levels; the graph values denote average \pm SD for 3–5 mice/group.

but also in cell compartments such as mitochondria, Golgi, nucleus, or lipid droplets, and both caveolins participate not only in endocytosis but also in lipid metabolism, inflammation, and proliferation.⁸⁷ PbONPs in the liver were accumulated in the mitochondria of the hepatocytes (Figure 8E). Thus, reduced expression of *caveolin 2* after clearance can indicate altered trafficking of nanoparticles through the hepatocyte mitochondria. However, another cause of decreased expression of *caveolin 2* could be alteration of lipid processing and their accumulation (steatosis) observed after PbONP inhalation, as *caveolin 2* is also involved in lipid metabolism.⁸⁹

PbONPs in the kidneys (Figure 8F, Figure 2) were found to be located freely in the cytoplasm of the epithelial cells of nephron tubules; thus, our data support the hypothesis that PbONPs in this secondary organ probably do not need any specific transport endocytic mechanism and pass easily through kidney biological membranes, as was documented for other types of metal nanoparticles.⁸² Here, no statistically significant changes were observed in the expression of all analyzed genes (*caveolin 1*, *caveolin 2*, *clathrin*) among controls, PbO-exposed groups, and clearance groups (Figure 8D).

ABC Transporters Were Significantly Deregulated in the Lungs of Animals Exposed to PbONPs. The family of mammalian ABC transporters consists of 48 members, and these can be expressed as channels, receptors, and transporters and serve as efflux transporter proteins protecting cells.⁹⁰ ABC transporters play crucial roles in detoxification by transporting a wide variety of endogenous compounds and xenobiotics such as drugs, toxic chemicals, or heavy metals.⁹⁰ They are predominantly expressed in excretory organs (liver, kidney) or physiological barriers such as the blood–brain barrier, blood–placenta barrier, or blood–air barrier in the lungs. In these barriers, ABC transporters function to limit the accumulation of drugs.⁹¹ Previous studies have demonstrated that heavy metals can be eliminated from cells by some ABC transporters; however, the precise role of ABC transporters in heavy metal efflux or nanoparticle removal from cells has not yet been analyzed.²⁵

Here, we assessed the role of several ABC transporters (ABCB1a, *p*-glycoprotein; ABCC2, MRP2; ABCC3, MRP3; ABCG2, BCRP) in the clearance of lead nanoparticles from lungs, livers, and kidneys (Figure 9A–C).

ABCB1 (*p*-glycoprotein), several transporters from subfamily “C”, and ABCG2 (BCRP) belong to the main transporters with large significance in drug efflux. In the lungs, ABCC2 (MRP2) and ABCC7 (CFTR) were found to be expressed in the apical parts of the epithelial cells, and ABCG2 was found to be expressed as a transporter in the lungs of dairy animals.^{92,93} However, to our knowledge, the possible involvement of any ABC transporter in lead clearance from the lungs has not been studied yet.

In the lungs, the expression levels of *Abcb1a* and *Abcc2* were only slightly decreased without statistical significance among controls, the 11-week PbONP inhalation group, and the clearance group (Figure 9A). Moreover, clearance partially restored their expression to the level of corresponding controls. Several single nucleotide polymorphisms were reported in *Abcb1*; thus, more significant outcomes can be observed during experiments with other isoforms of analyzed genes (such as *Abcb1b*, *Abcb1c*), which will require further analysis.⁹⁰ Also, the protein analysis of ABCB1 in the lung exhibited a similar expression pattern to the mRNA level (Figure 10A).

On the other hand, the mRNA expression level of *Abcg2* was statistically significantly upregulated ($p < 0.05$) after 11 weeks of PbONP inhalation, and the expression level was rescued in the clearance group ($p < 0.05$), while on protein level changes were just minute (Figure 10A). Increased expression of protein ABCG2 was previously found in lung stem cell populations.⁹⁴ Moreover, increased levels of this protein were observed after exposure to fine particulate matter (PM_{2.5}), and it was used as a marker of cancer stem cells in the lung.⁹⁵ PM_{2.5} samples were collected from polluted cities and displayed the abundant presence of metal ions, such as Fe, Al, Cu, and Pb. In our experiment, the gene *Abcg2* was identified as being significantly deregulated by PbONP inhalation. Thus, the ABCG2 transporter can be involved in lead transport from the pneumocytes; however, a functional assay with specific ABC transporter inhibitors has to follow these findings in the future. Unquestionably, the additional types of ABC transporters or SLC transporters can also play a role in complex molecular processes contributing to efficient cellular mechanisms of lead clearance from the lungs.

Different ABC Transporters Were Deregulated in the Livers of PbONP-Exposed Animals. ABC transporters in

the liver play crucial roles in bile formation and detoxification of exogenous compounds. The function of ABC transporters in heavy metal efflux was studied predominantly in fish or *in vitro* in cell lines.^{91,96–98} The increase in metal drug efflux by ABC transporters is also a major mechanism of multidrug resistance in tumor cells. However, to our knowledge, the role of any ABC transporter in lead clearance from the liver in mammals has not been analyzed yet.

Here, we investigated the transporters ABCB1a, ABCC2, and ABCG2, which are proteins in the canalicular (or apical) membranes of hepatocytes, and the ABCC3 protein localized in the sinusoidal (basolateral) membranes of hepatocytes.^{99–101} In the liver, the expression level of *Abcb1a* was statistically significantly downregulated ($p < 0.01$) in the clearance group (Figure 9B) at the RNA level; however protein analysis did not exhibit significant changes (Figure 10B). The *Abcc2* gene in mouse liver was upregulated in the inhaled group and statistically significantly in the clearance group relative to the controls just on the RNA level (Figure 9B). This was also observed in zebrafish liver exposed to lead for 24 h.⁹¹ The *Abcc2* gene is predominantly involved in bilirubin excretion into the bile canaliculus; therefore lead efflux into bile can represent one of the possible mechanisms involved in their removal from hepatocytes.¹⁰⁰ As lead can alter the expression of this gene, changes in bile production could occur following PbONP exposure. Interestingly, the alteration in gene expression of *Abcc2* correlates with the observed decreased level of bilirubin in blood after 6 weeks of PbONP inhalation, which could be affected by the upregulation of this gene.

The *Abcc3* gene was significantly upregulated in the liver in the clearance group at both the mRNA and protein level (Figures 9B, 10B). This gene has been suggested as mediating the removal of toxic anions from hepatocytes, predominantly into sinusoidal blood due to its high affinity for glucuronide conjugates; however, its role in heavy metal clearance is less clear.¹⁰⁰ On the other hand, the expression level of *Abcg2* was not altered in the liver parenchyma (Figures 9B, 10B).

Previously, the effects of gold nanoparticles on gene expression of different ABC transporters (including ABCB1, ABCC2, ABCC3, and ABCG2) have been investigated in human hepatocellular carcinoma cell lines.¹⁰¹ Gold nanoparticle treatment significantly downregulated the levels of all these genes. This is in contrast with our findings where upregulation of several transporters was observed following the inhalation of PbONPs. Thus, the results from our recent analysis demonstrate that the upregulation of ABC transporters in the liver can be an important mechanism for the clearance of lead from this organ. It is possible that some ABC transporters could be modulated by oxidative stress signaling, as proposed in another study with heavy metals, which will be interesting to follow in the future.¹⁰²

Expression of ABC Transporters in the Kidneys Was Not Significantly Altered in Animals Exposed to PbONPs. Previously, ABCC2 (MRP2) and ABCG2 (BCRP) were proposed as being the main ABC transporters involved in lead efflux from the kidneys.²⁵ Following PbONP inhalation, we identified only a small upregulation of *Abcc2* gene expression (Figure 9C) or protein level (Figure 10C). The levels of gene expression of *Abcg2* were practically unaltered. Therefore, we also analyzed other members of these transporters and observed increased expression levels of *Abac3* after PbONP inhalation, while clearance restored the

lead level to that of the corresponding controls. However, observed changes in gene or protein expression were not statistically significant due to higher variability among animals (Figures 9C, 10C).

As quantification of small expression changes from tissue samples can be affected by high variability among biological replicates, the involvement of ABC transporters in kidney lead clearance will be essential to further follow.

CONCLUSIONS

The actual production and use of the enormous amount of nanosized particles in all branches of human activities has caused increased nanoparticle exposure to the human organism. Research concerning the unique positive features of NPs has the same priority as research regarding its possible negative effects on live cells and tissues. The inhalation of NPs is the most frequent route of exposure to NPs of all types, including metal NPs. Understanding of mechanisms contributing to nanoparticle clearance represents a key question whose revealing will enable the prevention of and/or eliminate the damage resulting from exposure to metal NPs.

Here, we uncovered high variability in the ability to clear inhaled lead nanoparticles among individual organs, with the highest ability being found in the lungs and the lowest in long bones. Our data suggested ABCC3 as a possible transporter involved in clearance of Pb/PbONPs in the liver and ABCG2 transporter in the lungs. Moreover, the expression of *caveolin 1*, *caveolin 2*, and *clathrin* demonstrated tissue-specific responses to lead exposure and its clearance. Especially in the lungs, *caveolin 1* and *caveolin 2* expression was partially rescued during the clearance period. We envisage that a detailed understanding of mechanisms by which individual organs physiologically remove lead nanoparticles will help to design advance strategies of how such mechanisms can be enhanced to more effectively fight against increasing exposure to environmental pollutants.

METHODS

Animals. Adult female mice (CD-1(ICR) BR strain) were obtained from the Animal Facility of the Masaryk University (Brno, Czech Republic) and were allowed to acclimatize to laboratory conditions for at least 1 week before the inhalation experiments. Commercial feed and drinking water were provided *ad libitum*.

Preparation of PbONPs. PbONPs were prepared in the same way as in a previous study.²⁸ PbONPs were generated continuously *in situ* in a hot-wall tube flow reactor using an evaporation–oxidation–condensation technique in which a ceramic crucible containing a small amount of lead wire was placed inside the ceramic work tube of a vertically oriented furnace (Carbolite TZF 15/50/610). The molten lead was evaporated at the center of the furnace at a temperature of 830 °C. The formed metal vapor condensed to form Pb NPs, which were carried out of the furnace by an inert nitrogen gas stream and diluted with a stream of air, during which the lead was oxidized to lead oxide. Both flow rates were set at 3 L/min using mass flow controllers. Resulting PbONPs were diluted in the second step by a stream of air (20 L/min) and used for whole-body inhalation experiments.

Exposure to PbONPs. The characteristics of the inhalation chambers have been described in a previous study.²⁷ Adult female mice, with an average weight of approximately 24 g, were continuously exposed to PbONPs for 11 weeks (24 h/day, 7 days/week). Control animals were exposed to the same air as treated animals without the addition of nanoparticles.

The samples from the controls and the PbO-inhaled group of mice were continuously analyzed during the whole duration of the 11-week experiment. At the designated time points of the inhalation period (2

weeks, 6 weeks), 10 biological replicates in the control (ctr/2w, ctr/6w) and inhaled groups (PbO/2w, PbO/6w) were sacrificed, and lung, liver, kidney, spleen, femur, and blood were weighed and collected for chemical, biochemical, histopathological, ultramicroscopic, immunohistochemical, histochemical, and immunofluorescent analyses, elemental imaging, and the study of gene expression of selected markers.

Additionally, one group of mice inhaled air with PbONPs for 6 weeks (24 h/day, 7 days/week) and then inhaled clean air for the next 5 weeks (this group is annotated as the clearance group PbO/cl). At the end of the inhalation period (11 weeks), 10 biological replicates in the control (ctr/11w), in PbO-exposed (PbO/11w), and clearance groups (PbO/cl) were sacrificed, and selected organs were examined in the same manner as in previous groups of the experiment.

Characterization of Generated PbONPs. The main characterization of generated PbONPs is presented in Table 1.

The distribution of NPs concerning particle number concentration was continuously measured directly inside the exposure cages using an SMPS (model 3936L72, TSI Inc., Shoreview, MN, USA). The long-term stability of PbONP generation was high. The mass concentration of PbONPs was 78.0 $\mu\text{g PbO}/\text{m}^3$ during the inhalation experiment. Mass concentration of generated PbONPs was calculated by dividing the mass of PbONPs collected on the filter by the volume of the air sample that passed through the filter.

Generated PbONPs were sampled on nitrocellulose filters (pore size 0.45 μm , diameter 25 mm, Millipore, Bedford, MA, USA). Filters were dissolved in HNO_3 using a UniClever microwave mineralizer (Plazmatronika, Wroclaw, Poland), and Pb content in the sample was determined using AAS (AAAnalyst 600, PerkinElmer Inc., Shelton, CT, USA).

The size and shape of generated PbONPs were characterized by electron microscopy (EM). Immediately after generation at the furnace output, PbONPs were collected by electrostatic precipitation using a nanometer aerosol sampler (model 3089, TSI) on EM grids (copper S160-4, 3 mm in diameter, 400 mesh grids, Agar Scientific, Electron Technology, Stansted, Essex, UK). The samples were analyzed using a Magellan 400 L XHR microscope (FEI Company, Hillsboro, OR, USA), operating in the scanning transmission electron microscope (STEM) mode. The STEM results show that the PbONPs observed in the gas phase by an SMPS were formed from agglomerates (size range approximately 40–50 nm) of primary particles of 0.4–0.5 nm in diameter (Figure 1E).

The estimated deposited dose corresponding to PbO over the 11-week inhalation period was 0.88 μg of PbO per gram of mouse body weight and 0.48 μg of PbO per gram of mouse body weight for the clearance group.

Histological Analysis. Samples of organs (lung, liver, kidney, and spleen) for histological analyses were fixed overnight in 10% buffered neutral formaldehyde in a fridge and after that immersed in a series of increasing concentrations of ethanol, xylene, and paraffin wax. Serial histological sections of 5 μm thickness were prepared, and selected slices were stained by hematoxylin–eosin, by Masson Green Trichrome (GT), and Sirius Red–Alcian Blue for analysis of collagen fibers. Toluidine Blue was used to detect mastocytes.

Samples of lung, liver, and kidney were immersed in 10% sucrose in PBS in a fridge overnight. The next day, samples were embedded into O.C.T. compound (Agar Scientific Gardena, CA, USA) and stored at -25 °C for subsequent analysis. The cryosections of liver samples were used for detection of lipids by the Oil Red staining method. Further, the cryosections of 20 μm thickness of lung, liver, and kidney samples were prepared and used for LA-ICP-MS imaging.

Photos of the slices were taken by a light microscope (Leica DM5000 B, Leica Microsystems GmbH, Vienna, Austria) and a digital color camera (Leica DFC480, Leica Microsystems GmbH, Vienna, Austria).

Immunohistochemistry. After deparaffinization and rehydration of the sections, citrate buffer (pH = 6) was used as a pretreatment in a 97 °C water bath. For inhibition of nonspecific secondary antibody binding, sections were incubated with a blocking serum (Vectastain ABC kit, rabbit IgG, PK-4001, Vector Laboratories, USA; Vectastain

ABC kit, mouse IgG, PK-4002, Vector Laboratories, USA) for at least 20 min at room temperature (RT) and were then incubated with the primary antibody (PCNA, SOX2, CD68, MPO; detailed information in Table S3).

After application of biotinylated secondary antibody (Vectastain ABC kit, rabbit IgG, PK-4001, Vector Laboratories, USA; Vectastain ABC kit, mouse IgG, PK-4002, Vector Laboratories, USA) for 30 min at RT, slices were incubated with the peroxidase-conjugated avidin–biotin complex (Vectastain ABC kit, rabbit IgG, PK-4001, Vector Laboratories, USA; Vectastain ABC kit, mouse IgG, PK-4002, Vector Laboratories, USA) for 30 min at RT. Chromogen substrate diaminobenzidine (Liquid DAB+ substrate chromogen system, K3468, DAKO, USA) was used for visualization of positive cells. Counterstaining of slices with hematoxylin was then performed. A negative control of the sample was obtained by omitting the primary antibody from the labeling protocol.

Photos were taken by a light microscope (Leica DMS5000 B, Leica Microsystems GmbH, Vienna, Austria) and a digital color camera (Leica DFC480, Leica Microsystems GmbH, Vienna, Austria).

Detection of Apoptotic Cells. The apoptotic cells were detected by the terminal deoxynucleotidyl transferase dUTP nick end labeling (TUNEL) method according to the manufacturer's protocol (ApopTag peroxidase *in situ* apoptosis detection kit, S7100, Merck, USA). Proteinase K was used as a pretreatment for 20 min at RT. For visualization, chromogen substrate diaminobenzidine (Liquid DAB+ substrate chromogen system, K3468, DAKO, USA) was applied. Slices were counterstained with hematoxylin. A negative control was obtained by omitting the TdT enzyme from the protocol.

Photos were taken by a light microscope (Leica DMS5000 B, Leica Microsystems GmbH, Vienna, Austria) with the use of a digital color camera (Leica DFC480, Leica Microsystems GmbH, Vienna, Austria).

Immunofluorescence. After deparaffinization and rehydration, samples were pretreated in citrate buffer (pH = 6) in a 97 °C water bath. Blocking serum (Vectastain ABC kit, rabbit IgG, PK-4001, Vector Laboratories, USA) applied for at least 20 min at RT was used for inhibition of nonspecific secondary antibody bindings.

After that, samples were incubated with primary antibody (SOX9, Na⁺/K⁺-ATPase; detailed information in Table S4). Secondary antibody (goat anti-rabbit IgG (H+L), Alexa Fluor 488, R37116, Invitrogen, USA) was applied for 40 min at RT. Sections were covered with a coverslip in reagent containing DAPI (Fluoroshield with DAPI, D9564, Sigma-Aldrich, USA). Photos were taken under a fluorescence microscope (Leica DM LB2, Leica Microsystems GmbH, Vienna, Austria) and a digital color camera (Leica DFC480, Leica Microsystems GmbH, Vienna, Austria).

Transmission Electron Microscopy (TEM). Samples of lungs, livers, and kidneys were fixed in 3% glutaraldehyde for 24 h, washed three times in 0.1 M cacodylate buffer, and postfixed in 1% OsO₄ solution for 1.5 h. After washing in cacodylate buffer, all samples were dehydrated in a series of increasing concentrations of ethanol, followed by acetone, and embedded in the epoxy resin Durcupan. From selected parts of the samples, ultrathin sections (60 nm thick) were prepared for TEM analysis. Sections were cut using a Leica EM UC6 ultramicrotome (Leica Microsystems GmbH, Vienna, Austria) and placed on Formvar-coated nickel grids.

Some sections were without further contrasting for analysis of nanoparticles in TEM. The other sections were contrasted with uranyl citrate and lead acetate for studying cell architecture. All sections were observed using a Morgagni 268 TEM (FEI Company, Eindhoven, The Netherlands), and designated structures were measured using iTEM software. Photographs were taken using a Veleta CCD camera (Olympus, Münster, Germany).

Biochemical Analysis of Blood. Blood samples (of the control group of animals, the experimental group exposed to the PbONPs, and the clearance group of animals at designated time points) were collected by cardiac puncture into 1 mL lithium heparin tubes (TAPVAL, Dispolab, Czech Republic). The blood samples were centrifuged at 1000g for 15 min. Biochemical parameters were determined using a clinical chemistry analyzer, Abbott Architect c4000 (Abbott Laboratories, IL, USA), wet chemistry system.

LA-ICP-MS Analysis. The cryosections of lungs, kidneys, and livers were analyzed by laser ablation with LA-ICP-MS to get elemental distributions in these sections. The LA-ICP-MS setup consists of a UP213 laser ablation system (NewWave Research, USA) and an ICP-MS Agilent 7500ce (Agilent Technologies, Japan). The laser ablation of the samples was done with a laser spot diameter of 100 μm, scan speed of 200 μm/s, repetition rate of 10 Hz, and a laser beam fluence of 3 J/cm². The content of iron (Fe) and lead (Pb) was quantified using a series of agarose gels doped with a known amount of Fe and Pb.

Imaging of PbONPs in tissue sections was done under different LA-ICP-MS parameters than elemental imaging of tissues. For this purpose, the laser beam diameter was diminished to 20 μm and the scan speed was 200 μm/s. During this imaging, isotope ²⁰⁸Pb with the integration time of 1 ms was measured. The size of imaged kidney and liver tissue samples was 1.2 × 1.6 mm for exposed samples, 0.8 × 0.4 mm for control kidney, and 1.0 × 0.4 for control liver.

Moreover, the filter with captured PbONPs was ablated to uncover the range of intensities of Pb. The intensities of Pb varied from 5 counts, and the maximal measured intensity on the filter was 770 counts (Figure S5).

Determination of Lead in Mouse Blood and Organs. Blood samples (one-half of the analyzed group at each time point) were collected by cardiac puncture into 1 mL plastic Eppendorf tubes containing a small amount of heparin. Whole blood was divided into three fractions by centrifugation of blood cells, precipitation of proteins using methanol (300 μL), and separation of the remaining supernatant. Samples were stored at 5 °C for subsequent analysis.

In the analysis of organs, the weights of individual organs were determined, and the values were recorded for later quantitative evaluation.

The individual organs and blood fractions were decomposed by microwave (MW)-assisted digestion in concentrated subboil grade (quartz distillation system model MSBQ 2, Maassen, Eningen, Germany) nitric acid, *i.e.*, liver in 5 mL, lung spleen, and kidney in 3 mL, blood cells in 2 mL, and femur and other blood fractions in 1 mL of acid. The samples were treated in precleaned quartz tubes of a closed pressurized autoclave system (UltraWave, Milestone s.r.l., Italy). The decomposition program consisted of four steps: first step, 10 min with a temperature ramp between 100 and 120 °C; second step, 5 min with a temperature ramp between 120 and 200 °C; third step, 3 min with temperature ramp between 200 and 250 °C; fourth step, 5 min at 250 °C. After cooling (a duration of approximately 10 min), digests were quantitatively transferred to high-density polyethylene vials and diluted and adjusted with ultrapure water (Ultra Clear system, SB Barsbüttel, Germany) to the final mass of 10 g for organs, 4 g for blood cells, and 3 g for femur and other blood components, respectively. Simultaneously, blank samples (typically *n* = 30 per sampling series) were processed analogously.

The content of lead in the digests was determined by electrothermal atomic absorption spectrometry employing AAnalyst 600 PerkinElmer (USA) instrumentation under recommended conditions. A mixture of ammonium phosphate and magnesium nitrate was used as a combined chemical modifier. The method of standard addition calibration was applied for quantitation.

Determination of Element Content (Na, K, Mg, Ca) in Mouse Organs. The content of basic element components (Na, K, and Ca) in mouse organs was determined in the same sample solution prepared for determination of lead. After proper dilution of sample solutions, the concentrations of Na, K, Mg, and Ca were determined by flame atomic absorption spectrometry employing ContrAA 300 Analytik Jena (Germany) High Resolution Continuum Source AAS instrumentation under recommended conditions, using acetylene–air flame (Na, K, Mg) and acetylene–nitrous oxide flame (Ca), respectively. Measurement was performed at prominent analytical lines (Na 589.0 nm, K 766.5 nm, Mg 285.2 nm, and Ca 422.7 nm, respectively). Quantitation calibration was based on certified analyte standard solutions, Astatol (1 ± 0.002 g/L) (Analytika Ltd. Prague, Czech Republic).

qRT-PCR Analysis. Total RNA was extracted using the RNeasy mini kit (Qiagen). Complementary DNA was synthesized according to the manufacturer's instructions using a High-Capacity RNA-to-cDNA kit (Applied Biosystems).

qRT-PCR was analyzed with a LightCycler 480 (Roche). The number of analyzed cDNA samples was $n = 3-5$ for each group. Gene expression values for each sample were expressed in terms of the threshold cycle normalized to glyceraldehyde-3-phosphate dehydrogenase (*Gapdh*; ID Mm99999915_g1) or beta-actin (*Actb*; ID Mm00607939_s1) expression.

Abcc3 was analyzed with the following program: initial activation step at 95 °C for 5 min, followed by 40 cycles at 95 °C for 10 s, annealing temperature for 10 s, and 72 °C for 10 s. The sequences of primers of gene *Abcc3* are in Table S5. Gene expression values were normalized to *Gapdh*.

TaqMan gene expression assays of *Abcb1a* (ID Mm00440761_m1), *Abcc2* (ID Mm01199458_g1), and *Abeg2* (ID Mm00496364_m1) were performed with the following program: initial activation step at 95 °C for 20 s, followed by 40 cycles at 95 °C for 3 s, annealing temperature at 60 °C for 30 s. Values of ABC transporter expression were normalized to *Gapdh*.

Cav1 (ID Mm00483057_m1), *Cav2* (ID Mm00516827_m1), and *Cltc* (ID Mm01303974_m1) were analyzed with the following program: initial activation step at 95 °C for 10 min, followed by 40 cycles at 95 °C for 15 s, annealing temperature at 60 °C for 60 s. Gene expression values of these genes were normalized to *Actb* expression.

Western Blot Analysis. The dissected tissue was washed with ice cold 1× PBS to remove blood and stored at -80 °C. The samples with additional SDS lysis buffer were homogenized by needles with decreasing diameter and by an ultrasonic homogenizer. The clear samples were obtained as supernatant after centrifugation (lysates were cleared by centrifugation).

Protein concentrations of all samples were determined using the DC protein assay kit (Bio-Rad, USA). Lysates were supplemented with Bromophenol Blue (0.01%) and β -mercaptoethanol (143 mM) and incubated for 5 min at 95 °C. Equal amounts of total protein (10 μ g) were separated with SDS-PAGE and transferred onto a polyvinylidene difluoride membrane (Immobilon-P PVDF Membrane, Merck Millipore, Germany) using established procedures. The membranes were blocked in TBS (20 mM Tris-HCl pH 7.2, 140 mM NaCl, 0.1% Tween 20) with 5% nonfat milk. Proteins were immunodetected using appropriate primary and secondary antibodies and visualized by ECL-Plus reagent (Amersham Pharmacia Biotech, Piscataway, NJ, USA) according to the manufacturer's instructions. Primary antibodies were used as follows: rabbit polyclonal antibody against BCRP (sc-25822, Santa Cruz Biotechnology), mouse monoclonal antibody against MDR1 (P7965, Sigma-Aldrich), rabbit polyclonal antibody against MRP2 (24893-1-AP, Proteintech), mouse monoclonal antibody against MRP3 (ab3375, Abcam), and rabbit polyclonal antibody against GAPDH (sc-25778, Santa Cruz Biotechnology).

ASSOCIATED CONTENT

Supporting Information

The Supporting Information is available free of charge at <https://pubs.acs.org/doi/10.1021/acsnano.9b08143>.

Histopathological changes in the lungs after 6 and 11 weeks of PbONP inhalation in the experiment; histopathological changes in the liver after 6 and 11 weeks of PbONP inhalation in the experiment; list of antibodies used for immunohistochemical analysis; list of antibodies used for immunofluorescent analysis; primers for qPCR; lung after 3 days of PbONP inhalation; ultrastructure of kidney after PbONP exposure; content of elements (sodium, potassium, and calcium) in lung, liver, and kidney during subchronic PbONP inhalation; weight of mice during PbONP inhalation, lung, kidney, and spleen weight coefficient at

different time points (2, 6, and 11 weeks); histogram of intensities of ^{208}Pb obtained at laser ablation of filter (PDF)

AUTHOR INFORMATION

Corresponding Author

Marcela Buchtová – Laboratory of Molecular Morphogenesis, Institute of Animal Physiology and Genetics, v.v.i., Czech Academy of Sciences, Brno 602 00, Czech Republic; Section of Animal Physiology and Immunology, Department of Experimental Biology, Faculty of Science, Masaryk University, Brno 625 00, Czech Republic; orcid.org/0000-0002-0262-6774; Email: buchtova@iach.cz

Authors

Jana Dumková – Department of Histology and Embryology, Faculty of Medicine, Masaryk University, Brno 625 00, Czech Republic

Tereza Smutná – Department of Histology and Embryology, Faculty of Medicine, Masaryk University, Brno 625 00, Czech Republic; Laboratory of Molecular Morphogenesis, Institute of Animal Physiology and Genetics, v.v.i., Czech Academy of Sciences, Brno 602 00, Czech Republic

Lucie Vrlíková – Laboratory of Molecular Morphogenesis, Institute of Animal Physiology and Genetics, v.v.i., Czech Academy of Sciences, Brno 602 00, Czech Republic

Hana Kotasová – Department of Histology and Embryology, Faculty of Medicine, Masaryk University, Brno 625 00, Czech Republic

Bohumil Dočekal – Institute of Analytical Chemistry, v.v.i., Czech Academy of Sciences, Brno 602 00, Czech Republic

Lukáš Čapka – Institute of Analytical Chemistry, v.v.i., Czech Academy of Sciences, Brno 602 00, Czech Republic

Michaela Tvrdonová – Department of Chemistry, Faculty of Science, Masaryk University, Brno 625 00, Czech Republic; orcid.org/0000-0002-1686-4423

Veronika Jakešová – Laboratory of Molecular Morphogenesis, Institute of Animal Physiology and Genetics, v.v.i., Czech Academy of Sciences, Brno 602 00, Czech Republic

Vendula Pelková – Department of Histology and Embryology, Faculty of Medicine, Masaryk University, Brno 625 00, Czech Republic

Kamil Krůmal – Institute of Analytical Chemistry, v.v.i., Czech Academy of Sciences, Brno 602 00, Czech Republic; orcid.org/0000-0001-5030-8685

Pavel Coufalík – Institute of Analytical Chemistry, v.v.i., Czech Academy of Sciences, Brno 602 00, Czech Republic

Pavel Mikuška – Institute of Analytical Chemistry, v.v.i., Czech Academy of Sciences, Brno 602 00, Czech Republic

Zbyněk Večeřa – Institute of Analytical Chemistry, v.v.i., Czech Academy of Sciences, Brno 602 00, Czech Republic

Tomáš Vaculovič – Department of Chemistry, Faculty of Science, Masaryk University, Brno 625 00, Czech Republic

Zuzana Husáková – Department of Chemistry, Faculty of Science, Masaryk University, Brno 625 00, Czech Republic

Viktor Kanický – Department of Chemistry, Faculty of Science, Masaryk University, Brno 625 00, Czech Republic

Aleš Hampl – Department of Histology and Embryology, Faculty of Medicine, Masaryk University, Brno 625 00, Czech Republic

Complete contact information is available at: <https://pubs.acs.org/doi/10.1021/acsnano.9b08143>

Author Contributions

[#]J. Dumková and T. Smutná contributed equally.

Author Contributions

M.B., Z.V., and P.M. conceived and designed the experiments. T.S., L.V., H.K., V.P., V.J., B.D., P.M., K.K., L.C., Z.H., M.T., and P.C. performed experiments. J.D., T.S., M.T., T.V., V.K., and M.B. analyzed the data. M.B., V.K., and A.H. contributed reagents and materials. J.D., T.S., M.B., P.M., and A.H. wrote the paper. All authors read and approved the final manuscript.

Notes

The authors declare no competing financial interest.

ACKNOWLEDGMENTS

The work was supported by the Czech Science Foundation (grant no. P503/12/G147 to P.M. lab, 17-12774S to T.V. lab and experiments during revisions were supported by grant no. 20-02203S). The authors would like to thank Dobromila Klemová for help with the processing of samples and Daniela Dumková for the assistance and advice on the graphic editing.

REFERENCES

- (1) Wuana, R. A.; Okieimen, F. E. Heavy Metals in Contaminated Soils: A Review of Sources, Chemistry, Risks and Best Available Strategies for Remediation. *ISRN Ecol.* 2011, 2011, 1–20.
- (2) Pokras, M.; Kneeland, M. Lead Poisoning: Using Transdisciplinary Approaches to Solve an Ancient Problem. *Ecohealth* 2008, 5, 379–385.
- (3) Karami, H.; Karimi, M. A.; Haghdar, S.; Sadeghi, A.; Mir-Ghasemi, R.; Mahdi-Khani, S. Synthesis of Lead Oxide Nanoparticles by Sonochemical Method and Its Application As Cathode and Anode of Lead-Acid Batteries. *Mater. Chem. Phys.* 2008, 108, 337–344.
- (4) Hu, Y.; Yang, J.; Zhang, W.; Xie, Y.; Wang, J.; Yuan, X.; Kumar, R. V.; Liang, S.; Hu, J.; Wu, X. A Novel Lead Oxide Combined with Porous Carbon Skeleton Synthesized from Lead Citrate Precursor Recovered from Spent Lead-Acid Battery Paste. *J. Power Sources* 2016, 304, 128–135.
- (5) Minigalieva, I. A.; Katsnelson, B. A.; Panov, V. G.; Privalova, L. I.; Varaksin, A. N.; Gurvich, V. B.; Sutunkova, M. P.; Shur, V. Y.; Shishkina, E. V.; Valamina, I. E. *In Vivo* Toxicity of Copper Oxide, Lead Oxide and Zinc Oxide Nanoparticles Acting in Different Combinations and Its Attenuation with a Complex of Innocuous Bioprotectors. *Toxicology* 2017, 380, 72–93.
- (6) Yang, D.; Cao, M.; Zhong, Q.; Li, P.; Zhang, X.; Zhang, Q. All-Inorganic Cesium Lead Halide Perovskite Nanocrystals: Synthesis, Surface Engineering and Applications. *J. Mater. Chem. C* 2019, 7, 757–789.
- (7) Miri, A.; Sarani, M.; Hashemzadeh, A.; Mardani, Z.; Darroudi, M. Biosynthesis and Cytotoxic Activity of Lead Oxide Nanoparticles. *Green Chem. Lett. Rev.* 2018, 11, 567–572.
- (8) Bláhová, L.; Nováková, Z.; Večeřa, Z.; Vrlíková, L.; Dočekal, B.; Dumková, J.; Křůmal, K.; Mikuška, P.; Buchtová, M.; Hampl, A. The Effects of Nano-Sized PbO on Biomarkers of Membrane Disruption and DNA Damage in a Sub-Chronic Inhalation Study on Mice. *Nanotoxicology* 2020, 14, 1–18.
- (9) Bushueva, T.; Minigalieva, I.; Panov, V.; Kuznetsova, A.; Naumova, A.; Shur, V.; Shishkina, E.; Gurvich, V.; Privalova, L.; Katsnelson, B. More Data on *In Vitro* Assessment of Comparative and Combined Toxicity of Metal Oxide Nanoparticles. *Food Chem. Toxicol.* 2019, 133, 110753.
- (10) Hu, X.; Xu, X.; Ding, Z.; Chen, Y.; Lian, H. *In Vitro* Inhalation/Ingestion Bioaccessibility, Health Risks, and Source Appointment of Airborne Particle-Bound Elements Trapped in Room Air Conditioner Filters. *Environ. Sci. Pollut. Res.* 2018, 25, 26059–26068.
- (11) Agency for Toxic Substances and Disease Registry (ATSDR). https://www.atsdr.cdc.gov/csem/lead/docs/CSEM-Lead_toxicity_508.pdf (accessed 2019-8-15).
- (12) Agency for Toxic Substances and Disease Registry (ATSDR). <https://www.atsdr.cdc.gov/csem/csem.asp?csem=7&po=8> (accessed 2016-3-22).
- (13) Huang, K.; Zhuang, G.; Lin, Y.; Wang, Q.; Fu, J.; Fu, Q.; Liu, T.; Deng, C. How To Improve the Air Quality Over Megacities in China: Pollution Characterization and Source Analysis in Shanghai Before, During, and After the 2010 World Expo. *Atmos. Chem. Phys. Discuss.* 2013, 13, 3379–3418.
- (14) Gurjar, B.; Ravindra, K.; Nagpure, A. Air Pollution Trends Over Indian Megacities and Their Local-To-Global Implications. *Atmos. Environ.* 2016, 142, 475–495.
- (15) Li, Q.; Zheng, J.; Xu, S.; Zhang, J.; Cao, Y.; Qin, Z.; Liu, X.; Jiang, C. The Neurotoxicity Induced by PM2.5 Might Be Strongly Related to Changes of the Hippocampal Tissue Structure and Neurotransmitter Levels. *Toxicol. Res.* 2018, 7, 1144–1152.
- (16) Coufalík, P.; Mikuška, P.; Matoušek, T.; Večeřa, Z. Determination of the Bioaccessible Fraction of Metals in Urban Aerosol Using Simulated Lung Fluids. *Atmos. Environ.* 2016, 140, 469–475.
- (17) Pérez, N.; Pey, J.; Querol, X.; Alastuey, A.; López, J.; Viana, M. Partitioning of Major and Trace Components in PM10–PM2.5–PM1 at an Urban Site in Southern Europe. *Atmos. Environ.* 2008, 42, 1677–1691.
- (18) Shah, M. H.; Shaheen, N.; Nazir, R. Assessment of the Trace Elements Level in Urban Atmospheric Particulate Matter and Source Apportionment in Islamabad, Pakistan. *Atmos. Pollut. Res.* 2012, 3, 39–45.
- (19) Querol, X.; Viana, M.; Alastuey, A.; Amato, F.; Moreno, T.; Castillo, S.; Pey, J.; De la Rosa, J.; De La Campa, A. S.; Artíñano, B. Source Origin of Trace Elements in PM from Regional Background, Urban and Industrial Sites of Spain. *Atmos. Environ.* 2007, 41, 7219–7231.
- (20) Mitra, P.; Sharma, S.; Purohit, P.; Sharma, P. Clinical and Molecular Aspects of Lead Toxicity: An Update. *Crit. Rev. Clin. Lab. Sci.* 2017, 54, 506–528.
- (21) Daley, G. M.; Pretorius, C. J.; Ungerer, J. P. Lead Toxicity: An Australian Perspective. *Clin. Biochem. Rev.* 2018, 39, 61.
- (22) Lebedova, J.; Novakova, Z.; Vecera, Z.; Buchtova, M.; Dumkova, J.; Docekal, B.; Blahova, L.; Mikuska, P.; Misek, L.; Hampl, A.; Hilscherova, K. Impact of Acute and Subchronic Inhalation Exposure to PbO Nanoparticles on Mice. *Nanotoxicology* 2018, 12, 290–304.
- (23) Griffin, T. B.; Coulston, F.; Wills, H.; Russell, J. C. Biologic Effects of Airborne Particulate Lead on Continuously Exposed Rats and Rhesus Monkeys. *Environ. Qual. Saf., Suppl.* 1975, 2, 202–220.
- (24) Griffin, T. B.; Coulston, F.; Wills, H.; Russell, J. C. Clinical Studies on Men Continuously Exposed to Airborne Particulate Lead. *Environ. Qual. Saf., Suppl.* 1975, 2, 221–240.
- (25) Orr, S.; Bridges, C. Chronic Kidney Disease and Exposure to Nephrotoxic Metals. *Int. J. Mol. Sci.* 2017, 18, 1039.
- (26) Lee, S.; Choi, J.; Shin, S.; Im, Y. M.; Song, J.; Kang, S. S.; Nam, T. H.; Webster, T. J.; Kim, S. H.; Khang, D. Analysis on Migration and Activation of Live Macrophages on Transparent Flat and Nanostructured Titanium. *Acta Biomater.* 2011, 7, 2337–2344.
- (27) Večeřa, Z.; Mikuška, P.; Moravec, P.; Smolík, J. *Unique Exposure System for the Whole Body Inhalation Experiments with Small Animals*; Nanocon, 2011; pp 652–654.
- (28) Dumková, J.; Smutná, T.; Vrlíková, L.; Le Coustumer, P.; Večeřa, Z.; Dočekal, B.; Mikuška, P.; Čapka, L.; Fictum, P.; Hampl, A.; Buchtová, M. Sub-Chronic Inhalation of Lead Oxide Nanoparticles Revealed Their Broad Distribution and Tissue-Specific Subcellular Localization in Target Organs. *Part. Fibre Toxicol.* 2017, 14, 55.
- (29) Pietroiusti, A.; Bergamaschi, E.; Campagna, M.; Campagnolo, L.; De Palma, G.; Iavicoli, S.; Leso, V.; Magrini, A.; Miragoli, M.; Pedata, P.; Palombi, L.; Iavicoli, I. The Unrecognized Occupational Relevance of the Interaction between Engineered Nanomaterials and the Gastro-Intestinal Tract: A Consensus Paper from a Multi-disciplinary Working Group. *Part. Part. Fibre Toxicol.* 2017, 14, 47.

- (30) Tran, C.; Buchanan, D.; Cullen, R.; Searl, A.; Jones, A.; Donaldson, K. Inhalation of Poorly Soluble Particles. II. Influence of Particle Surface Area on Inflammation and Clearance. *Inhalation Toxicol.* **2000**, *12*, 1113–1126.
- (31) Oberdörster, G. Pulmonary Effects of Inhaled Ultrafine Particles. *Int. Arch. Occup. Environ. Health* **2000**, *74*, 1–8.
- (32) Brown, D. M.; Wilson, M. R.; MacNee, W.; Stone, V.; Donaldson, K. Size-Dependent Proinflammatory Effects of Ultrafine Polystyrene Particles: A Role for Surface Area and Oxidative Stress in the Enhanced Activity of Ultrafines. *Toxicol. Appl. Pharmacol.* **2001**, *175*, 191–199.
- (33) Chuang, H.-C.; Chen, L.-C.; Lei, Y.-C.; Wu, K.-Y.; Feng, P.-H.; Cheng, T.-J. Surface Area As a Dose Metric for Carbon Black Nanoparticles: A Study of Oxidative Stress, DNA Single-Strand Breakage and Inflammation in Rats. *Atmos. Environ.* **2015**, *106*, 329–334.
- (34) Schmid, O.; Stoeger, T. Surface Area is the Biologically Most Effective Dose Metric for Acute Nanoparticle Toxicity in the Lung. *J. Aerosol Sci.* **2016**, *99*, 133–143.
- (35) Human Respiratory Tract Model for Radiological Protection. A Report of a Task Group of the International Commission on Radiological Protection. *Ann. ICRP* **1994**, *24*, 1–482.
- (36) Moravec, P.; Kupčík, J.; Vodička, P.; Schwarz, J. Generation of ZnO Nanoparticles for Long-Term Exposure Experiments. *Aerosol Sci. Technol.* **2019**, *53*, 172–183.
- (37) Kuuluvainen, H.; Rönkkö, T.; Järvinen, A.; Saari, S.; Karjalainen, P.; Lähde, T.; Pirjola, L.; Niemi, J. V.; Hillamo, R.; Keskinen, J. Lung Deposited Surface Area Size Distributions of Particulate Matter in Different Urban Areas. *Atmos. Environ.* **2016**, *136*, 105–113.
- (38) Braakhuis, H.; Gosens, I.; Krystek, P.; Boere, J.; Cassee, F.; Fokkens, P.; Post, J.; van Loveren, H.; Park, M. Particle Size Dependent Deposition and Pulmonary Inflammation after Short-Term Inhalation of Silver Nanoparticles. *Part. Fibre Toxicol.* **2014**, *11*, DOI: 10.1186/s12989-014-0049-1.
- (39) Wiseman, C. L.; Zereini, F. Characterizing Metal (Loid) Solubility in Airborne PM10, PM2.5 and PM1 in Frankfurt, Germany Using Simulated Lung Fluids. *Atmos. Environ.* **2014**, *89*, 282–289.
- (40) Abid, A.; Anderson, D.; Das, G.; Van Winkle, L.; Kennedy, I. Novel Lanthanide-Labeled Metal Oxide Nanoparticles Improve the Measurement of *In Vivo* Clearance and Translocation. *Part. Fibre Toxicol.* **2013**, *10*, 1.
- (41) Kreyling, W. G.; Semmler-Behnke, M.; Seitz, J.; Scymczak, W.; Wenk, A.; Mayer, P.; Takenaka, S.; Oberdörster, G. Size Dependence of the Translocation of Inhaled Iridium and Carbon Nanoparticle Aggregates from the Lung of Rats to the Blood and Secondary Target Organs. *Inhalation Toxicol.* **2009**, *21*, 55–60.
- (42) Pietrousti, A.; Stockmann-Juvala, H.; Lucaroni, F.; Savolainen, K. Nanomaterial Exposure, Toxicity, and Impact on Human Health. *Wiley Interdiscip. Rev.: Nanomed. Nanobiotechnol.* **2018**, *10*, No. e1513.
- (43) Buckley, A.; Warren, J.; Hodgson, A.; Marczylo, T.; Ignatyev, K.; Guo, C.; Smith, R. Slow Lung Clearance and Limited Translocation of Four Sizes of Inhaled Iridium Nanoparticles. *Part. Fibre Toxicol.* **2017**, *14*, 5.
- (44) Detampel, P.; Ganguly, A.; Tehranian, S.; Green, F.; Singha, S.; Santamaria, P.; Jeje, A. A.; Cho, C. S.; Petri, B.; Amrein, M. W. *In Vivo* Clearance of Nanoparticles by Transcytosis Across Alveolar Epithelial Cells. *PLoS One* **2019**, *14*, 1–13.
- (45) Kreyling, W. G.; Semmler-Behnke, M.; Seitz, J.; Scymczak, W.; Wenk, A.; Mayer, P.; Takenaka, S.; Oberdörster, G. Size Dependence of the Translocation of Inhaled Iridium and Carbon Nanoparticle Aggregates from the Lung of Rats to the Blood and Secondary Target Organs. *Inhalation Toxicol.* **2009**, *21*, 55–60.
- (46) Anyanwu, B.; Ezejirofor, A.; Igweze, Z.; Orisakwe, O. Heavy Metal Mixture Exposure and Effects in Developing Nations: An Update. *Toxics* **2018**, *6*, 65.
- (47) Obiri, S.; Yeboah, P.; Osae, S.; Adu-Kumi, S. Levels of Arsenic, Mercury, Cadmium, Copper, Lead, Zinc and Manganese in Serum and Whole Blood of Resident Adults from Mining and Non-Mining Communities in Ghana. *Environ. Sci. Pollut. Res.* **2016**, *23*, 16589–16597.
- (48) Li, Q. Z.; Hu, X. L.; Bai, Y. P.; Alattar, M.; Ma, D.; Cao, Y. H.; Hao, Y. L.; Wang, L. H.; Jiang, C. Y. The Oxidative Damage and Inflammatory Response Induced by Lead Sulfide Nanoparticles in Rat Lung. *Food Chem. Toxicol.* **2013**, *60*, 213–217.
- (49) Brito, J.; McNeill, F.; Webber, C.; Chettle, D. Grid Search: An Innovative Method for the Estimation of the Rates of Lead Exchange between Body Compartments. *J. Environ. Monit.* **2005**, *7*, 241–247.
- (50) Yang, L.; Kuang, H.; Zhang, W.; Aguilar, Z.; Wei, H.; Xu, H. Comparisons of the Biodistribution and Toxicological Examinations after Repeated Intravenous Administration of Silver and Gold Nanoparticles in Mice. *Sci. Rep.* **2017**, *7*, 1–12.
- (51) Lietman, S.; Germain-Lee, E.; Levine, M. Hypercalcemia in Children and Adolescents. *Curr. Opin. Pediatr.* **2010**, *22*, 508–515.
- (52) Serfilippi, L. M.; Stackhouse Pallman, D. R.; Russell, B.; Spainhour, C. B. Serum Clinical Chemistry and Hematology Reference Values in Outbred Stocks of Albino Mice from Three Commonly Used Vendors and Two Inbred Strains of Albino Mice. *J. Am. Assoc. Lab. Anim. Sci.* **2003**, *42*, 46–52.
- (53) Lentini, P.; Zanolli, L.; Granata, A.; Signorelli, S. S.; Castellino, P.; Dell'Aquila, R. Kidney and Heavy Metals-The Role of Environmental Exposure. *Mol. Med. Rep.* **2017**, *15*, 3413–3419.
- (54) Haque, S. K.; Ariceta, G.; Badle, D. Proximal Renal Tubular Acidosis: A Not So Rare Disorder of Multiple Etiologies. *Nephrol., Dial., Transplant.* **2012**, *27*, 4273–4287.
- (55) Shakeel, M.; Jabeen, F.; Shabbir, S.; Asghar, M.; Khan, M.; Chaudhry, A. Toxicity of Nano-Titanium Dioxide (TiO₂-NP) Through Various Routes of Exposure: A Review. *Biol. Trace Elem. Res.* **2016**, *172*, 1–36.
- (56) Wan, R.; Mo, Y.; Zhang, Z.; Jiang, M.; Tang, S.; Zhang, Q. Cobalt Nanoparticles Induce Lung Injury, DNA Damage and Mutations in Mice. *Part. Fibre Toxicol.* **2017**, *14*, 38.
- (57) Bermudez, E.; Mangum, J.; Wong, B.; Asgharian, B.; Hext, P.; Warheit, D.; Everitt, J. Pulmonary Responses of Mice, Rats, and Hamsters to Subchronic Inhalation of Ultrafine Titanium Dioxide Particles. *Toxicol. Sci.* **2004**, *77*, 347–357.
- (58) Bai, K.; Chuang, K.; Chen, J.; Hua, H.; Shen, Y.; Liao, W.; Lee, C.; Chen, K.; Lee, K.; Hsiao, T.; Pan, C.; Ho, K.; Chuang, H. Investigation into the Pulmonary Inflammopathology of Exposure to Nickel Oxide Nanoparticles in Mice. *Nanomedicine* **2018**, *14*, 2329–2339.
- (59) Haste, L.; Hulland, K.; Bolton, S.; Yesilkaya, H.; McKechnie, K.; Andrew, P. Development and Characterization of a Long-Term Murine Model of *Streptococcus pneumoniae* Infection of the Lower Airways. *Infect. Immun.* **2014**, *82*, 3289–3298.
- (60) Dong, X.; Zhu, Y.; Cai, H.; Lv, C.; Gao, Y.; Yu, Z.; Xue, F. Studies on the Pathogenesis of a Chinese Strain of Bovine Parainfluenza Virus Type 3 Infection in Balb/c Mice. *Vet. Microbiol.* **2012**, *158*, 199–204.
- (61) Lebedova, J.; Blahova, L.; Vecera, Z.; Mikuska, P.; Docekal, B.; Buchtova, M.; Miskal, I.; Dumkova, J.; Hampl, A.; Hilscherova, K. Impact of Acute and Chronic Inhalation Exposure to CdO Nanoparticles on Mice. *Environ. Sci. Pollut. Res.* **2016**, *23*, 24047–24060.
- (62) Clausen, M. V.; Hilbers, F.; Poulsen, H. The Structure and Function of the Na, K-ATPase Isoforms in Health and Disease. *Front. Physiol.* **2017**, *8*, 371.
- (63) Sarkar, A.; Hochedlinger, K. The Sox Family of Transcription Factors: Versatile Regulators of Stem and Progenitor Cell Fate. *Cell Stem Cell* **2013**, *12*, 15–30.
- (64) Yin, C. Molecular Mechanisms of Sox Transcription Factors During the Development of Liver, Bile Duct, and Pancreas. *Semin. Cell Dev. Biol.* **2017**, *63*, 68–78.
- (65) Furuyama, K.; Kawaguchi, Y.; Akiyama, H.; Horiguchi, M.; Kodama, S.; Kuhara, T.; Hosokawa, S.; Elbahrawy, A.; Soeda, T.; Koizumi, M.; Masui, T.; Kawaguchi, M.; Takaori, K.; Doi, R.; Nishi, E.; Kakinoki, R.; Deng, J.; Behringer, R.; Nakamura, T.; Uemoto, S. Continuous Cell Supply from a Sox9-Expressing Progenitor Zone in

- Adult Liver, Exocrine Pancreas and Intestine. *Nat. Genet.* 2011, 43, 34–41.
- (66) Font-Burgada, J.; Shalpour, S.; Ramaswamy, S.; Hsueh, B.; Rossell, D.; Umemura, A.; Taniguchi, K.; Nakagawa, H.; Valasek, M.; Ye, L.; Kopp, J.; Sander, M.; Carter, H.; Deisseroth, K.; Verma, I.; Karin, M. Hybrid Periportal Hepatocytes Regenerate the Injured Liver without Giving Rise to Cancer. *Cell* 2015, 162, 766–779.
- (67) Hanley, K.; Oakley, F.; Sugden, S.; Wilson, D.; Mann, D.; Hanley, N. Ectopic SOX9 Mediates Extracellular Matrix Deposition Characteristic of Organ Fibrosis. *J. Biol. Chem.* 2008, 283, 14063–14071.
- (68) Dorrell, C.; Erker, L.; Schug, J.; Kopp, J.; Canaday, P.; Fox, A.; Smirnova, O.; Duncan, A.; Finegold, M.; Sander, M.; Kaestner, K.; Grompe, M. Prospective Isolation of a Bipotential Clonogenic Liver Progenitor Cell in Adult Mice. *Genes Dev.* 2011, 25, 1193–1203.
- (69) Bourassa, M.; Miller, L. Metal Imaging in Neurodegenerative Diseases. *Metalomics* 2012, 4, 721–738.
- (70) Kapoor, S. C.; van Rossum, G. D. Effects of Pb²⁺ Added *In Vitro* on Ca²⁺ Movements in Isolated Mitochondria and Slices of Rat Kidney Cortex. *Biochem. Pharmacol.* 1984, 33, 1771–1778.
- (71) Zareba, G.; Chmielnicka, J. Effects of Tin and Lead on Organ Levels of Essential Minerals in Rabbits. *Biol. Trace Elem. Res.* 1989, 20, 233–242.
- (72) Zhang, D.; Gao, J.; Zhang, K.; Liu, X.; Li, J. Effects of Chronic Cadmium Poisoning on Zn, Cu, Fe, Ca, and Metallothionein in Liver and Kidney of Rats. *Biol. Trace Elem. Res.* 2012, 149, 57–63.
- (73) Victory, W.; Miller, C.; Zhu, S.; Goyer, R. Effect of Different Levels and Periods of Lead-Exposure on Tissue-Levels and Excretion of Lead, Zinc, and Calcium in the Rat. *Toxicol. Sci.* 1987, 8, 506–516.
- (74) Rodriguez, J.; Mandalunis, P. M. A Review of Metal Exposure and Its Effects on Bone Health. *J. Toxicol.* 2018, 2018, 11.
- (75) Cretacci, Y.; Parsons, P. Localized Accumulation of Lead Within and Among Bones from Lead-Dosed Goats. *Environ. Res.* 2010, 110, 26–32.
- (76) Ishii, C.; Nakayama, S.; Kataba, A.; Ikenaka, Y.; Saito, K.; Watanabe, Y.; Makino, Y.; Matsukawa, T.; Kubota, A.; Yokoyama, K.; Mizukawa, H.; Hirata, T.; Ishizuka, M. Characterization and Imaging of Lead Distribution in Bones of Lead-Exposed Birds by ICP-MS and LA-ICP-MS. *Chemosphere* 2018, 212, 994–1001.
- (77) Lu, H.; Yuan, G.; Yin, Z.; Dai, S.; Jia, R.; Xu, J.; Song, X.; Li, L.; Lv, C. Effects of Subchronic Exposure to Lead Acetate and Cadmium Chloride on Rat's Bone: Ca and Pi Contents, Bone Density, and Histopathological Evaluation. *Int. J. Clin. Exp. Pathol.* 2014, 7, 640–647.
- (78) Leonas, R.; Noor, Z.; Rasyid, H. N.; Madjid, T. H.; Tanjung, F. A. Effect of Lead Nanoparticles Inhalation on Bone Calcium Sensing Receptor, Hydroxyapatite Crystal and Receptor Activator of Nuclear Factor-Kappa B in Rats. *Acta Inf. Med.* 2016, 24, 343.
- (79) Kilborn, S.; Trudel, G.; Uthoff, H. Review of Growth Plate Closure Compared with Age at Sexual Maturity and Lifespan in Laboratory Animals. *Contemp. Top. Lab. Anim. Sci.* 2002, 41, 21–26.
- (80) Alvarez-Lloret, P.; Lee, C. M.; Conti, M. I.; Terrizzi, A. R.; González-López, S.; Martínez, M. P. Effects of Chronic Lead Exposure on Bone Mineral Properties in Femurs of Growing Rats. *Toxicology* 2017, 377, 64–72.
- (81) Monir, A.; Gundberg, C.; Yagerman, S.; van der Meulen, M.; Budell, W.; Boskey, A.; Dowd, T. The Effect of Lead on Bone Mineral Properties from Female Adult C57/BL6 Mice. *Bone* 2010, 47, 888–894.
- (82) Beddoes, C.; Case, C.; Briscoe, W. Understanding Nanoparticle Cellular Entry: A Physicochemical Perspective. *Adv. Colloid Interface Sci.* 2015, 218, 48–68.
- (83) Gumbleton, M. Caveolae as Potential Macromolecule Trafficking Compartments Within Alveolar Epithelium. *Adv. Drug Delivery Rev.* 2001, 49, 281–300.
- (84) Yameen, B.; Choi, W.; Vilos, C.; Swami, A.; Shi, J.; Farokhzad, O. Insight into Nanoparticle Cellular Uptake and Intracellular Targeting. *J. Controlled Release* 2014, 190, 485–499.
- (85) Galbiati, F.; Volonte, D.; Engelman, J.; Watanabe, G.; Burk, R.; Pestell, R.; Lisanti, M. Targeted Downregulation of Caveolin-1 is Sufficient To Drive Cell Transformation and Hyperactivate the p42/44 MAP Kinase Cascade. *EMBO J.* 1998, 17, 6633–6648.
- (86) Racine, C.; Belanger, M.; Hirabayashi, H.; Boucher, M.; Chakir, J.; Couet, J. Reduction of Caveolin 1 Gene Expression in Lung Carcinoma Cell Lines. *Biochem. Biophys. Res. Commun.* 1999, 255, 580–586.
- (87) de Almeida, C. Caveolin-1 and Caveolin-2 Can Be Antagonistic Partners in Inflammation and Beyond. *Front. Immunol.* 2017, 8, 1530.
- (88) Naota, M.; Shimada, A.; Morita, T.; Yamamoto, Y.; Inoue, K.; Takano, H. Caveolae-Mediated Endocytosis of Intratracheally Instilled Gold Colloid Nanoparticles at the Air-Blood Barrier in Mice. *Toxicol. Pathol.* 2013, 41, 487–496.
- (89) Ostermeyer, A.; Paci, J.; Zeng, Y.; Lublin, D.; Munro, S.; Brown, D. Accumulation of Caveolin in the Endoplasmic Reticulum Redirects the Protein to Lipid Storage Droplets. *J. Cell Biol.* 2001, 152, 1071–1078.
- (90) El-Awady, R.; Saleh, E.; Hashim, A.; Soliman, N.; Dallah, A.; Elrasheed, A.; Elakraa, G. The Role of Eukaryotic and Prokaryotic ABC Transporter Family in Failure of Chemotherapy. *Front. Pharmacol.* 2017, 7, 535.
- (91) Long, Y.; Li, Q.; Zhong, S.; Wang, Y.; Cui, Z. Molecular Characterization and Functions of Zebrafish ABCG2 in Cellular Efflux of Heavy Metals. *Comp. Biochem. Physiol., Part C: Toxicol. Pharmacol.* 2011, 153, 381–391.
- (92) Li, C.; Schuetz, J. D.; Naren, A. P. Tobacco Carcinogen NNK Transporter MRP2 Regulates CFTR Function in Lung Epithelia: Implications for Lung Cancer. *Cancer Lett.* 2010, 292, 246–253.
- (93) Lindner, S.; Halwachs, S.; Wassermann, L.; Honscha, W. Expression and Subcellular Localization of Efflux Transporter ABCG2/BCRP in Important Tissue Barriers of Lactating Dairy Cows, Sheep and Goats. *J. Vet. Pharmacol. Ther.* 2013, 36, 562–570.
- (94) Marriott, S.; Baskir, R. S.; Gaskill, C.; Menon, S.; Carrier, E. J.; Williams, J.; Talati, M.; Helm, K.; Alford, C. E.; Kropfski, J. A. ABCG2^{pos} Lung Mesenchymal Stem Cells are a Novel Pericyte Subpopulation that Contributes to Fibrotic Remodeling. *Am. J. Physiol.: Cell Physiol.* 2014, 307, C684–C698.
- (95) Wang, Y.; Zhong, Y.; Hou, T.; Liao, J.; Zhang, C.; Sun, C.; Wang, G. PM2.5 Induces EMT and Promotes CSC Properties by Activating Notch Pathway *In Vivo* and *In Vitro*. *Ecotoxicol. Environ. Saf.* 2019, 178, 159–167.
- (96) Paetzold, S. C.; Ross, N. W.; Richards, R. C.; Jones, M.; Hellou, J.; Bard, S. M. Up-Regulation of Hepatic ABCG2, ABCG2, CYP1A1 and GST in Multixenobiotic-Resistant Killifish (*Fundulus heteroclitus*) from the Sydney Tar Ponds, Nova Scotia, Canada. *Mar. Environ. Res.* 2009, 68, 37–47.
- (97) Kim, H.-R.; Lee, K.-Y.; Ahn, S.-G.; Lee, B.-H.; Jung, K.-T.; Yoon, J.-H.; Yoon, H.-E.; Oh, S.-H. Transcriptional Regulation, Stabilization, and Subcellular Redistribution of Multidrug Resistance-Associated Protein 1 (MRP1) by Glycogen Synthase Kinase 3 α : Novel Insights on Modes of Cadmium-Induced Cell Death Stimulated by MRP1. *Arch. Toxicol.* 2015, 89, 1271–1284.
- (98) Chen, M.; Yin, H.; Bai, P.; Miao, P.; Deng, X.; Xu, Y.; Hu, J.; Yin, J. ABC Transporters Affect the Elimination and Toxicity of CdTe Quantum Dots in Liver and Kidney Cells. *Toxicol. Appl. Pharmacol.* 2016, 303, 11–20.
- (99) Keppler, D.; König, J.; Büchler, M. The Canalicular Multidrug Resistance Protein, cMRP/MRP2, a Novel Conjugate Export Pump Expressed in the Apical Membrane of Hepatocytes. *Adv. Enzyme Regul.* 1997, 37, 321–333.
- (100) Köck, K.; Brouwer, K. A Perspective on Efflux Transport Proteins in the Liver. *Clin. Pharmacol. Ther.* 2012, 92, 599–612.
- (101) Choi, K.; Joo, H. Assessment of Gold Nanoparticles-Inhibited Cytochrome P450 3A4 Activity and Molecular Mechanisms Underlying Its Cellular Toxicity in Human Hepatocellular Carcinoma Cell Line C3A. *Nanoscale Res. Lett.* 2018, 13, 279.
- (102) Tian, J.; Hu, J.; Liu, G.; Yin, H.; Chen, M.; Miao, P.; Bai, P.; Yin, J. Altered Gene Expression of ABC Transporters, Nuclear

Receptors and Oxidative Stress Signaling in Zebrafish Embryos Exposed to CdTe Quantum Dots. *Environ. Pollut.* 2019, 244, 588–599.